PROCEEDINGS

SPIE—The International Society for Optical Engineering

Smart Structures and Materials 1997

Smart Materials Technologies

Wilbur C. Simmons
Ilhan A. Aksay
Dryver R. Huston
Chairs/Editors

3–4 March 1997
San Diego, California

19970421 038

DTIC QUALITY INSPECTED 4

Volume 3040

REPORT DOCUMENTATION PAGE

Public reporting burden for this collection of information is estimated to average 1 hour per response, including the time for reviewing instructions, searching existing data sources, gathering and maintaining the data needed, and completing and reviewing the collection of information. Send comment regarding this burden estimates or any other aspect of this collection of information, including suggestions for reducing this burden, to Washington Headquarters Services, Directorate for information Operations and Reports, 1215 Jefferson Davis Highway, Suite 1204, Arlington, VA 22202-4302, and to the Office of Management and Budget, Paperwork Reduction Project (0704-0188), Washington, DC 20503.

1. AGENCY USE ONLY *(Leave blank)*	2. REPORT DATE April 1997	3. REPORT TYPE AND DATES COVERED Technical Report

4. TITLE AND SUBTITLE Smart Materials Technologies	5. FUNDING NUMBERS DAAG55-97-1-0121
6. AUTHOR(S) Wilbur C. Simmons, Ilhan A. Aksay, Dryver R. Huston	

7. PERFORMING ORGANIZATION NAMES(S) AND ADDRESS(ES) International Society for Optical Engineering Bellingham, WA 98227	8. PERFORMING ORGANIZATION REPORT NUMBER

9. SPONSORING / MONITORING AGENCY NAME(S) AND ADDRESS(ES) U.S. Army Research Office P.O. Box 12211 Research Triangle Park,, NC 27709-2211	10. SPONSORING / MONITORING AGENCY REPORT NUMBER ARO 35794.1-MS-CF

11. SUPPLEMENTARY NOTES

The views, opinions and/or findings contained in this report are those of the author(s) and should not be construed as an official Department of the Army position, policy or decision, unless so designated by other documentation.

12a. DISTRIBUTION / AVAILABILITY STATEMENT Approved for public release; distribution unlimited.	12 b. DISTRIBUTION CODE

13. ABSTRACT *(Maximum 200 words)*

no abstract furnished

14. SUBJECT TERMS			15. NUMBER IF PAGES
			16. PRICE CODE

17. SECURITY CLASSIFICATION OR REPORT UNCLASSIFIED	18. SECURITY CLASSIFICATION OF THIS PAGE UNCLASSIFIED	19. SECURITY CLASSIFICATION OF ABSTRACT UNCLASSIFIED	20. LIMITATION OF ABSTRACT UL

Smart Structures and Materials 1997

Smart Materials Technologies

Wilbur C. Simmons
Ilhan A. Aksay
Dryver R. Huston
Chairs/Editors

3–4 March 1997
San Diego, California

SPIE

P

PROCEEDINGS
SERIES

Volume 3040

SPIE is an international technical society dedicated to advancing engineering and scientific
applications of optical, photonic, imaging, electronic, and optoelectronic technologies.

Printed in the United States of America.

Contents

SESSION 7   POSTER SESSION

Conference Committee

Conference Chairs

Wilbur C. Simmons, U.S. Army Research Office
Ilhan A. Aksay, Princeton University
Dryver R. Huston, University of Vermont

Program Committee

Roshdy George S. Barsoum, Office of Naval Research
Gregory Paul Carman, University of California/Los Angeles
John P. Coulter, Lehigh University
Thomas M. Donnellan, Northrop Grumman Corporation
Carolyn M. Dry, University of Illinois/Urbana-Champaign
Nesbitt W. Hagood, Massachusetts Institute of Technology
Dimitris C. Lagoudas, Texas A&M University
Charles Y. C. Lee, Air Force Office of Scientific Research
S. C. Liu, National Science Foundation
Shuichi Miyazaki, University of Tsukuba (Japan)
Ratnakar R. Neurgaonkar, Rockwell International Science Center
Robert K. Prud'homme, Princeton University
Mohsen Shahinpoor, University of New Mexico
Susan Trolier-McKinstry, The Pennsylvania State University
Jan VanHumbeeck, Katholieke Universiteit Leuven (Belgium)
John B. Warren, Brookhaven National Laboratory

Session Chairs

1 Thermomechanical Systems: Switches I
Robert R. Reeber, U.S. Army Research Office
Salvatore Torquato, Princeton University

2 Thermomechanical Systems: Switches II
Robert R. Reeber, U.S. Army Research Office
Salvatore Torquato, Princeton University

3 Electromechanical Systems
Chin Teh Sun, Purdue University

4 Compliant Smart Materials and Complex Fluids I
Gordon G. Wallace, University of Wollongong (Australia)
K. T. Ramesh, Johns Hopkins University

5 Compliant Smart Materials and Complex Fluids II
Gordon G. Wallace, University of Wollongong (Australia)
K. T. Ramesh, Johns Hopkins University

Keynote Address

Dual Use Smart Materials For The MMC Century

Wilbur C.. Simmons*

Materials Sciences Division, US Army Research Office, RTP, NC

ABSTRACT

Research activities in smart materials at the Army Research Office (ARO), over the past decade is briefly reviewed. Status of the current program is discussed. The current symposia is previewed and a look to the future needs and opportunities for smart materials research is presented.

1. INTRODUCTION

From the very beginnin, humans have used materials in smart ways, for new purposes for which they were not originally intended, e.g., using straws to fish out food from ant hills, and using stones and sticks to fashion tools. Continuing to increase the sophistication of our available materials, the weaving of cloth was, perhaps, the first biomimetic material in it's mimicry of animal hides. It was lighter, more comfortable and it did not smell as bad as animal hides. Later refinements in ceramics, metals and tools altered our life styles and the way wars were fought. As each new material property was discovered and refined, new smart uses were found. Thermal expansion of mercury was used as a temperature indicator and later as a switch. Bimetallic strips were developed in the same manner for their response to temperature and being more versatile as detectors and actuators. As we shall see later in this symposia, a simple property such as thermal expansion or Poisson's ratio can still be manipulated and form the basis for new sensors and actuators materials. Clever adaptation of material properties, crystal structures, phase changes and architecture at all dimensions have thus led to a wide variety of materials used as sensors and/or actuators designed to respond to the environment in a purposeful way, i.e. to control the temperature of a room. These materials are called "active or adaptive materials"; however, many are popularly referred to as "smart or intelligent" materials. An unambiguous definition of smart materials is illusive. A clever utilization of a shape memory element can replace an entire smart system (thermocouple, control logic and motor/actuator). It can also be said that it replaces the need for man to think about the ambient and consciously make an adjustment for temperature control. Thus, judicious use of a material can replace a smart system and/or replace human intervention. It is difficult to separate the smartness of the inventor or engineer from the "smartness" of the material.

Smart structures and smart materials research is a relatively new interdisciplinary field that seeks to apply the optimized designs and functionalities found in the biological world to non-biologically based structures. To that end, the activities involved range from research on enabling technologies such as materials, sensing, actuation, algorithms and architectures to the development of fully integrated smart structures. A smart structure/material is a non-biological physical structure having the following attributes: it senses the environment, it responds in a purposeful way through design or by means of a logic controller element. This is a biological pattern of functioning. The ultimate benefit from successful research in smart structures/materials will be the creation of physical structures that perform their functions without human intervention.

2. PROGRESS

In the late eighties the US Army Research Office initiated a research thrust in the area of smart materials and structures with several national workshops, international symposia and an extensive multidisciplinary research program through the Department of Defense University Research Initiative (URI). Smart structures were considered to be structures that contained embedded sensors and actuators with associated modern control systems that can respond to external stimuli in proportion to intensity. Research areas that were promoted included aspects of materials science, electronics, biosystems, mechanical systems, and mathematical modeling. Specifically, new ideas were sought for research related to: embedded sensors and actuators (including optical, magnetic, electrical, chemical and mechanical); phase transitions such as those involved in shape memory; electrorheology; layered structures and composites; defect crystal structures (e.g.,photochromic glasses); biocomposites; piezoelectric ceramics; multifunctional macromolecules, and mathematical issues related to smart materials and structures. Initially, the research ramped up with individual and collective multidiciplinary groups of

investigators with three year grants. The program reached maturity in 1992 with about forty programs [1-39] including the initiation of three new five year URI block programs.[14-16] The level of effort was maintained rather constant for a number of years and began to ramp down as the single investigator programs completed their three year cycle and new grants were competitively awaded.[40-80] A new direction was embarked upon in FY96 with the establishment of four new programs[81-84] in the Multidisciplinary-URI (MURI) topic area of "Smart Structural Systems; Mesoscale Functional Design". The work is not only multidisciplinary but also multi-institutional, being conducted at MIT, Princeton, Harvard, Drexel, UCLA and CWRU. New processing techniques are required to produce entire sensor, actuator and control functions in unit cells of less than 1 mm cube. At this scale of architecture the arrays are perceived to act as a smart materials property. Microprinting of metal, insulator and actuator materials has been demonstrated. Additional composite architecture is achieved by tape layering and by 3D-rapid prototyping photo lithography techniques. Local and global response requires microprinting of circuits and elements. The latest FY97 MURI topic on "Design and Control of Smart Structures" will address mathematical issues in local-global control, simulation and modeling. Results of the competition will be announced after this paper is sent to press. Individual investigator programs in smart materials and structures have continued in all disciplines at ARO.[1-84]

3. FUTURE REQUIREMENTS / OPPORTUNITIES

Various forward looking scenarios of what the Army may encounter in 10-20 years, and the conditions under which it may have to operate, suggest areas of high priority DoD research in smart materials and structures. Some general assumptions are:

      a. Lightweight materials and systems for global deployment.
      b. Urban environment: 360 degree close range threats (not stand off 2-3 kilometers)
      c. Terrorists threats call for vigilance and detection.
      d. Drug interdiction, detection and tracking.
      e. Explosives, nuclear detection, tracking, and neutralization.
      f. Multifunctional requirements for materials, e.g., strength, erosion resistance, and stealth.
      g. Simplification of tasks (automatic controlled response).
      h. Laser eye protection.

The US Army and DoD continues to recognize and supporte this area with multidiciplinary programs involving aspects of materials science, electronics, biosystems, earth sciences, engineered systems and mathematical modeling. Specifically, new ideas are sought to embed or integrate sensors and actuators at the mesoscale or molecular level, for optical, magnetic, electrical, chemical, and mechanical devices. Computer logic chips may also be embedded in a distributed way. One large area for future civilian and military dual use deals with the need for a biomimetic nose to detect, discriminate and alarm the presents of chemical explosives, illegal drugs and biological agents. Molecular recognition and signal transduction must be highly sensitive and selective yet robust and regenerative. The use of actuators and sensors at milli- and micro-scales is changing the way we think about the design and control strategies of smart and adaptive structures. Control of shape at both macro and micro scales, including the use of large arrays of actuators, is desired for adjusting and focusing mirrors, vibration (noise) suppression, individualized contour seats, suppressing combustion instabilities, and changing the aerodynamic flow characteristics of aircraft. The possibility of using biologically inspired designs for the control of large numbers of micro actuators suggests a solution to the problem of designing muscle-like systems suitable for robotic fingers and arms. One of the advantages that needs to accrue from smart and adaptive materials is their ability to repair themselves and to be fault tolerant. Related to this is the necessity for smart systems with their multiple sensors and actuators to organize themselves into a system which is capable of some overall functioning with both normal and degraded modes of operation.

Over the last few years, with the downsizing of the military establishment and the government's reduced budgets, research in all agencies, DoD, DoE, etc., has sought to be more responsive to defense and to commercial interests (Dual Use). Future research in smart materials, as in all other areas of government funded research, will be highly competitive.

4. SYMPOSIA HIGHLIGHTS

This symposia presents the latest research in the area of smart materials and active materials for sensors and actuators components integrated into smart structures technology. Materials synthesis, processing, and characterization in the following active material systems are reported:

* shape memory alloys
* piezoelectric ceramics, polymers and films
* ferroelastic solids and films
* electrostriction materials
* electro- and magneto-rheological (ER and MR) fluids
* artificial polymer muscles
* meso-scale integrated composites
* biomimetic approaches for smart material architectures
* muitilayer and arrays of sensors and actuators in a distributed controlled "material"
* smart polymer and polymer composites
* multifunctional macromolecules
* signal transducting biomimetic materials
* recognition molecules
* modeling of smart material
* medical applications

The most notable shift in direction to the reported research activity is in the move toward macro-scale embedded systems and meso-scale (10^{-6} to 10^{-2}m) integrated smart composites. Rather than discrete actuators or sensors, more attention is given to a composite material response: a slab of material that warps purposefully or changes its surface contour; or monitors its health locally; or alters its physical characteristics locally. Small scale architecture was presented as a means to achieve an engineered negative Poisson's ratio utilized to increase the sensitivity of hydrophones. New techniques of patterning and constructing submillimeter sensors, actuators and distributed control elements suggest many structural and medical applications for this technology.

The level of integration in biological systems is far more advanced than in synthetic smart materials and systems. However, our evolving understanding of how biological organisms organize, create, and synthesize systems with smart functions has inspired the research community and already lead to biomimetic material systems. Concepts from biological systems can be used in the synthesis and design of the next generation of advanced materials which function as smart systems. Recent developments only promise the opportunities that lie ahead.

REFERENCES

Note that the following references are to research programs funded by the U.S. Army Research Office and indicate: a) the principal investigator's name; b) the performing institution; c) the ARO grant identification number; and d) the Defence Technical Information Center (DTIC) work unit summary identification number. Additional information may be obtained from the National Technical Information Service (NTIS) 5285 Port Royal Road, Springfield, VA, 22161.

1   E. Mintz, Clark Atlanta University, "Novel Electroactive Polymers and BLock Copolymers", ARO Grant #27141-CH, DTIC-DA320433.
2. C. J. Eckhardt & P. J. Dussault, University of Nebraska, "Molecular Devices Based on New Monolayer Forming Systems, ARO Grant #27195-CH, DTIC-DA320581.
3. T. J. Meyer & R. W. Linton, University of North Carolina, "Photochemistry in Thin Polymeric Films", ARO #27664-CH.
4. R. K. Gilpin, Kent State University, "Development of Novel Switchable Protein Surfaces", ARO Grant #27695-CH, DTIC-DA321897.
5. S. L. Regen, Lehigh University, "Ion Paired Amphiphiles", ARO Grant #28752-CH.
6. W. Rosen, University of Rhode Island, "The Preparation and Study of Some Macrocyclic Polyether Substituted Poly(iminomethylenes): Smart Polymers Having Externally Controlled Complexation Properties", ARO Grant #30876-CH.

7. C. J. Eckhardt, University of Nebraska,, "Two Dimensional Crystals and Nanostructured Materials", ARO Grant #30877-CH, DTIC-DA322629.

8. P. Song, University of Nebraska, "Photo-Signal Transduction ion Motile Ciliate Blepharisma", ARO Grant #28748-LS, DTIC-DA322110.

9. K. A. Marx, University of Lowell, "Intelligent Materials and Structures Based on Ordered Assemblies of DNA and Protein Incorporated within Electroactive Polymeric Systems", ARO Grant #28749-LS, DTIC-DA322133.

10. H. T. Tien, Michigan State University, "Electrical and Electronic Properties of Self-Assmbled Lipid Bilayers", ARO Grant #28750-LS, DTIC-DA322130.

11. W. E. Stites, University of Arkansas, "De Novo Design of Protein-Protein Interactions", ARO Grant #30875-LS, DTIC-DA322637.

12. M. H. Thursby, Florida Institute of Technology, "Smart Electromagnetic Structures: A New Approach to Smart Structures", ARO Grant #27191-EL, DTIC-DA320438.

13. R. Pinizzotto, University of North Texas, "The Genius Chip: Three-Dimensional Ferroelectric Integrated Circuits", ARO Grant #30872-EL, DTIC-DA322625.

14. C. A. Rogers, Virginia Polytechnic Institute and State University, "Smart Materials, Structures, and Mathematical Issues for Active Damage Control", ARO Grant #30364-EG.

15. L G. Tadjbakhsh & K.C. Craig, Rensselaer Polytechnic Institute, "Interdisciplinary Basic Research in Smart Materials and Structures", ARO Grant #30378-EG, DTIC-DA322479.

16. I. Chopra, University of Maryland, "Smart Structures Technology: Innovations and Applications to Rotorcraft Systems", ARO Grant #30380-EG.

17. M. V. Gandhi & B. S. Thompson, Michigan State University, "Smart Materials and Structures Incorporating Electrorheological Fluids: An Analytical and Experimental Investigation", ARO Grant #27149-EG, DTIC-DA320434.

18. S. P. Joshi, University of Texas at Arlington, "Damage Survivable and Damage Tolerant Laminated Composites with Optimally Placed Piezoelectric Layers", ARO Grant 27167-EG, DTIC-DA320436.

19. A. M. Baz, The Catholic University of America, "Active Control of Nitinol Reinforced Smart Structural Composites", ARO Grant #27216-EG, DTIC-DA320441.

20. V. S. Rao, T. J. O 'Keefe & L. R. Koval, University of Missouri at Rolla, "Use of Shape Memory Alloys in the Robust Control of Smart Structures", ARO Grant #27686-EG, DTIC-DA321902.

21. M. V. Vandhi & B. S. Thompson, Michigan State University, "Smart Composite Structures Featuring Embedded Hybrid Actuation and Sensing Capabilities", ARO Grant #27712-EG.

22. H. S. Tzou, T. R. Tauchert & G. E. Blandford, University of Kentucky, "Development of "Smart" Piezothermoelastic Laminae: Theory and Applications", ARO Grant #28754-EG, DTIC-DA322115.

23. D. J. Inman, Virginia Polytechnic Institute and State University, and E. Garcia, Vanderbilt University, "Programmable Materials and Structures", ARO Grant #28755-EG, DTIC-DA322116.

24. J. P. Coultler, Lehigh University, "Electrorheological Material Based Smart Structure", ARO Grant #30874-EG, DTIC-DA322621.

25. E. L. Chronister, University of California at Riverside, "Ultrafast Frequency Agile Optical Materials: Organically Doped Sol-Gel Glasses", ARO Grant #27185-MS, DTIC-DA320437.

26. N. Shaikh, University of Nebraska,, "Smart Structural Composites: Piezoelectric Film Deposition on Intercalated Carbon Fibers", ARO Grant #27198-MS, DTIC-DA320439.

27. M. T. Shaw, University of Connecticut, "Electrorheological Fluids: A Structural Approach to Mechanisms", ARO Grant #27210-MS, DTIC-DA320440.

28. L. Cartz, Marquette University, "Thermal Actuators of Mica Layer Structures", ARO Grant #27572-MS, DTIC-DA321918.

29. A. D. Hamilton & S. G. Weber, University of Pittsburgh, "Organic Materials that Respond to Molecules", ARO Grant #27724-MS, DTIC-DA321890.

30. J. E. Furneaux & B. Mason,University of Oklahoma, and B.B. Goldberg, Boston University, "Dimensionally Self-Regulating Materials", ARO #28746-MS, DTIC-DA322134.

31. D.H. Reneker, University of Akron, "Macromolecular Smart Materials and Structures", ARO Grant #28747, DTIC-DA322088.

32. M. G. Kuzyk, Washington State University, "Smart Opto-Mechanic Based Devices", ARO Grant #30878-MS, DTIC-DA322623.

33. R. B. Meyer, Brandeis University, "Development of a Liquid Crystal Smart Reflector", ARO Grant #30879-MS, DTIC-DA322622.

34. W. J. Brittain, University of Akron, "Static and Mobile Polymer Surfaces of Well Defined Structure", ARO Grant

#30880-MS, DTIC-DA322631.

35. W. W. Hager & R. Rostamian, University of Maryland Baltimore County, "Analysis and Optimization of Elastic Materials", ARO Grant #27022-MA, DTIC-DA320423.

36. R. D. James, University of Minnesota, "Research on the Improvement of Shape Memory and Magnetostrictive Materials", ARO Grant #27063-MA, DTIC-DA320428.

37. T. J. Pence, Michigan State University, "Rapidly Activated Dynamic Phase Transitions in Non- Linear Solids", ARO Grant #27077-MA, DTIC-DA320429.

38. H. Hattori, West Virginia University, "Problems Realted to Conservations Laws: Phase Transitions and Viscoelasticity", ARO Grant #27130-MA, DTIC-DA320432.

39. E. L. Chronister, University of California at Riverside, "Ultrafast Photochromic Sol-Gel Glasses and Fiber Optics", ARO Grant #30873-PH, DTIC-DA322613.

40. J.N. Reddy, Texas Engineering Experiment Station, "Computational Approaches for Smart Materials and Structural Systems Including Nonlinearitites", ARO Grant #34766-EG, DTIC-DA349418.

41. A. Chattopadhyay, Arizona State University, "Modeling and Analysis of Composites Using Smart Materials Optimization Techniques", ARO Grant #33180-EG, DTIC-DA349408.

42. J.C. Spence, Arizona State University, "Molecular Structure for Smart Materials - Proof of Concept", ARO Grant #35751-MS, DTIC-DA349480.

43. F. Mako, FM Technologies, Inc., "Pulsed Electron Beam Fabrication of Smart Materials", DTIC-DA363234.

44 .M.V. Gandhi, Michigan State University, "Smart Composite Structures Featuring Embedded Hybrid Actuation and Sensing Capabilities", ARO Grant #27712-EG, DTIC-DA321940.

45. J. F. Vincent, Reading University (UK), "Catalogue of Sensory Systems From Nature", DTIC-DA328899.

46. P.A. Parrish, BDM Corporation, "Smart Materials/Structures Technical Analysis Proposal", ARO Grant #28608-MS, DTIC-DA322062.

47. K.V. Logan, Georgia Institute of Technology, "Smart Armor Conceptual Design", ARO Grant #29317-EG, DTIC-DA322295.

48. K.H. Wu, Florida International University, "Development of High Temperature Two-Way Shape Memory Alloys, ARO Grant #29150-MS, DTIC-DA322305.

49. D. Barrett, Naval Air Warfare Center, "Micromechanics of Shape Memory Composites", DTIC-DN103259.

50. D.J. Inman, Virginia Polytechnic Institute, "Smart Materials Structures and Mathematical Issues for Active Damage Control and Embedded Sensors for Intelligent Processing and Adhesives Monitoring", ARO Grant #30364-EG, DTIC-DA322531.

51. V. Birman, University of Missouri at Rolla, "Control of Sandwich and Composite Plates", ARO Grant #30270-EG, DTIC-DA322556.

52. W.A. Schulze, Alfred University, "Design and Construction of Smart Materials Based on Piezoresistive Sensors and Multilayer Actuators", ARO Grant #28745-MS, DTIC-DA322618.

53. Z. Suo, University of California at Santa Barbara, "An Investigation on Degradation Mechanisms for Ferroelectric Actuator Design", DTIC-DN053134.

54. Z. Suo, University of California at Santa Barbara, "An Investigation on Degradation Mechanisms for Ferroelectric Actuator Design", DTIC-DN450108.

55. K.W. Wang, Pennsylvania State University, "Semi-Active Vibration Control of Flexible Structures Via Adaptive Damping and Stiffness", DTIC-DA348609.

56. Z. Hu, North Texas State University, "Polymer Gel Sensors and Devices Controlled by Infrared Light and Ultrasound, ARO Grant #32112-CH, DTIC-DA348665.

57. A.M. Baz, Catholic University of America, "Active Constrained Layer Damping, ARO Grant #32110-EG, DTIC-DA348673.

58. M. Shahinpoor, University of New Mexico, "Ionic Polymeric Gels as Smart Materials and Artificial Muscles", ARO Grant #32115-MS, DTIC-DA348678.

59 .Y. Zhao, Wayne State University, "Smart Material Structures Using Nonlinear Photonic Bandgap and Photon Localization for Rejecting High-Intensity Laser Radiation, ARO Grant #32116-MS, DTIC-DA348679.

60. T.C. Corke, Illinois Institute of Technology, "Smart-Wall for Control of the Burst Cycle of Longitudinal Vortices in Turbulent Boundary Layers, ARO Grant #32111-EG, DTIC-DA348681.

61 .F. Khorrami, Polytechnic Institute of Brooklyn, NY, "Modeling, Identification, and Control Design for a Flexible Pointing System with Embedded Smart Materials", ARO Grant #32108-MA, DTIC-DA348682.

62. J. Parise, State University of New York at Stony Brook, "Smart Ferroelastic-Ferroelectric Heterostructures: Materials Development, Modeling and Testing", ARO Grant #32114-MS, DTIC-DA348672.

63 .V.S. Rao, University of Missouri at Rolla, "Nonlinear and Distributed Control of Smart Structures Using Artificial Neural Networks", ARO Grant #32109-MA, DTIC-DA348666.

64. M.L. Myrick,University of South Carolina, "Fiber Optic Chameleonic Skin", ARO Grant #32113-PH, DTIC-DA348715.

65. G.G. Wallace, Wollongong University, (Australia) "Growth and Differentiation of Cultured Cells on 'Smart Materials' Substrates", ARO Grant #32329-MS, DTIC-DA348738.

66. G.S. White, Department of Commerce, Gaithersburg, MD, "Mechanical Reliability of High Strain Actuators", DTIC-DN054261.

67. D.A. Shockey, SRI International, "A Granular Flow Model for Developing Smart Armor Ceramics", ARO Grant #30330-MS, DTIC-DA348966.

68. D.S. Flamm, SRI International, "Control Technology for Smart Materials", DTIC-DN450302.

69. F.M. Mako, FM Technologies, Inc. , "Pulsed Electron Beam Fabrication of Smart Materials, DTIC-DA362937.

70. E. Saarma, Active Control Experts, Inc., "Solid-State Hydraulic Actuator for Machine Tool Applications", DTIC-DA362997.

71. J.B. Ballance, Materials Research Society, "Materials for Smart Systems", DTIC-DN450001.

72. C.R. Fuller,Virginia Polytechnic Institute, "An Active Surface Coating for Acoustic Application", ARO Grant #33953-EG, DTIC-DA349035.

73. F. Straub, McDonnell Douglas Helicopter Co., "Smart Materials Actuated Rotor Technology Proposal", ARO Grant #33619-EG, DTIC-DA349077.

74. R.N. Grimes, University of Virginia at Charlottesville, "Designed Synthesis and Assembly of Molecular Building Blocks for New Materials", ARO Grant #34065-CH, DTIC-DA349329.

75. J.T. Koberstein, University of Connecticut, "Molecular Engineering and Smart Polymer Surfaces", ARO Grant #34536-MS, DTIC-DA349249.

76. E. Saarma, Active Control Experts, Inc., "High-Bandwidth, Large Stroke Actuator for Active Control Applications", DTIC-DA363119.

77. Q. Jiang, University of Nebraska, "Computer Simulation of Electric Fatigue", DTIC-DN054150.

78. J. Stilwell, Aerotech Engineering and Research, "Piezoceramic Ultrasonic Motor Technology for Aerospace Applications", DTIC-DA347358.

79. C. Kim, Naval Research Lab, "Composite Piezoelectric Assemblies for Torsional Actuators", DTIC-DN163956.

80. I. Lasiecka, University of Virginia at Charlottesville, "A Partial Differential Equation Approach to Robust Control Design of Smart Materials and Structures: Theoretical and Computational Apsects", ARO Grant #35170-MA, DTIC-DA349523.

81. N. Hagood, Massachusetts Institute of Technology, "Smart Structures Systems-Mesoscale Functional Design",ARO Grant #33913-EG.

82. I. Aksay, Princeton University, "Smart Material Systems through Mesoscale Patterning", ARO Grant #33905-MS, DTIC-DA349222.

83. G. P. Carman, University of California at Los Angeles, "Innovative Mesoscale Activation Devices for Use in Rotorcraft Systems", ARO Grant # 35895-MS.

84. M. Mehregamy, Case Western Reserve University, "MEMS Base Design and Control of Smart Structures", ARO Grant # 33910-EG.

SESSION 1

Thermomechanical Systems: Switches I

Modeling and Measuring the Response Times of Thin Film TiNi

Ken Ho[1], Peter Jardine[2], Greg P. Carman[1], and C.J. Kim[1]

[1]Mechanical & Aerospace Engineering, UCLA 38-137m Engineering IV, LA, CA 90095
[2]Northrop Grumman Corp., Military Aircraft Systems Division, El
Segundo CA 90245

ABSTRACT

The response time of TiNi has been the subject of several experimental and theoretical investigations over the past decade. One of the principal concerns with this material is the relatively low cycle speeds or operational bandwidth caused by the considerable length of time required to cool the material. In this paper a finite difference model of heat transfer including the latent heat dissipated during the phase transformation is used to predict the bandwidth of thin film TiNi. The film is modeled as a plate subjected to either forced or free convection along the exposed surfaces and clamped to a large thermal mass representative of silicon wafer at the ends of the specimens. Results indicate that both latent heat as well as the relative ratios of the transformation temperatures to ambient temperature strongly influence the bandwidth of the material. Good correlation between the analytical model and test data obtained on a 38 micron wire indicate the model contains the correct assumptions to predict bandwidths. The bandwidth of TiNi thin film are predicted to be on the order of 100 Hz necessary assuming that the transformation temperatures for the film are the same as the bulk material.

1.0 BACKGROUND

Since the original discovery of TiNi as a shape memory alloy, commercial interest has been dominated by their use as a high force low frequency actuators. This thermally driven systems has a cycle time typically less than a hertz which is limited by heat transfer processes required to transform the material from austenite to martensite. By reducing the materials thermal mass or by increasing heat transfer, it is plausible to increase the bandwidth significantly. Reducing the thermal mass can be achieved by manufacturing thin film TiNi micro-actuators with concomitant reductions in authority being addressed with a distributed network of micro-actuators rather than a single bulk actuator. The fact that IC processing technologies are being used to develop MEMS devices using sputtered thin film technologies provides impetus to develop TiNi micro-actuators. However, to accurately design this new class of micro-actuators the operational bandwidth needs to be better understood in order to determine its applicability to specific operational profiles. While there are many issues which need to be resolved in the area of TiNi micro-actuators, such as etching, sputtering reliability etc, bandwidth is clearly a primary concern from an application and design perspective.

Thin film TiNi actuators are well suited for MEMS devices because of their large work energy densities, compatibility with silicon IC processing, and low voltage requirements. Their specific energy density of 1J/gm is an order of magnitude larger than any alternative actuation mechanism such as electrostatics, magnetic, piezoelectric, and bimetallic [1 & 2]. A large work energy density permits smaller more robust actuator designs when compared to existing micro-actuators. Research pertaining to TiNi films has primarily concentrated on deposition, heat treatments, and thermomechanical characterization [3, 4, 5, & 6]. Only a small group of researchers has focused on engineering micro-devices from these thin films

due to the lack of reliable fabrication techniques. Among the few actuators investigated; Walker et al. [7] was one of the first to investigate TiNi for MEMS application, Kuribayashi et. al. [8] used TiNi films to actuate a microrobotic manipulator, Johnson et al. [9]developed a microvalve, and Lee et al. [10] developed a microgripper.

Because TiNi is a thermally driven actuator, its bandwidth is considerably lower than electrostatic or ferroelectric actuators. The response time of TiNi actuators is limited by heat dissipation during the cooling cycle[11,12, & 13]. Jardine measured a response of 50Hz for a 20 micron thick thin film TiNi cantilever and analytically suggested that 500Hz is possible with 2um films attached to a silicon substrate [11,13,14]. Yang et al. [15] indicated that a heat actuated bistable micro-beam could proceed with an operational bandwidth in excess of a kilohertz. These and other studies indicate that the bandwidth of heat actuated micro-structures such as TiNi could satisfy many high frequency operational requirements of the MEMS community. However, a systematic study of the bandwidth and its relation to material properties has been lacking in the literature and thus motivated this research

2.0 ANALYTICAL MODEL

The operational bandwidth of TiNi is controlled by the heat transfer from the material to its surroundings during the phase transformation from austenite to martensite. Parameters which influence this process include surface to volume ratios, conduction, convection, and latent heat. While the temperature rise time associated with the transformation from martensite to austenite can occur in the kilohertz range, the heat dissipation required to cool the material takes considerably longer and for many structural applications limits the bandwidth of the actuator to a hertz. In this paper we investigate the influence of surface to volume ratios on the bandwidth of an actuator fabricated from thin film. The free standing film is attached at the ends to a conducting surface held at room. All other exposed areas transfer heat by either free convection or forced convection to the surrounding air. The analysis is divided into a heating analysis and a cooling analysis with the cooling analysis subdivided between conduction/convection and latent heat.

2.1 Heat Analysis

The film was heated via Joule heating from a current source with a sufficient amount of power available. The time required to transform the material from martensite to austenite can be determined from power balance. Assuming that the material heats uniformly, an energy balance between power supplied to the film and internal heat generated in a material results in the following expression

$$Power = I^2 R = mC_p \frac{dT}{dt} + \frac{mQ}{dt} \qquad (2.1a)$$

where the first term represents the thermal mass and the second term represents latent heat. In incremental form we can rewrite 2.1a as follows

$$Power = I^2 R = \frac{m\left[(T_{max} - T_\infty)C_p + Q\right]}{\Delta t} \qquad (2.1b)$$

where m is mass, T_{max} (or A_f) and T_∞ are the film and ambient temperatures respectively, C_p: specific heat, Q: latent heat of transformation, R is the resistance of the film, and I is the current provided over some time increment Δt. Solving equation 2.1b for the time to heat a specimen Δt with a current I we have

$$t_h = \frac{mC_p\Delta T + mQ}{I^2 R}$$

(2.2)

Based on Equation 2.2 the time to heat a specimen is related to the inverse square of the current. Reducing the heating time can be achieved by increasing the current. Therefore, based on Equation 2.2 the transformation time from martensite to austenite is not a significant issue in regards to bandwidth of the material.

2.2 Cooling Analysis

A uniform temperature was assumed to exist in the material during the heating cycle, this assumption is not valid for the cooling analysis and requires a more accurate model. To permit temperature variations within the material a finite difference code was developed to analyze the cooling response of the film. The film was modeled as a plate clamped at the two ends of the specimen (Figure 1) with heat dissipation by free or forced convection on the two exposed surfaces, and conduction at the ends of the specimen. The ends were treated as heat sinks with a constant temperature of 25°C indicative of a large silicon substrate at room temperature. From symmetry arguments, only half of the plate was analyzed.

In developing a finite difference model, a uniform temperature distribution is assumed to exist in each element reducing the problem to a 1-dimensional heat transfer analysis (see Figure 2). This is a reasonable assumption since the Biot number ($B_i = hL_C/k < 0.1$) for the thin films used in this study is less than 0.1. The Biot number is a measure of the temperature drop in the solid relative to the temperature difference between the surface and air. In other words, a small B_i indicates a sufficiently large conduction rate is present within the solid relative to the convective heat dissipation, such that a uniform temperature within the element is maintained. For a given node i, we have heat fluxes due to conduction q_{in} from the adjacent right node $i+1$, q_{out} to the adjacent left node $i-1$, and convection losses through the exposed surfaces q_{conv}. Using this notation, the balance of heat flux in an element is:

$$mC_p dT/dt = -q_{conv} - q_{out} + q_{in}$$

(2.3a)

or

$$mC_p \frac{dT}{dt} = -2(w\Delta x + t\Delta x)h(T_i - T_\infty) + tw\left(\frac{k}{\Delta x}\right)(\Delta T_{in} - \Delta T_{out})$$

(2.3b)

Where h is the average convection heat transfer coefficient; k is the conduction coefficient; T_i is the elements temperature; m is the mass of the element; w, t, and Δx represent dimensions of the nodal elements of the TiNi material. The set of finite difference equations for this problem can be cast in the following form.

$$T_{o+1} = T_o - \frac{\Delta t}{mC_p}\left[2\Delta x(w+t)h(T_i - T_\infty) - \frac{twk}{\Delta x}\left(T_{i+1} + T_{i-1} - 2T_i\right)\right]$$

(2.4a)

$$T_{o+1} = T_o - \frac{\Delta t}{mC_p}\left[2\Delta x(w+t)h(T_i - T_\infty) - \frac{twk}{\Delta x}\left(T_i - T_{i-1}\right)\right]$$ (2.4b)

Equation 2.4b represents the element along the boundary where q_{in}=0 due to symmetry conditions. In Equations 2.4, T_{o+1} is the temperature of node i for the next time step, T_i, T_{i+1}, and T_{i-1} are the temperatures of the ith node, the right node and the left node respectively. Δt is the time step, m the mass of each node. Replacing the mass term (m) in equation 2.4 by the mass density (ρ) multiplied by the volume (V), the following parameters control the cooling rate of this material; surface area to volume ratio, heat convection coefficient, and heat conduction coefficient.

2.3 Latent Heat

The above derivation did not include the latent heat dissipated during the transformation process. During the heating and cooling cycles TiNi undergoes a phase transformation. The phase transformation occurs over a temperature range identified by austenite start and finish temperatures (A_s-A_f) during the heating cycle and martensite start and finish temperatures (M_s-M_f) during the cooling cycle. Phase transformation is endothermic during heating and exothermic upon cooling. Therefore, assuming sufficient power is available to heat the sample (2.1a) the endothermic cycle does not limit the bandwidth but the exotherm during the cooling cycle is a major concern.

To provide a tractable solution to this problem, we assumed that the austenite/martensite transformation proceeds until a critical temperature is reached, at which point the temperature remains constant until the entire latent heat is dissipated. For the results presented here we assumed that this temperature was the average of martensite start and finish temperatures ($[M_s + M_f]/2 = 47$ C). Considering only the temperature rise produced by latent heat an energy balance at each element gives

$\rho VC_p dT/dt + \rho VQ/dt = -q_{conv} - q_{cond(out)} + q_{cond(in)}$

Based on our assumption that the latent heat is dissipated at a constant temperature $dT/dt = 0$ and the heat flux equation becomes

$$\frac{\rho VQ}{\Delta t} = -A_s h(T_i - T_\infty) - A_c k \frac{\Delta T_{out}}{\Delta x} + A_c k \frac{\Delta T_{in}}{\Delta x}$$ (2.5a)

$$\frac{\rho VQ}{\Delta t} = -2(w\Delta x + t\Delta x)h(T_i - T_\infty) + tw\left(\frac{k}{\Delta x}\right)(\Delta T_{in} - \Delta T_{out})$$ (2.5b)

Further simplification produces the following finite difference equations

$$Q = -\frac{\Delta t}{\rho V}\left[2\Delta x(w+t)h(T_i - T_\infty) - \frac{twk}{\Delta x}\left(T_{i+1} + T_{i-1} - 2T_i\right)\right]$$ (2. 6a)

$$Q = -\frac{\Delta t}{\rho V}\left[2\Delta x(w+t)h(T_i - T_\infty) - \frac{twk}{\Delta x}\left(T_i - T_{i-1}\right)\right]$$ (2.6b)

where Equation 2.6b is for the node with boundary conditions $q_{in} = 0$. Once again, the time to dissipate the latent heat is controlled by the surface to volume ratio, the heat convection coefficient, and the heat conduction coefficient. Thus an incremental amount of latent heat is dissipated for each time step until all

the latent heat is dissipated, at which point the film resumes its original cooling profile defined in Equation 2.4.

2.4 Convection Heat Transfer Coefficient

The convection heat transfer coefficient h can be calculated with the Nusselt number Nu_L which is a measure of heat transfer at the surface. The Nusselt number includes information regarding local flow conditions at the surface, that is forced or free convection. The Nu_L is related to the heat transfer coefficient by the following

$$\overline{Nu}_L = \frac{\overline{h}L_c}{k_{air}}$$
(2.7)

where k_{air} is the thermal conductivity of air, and L_c is a characteristic length. The modeled developed includes both laminar and turbulent flow conditions. Under laminar flow conditions ($Ra_L < 10^9$) for a vertical plate the Nusselt number is given by the following empirical equations [16].

$$Nu_L = 0.68 + \frac{0.670\,Ra_L^{1/4}}{\left[1+(0.492/Pr)^{9/16}\right]^{4/9}}$$
(2.8a)

If flow conditions are turbulent the Nusselt number is given by

$$Nu_L = \left\{0.825 + \frac{0.387\,Ra_L^{1/6}}{\left[1+(0.492/Pr)^{9/16}\right]^{8/27}}\right\}^2$$
(2.8b)

Where Pr is the Prandlt number $Pr = \nu/\alpha$ representing the ratio of the kinematic viscosity ν over the thermal diffusivity α. For the results presented in this paper all flow conditions are laminar and Equation 2.8a are used. However, we do note that for turbulent flow patterns the Nusselt number is larger and we would expect to see cooling times which are quicker than presented here. The Rayleigh number Ra_L is analogous to the Reynolds number in fluid mechanics and is defined as

$$Ra_L = \frac{g\beta(T_s - T_\infty)L^3}{\nu\alpha}$$
(2.9)

where g is gravity, and β is the volumetric thermal expansion coefficient.

If the plates were horizontal, the flow conditions are different and the Nusselt numbers are given by the following relations:
at the upper surface of a heated plate

$$Nu_L = 0.54\,Ra_L^{1/4} \qquad (10^4 < Ra < 10^7)$$
(2.10a)

$$Nu_L = 0.15\,Ra_L^{1/3} \qquad (10^7 < Ra < 10^{11})$$
(2.10b)

and at the lower surface of a heated plate

$$Nu_L = 0.27\ Ra_L^{\ 1/4} \qquad\qquad (10^5 < Ra < 10^{10}) \qquad\qquad\qquad (2.10c)$$

The characteristic length L_C in Ra_L is now given by $L_C = A_S/P$ (surface area divided by the perimeter).

3.0 Experimental Set Up

In order to corroborate the analytical predictions an experimental setup was constructed to evaluate the response of both thin film TiNi and TiNi wire. A LVDT (linear variable displacement transducer) capable of micron resolution coupled to a data acquisition system monitors the displacement of the TiNi sample when pulsed with an arbitrary wave signal (Figure 3). The TiNi has a variable traction applied to the ends with the load in this case representing approximately 150MPa. When the TiNi material is heated to the austenite phase, the sample contracts and when it cools to the martensite phase it elongates due to the differences in Young's modulus between the two phases. The input wave signal or voltage pulse is produce by a 100W Keithley model 228A voltage/current source. The LVDT model 250-MHR and ATA-101 analog transducer amplifier are from Lucas Controls Inc. and provides up to kHz excitation times. LVDT signals were conditioned by the ATA-101 and sent to the Keithley Metrabyte DAS-8PGA A/D board. A Dell 486DX2-66 PC running Labtech Notebook version 7.20 was used to acquire the data from the DAS-8PGA. The system displayed in Figure 3 is housed in a thermal cycling chamber (Delta Design 9028) to permit operation of the thin film or wire at various temperatures to evaluate the material's response. At this writing the thin film systems had not been produced and only TiNi wire data are presented.

4.0 Analytical/Experimental Results

Analytical results for cooling a TiNi thin film with properties identified in Table I are presented in Figure 4. The film is modeled as a vertical plate with free convection on the exposed surfaces and conduction through the ends. In the 3-D plot of Figure 4, the vertical axes represents the temperature at a specific node, while the two horizontal axis represent either the geometric position in the TiNi film or the time. The plateau in the cooling profile indicates that the latent heat generated by the austenite to martensite phase transformation is being dissipated. This result suggests that the latent heat occupies a substantial time period and will significantly influence the bandwidth for this material. For this particular 1x4mmx4μm thin film, the finite difference model predicts a cooling time which provides an operational bandwidth for the material of 69 Hz. Studies done on varying the width of the film between 0.5 mm and 4 mm produced negligible shifts (less than 4%) in the bandwidth.

As a means to corroborate the analytical predictions, the response of a 38μm diameter wire 6cm long were measured and compared with results from the finite difference model. Analytical results produced by the model are provided in Figure 5. As with the thin film, a plateau region is reached in which the latent heat generated by the austenite to martensite phase transformation is being dissipated. This again occupies a major portion of the cooling curve. The cooling rate for the wire is considerably longer almost an order of magnitude larger than for the thin film results presented in Figure 4. For the wire the operational bandwidth is predicted to be 6.5 Hz which corresponds to a cooling time of 153 msec. While not shown in the figure, if the temperature at which latent heat dissipates is shifted upward 25 C (i.e. 75 C) the bandwidth of the material increases by a factor of two, that is 12 Hz. This indicates that magnitudes and relative ratios of the M_s and M_f temperatures strongly influence the bandwidth of the material.

Experimental tests results for a thin wire are provided in Figure 6. The top curve in the figure represents the wave signal to heat the specimen. An 8V source was applied for 0.1sec and caused the

sample to heat just above the austenite finish temperature. A number of tests were performed to ensure that this heating time did not cause an overshoot in temperature. The sample was permitted to cool for a sufficiently large time (i.e. 0.2 sec) to assess the samples bandwidth. The lower curve in Figure 6 presents displacement measurements in terms of voltage as a function of time. As can be seen the contraction (or increase in voltage from -2.8 to -1.5) of the element during the heating cycle closely follows the applied voltage. Upon removal of the current, the wire slowly returns to the original position prior to heating; thus indicating that the reverse transformation to martensite is complete. The time to return to this original position represents the cool down cycle used in calculating the bandwidth for the material. For this particular case the wire produced a bandwidth of approximately 5 Hz which is in reasonable agreement with the 6.5 Hz prediction of the model.

To further evaluate the accuracy of the model the response of TiNi wire at 0°C was examined. Shifting the ambient temperature by 25°C is analytically equivalent to shifting the transformation temperature of the material by 25°C. This is an important consideration for thin film where the transformation temperature of the material largely depends upon the manufacturing process and can vary by 50°C . In figure 7 the analytical results for a 38 micron wire in ambient temperatures of 0°C is presented. The cool down time is considerably shorter than for the previous ambient temperature of 25 C. For the ambient temperature of 0°C the model predicts an operational bandwidth of 10.2Hz (compared to 6 Hz for room temperature) or a cooling time of 97 msec.

Experimental results obtained for this wire are presented in Figure 8. While not shown in the figure, the driving voltage to heat the sample was the same as provided in Figure 6, or 8V for 0.1 sec followed by a similar cooling cycle of 0.2 sec. Therefore, the single curve presented in Figure 8 represents the displacement response of the wire. As the wire decreases its length from 1.5 volts to 1.9 volts, the sample changes from martensite to austentite. The differences in voltage output for the LVDT for this configuration over the previous room temperature operation is due to length changes in the sample. Test results in Figure 8 indicate that the operational bandwidth for this material is 20 Hz or a cooling time of 50 msec. This test data indicates a faster cool down time than suggested by the analytical model by a factor of two. A number of features associated with the experimental procedures may attribute to this discrepancy. Nonetheless the predictions are of the same order of magnitude as the test results.

In Figure 9, we present analytical results for thin film TiNi as a function of film thickness for three different transformation temperatures, that is $(M_s+M_f)/2$ = 33, 40, and 47°C. Results indicate that the bandwidth of the material with transformation properties similar to the bulk material approach 300 Hz as the thickness of the film is reduced to one micron, a size compatible with MEMS manufacturing. For film thickness of 4 microns, the bandwidths are 69, 52, and 29 Hz for samples with latent heat dissipated at 47, 40 and 33 °C respectively. For a film whose thickness is 1 micron, the bandwidths are 277, 212, and 119 for the three materials studied indicating that simple extrapolations based on film thickness is inappropriate. Furthermore, even though the transformation temperatures were reduced linearly (i.e. 7 °C), the corresponding reduction in bandwidths were nonlinear. Therefore, reducing the transformation temperatures causes a nonlinear increase in the time to cool the specimen or corresponding decreases in the operational bandwidth of the material. Based on the good agreement obtained between experimental and analytical results for the wire, the predictions presented in Figure 9 appear to be reasonable numbers but a number of comments are needed. First, thin film TiNi typically is Ni rich which lowers the transformation temperatures of the material. As presented in Figure 9, small changes in transformation temperatures with respect to ambient temperature significantly influence the bandwidth (e.g. almost a factor of three for a shift of 14°C). While not shown here shifts in M_s and M_f, even though their ratios remain constant, will also influence the bandwidth of a thin film TiNi structure.

5.0 Conclusions

In this paper a finite difference code which included latent heat was developed to predict the heating and cooling rate of thin film TiNi structures. The film was modeled as a flat plate either vertically or horizontally oriented with either free convection or forced convection along its exposed surfaces. Results indicated that the latent heat term contributes significantly to lowering the operational bandwidth of the material. Comparisons between analytical results and test data obtained on a 38 micron wire indicated good correlation suggesting the model is correctly depicting the operational bandwidth for the material. The bandwidth of TiNi micro-actuators fabricated with thin film were predicted to be on the order of 100 Hz assuming that transformation temperatures for the film were the same as the bulk material and the material was free standing. Furthermore, the three transformation temperatures A_f, M_f and M_s and there relative ratios contribute significantly to determining the bandwidth for these materials as do the relative structure of the micro-actuator itself.

ACKNOWLEDGEMENTS

REFERENCES

1. R.H. Wolf and A.H. Heuer, "TiNi (Shape Memory) Films on Silicon for MEMS Applications". J. of Microelectromechanical Sys. vol.4, no.4, pp206-212 (Dec. 1995).

2. J.D. Busch, M.H. Berkson, and A.D. Johnson, Phase transformations in sputtered NiTi film: effects of heat treatment and precipitates. Mat. Res. Soc. Symp. Proc. vol.230, pp91-96 (1992).

3. Johnson, A.D., et al.,"High Transition Temperature Shape Memory Alloy Film," SPIE V. 2441, pp. 165-170, 1995.

4. Jardine, A.P., "Deposition Parameters for Sputter Deposited Thin Film TiNi," Materials for Smart Systems Symposium, Boston Ma., Mater Res Soc., 1995, pp. 293-298.

5. Busch, J.D., Johnson, A.D., Lee, C.H. and Stevenson, D.A., "Shape-Memory Properties in Ni-Ti Sputter-Deposited Film," Journal of Applied Physics **68** (12), Dec 1990, pp. 6224-6228.

6. Miyazaki, et al., "Shape Memory Characteristics of Sputter Deposited TiNi Base Thin Films," SPIE V. 2441, pp. 156-164, 1995.

7. Walker, K.J. Gabriel, M. Mehregany, Thin-film processing of TiNi shape memory alloy. Sensors and Actuators, A21-A23, pp243-246 (1990).

8. J.D. Busch and A.D. Johnson, "Prototype Micro-valve actuator". IEEE CH2832-4, pp40 (1990).

9. K. Kuribayashi, T. Taniguchi, M. Yositake, and S. Ogawa, "Micron sized arm using reversible TiNi alloy tin film actuators". Mat. Res. Soc. Symp. Proc., vol.276, pp167-176 (1992).

10. Lee A. P., Ciarlo D. R.,Krulevitch P., Lehew S., Trevino J.,, & Northrup A., "A Practical Microgripper by Fine Alignment, Eutectic Bonding and SMA Actuation," Transducers 95, Eurosensors IX, pp. 368- 373.

11. A.P. Jardine, et. al. "Characterization of the deposition and materials parameters of thin film TiNi for microactuators and smart material". Mat. Charac. vol.32, pp169-178, (1994).

12. A. Baz, K. Iman and J. McCoy, "The dynamics of helical shape memory actuators". J. of Intelligent Mat. Sys. and Struc. vol.1, pp105 (Jan. 1990).

13. A.P. Jardine, et. al., "Dynamics of thin film TiNi cantilevers on Si". Proceedings MRS Symp. vol.311, pp161 (1993).

14. A. Peter Jardine, Cycling times of thin-film NiTi on Si. Mat Res. Soc. Symp. Proc., vol.246, pp427 (1992).

15. Yang Y., Kim CJ, Matoba H., and Muller R.S., "Thermal Analysis of a Bistable Microactuator," Dynamcis Systems and Control: V.2, DSC-V. 55-2, ASME 1994, pp. 687-693.

16. Incropera and D.P. De Witt, Fundamentals of Heat and Mass Transfer. John Wiley and Sons, third edition, N.Y., (1990).

Table I   Values used in the heat analysis model.

Constants	definition	value	units
g	gravitational acceleration	9.8	m/s^2
ν	kinematic viscosity (air)	26.4×10^{-6}	m^2/s
α	thermal diffusivity (air)	38.3×10^{-6}	m^2/s
β	volumetric thermal expansion coefficient	$1/T_f$	1/K
k	thermal conductivity (TiNi)	0.21	W/K cm
k_{air}	thermal conductivity (air)	33.8×10^{-5}	W/cm K
T_∞	ambient temperature	25	C
ρ	density (TiNi)	6.45	g/cc
Rs	Sheet resistance of TiNi	80×10^{-6}	Ω cm
R	Resistance	R=Rs l/wt	Ω
Q	latent heat of transformation	25.0	J/g
C_p	specific heat (TiNi)	0.23	J/g K
L	charac. length (half film length)	0.2	cm
dx	width of node elem. ($l/40$)	1×10^{-2}	cm
w	film width	0.1	cm
l	film length	0.4	cm
t	film thickness	4×10^{-4}	cm
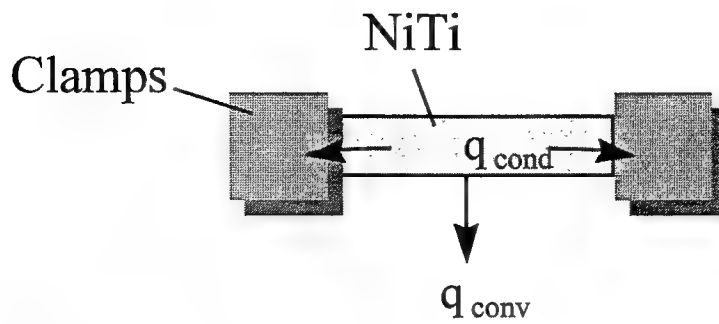
Figure 1: Illustration of physical model used to analyze the heat transfer in thin film TiNi clamped to slicon at the ends.
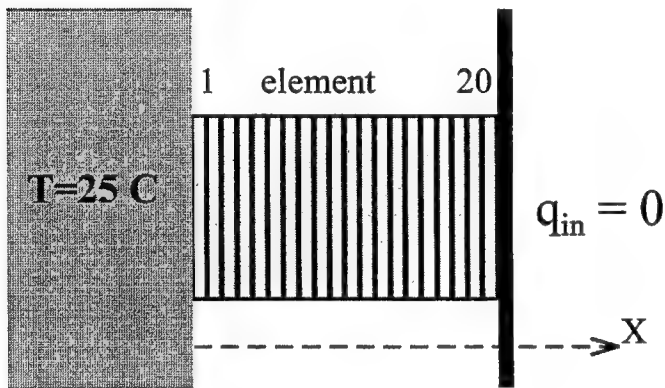
Figure 2: Schematic of finite difference model with 20 nodal elements.

SCHEMATIC
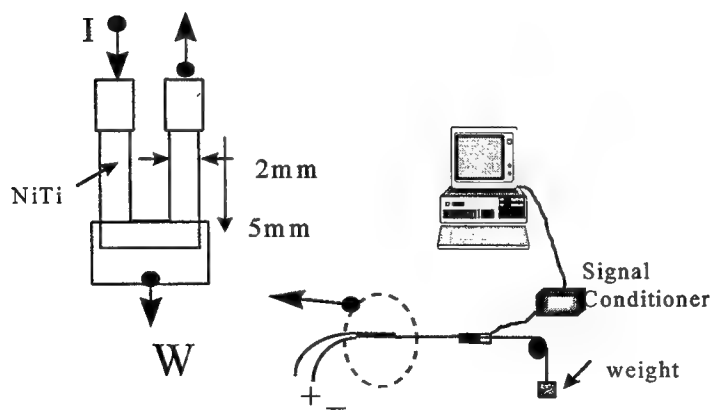
Figure 3 : Illustration of the test setup to measure the response time of thin film TiNi.
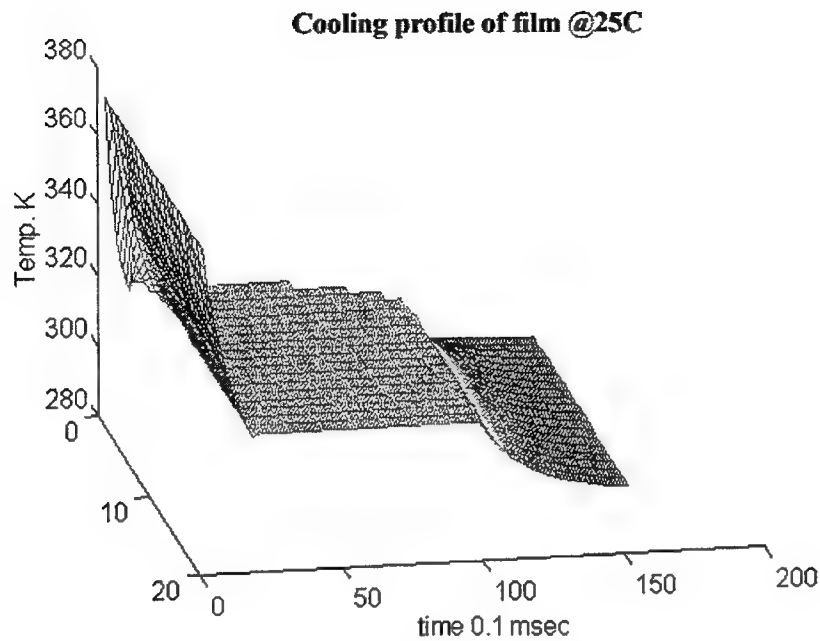
Figure 4: Cooling profile for thin film TiNi 4 microns thick in an ambient environment of 25 degrees Celsius.
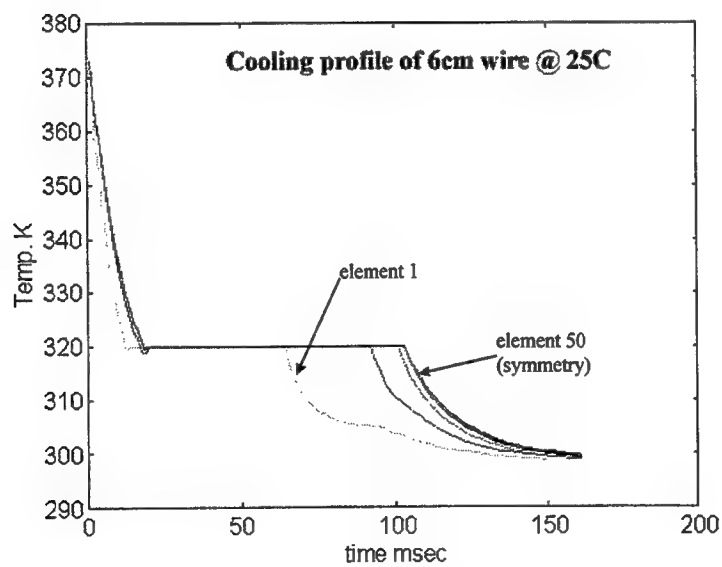
Figure 5: Analytical results for the cooling profile at different element location of a 38 micron diameter wire in an ambient environment of 25 degree Celsius.

wire 0.1 Heat 0.2sec cool
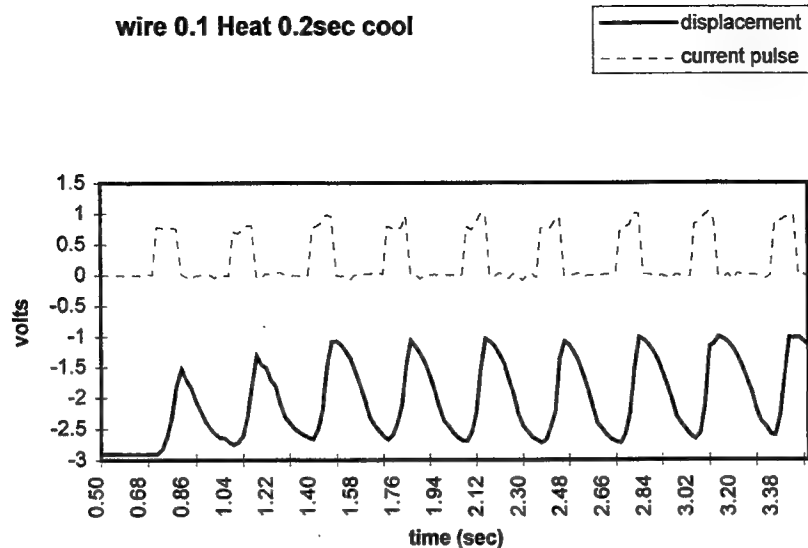
Figure 6: Experimental results for the heating and cooling of a 38 micron diameter wire with ambient environment of 25 degree Celsius. The top curve represents the voltage supplied to the wire and the bottom curve provides the LVDT output.
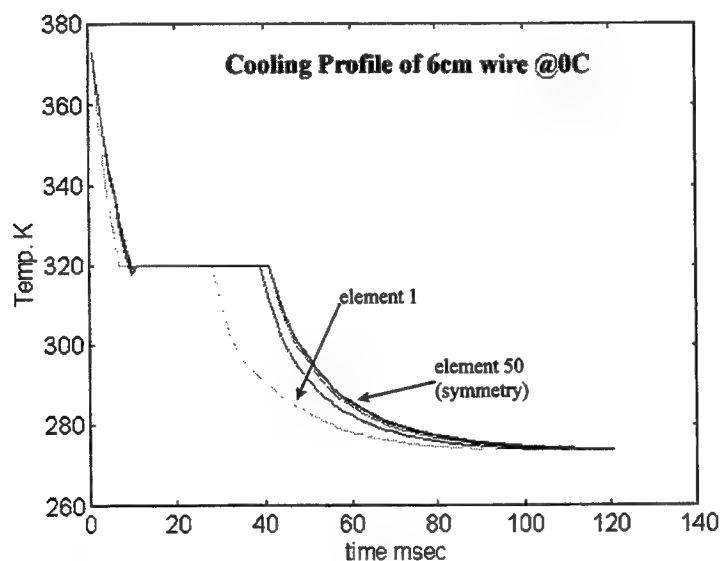
Figure 7: Analytical results for the cooling profile at different element location of a 38 micron diameter wire in an ambient environment of 0 degree Celsius.

0 C 0.1 sec heat 0.2 sec cool
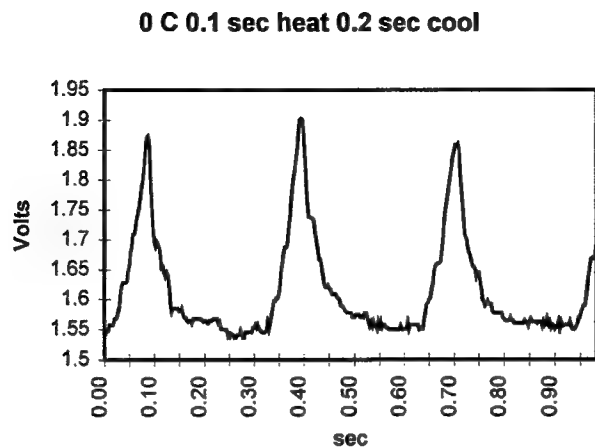
Figure 8: LVDT response for the heating and cooling of a 38 micron diameter wire with ambient environment of 0 degree Celsius.
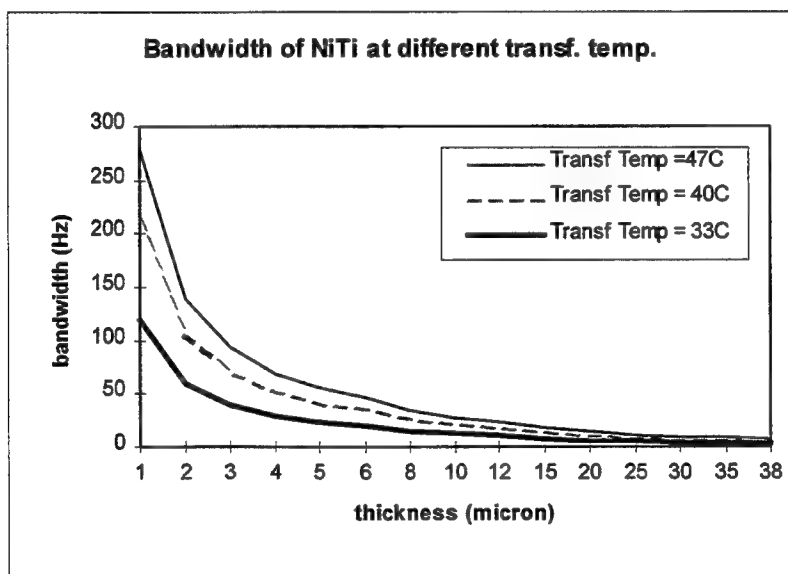
Figure 9: Bandwidth for a thin film with three different martensite phase transformation temperatures.

22

Design for shape memory alloy rotatory joint actuators using shape memory effect and pseudoelastic effect

Guoping Wang and Mohsen Shahinpoor

Artificial Muscles Research Institute, School of Engineering, University of New Mexico
Albuquerque, New Mexico 87131

ABSTRACT

A new design for shape memory alloy rotatory joint actuators using shape memory effect and pseudoelastic effect is presented. In this design, one SMA wire works with its shape memory effect, while the other SMA wire works with its pseudoelastic effect. The pseudoelastic type of SMA wire provides the shape memory type of SMA wire with bias force, and therefore, the bias spring in a bias force type of SMA actuator can be eliminated. A quasi-static analysis of this type of actuators is performed which incorporates a varying load torque. General stress-strain relation and stress-temperature relation of the shape memory effect wire and a formula for an equivalent spring rate of the pseudoelastic wire are derived. Liang and Rogers' model for shape memory materials is used for the analysis. An experimental method to obtain the equivalent spring rate is also described. Design formulas for a simplified design are derived based on the quasi-static analysis of the actuator.

Keywords: shape memory alloy, rotatory joint actuator.

1. INTRODUCTION

Shape memory alloys (SMA) have found a wide range of applications because of their unique shape memory effect (SME) and pseudoelastic effect (PEE). Shape memory effect of SMA materials has been widely exploited in design of SMA force and displacement actuators. But pseudoelastic effect of SMA materials has received little attention in design of SMA force and displacement actuators. Liang and Rogers[1] presented a design for SMA force and displacement actuators, based on the thermomechanical constitutive relations for shape memory materials which had been previously developed by Liang and Rogers.[2] The design covers both bias spring SMA actuators and differential SMA force actuators which exploit shape memory effect of SMA materials. A dead weight load was considered.

Wang and Shahinpoor[3] presented a simplified design approach for a bias force type of SMA rotatory joint actuators which incorporates a sinusoidal load torque. A concept of allowable variation of bias stress within working range was introduced in that design. This concept incorporates design considerations on utility of SMA material's load capacity, spring constant and geometric parameters of the bias spring. It provides explicit physical meanings related to those design considerations and yields a very simple design procedure. A smaller variation of bias stress relates to a softer and longer spring, and takes away less load capacity of the actuating SMA wire during actuating process. On the other hand, a larger variation of bias stress means a stiffer and shorter spring, and takes away more load capacity of the actuating SMA wire during actuating process. For that design, the stress-strain states of the SMA wire within working range can be determined and are depicted by the curve B to C in Figure 1, where states B (σ_0, ε_0, T_0) and C (σ_a, ε_a, T_a) are pre-determined through uniaxial material tests on the SMA wire which is to be used in a designed SMA actuator. As a trade-off for simplicity of design, that design does not provide a temperature value for a state within states B and C. For many cases, maximum output force and displacement range of a SMA actuator are important, not an exact temperature value under a certain displacement or a certain load. For those cases, this simplified design approach is justified.

This paper describes a new design for a bias force type of SMA rotatory joint actuators using two contractile SMA wires, one of which is passive and functional with its pseudoelastic effect and acts as a bias spring. The main advantage of this design is the elimination of a bias spring in a bias force type of SMA actuator. This advantage is
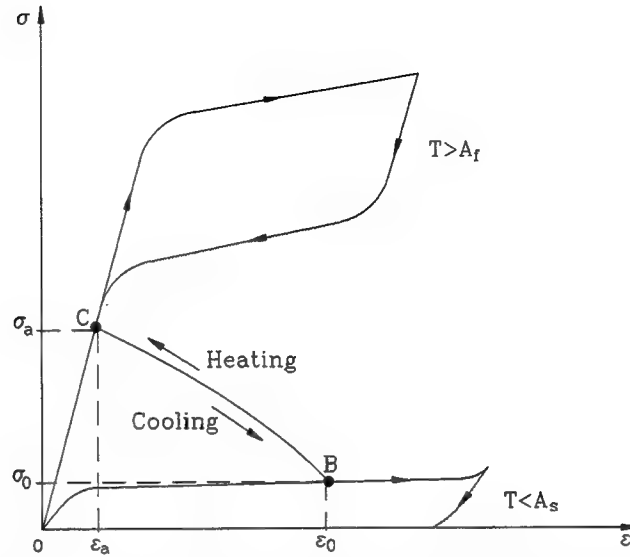
Figure 1: Working States of a SMA wire in a bias force type of SMA actuator

critical when the SMA actuator is to be used in biomechanical applications where a stressed spring is one of safety concerns.

2. QUASI-STATIC ANALYSIS OF THE SMA ROTATORY JOINT ACTUATOR

Figure 2 is a schematic of a type of SMA rotatory joint actuator using both shape memory effect and pseudoelastic effect of shape memory alloys. In this type of actuators, two types of SMA wires are used, one SME type and the other PEE type. In Figure 2, the SME wire works as an actuating component, while the PEE wire acts as a bias spring to provide the actuating SME wire with bias force, i.e., restoring force to strain the SME wire back to its initial position when the SME wire is cooled. The definitions of the symbols in Figure 2 are listed below:

α: angular displacement of the rotatory joint actuator;
r: radius of the plenary joint in the rotatory joint actuator;
W: weight of the link, which is the load of the rotatory joint actuator;
s: equivalent torque arm of the link mass with respect to joint center;
F: actuating force provided by the SMA wire;
R: resistant force (bias force) from the pseudoelastic effect wire;
Δl: actuating displacement, the length change of the SME wire to bring the link from its initial position to its actuated position;
k: equivalent spring rate of the pseudoelastic effect (PEE) wire.

In this paper, σ, ε, A, and l represent stress, strain, cross-section area, and zero strain length of a shape memory alloy wire, respectively. Variables with superscript 'SM' are variables for the shape memory effect wire, and the variables with superscript 'PE' are variables for the pseudoelastic effect wire. Variables with subscript '0' represent the values of the variables at the initial link position α_0, and the variables with subscript 'a' the values of the variables at the fully actuated link position α_{max}. The friction on the joint surface is assumed to be negligible.

24
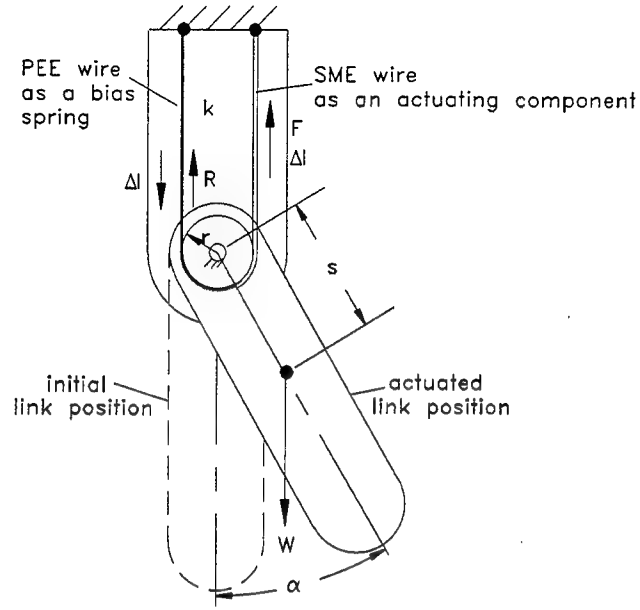
Figure 2: Schematic of a SMA rotatory actuator using shape memory effect and pseudoelastic effect

2.1. Thermomechanical relation for the SMA rotatory joint actuators

A quasi-static analysis of the SMA joint actuators is assumed in this paper to reduce the complexity of the problem, and therefore the inertia of the link mass is not considered.

The moment equilibrium equation of the link at an arbitrary angular displacement α can be written as

$$(A^{SM}\sigma^{SM} - A^{PE}\sigma^{PE})r - \tau = 0 \tag{1}$$

where τ is the output torque of the actuator at position α. The thermomechanical stress of the SME wire, σ^{SM}, and the isothermal stress of the PEE wire, σ^{PE}, are described in the following sections.

The initial condition of the actuator system is

$$(A^{SM}\sigma_0^{SM} - A^{PE}\sigma_0^{PE})r - \tau_0 = 0 \tag{2}$$

And the angular displacement α can be expressed as

$$\alpha = \alpha_0 + \frac{l^{SM}(\varepsilon_0^{SM} - \varepsilon^{SM})}{r} \tag{3}$$

or

$$\alpha = \alpha_0 + \frac{l^{PE}(\varepsilon^{PE} - \varepsilon_0^{PE})}{r} \tag{4}$$

2.2. Isothermal stress-strain relation of the PEE wire

By Liang and Rogers,[2] the stress increment of the PEE wire under constant temperature can be written as

$$\sigma^{PE} - \sigma_0^{PE} = D^{PE}(\varepsilon^{PE} - \varepsilon_0^{PE}) + \Omega^{PE}(\xi^{PE} - \xi_0^{PE}) \tag{5}$$

where D^{PE} and Ω^{PE} are the Young's modulus and phase transformation tensor of the PEE wire material, respectively. Since the PEE wire is passive and not heated during operation of the actuator, it is considered to have a constant temperature. The ξ^{PE} is the martensite fraction of the PEE wire, and its relation to material properties and its dependance on transformation history are described by Liang and Rogers.[2]

To model the PEE wire as an equivalent bias spring, we can also write the stress-strain relation of the PEE wire as

$$\sigma^{PE} - \sigma_0^{PE} = \frac{kl^{PE}}{A^{PE}}(\varepsilon^{PE} - \varepsilon_0^{PE}) \tag{6}$$

where k is an equivalent spring rate of the PEE wire for the process from the state $(\sigma_0^{PE}, \varepsilon_0^{PE}, T_0)$ to the state $(\sigma^{PE}, \varepsilon^{PE}, T_0)$.

Equations (5) and (6) yield

$$k = \frac{A^{PE}E^{PE}}{l^{PE}} \tag{7}$$

where E^{PE} is an equivalent elastic modulus of the PEE wire for the same process and is expressed by

$$E^{PE} = D^{PE} + \frac{\Omega^{PE}(\xi^{PE} - \xi_0^{PE})}{\varepsilon^{PE} - \varepsilon_0^{PE}} \tag{8}$$

The value of E^{PE} can be obtained in two ways. One is to use a constitutive model for shape memory materials, such as the model by Liang and Rogers,[2] and simulate a transformation process numerically. But it needs the values of material properties such as D^{PE}, Ω^{PE}, a_M, b_M, M_f, etc. The other way is to obtain the value of E^{PE} through a uniaxial material test on the PEE wire. Figure 3 (b) is a schematic of working states of the PEE wire. The slope of the dashed line from point B to point C in Figure 3 (b) is the equivalent elastic modulus E^{PE} for the process from state B to state C. This is obvious by considering equations (6) and (7). After E^{PE} is determined, the equivalent spring rate k can be calculated by using equation (7).

2.3. Thermomechanical relations of the SME wire

When a SME wire is used as an actuating component in an actuator, the fundamental for it to work is its behavior of large recoverable strain, which is named the shape memory effect. This is depicted in Figure 3 (a). Two stress vs. strain curves of a SMA wire are shown in the figure. One represents its behavior at a high temperature T_a, which is higher than its Austenite finish temperature A_f. The other represents its behavior at a low temperature T_0, which is lower than its austenite start temperature A_s. At a temperature lower than A_s, the SME wire is easily stretched to elongate because of the bias force provided by the PEE wire and the stress-induced martensitic transformation occurred in the SME wire. A state of the SME wire in an assembled actuator at this low temperature T_0 is represented by point B $(\sigma_0^{SM}, \varepsilon_0^{SM}, T_0)$ in Figure 3 (a). At a temperature higher than A_f, the SME wire is mostly at austenitic phase. The reverse phase transformation of the SME wire induced by heating the SME wire makes the SME wire
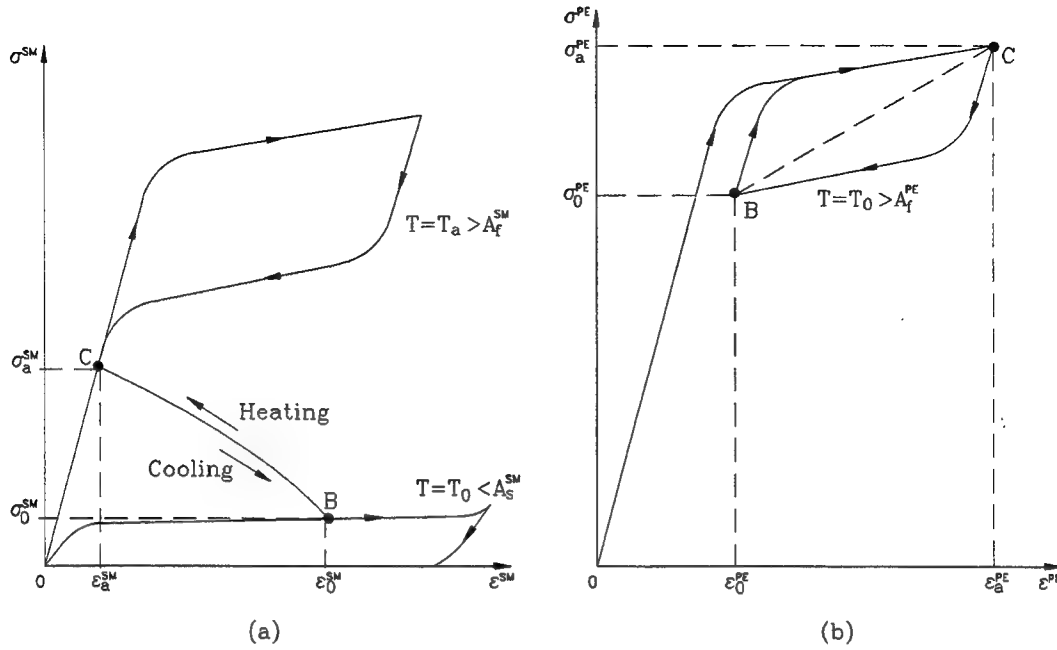
Figure 3: (a) Working states of the SME wire; (b) Working states of the PEE wire

contract and introduces a large recovery stress to actuate the link. A state of the SME wire in an assembled actuator at this high temperature T_a is represented by point C ($\sigma_a^{SM}, \varepsilon_a^{SM}, T_a$) in Figure 3 (a). The stress difference between σ_a^{SM} and σ_0^{SM} provides force output of a SMA actuator, while the strain difference between ε_0^{SM} and σ_a^{SM} provides displacement output of the SMA actuator.

By Liang and Rogers,[2] the thermomechanical constitutive relation for the SME wire is

$$\sigma^{SM} - \sigma_0^{SM} = D^{SM} (\varepsilon^{SM} - \varepsilon_0^{SM}) + \Theta^{SM} (T - T_0) + \Omega^{SM} (\xi^{SM} - \xi_0^{SM}) \tag{9}$$

where D^{SM}, Θ^{SM}, Ω^{SM}, and ξ^{SM} are the young's modulus, thermoelastic tensor, phase transformation tensor, and martensite fraction of the SME wire, respectively.

Equations (1) to (4), and (6) yield the general stress-strain relation of the SME wire of the actuator:

$$\sigma^{SM} - \sigma_0^{SM} = \frac{kl^{SM}}{A^{SM}} (\varepsilon_0^{SM} - \varepsilon^{SM}) + \frac{\tau - \tau_0}{rA^{SM}} \tag{10}$$

Substituting equation (10) into equation (9) leads to the general stress-temperature relation of the SME wire:

$$\sigma^{SM} - \sigma_0^{SM} = \Theta' (T - T_0) + \Omega' (\xi^{SM} - \xi_0^{SM}) + \frac{\tau - \tau_0}{r [A^{SM} + (kl^{SM})/D^{SM}]} \tag{11}$$

where

$$\Theta' = \frac{\Theta^{SM}}{1 + \dfrac{A^{SM}D^{SM}}{kl^{SM}}}$$

$$\Omega' = \frac{\Omega^{SM}}{1 + \dfrac{A^{SM}D^{SM}}{kl^{SM}}}$$

The last terms in equations (10) and (11) represent the influence of a varying load torque.

3. DESIGN FORMULAS

Most commercial SMA wires are not supplied with data of all material properties required by a certain constitutive model of shape memory materials. Therefore material tests are required on a purchased SMA wire to obtain data of these material properties in order to use a constitutive model. This is not convenient.

The purpose of this paper is to present a design for satisfaction of a given requirement of maximum displacement and maximum load. The advantage of this design is simplicity without the need of values of those material properties required by a constitutive model of shape memory materials. The disadvantage is the information loss of intermediate states within working range. The procedure and formulas for this design are described below which are based on the previous quasi-static analysis.

Through uniaxial tests on the SME wire, the actuating capacity of the SME wire, i.e., the values of $\sigma_a^{SM} - \sigma_0^{SM}$ and $\varepsilon_0^{SM} - \varepsilon_a^{SM}$, is determined. The lager the values, the better the SME wire for actuator purposes. For long life of a SMA actuator, a value about 4% for ε_0^{SM} is considered in this design. Through a uniaxial test on the PEE wire, the working states B and C of the PEE wire can be selected. The same consideration on maximum strain applies to the PEE wire. These tests determine σ_0^{SM}, σ_a^{SM}, ε_0^{SM}, ε_a^{SM}, σ_0^{PE}, σ_a^{PE}, ε_0^{PE}, and ε_a^{PE}. A process from state B to state C means a full activation process of the actuator.

Considering the maximum output torque τ_{max} at the maximum displacement α_{max} in equation (1), then combining equations (1) and (2), we can found the cross-section areas of the SME wire and the PEE wire as:

$$A^{SM} = \frac{\dfrac{\tau_{max}}{r}\left(1 - \dfrac{\tau_0}{\tau_{max}}q^{PE}\right)}{\sigma_a^{SM}(1 - q^{SM}q^{PE})} \tag{12}$$

$$A^{PE} = \frac{\dfrac{\tau_{max}}{r}\left(q^{SM} - \dfrac{\tau_0}{\tau_{max}}\right)}{\sigma_0^{PE}(1 - q^{SM}q^{PE})} \tag{13}$$

where variables with subscript 'a' represent the values of the variables at maximum actuator displacement α_{max}. q^{SM} and q^{PE} are stress ratios which are expressed as

$$\begin{cases} q^{SM} = \sigma_0^{SM}/\sigma_a^{SM} \\ q^{PE} = \sigma_a^{PE}/\sigma_0^{PE} \end{cases} \tag{14}$$

Similarly, the lengths of the SME wire and the PEE wire can be found from equations (3) and (4) as:

$$l^{SM} = \frac{r(\alpha_{max} - \alpha_0)}{\varepsilon_0^{SM} - \varepsilon_a^{SM}} \tag{15}$$

$$l^{PE} = \frac{r(\alpha_{max} - \alpha_0)}{\varepsilon_a^{PE} - \varepsilon_0^{PE}} \tag{16}$$

where

$$\tau_{max} = \begin{cases} Ws\sin(\alpha_{max}), & \text{for} \quad \alpha_{max} \leq 90^o \\ \\ Ws, & \text{for} \quad \alpha_{max} > 90^o \end{cases} \tag{17}$$

Using PEE wire instead of a normal spring provides more degrees-of-freedom when deciding a spring rate of a bias spring. Instead of one parameter, spring constant k, of a normal spring, an equivalent bias spring made from a PEE wire provides three degrees-of-freedom, see equation (7). A designer can decide lengths of the SME wire and the PEE wire to satisfy a required maximum displacement, and decide cross-section areas of the SME wire and the PEE wire to satisfy the bias stress need by the SME wire and a required maximum load. The displacement requirement and the load requirement of a design are decoupled in this regard.

The initial strain ε_0^{SM} should be realized at assembly to set proper initial condition. The bias force provides the SME wire with a stable initial state and therefore improves reversibility of the actuator. Heating response time of the actuator can be controlled by electric current of resistive heating of the SME wire. Cooling response time depends on a cooling method. For a passive free convection, cooling time can be very long for a large cross-section area of the SME wire. An active cooling system may be considered if improvement of cooling response is necessary and is cost-effective for certain applications.

4. CONCLUSION

A design for a bias force type of SMA rotary joint actuators is presented. This type of SMA actuators use two types of SMA wires, one SME type, the other PEE type. A bias spring is not needed. A quasi-static analysis of this type of SMA actuators provides general stress-temperature relation and general stress-strain relation of the SME wire which can be used for design analysis. Expressions for an equivalent spring rate of the PEE wire is derived, and an experimental method of acquiring the equivalent spring rate is described. A simplified design based on the quasi-static analysis yields very simple design formulas, which can be used in design for satisfaction of required maximum displacement and maximum load. A trade-off for this simplicity exists. Between the initial condition and the maximum displacement configuration of a designed actuator, stress-strain-temperature states of both SMA wires are not quantitatively predicted.

5. ACKNOLEDGEMENT

6. REFERENCES

1. C. Liang and C. A. Rogers, "Design of Shape Memory Alloy Actuators," *Journal of Mechanical Design*, Vol.

114, pp. 223-230, 1992.

2. C. Liang and C. A. Rogers, "One-Dimensional Thermomechanical Constitutive Relations for Shape Memory Materials," *Journal of Intelligent Material Systems and Structures*, Vol. 1, No. 2, 1990.

3. G. Wang and M. Shahinpoor, "A new design for a rotatory joint actuator made with a shape memory alloy contractile wire," *Proc. SPIE 1996 Smart Structures and Materials Conference*, Mathematics and Control in Smart Structures, edited by V. V. Varadan, Vol. 2715, 1996.

Characteristic studies of modified Cu-Zn-Al shape memory alloy with Mn and Zr addition

W. H. Zou, Christina W. H. Lam, C. Y. Chung and Joseph K. L. Lai

Department of Physics and Materials Science, City University of Hong Kong
83 Tat Chee Avenue, Kowloon, Hong Kong

ABSTRACT

As a modification of Cu-Zn-Al shape memory alloy (SMA), the characteristics of Cu-21Zn-6Al-1Mn-0.5Zr (wt%) SMA are examined and compared with that of Cu-21Zn-6Al (wt%) SMA in the present work. After added Zr into the Cu-Zn-Al alloy, the average grain size of Cu-Zn-Al-Mn-Zr alloy is reduced from 300μm (that of Cu-Zn-Al alloy) to 75μm. Two Zr-rich new phases were found in Zr added alloy by means of transmission electron microscopy. The tensile testing results and scanning electron microscopy observations show that the strength of grain boundary and the ductility of the Mn, Zr added alloy were enhanced. This has made the alloy exhibit better mechanical property than ordinary Cu-Zn-Al SMA. Moreover, upon ageing, the reordering phenomenon was not serious when the ageing temperature was below 200°C in Cu-Zn-Al-Mn-Zr alloy while significant decrease of order degree and shape memory capacity were found for Cu-Zn-Al alloy.

1. INTRODUCTION

Shape memory Alloys (SMA) based on Ni and Ti has demonstrated the best shape memory properties and good corrosion resistance. They are widely used in many commercial applications. However, Ni-Ti in its finished form is very expensive because of the fabrication difficulties associated with melting and forming.

Cu-based SMAs serve as economic alternatives to Ni-Ti SMA because of their lower price. Cu-Zn-Al are now the most popular Cu-based SMA and are presently available in the market. However, they do not always exhibit sufficient thermal stability and mechanical strength. They suffer from martensite stabilisation[1] which causes increase in reverse transformation temperatures when they are aged in the martensite state. Ageing in parent phase will result in the change of the degree of order and the formation of precipitations[2]. Intergranular cracking usually occurs during processing and service because of the large anisotropy and large grain size of the alloy[3]. They also exhibit low ductility problems.

Many attempts have been made to improve the mechanical properties and thermal stability of the martensitic transformation. With the increase of the Mn concentration in Cu-Al-Ni SMA, the thermoelastic and pseudoelastic behaviours were found enhanced. The ductility of the alloy was improved[4]. On the other hand, elements such as B, V, Zr and Ti were chosen to be added to refine grains of the parent phase in Cu-based SMAs. Zr addition was found good in lowering grain growth rate to zero during annealing at 800°C in Cu-Zn-Al alloy. Zr-rich particles were observed at grain boundaries which were believed to be responsible for the grain refining effect[5].

Mn and Zr were added into Cu-Zn-Al alloy to refine the grains, to improve the ductility and to suppress the stabilisation of the martensite. In the current work, the characteristic of the transformation and the mechanical properties are studied. Detailed microstructural examination were performed to understand the effect of the Zr-rich precipitates formation on the characteristics of Cu-Zn-Al-Mn-Zr alloy. The composition and structure of Zr-rich precipitates were also studied in detail

Authors information -
W.H.Z. (correspondence): Email: rmwhz@cityu.edu.hk
C.W.H.L. : Email: apclam@cityu.edu.hk
C.Y.C. : Email: appchung@cityu.edu.hk
J.K.L.L. : Email: apjoelai@cityu.edu.hk

using energy dispersive X-ray spectroscopy (EDXS) and transmission electron microscopy (TEM). Furthermore, the thermal stability of the new alloy is studied through ageing.

2. EXPERIMENTAL

Cu-21Zn-6Al-1Mn-0.5Zr (wt%) and Cu-21Zn-6Al (wt%) alloys were prepared by melting elements with industrial purity in an induction furnace. The ingots were hot rolled to 1mm plates. The specimens were then solid solution treated at 850°C for 5min. One batch of specimens was directly quenched into the ice water (D.Q.). Another batch was step quenched (S.Q.) into hot water at 100°C for 30 minutes and then quenched into ice water. The transformation characteristics were determined using differential scanning calorimeter (DSC). The heating and cooling rates were ±20°C/min. Transmission electron microscopy (TEM) observations were carried out using a Philips CM-20 transmission electron microscope attached with a EDAX DX-4 energy dispersive X-ray spectroscope operating at 200kV. Micrographs were taken in optical microscope and JEOL-820 scanning electron microscope (SEM). Tensile tests were done in an Instron 4206 tensile tester at strain rate of 1mm/min.

3. RESULTS

3. 1 Microstructure of Cu-Zn-Al-Mn-Zr SMA

The addition of Zr has significant effect on grain refinement. Fig. 1 (a) and (b) are optical micrographs of Cu-Zn-Al and Cu-Zn-Al-Mn-Zr alloys. The average grain size of Cu-Zn-Al alloy is about 300μm and that of Cu-Zn-Al-Mn-Zr alloy was reduced to only 75μm. Zr-rich precipitates formed in the Cu-Zn-Al-Mn-Zr alloy, which were identified by electron diffraction and TEM-EDXS analysis. The average sizes of precipitates in the alloy ranged from 0.1μm to 1μm and possess incoherent interfaces with the parent phase matrix.

The structure types of martensite and parent phase in Cu-Zn-Al-Mn-Zr SMA are determined to be $M18R_1$ and DO_3 respectively by selected area electron diffraction analysis. Fig. 2 (a) and (b) are the typical TEM bright field images of Cu-Zn-Al-Mn-Zr alloy. Fig. 2 (a) shows the morphology of the martensite phase and the parent phase in the alloy. The "tweed" contrast of the parent phase is due to the premartensitic effect. Fig.2 (b) shows the morphology of a Zr-rich precipitate formed in the Cu-Zn-Al-Mn-Zr alloy. Energy dispersive X-ray spectroscopy microanalysis and electron diffraction analysis in TEM were used to determine the composition and the structure of precipitates. The results reveal that there are two kinds of Zr-rich phases formed in the alloy. The results of quantitative compositional microanalysis are listed in Table I, which suggests that the two precipitates are all new Cu-Zr-Al-Zn phases with the compositions of $Cu_2Zr(Al, Zn)_1$ and $Cu_3ZrAlZn$ (at%). They will be named as Z_1 and Z_2 phase respectively hereafter. Selected area electron diffraction (SAED) was used to determine the
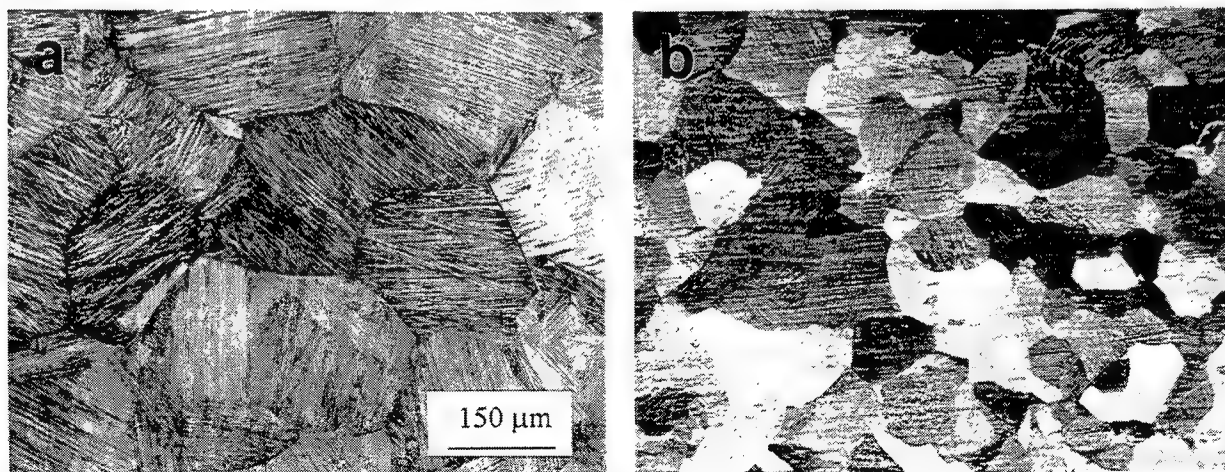
Fig. 1   Optical micrographs of S.Q. (a) Cu-Zn-Al SMA and (b) Cu-Zn-Al-Mn-Zr SMA.
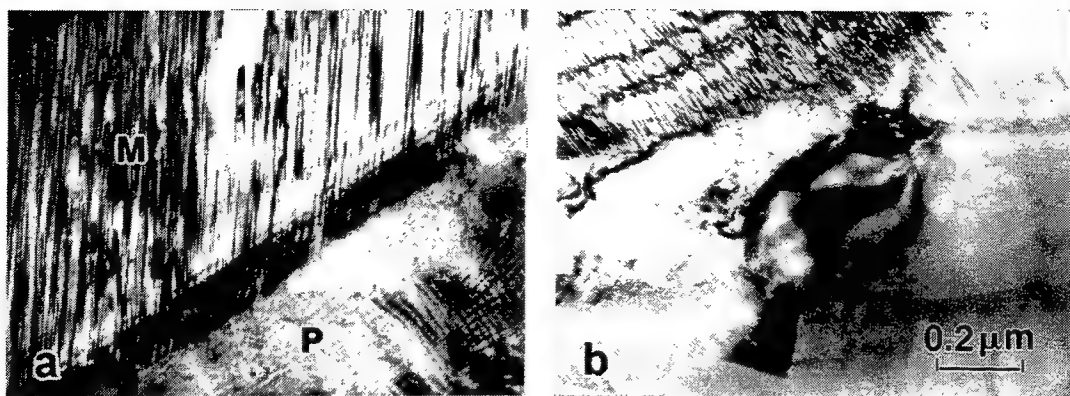
Fig. 2   TEM bright field images of Cu-Zn-Al-Mn-Zr specimen showing the different phases. (a) martensite phase and parent phase; (b) a Zr-rich phase located in the matrix.

crystallographic structure of the phases. The systematic SAED patterns were taken by tilting the TEM foils around the low index axes. The corresponding experimental angles between the neighbouring SAED patterns were recorded. Fig. 3 and Fig. 4 show the systematic SAED patterns of the Z_1 and Z_2 phases The angles between the neighbouring patterns labelled in Fig. 3 are the experimental values. The SAED patterns in Fig. 3 indicate the crystal structure of the Z_1 phase is face-centred cubic with lattice parameter of $a = 1.234$nm. In Fig. 4, the main reflection spots of Z_2 phase can be indexed by a base-centred orthorhombic unit cell with lattice parameter being $a = 0.481$nm; $b = 0.833$nm; $c = 0.826$nm. In Fig. 4 (d) - (h), each main reflection spot is accompanied by several satellite spots which derived from an incommensurate modulation structure. The modulation wave vector is along $(010)_{Z1}$ and the period of the modulation is about 1.96nm.

3. 2 Transformation Characteristics

The reverse transformation behaviour of differently heat treated Cu-Zn-Al and Cu-Zn-Al-Mn-Zr alloys were examined using DSC. Figs. 5 (a) - (d) are the heating and cooling curves for Cu-Zn-Al and Cu-Zn-Al-Mn-Zr. The step quenched Cu-Zn-Al and Cu-Zn-Al-Mn-Zr exhibited good reverse and forward transformations. However, the results show that martensite stabilisation has occurred seriously in direct quenched Cu-Zn-Al alloy. No reverse transformation peak was detected in this sample. With the addition of Mn and Zr, Cu-Zn-Al-Mn-Zr showed transformation peaks in both heating and cooling curves. Martensite stabilisation has been suppressed. The transformation temperatures of the differently heat treated alloys are listed in Table II.

Table I Results of TEM-EDXS microanalysis of the Zr rich precipitates and the matrix.

phases	Cu	Zn	Al	Mn	Zr	
precipitate 1	49.7	8.1	7.2	—	35.0	(wt%)
(Z_1 phase)	50.2	7.9	17.3	—	24.6	(at%)
precipitate 2	56.1	10.3	5.0	—	28.6	(wt%)
(Z_2 phase)	57.4	10.3	11.9	—	20.4	(at%)
matrix	73.2	21.8	4.4	0.6	—	(wt%)

Table II   Transformation temperatures of differently heat treated samples

Alloy	Heat Treatment	Mf (°C)	Ms (°C)	As (°C)	Af (°C)
Cu-Zn-Al	D.Q.	-	-	-	-
	S.Q.	49	72	68	87
Cu-Zn-Al-Mn-Zr	D.Q.	-10	20	5	35
	S.Q.	10	30	20	42
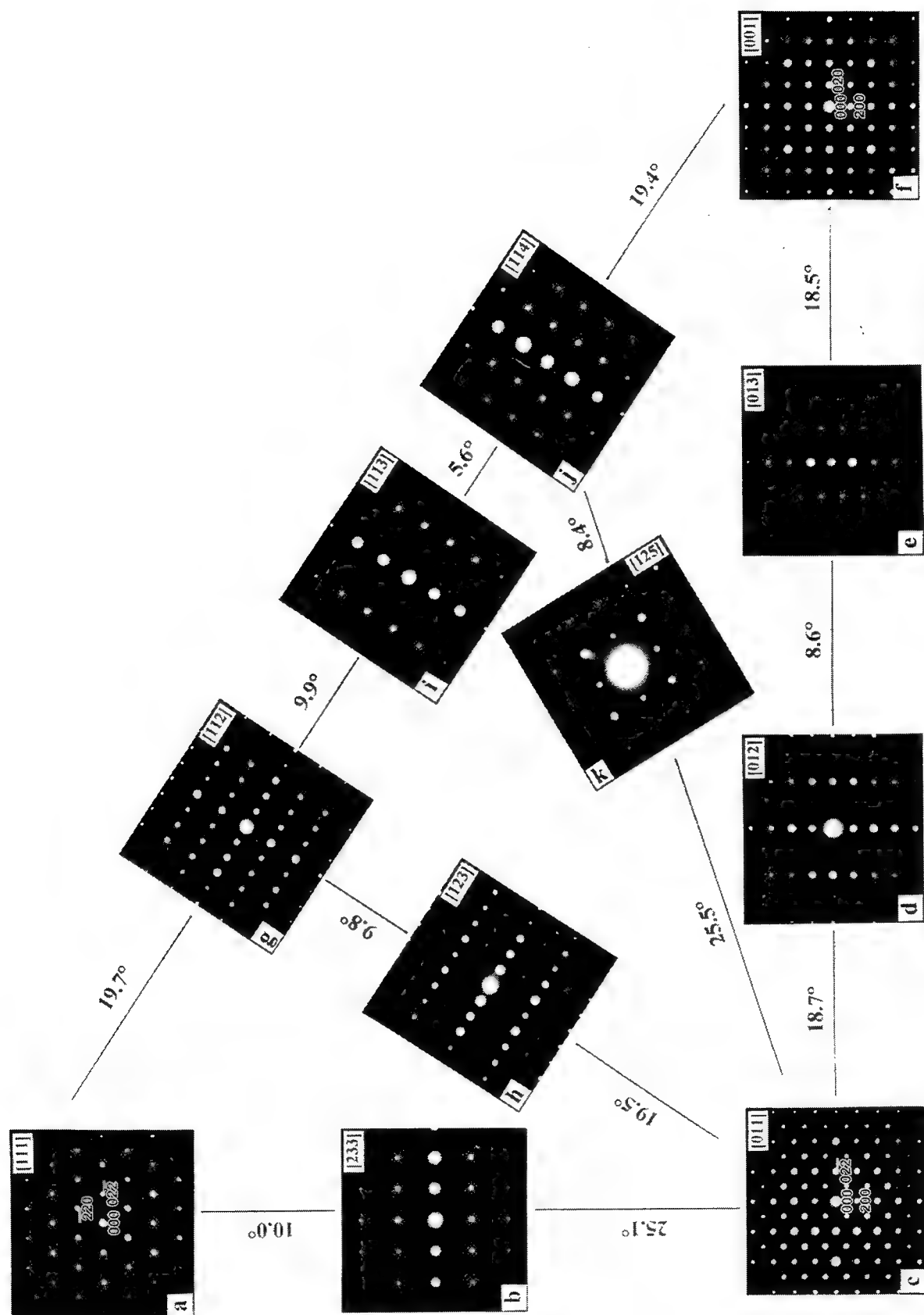
Fig. 3 Systematic selected area electron diffraction patterns of Z_1 precipitate. The angles between the neighbouring patterns labelled in the figure are experimental values.

34
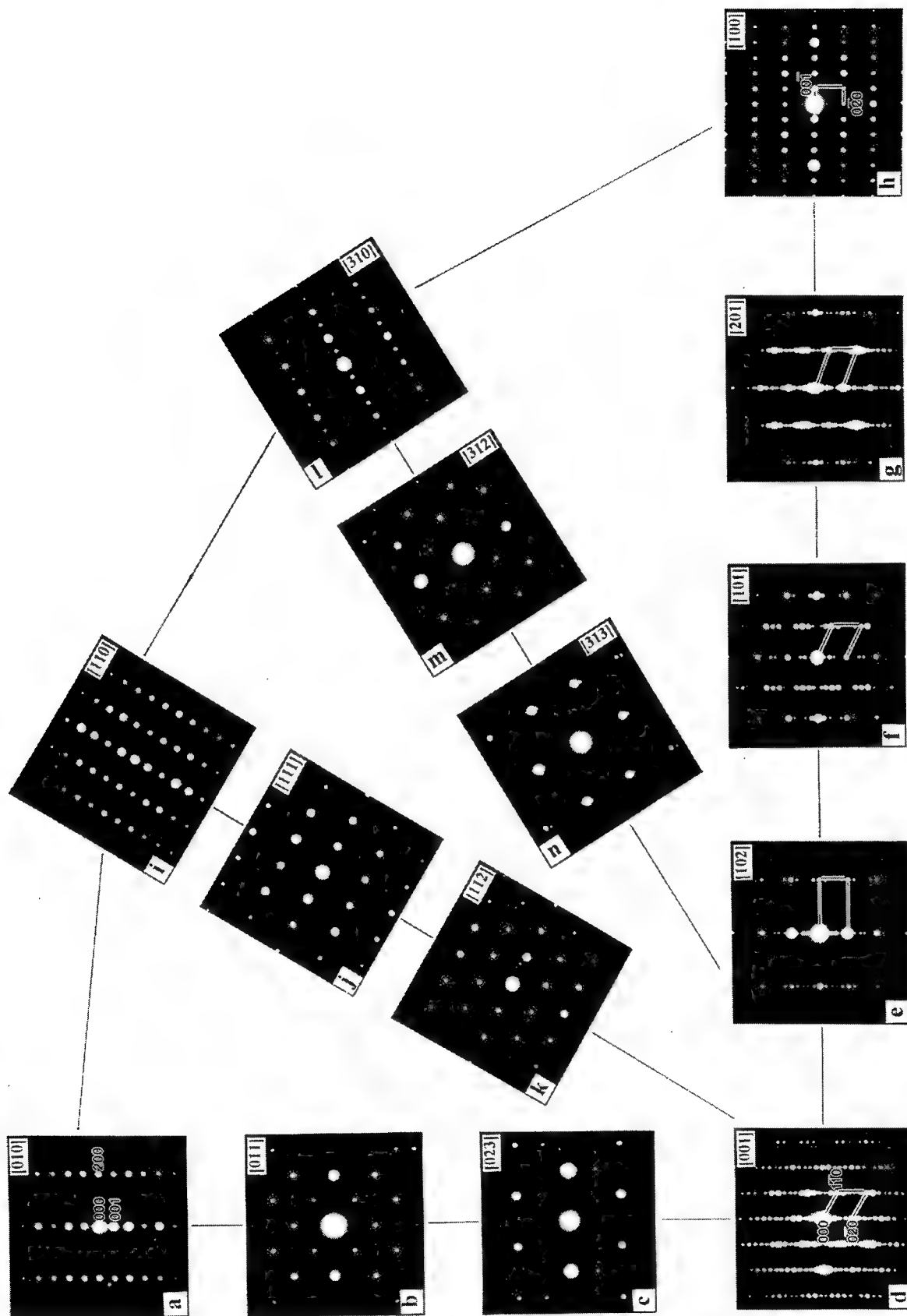
Fig. 4   Systematic selected area electron diffraction patterns of Z_2 precipitate.

35
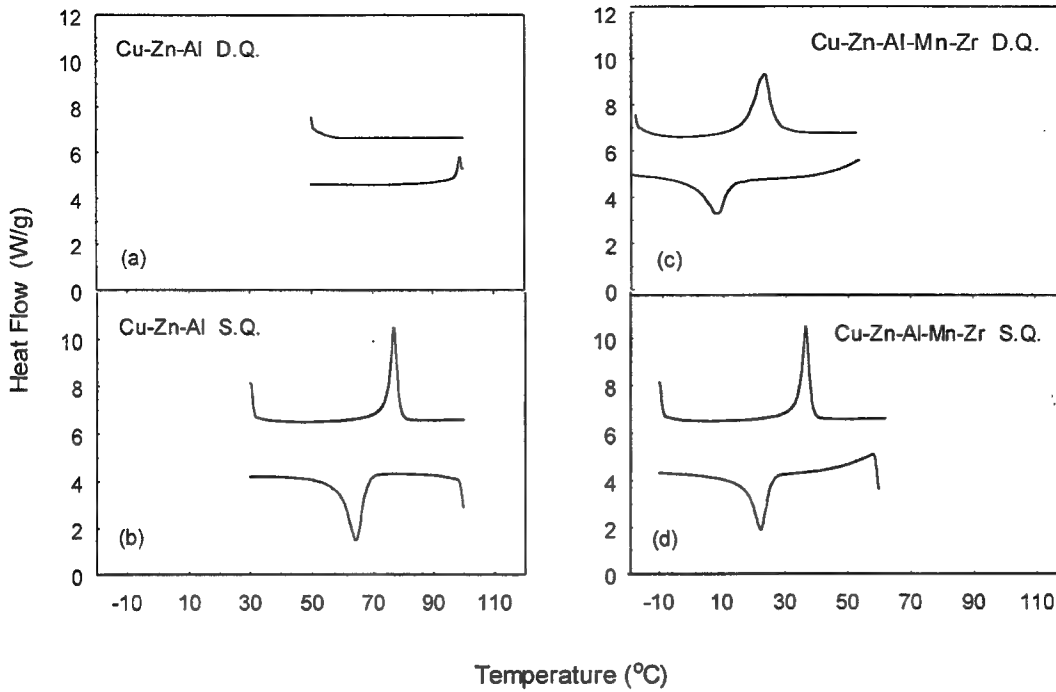
Fig.5   DSC heating and cooling curves for (a) D.Q. Cu-Zn-Al, (b) S.Q. Cu-Zn-Al, (c) D.Q. Cu-Zn-Al-Mn-Zr and (d) S.Q. Cu-Zn-Al-Mn-Zr, positive peak represents endothermic transformation.

3. 3 Fracture property

Fig. 6 reveals the typical stress-strain curves of the two S.Q. alloys tested at room temperature (20°C), which are all in the martensite state. The results show that the grain refined Cu-Zn-Al-Mn-Zr alloy possesses a significantly higher fracture stress and fracture strain compared to the Cu-Zn-Al alloy.
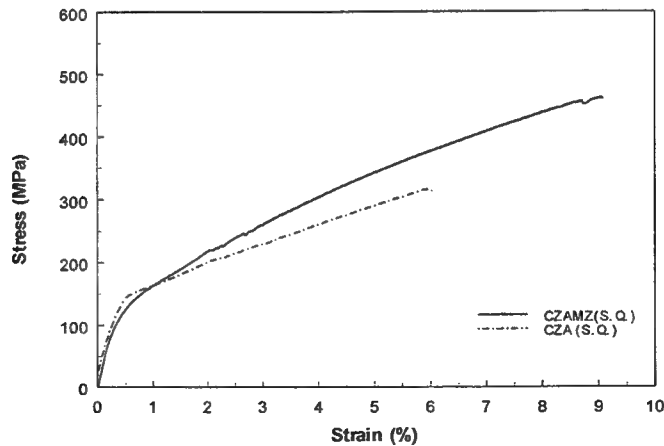
Fig. 6   The stress-strain curves for Cu-Zn-Al and Cu-Zn-Al-Mn-Zr alloys. The tests were performed at room temperature ($<A_s$) while the alloys were all in martensite state.
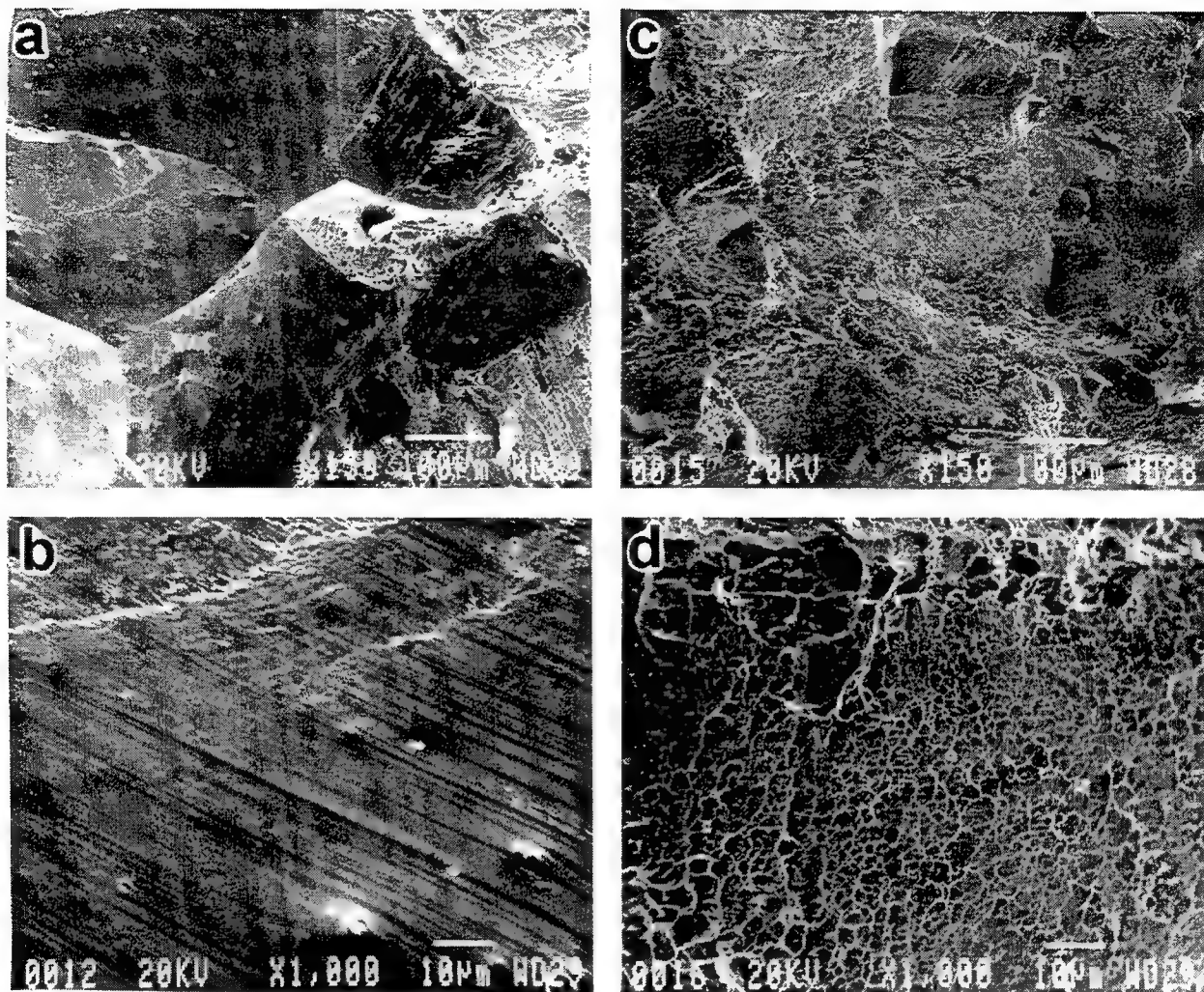
Fig. 7 SEM micrographs of Cu-Zn-Al (a), (b) and Cu-Zn-Al-Mn-Zr (c), (d) showing the morphology of the fracture surface of the two alloys.

The fractographs of the two alloys after the tensile tests were examined by SEM. Fig. 7 shows the typical SEM micrographs of the fracture surface. Fig. 7 (a) and (b) were obtained from Cu-Zn-Al alloy, which exhibited the apparent characteristics of intergranular fracture. However, the additions of Mn and Zr have caused a large changes in the morphology of the fracture surface. The typical morphology of the fracture surface of Cu-Zn-Al-Mn-Zr alloy is shown in Fig. 7 (c) and (d). The river like characteristic of the ductile failure can be seen and the fracture mode is mainly transgranular. So the Zr has strengthened the grain boundary and this is considered to be one of the important factors which improved the mechanical properties of the Cu-Zn-Al-Mn-Zr alloy as compared to Cu-Zn-Al alloy.

3.4   Thermal Stability

Fig.8 depicts the change in peak temperatures of the forward and reverse martensitic transformations obtained from DSC curves for Cu-Zn-Al and Cu-Zn-Al-Mn-Zr alloys after ageing at different temperatures for 6 hours. The transformation temperatures decreased slightly when the alloys were aged below 100°C. Larger drops were found for both alloys when aged at 150°C. After ageing at 200°C, no martensitic transformation can be found in the Cu-Zn-Al alloy; however, it was still present in the Cu-Zn-Al-Mn-Zr alloy. Transformation enthalpies were obtained by integrating the area of the DSC transformation peaks. Fig.9 shows the change of enthalpy in the forward martensitic transformation with respect to ageing temperatures. The enthalpies were not changed much after ageing at temperature below 150°C but dropped more significantly
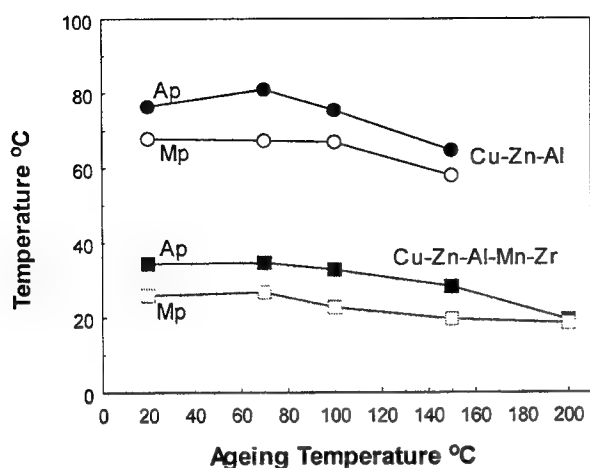
Fig.8 Peak temperatures for Cu-Zn-Al and Cu-Zn-Al-Mn-Zr during reverse (Ap) and forward (Mp) transformations at different ageing temperatures.
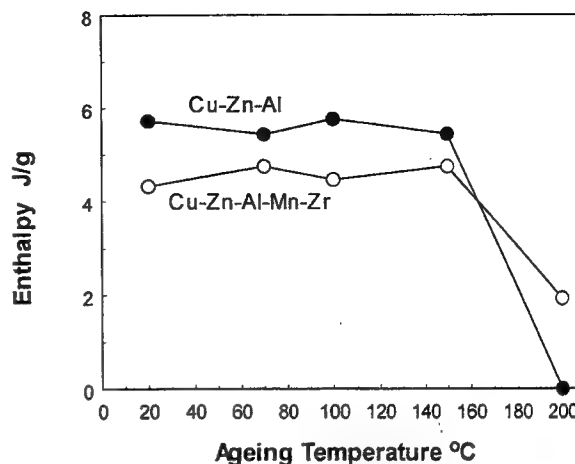
Fig.9 Change in transformation enthalpy in forward transformation of Cu-Zn-Al and Cu-Zn-Al-Mn-Zr with respect to ageing temperatures.

after ageing at 200°C. This implies that the volume of transformable parent phase will decrease when ageing temperatures are high enough. The parent phase should either have stabilised or decomposed to the equilibrium phases. This phenomenon is more severe in Cu-Zn-Al than in Cu-Zn-Al-Mn-Zr alloy after ageing at 200°C as the volume of transformable parent phase in Cu-Zn-Al has dropped to zero. Both alloys show no martensitic transformation after ageing at 300°C.

Splitting parameters were calculated from $(\bar{1}22)_M - (202)_M$, $(1210)_M - (\bar{2}010)_M$ and $(040)_M - (320)_M$ line pairs of X-ray diffraction (XRD) spectrum taken at room temperature. Fig.10 shows the change in splitting parameters with ageing. The splitting parameters of Cu-Zn-Al drop steadily with increasing ageing temperatures. The higher the ageing temperature, the drop became more severe. However, the splitting parameters of Cu-Zn-Al-Mn-Zr were not changed much. From the XRD results, φ and x-parameter can be calculated using the lattice parameters where $\varphi=2\tan^{-1}(b/2a)$ and $x=1/3+(c/9a)\cos\beta$. Table III summarise the lattice parameters, φ and x-parameters. For Cu-Zn-Al alloy, with ageing, (i) $\rho 1$, $\rho 2$, $\rho 3 \rightarrow 0$; (ii) $\beta \rightarrow 90°$; (iii) $\varphi \rightarrow 60°$; and (iv) $x \rightarrow 1/3$. These trends imply that the M18R martensite changes from M18R$_1$ towards N18R$_1$ structure upon ageing. For Cu-Zn-Al-Mn-Zr, the changes in these parameters were less obvious when aged below 150°C.
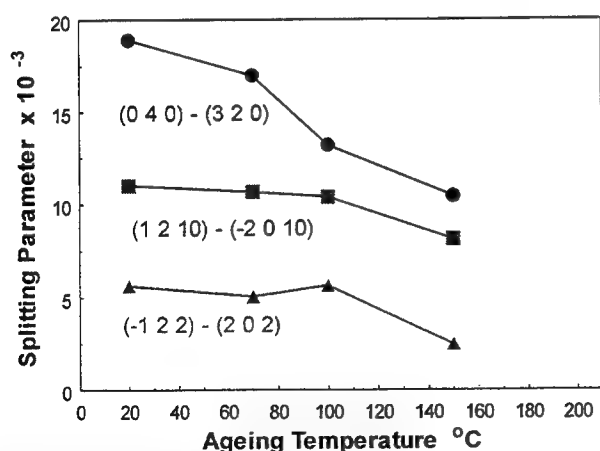
Fig.10a Change of splitting parameters of Cu-Zn-Al with respect to ageing temperature.
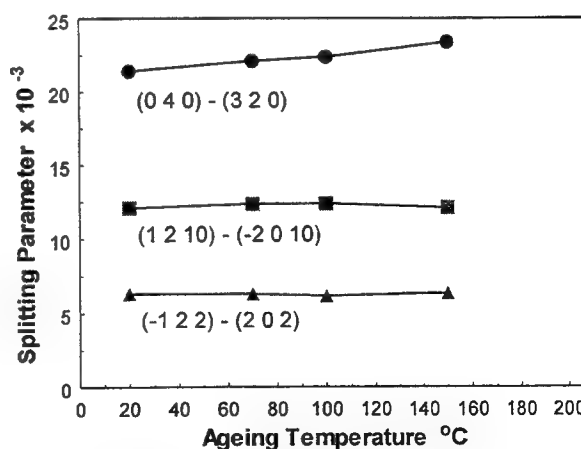
Fig. 10b Change of splitting parameters of Cu-Zn-Al-Mn-Zr with respect to ageing temperatures.

Table III   Lattice parameters for Cu-Zn-Al and Cu-Zn-Al-Mn-Zr after different thermal treatments

Alloy	Ageing	Lattice Parameters				φ°	x
		a (nm)	b (nm)	c (nm)	$\beta\,^\circ$		
Cu-Zn-Al	S.Q.	0.4423	0.5298	3.818	88.80	61.83	0.3534
	70°C	0.4432	0.5295	3.821	88.76	61.70	0.3540
	100°C	0.4430	0.5304	3.817	88.95	61.81	0.3508
	150°C	0.4448	0.5289	3.833	89.15	61.46	0.3475
Cu-Zn-Al-Mn-Zr	S.Q.	0.4416	0.5308	3.818	88.69	62.01	0.3553
	70°C	0.4420	0.5318	3.821	88.63	62.06	0.3563
	100°C	0.4421	0.5317	3.824	88.63	62.04	0.3562
	150°C	0.4425	0.5322	3.824	88.74	62.04	0.3544

By microstructural examination, typical martensite morphology can be found in step quench, 70°C aged Cu-Zn-Al and Cu-Zn-Al-Mn-Zr samples and 150°C aged Cu-Zn-Al-Mn-Zr samples. Bainite start to precipitate in 200°C aged samples. In Cu-Zn-Al, all the parent phase changed to bainite during 150°C ageing while in Cu-Zn-Al-Mn-Zr about 70% has been changed as the amount of martensitic transformation has dropped 70%. After 300°C ageing, large area of α and β phases were found.

4. DISCUSSIONS

The fine structure of Cu-Zn-Al-Mn-Zr alloy has been examined. Besides the martensite and parent phase, only some Zr rich precipitates with size around 0.1~1μm were observed in the alloy. These precipitates possess specific orientation relationship and incoherent interfaces with the parent phase matrix. No smaller coherent precipitates have been found. This situation is different from most of Cu-based SMAs with grain refinement element additions, such as, V-doped Cu-Zn-Al alloy, Zr-, Cr- or B-doped Cu-Al-Ni alloys. In these grain refinement elements doped SMAs, there are some fine precipitates, such as the X_S and X_{SS} phases in Cu-Al-Ni-Mn-Ti SMA[6,7], formed in the matrix which possess semi-coherent or coherent interfaces with the matrix. To a first approximation, the pinning force of precipitates on per unit of boundary is inversely proportional to the mean particle radius. Thus, these very fine coherent or semi-coherent precipitates (usually with size of several 10nm) in some Cu-based SMAs are thought to be effective in suppressing grain coarsening during hot working, homogenisation and/or betatization treatment. However, on the other hand, they can also have the effect of pinning the martensite/parent phase or martensite/martensite interfaces, and obstruct the movement of these interfaces during the process of martensitic transformation. So in some SMAs with addition of grain refining elements, although the grain size can be greatly reduced, other adverse effects are produced at the same time. For the present Cu-Zn-Al SMA with Zr and Mn additions, grain refinement is significant and the mechanical properties were improved, but only very large Zr-rich precipitates are formed. So from this point of view, Zr addition in Cu-Zn-Al-Mn-Zr alloy does not have adverse effect on martensitic transformation.

The S.Q. specimens of Cu-Zn-Al and Cu-Zn-Al-Mn-Zr alloys exhibited both good reverse and forward martensitic transformation properties. That is due to the annihilation of supersaturated vacancies in the parent phase matrix during the S.Q. treatment. Serious martensite stabilisation has occurred in D.Q. Cu-Zn-Al alloy. Martensite stabilisation in Cu-based SMAs is related to the structure and degree of order of the martensite phases[8]. The degree of order of differently heat treated Cu-Zn-Al and Cu-Zn-Al-Mn-Zr alloy have been investigated in our previous work[9]. The B2 and DO₃ order degree of both S.Q. Cu-Zn-Al and Cu-Zn-Al-Mn-Zr specimens were all higher than that of D.Q. specimens. However, for S.Q. Cu-Zn-Al-Mn-Zr alloy, the increase of B2 and DO₃ order degree did not result in the increase of the splitting of $(\bar{1}22)_M - (202)_M$ and $(12\bar{1}0)_M - (\bar{2}010)_M$ line pairs. This may imply that the orthorhombic distortion of martensite phase does not possess a simple relationship with the variations of order degree in Cu-Zn-Al-Mn-Zr alloy. In other words, changes in orthorhombic distortion should not be interpreted as an equivalence of variation in order degree.

When both Cu-Zn-Al and Cu-Zn-Al-Mn-Zr alloys were aged at parent phase, Cu-Zn-Al suffered from decrease of the monoclinicity and lower of transformation temperature. The martensite structure became more closer to N18R. When they were aged at temperature higher than 150°C, bainite started to precipitate and reduced the amount of transformable

martensite. Contrastly, the change in the monoclinicity and transformation temperatures of martensite were less obvious for Cu-Zn-Al-Mn-Zr alloy. The addition of Mn and Zr has lowered the diffusion rate of the constituent atoms and suppressed the rate of disordering. However, further ageing will also lead to precipitation of bainite and then equilibrium phases. Bainite precipitate occurs in both alloys when aged at 200°C. Although both alloys are thermally unstable at 200°C, the splitting parameters and transformation temperatures of Cu-Zn-Al-Mn-Zr alloy shift less than ordinary Cu-Zn-Al alloy when aged below 150°C.

5. ACKNOWLEDGMENT

6. REFERENCES

1. J. Van Humpback, J. Janssen, N. Mwamba, and L. Delaey, "The stabilisation of step-quenched copper-zinc-aluminium martensite, part I: The reverse transformation temperatures ", *Scripta Metall.* **18,** pp. 893-898, 1984.
2. S. Miyazaki, and K. Otsuka, "Development of shape memory alloys", *ISIJ International* **29,** no.5, pp. 353-377, 1989.
3. R. Oshima, and N. Yoshida, "Fatigue of thermoelastic Cu-Zn-Al alloys ", *ICOMAT-82,* pp. 803-808, 1982.
4. M.A. Morris, and T. Lipe, "Microstructural influence of Mn additions on thermoelastic and pseudoelastic properties of Cu-Al-Ni alloys " *Acta Metall* **42,** pp. 1583-1594, 1994.
5. J.S. Lee, and C.M. Wayman, "Grain refinement of Cu-Zn-Al shape memory alloys ", *ICOMAT-86,* pp. 920-925, 1986.
6. K. Adachi, K. Shoji, and Y. Hamada, "Formation of X phases and origin of grain refinement effect in Cu-Al-Ni shape memory alloys added with titanium", *ISIJ International* **29,** pp. 378-387, 1989.
7. Hurtado, P. Ratchev, J. Van Humbeeck, and L. Delaey, "A fundamental study of the x-phase precipitation in CU-Al-Ni-Ti-(Mn) shape memory alloys", *Acta mater.* **44,** pp. 3299-3306, 1996.
8. X. Qi, B. H. Jiang and T. Y. Hsu, "The effect of martensite ordering on shape memory effect in a copper-zinc-aluminium alloy", *Mater. Sci. Engng.* **93,** pp. 205-211,1987.
9. W.H. Zou, C.W.H. Lam, C.Y. Chung, and J.K.L. Lai, "Improvement of the shape memory characteristics of a Cu-Zn-Al alloy with manganese and Zirconium addition", *Scripta Mater.,* in press.

Preparation of new PTCR material
by particle electrification processing

Norio Shinya, Takehiro Dan, Mitsuru Egashira,
Junro Kyono and Hiroshi Fudouzi

National Research Institute for Metals
2-1, Sengen 1-chome, Tsukuba 305, Japan

ABSTRACT

The purpose of the present work is to develop the materials with new functions by combining two kinds of particles electrified reciprocally. This paper reports a preparation method and the positive temperature coefficient of resistivity(PTCR) properties of complex particles consisting of semiconductive $BaTiO_3$ granules and metallic indium powder particles.

The conclusions obtained by the present experiment are as follows.
(1) Vibrating cylindrical electrode can forced-electrify metal, semiconductor and insulator particles positively or negatively.
(2) When the particles electrified reciprocally are mixed in the same region at the same time, complex particles can be created by the electrostatically attractive force working between the two kinds of particles.
(3) Indium-semiconductive $BaTiO_3$ complex particles made by this processing offer the new PTCR material which can be used in arbitrary shapes by filling and packing or drawing and painting.

1. INTRODUCTION

The authors has already proposed the concepts of powder particles assembly for the creation of multi-functional materials in 1994[1] and undertaken the development of fundamental techniques for the preparation of complex particles by a forced electrification processing. The purpose of the present work is to develop the materials with new functions by combining two kinds of particles electrified reciprocally. This paper describes a preparation method and the positive temperature coefficient of resistivity(PTCR) properties of complex particles consisting of semiconductive $BaTiO_3$ particles and metallic indium particles[2].

2. EXPERIMENTALS

Semiconductive $BaTiO_3$ particles used in the present experiment were pressed at the load of 320 kgf/cm^2, heat-treated at 1330℃ for an hour and cooled down at the rate of 110℃/hr. The raw materials were supplied by Mitsui Mining Material Co., Ltd. Metallic In particles of under 20 μm diameter fabricated using the centrifugal spray method were supplied by Mitsuwa Chemical Co., Ltd. Figure 1 shows the morphology of these particles.

An electrification apparatus consists of a cylindrical brass electrode which was 4 mm inside diameter and 21 mm long, a grounded counter-electrode, piezoelectric de-
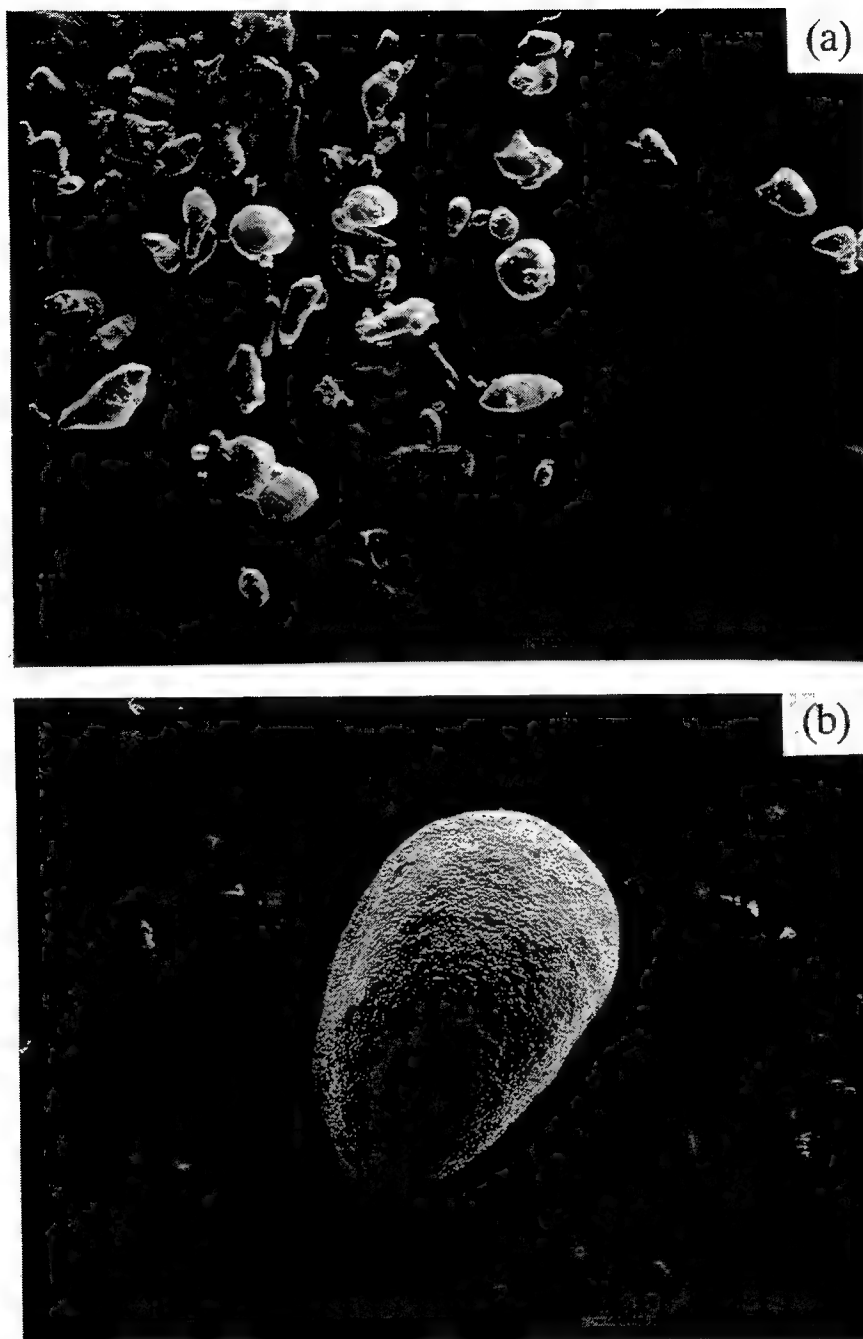
Fig. 1   Scanning electron micrographs of constituent particles.
  (a) metallic indium powder particles.
  (b) semiconductive BaTiO₃ particle.

vices which vibrated the above-mentioned electrode, a high voltage electric source for particle charging and another electric source for the vibration, as shown in Fig. 2. A pair of cylindrical electrodes were prepared for negative and positive charging, respectively.

Electrification processing was carried out as follows. At first two kinds of particles were inserted into the cylindrical electrodes, respectively. The high voltage of direct current was loaded to each electrode positively or negatively, respectively. The electric voltage for vibration of these electrodes was also loaded in order to promote the particles movement. After holding these conditions, the electrode ends were opend at the same time in order to spray the two kind of particles into the same region. They were mixed and combined each other by the electrostatic force.

The determination of charge quantity of particles is described below. A Farady cage, which was electrostatically shielded by a stainless steel mesh with 1.5 mm opening, was located just under the open end of the cylindrical electrode. This mesh prevented gaseous ions from flowing into the cage together with the charged particles. The charge quantity in the Farady cage was measured by a degital electrometer.

The PTCR characteristics of complex particles were measured as follows. The cell for the measurements consisted of alumina tube (1.8 mm inner diameter, 7 mm long), stainless steel rods as electrodes and In foils. The room in the cell was filled with particles to be determined. Figure 3 shows the configuration of this cell. This cell was set in an oven and heated. The resistivity of this cell was measured under a constant electric current by a coulombmeter from the room temperature to near the melting point of metallic indium.
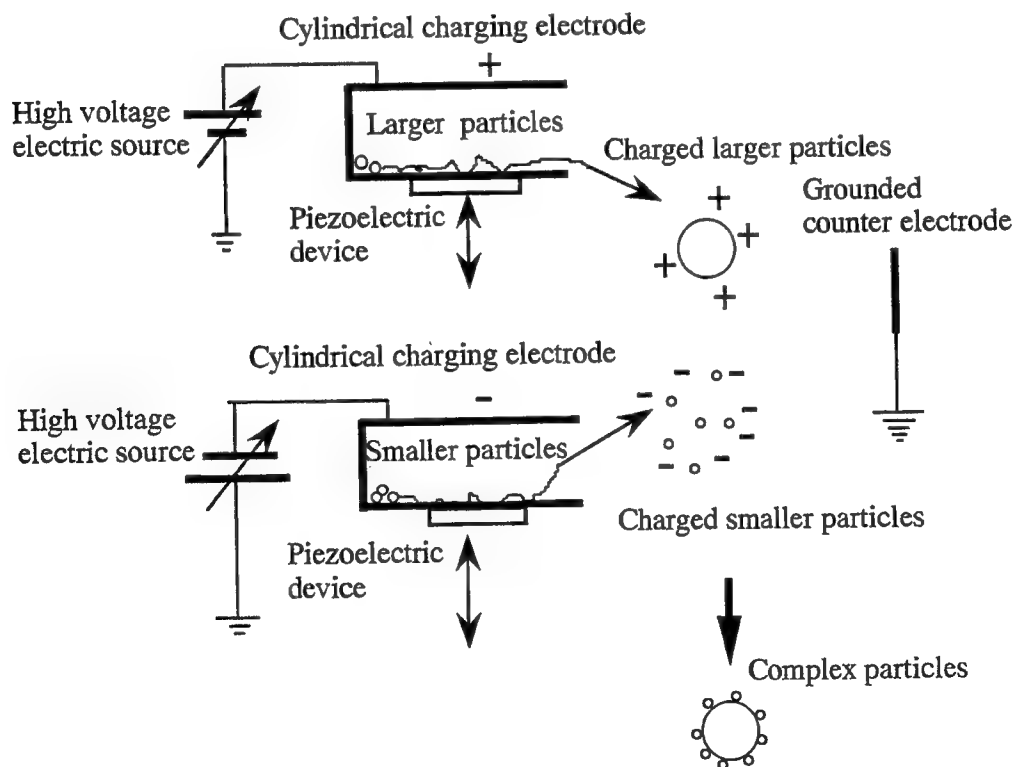
Fig. 2   Schematic diagram of particle electrification apparatus.
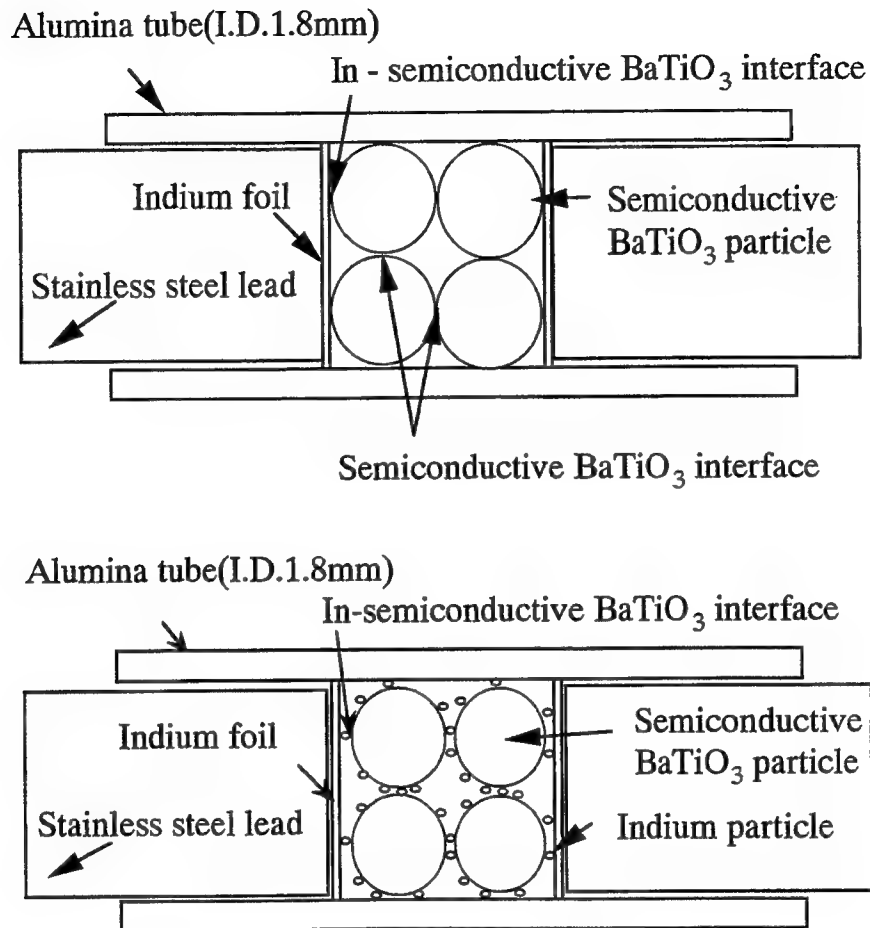
Fig.3   Configuration of the packing cells for PTC
        characteristics measurements.
        Above: A cell filled with semiconductive
                 BaTiO$_3$ particles.
        Below: A cell filled with complex particles

3. EXPERIMENTAL RESULTS AND DISCUSSION

It is very important in the electrification process of particles that the charge quantity of particles is measured precisely. Gold particles, which are stable physically and chemically, were used for the determination of the charge quantity. The diameter of the gold particle was $400\,\mu$m. Figure 4 shows an example of these determinations. A distinguished jump in the charge quantity was observed. Figure 5 summarizes these results, that
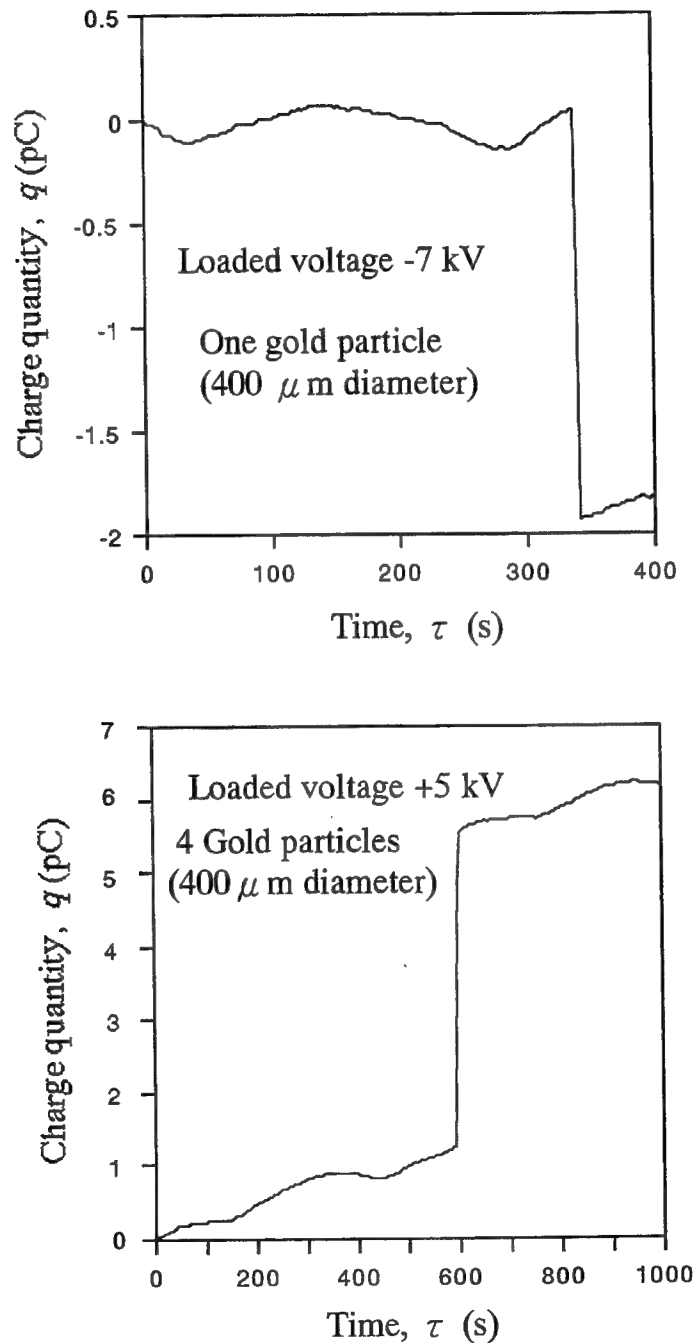
Fig. 4   Examples of charge quantity measurements.

is, the relationship between the charge quantity per particle and the electrostatic field strength. In this figure, a dotted line shows the theoretical relationship between the maximum charge quantity q_i by the induction charging and the electrostatic field strength E.

$$q_i = 1.65 \times 4\pi \varepsilon_0 r^2 E \qquad (1)$$

On the other hand, a solid line indicates that by the corona charging,

$$q_c = 4\pi p \varepsilon_0 r^2 E \qquad (2)$$

where q_c is the maximum charge quantity by corona charging, respectively, ε_0 is the dielectricity in vacuum(8.8541×10^{-12} F/m), r is the radius of particle(m), E is the electrostatic field strength(V/m), p is a constant depending on materials and defined by the relationship

$$p = 2(\varepsilon_s - 1)/(\varepsilon_s + 2) + 1 \qquad (3)$$

ε_s is the specific dielectric constant of the particle. As the particle is conductive in the present case, ε_s becomes ∞. Therefore, p is equal to 3. It is apparent from Fig. 5 that the charge quantity is considerably larger than those theoretical relationships. These results may be ascribed to the concentration of the electrostatic field at the end of the charging electrode. Figure 6 is the contour diagram of electrostatic field strength near the electrode end. β is the field concentration factor and indicates the extent of concentration of electrostatic field strength.
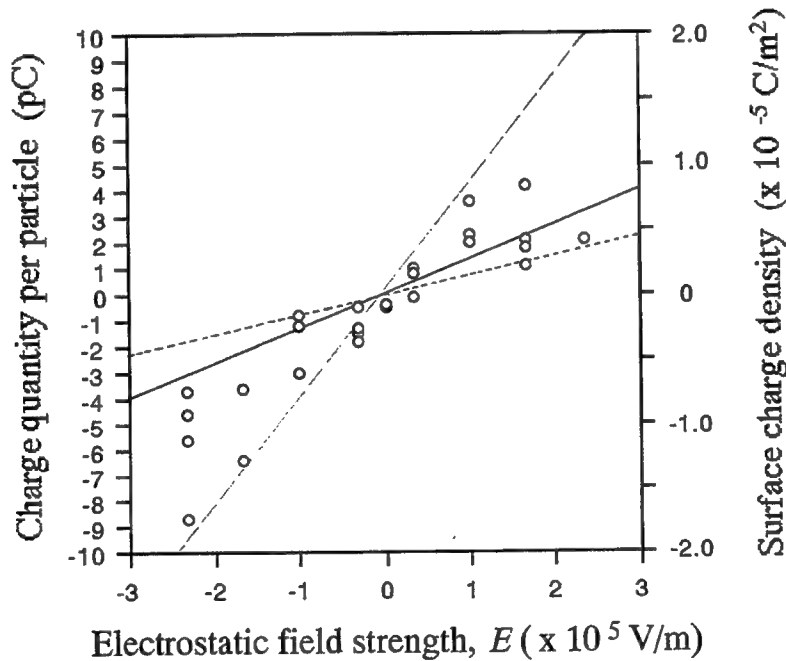
Fig. 5   Relationship between electrostatic field strength and charge quantity per particle or surface charge density.

Calculated relationship (β : field concentration factor)
dotted line: induction charging(β =1).
solid line: corona charging(β =1).
broken line: corona charging(β =3).
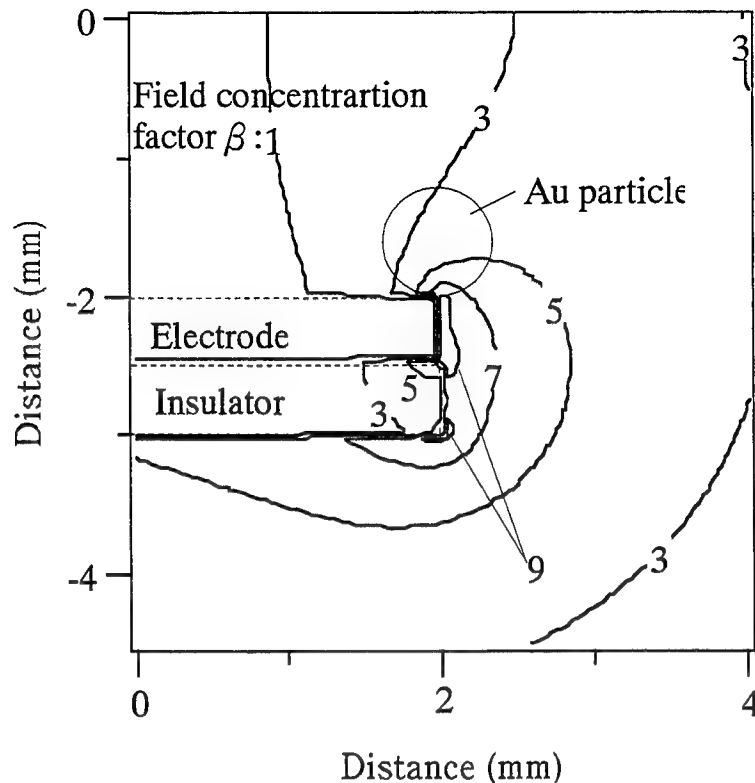
Fig. 6   Contour diagram of the field concentration factor
in the neighborhood of electrode.

A scanning electron microscopic images of the complex particles which were created by use of this forced electrification apparatus(±4 kV, 30 min) is shown in Fig. 7. It shows that the morphology of the complex particles does not depend on the polarity of constituent particles during the processing. Figure 8 shows the surface of particles. It is apparent that metallic In particles are attached to the surface of semiconductive $BaTiO_3$ particles dispersively or discontinuously by the coulomb's force.

Figure 9(a) shows the PTCR characteristics of the complex particles cell as described above. On the otherhand, those of the only semiconductive $BaTiO_3$ particles cell are shown in Fig. 9(b). It is definite that the electric resistivity of the complex particles cell is smaller than that of the only semiconductive $BaTiO_3$ particles cell at the room temperature. These results are ascribed to the low resistivity of metallic In particles between semiconductive $BaTiO_3$ particles and a good ohmic contact between In and semiconductive $BaTiO_3$. This material can be used in arbitrary shapes and forms, different from traditional PTC materials which were sintered rigidly.

4. CONCLUSIONS

In order to confirm the fundamental techniques of particles assembly, a forced electrification apparatus with vibrating cylindrical electrodes was introduced. By use of this apparatus, the charging behavior of the several kinds of particles was observed. The results obtained are as follows.
(1) The forced electrification apparatus electrified several kinds of particles, metals, semiconductors and insulators, positively or negatively.
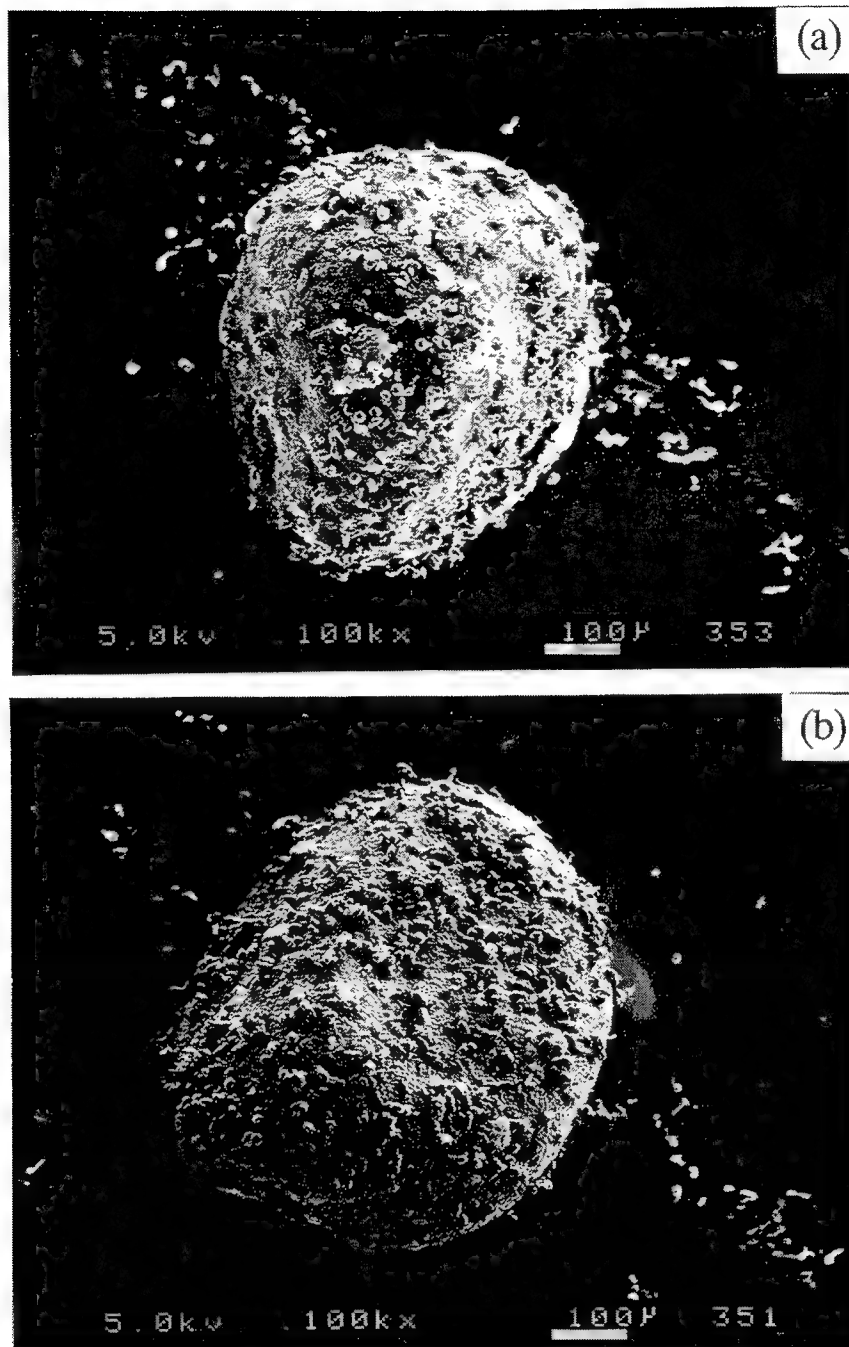
Fig. 7   Scanning electron micrographs of complex particles.
        (a) In(−)-semiconductive BaTiO₃(+) complex particle.
        (b) In(+)-semiconductive BaTiO₃(−) complex particle.
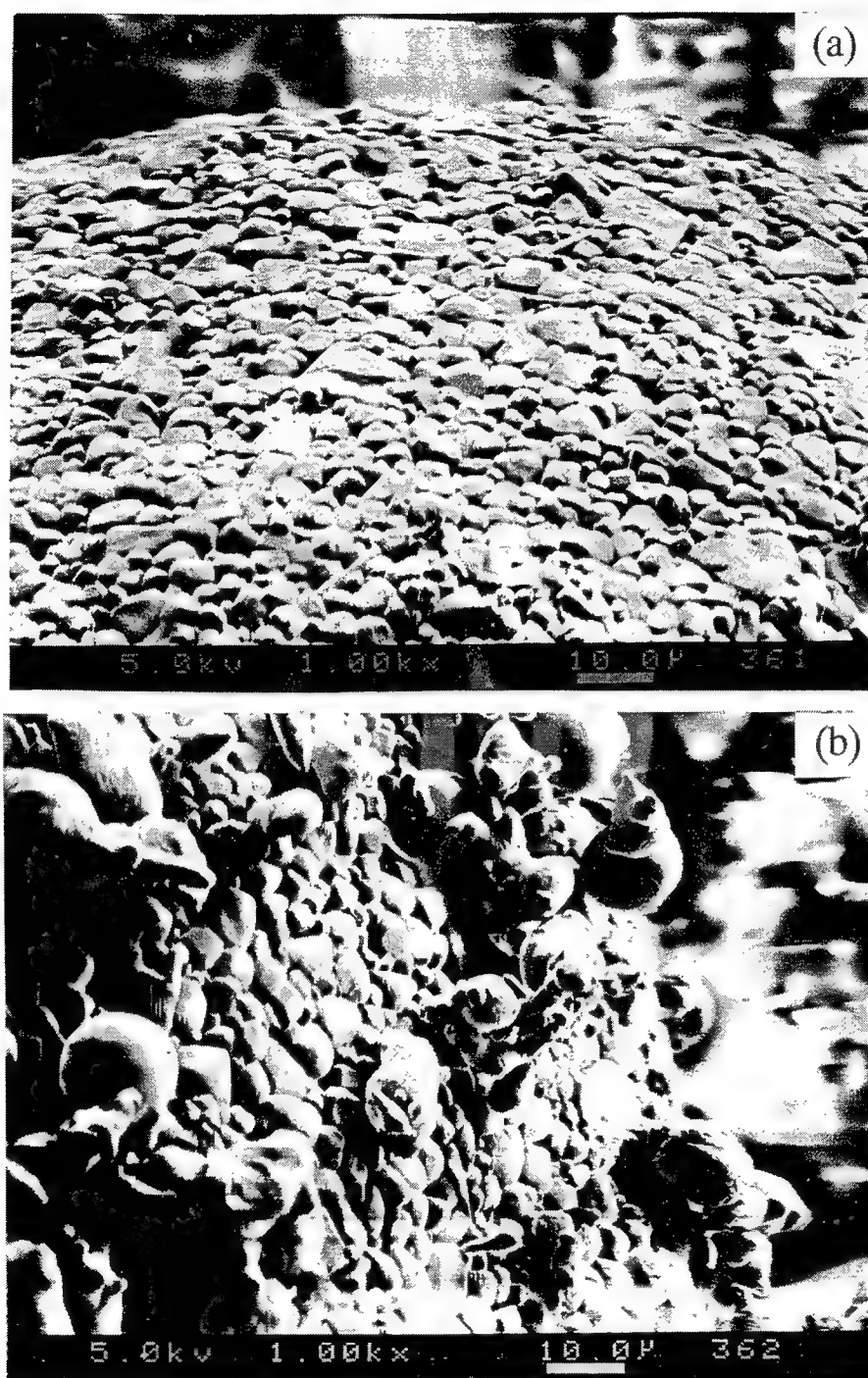
Fig. 8　Scanning electron micrographs of the particle surface.
　　　(a) semiconductive BaTiO₃ particle.
　　　(b) In-semiconductive BaTiO₃ complex particle.
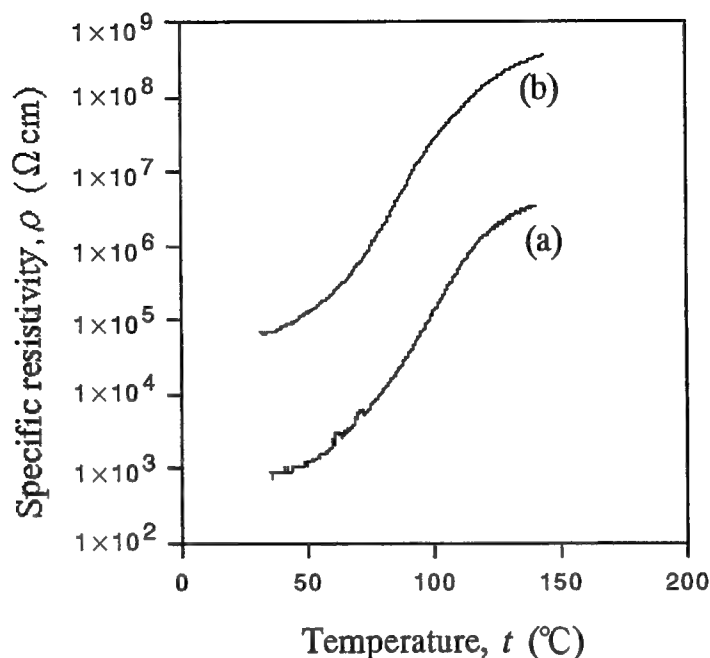
Fig. 9 PTC characteristics of the particles packing cells.
(a) In-semiconductive BaTiO₃ complex particles.
(b) semiconductive BaTiO₃ particles.

(2) In consideration of the effective electrostatic field strength, the charge quantity per particle is estimated theoretically.
(3) By means of such a forced electrification processing complex particles were prepared. This complex particle consists of semiconductive BaTiO3 particle as the core and metallic In particles which were adhered to the surface of the core particle dispersively and discontinuousdly.
(4) Agglomeration consisting of such complex particles can be used as PTC materials.
(5) This PTC material can be used in arbitrary forms and shapes, different from traditional PTC materials.

REFERENCES

1. N. Shinya, M. Egashira and H. Fudouzi: Powder Particles Assembly Using Electron Beam for Creation of Multi-Functional Materials, Proc. of the 2nd International Conference on Intelligent Materials, 1142-1151, Technomic Publishing Co. Inc., 1994.
2. T. Dan, M. Egashira, J. Kyono, H. Fudoji and N. Shinya: Preparation of New PTCR Material by Particle Electrification Processing, Extended Abstracts of the 5th Symposium on Intelligent Materials & UK-JAPAN Seminar on Intelligent Materials, 47-49, Soc. of Non-Traditional Technology Intelligent Materials Forum, 1996.

SESSION 2

Thermomechanical Systems: Switches II

Design of materials with extreme thermal expansion using a three-phase topology optimization method

O. Sigmund and S. Torquato

Princeton Materials Institute and Department of Civil Engineering and Operations Research, Princeton University, Princeton, New Jersey, 08540

ABSTRACT

We show how composites with extremal or unusual thermal expansion coefficients can be designed using a numerical topology optimization method. The composites are composed of two different material phases and void. The optimization method is illustrated by designing materials having maximum thermal expansion, zero thermal expansion, and negative thermal expansion. Assuming linear elasticity, it is shown that materials with effective negative thermal expansion coefficients can be obtained by mixing two phases with positive thermal expansion coefficients and void. We also show that there is no mechanistic relationshipbetween negative thermal expansion and negative Poisson's ratio.

1. INTRODUCTION

In light of the manifest technological importance of determining the effective properties of composite materials, an enormous body of literature has evolved based upon direct measurement, empirical relations, and approximate as well as rigorous theoretical methods.[1-5] Of particular interest is the "reverse engineering" problem of specifying the desired properties that one would like the material to be endowed with and then going about finding the appropriate material (or materials) and material structure that will achieve the desired properties. Such a study clearly cannot be carried out experimentally because of the enormous number of variables that are involved. Here we describe a systematic procedure to design composite materials with exotic thermal-expansion behavior. Materials with extreme or unusual thermal expansion behavior are of interest from both a technological and fundamental standpoint. Of particular practical interest are materials with zero thermal expansion, maximum thermal expansion or force, and negative (i.e., minimum) thermal expansion.

Zero-thermal-expansion materials are needed for use in structures subject to temperature changes such as space structures, bridges and piping systems. Materials with maximum unidirectional thermal displacement or force can be employed as ``thermal" actuators. A fastener made of a negative thermal expansion coefficient material, upon heating, can be inserted easily into a hole. When cooled down, it will expand, fitting tightly into the hole and upon heating can be easily removed.

A negative thermal expansion material has the counterintuitive property of contracting upon heating. There are existing materials with negative expansion coefficients. Glasses in the titania-silica family have *isotropic* negative expansion coefficients at room temperature.[6] At very low temperatures (<100 K), silicon and germanium[7] as well as $Bi_{2.2}$ $Sr_{1.8}CaCu_2O_x$ superconductor single crystals[8] have negative expansion coefficients. Materials with *directional* negative expansion coefficients at room temperature include Kevlar, carbon fibers, plastically deformed (anisotropic) Invar (Fe-Ni alloys)[9] and certain molecular crystalline networks.[10] The negative expansion mechanism of these molecular-level networks is based on un-twisting of helical chains; but currently these materials cannot be made in extended form.

The purpose of this paper is to review some recent work of ours on composites with extremal thermal expansion behavior first described in a brief report[11] and subsequently elaborated upon in detailed paper.[12]

2. TOPOLOGY OPTIMIZATION PROCEDURE

We use a topology optimization procedure [11, 12] to determine the distribution of two different bulk material phases and a void phase in order to design composites with extremal or unusual thermal expansion behavior. Three phases are used (as opposed to two phases) since one can achieve composite properties beyond those of the individual components.[13] Microstructural variation is limited to one length scale in a unit cell as this is most easily manufacturable. An interesting question arising from the work of Baughman and Galvão [10] is whether there is a mechanistic relationship between negative thermal expansion and negative Poisson's ratio? Negative Poisson's ratio materials expand laterally when pulled axially and can be made by processing foams with rentrant (non-convex) cells Lakes.[14] We will show that isotropic materials with *negative* thermal expansion coefficients and *positive* Poisson's ratios exist, and can be made by mixing two phases with positive thermal expansion coefficients and void. We first describe briefly the optimization procedure and then present results for specific design examples.

Assuming two-dimensional linear elasticity, perfect bonding between the material phases, uniform temperature distribution and constant isotropic material properties, thermoelastic behavior of materials can be described by the constitutive relations

$$\sigma = C[\varepsilon - \alpha \Delta T] = C\varepsilon - \beta \Delta T \tag{1}$$

$$\text{where} \quad C = \frac{E}{1 - v^2} \begin{pmatrix} 1 & v & 0 \\ v & 1 & 0 \\ 0 & 0 & \frac{1-v}{2} \end{pmatrix}, \tag{2}$$

σ and ε are the stress and strain tensors, E and v are the Young's modulus and Poisson's ratio of the considered material and ΔT is the temperature change. The thermal strain tensor α is the resulting strain of a material allowed to expand freely, whereas the thermal stress tensor $\beta = C\alpha$ is the stress per degree Kelvin in the material constrained not to expand. For the three-phase composite of interest, relation (1) is valid on a local scale (with subscripts 0, 1, and 2 appended to the thereoelastic properties) and the macroscopic scale (with subscript * appended to the properties). In the latter case, the stresses and strains are averages over local stresses and strains, respectively.

The topology optimization procedure proposed here essentially follows the steps of conventional procedures.[15, 16] The design domain is the periodic base cell and is initialized by discretizing it into 3600 finite elements. The problem consists in finding the optimal distribution of the two base materials and void, such that the objective function is minimized. The objective function can be any combination of the individual components of the effective thermal strain and stress tensors $(\alpha_*)_{ij}$ and $(\beta_*)_{ij}$, with constraints on the bulk modulus and symmetry, i.e.,

$$\begin{aligned}
&\textit{Optimize} : \text{Combination of } (\alpha_*)_{ij} \text{ or } (\beta_*)_{ij}, \\
\\
&\textit{Variables} : \text{Distribution of two material phases} \\
&\qquad\qquad\quad \text{and void in the periodic base cell}, \\
\\
&\textit{Subject to} : \text{Constraints on volume fractions } c_i, \\
&\qquad\qquad\quad : \text{Symmetry constraints}, \\
&\qquad\qquad\quad : \text{Lower bound on bulk modulus } k_* \text{ or} \\
&\qquad\qquad\quad \text{Young's modulus } E_* .
\end{aligned} \tag{3}$$

The optimization procedure solves a sequence of finite element problems followed by changes in material type (density) of each of the finite elements, based on sensitivities of the objective function and constraints with respect to design changes. In contrast to conventional procedures, we use an "artificial" material model [17,18,] i.e., properties in a given element are some fraction of solid material properties.

3. DESIGN EXAMPLES

To benchmark the optimization algorithm, we first check to see how close we can approach newly developed rigorous upper and lower bounds on the effective isotropic thermal coefficients α_* and β_* for three-phase composites obtained by Gibiansky and Torquato [19]. The material data for the phases are chosen as $E_2/E_1 = 1$, $\nu_1 = \nu_2 = 0.3$, $\alpha_2/\alpha_1 = 10$, $c_0 = 0.5$ and $c_1 = c_2 = 0.25$. For computational reasons, the void phase is given a small stiffness, $E_0/E_1 = 10^{-4}$, which, however, does not have significant structural effect. *Note that the volume fractions c_i are held fixed for this hypothetical composite, to allow for comparison with the bounds and for easy interpretation of the results.* The bounds on α_* are most naturally expressed in terms of the effective bulk modulus $k_* = E_*/2(1+\nu_*)$.

We consider the following four *hypothetical* design examples constrained to be elastically isotropic:

(a) Minimization of the *isotropic* thermal strain coefficient α_*/α_1 with a lower bound constraint on the effective bulk modulus given as 10% of the theoretically attainable bulk modulus, i.e. $k_*/k_1 = 0.0258$. Horizontal geometric symmetry is specified.

(b) Minimization of the isotropic thermal strain coefficient α_*/α_1 with lower bound constraint on effective bulk modulus given as 10% of the theoretically attainable bulk modulus. Four-fold geometric symmetry is specified.

(c) Maximization of the effective bulk modulus k_*/k_1 for fixed zero thermal expansion ($\alpha_*/\alpha_1 = 0$). Horizontal reflection symmetry is specified.

(d) Maximization of isotropic thermal stress coefficient β_*/β_1. Four-fold symmetry is specified.

Three by three arrays of the resulting optimal base-cell topologies are shown in Figs. 1 and 2; their associated effective properties are given in Ref. 12. The solutions obtained by the design procedure turn out to be very close to the new bounds, thus validating the numerical procedure. One can get even closer to the bounds using finer discretizations; however, this has not been done for computing-time reasons. Note that extreme values of the thermal strain coefficients are only possible for low bulk moduli. If we simply tried to minimize (or maximize) the thermal strain α_*, we would end up with a *very weak* material. Therefore, there is a tradeoff between extremizing thermal strain coefficients on the one hand and ending up with a stiff material on the other.

The actual mechanisms behind the extreme thermal expansion coefficients of the materialstructure can be difficult to understand. To visualize one of the mechanisms, the (exaggerated) displacements, due to an increase in temperature of the microstructure in Fig. 1, is shown in Fig. 3. Studying Fig. 3, we note that there appears to be contact between parts of the microstructure. This contact is only due to the magnification of the displacements used in the illustration. The simple linear modelling used here can not take such problems into account. Nevertheless, it would be interesting to extend the analysis to include non-linear behavior including contact, which would open up for a whole new world of interesting design possibilities. We will leave these extensions to future studies.

When allowing low bulk moduli [as in examples (a) and (b)], the main mechanism behind the extreme (negative) thermal expansion is the *reentrant cell structure* having bimaterial components which bend and cause large deformation when heated. The bimaterial interfaces of design examples (a) and (b) bend and make the cell contract, similar to the behavior of negative Poisson's ratio materials[14]. If a higher effective bulk modulus is specified, as in example (c), the intricate bi-material mechanisms are less pronounced resulting in a less extreme expansion ($\alpha_* = 0$). Finally, maximizing the expansive stress, as in example (d), results in a structure without bimaterial mechanisms, where the high expansion phase (cross hatched phase) is arranged such that it maximizes the horizontal and vertical expansion.

Design examples (a) and (b) in Fig. 1 demonstrate how two, topologically, very different microstructures can have (almost) the same value of the objective function. The only difference between the two examples is the specified geometric symmetry.

To design real new materials with extreme thermal expansion, the two base materials should be of similar stiffness but widely differing thermal expansions. Two materials fulfilling this requirement are *isotropic* Invar (Fe-36%Ni) and nickel,

which have Young's moduli of 150 GPa and 200 GPa, respectively, thermal expansion coefficients of 0.8 μ m / (mK) and 13.4 μ m/($m\ K$), and Poisson's ratios of 0.31 for both. In Refs. 11 and 12 we considered the following design examples:

(e) : minimization of the *isotropic* thermal stress coefficient β_* and horizontal reflection symmetry;

(f) : minimzation of the *vertical* thermal stress $(E_*)_2(\alpha_*)_{22}$ and horizontal and vertical reflection symmetry; and

(g) : maximization of the *vertical* strain $(\alpha_*)_{22}$ with the constraint on the vertical Young's modulus $(E_*)_{22}\ 5 \geq$ GPa and horizontal   and vertical reflection symmetry.

For examples (e)-(g), *the phase volume fractions c_i are unconstrained*, allowing for a wider range of minimum and maximum values.

The resulting optimal topologies are shown in Refs. 11 and 12 and the corresponding effective properties are listed in Table I. As the optimal structures of design examples (f) and (g) are anisotropic, Table I lists two numbers: for α_*, E_* and β_* these are the associated horizontal and vertical components, respectively, and for ν_* these are the components $(\nu_{12})_*$ and $(\nu_{21})_*$.[12]

To overcome the positive thermal expansion of other surrounding materials, we seek to maximize the *contraction force*, i.e., minimize β_* as in example (e). The *isotropic* vertical contraction stress (per degree Kelvin) of example (e) is $E_*\ \alpha_* =$ 73.6kPa/K. Relaxing the isotropy requirement, as in example (f), reduces this *directional* value to $(E_*)_2(\alpha_*)_{22} = -137.7$kPa/K. If *maximum* expansion stress is desired, the best choice is to use solid nickel material in all cases.

The isotropic negative thermal expansion materials in examples (a), (b) and (e) both have positive Poisson's ratios (0.52 and 0.06, respectively), *showing that there is no mechanistic relationship between negative thermal expansion and negative Poisson's ratio*. In example (g) we see again that anisotropy can lead to very high *directional* expansion coefficients. The vertical coefficient of $(\alpha_*)_{22}$ of example (g) is 2.6 times higher than for solid nickel, but at the cost of a low vertical Young's modulus. (2.5% of nickel).

4. DISCUSSION

We have proposed a method to design material microstructures with extreme thermoelastic properties. The optimization procedure has been shown to be very accurate in producing the optimal microstructures. Our obtained values are quite close to the Gibiansky-Torquato bounds, which are the best available rigorous bounds, thus validing the optimization procedure. We have shown that extreme thermal expansion behavior can be obtained but at the cost of a low bulk modulus. Therefore, there is a tradeoff between extremizing thermal strain coefficients on the one hand and ending up with a stiff material on the other. We have also shown that extreme directional thermal expansion can be obtained by allowing anisotropy of the composites.

In practice, how can our optimally designed materials be manufactured? They may be fabricated with cell sizes down to 10-50 microns using surface micromachining techniques as seen for materials with negative Poisson's ratios in Larsen, Sigmund and Bouwstra[20] or stereolithography techniques.[21] Furthermore, it will be interesting to examine whether the lessons learned from this continuum analyses can be exploited to optimally design and synthesis of materials at the molecular level (e.g. Baughman and Galvão.[10]

Finally, we note that the method is applicable to design of smart materials (piezoelectric or shape-memory-alloy inclusions). We are in the process of applying the topology optimization method to find the three-dimensional structures that optimize the piezoelectric properties of the material for use as actuators or sensors.[21] The extension to three dimensions is straight forward, but computer time will increase dramatically.

TABLE I. Thermoelastic parameters for optimal microstructures made of Invar (phase 1) and nickel (phase 2). Note that for the isotropic example (e), $\beta_* = E_*\alpha_*/1 - \nu_*\} = 2k_*\alpha_*$.

Material	α_* $\mu\ m/(mK)$	E_* GPa	ν_*	β_* kPa/K	c_1/c_2
Invar	0.8	150	0.31	174	1/0
Nickel	13.4	200	0.31	3884	0/1
e	-4.97	14.8	0.055	-77.6	0.60/0.28
f	5.42/-4.68	69.9/29.5	0.059/0.025	372/-129	0.60/0.30
g	23.4/35.0	1.09/5.00	-.135/-.621	2.01/174	0.38/0.46

ACKNOWLEDGMENTS

REFERENCES

1. M. J. Beran, *Statistical Continuum Theories*, (Wiley, New York, 1968).

2. R. M. Christensen, *Mechanics of Composite Materials*, (Wiley, New York, 1979).

3. G. W. Milton and N. Phan-Thien, Proc. R. Soc. Lond. A **380**, 305 (1982).

4. Z. Hashin, J. Appl. Mech. **50**, 481 (1983).

5. S. Torquato, Appl. Mech. Rev., **44**, 37 (1991).

6. P. C. Schultz and H. T. Smyth, in Amorphous Materials (Eds. R. Douglas and B. Ellis, Wiley, New York, 1970).

7. H.-M. Kagaya and T. Soma, Solid State Commun. **85**, 617 (1993).

8. Z. J. Yang *et~al.*, J. of Superconductivity **8**, 233 (1995).

9. G. Hausch, R. Bächer, and J. Hartmann, Physica B **161**, 22 (1989).

10. R. H. Baughman and D. S. Galvão, Nature **365**, 735 (1993).

11. O. Sigmund and S. Torquato, Appl. Phys. Lett. **69**, 3203 (1996).

12. O. Sigmund and S. Torquato, J. Mech. Phys. Solids, in press.

13. R. Lakes, private communication.

14. R. Lakes, Science **235**, 1038 (1987).

15. M. P. Bendsøe and N. Kikuchi, Comp. Meth. Appl. Mech. Eng. **71**, 197 (1988).

16. M. P. Bendsøe, *Methods for the optimization of structural topology*, Springer, Berlin, (1995).

17. O. Sigmund, Ph.D. thesis, Technical University of Denmark, Department of Solid Mechanics, 1994.

18. O. Sigmund, Int. J. Solids Structures **31**, 2313 (1994).

19. L. V. Gibiansky and S. Torquato, J. Mech. Phys. Solids, in press.

20. U. D. Larsen, O. Sigmund, and S. Bouwstra, in *IEEE, International Workshop on Micro Electro Mechanical Systems MEMS-96}* (1996)

21. O. Sigmund, S. Torquato and I. A. Aksay, in preparation.

Further author information -

O.S.: Present and permanent address: Dept. of Solid Mechanics, Technical University of Denmark, DK-2800, Lyngby, Denmark.
E-mail: sigmund@fam.dtu.dk

S.T.: E-mail: torquato@matter.princeton.edu
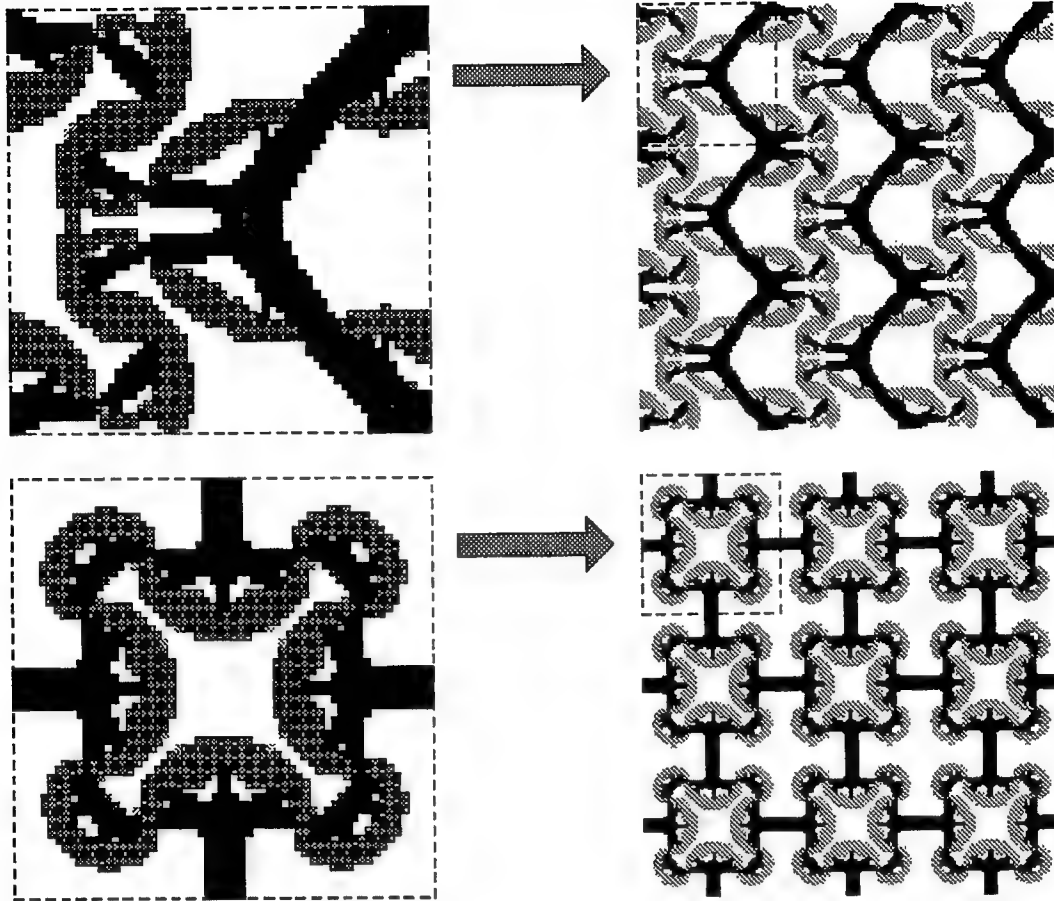
FIG. 1. Optimal microstructures for minimization of effective thermal strain coefficient for design examples **(a)** (top) and **(b)** (bottom). The white regions denote void (phase 0), the filled regions consist of low expansion material (phase 1) and the cross-hatched regions consist of high expansion material (phase 2).
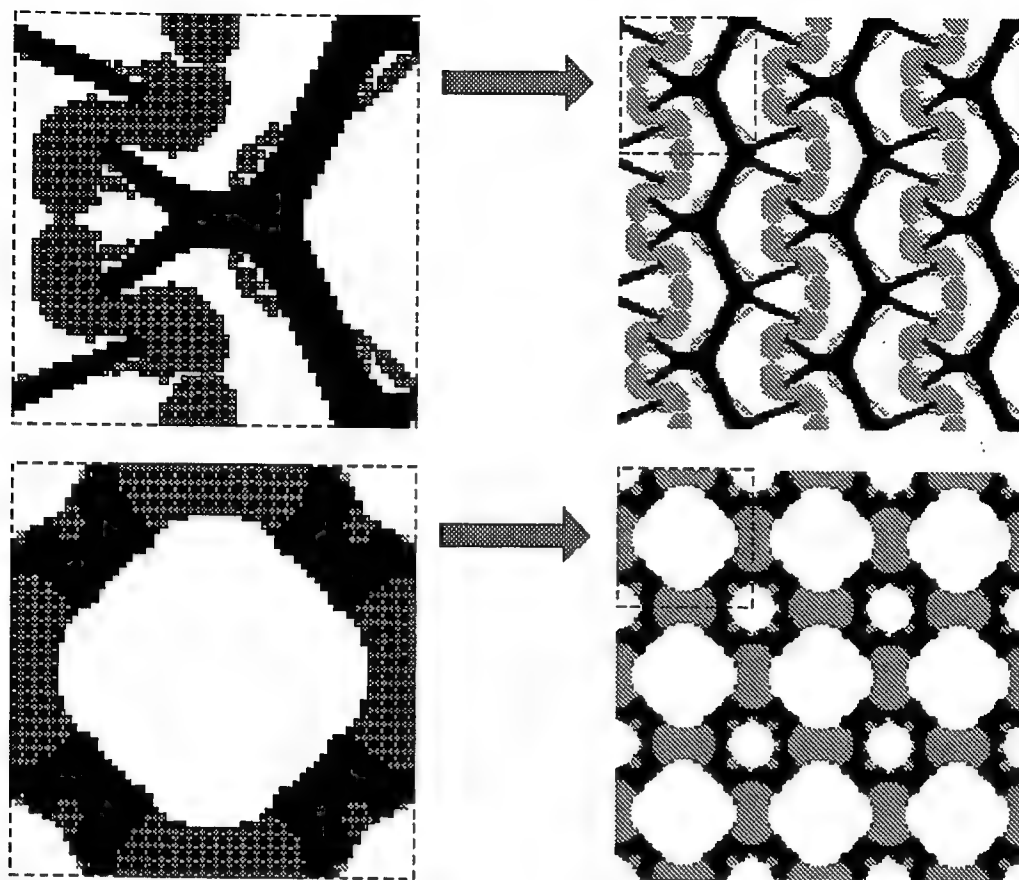
FIG. 2. Optimal microstructures for maximization of bulk modulus with zero thermal expansion for design example **(c)** (top) and maximization of effective thermal stress coefficient for design example **(d)** (bottom). The white regions denote void (phase 0), the filled regions consist of low expansion material (phase 1) and the cross-hatched regions consist of high expansion material (phase 2).
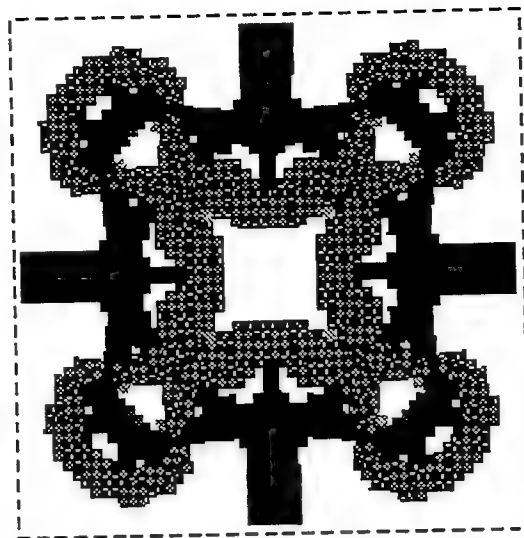
FIG. 3. Thermal displacement of microstructure in Fig. 1 (bottom).

Fiber optic switching devices constructed from thermally stable materials

A. Paige Clifton Furrow[1], Jennifer Grace[2], Jonathan Greene[1], Dr. Kent A. Murphy[3], and
Dr. Richard O. Claus[3]

[1]F&S Inc., Blacksburg, VA 24062
[2]has since moved to U.S. Precision Lens, Cincinnati, OH
[3]Fiber & Electro-Optics Research Center, Bradley Department of Electrical Engineering,
Virginia Tech, Blacksburg, VA 24061

ABSTRACT

In the past, optical fiber switches have typically been constructed from plastics or
ceramics. However, the inability of these materials to operate effectively at high
temperatures has greatly restricted the utilization of these devices. Recently, fiber optic
switches have been manufactured from two thermally stable materials: carbon-carbon and
BS50, a high temperature ceramic. The integration of these dimensionally stable materials
into the fabrication of the optical switch will allow the switch to be utilized in an
increased number of applications including optics, aerospace, mechanical, medical, and
electronics. Preliminary testing included examining these new optical switches for
structural damage due to the manufacturing process and testing the switches to
demonstrate that the fibers could be realigned after processing. The tests concluded that
no structural damage was induced, and the critical fiber realignment was achieved.

1. INTRODUCTION

Optical switches are primarily recognized for their use in communication systems.
Efficient switches must possess desirable optical properties such as small light reflection,
low insertion loss, and low optical crosstalk. The switches should also have low power
consumption and should be compact and inexpensive.[1] Numerous switches are available
which possess these characteristics. However, many feasible applications are unable to
take advantage of optical switches because the switches are unable to withstand certain
environmental conditions, such as large temperature fluctuations which result in fiber
misalignments. For example the thermal expansion of typical ceramics and plastics is .5 x
10^{-6} to 13.5 x 10^{-6} ($°C^{-1}$) and 50 x 10^{-6} to 220 x 10^{-6} ($°C^{-1}$) respectively. Therefore, for
the further integration of optical fiber switches into civilian and military infrastructure, it
is necessary to demonstrate higher performance levels over environmental conditions.
One specific example where this is true is flight-worthy applications. The optical fiber

components used in these systems need to be rugged and provide consistent performance despite being subjected to a wide range of temperatures.

Optical fiber switches are especially critical components because they form the basis of optical fiber distribution networks. These devices need to maintain accurate fiber alignment over extended lifetimes while performing optical fiber switching and alignment with millisecond response times. Optical switch technology would benefit substantially if they were constructed from thermally stable materials. The critical alignment that is maintained between multiple fibers is severely limited due to thermal expansion of the alignment ferrules, and this problem has limited the applications of switch devices in the past.

Recently, optical fiber switches have been constructed using two types of thermally stable materials, graphite and BS50 ceramic. The thermal expansion of both of these materials is <1 x 10^{-6} ($°C^{-1}$). The thermal expansion of BS50 is also tailorable to fit specific applications. Research shows that these new switches possess both desirable optical characteristics and dimensional stability. There is no evidence of damage due to the manufacturing process, and critical fiber alignment is maintained after material processing.

2.EXPERIMENTAL

2.1 Materials

Two different thermally stable filler materials were mixed with a polyimide matrix to form the fiber optic switches. The fillers were natural graphite flakes #2 (120 - 150 μm in diameter) supplied by Dixon Corporation and BS50 (an NZP ceramic) supplied by LoTEC, Incorporated. The matrix resin was LaRC^{TM}-SI (2% offset), furnished by Imitec, Incorporated. The solvent N-methyl-pyrrolidinone (NMP) was provided by Aldrich Chemical Company. All materials were used as received.

2.2.1 Coating Process

A predetermined amount of LaRC^{TM}-SI was dissolved in NMP at room temperature to form two solutions. The graphite and BS50 dry filler particles were each added to a solution to form a thick paste. The mixtures contained 5% (w) and 10% (w) LaRC^{TM}-SI respectively. The mixtures were placed in a vacuum oven at 260°C and the solvent was removed. The mixtures were then ground into fine particles of useable material.

2.2.2 Switch Manufacturing Process

A specific amount of each powder was measured and placed in a rectangular stainless steel mold. Two ceramic fiber ferrules (either singlemode or multimode) were embedded in the powder as shown in Figure 1. The mold was placed in a press where it experienced a pressure of 12,000 psi at 300°C for one hour. The mold was allowed to cool to 150°C; then the consolidated piece was removed from the mold. The consolidated parts are referred to as microcomposites. The photographs in Figure 2 illustrate the microcomposite manufacturing process. Following consolidation, the microcomposites were cut lengthwise along their centerline using an Ecomet automated diamond saw. An alignment pin was placed in one ferrule and an optical fiber was placed in the remaining ferrule. In this configuration, one of the halves remains fixed, and the other rotates about the pin to obtain the desired alignment. Figure 3 illustrates this optical switch arrangement.

3. TESTING AND PERFORMANCE OF THE OPTICAL SWITCHING DEVICE

The desired performance of the microcomposite optical switch is a function of its robustness and ability to realign properly following the manufacturing process. Both factors were thoroughly researched after processing. The integrity of the microcomposite optical switch was investigated using an optical microscope. The surfaces, primarily the cut edges, were carefully examined for microcracking and voids. The embedded fiber ferrules were scrutinized for cracking which could have resulted from the large amount of pressure applied during processing. Microscopic observations showed that the pieces were well consolidated with no cracks or voids, and the fiber ferrules maintained their original structure and strength.

The ability of the of the two switch halves to be realigned properly after processing and cutting was tested by transmitting light through linked optical fibers and modulating one half of the optical switch using a piezoelectric-based actuator, THUNDER™. The THUNDER™ actuator was mounted perpendicular to one of the microcomposite switch halves and positioned so that it contacted the edge of the microcomposite as shown in Figure 4. The microcomposite switch linked two multimode fibers through which light was being transmitted to an optical detector when the fibers were aligned. The detector was connected to an oscilloscope so that the optical throughput could be monitored during the test as shown in Figure 5. Figure 6 shows data obtained from modulating the THUNDER™ actuator at approximately 1 Hz. The top line is the sinusoidal signal driving the THUNDER™ wafer, and the bottom line shows the monitored optical signal as the switch is modulated through the off and on states, respectively. This verifies that the switch can be realigned properly after manufacturing.

Embedded ceramic ferrules
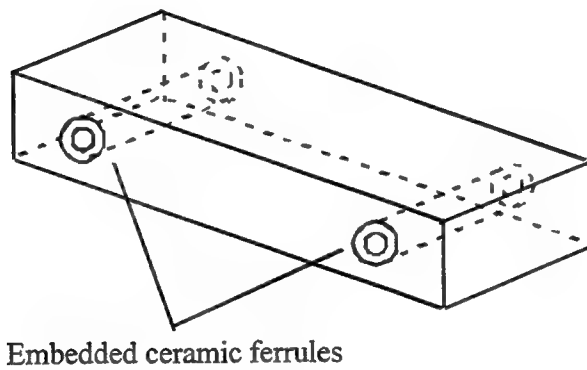
Figure 1. Position of embedded ceramic ferrules in the powder.
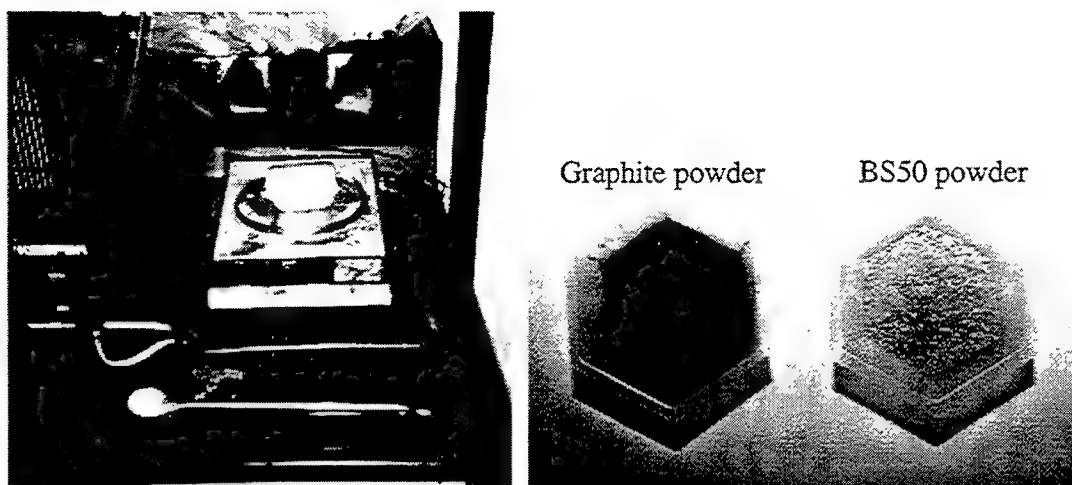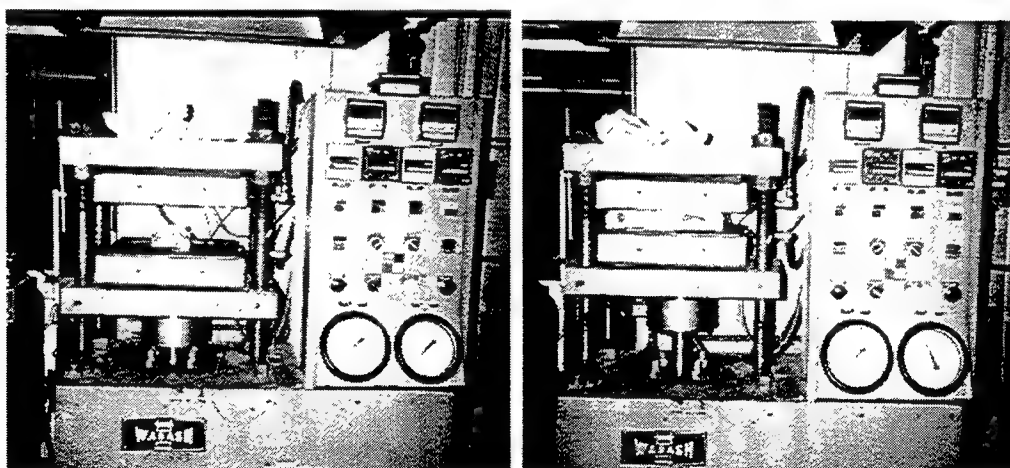
Figure 2. Microcomposite manufacturing process: (a) BS50 or graphite powder mixed with LaRC™-SI is weighed, and (b) is placed in a microcomposite mold, then (c) the mold is placed under 12,000 psi at 300°C
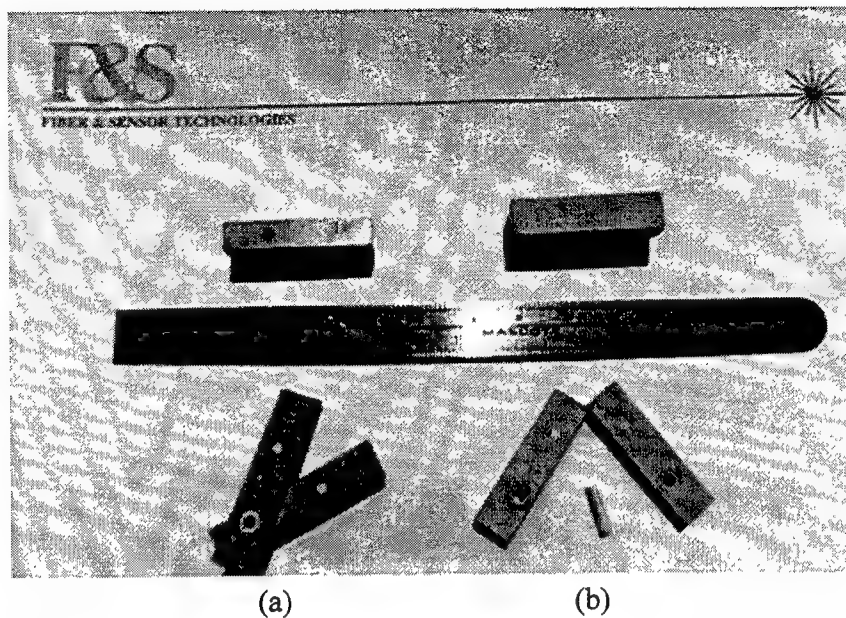
Figure 3. Microcomposite optical fiber switches: (a) graphite with 10% LaRC$^{\text{TM}}$-SI (b) BS50 ceramic with 10% LaRC$^{\text{TM}}$-SI.
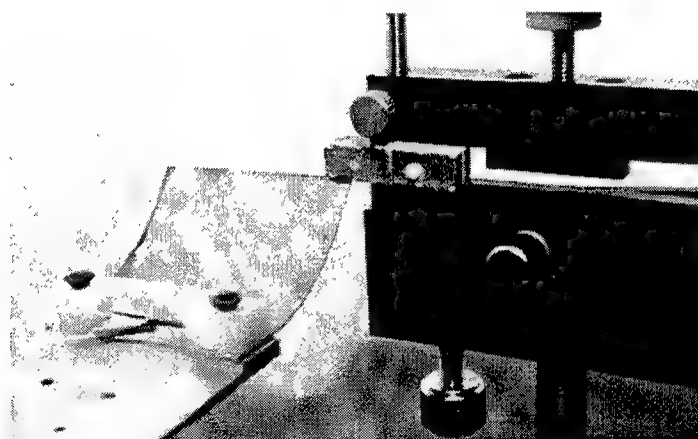
Figure 4. Microcomposite optical fiber switch with THUNDER$^{\text{TM}}$ actuator.
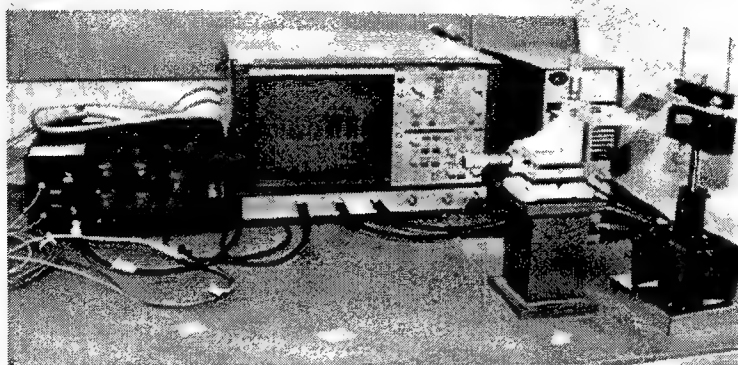
Figure 5. Experimental set-up for switch test.
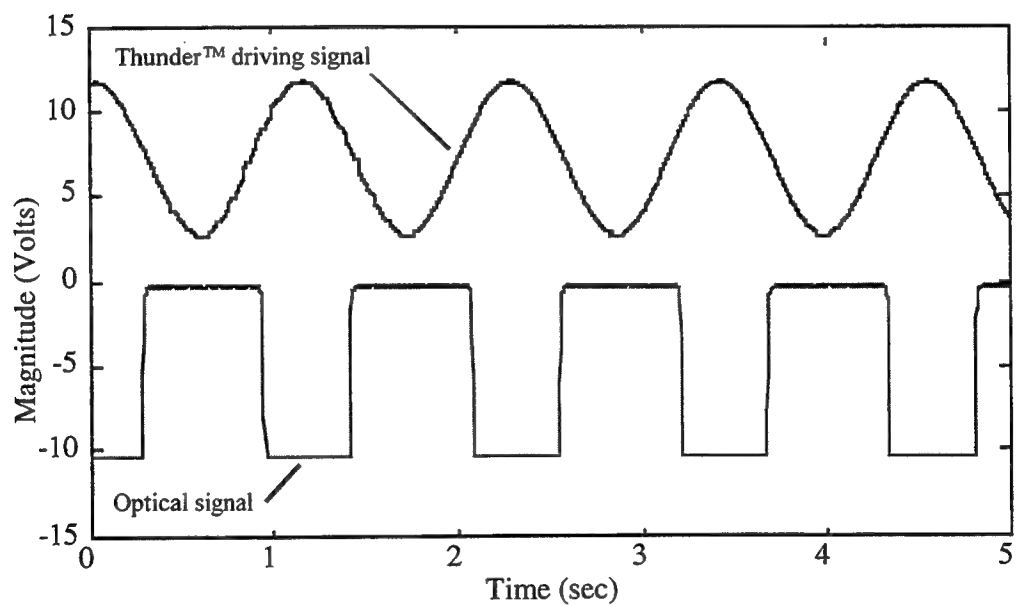
Figure 6. Experimental data for microcomposite optical switch.

4. SUMMARY AND CONCLUSIONS

An optical switching device has been developed using thermally stable microcomposite materials. Preliminary testing indicates the switch is structurally robust and capable of being realigned after an intense manufacturing process. In the future, a considerable amount of testing will be done to further investigate the optical, thermal, and mechanical characteristics of this switch.

The use of this new microcomposite technology will lead to the rapid, high-volume manufacture of optical fiber switches by allowing them to be cut from a continuous mold along an assembly line.

5. ACKNOWLEDGEMENTS

REFERENCES

1.   Shinji Nagaoka, "Optomechanical Switches for Fiber-Optic Communication Systems", SPIE Vol. 2576, pp. 383-389.

SESSION 3

Electromechanical Systems

A comparative analysis of piezoelectric bending-mode actuators

V. D. Kugel, Sanjay Chandran, and L. E. Cross

Intercollege Materials Research Laboratory, The Pennsylvania State University, University Park, PA
16802

ABSTRACT

During the last several years novel piezoelectric bending actuators have been developed: RAINBOW, CERAMBOW, CRESCENT, d_{33} bimorph and THUNDER. A comparative experimental investigation of electromechanical characteristics of these devices along with conventional d_{31} bimorph and unimorph actuators was conducted in this work. All transducers were fabricated from soft piezoelectric ceramics. The experimental results show that d_{33} bimorph and unimorph elements have superior quasistatic characteristics as compared to other type of bending-mode actuators. All these piezoelectric devices demonstrate a significant dependence of electromechanical performance on the magnitude of the driving electric field. It was found that the decrease in the mechanical quality factor and resonant frequency of bending vibrations in d_{31} unimorph, RAINBOW, CRESCENT (CERAMBOW) and THUNDER with increasing electric field is much smaller than that in bimorph and d_{33} unimorph actuators. The dependence of the behavior of these devices on the operating conditions governs the selection of a particular device for a specific application.

Keywords: piezoelectric actuators, bimorph, unimorph, RAINBOW, CRESCENT, CERAMBOW, THUNDER

1. INTRODUCTION

Piezoelectric ceramics have a relatively high electromechanical coupling coefficient which makes them very attractive for applications involving efficient transformation of electrical energy into mechanical energy and vice versa. Therefore piezoelectric actuators fabricated from these ceramics have significant potential for use as sensors and actuators in smart systems. Some of the most popular types of piezoelectric devices are bending actuators, in which applied electric field causes mechanical bending because of the piezoelectric effect. A classical example of such a device is piezoelectric bimorph actuator[1] consisting of two similar electroded piezoelectric plates poled along their thickness and adhesively bonded together. A schematic view of the piezoelectric bimorph cantilever with rectangular cross-section is shown in Fig. 1a. The flexural displacement η under applied voltage U (Fig. 1b) is caused by the piezoelectric effect in the direction perpendicular to the polar (Z) axis (piezoelectric d_{31} coefficient).

(a)   (b)
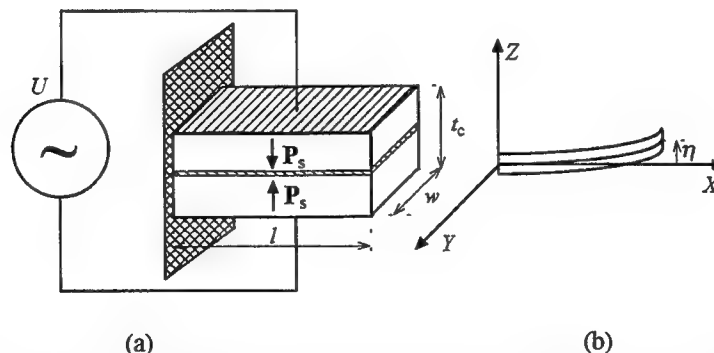
Fig. 1. (a) A schematic view of the piezoelectric d_{31} bimorph cantilever with series connection. $\mathbf{P}_s$ denotes the vector of the spontaneous polarization. (b) Flexural displacement of the transducer in the ZX plane under the applied voltage.

Another widely used bending actuator is unimorph (Fig. 2).[2] The unimorph actuator consists of the non-piezoelectric and electroded piezoelectric plates bonded together. Here, like in the piezoelectric bimorph, the piezoelectric effect in the direction perpendicular to the polar axis (coefficient d_{31}) generates flexural displacement.
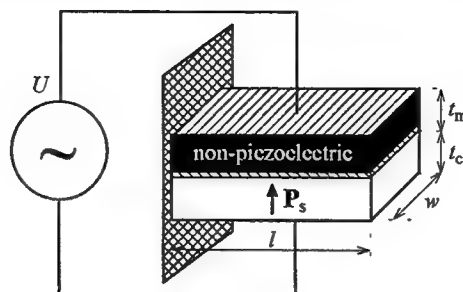
Fig. 2. A schematic view of the piezoelectric d_{31} unimorph cantilever with rectangular cross-section.

A new type of bending piezoelectric actuator named RAINBOW (standing for Reduced And Internally Biased Oxide Wafer) has recently been developed.[3] This is a monolithic bender in which the ceramic is subjected to a selective high temperature reduction with graphite in an oxidizing atmosphere resulting in a reduced non-piezoelectric layer with metallic electrical conductivity and an unreduced piezoelectric layer. The resulting stress-biased monolithic unimorph has domelike structure (Fig. 3) because of difference in the thermal contraction of reduced and non-reduced parts of the ceramic plate. It was stated that the actuator can generate significant axial displacement.[4]
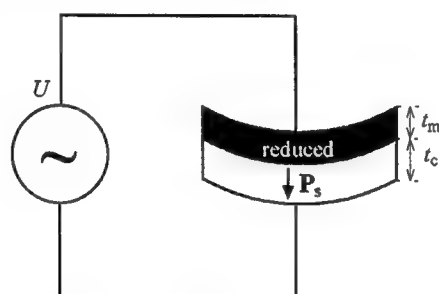
Fig. 3. A schematic view of RAINBOW actuator.

CERAMBOW (stands for CERAMic Biased Oxide Wafer) piezoelectric actuator is another stress-biased unimorph actuator in which metal and electroded ceramic plates are cemented together at an elevated temperature using appropriate solder.[5] Curvature develops as the CERAMBOW is cooled to room temperature since the metal and ceramics have different coefficients of the thermal expansion. CERAMBOW has the same shape as RAINBOW (Fig. 4). A much more reliable way for stress-biased actuators fabrication has been suggested by the authors. Dome shape of this stress-biased unimorph named CRESCENT (Fig. 4) is achieved by bonding metal and electroded piezoelectric plates at a high temperature using special epoxies (curing temperature is 200-400 °C). If fabricated at the same temperature, the CERAMBOW and CRESCENT have similar electromechanical properties.

Another new class of bimorph and unimorph actuators utilizing piezoelectric d_{33} coefficient has recently been developed.[6] This caterpillar-type piezoelectric d_{33} transducer consists of piezoelectric segments bonded by a polymeric agent by a dicing and layering technique (Fig. 5). It is the piezoelectric effect along polar axis $\mathbf{P_s}$ (coefficient d_{33}) that causes flexural displacement in these transducers. Since piezoelectric d_{33} coefficient in commercial piezoelectric ceramics is 2-2.2 time large than d_{31}, this transducer generates significantly higher displacement than conventional piezoelectric d_{31} bimorph and unimorph actuators.
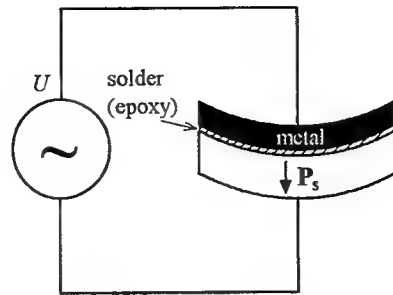
Fig. 4. Schematic view of CERAMBOW (CRESCENT).
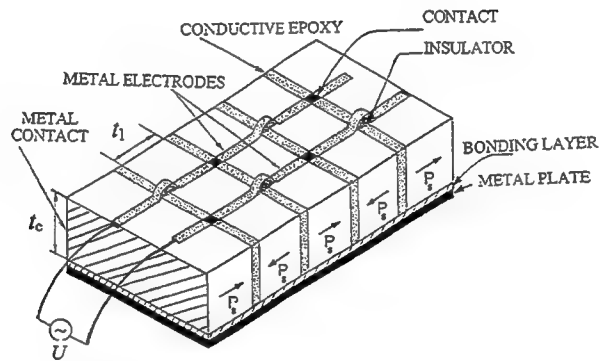
Fig. 5. A schematic view of the caterpillar-type d_{33} unimorph actuator. In the case of a bimorph consisting of two similar piezoelectric plates, the metal plate is replaced by the same piezoelectric plate.

Recently, another type of unimorph stress-biased piezoelectric actuator - THUNDER - (stands for THin layer Unimorph DrivER and sensor) has been reported.[7] The technique of THUNDER fabrication consists of high temperature bonding (300-350 °C) of an electroded ceramic plate with metal foils using LARC[tm]-SI polyimide adhesive developed at NASA. The foils are cemented from both surfaces of the ceramic plate and the thickness of the metal foils on one surface of the ceramic plate is much thicker than on the other (Fig. 6). After the high temperature bonding the structure is given an additional bent by mechanical pressing to increase curvature. No published data are available to date for evaluating electromechanical properties of THUNDER.
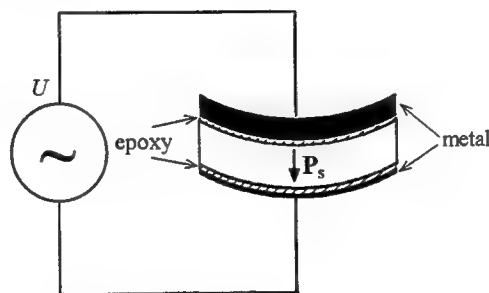
Fig. 6. Schematic view of THUNDER.

Thus, several new types of piezoelectric bending actuators have emerged during the last several years. A comparative analysis of their electromechanical properties is indeed the need of the hour. Therefore this work was undertaken in attempt to find and use unified criteria for the device characterization. The approach used is described in

section 2. Experimental procedure and results are presented in section 3. Finally, discussion and summary are given in section 4.

2. REPRESENTATION OF EXPERIMENTAL DATA

Actuators consisting of plates with rectangular cross-section have only been considered in this work. Since in many instances piezoelectric bending actuators are used in the cantilever configuration where one end of the actuator is clamped and the second one vibrates under or without an external load (Fig. 1), this configuration was used for the actuator characterization.

In the cantilever configuration mechanical load is usually applied to the vibrating end of the cantilever. Therefore the most important quasistatic characteristics are the free displacement η (Fig. 1) of the vibrating end and the blocking force F_{bl} when $\eta=0$. For piezoelectric bimorph and unimorph actuators[6]

$$\eta = \frac{3}{2}d\frac{l^2}{t}k_d E,$$

$$F_{bl} = \frac{3}{8}\frac{d}{s}\frac{wt_c^2}{l}k_{df}E,$$

(1)

where d is the piezoelectric coefficient of ceramics, s is the mechanical compliance of ceramics in the direction X under the constant electric field E (Fig. 1), $E = U/t_c$ for all actuators except for d_{33} bimorph and unimorph for which $E = U/t_1$ (Fig. 5), l, w, and t_c are the dimensions of the piezoelectric plate of the cantilevers (Figs. 1 and 2), and k_d and k_{df} are displacement and blocking force coefficients, respectively. For conventional piezoelectric d_{31} bimorph and unimorph actuators (Figs. 1 and 2) piezoelectric coefficient d_{31} and mechanical compliance s_{11}^E should be used in equation (1); for d_{33} transducers d_{33} and s_{33}^E should be used.

For bimorph cantilevers displacement and blocking force coefficients in equation (1) are equal to 1, for unimorph cantilevers without internal stress bias (Figs. 2 and 5) they can be expressed as[6]

$$k_d = \frac{2xy(1+x)}{1+4xy+6x^2y+4x^3y+x^4y^2}, \quad x = \frac{t_m}{t_c}, \quad y = Y_m s,$$

$$k_{df} = 2xy\frac{1+x}{1+xy},$$

(2)

where t_m is the thickness of the non-piezoelectric plate (Fig. 2) and Y_m is the Young's modulus of the non-piezoelectric plate. As follows from the analysis of equation (2) factors k_d and k_{df} depend on the ratio of thicknesses x and Young's moduli y of non-piezoelectric and piezoelectric plates. The larger y is, the higher the value of k_d and k_{df} for optimum x. Analysis shows that maximum value of k_d is 0.5 and corresponding k_{df} is 2.

For stress-biased unimorph actuators like RAINBOW, CERAMBOW, and CRESCENT, mechanical stress arising in these structures during device fabrication and poling, changes electromechanical properties of ceramics. Therefore equation (1) for these actuators can be written as

$$\eta = \frac{3}{2}d_{31}\frac{l^2}{t}k_d k_p E,$$

$$F_{bl} = \frac{3}{8}\frac{d_{31}}{s_{11}^E}\frac{wt_c^2}{l}k_{df}k_{pm}E,$$

(3)

where d_{31} and s_{11}^E are the piezoelectric and mechanical compliance coefficients of the piezoelectric ceramics before the device fabricating, k_p and k_{pm} are coefficients equal to relative change in d_{31} and d_{31}/s_{11}^E respectively as a result of the acting mechanical stress. Coefficients k_d and k_{df} in equation (3) should be calculated using equation (2) for values of piezoelectric and electromechanical coefficients of the piezoelectric plate poled under mechanical stress. Equation (3) is also valid for THUNDER but in this case k_d and k_{df} are not described by equation (2).

One more important quasistatic electromechanical characteristic of the actuators is their electrical admittance Y:

$$Y = j\omega\frac{lw}{t_c}\varepsilon_{33}^T k_Y,$$

(4)

where ω is the angular frequency, ε_{33}^T is the component of the tensor of the dielectric permittivity of ceramics and k_Y is the factor depending on the corresponding mechanical coupling coefficient and a change in the dielectric permittivity as a result of the devices fabricating.

Thus as is seen from equations (1-4) quasistatic electromechanical characteristics of actuators with **the same dimensions** of piezoelectric part of the devices, **the same electric field**, and **the same frequency** can be normalized with respect to actuator chosen as a standard. It is convenient choose d_{31} **bimorph actuator** (Fig. 1) as this standard. Therefore the tip displacement η, blocking force F_{bl} and electrical admittance Y of all above described transducers fabricated using **the same piezoelectric ceramics** can be expressed as

$$\eta = \eta^{bimorph} f_m^{\eta},$$
$$F_{bl} = F_{bl}^{bimorph} f_m^F,$$
$$Y = Y^{bimorph} f_m^Y,$$

(5)

where f_m^{η}, f_m^F, f_m^Y are individual figures of merit characterizing the tip displacement, blocking force and electrical admittance of a specific bending actuator, respectively.

The mechanical work W_{mc} that can be produced by the bending-mode actuators is proportional to the product of the multiplication of the tip displacement η and the blocking force :

$$W_{mc} \propto \eta F_{bl} .$$

(6)

Quasistatic electrical energy W_{el} accumulated in the transducer is proportional to its dielectric permittivity ε, the volume of the piezoelectric plate and the square of electric field E. Using equation (4), the following relation is obtained:

$$W_{el} \propto \frac{Y}{\omega} t_c^2 E^2 ,$$

(7)

The ratio of the mechanical work to the input electrical energy can serve as an overall figure of merit for the electromechanical efficiency of the piezoelectric actuator,

$$\text{integral figure of merit} = \frac{W_{mc}}{W_{el}} \propto \frac{\eta F_{bl}}{Y} \frac{\omega}{t_c^2 E^2} .$$

(8)

Using equation (5) the overall figure of merit relative to that of piezoelectric d_{31} bimorph, f_m, can be written as

$$f_m = \frac{f_m^{\eta} f_m^F}{f_m^Y} .$$

(9)

Thus, the relative factors f_m^{η}, f_m^F, f_m^Y, and f_m make it possible to describe quasistatic electromechanical characteristics of bending-mode piezoelectric actuators in the cantilever configuration. It is important to note that the actuators under consideration should be fabricated using the same piezoelectric ceramics and should have the same dimensions of the active piezoelectric part. All quasistatic characteristics should be measured for the same amplitude and frequency of the applied electric field since electromechanical properties of piezoelectric ceramics depend on the amplitude and frequency of the electric field.[8] Experimental results[6,8] show that despite a significant dependence of quasistatic electromechanical characteristics of piezoelectric actuators fabricated from soft piezoelectric ceramics on the applied electric field, the changes of these characteristics for different actuators show almost the same variation. Therefore it is enough to find f_m^{η}, f_m^F, f_m^Y, and f_m for one value of the applied electric field.

Since in many cases bending-mode actuators are operated near the fundamental frequency of bending vibrations, resonant characteristics of the actuators are also important. The values of the fundamental resonant frequency ν_r and the mechanical quality factor Q_m can be chosen to characterize resonant properties. The fundamental resonant frequency of the piezoelectric d_{31} bimorph cantilever with rectangular cross-section is[9]

$$\nu_r = \frac{1.875^2}{4\pi} \frac{t_c}{l^2} \frac{1}{\sqrt{3 s_{11}^E \rho_c}} ,$$

(10)

where ρ_c is the density of the ceramics. The resonant frequency of the piezoelectric d_{31} unimorph with rectangular cross-section is expressed as[10]

$$\nu_r = \frac{1.875^2}{4\pi} \frac{t_c}{l^2} \frac{1}{\sqrt{3 s_{11}^E \rho_c}} \sqrt{\frac{k_{df}}{k_d (1 + xz)}} , \qquad z = \frac{\rho_m}{\rho_c} ,$$

(11)

where ρ_m is the density of the non-piezoelectric plate. Thus, it is evident that the resonant frequency of the unimorph cantilever is a function of the resonant frequency of the piezoelectric plate (bimorph). For calculating the fundamental

resonant frequency of piezoelectric d_{33} bimorph and unimorph, s_{33}^E should be used in equations (10) and (11) instead of s_{11}^E. Equation (11) is also valid for RAINBOW, CERAMBOW, and CRESCENT cantilevers but in this case, the mechanical compliance of the stress-biased piezoelectric plate should be used in the calculations. For THUNDER too, the resonant frequency is a function of the resonant frequency of piezoelectric plate which is described by equation (10) but the actual dependence is a more complicated function of x, y and z. Based on the analysis described above, the resonant frequency of the bending mode actuators can be related to the resonant frequency of the piezoelectric d_{31} bimorph which has the same dimensions of the active piezoelectric plate, using the equation

$$\nu_r = \nu_r^{bimorph} f_m^\nu, \tag{12}$$

where f_m^ν is the figure of merit characterizing the fundamental resonant frequency of the bending-mode transducer. It is known[8] that the fundamental resonant frequency depends on the magnitude of the applied electric field. Therefore another important parameter to be considered is the relative change in the resonant frequency $\Delta\nu_r/\nu_r$ as a function of the electric field.

The mechanical quality factor Q_m is another important resonant characteristic. Since mechanical vibrations of the piezoelectric bending-mode actuators are described by fourth-order differential equation[9] and not by a second order one, Q_m should be defined appropriately. By analogy with the definition of Q_m for damped harmonic **vibrator without frequency dispersion** of the relevant electromechanical parameters of the system, Q_m can be expressed as[11]

$$Q_m = \frac{\eta_r}{\eta}, \tag{13}$$

where η_r is the amplitude of resonant vibrations. The amplitude of resonant vibrations depends on mechanical losses in the actuator[9] and is also very sensitive to the way the cantilever is clamped. Therefore it is preferable to compare the relative change $\Delta Q_m/Q_m$ as a function of the electric field instead of Q_m.

Thus, relative factors f_m^η, f_m^F, f_m^Y, and f_m are used to characterize quasistatic electromechanical characteristics and f_m^ν, $\Delta\nu_r/\nu_r$, and $\Delta Q_m/Q_m$ are used to characterize resonant properties of bending-mode piezoelectric actuators in the cantilever configuration.

3. EXPERIMENTAL PROCEDURE AND EXPERIMENTAL RESULTS

All transducers investigated were fabricated from soft piezoelectric ceramics and had a rectangular cross-section and the following dimensions: 0.4-2.5 mm in thickness, 5-15 mm in width, and 15-35 mm in length. Piezoelectric bimorph and metal/piezoelectric unimorph actuators were fabricated from PKI550 (Piezo Kinetic, Inc.) ceramic plates poled along their thickness. This category of piezoelectric ceramics is analogous to soft piezoelectric ceramics PZT5H. Stainless steel SS302 was used to make the unimorphs because of its very high Young's modulus and, consequently, high theoretical ratio of Young's moduli $y=3.05$ (equation (2)). The plates were bonded using commercial J-B Weld epoxy (J-B Weld Company). Piezoelectric d_{33} bimorphs were fabricated by a dicing and layering technique.[6] Theoretical ratio of Young's moduli for the d_{33} unimorph is $y=3.90$. The ceramic plates in the stack were bonded using commercial conductive adhesives EP21TDCS (Master Bond, Inc.) and E-Solder 3025 (Insulating Materials, Inc.). J-B Weld epoxy was used for bonding metal and sliced ceramic plates. Each piezoelectric segment in the piezoelectric plates (Fig. 5) had the following dimensions: $t_c = t_1 = 1.09$ mm, $w = 11$ mm. As follows from equation (2), electromechanical characteristics of d_{31} and d_{33} unimorph actuators depend on the ratio of thicknesses x and Young's moduli y of non-piezoelectric and piezoelectric plates. Theoretical analysis shows[10] that maximum value of the displacement factor f_m^η and overall figure of merit f_m correspond to different values of x. Therefore, only devices exhibiting maximum quasistatic tip displacement were chosen. Experimental study showed[6,10] that for SS302/PKI550 unimorphs optimum x lies between 0.2 and 0.35.

CRESCENTs were fabricated from PKI550 and SS302 using several types of high temperature epoxies. Since the Curie temperature ~200 °C was lower than the device fabrication temperature, the actuators were poled after their fabrication. It was found that tip displacement factor f_m^η for CRESCENT depends not only on the x and y factors but also on the curing temperature T_{cr}; therefore only CRESCENTs possessing maximum f_m^η were used for a comparative study. For actuators with $t_c=1$ mm and $t_m=0.37$ mm the optimal curing temperature was around 250-260 °C. The radius of the curvature of the transducer before poling was 0.4 m and after poling it increased to 0.8-0.9 m.

Since figures of merit are defined for elements with the same dimension of the piezoelectric part, the experimental data obtained for actuators fabricated from PKI550 with different dimensions were recalculated for a device with standard dimensions of piezoelectric plate.

RAINBOW actuators were cut from piezoelectric RAINBOW disks which were purchased from Aura Ceramics, Inc. RAINBOW disks are fabricated from C3900 ceramics which is analogous to PZT5H. The thickness of the devices was 0.46-0.48 mm, the thickness of the piezoelectric (unreduced) part t_c was approximately 0.27-0.29 mm. The thickness of the reduced layer was 0.12 mm and the thickness of conductive epoxy layer which served as electrode was 0.07 mm.

THUNDER actuators were fabricated from soft piezoelectric ceramics PZT5A and Al foil. Three layers of the foil were cemented on one side of the ceramic plate and one layer on the other side. Curing temperature was 300-320 °C. The thickness of the THUNDERs was 0.41 mm, the thickness of piezoelectric plates was 0.2 mm. The radius of the actuator curvatures after poling was approximately 0.33 m. After the high temperatures bonding followed by poling (first stage) the devices were additionally bent by mechanical pressing (second stage) and the radius of the curvature decreased to 0.14 m. Measurements of piezoelectric characteristics were conducted after the first and second stages.

Individual figures of merit of RAINBOW and THUNDER actuators were calculated using their experimental data and theoretical calculations for bimorph actuators from the same piezoelectric ceramics having the same dimensions.

The tip displacement of actuators was measured by a photonic sensor MTI 2000 (MTI Instruments Division). The blocking force was measured by means of a load cell ELF-TC500 (Entran Devices, Inc) and the electrical admittance was measured my means of a lock-in amplifier SR830 DSP (Stanford Research Systems, Inc). A complete description of the experimental set-up is given elsewhere.[8] Electromechanical characteristics were measured in quasistatic regime and at the fundamental frequency of bending vibrations. In the quasistatic regime the measurement frequency was at least ten times smaller than the fundamental resonant frequency.

Experimental figures of merit f_m^n, f_m^F, f_m^Y, f_m, and f_m^v representing electromechanical characteristics of the actuators studied are given in the Table. These values were obtained for low applied electric field (less than 20 V/cm). Dependencies of the resonant frequency and mechanical quality factors on the electric field are shown in Figs. 7 and 8, respectively. Resonant characteristics of CRESCENT actuators were similar to that of d_{31} unimorphs. No significant difference in almost all measured electromechanical properties of THUNDER actuators after the first and second stages of their fabrication was observed. Only mechanical quality factor decreased by 23% after the second stage.

Table. Figures of merit of bending-mode piezoelectric actuators in the cantilever configuration.

TYPE OF PIEZOELEMENT	Tip displacement factor f_m^n	Blocking force factor f_m^F	Admittance factor f_m^Y	Overall figure of merit f_m	Resonant frequency factor f_m^v
d_{31} Bimorph	1	1	1	1	1
d_{31} Unimorph $x=0.34, y=3.05$	0.41	1.8	1.0	0.74	1.7
RAINBOW	0.19-0.22	0.1-1.2	0.66	0.03-0.40	1.2-1.4
CRESCENT 250 °C (CERAMBOW) $x=0.34, y\cong3.05$	0.44	1.75	0.91	0.85	1.7
THUNDER (3Al/PZT5A/Al)	0.12	0.36-1.0	0.90	0.05-0.13	2.1
d_{33} Bimorph	2.5	1.52	~1	3.80	0.84
d_{33} Unimorph $x=0.34, y=3.90$	0.72	3.5	~1	2.52	1.7

Analysis of d_{31} bimorphs experimental data showed that the experimental tip displacement and its theoretical value calculated according to equation (1) are in good agreement. Averaged experimental value of the blocking force was 33% less than theoretical one given by equation (1) and the averaged experimental value of the resonant frequency of cantilevers was 13% smaller that theoretical one (equation (10)). Nevertheless, the resonant frequency of these bimorph actuators with free-free boundary conditions (non of the ends is clamped) coincided with the theoretical one. For d_{31} unimorph actuators

the same tendency was observed: the blocking force was smaller by 13% and the resonant frequency was smaller by 12% than corresponding theoretical values. In d_{33} bimorphs the blocking force was smaller by 42% and the resonant frequency was smaller by 17% than corresponding theoretical values. The discrepancy was smaller for d_{33} unimorphs: the blocking force was smaller by 7% and the resonant frequency was smaller than the corresponding theoretical values by 3%. There may be several reasons for these discrepancies. Firstly, under the applied electric field, piezoelectric cantilever bends not only along the X axis but also along the Y axis (Fig. 1). In theoretical calculations bending along the Y axis was neglected. Bending along the Y axis may affect the blocking force and resonant frequency of actuators. The second reason is that the cementing epoxy whose thickness was neglected in the calculations, may also change electromechanical properties of the actuators. We were unable to conduct the same analysis for RAINBOW, CRESCENT and THUNDER actuators since exact electromechanical properties of these devices are unknown.

As seen from the Table, the blocking force factor for RAINBOW does not have an exact value. This is because the blocking force showed significant dependence on the external load. The force increased markedly with increasing mechanical pre-stress which can be generated externally by the horizontal displacement of the load cell stuck to the vibrating end of the actuator. It was also found that if the load cell was pressed against the vibrating end the measured blocking force was an order of magnitude large than that for the case when the load cell was glued to the vibrating end of RAINBOW cantilevers. A significant scattering in the measured blocking force factor f_m^F of THUNDERs (see Table) is probably caused by experimental limitations since it is very difficult to attach the vibrating end of THUNDER having a curved shape and the load cell head having a flat surface.
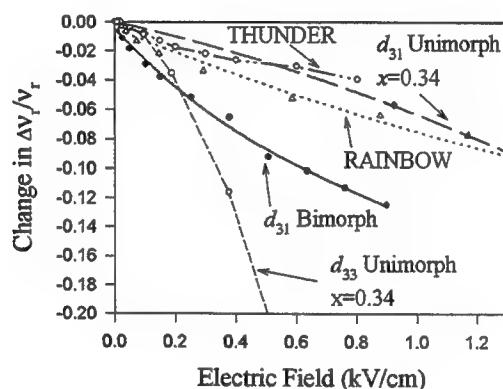
Fig. 7. Dependence of the resonant frequency v_r of bending vibrations on the electric field (rms). Low-field resonant frequency is: 1394 Hz (d_{31} bimorph), 1015 Hz (d_{31} unimorph), 1029 Hz (d_{33} unimorph), 595 (RAINBOW), and 227 Hz (THUNDER).
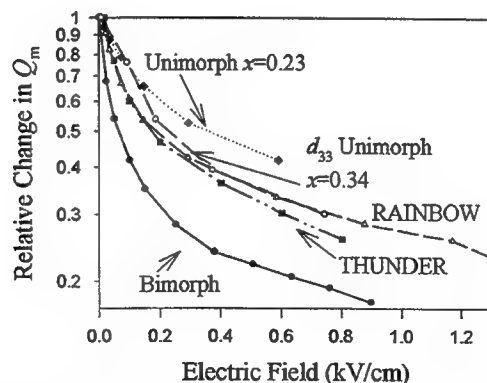
Fig. 8. Dependence of the relative mechanical quality factor on the electric field (rms). Low-field quality factor Q_m is: 55 (d_{31} bimorph), 48 (d_{31} unimorph), 25 (d_{33} unimorph), 62 (RAINBOW), and 137 (THUNDER, after first stage).

77

4. DISCUSSION AND SUMMARY

As follows from the Table, d_{33} bimorph and unimorph actuators have the best quasistatic electromechanical characteristics with respect to the blocking force and overall figure of merit. The reason for this is that piezoelectric d_{33} coefficient and corresponding coupling factor k_{33} are 2-2.2 times large than d_{31} and k_{31}. d_{31} bimorph generates higher tip displacement than d_{33} unimorph but its blocking force is significantly lower. d_{31} bimorph is followed by CRESCENT (CERAMBOW) and d_{31} unimorph actuators. It is interesting that the CRESCENT fabricated at the optimal temperature has a higher tip displacement, and overall figure of merit than d_{31} unimorph fabricated from the same materials. It means that the average piezoelectric d_{31} coefficient of the piezoelectric plate poled under certain mechanical bending stress is higher and corresponding dielectric permittivity ε_{33}^T lower than that of the starting material. A probable reason is that there are specific domain structures that are formed during poling. Two experimental facts support this hypothesis: the first one is a significant increase in the radius of the transducer curvature after poling. The second fact is that after separation of the metal and ceramic plates in the poled CRESCENT, the ceramic plate retained its curved shape which implies that there is practically no mechanical stress in the transducer. Moreover, effect of the longitudinal stress cannot explain the increase in the tip displacement since experimental results[12] show that longitudinal stress decreases piezoelectric d_{31} coefficient. If the CRESCENT is prepared above the optimal temperature residual mechanical stress may decrease piezoelectric d_{31} coefficient.

As is seen from the Table, RAINBOW and THUNDER actuators have lowest quasistatic figures of merit. Since reduced layer in RAINBOW actuator has a Young's modulus[13] much lower than stainless steel used for d_{31} unimorph fabrication, displacement factor k_d for this actuator is less than that for unimorphs. In addition as follows from the analysis of equation (2), the ratio of thickness of the reduced and active piezoelectric layers is less than the optimal one. The same reason can explain inferior quasistatic behavior of THUNDERs. Also, these devices have metal foils from both sides that decrease tip displacement. Since the thickness of the piezoelectric plates in the device was relatively small, the adhesive layers can also decrease f_m^n.

As seen from Fig. 7, the fundamental resonant frequency of bending-mode actuators depends on the applied electric field. Large sensitivity of the resonant frequency of d_{33} unimorph to electric field can be due to the fact that at a high level of mechanical stress which exists at a high level of resonant vibrations the epoxy bonding the piezoelectric segments becomes soft due to non-linear strain-stress relationship in the polymer materials. Resonant properties of d_{33} bimorph were not measured but based on the above discussion, this device should be even more sensitive to high electric field because it does not have the stabilizing metal plate. Relatively high dependence of v_r of d_{31} bimorph can be caused by an increase of the mechanical compliance of the piezoelectric ceramics with increasing electric field.[8] The effect of mechanical "softening" of the piezoelectric ceramics in all d_{31}-type unimorph devices is less significant since they have non-piezoelectric part whose properties do not depend on the electric field.

All actuators demonstrate a significant decrease of the mechanical quality factor with increasing electric field (Fig. 8). The most sensitive device studied was the d_{31} bimorph. Since the amplitude of resonant vibrations is inversely proportional to the mechanical losses at the resonance[9], the mechanical losses increase significantly under high electric field. At the electric field 1 kV/cm the mechanical quality factor decreases by an order of magnitude as compared to its low-field value. Since in unimorph-type structures there is non-piezoelectric part in which the mechanical losses do not depend on the applied electric field, the decrease of Q_m in these actuators is more gradual.

It should be noted that there is one more important figure of merit that has not been considered in this work. It is mechanical failure at resonance. Our results showed that at a high level of mechanical vibrations at resonance the actuators fracture. The fracture occurred at the surface of ceramic plates in the region where actuators were clamped since this area is subjected to the highest level of stress. Analysis of experimental data showed that fracture of d_{31} bimorph and unimorph transducers at resonance occurs if the maximum stress at the clamped surface reaches 30-50 MPa. In this case mechanical failure occurs in several seconds. Clearly, unimorph actuators having metal plates, such as d_{31} and d_{33} unimorph, CRESCENT, CERAMBOW, and especially THUNDER, are more reliable in a sense that even if mechanical failure of ceramics occurs the actuators do not fracture since metals like steel or Al have much higher fracture toughness than ceramics.

It is worthwhile to note that the straight or slightly curved shape of bending-mode actuators is not optimal in terms of overall figure of merit f_m. For instance, theoretical calculations show that L-shaped d_{31} bimorph cantilever (Fig. 9) has higher blocking force factor f_m^F and overall figure of merit f_m than straight d_{31} bimorph with the same dimensions. This is because in a conventional straight structure, bending moment generated in the actuator works against the blocking force

applied to the vibrating end. Therefore this force blocks the movement of the actuator's tip only. In the L-shaped structure, application of the horizontal force produces a mechanical moment on the horizontal part of the actuator. Thus, the blocking force should almost prevent displacement in the whole bottom part of the transducer consequently the magnitude of the corresponding blocking force should be higher in this case.

ELEMENT	Tip displacement factor f_m^η	Blocking force factor f_m^F	Admittance factor f_m^Y	Overall figure of merit f_m	Resonant frequency factor f_m^ν
d_{31} Bimorph	1	1	1	1	1
L-shaped d_{31} Bimorph ($l_1=l_2=0.5l$)	0.75	1.5	1.0	1.125	1.32
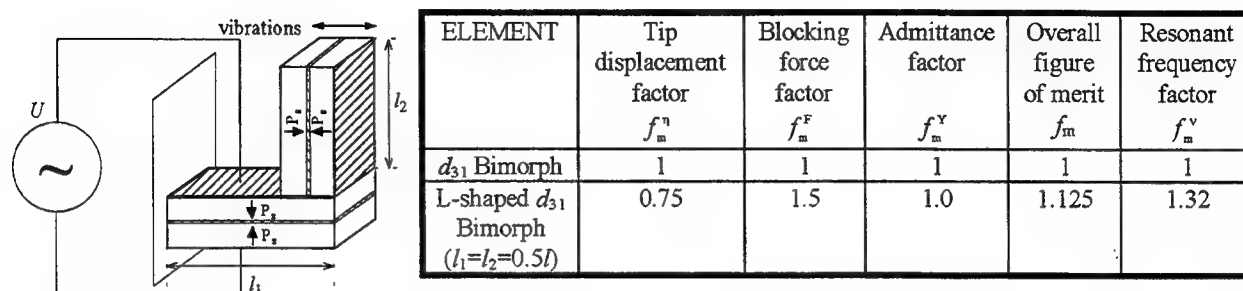
Fig. 9. Schematic view of L-shaped d_{31} bimorph and theoretical figures of merit of this device with $l_1=l_2=0.5l$.

In summary, a comparative experimental investigation of electromechanical characteristics of piezoelectric d_{31} and d_{33} bimorph and unimorph actuators, RAINBOW, CRESCENT (CERAMBOW), and THUNDER actuators in cantilever configuration has been conducted. The tip displacement, blocking force, and electrical admittance were chosen to characterize quasistatic properties and the resonant frequency and mechanical quality factor were chosen to characterize the behavior at the fundamental frequency of bending vibrations. The experimental results show that d_{33} bimorph and unimorph actuators have superior quasistatic characteristics as compared to other types of bending-mode actuators. It was found that resonant frequency and especially mechanical quality factor of all actuators depend on the applied electric field. d_{31} unimorph, RAINBOW, CRESCENT (CERAMBOW), and THUNDER were found to be less dependent on the applied electric field than d_{31} bimorph and d_{33} bimorph and unimorph actuators. These results indicate that the choice of devices for a particular application depends on conditions under which the device will operate.

ACKNOWLEDGMENTS

REFERENCES

1. W. P. Mason, *Electromechanical Transducers and Wave Filters* (D. Van Nostard Company, New York, 1942). pp. 199-200, 209-215.
2. M. R. Steel, F. Harrison, and P. G. Harper, "The piezoelectric bimorph: An experimental and theoretical study of its quasistatic response", *J. Phys. D: Appl. Phys.* **11**, pp. 979-989, 1978.
3. G. H. Haertling, "Rainbow ceramics - a new type of ultra-high-displacement actuator", *Amer. Cer. Soc. Bulletin* **73**, pp. 93-96, 1994.
4. G. H. Haertling, "Chemically reduced PLZT ceramics for ultra-high displacement actuators", *Ferroelectrics* **154**, pp. 101-106, 1994.
5. E. Furman, "Stress-enhanced ferroelectric materials and structures", *Annual report Part III "Studies of RAINBOW and CERAMBOW electromechanical properties"*, The Gilbert C. Robinson Department of Ceramic Engineering, Clemson University, 1995.
6. V. D. Kugel, Sanjay Chandran, and L. E. Cross, "Caterpillar-type piezoelectric d_{33} bimorph transducer", *Appl. Phys. Lett.* **69**, pp. 2021-2023, 1996.
7. R. L. Fox, R. G. Bryant, and J. M. Bacon "THUNDER ACTUATOR" (NASA Langley Research Center), private communication, 1996.
8. V. D. Kugel, Q. M. Zhang, Baomin Xu, Qing-ming Wang, Sanjay Chandran, and L. E. Cross, "Behavior of Piezoelectric Actuators under High Electric Field", Accepted to *IEEE Proceedings on Application of Ferroelectrics, ISAF'96* (1996).

9. V. D. Kugel, Baomin Xu, Q. M. Zhang, and L. E. Cross, "Bimorph-Based Piezoelectric Air Acoustic Transducer: Model", Submitted to *Sensors and Actuators A* (1996).

10. V. D. Kugel and L. E. Cross, unpublished.

11. R. F. Steidel, Jr., *An Introduction to Mechanical Vibrations* (John Willey & Sons: New York, 1979). pp. 212-216.

12. Q. M. Zhang, J. Zhao, K. Uchino, and J. Zheng, "Change in the weak field properties of $Pb(ZrTi)O_3$ piezoceramics with compressive uniaxial stresses and its links to the effect of dopants on the stability of the polarization in materials", To be published in *J. Mater. Research* **12**, 1997.

13. E. Furman, G. Li, and G. H. Haertling, An investigation of the resonance properties of RAINBOW devices", *Ferroelectrics* **160**, pp. 357-369, 1994.

Rainbow actuators and sensors: a new smart technology

Gene H. Haertling

The Gilbert C. Robinson Department of Ceramic Engineering
Clemson University, Clemson, SC 29634-0907

ABSTRACT

Recent developments in the technology of ferroelectric, piezoelectric, electrostrictive and antiferroelectric ceramic actuators have clearly demonstrated that the materials required for future applications such as positioners, levelers, pumps, vibration-free structures and variable-focus elements will need to be more sophisticated (multifunctional and smart), more economical and possess a higher degree of performance than presently available. One recently developed method for producing considerably higher-than-normal displacement in these materials is known as the RAINBOW (Reduced and INternally Biased Oxide Wafer) technology. This acronym denotes the basic active structure of the Rainbow device which is produced by a special high temperature chemical reduction process. In its most basic sense, a Rainbow can be considered to be a pre-stressed, monolithic, axial-mode bender; however, because of its unique dome or saddle-shaped configuration, it is able to produce much higher displacements (up to several mm depending on size) and sustain moderate loads (up to 10 kg depending on thickness) than normal benders such as unimorphs and bimorphs. The technology of producing and characterizing such Rainbows as well as methods for increasing their utility by means of stacked actuators for increased linear displacement and matrix arrays for enhanced coverage in wide-area applications such as smart skins, autoleveling structures and deformable coatings are described.

Keywords: ferroelectrics, piezoelectrics, electrostrictors, actuators, sensors, Rainbow devices, PLZT, smart structures, actuator arrays, pre-stressed structures

1. INTRODUCTION

The recently renewed, worldwide interest in ferroelectric, piezoelectric, electrostrictive and antiferroelectric ceramics by a number of commercial, industrial and government agencies has been brought about as a result of their unique combination of properties (dielectric, electromechanical, photomechanical, electrooptic, memory, etc.) which make them nearly ideal candidates for a variety of actuating and/or sensing applications where small size, low weight, low or high force, small displacement and variable sensitivities are required. Such applications include automobile and home utility improvements, industrial automation, systems for national security, aircraft control and maneuverability, data processing, entertainment, communications and space exploration, Furthermore, since they are capable of the combined functions of actuating, sensing and controlling in response to an external environment or condition, they belong to that special class of multifunctional ceramics known as "smart" materials.[1]

In spite of their many obvious advantages in these applications, such ceramics are still limited in their ability to deliver high energy or power; e.g., a ceramic linear actuator being able to simultaneously generate high displacement and high force under static or quasi-static conditions is still beyond the scope of present ceramic technologies . In general, such actuators can generate significant force ($>10^3$ N) with very little movement (on the order of microns), or they can deliver millimeters of displacement via strain-amplifying techniques with little or no force; but not both at the same time. The first of these is typified by the monolithic or multilayer, direct extensional actuator while the second is typical of a bimorph (two opposed active ceramic elements) or unimorph (one ceramic element with inactive metal substrate) actuator. Deliverable energy densities per unit mass for the PZT and PMN-based, direct extensional actuators were reported by Giurgiutiu and co-workers[2] to range from 0.2 to 1 J/kg at an overall average electrical-to-mechanical conversion efficiency of 20%.

An assessment of the present-day ceramic actuator technologies for ceramic materials is given in Figure 1. As seen from the figure, direct extensional configurations, composite flextensional structures and bending-mode devices are all used
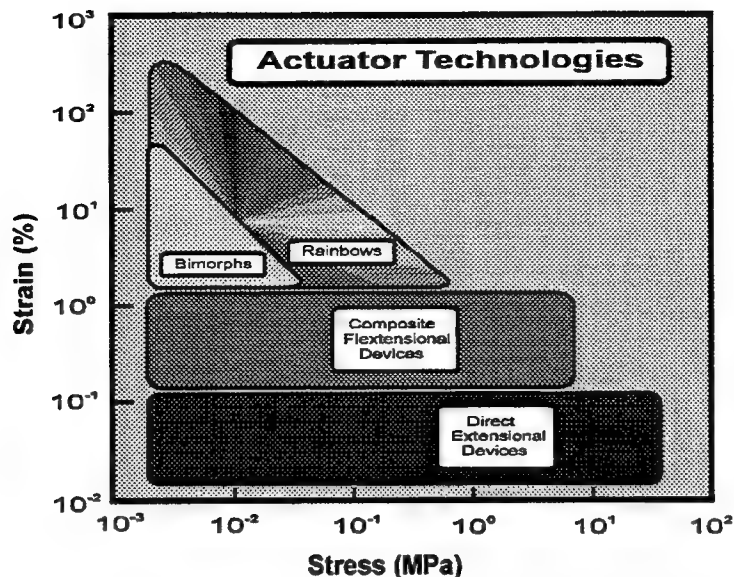
Figure 1. A comparison of ceramic actuator technologies.

to achieve an electromechanical output. Trade-offs between stress generating/load-bearing capability and strain (displacement) must usually be made when designing for particular applications. Maximum displacement can be seen to be achieved with composite or bender structures; however, this is usually accomplished at the expense of less load-bearing capability. A more recently developed strain-amplifying method for piezoelectric and electrostrictive ceramic materials is known as the RAINBOW (Reduced And Internally Biased Oxide Wafer) technology. A complete reference listing for the Rainbow technology is given in references 3 through 17. The properties of the Rainbow are such that it is classified as a pre-stressed, bender actuator which expands the load-bearing capability of the conventional benders while at the same time maintaining or increasing their mechanical displacement characteristics. Key features of the Rainbows are their simplicity, ease of processing, flexibility and surface mountable configuration. Rainbow actuators have been successfully fabricated from all of the common high-lead containing ferroelectric, piezoelectric, electrostrictive and antiferroelectric compositions such as PZT, PLZT, PSZT, PBZT, PNZT, PBiZT, PZT-5A, PZT-5H, PZT-4 and PMN-PT.[9,11,14]

The purpose of this paper is to describe the Rainbow technology in terms of materials, processing, properties and applications. Methods for increasing their utility via cascading arrangements for increased displacement and matrix arrays for wide-area coverage are also described.

2. RAINBOW MATERIALS AND PROCESSING

2.1 Rainbow materials

Although a number of different compositions have been successfully prepared as Rainbows, those most compatible to the specific processes used and most amenable to achieving the desired properties are in the PLZT solid solution family. Typical high displacement, ferroelectric compositions are 1/53/47 (La/Zr/Ti) and 5.5/56/44 for low and high dielectric constant applications, respectively; whereas, the usual compositions for the electrostrictive-type applications are 9/65/35 or 8.4/70/30. These specific compositions are pointed out in the PLZT phase diagram given in Figure 2. As may be noted, the ferroelectric materials are morphotropic phase boundary compositions, and the non-memory, electrostrictive materials are compositionally located along the ferroelectric-to-paraelectric phase boundary.[9]

2.2 Rainbow processing

The Rainbow technology fundamentally consists of a new processing method that is applied to standard, high lead-containing ferroelectric, piezoelectric and electrostrictive ceramic wafers which are transformed by the process into a
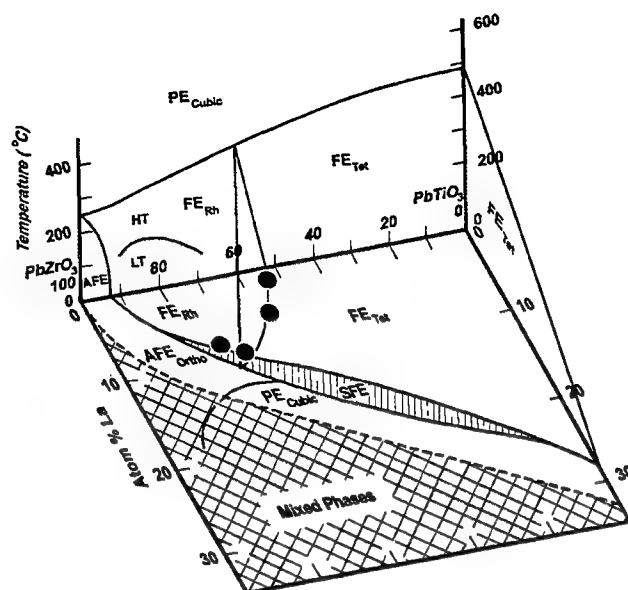
Figure 2. Room temperature phase diagram of the PLZT solid-solution system along with the PZT system vs. temperature. The specific compositions (8.4/70/30, 9/65/35, 5.5/56/44, 1/53/47) are indicated by the bold black circles, left to right, respectively.

monolithic, composite structure consisting of a stressed dielectric and a chemically reduced, electrically conductive layer which acts as the stressing element as one of the electrodes for the final device. Since all of the materials are ferroelectric or electrically-enforced ferroelectric materials, they are multifunctional and smart, by nature, and are thus capable of performing both actuator and sensor functions, simultaneously.

The high temperature chemical reduction process involves the local reduction of one surface of a planar ceramic plate, thereby achieving an anisotropic, stress-biased, dome or saddle-shaped wafer with significant internal tensile and compressive stresses which act to increase the overall strength of the material and also provide its unusually high displacement characteristics. According to previously reported work, the chemical reduction process proceeds via simple reactions consisting of the oxidation of the solid carbon (graphite) block to carbon monoxide and further oxidation of the carbon monoxide gas to carbon dioxide with the associated loss of oxygen from the PLZT oxide in contact or in near contact with the graphite block.[5] Figure 3 shows cross sections of the dome curvature and a fracture surface which are typical of the Rainbow ceramics.
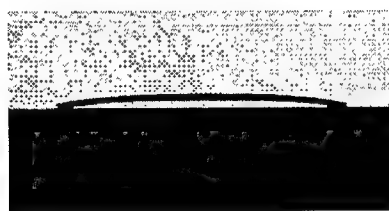
(a)
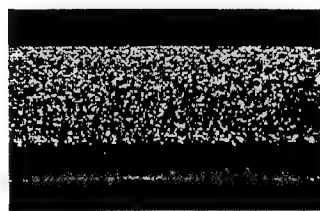
(b)

Figure 3. Cross-sectional views of PLZT 5.5/56/44 Rainbow wafer illustrating (a) dome profile and (b) fracture surface of reduced layer (bottom portion) and unreduced PLZT (top portion).

Rainbow ceramics are produced from conventionally sintered or hot pressed ceramic wafers by means of a few simple steps requiring approximately two hours of additional time. A Rainbow is produced from an as-received wafer by

placing it on a flat graphite block, placing a protective zirconia plate of the same size on top of the wafer and introducing the assembly into a furnace held at temperature in a normal air atmosphere. The part is treated at a temperature of 975°C for one hour, removed from the furnace while hot and cooled naturally to room temperature in about 45 minutes. A reduced, cermet layer, approximately 150 um thick, is produced in the wafer under these treatment conditions, When cool, the dome or saddle-shaped wafer is lifted from the graphite block; brushed and sanded lightly on the reduced (concave) side to remove any metallic lead particles and to expose the electrically conductive, reduced cermet beneath the thin, reoxidized layer; and then electroded for test and evaluation. A variety of electrodes can be used such as epoxy silver, fired-on silver and vacuum-deposited metals. After applying appropriate electrodes, the Rainbow is completed and ready for operation. It should be noted that although Rainbows are processed in bulk wafer form, after heat treatment they may be diced or scribed into smaller elements (~ 1 mm^2) for a pick-and-place operation onto a smart hybrid circuit. This technique is possible since each individually diced element possesses a smaller but similar dome structure with a radius of curvature identical to the larger wafer. Even though the displacements of the smaller individual elements are proportionately less than the parent wafer, they nevertheless, are large enough (5 - 50 microns) to be useful in some devices as actuators and sounders or as sensors. Some typical examples of sizes and shapes of Rainbows are shown in Figure 4.
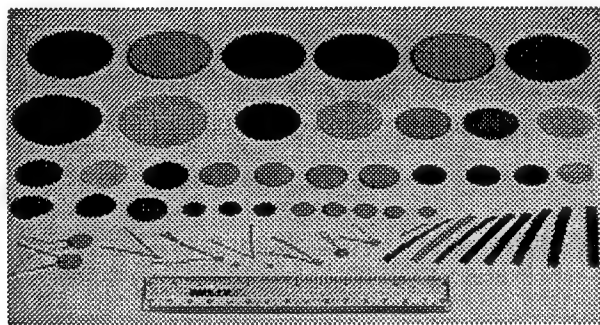
Figure 4. Typical examples of sizes and shapes of Rainbow elements

2.3 Rainbow operation

In regard to operation, a Rainbow is similar to a device known in the industry as a unimorph bender. A unimorph is composed of a single piezoelectric element externally bonded to a flexible metal foil which is stimulated into action by the piezoelectric element when activated with a ac or dc voltage and results in an axial buckling or displacement as it opposes the movement of the piezoelectric element. However, unlike the unimorph, the Rainbow is a monolithic structure with internal compressive stress bias on the piezoelectric element; thus producing the dome structure, rendering it more rugged and able to sustain heavier loads that normal. The integral electrode (usually the bottom electrode) consists of metallic lead intimately dispersed throughout the semiconductive, porous oxide layer. The change in shape of the wafer after reduction is believed to be due to (1) the reduction in volume of the bottom reduced layer (largely metallic lead) compared to the unreduced material as a result of the loss of oxygen from the lattice, (2) the differential thermal contraction between the reduced and unreduced layers on cooling to room temperature and (3) any change in volume which may occur on cooling through the Curie point as the material undergoes a phase transformation from a smaller, non-polar, cubic unit cell to a larger, polar, ferroelectric unit cell.

Like other piezoelectric devices, Rainbows may be operated with a dc, pulse dc, or ac voltage; however, when driven with ac, the largest displacements are usually achieved at 100 Hz or less. In operation, the dome height of the Rainbow varies as a function of the magnitude and polarity of the voltage. When a given polarity of voltage is applied, the dome decreases in height depending on the magnitude of the voltage; and alternatively, when the polarity is reversed, the dome increases. The large axial motion of the dome is largely due to contributions from (1) a lateral contraction produced in the material via the d_{31} coefficient and (2) a stress-directed domain switching process near the top surface wherein c-axis domains lying in the plane of the wafer as a result of the tensile stress are induced by the electric field to switch to a position normal (90°)to the plane. It should be remembered that the 180° domains that reorient in the electric field do not cause a change in shape for the Rainbow. A model of this effect is illustrated in Figure 5.
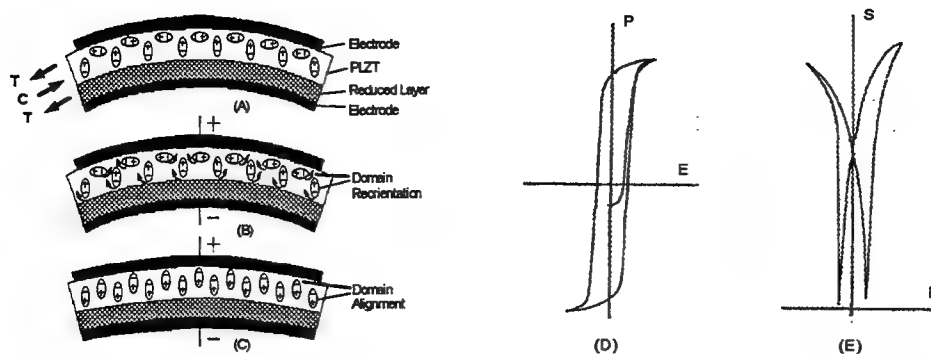
Figure 5. A model of the changes taking place during operation of a Rainbow wafer, depicting various stages of domain alignment and reorientation in a Rainbow actuator: (A) as processed and electroded, (B) first application of voltage causing domain reorientation, (C) complete application of voltage producing near complete domain alignment and flattening of the wafer, (D) the asymmetrical hysteresis loop obtained on the first application of voltage indicating partial, stress-induced (ferroelastic) poling and (E) the asymmetrical strain loop obtained on first application of voltage.

3. PROPERTIES

3.1 Dielectric properties

The temperature dependent dielectric behavior for two PLZT compositions; i.e., 1/53/47 and 9/65/35, are shown in Figure 6. It can be seen from the figure that a gradual rise occurs in the relative dielectric constant (1 kHz) of 1/53/47
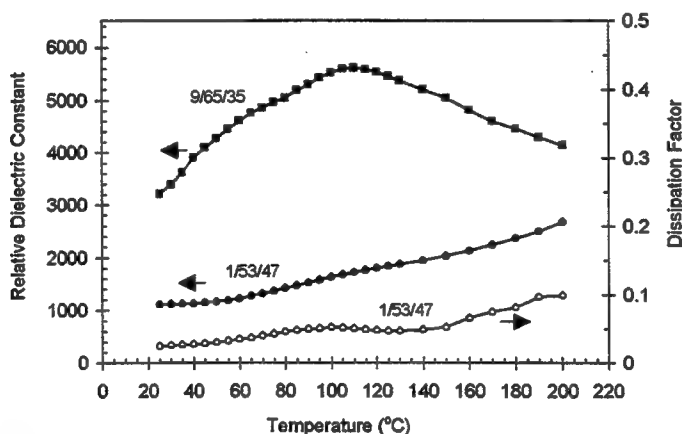
Figure 6. Temperature dependent dielectric properties of PLZT Rainbow wafers.

from a room temperature value of approximately 1100 to about 2700 at 200°C. No peak is observed in this range for this composition because its Curie point is 330°C. On the other hand, composition 9/65/35 shows a change in dielectric constant from 3200 to 5700 over this same temperature range with a peak occurring at 105°C, which is its usual Curie point as determined from small signal measurements. Since this composition is an electrostrictive, relaxor-type material, this Curie point does not coincide with its loss in polarization which occurs at about 20°C; thus, making it one of the most sensitive, high displacement, electrostrictive Rainbow materials. It may be noted that the dielectric constants for both compositions and also the dissipation factor for 1/53/47 are comparable to previously reported values, and this indicates that the Rainbow reduction process does not substantially change the dielectric properties of the unreduced part of the structure.

3.2 Hysteresis loops

Typical examples of dc hysteresis loops for compositions 1/53/47 and 9/65/35 are given in Figure 7. The loop in Figure 7(A) was taken on the ferroelectric Rainbow element (1/53/47) in its virgin condition before any other measurements
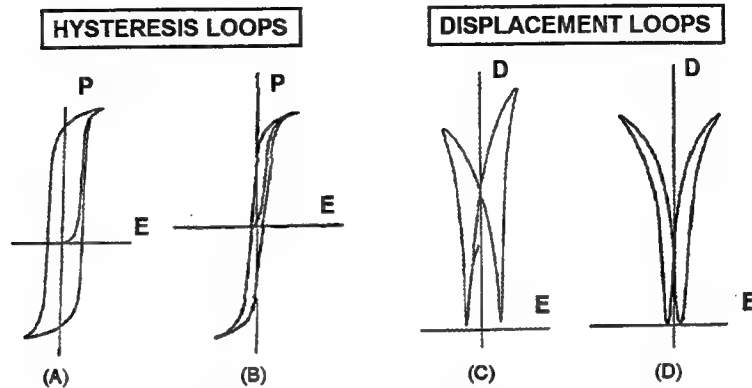
Figure 7. Hysteresis loops (P vs. E) and electromechanical displacement loops (D vs. E) for PLZT Rainbows 1/53/47 (A and C) and 9/65/35 (B and D), respectively.

were made. It should be noted that on the initial application of positive voltage to +450V there was approximately 60% of the total remanent polarization switched rather than the usual 50% one ordinarily observes in a virgin, randomly oriented ceramic.. This behavior is highly unusual and indicates that the Rainbow ceramic was partially poled before testing. Additional audio and piezoelectric tests of other virgin parts also indicated that the elements were partially poled to varying degrees; i.e., some very little and others as high as 75%.

One explanation for this condition occurring in the electrically virgin state is that the mechanical compressive and tensile stresses produced in the Rainbow wafer during processing are acting together to switch some of the domains in this soft ferroelectric/ferroelastic material. Since uniform stress is a symmetrical quantity, it is recognized that it alone is insufficient to produce a net polarization in a given direction even though it may be of sufficient magnitude to switch domains; however, a stress gradient such as produced by the Rainbow bending process is a vector quantity and can, indeed, produce the observed effect. This non-uniform stress is believed to be responsible for the partial poling of the Rainbow wafers. Measured properties on the above 1/53/47 wafer were: P_R = 44.8 uC/cm^2, E_C = 7.5 kV/cm, dielectric constant = 1210 and dissipation factor = 0.047.

The virgin loop of Figure 7(B) is a typical one for the electrostrictive (9/65/35) type of Rainbow materials and is very similar to that obtained on bulk electrooptic material. Measured properties on this wafer were: $P_{10kV/cm}$=28.3 uC/cm^2, dielectric constant = 3142 and dissipation factor = 0.085. As a matter of course, no unsymmetrical hysteresis loops were observed in the electrostrictive materials, and none was expected, since there are no stable domains in these materials at zero electric field. Conceivably, a high enough stress could precipitate stable domains in a very near-ferroelectric material, however, this was not experimentally confirmed

3.3 Electromechanical displacement loops

Displacement vs. electric field (butterfly) loops for the Rainbow wafers described above are also shown in Figure7. Figure 7(C) illustrates the Rainbow axial motion as the sample is electrically switched from zero to +450V, to -450V and back to zero, however, in this case this loop was not taken on the virgin wafer. It may be noted that this loop is remarkably similar to that observed when measuring the direct extensional (longitudinal, lateral) displacements via the piezoelectric d_{33} or d_{31} coefficients. The value of displacement in the + voltage direction was measured at 190.5 um, and the total amount of displacement (+/-) was 432 um.

Figure 7(D) shows the displacement loop of the electrostrictive Rainbow material (9/65/35) mentioned above. Since 9/65/35 is a relaxor material there should be little or no memory, and the same value and sign of displacement

should be obtained whether a + or a - voltage is applied. One can see by switching this sample through a full voltage loop that a small amount of remanent displacement (strain) is present which is probably due to the close proximity of this composition to a FE phase. A further indication of this incipient FE phase is the higher than normal value of P_{10} (P_{10} = 28.3 vs. a more normal 18.0 uC/cm^2) as given above. Measured value of total displacement for this wafer was 178 um.

3.4 Voltage dependent displacement characteristics

The displacement characteristics as a function of applied voltage are given in Figure 8 for some selected compositions. One of the most striking features of this figure is the very high displacements achieved by these Rainbow
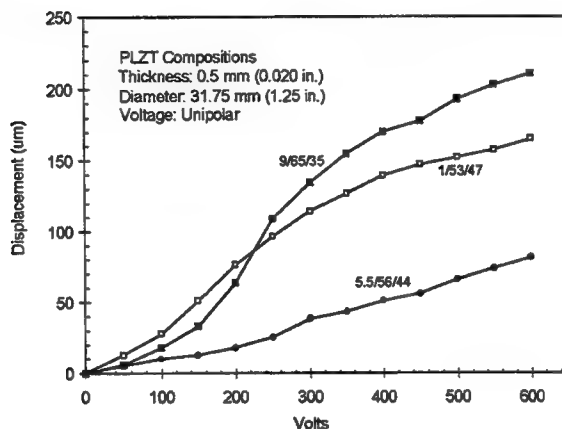
Figure 8. Axial dislacement characteristics of Rainbow PLZT compositions as a function of voltage.

ceramics at moderate electric fields; e.g., 400 volts is equivalent to an electric field of 10 kV/cm. Composition 9/65/35 is noted to possess the highest displacement of 210 um at a maximum voltage of 600 volts, however, its displacement is characteristically non-linear because of its electrostrictive nature. Compositions 1/53/47 and 5.5/56/44 are ferroelectric materials, and thus, are more linear in behavior. As a general rule, the displacements of the ferroelectric materials are lower than those of the electrostrictive compositions, particularly when operated at higher voltages and one polarity; however under bipolar operation, the displacement values of the ferroelectric materials will commonly be double the values shown in the figure.

Figure 9 illustrates the unusually large range of displacements obtained for Rainbows as a function of thickness,
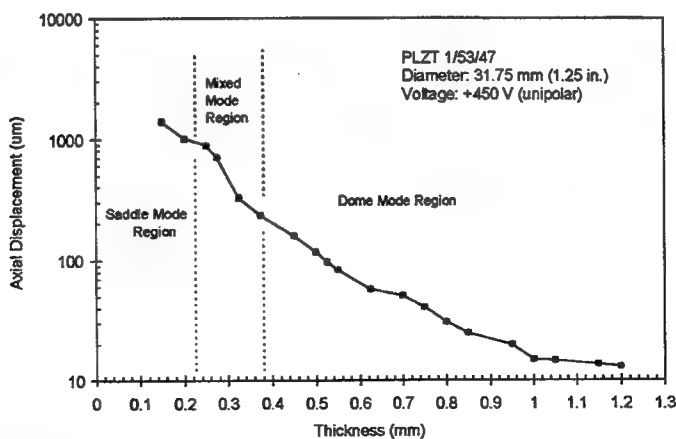
Figure 9. Displacement characteristics of Rainbow PLZT 1/53/47 as a function of wafer thickness.

where thickness is plotted against the log of displacement. Wafer thickness has been found to have a significant effect upon axial displacement primarily because of the change in motional mode; i.e., from dome (spherical) to saddle (cylindrical) flexing, as the wafer thickness is reduced to approximately one-hundredth of the diameter. For example, a 31.75 mm (1.25 inch) diameter wafer usually develops a saddle-mode configuration when its thickness is less than 0.32 mm (0.013 inch). Saddle-mode operation provides maximum displacement with minimum load bearing capability (<100 grams); and therefore, should only be considered for special applications. It can also be seen from the figure that there is a thickness-dependent mixed mode region separating the other two modes. Replotting the data (in the dome-mode region) as displacement vs. $1/\text{thickness}^2$ reveals a near linear relationship and demonstrates that the displacement is inversely proportional to the square of the wafer thickness as shown in Figure 10.
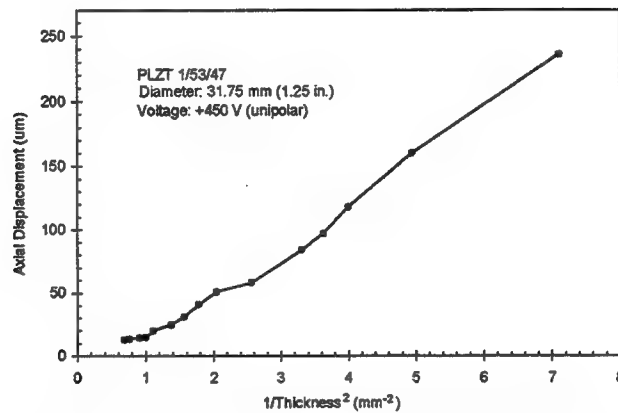
Figure 10. Replot of data from the dome-mode region of Figure 9 for Rainbow 1/53/47

The dependence of the axial displacement of a Rainbow wafer on its diameter is shown in Figure 11 where displacement is plotted against the wafer diameter squared. As can be seen, an excellent linear relationship is obtained.
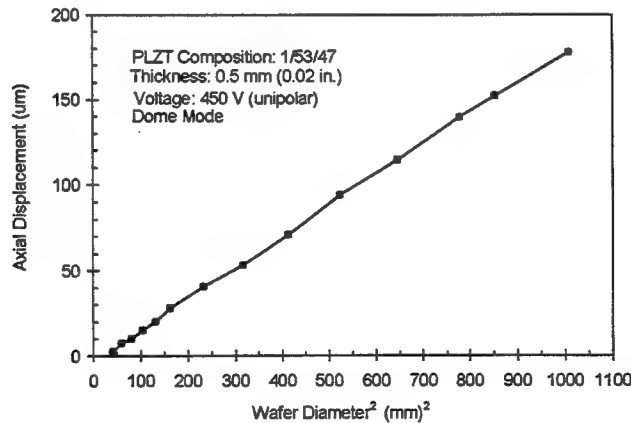
Figure 11. Axial displacement of Rainbow PLZT 1/53/47 as a function of the wafer diameter squared.

Thus, the data from both Figures 10 and 11 confirm that a Rainbow behaves very much like a normal bending actuator according to the equation: [18]

$$y = 3/2 * d_{31} * d^2/t^2 * V$$

or, in general,

$$y = m * d^2/t^2 * V$$

where y is the axial displacement, d_{31} is the lateral piezoelectric coefficient, m is a constant (1×10^{-4} um/V), d is the wafer diameter, t is the wafer thickness and V is the applied voltage. Maximum displacement is accordingly obtained with larger diameter and thinner wafers. A maximum displacement of 3mm at an operating voltage of 450 V has been obtained, to date, with a single Rainbow wafer having a diameter of 100 mm and a thickness of 0.375 mm.

The effect of an unconstrained axial point load on the displacement of an activated Rainbow is given in Figure 12 for
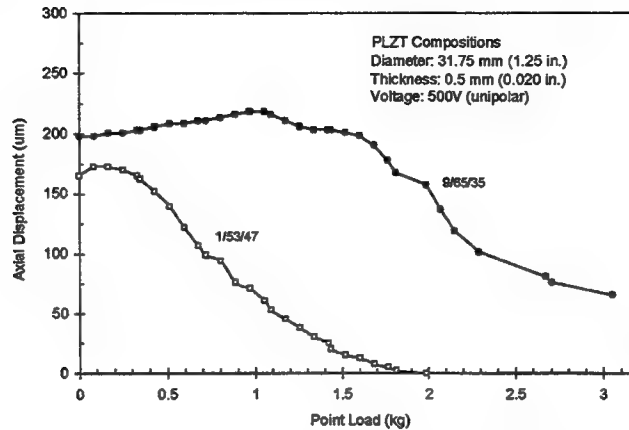
Figure 12. Concentrated (point) load-bearing characteristics of Rainbow PLZT Compositions

compositions 1/53/47 and 9/65/35. PLZT 1/53/47 can be seen to be relatively ineffective when loaded with a dead weight of 1.5 kg (3.3 lbs), whereas, composition 9/65/35 is still effective at a load of over 3 kg. This result is not too surprising since the elastic modulus of 9/65/35 (10.9×10^4 MPa) is noticeably higher than that of 1/53/47 (7.8×10^4 MPa). Another point to note from the figure is the increase in displacement with the introduction of a finite amount of load on the device. This effect was previously reported by Furman, et al.,[8] and is believed to be due to the lowering of the stiffness of the ceramic when the ferroelectric phase is field enforced. This decrease in elastic modulus with field leads to an increased flattening of the wafer under load; however, when the field is removed, the material become stiffer again and the original height (curvature) of the wafer is restored. This phase transformation effect leads to a increased range of displacement up to an amount of loading which can be readily accommodated by the wafer without the electric field. As a function of frequency, 9/65/35 is also superior to 1/53/47 in that its displacement is relatively constant from 0.1 Hz to several hundred Hertz.

Another concern of actuator designers is the amount of force that can be generated by an actuator when voltage is applied. This is shown in Figure 13 for a 1/53/47 Rainbow of standard size. As can be seen, the force generated is a linear
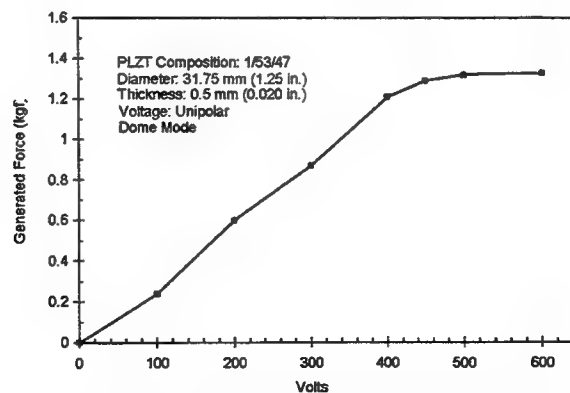
Figure 13. Effect of applied voltage on the force generated by a PLZT 1/53/47 Rainbow wafer.

function of voltage until the onset of saturation for this particular configuration. A maximum force of 1.3 kgf was achieved at 450 volts.

3.5 Rainbow stacks and arrays

Previous work on high displacment Rainbow actuators has shown that they possess the capability to be configured into linear stacks for higher displacement devices or into larger area arrays for actuator/sensor functional components. The stacking arrangement consisted of linearly cascading several Rainbow elements together in multiple groups of two in a clamshell arrangement and then bonding these clamshells together into a single unit. Sending/receiving arrays, on the other hand, were individually placed side-by-side (sandwiched between to thin layers of ductile metal foil and bonded together with conductive Ag epoxy) in order to maximize their area while minimizing their thickness. Thus, stacks consisted of Rainbows arranged mechanically in series and electrically in parallel while arrays were Rainbows arranged both mechanically and electrically in parallel. Individually addressed elements in some of the arrays were achieved by employing a matrix scheme wherein separate bottom electrodes made up the rows and separate top electrodes were the columns. Operation of a single Rainbow was then obtained by applying voltage between a row and column electrode. Typical examples of stacks and arrays are shown in Figure 14.

(A)   (B)   (C)
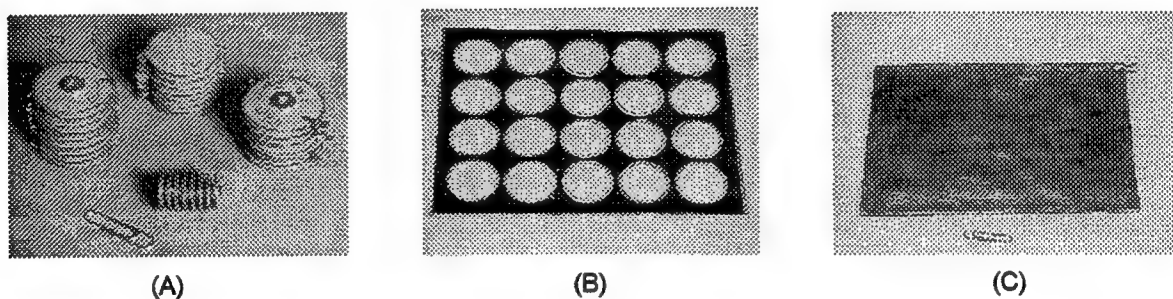
Figure 14. Examples of (A) Rainbow stacks and a Rainbow array showing (B) the individual Rainbow elements before applying the top metal foil and (C) completed smart skin array 1.25 mm thick.

The characteristics of the PLZT Rainbow stacks were evaluated as a function of wafer thickness, wafer diameter, point load-bearing capability and unipolar or bipolar voltage displacement. These data are given in Figure 15. First it can
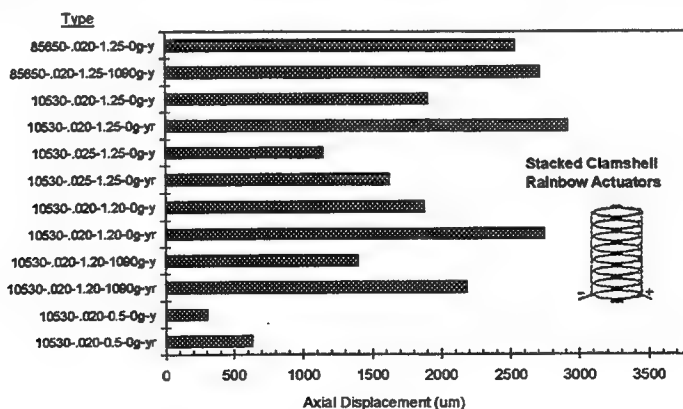
Figure 15. Displacement characteristics of various types of eight-unit Rainbow clamshell actuators. Type legend: composition/wafer thickness in inches/wafer diameter in inches/point load in grams/bipolar (yr) or unipolar (y) voltage displacement.

be seen that bipolar operation always achieves higher displacement by at the expense of higher non-linearity; secondly, in unipolar operation the 8.5/65/35 material achieved higher displacements and could sustain higher loads than the 1/53/47

material; however, in bipolar operation the 1/53/47 was superior in terms of displacement; and thirdly, small compact actuators, 12.7 mm dia. x 24 mm long, were capable of achieving moderate displacements (308 um) under modest loads of 1 kg. or less. In general, total displacements were found to scale linearly with the number of individual Rainbow elements. In regard to the arrays, several different Rainbow arrays consisting of up to 42 Rainbow elements were evaluated

4.0 APPLICATIONS

A number of examples of applications are given in this section in order to demonstrate the versatility of the Rainbow technology. These working models are essentially discrete, proof-of-principle devices which require further engineering, design, miniaturization and modifications in order for them to be suitable for hybrid microelectronics or integrated structures. A number of advantages and features of the Rainbows are: (1) simplicity, (2) solid-state, (3) monolithic, (4) pre-stressed for greater strength and durability, (5) can sustain or generate moderate loads, (6) surface mountable, (7) very high axial displacement, (8) above-the-plane displacement, (9) no bonding layers, (10) temperature compensation possible, (11) can be stacked to multiply displacement and (12) can be fabricated into large area arrays.

Chassis Speaker

Table Leveler

Jet Pump

Substrate Pump

Toys

Remote Tweezer

Cavity Pump
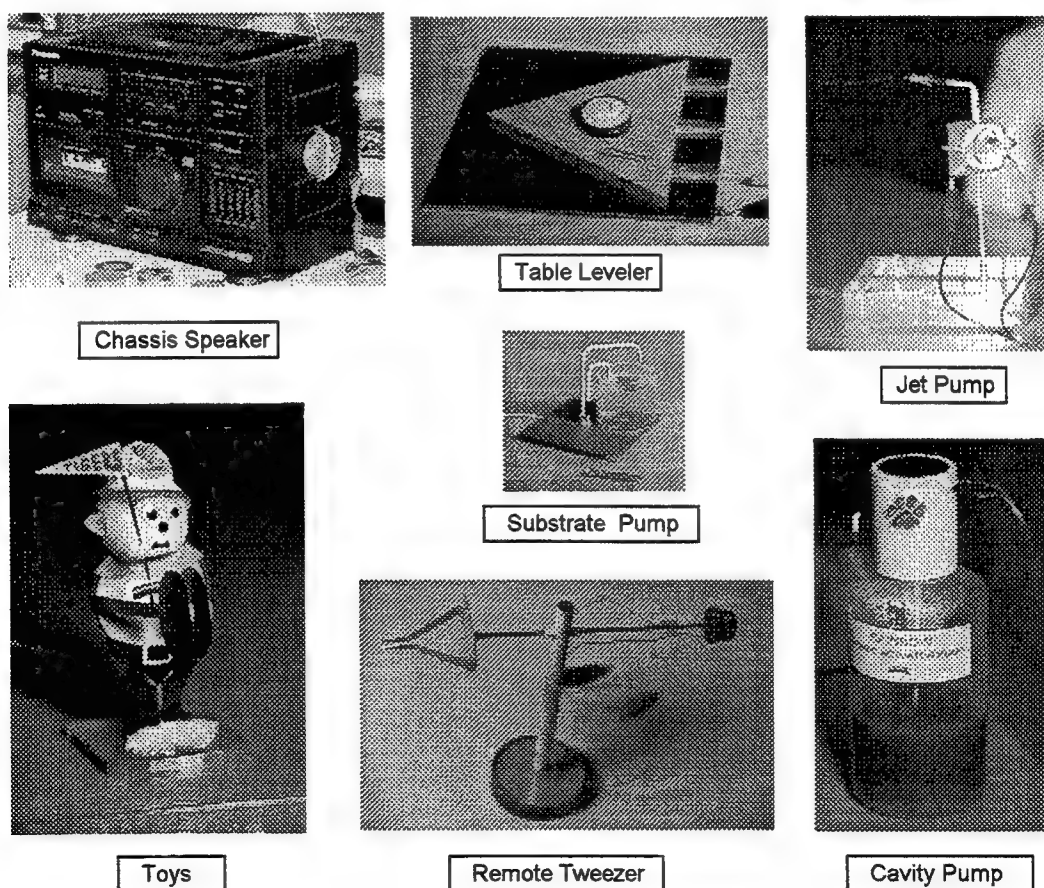
Figure 16. Examples of working model devices using Rainbow ceramics as actuators

The Rainbow devices shown in Figure 16 are typical examples of a number of applications envisioned for this technology. As can be seen, they range from actuators to speakers, and remote handlers to pumps. A more extensive list of applications include (1) linear actuators, (2) cavity/piston pumps, (3) loud speakers, (4) reciprocating motors, (5) relays/switches/thermostats, (6) sensors, (7) hydrophones/hydroprojectors, (8) variable-focus mirrors/lenses, (9) optical deflectors/scanners, (10) vibrating delivery systems, (11) liquid delivery systems, (12) antivibration/noise-cancelling devices, (13) sonic and ultrasonic devices and (14) auto-leveling platforms.

91

5. CONCLUSIONS

The prospects for utilizing Rainbows in discrete hybrid and integrated microelectronics are promising for future applications involving smart ceramics such as ferroelectrics, piezoelectrics, electrostrictive and antiferroelectric materials. Rainbows have opened up a new dimension in high displacement actuators. The key to adapting these materials to specific devices and applications is the manner in which answers are found to questions concerning their reproducibility, reliability, longevity and cost effectiveness. Further development and design work are obviously needed in order to answer these questions.

ACKNOWLEDGEMENTS

REFERENCES

1. R.E. Newnham and G.R. Ruschau, "Smart electroceramics", *Bull. Am. Ceram. Soc.* **75**, pp. 51-61, 1996.
2. V. Giurgiutiu, Z. Chaudhry and C.A. Rogers, "Energy-based comparison of solid-state actuators", Virgina Tech Report No. CIMSS 95-101, Center for Intelligent Material Systems and Structures, 1995.
3. G.H. Haertling, "Rainbow ceramics - a new type of ultra-high displacement actuator", *Bull. Am. Ceram. Soc.* **73**, pp. 93-96, 1994.
4. G.H. Haertling, "Method for making monolithic prestressed ceramic devices", U.S. Patent No. 5,471,721, December 5, 1995.
5. G.H. Haertling, "Chemically reduced PLZT ceramics for ultra-high displacement actuators", *Ferroelectrics* **154**, pp. 101-106, 1994.
6. E. Furman, G. Li and G.H. Haertling, "An investigation of the resonance properties of rainbow devices", *Ferroelectrics* **160**, pp. 357-369, 1994.
7. S. Sherrit, H.D. Wiederick, B.K. Mukherjee and G.H. Haertling, "The dielectric, piezoelectric and hydrostatic properties of PLZT based Rainbow ceramics", *Proc. of the 9th IEEE Intl. Meeting on Appl. of Ferroelectrics*, pp. 390-393, University Park, PA, 1994.
8. E. Furman, G. Li and G.H. Haertling, "Electromechanical properties of Rainbow ceramics", *Proc. of the 9th Intl. Meeting on Appl. of Ferroelectrics*, pp. 146-149, University Park, PA, 1994.
9. G.H. Haertling, "Compositional study of PLZT Rainbow ceramics for piezo actuators", *Proc. of the 9th Intl. Meeting on Appl. of Ferroelectrics*, pp. 313-318, University Park, PA, 1994.
10. C. Elissalde and L.E. Cross, "Dynamic characteristics of Rainbow ceramics", *J. Am. Ceram. Soc.* **78**, pp. 2233-36, 1995.
11. G. Li, E. Furman and G.H. Haertling, "Composition and microstructure of chemically reduced PLZT ceramics", *Ferroelectrics*, **182**, pp. 69-76, 1996.
12. K.M. Nair and V.N. Shukla, *Hybrid Microelectronic Materials*, pp. 71-96, ACerS Ceramic Transactions, Vol. 68,., Westerville, OH, 1996.
13. C. Elissalde, L.E. Cross and C.A. Randall, "Structural-property relations in a reduced and internally biased oxide wafer (RAINBOW) actuator material", *J. Am. Ceram. Soc.* **79**, pp. 2041-48, 1996.
14. G. Li, E. Furman and G.H. Haertling, "Fabrication and properties of PSZT antiferroelectric Rainbow actuators", *Ferroelectrics* **188**, pp. 223-236, 1996.
15. D.E. Dausch, "The effects of excess PbO addition and composition variation on the processing and properties of tape cast PLZT Rainbow actuators", *Proc. of the 10th Intl. Meeting on Appl. of Ferroelectrics*, East Brunswick, NJ, 1 996. (to be published)
16. G. Li and G.H. Haertling, "The piezoelectric, pyroelectric and photoelectronic properties of PLZT Rainbow ceramics", *Proc. of the 10th Intl. Meeting on Appl. of Ferroelectrics*, East Brunswick, NJ, 1996. (to be published)
17. G.H. Haertling, "Stress-induced effects in PLZT ceramics", *Proc. of the 10th Intl. Meeting on Appl. of Ferroelectrics*, East Brunswick, NJ, 1996. (to be published)
18. R.C. Buchanan, *Ceramic materials for electronics*, p. 187, Marcel Dekker, Inc., New York, 1991.

Multilayer electromechanical composites with controlled piezoelectric coefficient distribution

James S. Vartuli,[a] David L. Milius,[a] Xiaoping Li,[b] Wan Y. Shih,[a,b] Wei-Heng Shih,[b]
Robert K. Prud'homme,[a] and Ilhan A. Aksay[a]

[a]Department of Chemical Engineering and Princeton Materials Institute
Princeton University, Princeton, NJ 08544-5263
[b]Department of Materials Engineering
Drexel University, Philadelphia, PA 19104-2875

ABSTRACT

We have fabricated multilayer electromechanical composites with controlled piezoelectric coefficient distributions using tape casting. Tapes of doped lead zirconate titanate were cut and stacked in accordance with their characteristic electromechanical coupling values and modulus of elasticity. This technique is an extremely versatile method to fabricate displacement actuators to fabricate monolithic ceramic parts with controlled material property gradients. To obtain a quantifiable method to optimize this type of transducer, we have devised a processing model. Given the functional distribution of the electromechanical coupling coefficient, d_{31}, and the functional distribution of elastic modulus through the thickness of the transducer, the analysis predicts the displacement as a function of loading. The tape casting method coupled with the model provides an actuator that maximizes displacement and generated force for the given material properties.

Keywords: actuator, multilayer, piezoelectric, tape casting

1. INTRODUCTION

There has been a continuous effort to improve piezoelectric actuator systems so that simultaneously large displacements, on the order of hundreds of microns, can be obtained while subjected to large forces, on the order of Newtons. Two recently developed piezoelectric actuators, moonies[1] and rainbows,[2] have made significant improvements in obtainable displacements and generated forces. Both contain a shell-like structure and obtain large axial displacements at the apex of the shell through bending stresses. We focus on the rainbow and seek ways to improve the displacement and load bearing properties.

Rainbows achieve their bending stress from a variation in the d_{31} value of electromechanical coupling across the thickness of the actuator. The gradient in d_{31} is obtained by selectively reducing one side of a plate (with respect to oxygen content). Rainbows, although achieving large displacements while sustaining moderate loads, are limited from a processing standpoint. Chemical reduction produces only one functional gradient in electromechanical properties across the thickness of the actuator. The resulting functional gradient does not follow the theoretically expected hyperbolic tangent diffusion relation, but contains a pre-reduction zone.[3] The grain boundaries within the intermediate pre-reduction zone are modified by the reduction. We present a processing scheme that can customize an actuator for a given function, by providing considerable control over the material property gradients. Our approach permits sharp functional gradients that are not severely altered by solid state diffusion.[4]

Utilizing the benefits of creating displacement through a transverse bending stress, we started to process transducer plates with d_{31} variations made by the tape casting method. This versatile fabrication route produces 25 to 60 μm, uniform sheets of lead zirconate titanate (PZT), that serve as the building block of the actuator. Individual sheets of piezoelectric material can be stacked according to different material properties. We have developed a computational model that serves as

a useful guide in the processing. The analysis supplies quantified design characteristics to produce a transducer with the greatest displacement and load bearing abilities for the given material constants. Incorporating this information with the tape cast processing strategy, we can produce "tailor-made" actuators.

2. PROCESSING OF TRANSDUCERS

Tape casting is frequently utilized in the electronics industry for a variety of applications. Thin, uniform tapes can be made with ceramic contents that exceed 50 volume percent. This process is a natural choice for the fabrication of materials with functional gradients. We have made stable suspensions of various PZT powders that have d_{31} values ranging from -262×10^{-12} to -3×10^{-12} m/V.[5] The mixing of different powders allows the creation of a continuous array of properties.

An outline of the process is shown in Fig. 1. The suspensions are mixed with polymers and an appropriate solvent. The polymers provide mechanical integrity and flexibility to the tape. A flat doctor blade sweeps the liquid mixture across a substrate. Within several minutes the cast tape is dried, cut, and separated from the backing. Any desired shape could be stamped from the tapes, but preliminary experiments use simple rectangular and circular pieces. The material is subsequently stacked in the desired order. Heat and pressure make the stacked structure into a laminated monolith by inter-diffusing the long chain polymers across adjacent tapes.
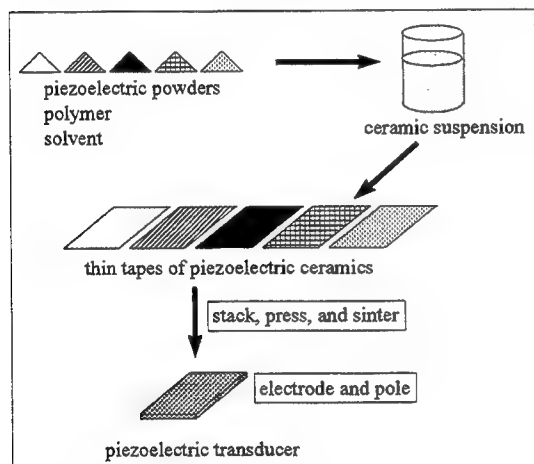
Figure 1: Outline of the processing steps

During the sintering step, the discrete layers create a fully dense monolith without the aid of external pressure, producing a multilayer electromechanical composite with a "custom made" piezoelectric coefficient distribution. We should preface here that the piezoelectric coefficient distribution within the sintered specimen will be slightly different from that of the unsintered piece, due to diffusion of the PZT dopants. This would result in a smoothing of any sharp material property interfaces, as observed by Wu, et al. at the Naval Research Laboratory.[6] Wu, et al noticed that a dopant used to alter resistivity diffused to produce a continuous, nearly linear gradient across the actuator thickness. With our approach of varying the PZT powders, our chemical analysis by energy dispersive spectroscopy shows that sharp material property interfaces remain after sintering.[4] This technique provides a predictable control of material property distributions enabling the desired green structure to remain after sintering. The following sections describe why control is so important to actuator performance.

3. MODELING FOR FLEXTENSIONAL TRANSDUCERS

The following is a model that we are currently using to guide our fabrication. This multilayer thin plate model provides insight on the key phenomena. The theory is a natural extension to tape cast processing. First, we define a multilayer laminate composed of "n" layers. Each layer has defined values for the modulus of elasticity, the electromechanical coupling value of d_{31}, and the thickness.

The effect of the electromechanical coupling, d_{33} is assumed insignificant. In the case that the length of the actuator is large relative to the thickness, this assumption is true. The model is limited to the linear region of displacement vs. voltage relationship. Finally, the present analysis uses the beam geometry of which bending effects along the width are neglected. For a transducer that is much longer than it is wide, this assumption will not introduce appreciable error. For the case that the width of the plate is comparable to the length, the model can be generalized to include the contribution from the whole dimension.

This section borrows ideas from a recent publication by Shih, et al.[7] Shih, et al.'s two layer model is made more general to include many thin layers that can closely approximate a continuum. We examine the specific case of placing a

distributed force that spans the width of the transducer at the length's mid-point and finding the resulting displacement at this location. Figures 2 and 3 define the geometry. There are two boundary conditions that must be satisfied:

(i) The sum of the bending stress must equal zero,

$$\sum_{x=1}^{n} \int_{t_{x-1}}^{t_x} E_x \left(z - t_{np} \right) dz = 0 \text{ , and} \tag{1}$$

(ii) the sum of the lateral stresses equals zero,

$$\sum_{x=1}^{n} \int_{t_{x-1}}^{t_x} E_x \left(c - d_{31,x} \varepsilon \right) dz = 0 . \tag{2}$$

We solve for t_{np} and c, where

n = total number of layer,	z = distance from t_0,
t_x= the position at the top of layer x,	E_x = modulus of elasticity of layer x,
$d_{31,x}$ = the d$_{31}$ value of layer x,	ε = the electric field,
t_{np} = the position of the neutral plane,	r = the radius of curvature,
c = the constrained in plane strain,	t_0 = the position at the bottom of the first layer,
L = length of the beam	which is taken as the origin.
E = modulus of elasticity	I = moment of inertia
v = deflection of the beam	b = width of beam
F = distributed force along mid-point	x = position on the actuator.

Following the fundamental equation of beam theory:

$$\frac{d^2 v}{dx^2} = -\frac{M}{EI}, \tag{3}$$

the displacement is expressed as a function of the bending moment.
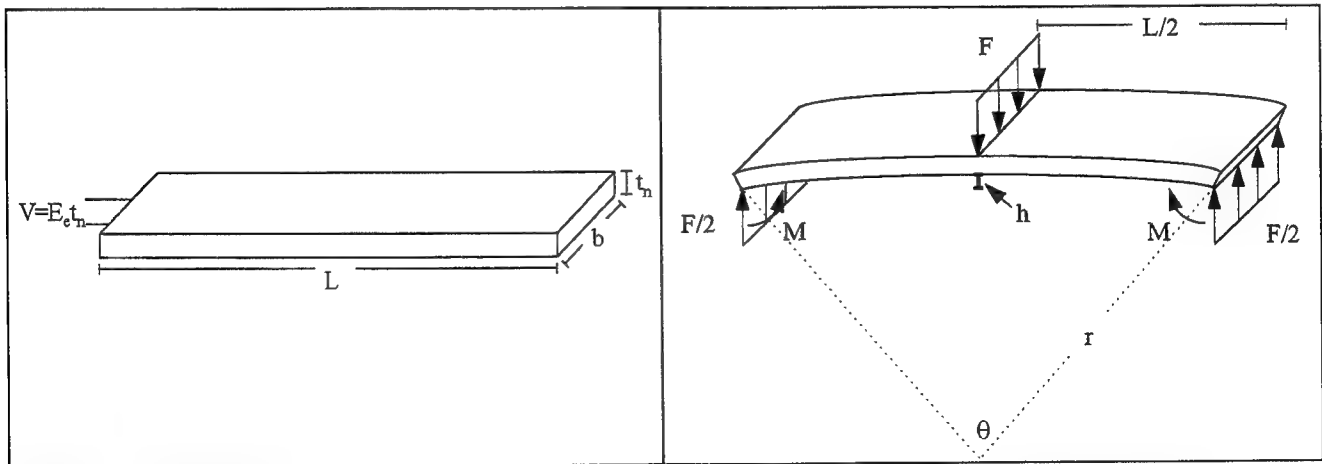
Figure 2: Geometry without load (symbols defined above).   Figure 3: Geometry with load (symbols defined above)

Using the results from Eqs. (1) and (2), we have values for t_{np} and c. The bending moment generated from the piezoelectric effect is calculated as follows:

$$M = b \sum_{x=1}^{n} \int_{t_{x-1}}^{t_x} E_x \left(d_{31,x} E_e - c \right) \left(z - t_{np} \right) dz \tag{4}$$

The displacement of a point on the actuator can be calculated from substituting (3) into (4), and is shown below:

$$EIv(x) = \frac{M}{2} \left(x^2 - Lx \right) - \frac{F}{48} \left(4x^3 - 3L^2 x \right) \text{ for } 0 \leq x \leq \frac{L}{2}. \tag{5}$$

The product of elastic modulus and moment of inertia of a laminated composite can be calculated as:

$$EI = b \sum_{x=1}^{n} \int_{t_{x-1}}^{t_x} E_x \left(z - t_{np} \right)^2 dz \tag{6}$$

Simplifying the above analysis to a two layer composite without a load, yields exact agreement with Timoshenko's analytic model of bi-metal thermostats.[8]

4. RESULTS

The following three examples, Figs. 4, 5, and 6, display different functional variations of d_{31} across the thickness of the actuator. Figure 7 compares the results. Figures 4, 5, and 6, are a step function, linear function, and diffused step function, respectively. Each type of actuator has a graph that displays the relationship between displacement and generated force along with the corresponding work under these conditions. The following conditions were held constant for each sample calculation:

   (i) length = 25.4 mm, width = 12.7 mm, thickness = 0.6 mm,
   (ii) modulus of elasticity is constant at 6.4×10^{10} N/m^2,
   (iii) voltage drop = -500 V; producing an electric field = -8.3×10^5 V/m,
   (iv) variation is d_{31} from maximum to minimum absolute value is 167×10^{-12} m/V, and
   (v) the plane of neutral stress is constant at the center of the thickness = 0.3 mm.

A number of important design criteria were obtained from the modeling of the transducers. An actuator that moves a large distance while supporting a large load is more desirable. Typically this quantity, the maximum amount of obtainable work for a given electric field, provides a value to judge the usefulness of a given actuator. The following are the conditions for the axial d_{31} distributions that optimize the obtainable work:

   (i) maximize the difference between the d_{31} values of the top and bottom layers,
   (ii) a step-wise distribution of d_{31} is the optimal functional distribution, and
   (iii) place the steepest part of the slope, or the step in d_{31} on the plane of neutral stress.

Condition (i) is trivial and needs no explanation. Condition (ii) is verified by Table 1. Condition (iii) can be obtained analytically by maximizing M in Eq. (5). The maximum generated moment is obtained only when the plane of neutral stress lies on the interface of the two layers. The computational model, outlined above, will verify condition (iii) for the functional form of the gradient in d_{31} that is displayed in Fig. 6.

The step function is shown to be the optimal design to achieve maximum amount of work. However this d_{31} profile is not readily achievable with our process, due to diffusion of the PZT dopants at sintering temperatures.[6] We expect a d_{31} that more closely approximates the diffused step function shown in Fig. 6.

5. CONCLUSIONS

The tape casting method to fabricate multilayer electromechanical composites with controlled piezoelectric coefficient distributions has been demonstrated. "Tailor-made" actuator designs can be accomplished to achieve the optimal displacement and load bearing properties. A computational model has been developed to guide the processing for given material constants and comparisons between different designs can be made and judged without the need for numerous experiments and testing. A step functional variation of d_{31}, with the interface placed on the plane of neutral stress has been shown to be the optimized arrangement. The tape casting method is a processing method that is well suited to ensure that these design requirements are made with a high degree of accuracy.

ACKNOWLEDGMENTS
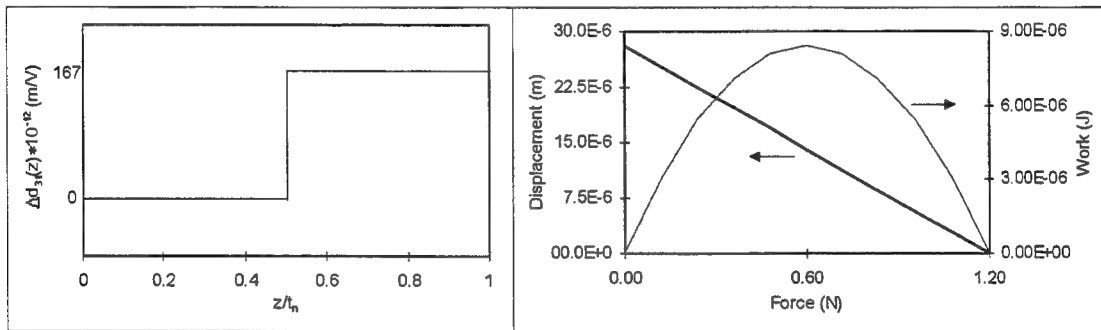
Figure 4: Step function in d_{31}, with accompanying displacement and work vs. force diagram.
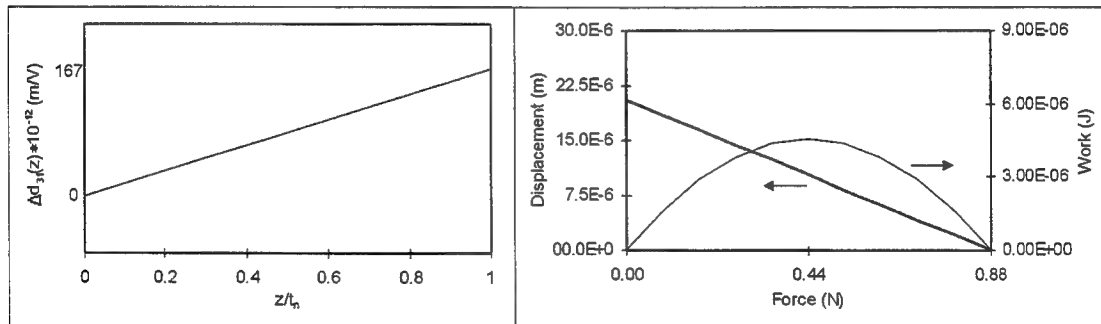
Figure 5: Linear function in d_{31}, with accompanying displacement and work vs. force diagram.
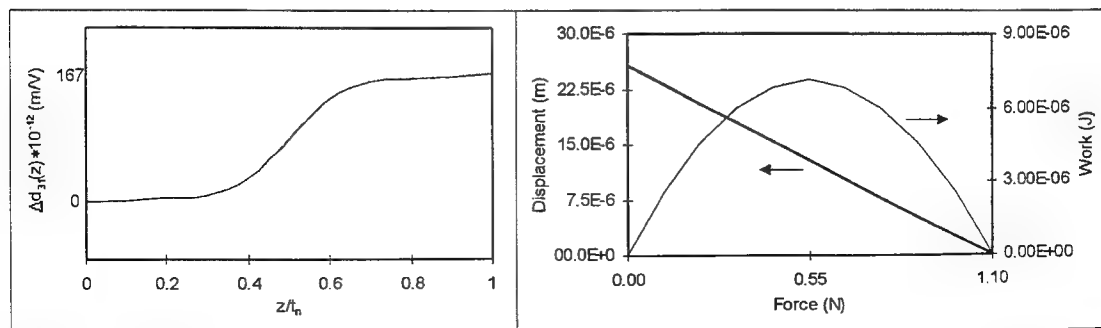
Figure 6: Diffused step function in d_{31}, with accompanying displacement and work vs. force diagram.

	Step Function	Linear Function	Diffused Step Function
Displacement at zero load	28.1 μm	20.6 μm	25.8 μm
Force at zero displacement	1.20 N	0.88 N	1.10 N
Maximum amount of obtainable work	8.43×10^{-6} J	4.54×10^{-6} J	7.12×10^{-6} J

Table 1: Outline of results from Figs. 4, 5, and 6.

REFERENCES

1. Y. Sugawara, K. Onistsuka, S. Yoshikawa, Q. C. Xu, R. E. Newnham, and K. Uchino, "Metal-Ceramic Composite Actuators," *J. Am. Ceram. Soc.*, **75** [4] 996-98 (1992).

2. G. H. Haertling, "Rainbow Ceramics: A New Type of Ultra-High Displacement Actuators," *Am. Ceram. Soc., Bull.*, **73** [1] 93-96 (1994).

3. C. Elissalde, L. E. Cross, and C. A. Randall, "Structural-Property Relations in a Reduced and Internally Biased Oxide Wafer (RAINBOW) Actuator Material," *J. Am. Ceram. Soc.*, **79** [8] 2041-48 (1996).

4. J. S. Vartuli, D. L. Milius, R. K. Prud'homme, and I. A. Aksay, results to be published.

5. EDO Corporation, Ceramic Operations, Salt Lake City, Utah.

6. C. C. M. Wu, M. Kahn, and W. Moy, "Piezoelectric Ceramics with Functional Gradients: A New Application in Material Design," *J. Am. Ceram. Soc.*, **79** [3] 809-12 (1996).

7. W. Y. Shih, W. H. Shih, and I. A. Aksay, "Scaling Analysis for the Axial Displacement and Pressure of Flextensional Transducers," *J. Am. Ceram. Soc.*, (1997) (in press).

8. S. Timoshenko, "Analysis of Bi-Metal Thermostats," *J. of Optic. Soc. of Am.*, **11** [9] 233-55 (1925).

Field dependence of the complex piezoelectric, dielectric, and elastic constants of Motorola PZT 3203 HD ceramic

S. Sherrit[a], H. D. Wiederick[a], B. K. Mukherjee[a] and M. Sayer[b]

[a]Physics Dept., Royal Military College of Canada, Kingston, ON, Canada, K7K 5L0
[b]Physics Department, Queen's University, Kingston, ON, Canada, K7L 3N6

ABSTRACT

The design of ferroelectric/piezoelectric smart structures is limited by the accuracy to which the material properties of the sensor/actuator materials are determined. In particular, it is important to understand the effects of losses, dispersion, and the non-linearities that become significant when large fields are applied. This paper presents the small signal properties, including losses of Motorola PZT 3203 HD, a typical piezoelectric material , and it reports on the field dependence of the material constants for large electric fields. A set of PZT 3203 HD unloaded resonators manufactured by Motorola was cut to specifications outlined in the IEEE Standard on Piezoelectricity Std 176-1987, to ensure the appropriate boundary conditions of each resonance mode. Quasi-static measurements were performed on some of the samples at various field levels above and below the coercive field of the material. The impedance/admittance spectra of the resonators were measured for different values of the DC bias field. In both cases the average slope as a function of field, which is a measure of the piezoelectric or the dielectric constant, was found to increase linearly with the maximum field applied. The values of the material constants determined from the DC biased spectra were found to be smaller by a factor of 4-6. This is attributed to differences in the nature of the measurements. The quasistatic measurements are done at high field and low frequency and involve irreversible domain switching. The DC bias measurement is at high frequency and the AC measurement field is much smaller and the domain motion is reversible.

Keywords: Hysteresis, piezoelectric material constants, non-linearities, field dependence, PZT, reduced matrix

1. INTRODUCTION

There are a wide variety of conditions under which piezoelectric/ferroelectric materials can be characterized. The usefulness of these various techniques depends largely on the application for the material. Quasistatic techniques are useful in characterizing the properties of actuators. In the characterization of actuators, for example, a field is applied at various levels and the resultant strain is monitored as the field is increased and decreased. For a typical ferroelectric material a measurable hysteresis is noticed in the resultant strain which is due to reversible and irreversible domain wall motion in the material. A qualitative look at the effect of domains on the strain field curves is shown in Figure 1. Under a large field the 180° and 90° domain walls move to maintain a minimum in the domain energy. Contributions from the electrostatic and domain wall energies counteract each other and the underlying domain structure (size, shape and population) changes. In the process some of the domains engulf other domains or change shape irreversibly which contributes to the net strain and polarization.

Ferroelectric ceramics are also frequently characterized by resonance measurements as outlined in the IEEE Standard on Piezoelectricity Std-176-1987. A small AC signal couples to the piezoelectric coefficient to excite a strain wave in the material. At a critical frequency determined by the sample dimensions a resonance occurs. These resonances are determined experimentally by monitoring the electrical impedance or admittance of the sample as a function of the frequency. The measurement is very practical in that the elastic, dielectric, and piezoelectric constants can be determined
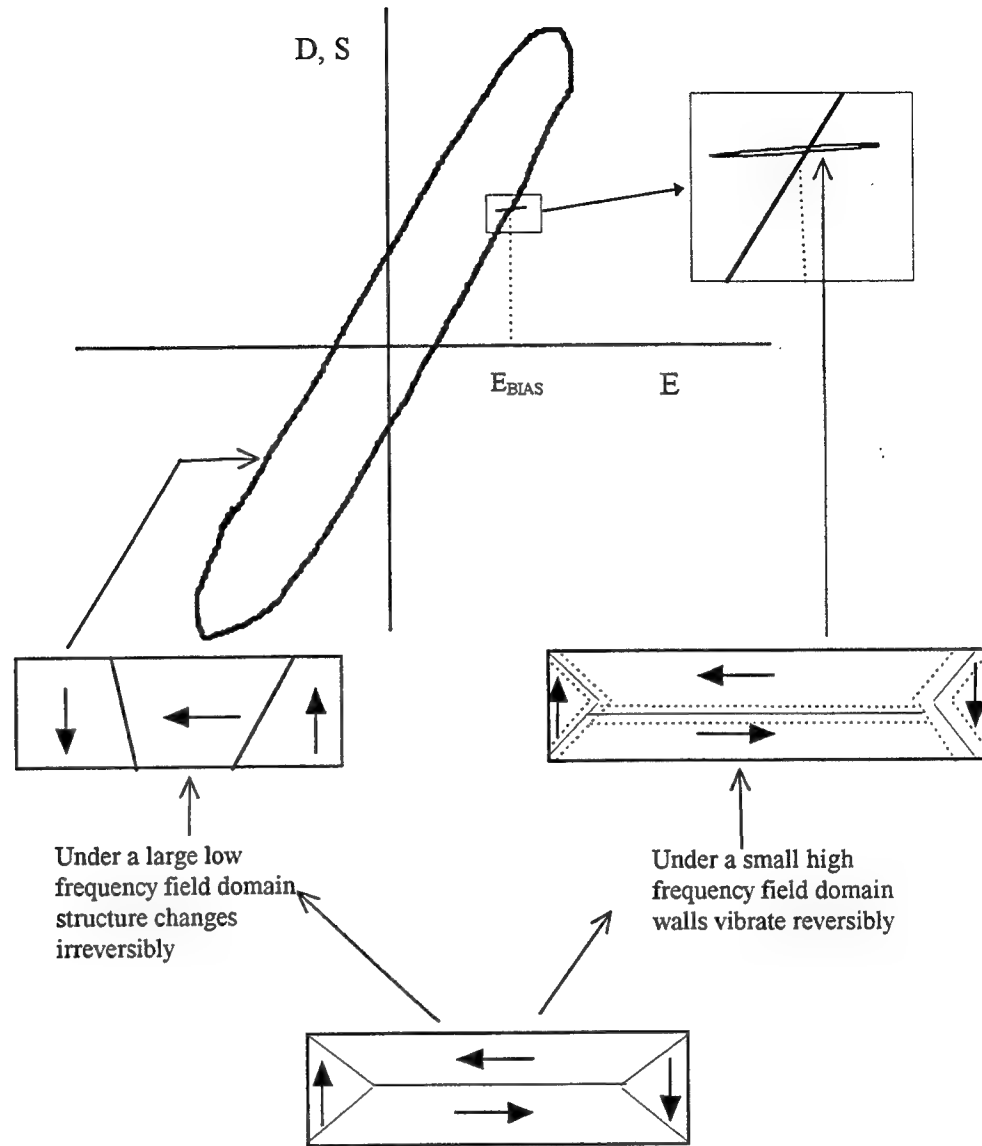
Figure 1: The relationship between the reversible and irreversible domain motion and the resultant strain or dielectric displacement as a function of the electric field. A portion of the smaller slope of the small AC field may be due to dispersion. A small hysteresis may also be present

from one measurement. Since the measurement signal is small, the excursions of the domain walls are small and the domain walls vibrate reversibly. The onset of irreversibility for 3 compositions of ferroelectric PZT materials has been studied by Zhang et.al.[1] They found that each material had a plateau region where the dielectric permittivity and the piezoelectric constant were independent of field. They attribute this field independence to reversible domain motion. Since the field of the AC signal is well below the critical fields of the plateau, it is clear that the small signal resonance measurement is actually a measurement of the reversible domain motion. For a biased resonator we are determining the reversible dependence at the bias field level. These curves however still have a hysteresis associated with them due to irreversible changes in the underlying domain structure due to the bias field.

2. QUASI-STATIC MEASUREMENTS

It has been known for some time now that the linear model of piezoelectricity could not explain some of the behavior of piezoelectric materials and the non-linear behavior has been studied by a variety of authors. Berlincourt and Kruegar[2] and Woolett and Leblanc[3] looked at the general aspects of non-linearity as a function of stress and field while Krueger[4,5,6,7], Brown and McMahon[8,9], Fritz[10] and Cao and Evans[11] studied the stress dependence of the dielectric elastic, and piezoelectric properties of piezoelectric ceramics.

The majority of the studies quoted above were done under quasi-static conditions where a stress ramp or an electric field is applied over some time and the properties are monitored as a function of the stress or electric field. One of the representations of the linear equations of piezoelectricity is

$$S_p = s_{pq}^E T_q + d_{pm} E_m$$
$$D_m = \varepsilon_{mn}^T E_n + d_{pm} T_p$$

(1)

where S, T, E, D are the strain, stress, electric field and the dielectric displacement respectively. The constants s^E, ε^T, d are the elastic compliance, dielectric permittivity and the piezoelectric constant respectively. The subscripts on the material coefficients designate the direction with respect to the poling direction of the piezoelectric ceramic. In the case of a length extension in the poling direction all the subscripts shown in (1) would be 3. The equations shown in (1) are phenomenological equations derived from thermodynamic potentials. The majority of quasistatic measurements use these equations as a starting point to interpret the results of quasistatic measurements. There is an experimental condition that can be imposed to simplify the measurement. It can be seen in equation (1) that if the stress is set to zero (sample free to expand), the equations in (1) are uncouple and the strain and dielectric displacement can be monitored as a function of the electric field. The uncoupled relationships are shown in Table 1.

Table 1: The quasi-static measurements that can be made in the 33 and 31 direction (along the poling axis) on a piezoelectric material with the stress set to zero

Linear Equations	Boundary Condition	Simultaneous Equations	
$S_3 = s_{33}^E T_3 + d_{33} E_3$ $D_3 = \varepsilon_{33}^T E_3 + d_{33} T_3$	$T_3 = 0$ (unclamped) Apply E_3-Measure S_3 and D_3	$S_3 = d_{33} E_3$	$D_3 = \varepsilon_{33}^T E_3$
$S_1 = s_{11}^E T_1 + d_{13} E_3$ $D_3 = \varepsilon_{33}^T E_3 + d_{13m} T_1$	$T_1 = 0$ (unclamped) Apply E_3-Measure S_1 and D_3	$S_1 = d_{13} E_3$	$D_3 = \varepsilon_{33}^T E_3$

The hysteresis loops for the Motorola 3203 HD material are shown in Figure 2. The curves exhibit the typical hysteresis behavior for a ferroelectric material. The dielectric displacement saturates at high fields. The value of the charge on the surface is dependent on the prior field on the sample and a saturated hysteresis loop is shown. The strain has the more complicated butterfly shape that is indicative of domain switching. The shape of both these curves is dependent on the size and change in the field. The field was cycled up to 2 MV/m and down to -2 MV/m in steps of 0.14 MV/m. On the strain versus electric field curve the useful piezoelectric region is near the center of the curve where the graph is seen to make an X shape. This X shape is due to two anti-parallel polarities that are allowed for this material. The slopes of each line of the X shape at zero field are the piezoelectric constants for each polarity. This value is not the same as the small signal piezoelectric constant determined from resonance data since a large portion of the strain is due to irreversible
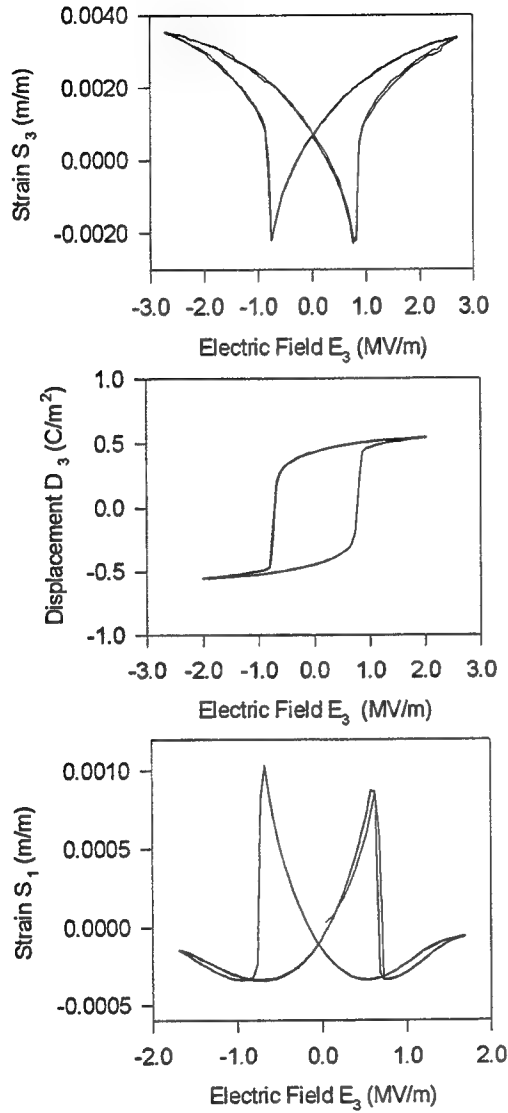
Figure 2. The quasistatic field dependence of the strain S_3, dielectric displacement D_3, and strain S_1 as a function of field to field levels above the coercive field
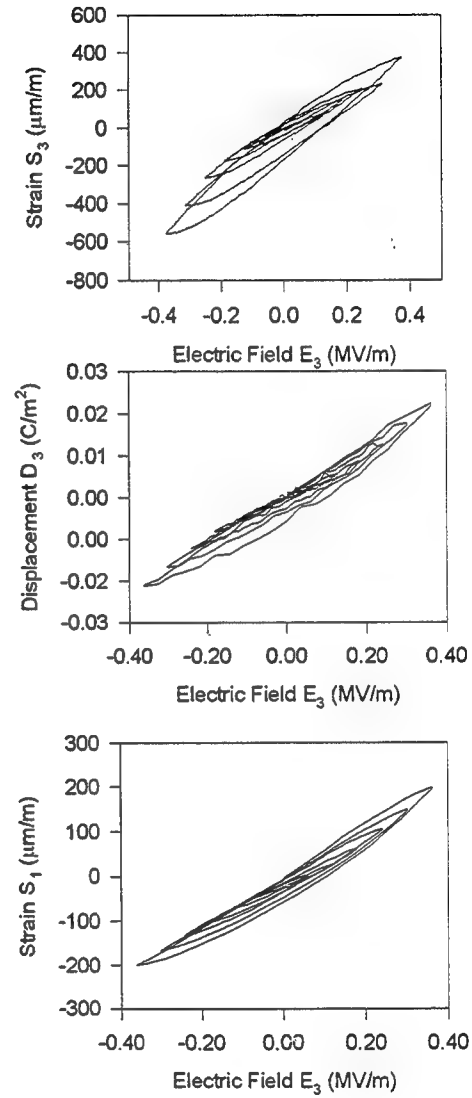
Figure 3. The quasistatic field dependence of the strain S_3, dielectric displacement D_3, and strain S_1 as a function of field to field levels below the coercive field. Six loops with different maximum fields are shown
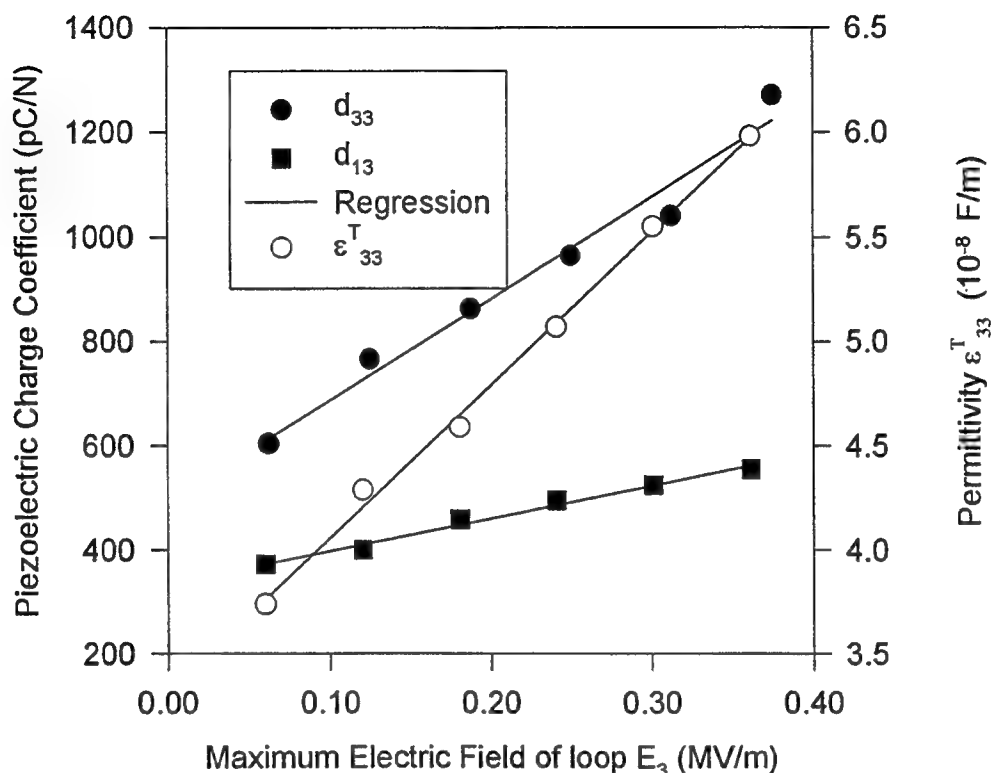
Figure 4. The quasistatic field dependence of the effective piezoelectric constant d_{33}, d_{13}, and permittivity ε_{33}^{T} as a function of field up to field levels below the coercive field. The slope is a measure of the higher order material coefficients.

domain motion as the field is ramped up to fields above the coercive field. When the sample is poled positively and a positive field is applied to the positive electrode the sample is dilated. When the sample is poled negatively the same field produces a contraction. The reason that both slopes are seen on this curve is that the maximum (2 MV/m) positive and negative applied field during the measurement exceeds the coercive field ($E_C = 0.5$-1.0 MV/m) during the measurement and the sample polarity is reversed.

The dependence of the piezoelectric constant on the field is apparent in the strain versus electric field curve. Consider the curve which has a positive slope with respect of the electric field. As the field is increased in the positive direction the slope of the curve which is a measure of the piezoelectric constant at this field level decreases. Conversely as the field in the negative direction is increased the slope increases which means that the piezoelectric constant will increase. The change in slopes is therefore directly related to the field dependence and the higher order material constants governing the strain in the material. This behavior is similar to what is measured by the field dependence of the various resonators. However in the case of the resonators a DC field is applied and the reversible piezoelectric constant or slope is measured at the DC field level using a small AC signal. The other obvious difference is that the quasi-static measurements are performed at much lower frequencies (mHz) while the resonance measurements are performed in the (MHz) frequency

range. The transverse strain hysteresis curve for the strain S_1 as a function of the electric field in the 3 direction is shown in the lower curve of Figure 2. The strain change during polarization reversal is opposite to the strain change found in S_3 found in the top curve of Figure 2.

Quasi-static measurements can also be used to examine the non-linear properties of these materials by making measurements at field levels below the coercive field. These measurements represent an averaged measurement since the strain and the slope is determined over some range in field. However from the point of view of an actuator designer this may be appropriate in that the strain level as a function of the field is the relationship of interest.

The strain S_3 as a function of the electric field for a rod is shown in Figure 3 for 6 different field levels. The slope and the hysteresis increases with an increase in the field range. Similar behavior is found in the strain S_1 and the dielectric displacement D_3 as a function of the electric field E_3, which are also shown in Figure 3. The slope of these curves were determined using linear regression. The hysteresis was ignored in the analysis of the slope. The slope of the curves show in Figure 3 are a measure of the average piezoelectric material constant and permittivity over the field range. The values of d_{33}, d_{13}, and ε_{33}^T as a function of the maximum field of the loop are shown in Figure 4. The relationship is seen to be linear. The quasi-static electrostrictive coefficients q_{33} and q_{13} were determined by taking the derivative of the d_{33} and d_{13} versus maximum electric field curves. The values are reported in Table 2 along with the electrodielectric constant determined from the slope of the ε_{33}^T data found in Figure 3. It should be noted that the saturated hysteresis curves shown in Figure 2 can be used to predict the general behavior of the curves shown in Figure 3. Each of the curves that produce the X shape at the origin of the strain curves can be represented by a linear and quadratic polynomial as a function of the electric field ($S=d_{33}E+q_{33}E^2$) . The quadratic component is the electrostrictive coefficient q_{33} or q_{13} and is related to the slope of the curves in Figure 4 which is equal to twice q_{33} or q_{13}. The dielectric displacement around the origin at the positive and negative polarization can also be represented by a function of the form $D = \varepsilon_{33}E+(\kappa_{33}/2)E^2$ and related directly to the slope of the permittivity as a function of the field (see Figure 4) where κ_{33} is the second order dielectric constant which we have called the electrodielectric constant. These relationships predict the linear relationship between the piezoelectric constant and the permittivity as a function of the field. This relationship is only approximate since the values shown in Figure 4 are determined from an average slope and plotted as a function of the maximum field of the loop. A true differential measurement is required to relate the two curves quantitatively. It should also be noted that these quasi-static measurements are for zero load.

3. RESONANCE MEASUREMENTS

Methods[12,13,14,15] for characterizing a piezoelectric material based on the IEEE Standards on Piezoelectricity[16] were used to characterize a set of aged Motorola 3203 HD resonators. These methods use the impedance equations described in the IEEE standard. However the material constants are defined as complex to account for losses. The length extensional mode is described by an equation of the form

$$Z = \frac{l}{i\omega A \varepsilon_{33}^S}\left(1-\frac{k_{33}^2 \tan\left(\frac{\omega}{4f_p}\right)}{\frac{\omega}{4f_p}}\right), \tag{2}$$

where l is the sample length, A is the electrode area, ε_{33}^S is the clamped permittivity, k_{33} is the complex length extensional coupling constant, the complex parallel frequency constant is defined by

$$f_p = \left[4\left(1-k_{33}^2\right)\rho s_{33}^E l^2\right]^{-1/2} = \left[4\rho s_{33}^D l^2\right]^{-1/2}, \tag{3}$$

and the complex length electromechanical coupling constant is defined by

$$k_{33}^2 = \frac{d_{33}^2}{\varepsilon_{33}^T s_{33}^E}. \tag{4}$$

The equation governing the resonance of the length thickness extensional mode is

$$Y(\omega) = \left(\frac{i\omega\varepsilon_{33}^T w_1 w_2}{t}\right)\left[1 - k_{13}^2\left[1 - \frac{\tan\left(\frac{\omega}{4f_s}\right)}{\frac{\omega}{4f_s}}\right]\right]$$

(5)

where t is the sample thickness, A $=w_1 w_2$ is the electrode area with w_1 being the longest lateral dimension of the electrode and w_2 being the smaller lateral dimension, ε_{33}^T is the complex free permittivity, and k_{13} is the complex length thickness extensional coupling constant. The complex series frequency constant defined by.

$$f_s = \left(\frac{1}{4\rho s_{11}^E w_1^2}\right)^{1/2}$$

(6)

is a function of the width w_1, the density ρ and the elastic compliance $s_{11}^E = \frac{s_{11}^D}{(1-k_{13}^2)}$. The DC field dependence of the

length thickness extensional and length extensional modes are shown in Figures 5 and 6. The field dependence of the small signal material constants is primarily linear. These curves are obtained from impedance resonance spectra. Each point represents the analysis of a spectra at a set DC bias. The slope of the small signal material constants as a function of the field is shown in Table 2 along with the slopes obtained from the quasi-static measurements below the coercive field. The values obtained from the quasi-static curves are seen to be 4 to 6 times greater than the slope obtained from the biased resonance spectra. The difference is these values can be explained in terms of the reversible and irreversible domain wall motion in the ferroelectric material and the different measurement frequencies as is shown in Figure 1.

Table 2: The electrostriction and electrodielectric constants determined from the quasi-static and DC biased resonance spectra.

Non linear Coefficient Real Part	Quasi-static Maximum E_{DC}=0.39MV/m $f < mHz$	Length thickness Resonator Maximum E_{DC}=0.39MV/m f =72 kHz	Length Resonator Maximum E_{DC}=0.016MV/m f =572 kHz
K_3 (Fm/V)	7.3×10^{-14}	1.8×10^{-14}	1.4×10^{-14}
q_3 (m²/V²)	9.5×10^{-16}	N/A	1.4×10^{-16}
q_1 (m²/V²)	3.1×10^{-16}	5.0×10^{-17}	N/A

The complete reduced piezoelectric, elastic, and dielectric matrix (C_∞ symmetry) for the Motorola 3203 HD material is presented in Table 3. The material constants including losses were determined from the length extensional, length thickness extensional, thickness shear, radial and thickness modes. The value of s_{13}^E was calculated using the equations presented by Smits[12] and by matrix inversion and the results are shown in Table 3. The measurements for each mode were performed on 4 different resonators with the same geometry and aspect ratios. The standard deviations are reported in Table 3 as a percentage of the average value for each material coefficient. The electromechanical coupling is also reported in Table 3. These values are determined from the fundamental resonance for each mode. The frequency of measurement is reported for each value. The value of the material constant may differ slightly depending on the frequency of measurement due to dispersion in the material properties.
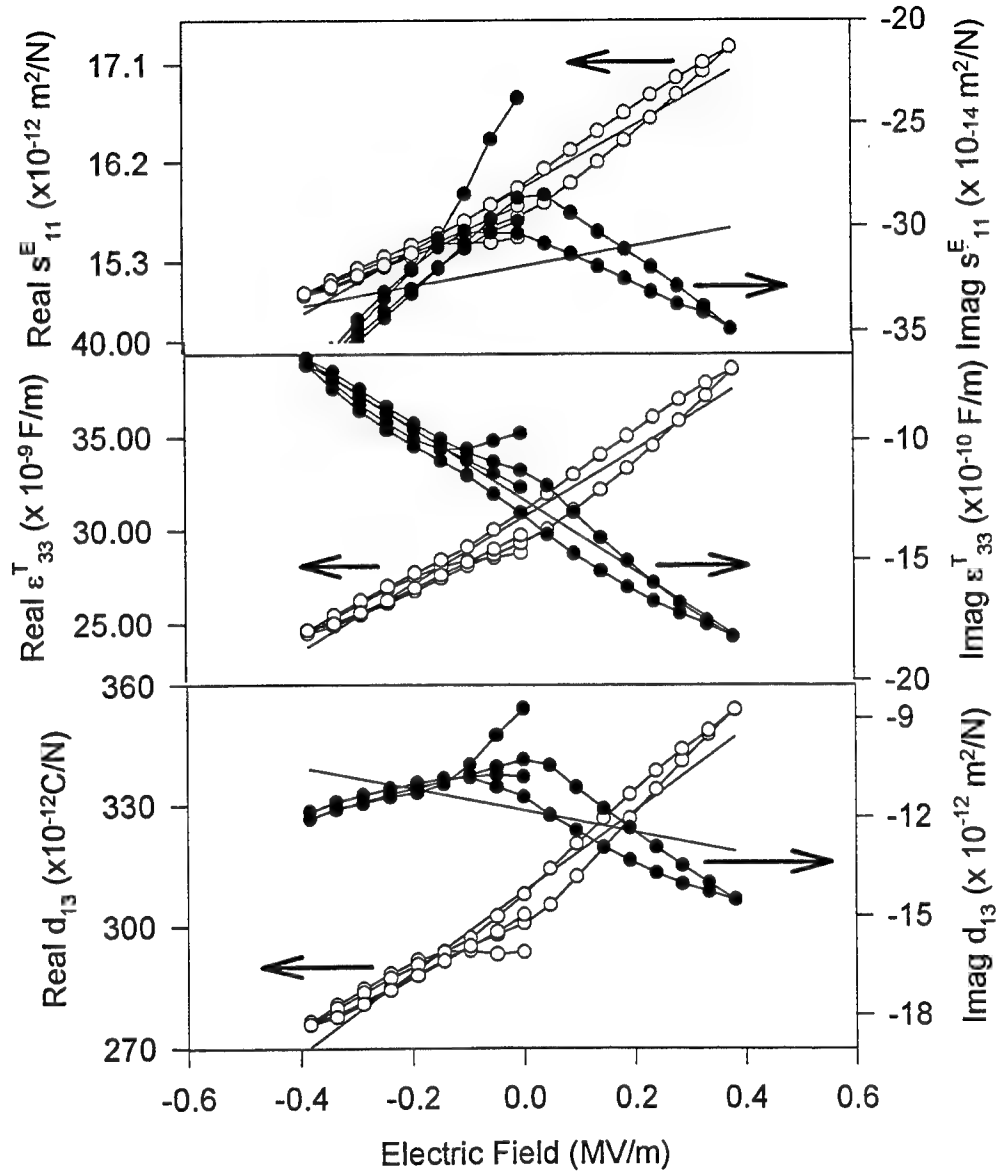
Figure 5 The length thickness mode material constants (s_{11}^{E}, ε_{33}^{T}, d_{13}) of Motorola 3203HD as a function of the DC bias field. The DC bias was stepped up to ±0.39 MV/m. The bias field is applied parallel to the poling direction for this mode. The linear portion of the field dependence is shown as a straight solid line. The curves show hysteresis. The linear field dependence is the result of a higher quadratic coefficient.
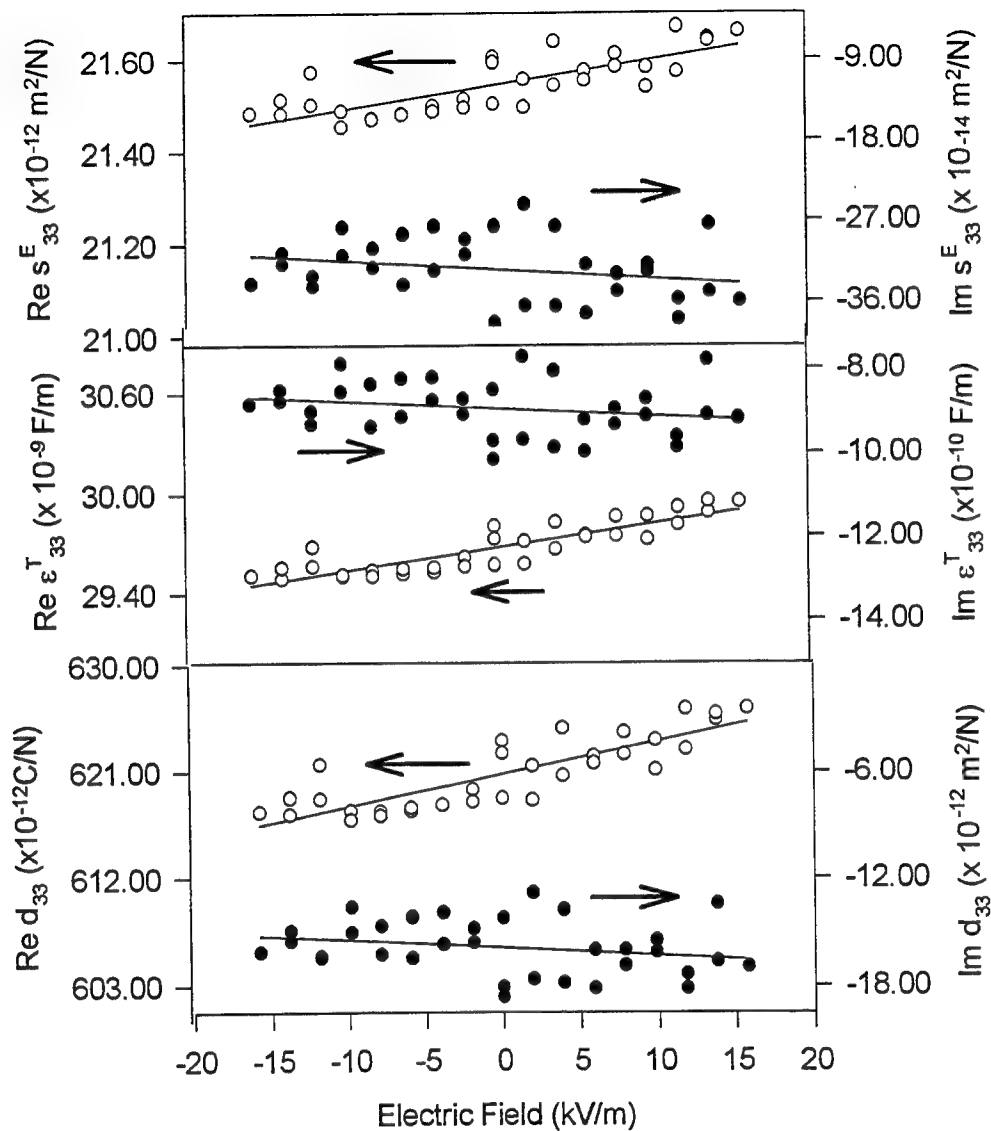
Figure 6. The length extensional mode material constants (s_{33}^E, ε_{33}^T, d_{33}) of Motorola 3203HD determined from the second resonance as a function of the DC bias field. The DC bias was stepped up to ± 0.016 MV/m. The bias field is applied parallel to the poling direction for this mode. The linear portion of the field dependence is shown as a straight solid line. The large scatter is due to the decrease in sensitivity of the measurement at lower field levels. The difference in the zero field values determined from the curve above and the values listed in Table 3 are due to dispersion.

Table 3: The reduced matrix of Motorola 3203HD PZT including the electromechanical coupling determined at the fundamental resonance of each mode

Material Constant	Mode	Frequency (kHz)	Value Real	Value Imag	% Standard Deviation Real	% Standard Deviation Imag
s_{11}^E (m^2/N) x10^{-11}	LTE	71.5	1.56	-0.030	0.63	5.2
s_{11}^E (m^2/N) x10^{-11}	RAD	150.9	1.55	-0.032	0.45	2.8
s_{11}^E (m^2/N) x10^{-11}	Average		1.56	-0.031		
s_{12}^E (m^2/N) x10^{-11}	RAD	150.9	-0.420	0.012	3.90	4.9
s_{13}^E (m^2/N) x10^{-11}	Calculated	Smits formula	-0.821	0.034	N/A	N/A
s_{13}^E (m^2/N) x10^{-11}	Calculated	Matrix inversion	-0.825	0.017	N/A	N/A
s_{33}^E (m^2/N) x10^{-11}	LE	199	1.89	-0.034	1.0	0.78
s_{55}^E (m^2/N) x10^{-11}	TS	2730	3.92	-0.13	2.9	4.3
s_{66}^E (m^2/N) x10^{-11}	Calculated	IEEE formula	2.28	-0.038	N/A	N/A
c_{33}^D (N/m^2) x10^{11}	TE	6390	1.77	0.023	2.0	11
d_{13} (C/N) x10^{-12}	LTE	71.5	-297	9.7	0.70	7.1
d_{13} (C/N) x10^{-12}	RAD	150.9	-293	10	0.68	5.8
d_{13} (C/N) x10^{-12}	Average		-295	9.9		
d_{33} (C/N) x10^{-12}	LE	199	564	-15	3.1	17
d_{15} (C/N) x10^{-12}	TS	2730	560	-30	4.6	11
ε_{11}^T (F/m) x10^{-8}	TS	2730	2.14	-0.13	0.44	6.8
ε_{33}^T (F/m) x10^{-8}	RAD	150.9	3.06	-0.11	1.1	6.5
ε_{33}^T (F/m) x10^{-8}	LT	71.5	2.83	-0.061	1.9	9.4
ε_{33}^T (F/m) x10^{-8}	Average		2.95	-0.083		
ε_{33}^S (F/m) x10^{-8}	TE	6390	1.06	-0.053	2.0	4.2
k_{33}	LE	199	0.763	-0.0029	0.52	45
k_{13}	LTE	71.5	0.447	-0.0054	0.90	16
k_{15}	TS	2730	0.611	-0.0034	3.1	37
k_P	RAD	150.9	0.706	-0.0062	0.45	6.1
k_t	TE	6390	0.536	-0.0050	0.46	12

4. CONCLUSIONS

The quasi-static and DC biased resonance spectra for Motorola 3203HD have been measured and the field dependence of the material constants determined using DC biased impedance spectra were found to be smaller by a factor of 4 to 6 times. The difference in the two measurements is attributed to reversible and irreversible domain motion. The excursions of the domain walls under large quasi-static fields are larger and irreversible while the small AC fields of the resonance measurement vibrate the domain walls reversibly. The complete reduced matrix for Motorola 3203 HD including losses is reported

5. ACKNOWLEDGMENTS

6. REFERENCES

[1] Zhang, Q.M., Pan, W.Y., Jang, S.J. And Cross, L.E., "Domain Wall Excitations and their Contributions to the Weak Signal Response of Doped Lead Zirconate Titanate Ceramics", J. Appl. Phys. 64, pp. 6445-6451, 1988

[2] Berlincourt, Don and Krueger, Helmut H.A.,"Domain Processes in Lead Titanate Zirconate and Barium Titanate Ceramics", J. Appl. Phys., 30, (11), pp. 1804-1810, 1959

[3] Woollett, R.S., Leblanc, C.L., "Ferroelectric Non-linearities in Transducer Ceramics", IEEE Trans on Sonics and Ultrasonics, (SU-20), pp. 24-31, January,1973

[4] Krueger, Helmut H.A., "Mechanical Properties of Ceramic Barium Titanate, Phys. Rev., 93, pp. 362, 1954

[5] Krueger, Helmut H.A. , "Stress Sensitivity of Piezoelectric Ceramics: Part 1., Sensitivity to Compressive Stress Parallel to the Polar Axis", J. Acoustical Society of America, 42, (3), pp.636-645, 1967

[6] Krueger, Helmut H.A., "Stress Sensitivity of Piezoelectric Ceramics: Part 2. Heat Treatment", J. Acoustical Society of America, 43, (3), pp.576-582, 1968

[7] Krueger, Helmut H.A., "Stress Sensitivity of Piezoelectric Ceramics: Part 3., Sensitivity to Compressive Stress Perpindicularl to the Polar Axis", J. Acoustical Society of America, 43, (3), pp.583-591, 1968

[8] Brown, R.F. And McMahon, G.W, "Material Constants of Ferroelectric Ceramics at High Pressure", Can. J. Physics, 40, pp.672-674, 1962

[9] Brown, R.F. and McMahon, G.W, "Properties of Transducer Ceramics Under Maintained Planar Stress", J. Acoustical Society of America, 38, pp.570-575, 1965

[10] Fritz, I.J., "Uniaxial Stress Effects in a 95/5 Lead Zirconate Titanate Ceramic", J. Appl. Phys., 49, (9), pp. 4922-4928, September, 1978

[11] Cao, Hengchu and Evans, Anthony, G, "Nonlinear Deformation of Ferroelectric Ceramics", J. of the American Ceramic Society, 76, (4), pp. 890-896, April, 1993

[12] Smits, J.G., "Iterative Method for Accurate Determination of the Real and Imaginary Parts of Materials Coefficients of Piezoelectric Ceramics", IEEE Trans on Sonics and Ultrasonics, (SU-23),(6), pp. 393-402, November, 1976

[13] Sherrit, S., Wiederick, H.D., Mukherjee, B.K. "Non Iterative Evaluation of the Real and Imaginary Material Constants of Piezoelectric Resonators", Ferroelectrics, 134, pp.111-119, 1992

[14] Sherrit, S., Gauthier, N., Wiederick, H.D., Mukherjee, B.K., "Accurate Evaluation of the Real and Imaginary Material Constants for a Piezoelectric Resonator in the Radial Mode", Ferroelectrics, 119, pp.17-32, 1991

[15] Alemany, C., Pardo, L., Jimenez, B., Carmona, F., Mendiola, J. and Gonsalez, A.M., "Automatic Iterative Evaluation of Complex Material Constants in Piezoelectric Ceramics", J. Phys. D (Appl. Phys.), 27, pp.148-155, 1994

[16] IEEE Standard on Piezoelectricity, ANSI/IEEE Std. 176-1987

Antiferroelectric-to-Ferroelectric Phase Switching Lead Lanthanum Zirconate Stannate Titanate (PLZST) Ceramics

Shoko Yoshikawa[a], Kelley Markowski[b], Seung-Eek Park,
Ming-Jen Pan, L. Eric Cross

Materials Research Laboratory, The Pennsylvania State University,
University Park, PA 16802

ABSTRACT

Electric field induced antiferroelectric (AFE) to ferroelectric (FE) phase transformations are accompanied by large strain and significant hysteresis. The properties of these materials can be tailored to fit specific applications such as high strain actuators and charge capacitors. As an attempt to reduce hysteresis, Barium and Strontium A-site substitution of the phase transformation behavior of $(Pb_{0.98-\delta}La_{0.02}A_{\delta})$ $(Zr_xSn_yTi_z)O_3$ (A=Ba, Sr) ceramics have been investigated. The ceramic samples in this study produced 0.2% to 0.3% strain level. Barium proved to be a strong FE stabilizer with decreasing both switching field and hysteresis, while Strontium proved to be a strong AFE stabilizer. Some practical data, including temperature stability and current requirements, are also to be discussed.

Keywords: lead zirconate stannate titanate ceramics, antiferroelectric-to-ferroelectric phase switching ceramics, field induced strain, field induced polarization

1. INTRODUCTION

Lead zirconate ($PbZrO_3$) and lead titanate ($PbTiO_3$) form a complete solid-solution series (lead zirconate titanate, or PZT) of great technological importance. It is used in various Zr:Ti ratios and with numerous dopants to manufacture a vast array of electronic and electromechanical devices.

The effects of pressure-enforced ferroelectric (FE) to antiferroelectric (AFE) in modified $PbZrO_3$ was originally studied by Berlincourt et al. for an application of shock-actuated power supplies[1,2]. The relatively recent work on the same ceramics are published from Sandia National Laboratories[3,4].

Triaxial phase diagram introducing lead stannate ($PbSnO_3$) for both Niobium (Nb) and Lanthanum (La) doped system have been developed from the large amount of compositional study pursued at Clevite Corporation[1,2] in 1960s.

---

[a] Shoko Yoshikawa: Correspondence: e-mail: sxy3@psuvm.psu.edu; Phone: (814) 863-1096; Fax: (814) 865-2326
[b] Kelley Markowski: Current address: Materials Systems Inc., Littleton, MA 01460

Our interest in these families of materials lies in their ability to produce large strain at the electric (E)-field induced tetragonal AFE (AFE_T) to rhombohedral FE transformation (FE_R)[5,6]. Depending on the compositional adjustments, the materials can exhibit shape memory effect as described by Uchino, et al.[7].

Our compositions, unlike the above example of FE-to-AFE transformation to release energy upon application of pressure, start from AFE_T phase and switches to FE phase upon application of E-field. For actuator application, it is, therefore, important to optimize the compositions to exhibit following characteristics:

1. Larger strain, thus larger displacement,
2. Lower hysteresis, thus less heat generation, and
3. Lower switching field, thus less E-field requirement.

We have shown previously[8,9] that the B-site compositional modification controls switching field, though hysteresis behavior has little influence.

The objective in this study, therefore, is to attempt to produce compositions with less hysteresis without sacrificing too much strain while maintaining relatively low switching E-field. A-site modifications were accomplished by the addition of Ba and Sr.

2. EXPERIMENTAL PROCEDURE

2.1 Sample preparation

The five compositions described as A, A1, A2, B, and C in Table 1 were prepared according to the formula. Figure 1 shows the location of these compositions in the PLZST ternary phase diagram. Polycrystalline ceramic materials investigated in this study were prepared by solid state reaction, using the appropriate amount of reagent grade raw materials of lead carbonate ($PbCO_3$), lanthanum oxide (La_2O_3), zirconium dioxide (ZrO_2), titanium dioxide (TiO_2), and tin oxide (SnO_2). The chemical purity of each of the raw materials was greater than 99%. Barium and strontium additions were made using the appropriate amounts of strontium carbonate ($SrCO_3$) and barium carbonate ($BaCO_3$), respectively. The sintering process was carried out in a lead rich environment in order to minimize lead volatilization. To further enhance densification and increase the electric field where dielectric breakdown occurs, the sintered specimens were hot isostatically pressed for 2 hours at 1200°C in an air atmosphere under a pressure of 20MPa. Disk samples were then prepared by polishing with silicon carbide and alumina polishing powders to achieve a flat and parallel surface onto which gold was sputtered as an electrode.

Table 1. PLZT compositions.

	COMPOSITION	Comments
A	$(Pb_{0.88}La_{0.02})(Zr_{0.66}Ti_{0.26})_{0.995}O_3$	0% Ba, Zr:Ti:Sn 66:8:26
A1	$(Pb_{0.93}Ba_{0.05}La_{0.02})(Zr_{0.66}Ti_{0.08}Sn_{0.26})_{0.995}O_3$	5%Ba,Sr:Ti:Sn 66:8:26
A2	$(Pb_{0.88}Ba_{0.10}La_{0.02})(Zr_{0.66}Ti_{0.08}Sn_{0.26})_{0.995}O_3$	10%Ba,Zr:Ti:Sn 66:8:26
B	$(Pb0.93Sr0.05La0.02)(Zr_{0.55}Ti_{0.15}Sn_{0.30})_{0.995}O_3$	5% Sr, FE region of phase diagram
C	$(Pb0.93Ba0.05La0.02)(Zr_{0.55}Ti_{0.15}Sn_{0.30})_{0.995}O_3$	5% Ba, FE region of phase diagram
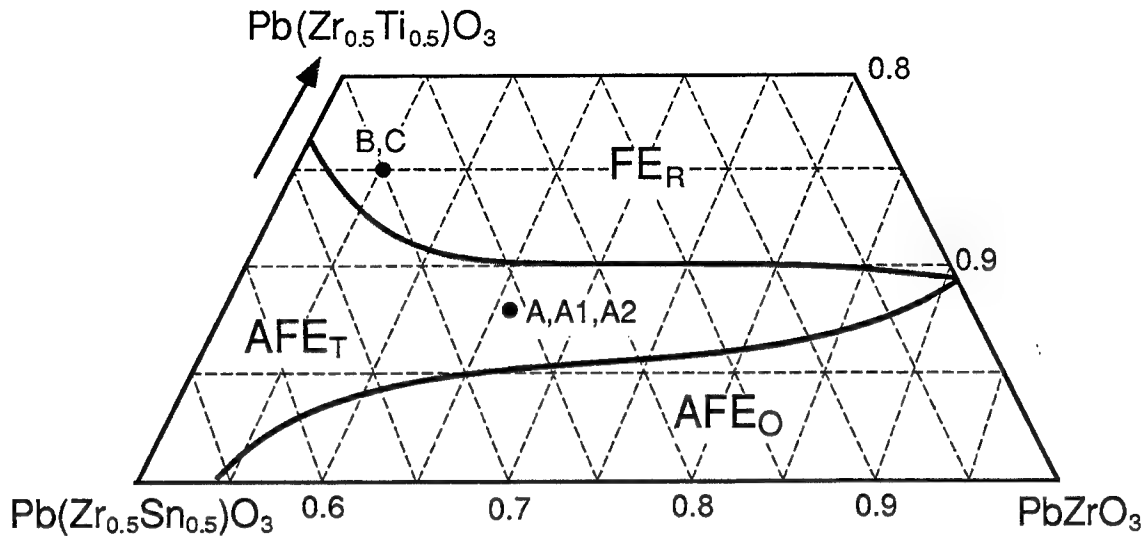
Figure 1: PLZST phase diagram and investigated compositions.

2.2 Characterization techniques

(a) Phase and microstructure

Calcined and sintered powders were examined by x-ray diffraction to insure phase purity and to identify the crystal structure. Typically, the samples showed a single phase within the detection limit of XRD (< 2%).

(b) Dielectric properties

Multifrequency meters (Hewlett Packard 4274A and 4275A LCR meters) were used in conjunction with a computer controlled temperature chamber (Delta Design Inc., Model MK 2300) to measure capacitance as a function of temperature and frequency. Capacitance was converted to dielectric permittivity using the sample geometry and permittivity of air. Measurements were taken from 100 Hz to 100 kHz at temperatures from -150°C to 250°C.

(c) Polarization and strain

High field measurements included polarization and strain hysteresis using a computer controlled modified Sawyer Tower system with a National Instruments Input Output card and linear variable displacement transducer (LVDT) sensor driven by a lock in amplifier (Stanford Research Systems, Model SR830). The voltage was supplied using a Trek 609C-6 high voltage DC amplifier. Through the LVDT sensor the strain of the samples can be measured with the applications of an applied field. Electric fields as high as ~ 100kV/cm were applied using an amplified sine waveform at 0.2 Hz. During testing the samples were submerged in Fluorinert (FC-40, 3M), an insulating liquid, to prevent arcing.

3.   RESULTS AND DISCUSSION

3.1   A-Site Modification

A-site modifications were based on tolerance factor, which can be described for perovskites with the general formula ABX_3 by:

$$t = (R_A + R_X) / (\sqrt{2}) (R_B + R_X)$$

where R_A = radius of A, R_B = radius of B and R_X = radius of X. Ba^{2+} (1.48Å) is larger than Pb^{2+} (1.32Å), and Sr^{2+} (1.27Å) is smaller than Pb^{2+}. When $t > 1$ the FE phase is stabilized when $t < 1$ the AFE phase is stabilized[10]. For Pb based compounds, however, only trends need to be considered because of the high polarizability of the Pb. Both Ba and Sr were considered as A-site additions only in this study. Ba being a FE stabilizer and Sr being a AFE stabilizer both potentially lowering T_{max} and subsequently suppressing hysteresis.

Figure 2 shows E-field induced polarization (a) and strains (b) for compositions A, A1, and A2. As anticipated, increased Ba^{2+} content clearly lowered switching field, and decreased hysteresis. It is important to note that the maximum strain is a function of applied electric field after the switching. The dielectric data is shown in Figure 3. This data showed a decrease T_{max} (associated with decreased hysteresis), increased K_{max} and increased T_{FE-AFE} (associated with decreased switching field) with increased Ba^{2+} content, though T_{FE-AFE} is not obvious in virgin sample. This also indicates that the operating temperature range is narrower as Ba^{2+} content increased (to be discussed below).

Figures 4 to 7 show the results of compositions B and C. The original location of the composition is in rhombohedral ferroelectric region (FE_R); therefore, the composition without Ba or Sr addition is ferroelectric. As anticipated from Sr being AFE stabilizer, as sintered composition B with 5% Sr addition showed antiferroelectric, and underwent AFE-to-FE transformation upon application of E-field (Figure 4). The switching field was approximately 50 kV/cm, and hysteresis was relatively small.

On the contrary, the same composition with Ba^{2+} addition instead of Sr^{2+} showed stable ferroelectric behavior, as shown in Figure 6. Dielectric data in Figure 7 showed a transition from FE to PE (paraelectric) without any AFE stable temperature range. It is determined from the fact that the cooling run (sample depoled by exposing temperature above T_{max}) showing higher dielectric constant than heating (E-field exposed sample) run, unlike the data in Figure 5.

3.2.   Temperature stability

Low field dielectric data, as discussed above, are important tools to determine temperature stability of each composition without actually measuring the strain in different temperature conditions. At very low temperature all of the compositions discussed in this study are ferroelectric. There are temperature regions in which compositions show AFE phase, which can be transformed to FE by E-field. Above T_{max}, the phase is PE so that only electrostrictive strain behavior can be observed.

General temperature behavior of this family of ceramics is shown in Figure 8 of temperature and E-field phase diagram. The shaded areas describe hysteresis. As the figure indicates, it is possible to decrease hysteresis by operating at a higher temperature, though strain level will be reduced.

(a)   (b)
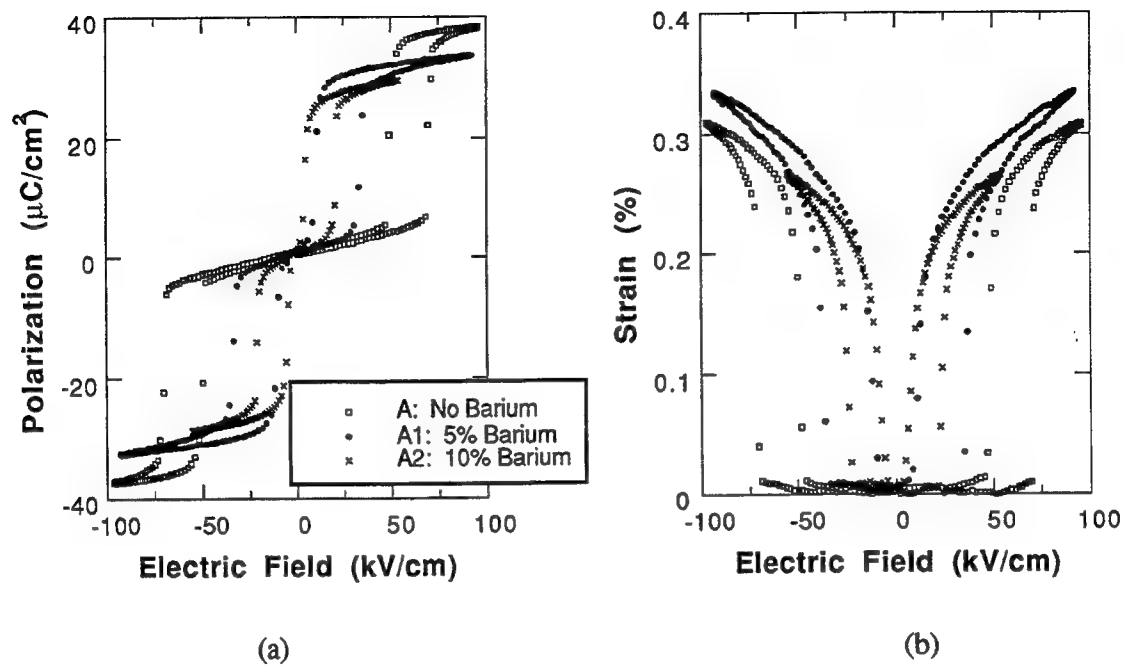
Figure 2:   Electrically induced polarization (a) and strain (b) for compositions A, A1, and A2.
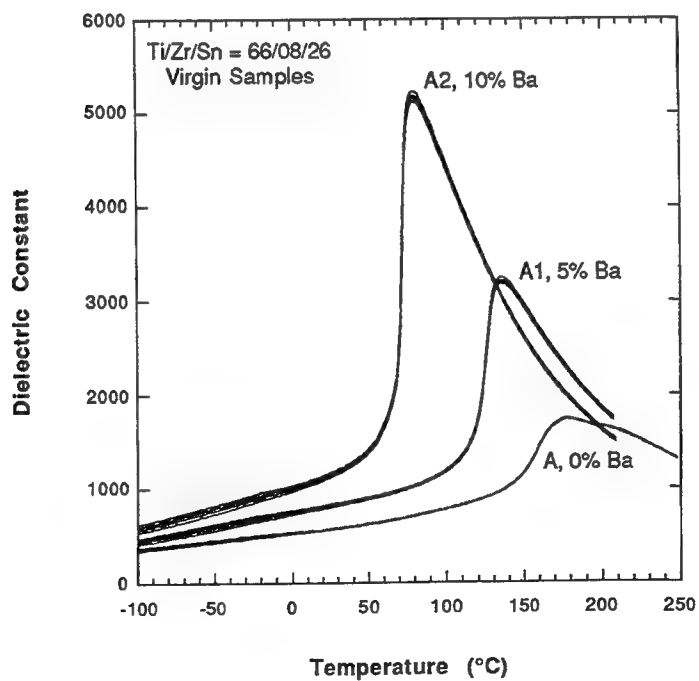
Figure 3:   Temperature dependence of dielectric constant for the compositions A, A1, and A2; (cooling) virgin sample.
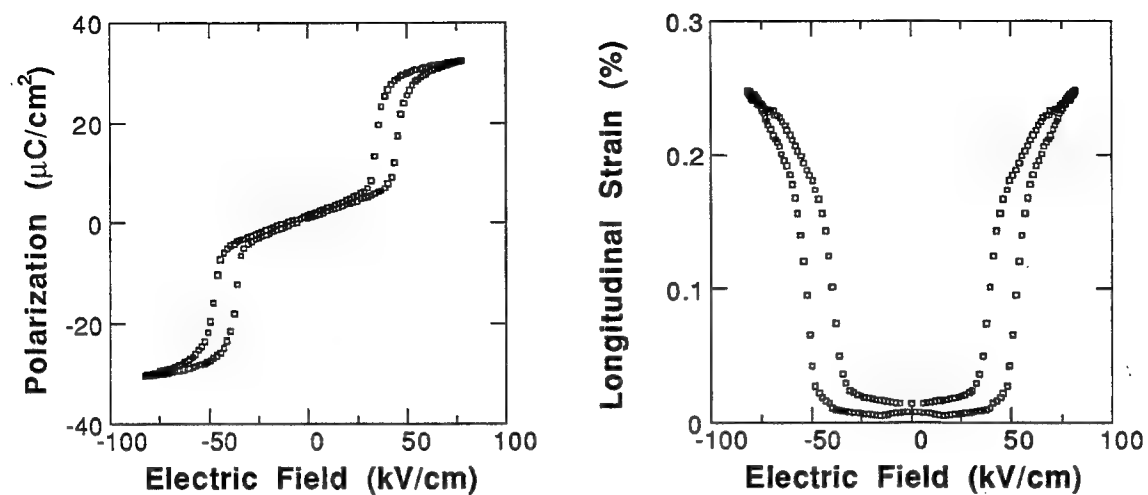
Figure 4:   Electrically induced polarization and strain for composition B.
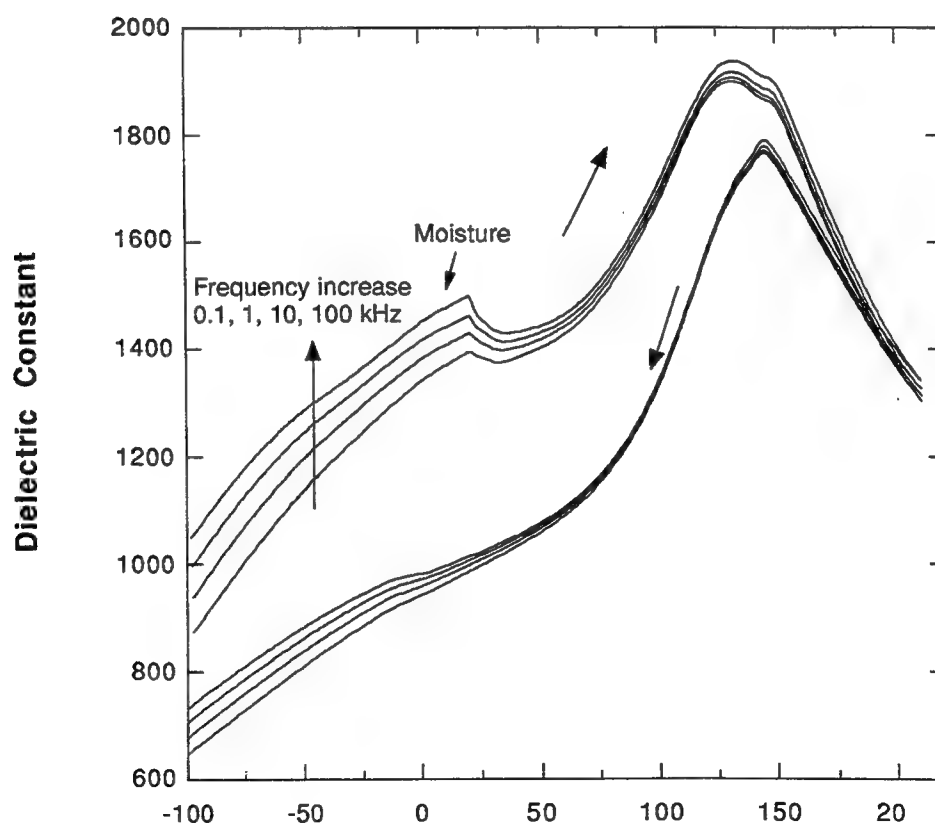
Figure 5:   Temperature dependence of dielectric constant for the composition B; poled sample, heating first, then cooling
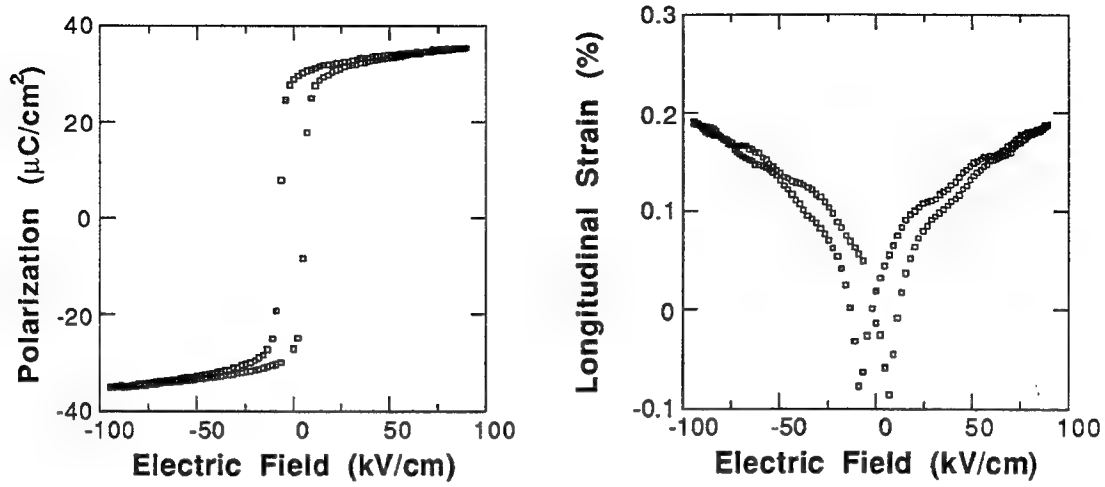
Figure 6: Electrically induced polarization and strain for composition C.
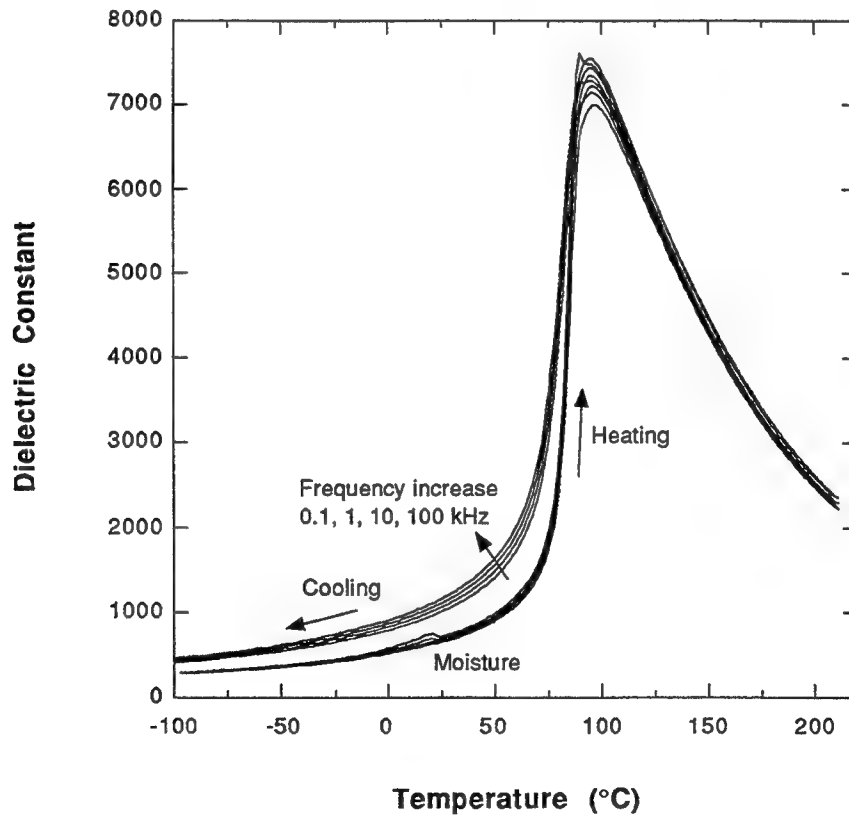
Figure 7: Temperature dependence of dielectric constant for the composition C; poled sample, heating first, then cooling

The above study of A-site modification showed that it is possible to decrease hysteresis and switching field at room temperature with, unfortunately, narrowing AFE temperature range. It is, therefore, critical to determine optimum composition based upon the requirements of a specific application and tailor the properties of the phase change materials.
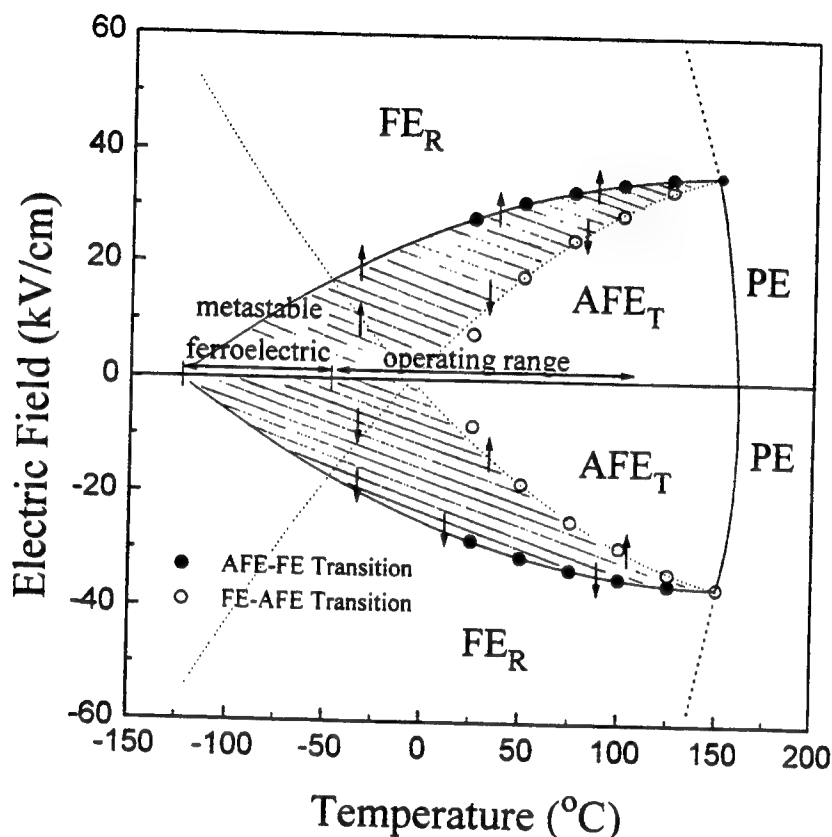
Figure 8: Temperature-electric field phase diagram. Shaded area indicates hysteresis.

3.3. Current requirement

Previous study[5] on compositional modification on the B-site also showed high field dielectric constants and loss by using DC bias field. As sharp increase and decrease in polarization hysteresis loop indicate, charge requirement to drive these ceramics as actuators can be quite high. Figure 9 shows the AC current required when one of the samples undergoes a phase transition from AFE-FE and subsequent switching back into the AFE phase by increasing and decreasing E-field. These measurements were completed at a low frequency (0.2 Hz) and represent relatively low current requirements. The current required at a higher frequency would be substantially higher and should be taken into account when the operating circuit for this material is designed. Current is lost in the time required to complete a measurement cycle (5 sec in this case), which accounts for the lack of symmetry in Figure 9.
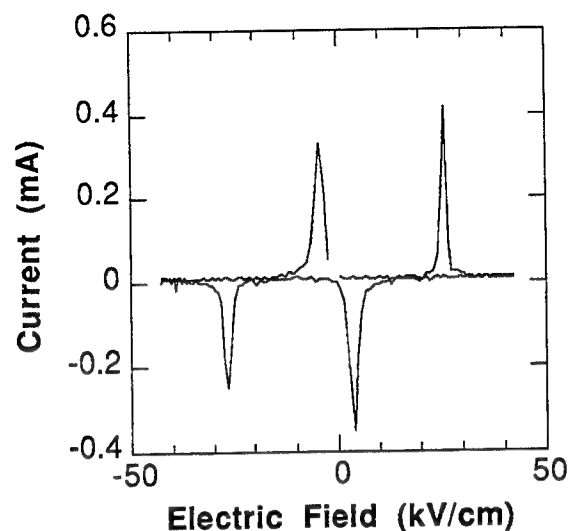
Figure 9:   Current requirements on phase switching (0.2 Hz).

4.   CONCLUSIONS

A-site compositional modification can be used along with B-site Ti:Sn ratio changes to modify the properties of phase switching ceramics, for example decreasing hysteresis. Sr additions have limited merit alone because they cause increases in the switching field and, therefore, increases in the field necessary to obtain maximum strain levels. Sr addition, however, suppressed hysteresis.

Ba additions proved to be a FE phase stabilizer, lowering both the amount of hysteresis and the switching field. It should be noted, however, that these changes also make the AFE temperature range smaller. The operation temperature and current requirement for this family of ceramics were also summarized. Ideally, with respect to application, a balance should be maintained between switching field, hysteresis and operating temperature range.

ACKNOWLEDGEMENTS

REFERENCES

1. D. Berlincourt, H.H.A. Krueger, and B. Jaffe, "Stability of Phases in Modified Lead Zirconate with Variation in Pressure, Electric Field, Temperature, and Composition," *J. Phys. Chem. Solids*, **Vol. 25**, 659–674 (1964).

2. B. Jaffe, "Antiferroelectric Ceramics with Field-Enforced Transitions: A New Nonlinear Circuit Element," *The Proceedings of the IRE*, **Vol. 49**[8], 1264–1267 (1961).

3. D.H. Zeuch, S.T. Montgomery, J.D. Keck, "Hydrostatic and triaxial compression experiments on unpoled PZT 95/5-2Nb ceramic: The effects of shear stress on the F_{R1} to A_O polymorphic phase transformation," *J. Mater. Res.*, **7**, pp. 3314–3332 (1992).

4. D.H. Zeuch, S.T. Montgomery, J.D. Keck, "Further observation on the effect of nonhydrostatic compression on F_{R1} to A_O polymorphic phase transformation in niobium doped, lead-zirconate-titanate ceramic," *J. Mater. Res.*, **9**, pp. 1322–1327 (1994).

5. K. Uchino and S. Nomura, "Electrostriction in PZT-Family Antiferroelectrics," *Ferroelectrics*, **Vol. 50**, 191–196 (1983).

6. W.Y. Pan, Q. Zhang, A. Bhalla, and L.E. Cross, "Field-Forced Antiferroelectric-to-Ferroelectric Switching in Modified Lead Zirconate Titanate Ceramics," *J. Am. Ceram. Soc.*, **Vol.[4]**, 571–578 (1989).

7. A. Furuta, K-Y Oh, and K. Uchino, "Shape Memory Ceramics and Their Application to Latching Relays," *Sensors and Materials*, **3.4**, 205–215 (1992).

8. S. Yoshikawa, N. Kim, T. Shrout, Q. Zhang, P. Moses, L.E Cross, "Field-Induced Lead Zirconate Titanate Stannate Antiferroelectric-to-Ferroelectric Phase Switching Ceramics, SPIE North American Conference on Smart Structure and Materials, *SPIE* **Vol. 2441**, p. 223–232.

9. K. Markowski, S-E. Park, S. Yoshikawa, L.E. Cross, "The Effect of Compositional Variations in the Lead Lanthanum Zirconate Stannate Titanate System on Electrical Properties," to be published in J. *Am. Ceram. Soc.*

10. K.J. Rao, C.N.R. Rao, Phase Transition in Soleds: An approach to the Study of the Chemistry and Physics of Solids," McGraw-Hill, New York (1978).

Moire Interferometer Applied to a Piezoceramic Containing a Simulated Void

S.S. Park[1], G.P. Carman[1], & S.B. Park[2]

[1]Mechanical & Aerospace Engineering, UCLA 38-137m Engineering IV, LA, CA 90095
[2]IBM Microelectronic Division, 1701 North Street Bldg. 257, Endicott NY, 13760

ABSTRACT

In this paper we describe the results of an ongoing experimental program to measure the strain distribution around a simulated void in a piezoceramic material subjected to large electric fields. The simulated void is a two-dimensional circular cylinder fabricated into the sample. Strain information is acquired with a Moire inteferometric system which permits both quantitative evaluation of surface strains and qualitative information regarding domain reorientation. Results indicate that large stresses/strains arise around the perimeter of the hole prior to domain reorientation. Domain switching initiates at the locations where the largest stress/strain occurs around the perimeter of the simulated void and do so to reduce the localized concentrations. During this evolutionary process the material contains a multi-domain structure with regions polarized in 180° apart. Domain switching appears to be predominately 180° without any 90° domain reorientation occurring at the mesoscopic level. Results suggest that large stress/strain concentrations around voids could be a source for electric fatigue degradation.

1.0 INTRODUCTION

The use of piezoceramics in actuator systems to suppress vibrations, cancel noise, and to alleviate undesirable aerodynamic effects has received considerable attention in the last decade. However, many of these actuator applications require strokes substantially larger than the material was originally designed for. To generate the larger displacements, the materials are being exposed to increasingly larger electric fields which cause domain wall motion within the material. While domain wall motion creates larger displacements, it also causes spatially varying electric fields and mechanical stresses within the material. When exposed to repeated cycles for extended periods of time, the material electrically and mechanically degrades due to a variety of physical mechanisms which are not fully understood. Depending upon the particular piezoelectric material, this degradation can occur in a couple of cycles or millions of cycles. To develop new higher authority actuators with extended fatigue lives the scientific community must begin to understand the mechanisms which contribute to this degradation process in the context of domain wall movement.

In 1953 McQuarrie (1953) reported that repeated applications of large electric fields degrade the electro-mechanical properties of barium titanate. Since that original discovery, a number of research efforts have been conducted to understand the electric fatigue process in a variety of different piezoceramic compositions. While the origin of fatigue is still unclear, there are three accepted mechanisms contributing to ferroelectric fatigue. They are 1) domain pinning/space charges (Pan 1992), 2) electrode attachment (Taylor 1967), and 3) internal stress concentrations (Carl 1975). For example, Carl (1975) and later Chung et al. (1989) observed that electric fatigue caused microcracking which was qualitatively attributed to the internal stresses developed between grains, thermal-expansion anisotropy, or stress induced by large electric fields. Jiang and Cross (1993) showed that PZT ceramics with higher

densities (i.e. fewer voids) had a longer fatigue life compared to those with lower densities. They attributed material degradation to space charges which developed along the surface of the voids causing the domain structures to be "pinned". By thermally treating the material, they reported that D-E hysteresis loops could be partially recovered indicating that the space charges were removed. Following up on the work of Taylor (1967), Jiang et al. (1994) attributed the fast fatigue of PLZT ceramics to contaminated surfaces instead of intrinsic structure deterioration or changes in domain distribution. They indicated that inappropriate electrode attachment or surface preparations can adversely effect the fatigue life of piezoelectric materials. Recently, Wang et al. (1996) suggested that electric fatigue of PZT-5H was the result of spatially variant electric fields around internal anomalies such as voids which generate large mechanical stresses caused by localized domain reorientation. While all of these contribute to the fatigue process, new actuator materials will inevitably use domain wall movement to achieve larger displacements. This means that internal stresses caused by non-aligned domains is a key issue for developing a fatigue resistant actuator.

In this paper, a Moiré inteferometry method is used to study the strain concentration around a simulated void in a piezoelectric ceramic. This study is based on the previous work of Wang (1996) indicating that fatigue degradation is the result of internal stress/strain concentrations generated by the spatially variant electric fields around voids. While previous researchers such as Mollenhauer et al. (1992) have used the Moiré technique to understand strain transfer between a piezoceramic patch and a plastic substrate, to our knowledge the Moire method has not been previously used to monitor internal stress/strain concentrations during large electric field excursions. In a previous publication (Park et al. 1996) we on the use of a Moire method to measure the strain concentrations between dissimilar oriented domain structures. In this paper we extend this concept for measuring strains around a simulated void to help understand the role of microvoids in the electric fatigue of peizocermamics.

2.0 EXPERIMENTAL SETUP

The material used in this study was a commercially available PZT-5H. This material was chosen because it generates relatively large strains (e.g. 3000 microstrain or 0.3% achievable) when compared to other piezoelectric ceramics and it is used in piezoelectric motors (Anon 1990). The material was polled at a temperature of 90° C in an electric field of 3 MV/m for five minutes. Throughout this manuscript the original poling direction will be referred to as x_3 regardless of subsequent domain wall movement which is consistent with standard piezoelectric nomenclature (Cady 1946). The orthogonal axis on the same plane will be referred as x_1.

The specimen used for this study is cut to size with a ceramic saw equipped with a diamond blade. Care is taken to ensure that the blade does not induce any anomalies in the material which would influence the results. A 4.74mm diameter carbide drill creates a simulated two-dimensional void in the material in the form of a continuous circular cylinder (see Figure 1). A coolant is used during the drilling process to prevent any local heating which might influence the material characteristics. A grinder process using 1000 grid polish followed by a 5 μm grid polish is used to smooth the exposed surfaces of the specimen for two reasons. First, Moiré interferometery requires a relatively flat smooth specimen to obtain accurate measurements and second any surface defects induced during manufacturing can potentially be removed.
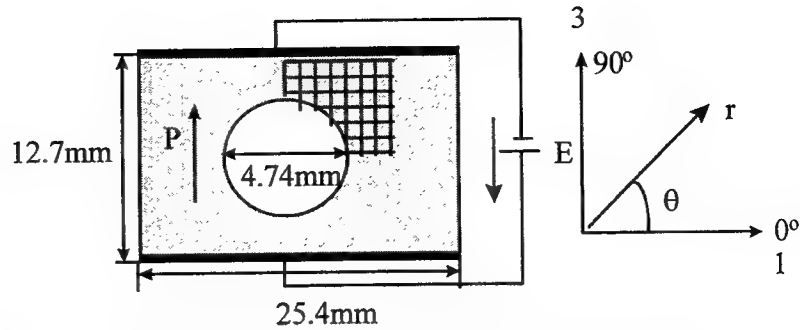
Figure 1. An illustration of the specimen and grating used and this study.

As illustrated in Figure 2, the procedures to place a grating on the specimen are as follows. The epoxy used for the replication was a F-117 bipax epoxy which was initially degassed in a centrifuge for five minutes to eliminate any air bubbles in the epoxy and provide a clean replication. A drop of epoxy is placed on the grating and subsequently attached to the specimen with a 0.1N force to promote bonding and to reduce epoxy thickness. Following cure, an M-Coat C silicone rubber is applied to all exposed surfaces to prevent problems associated with electrical breakdown of air. To prevent electric conduction through aluminum coating, the coating is dissolved with a 50% concentration of NaOH for one minute, leaving only an epoxy grating in its place. The loss in the reflection associated with removal of the aluminum coating is partially compensated for by both increasing the intensity of the laser source and using a CCD camera to record fringe patterns. A specially designed plexi-glass structure is used to hold the specimen in the Moiré apparatus and prevent electrical conduction.
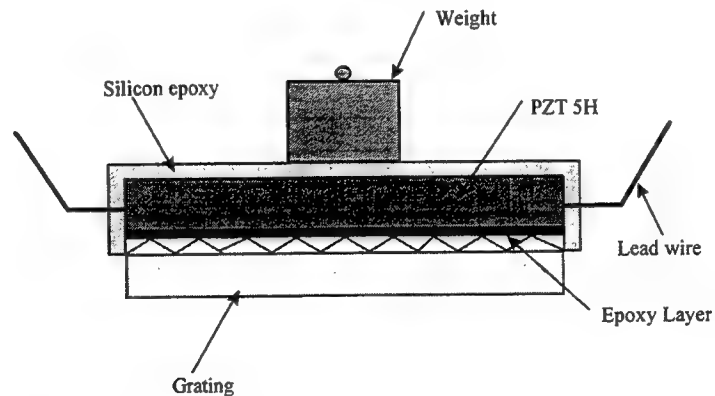
Figure 2. An illustration of the replication process to attach a grating to the specimen

In this experiment a four beam Moiré interferometry system is used . Figure 3 shows the PEMI (Portable Engineering Moire Interferometer) unit that was used for this experiment. The laser source for this system has a wave length of 633 *nm* and the reference grating frequency on the specimen is *f*=2400 *lines/mm*. When the specimen deforms, constructive and destructive interference of the laser causes fringes to be generated (Post 1994). For the test reported on in this manuscript, a CCD camera is used to acquire the image and subsequently digitized with a frame grabber rather than using a shutter camera displayed in Figure 3. A CCD camera provides the opportunity to record time dependent phenomena and provides better sensitivity for the fringes obtained from the epoxy grating.

Figure 3. An photograph of the Moire apparatus used in this study.

Following specimen preparation, the sample is mounted in the Moiré system and a null field is generated in the absence of the electrical field. For analytical convenience, carrier fringes of rotation are added which generate uniformly spaced horizontal lines in U-field and vertical lines in V-field. The application of an electric field to the specimen causes the material to deform and alters the fringes in very distinct fashions. For example, if an electric field is applied parallel to the positive x_3 axis, the sample elongates and the carrier fringes rotate clockwise. If the electric field is applied in the negative x_3 direction the sample contracts and the carrier fringe rotate counterclockwise. Therefore, when a specimen undergoes 180° domain switching, where the material abruptly switches from a contraction state to an elongation state, the carrier fringes will suddenly rotate in the opposite direction. While for the test scenario illustrated in Figure 1, one might expect the sample to undergo only 180° domain switching there is a possibility that 90° domain switching will occur. This is due to the fact that an applied E^0 generates both an E_3 and E_1 around the simulated void (Park et al. 1997b). Park 1997a discusses in detail the electric field distribution for the particular case discussed in this manuscript. Therefore, in this experiment care must be taken to explore the possibility of both 180^0 and 90^0 switching phenomena around the simulated void.

3.0 EXPERIMENTAL RESULTS

In this section the measured strain concentration around a simulated void in a material subjected to a large electric field is presented. The radius of the void is defined to be r_a (i.e., $r = 2.37$ mm) in the following discussion. The material is poled in the positive x_3 axis and an electric field is applied in the negative x_3 axis to generate the results described in this section. Experimental results for three different electric fields are presented. i.e., $E^0 = -0.63$MV/m, -0.83 MV/m, and -0.86 MV/m. An electric field value of -0.86 MV/m represents an electric field slightly lower than the coercive field in a sample without a simulated void. However, due to the electric field concentration caused by the hole polarization switching can essentially finish in this sample at - 0.86MV/m if held for a sufficient length of time.

-0.63MV/m

-0.83MV/m

-0.86MV/m

Figure 4. Contour plots of ε_{33} for three different applied electric field values

In Figure 4, contour plots of the measured strain values ε_{33} for the three electric fields are presented. At -0.63 MV/m the maximum strain is -1300 microstrains and occurs at $\theta = 0°$ and $r = r_a$ while the minimum strain is -150 microstrains and occurs at $\theta = 90°$ and $r = r_a$. In the far field (i.e., $r \gg r_a$) the strain quickly becomes uniform with a magnitude approaching -960 microstrain indicating that the influence of the hole is limited to a small region (i.e. less than 1.3 r_a). The non-uniform strain generated

around the hole is the result of the spatially variant electric field generated by the simulated void. The strain data in this figure also indicates that polarization reversal has not initiated at any location in the sample for an electric field value of -0.63 MV/m.

At -0.83 MV/m (Figure 4) the maximum strain is -1400 microstrain and the minimum strain is -700 microstrain. While the minimum strain occurred at the position expected (i.e., $\theta = 90°$ and $r = r_a$), the maximum strain was recorded in the far field region where the influence of the hole is negligible. At $\theta = 0°$ and $r = r_a$, the position one might expect the maximum strain to arise, the measured strain is only -600 microstrain. This value represents a 54% decrease in strain when compared to the lower electric field value of -0.63 MV/m. This result indicates that 180° polarization reversal has initiated in the local region around $\theta = 0°$ and $r = r_a$ where the electric field is the highest. When polarization switching begins the electric field causes the material to elongate rather than contract producing a mesoscopically measured strain which is lower than the far field value. The mechanical constraint by the surrounding region which has not switched causes the strain to remain in contraction even though the local region is attempting to elongate. Therefore, a localized region exists around the simulated void which is polarized 180° out of phase with the original poling direction.

At a value of -0.86 MV/m (Figure 4), 180° polarization switching has occurred in the vast majority of the material and can be considered complete. The maximum strain is 2200 microstrain at $\theta = 0°$ $r = r_a$, and represents a strain concentration of approximately 2 when compared to the far-field strain values for this electric field. At $\theta = 90°$ and $r = r_a$, the minimum strain occurred with the magnitude of -900 microstrain. The strain distribution appears to suggest some interesting phenomena occurring at $\theta = 45°$. From FEM analysis, the nominal electric field (E_3) for the region $\theta > 45°$ is below the coercive field level suggesting that this region remains polarized in the original poling direction. Based on the fringe patterns presented in Figure 5, this confirms the linear anlyatical results suggesting that a boundary exists between switched regions and non-switched region at $\theta = 45°$. Therefore, a portion of the material above the hole is still poled in the original poling direction. While not shown here the strain values (ε_{11}) follow the constant volume arguments for all electric field values. That is, ε_{33} is approximately two times the value for ε_{11}.
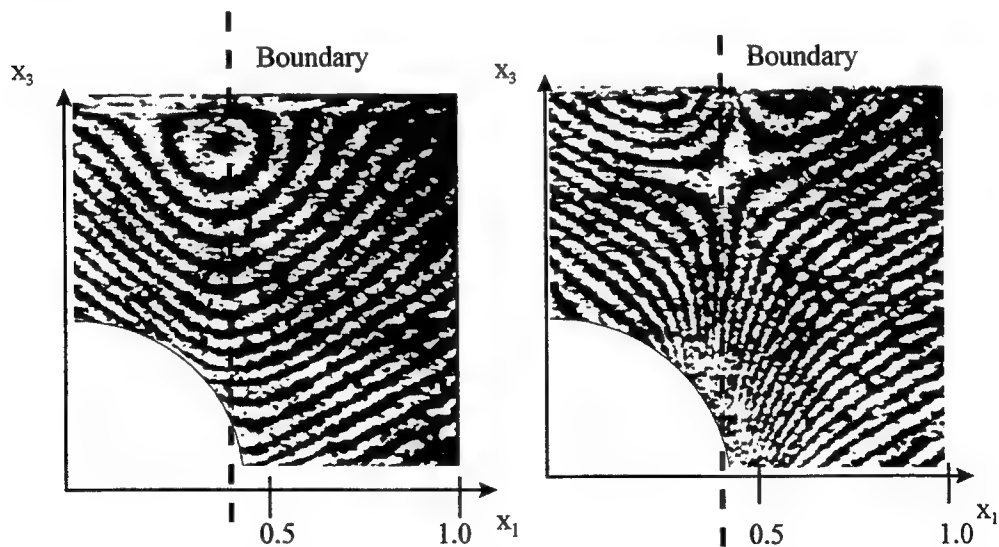
Figure 5. Fringe patterns from the U and V field for an electric field of -0.86 MV/m.

The shear strain for three different electric fields is shown in Figure 6. At -0.63 MV/m, the maximum shear strain occurred at 45° with a magnitude of 380 microstrain while minimum strain values of 0 occurred in the far field and at $\theta = 0°$ and $\theta = 90°$. Based on a linear finite element analysis (FEM) for this specific problem, E_1 is a maximum at $\theta = 45°$ while it is nearly zero in the far field region as well as $\theta = 0°$ and $\theta = 90°$. Therefore linear analysis provides an explanation of the locations of maximum and minimum shear indicating that domain switching has not initiated for this electric field value. The discussion of this figure is consistent with the results described for Figure 4 regarding the normal strains.

At -0.83 MV/m, the maximum shear strain was 950 microstrain, occurring again at 45°. The shear strain at $\theta = 0°$, $\theta = 90°$ and the far field were similar in magnitude and equal to a value of approximately 200 microstrain. The nonzero value of shear strain in the far-field suggests either dissimilar oriented domains are inducing shear or 90° switching is taking place. From a linear FEM analysis of this problem (Park 1997a), the maximum $E_1/E^0 = 0.65$ occurs at $\theta = 45°$ and $r = r_a$ resulting in an electric field value of $E_1 = 0.56$ MV/m for this particular case. From tests conducted on homogeneous specimens undergoing pure 90° switching, 90° polarization switching initiates at a value of approximately 0.6 MV/m and continues to evolve until 1.0MV/m is reached. For the case described here, E_1 at 45° is below the 0.6MV/m value (note: based on linear model) and should not induce any 90° domain switching in the material. Furthermore, the shear strain measured for this specimen in this region (i.e., 700 microstrain) supports the contention that 90° polarization switching has not occurred. In our previous study (Park et al. 1996) the shear strain at which switching commenced was nearly 3000 microstrain. Therefore, it is believed that for this particular sample 90° switching is not a source of the shear strain in the far-field. Rather, this strain is the result of strain induced by constrained regions during the 180° switching around $\theta = 45°$ (see Figure 5).

-0.63MV/m

−0.83MV/m
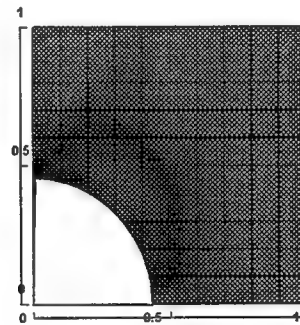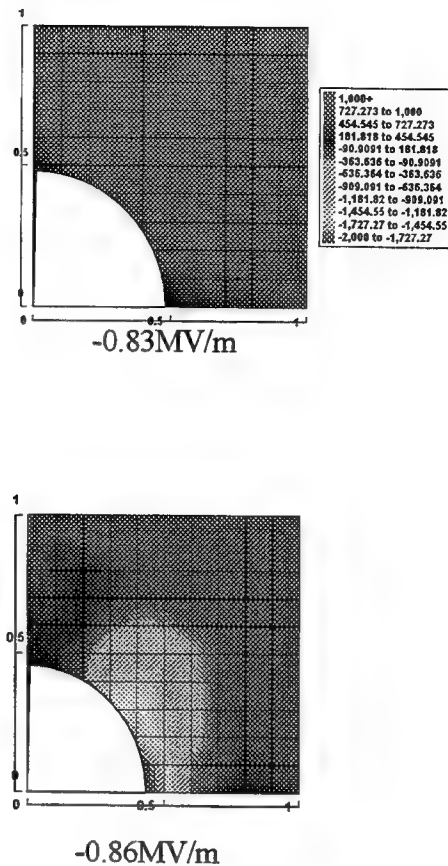
−0.86MV/m

Figure 6. Contour plots of γ_{13} for three different electric field values.

At −0.86 MV/m, the maximum shear shifted to 0° with a magnitude of −2000 microstrain. Except for this localized region, the shear strains in other portions of the ceramic were close to zero. When reviewing the magnitude and distribution of this shear strain, one discovers strong similarities with strain concentrations between regions 180° apart without the presence of a hole are present (see Park et al. 1996). Therefore, this result further indicates that 90° switching is not prominent in the domain reorientation around a simulated void.

4.0 CONCLUSIONS

Experimentally measured strain distributions around a circular cylindrical void in a piezoceramic subjected to large electric fields was measured using a Moire inteferometer. Results indicate that large stresses/strain arise around the perimeter of the hole prior to domain reorientation. Domain switching initiates at the locations with the largest stress/strains and switch in a manner so as to reduce the localized stress/strain concentrations. Domain switching in these samples appears to be predominately

any 90° domain reorientation occurring at the mesoscopic level. Domain switching initiates at critical locations around the simulated void and proceeds throughout the entire specimen rather than by homogeneous switching typical of bulk specimens. This causes localized regions of the ceramic to have a net polarization 180° out of phase with the rest of the material. In general these results indicate that local internal anomalies in the piezoeceramic such as voids generate large stress/strain concentrations when the specimen is exposed to large electric field excursions. These stresses/strains are believed to be a contributor to the electric fatigue degradation reported in large actuation ceramics.

ACKNOWLEDGEMENT

REFERENCES

Anon, "UHVL Inchworm® Motor Instruction Manual," Fishers, NY.Burleigh Instruments Inc., 1990.

Cady, W. G., Piezoelectricity, McGraw-Hill Book Co., New York, 1946.

Carl, K.,"Ferroelectric Properties and Fatiguing Effects of Modified PbTiO3 Ceramics," *Ferroelectrics*, 1975, V.9, pp. 23-32.

Chung, H.T., Shin, B.C., and Kim H.G., "Grain-Size Dependence of Electrically Induced Microcracking in Ferroelectric Ceramics," *Journal of the American Ceramic Society*,1989, Vol. 72, No. 2,pp. 327-329.

Jiang, Q.Y. and Cross, L.E., "Effects of Porosity on Electric Fatigue Behaviour in PLZT and PZT Ferroelectric Ceramics," *Journal of Material Science*, August 1993,Vol. 28, No. 16, pp. 4536-4543.

Jiang Q.Y., Subbarao, E.C., and Cross, L.E., "Effect of Composition and Temperature on Electric Fatigue of La-Doped Lead Zirconate Titanate Ceramics," *J. Appl. Phys.*, 1994,V. 75, No. 11,pp. 7433-7443.

McQuarie, "Time Effects in the Hystersis Loop of Polycrstalline Barium Titanate," *J. Appl. Phys.*, 1953,V. 24,pp. 1334-35.

Mollenhauer, D.H.; Griffin, O.H., Jr.,"Induced strain of actuation of surface bonded piezoceramic patches: a numerical and experimental study.," *Journal of Intelligent Material Systems and Structures*, May 1994, vol.5, (no.3):355-62.

Pan, W., Yue, Cheng-Feng, and Tosyali, O., "Fatigue of Ferroelectric Polarization and the Electric Field Induced Strain in Lead Lanthanum Zirconate Titanate Ceramics," *J. Am. Ceram. Soc.*, 1992,V.75, No. 6, pp. 1534-1540.

Park, S.S., " Measuring Strain Concentrations in Pieozceramics Undergoing Domain Motion with Moire," UCLA M.S. thesis, 1997a.

Park, S.B. and Carman G.P., "Optimal Properties for Piezoelectric Ceramics," *International Journal of Solids and Structures*, To appear 1997b

Park, S.B., Park S.S., Carman G.P., and Hahn, H.T., "Polarization Switching for Ferroelectric Materials," ASME WAM 1996, Proceedings ASME Aerospace Division, pp. 603-613.

Post, D., Han, B. and Ifju, P., High Sensitivity Moire: Experimental Analysis for Mechanics and Materials Springer-Verlag, 1994.

Taylor G.W., "Electric Properties of Niobium-Doped Ferroelectric Pb(Zr,Sn,Ti)03 Ceramics," *J. Appl. Phys.*, 1967,V. 38, pp. 4697-4706.

Wang, D., Fotinich, E., and Carman G.P., "Influence of Temperature on the Electro-Mechanical and Fatigue Behavior of Piezoelectric Ceramics," Submitted *Journal of Applied Physics*, Aug. 1996.

Fatigue behavior of piezoelectric ceramics

C. T. Sun and L. Z. Jiang
School of Aeronautics and Astronautics
Purdue University, West Lafayette, IN 47907

ABSTRACT

Fatigue behavior for a piezoceramic material was studied. Fatigue tests using compact tension specimens of PZT-4 under various combinations of electric and mechanical load were conducted to develop a crack growth law. Experimental results indicated that crack growth could be significantly influenced by electric fields.The fatigue crack growth cannot be accounted for by stress intensity factor alone. The result of this study indicates that the mechanical strain energy release rate is a single parameter that can account for the combined mechanical and electrical load that governs crack growth. A Paris law type of fatigue crack growth model was derived based on the fatigue tests.

Keywords: piezoceramics, fatigue, compact tension specimen, Vickers indentation

INTRODUCTION

Piezoelectric materials are currently receiving consideration in a number of actuator applications including precision positioning, vibration suppression and noise control. These materials offer promising application in many smart structures. The use of piezoceramics as actuators in smart structures demands that these materials perform under increasingly high electric and mechanical loads. Durability and reliability of actuators become important issues. Therefore, fracture (failure under monotonic mechanical and electrical loads) and fatigue (failure under cyclic loads) behaviors of piezoceramics must be understood and accurately modeled.

A crack in a material gives rise to a singular stress field near its tip. In a piezoelectric material a singular electric field is also induced if electric loading is applied. These strong mechanical and electrical fields produce crack driving forces that extend the crack in a catastrophic manner (fracture) or cumulative manner (fatigue). In either case, the presence of cracks would degenerate the mechanical as well piezoelectric performance of the actuator.

The phenomenon of crack growth has been studied extensively in many ceramics materials[1] but has only recently been investigated in piezoelectric ceramics. Caldwell and Bradt[2] studied slow crack growth in PZT using fatigue tests. White et al[3] studied the effects of cyclic stresses on crack extension at resonant frequency by including thermal dissipation. Cao and Evens[4] and Lynch[5] performed fatigue tests on Vickers indented specimens under cyclic electric fields above the coercive field and found that electric fatigue is characterized by step-by-step cleavage. Nishikawa et al[6] performed three point bending tests under cyclic mechanical loading. Tobin and Pak[7] showed that fatigue crack growth took place even at field amplitude as low as 5% of the poling field. All test results indicated that electric fields affect crack growth.

In metals, fracture and fatigue can be described well by using classical fracture mechanics. The parameter often used is the stress intensity factor. However, this parameter is not suitable for piezoceramics under combined mechanical and electrical loading since the stress intensity factor is independent of the electric field and is unable to include the effect of the electric field. Experimental efforts have attempted to observe fracture behavior under both mechanical and electrical loading. McHenry and Koepke[8] measured crack propagation velocities under electric fields and noted that electric fields increased crack speed and that crack propagation direction deviated from its original direction under strong electric fields. Tobin and Pak[7] performed Vickers indentation tests and found that the apparent fracture toughness of the material was reduced or increased depending on the direction of the applied electric field. Park and Sun[9,10] proposed the use of a mechanical strain

energy release rate to measure the apparent fracture toughness of piezoceramics. This new parameter can account for the effect of the electric field on fracture toughness.

In this paper, the mechanical strain energy release rate is employed to characterize fatigue crack growth in piezoceramics under various combined mechanical-electrical loading.

MECHANICAL ENERGY RELEASE RATE

Energy released from the cracked body which creates new crack surfaces during crack extension has been used in classical fracture mechanics. In piezoelectric materials, the total potential energy release rate can be expressed as a path-independent integral. For a cracked body shown in Fig. 1, this integral is given by

$$J = \int_{\Gamma} (Hn_2 - \sigma_{ij}n_j u_{i,2} + D_i E_3 n_i) d\Gamma, \quad i,j=2,3 \tag{1}$$

where $H = \frac{1}{2} C_{ijkl} s_{ij} s_{kl} - \frac{1}{2} \varepsilon_{ij} E_i E_j - e_{ikl} s_{kl} E_i$ is the electric enthalpy, σ_{ij}, s_{ij} and E_i are stresses, strains and electric fields, respectively; C_{ijkl}, e_{ikl} and ε_{ij} are elastic constants, piezoelectric constants and electric permitivities, respectively, and n_i is the unit normal vector to the contour Γ. The J-integral when used as a fracture criterion, would indicate that the presence of electric fields always impedes crack propagation. However, all available experimental observations indicate otherwise.

The mechanical strain energy release rate proposed by Park and Sun[8] includes only mechanical energy released as the crack extends. For Mode I loading, the mechanical strain energy release rate can be obtained using Irwine's crack closure method. We have

$$G_I^M = \lim_{\delta \to 0} \int_0^{\delta} \sigma_{33}(x_2) \Delta u_3 (\delta - x_2) dx_2 \tag{2}$$

where Δu_3 is the crack opening displacement near the crack tip. For PZT-4, we have

$$G_I^M = \frac{\pi a}{2} (2.28 \times 10^{-11} \sigma_{33}^{\infty}{}^2 + 2.21 \times 10^{-10} \sigma_{33}^{\infty} E_3^{\infty}) \quad (\text{N/m}) \tag{3}$$

in which σ_{33}^{∞} and E_3^{∞} are the remotely applied stress and electric field, respectively. Note that a negative electric field decreases the value of G_I^M and thus would increase the apparent toughness of the material.

Using G_I^M as a fracture criterion, Park and Sun[10] were able to predict fracture loads in PZT-4 piezoceramics under combined mechanical and electrical loading fairly accurately.

FATIGUE TEST USING COMPACT TENSION SPECIMEN

Experimental Procedure

The dimensions of the compact tension specimen and setup for the experiment are shown in Figures 1 and 2, respectively. The poling direction was along the X_3-axis. A conductive epoxy was used to make electrodes such that they were 13.2 mm apart. The side faces were polished in several steps starting with a 600 grit silicon carbide polishing wheel and finishing with a 0.5 μm grain sized alumina polishing pad. The crack was created by cutting the specimen with a 0.46 mm thick diamond wheel perpendicular to the poling direction resulting in a crack length of 6 mm. Subsequently, the crack tip was further sharpened by using a razor blade with diamond abrasive.
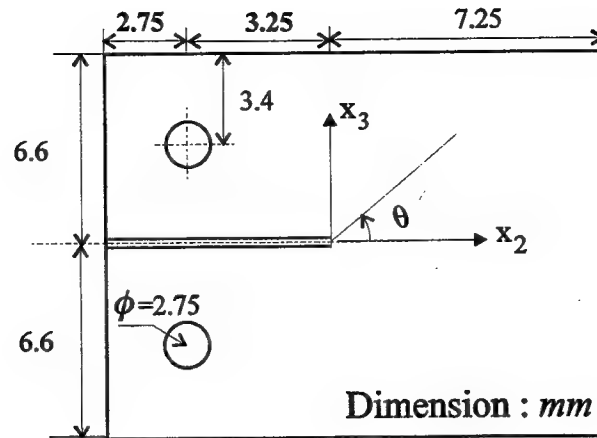
Figure 1. Compact tension specimen, PZT-4
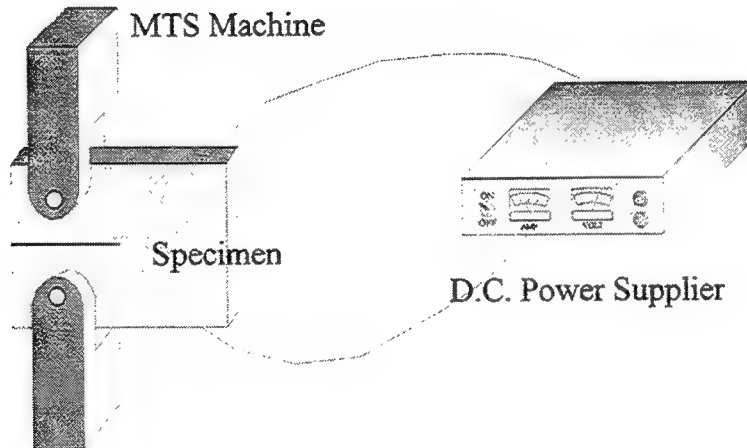
Figure 2. Setup for fatigue test using compact tesion specimen

Two types of loads were applied in the fatigue tests. In the first type of loading, the voltage was kept constant while the tension-tension cyclic mechanical load was applied. In the second type of loading, the specimen was under a constant tensile load while a time-varying electric field was applied. Table 1 lists the loading conditions.

Table 1. Loading conditions

	Mechanical	Electrical
Type 1 Loading	P_{max}=67 N, P_{min}=11 N	E=0.53 Mv/m
		E=0.23Mv/m
		E=0
		E=-0.23Mv/m
		E=-0.53Mv/m
Type 2 Loading	P=75N	E_{max}=0.15Mv/m, E_{min}=0
		E_{max}=0.08Mv/m, E_{min}=0

To prevent arcing between electrodes through the air, the specimen was submerged in silicon oil contained in a translucent plexi-glass tub. A traveling microscope was used to measure the crack length during the fatigue test.

Finite Element Analysis

The mechanical strain energy release rate corresponding to the crack growth history for each test was calculated using finite element analysis in conjuction with crack closure technique. The eight node plane strain element for piezoelectric materials in ABAQUS was used. Figure 3 shows a number of elements near the crack tip. The strain energy released during a virtual crack extension Δa would be the same as the work done in using the crack tip nodal force to close the crack opening displacement if the crack tip node were released. Since the virtual crack extension Δa is taken to be very small as compared with the crack length, the virtual crack opening can be approximated by the crack opening at the node right behind the crack tip. Using this modified crack closure technique, the mechanical strain energy release rate can be obtained as

$$G_I^M = \frac{1}{2\Delta a}\{F_3^e(u_3^{(a)} - u_3^{(b)}) + F_3^f(u_3^{(c)} - u_3^{(d)})\} \tag{4}$$

where F_3^i is the nodal force in the x_3 direction at the node i and $u_3^{(i)}$ is the nodal displacement in the x_3 direction at the node i.

Figure 3 Finite element mesh for the crack closure integral

Results

The crack growth histories corresponding to the two type of loading are presented in Figures 4 and 5, respectively. The test results clearly display the effect of electric field on fatigue crack growth. Specifically, note that a negative electric field tends to slow crack growth.

To establish a fatigue crack growth model similar to the Paris law for metallic materials, we obtained da/dN (crack growth per cycle) from the data of Figures 4 and 5. Subsequently, the $d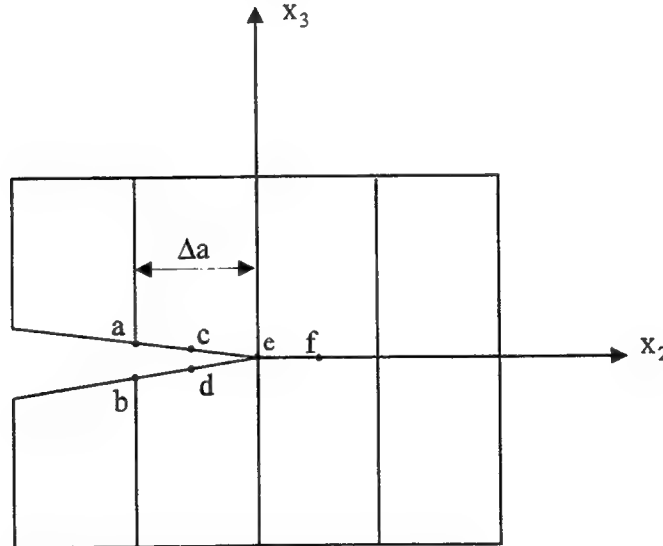a/dN$ data were plotted against the range of mechanical strain energy release rate ΔG_I^M with the result shown in Figure 6. It is interesting to note that in such a plot, all the crack growth curves generated under different loading conditions collapse almost into a single curve. This master curve can be expressed in the form of the Paris law as

$$\frac{da}{dN} = A(\Delta G_I^M)^n \quad \text{(cm/cycle)} \tag{5}$$

where $A = 4.5 \times 10^{-16}$, $n = 22.3$ and ΔG_I^M is in Nm/m^2.

Fatigue Test Using Vickers Indented Cracks

Vickers indentation technique is a popular technique for determining fracture toughness of brittle materials because of its simplicity. Sun and Park[11] extended this technique to include the piezoelectric effects in PZT piezoceramics. In this study, the precrack was produced by Vickers indentation and crack growth was generated by applying 60Hz AC electric fields. The crack lengths were measured with an optical microscope.

The electric load was applied using full wave, positive half wave and negative half wave electric fields. The peak value of the applied electric field was 5kv/cm. Figure 7 presents the normalized crack growth histories of the major crack which is perpendicular to the poling direction. It is evident that crack growth under the action of the positive half wave of electric field loading is significantly greater than that under the negative half wave loading. This phenomenon can be explained as follows. During the indentation with Vickers indentor, a plastic zone is created inside the half penny-shaped crack. Tensile residual stresses exist near the crack tip after indentation. A negative electric field when coupled with the crack tip tensile residual stress would yield a smaller mechanical strain energy release rate and thus less crack growth. A positive electric field through the coupling with the tensile residual stresses would produce a higher mechanical strain energy release rate that would produce greater fatigue crack growth. The growth of the crack would reduce the level of residual stress at the crack front and, thus, the crack growth rate.

CONCLUSION

Fatigue crack growth in PZT-4 piezoceramics has been investigated. The magnitude and direction of the electric field were found to significantly influence on the crack growth rate. The mechanical and electrical loads can be combined into a single parameter, the mechanical strain energy release rate, which can be used to characterize fatigue crack growth for various mechanical/electrical loading. A fatigue crack growth law similar to the Paris law has been derived and shown to be capable of describing the fatigue crack growth rate for PZT-4 piezoceramics.

ACKNOWLEDGMENT
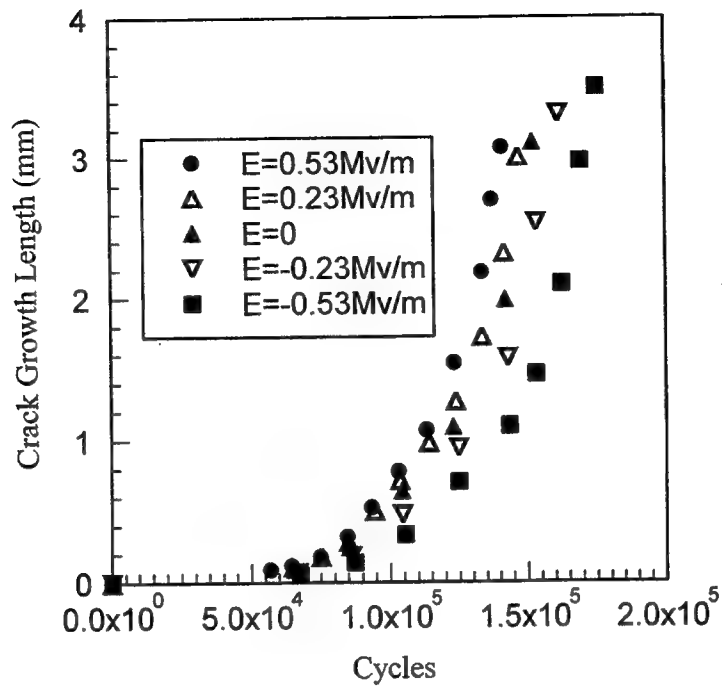
Figure 4. Crack growth vs. number of cyclic mechanical loads at constant electric field
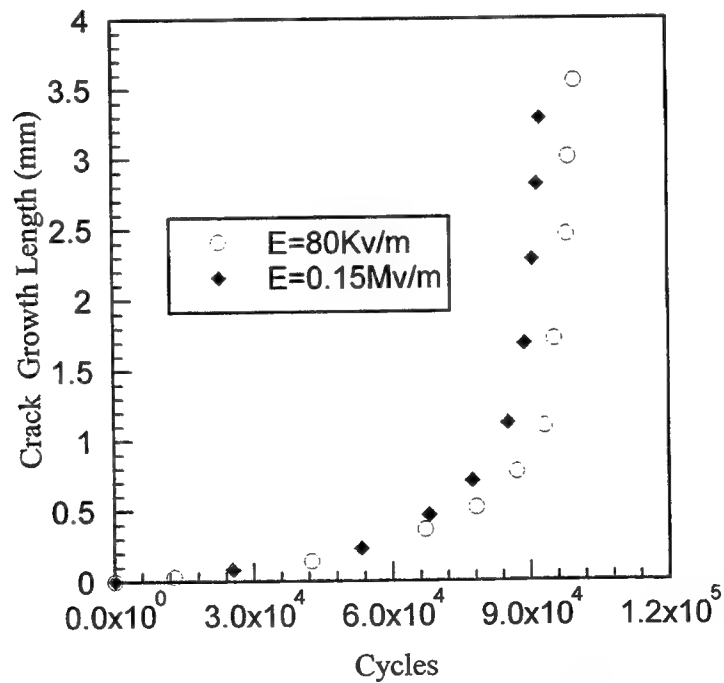
Figure 5. Crack growth vs. number of cyclics for cyclic electrical loading at constant mechanical load
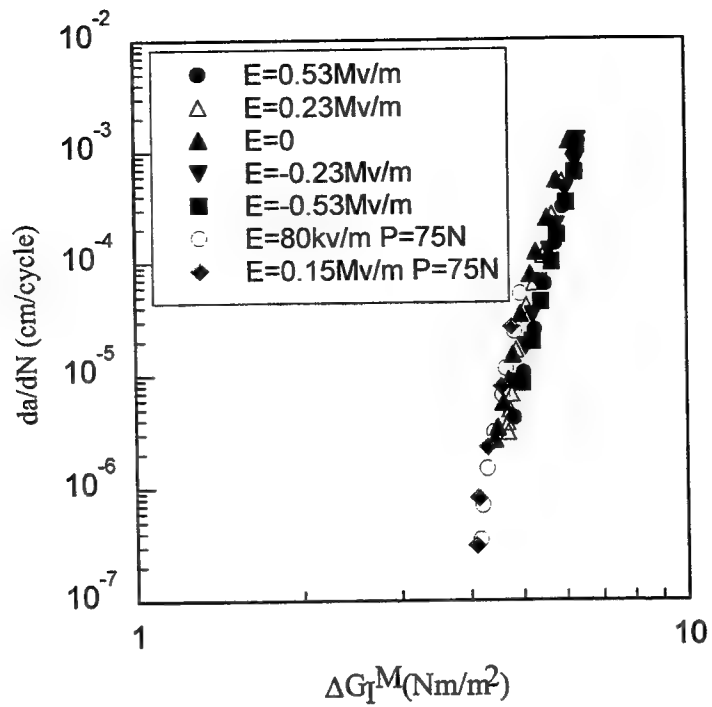
Figure 6. Crack growth rate da/dN vs. ΔG_I^M for both types of loading
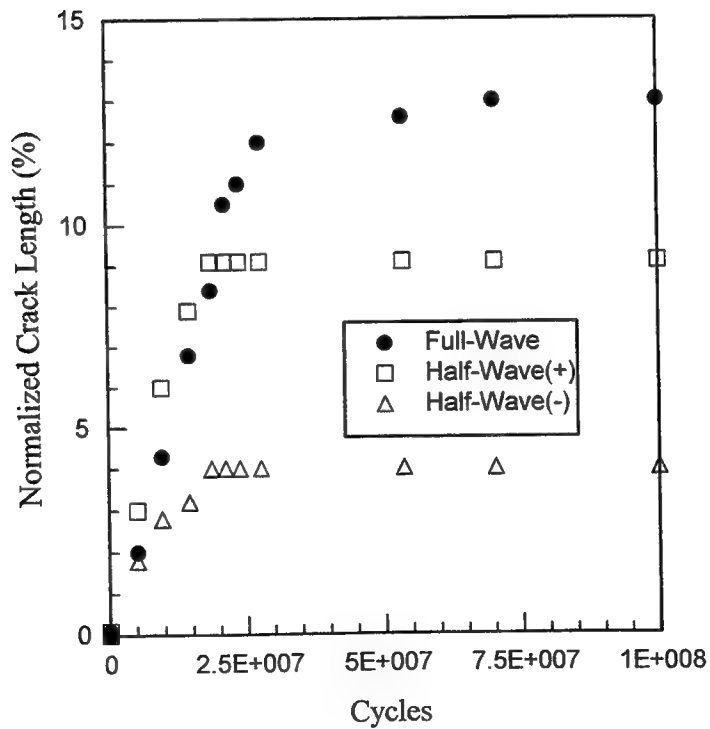
Figure 7. Fatigue crack growth under cyclic electric loading

REFERENCES

1. R. C. Bradt, D. P. H. Hasselman, D. Munz, M. Sakai, and V. Y. Shevchenko, *Fracture Mechanics of Ceramics*, Vol. **9**, Plenum Publishing Co., New York, New York, 1992.
2. R. F. Caldwell and R. C. Bradt, *J. Amer. Ceram. Soc.*, **60** , pp.169, 1977.
3. G. S. White, A. S. Raynes, M. D. Vaudin and S. W. Freiman, "Fracture bahavior of cyclically loaded PZT ", *J. Am. Ceram. Soc.*, **77**, 10, pp. 2603-2608, 1995.
4. H. C. Cao and A. G. Evans, "Electric-field-induced fatigue crack growth in piezoelectrics", *J. Amer. Ceram. Soc.*, **17**, pp.1783-1786, 1995.
5. C. S. Lnych, W. Yang, L. Collier, Z. Suo and R. M. McMeeking, "Electric field induced cracking in ferroelectric ceramics", *Ferroelectrics*, **166**, pp.11-30, 1995.
6. T. Nishkawa, J. Takahashi, A. Hattori and M. Takatsu, "Cyclic fatigue of electrically poled piezoelectric ceramics", *Fracture Mechanics of Ceramics*, Vol. **9**. Edited by Bradt, Hasselman, Munz, Sakai and Shevchenko, pp.493-500, 1992.
7. A. G. Tobin and Y. E. Pak, "Effect of electric fields on fracture behavior of PZT ceramics", **SPIE,** **1919**, pp.78-86, 1994.
8. K. D. McHenry and B. G. Koepke, "Electric field effects on subcritical crack growth in PZT", In *Fracture Mechanics of Ceramics*, Vol.5, R. C. Bradt, A. G. Evans, D. P. H. Hasselman and F. F. Lange, ed., Plenum Publishing Co., New York, NY, pp.337-352, 1978.
9. S. B. Park and C. T. Sun, "Effect of eletric fields on fracture of piezoelectric ceramics", *Int. J. Fracture*, **70**, 203-216, 1995.
10. S. B. Park and C. T. Sun, "Fracture criteria for piezoelectric ceramics", *J. Am. Ceram. Soc.*, **78**, 6, 1475-1480, 1995.
11. C. T. Sun and S. B. Park, "Determination of fracture toughness of piezoceramics under the influence of electric field using Vickers indentation", *Proc. 1995 N. Am. Conf. on Smart Structures and Materials*, 26 February-3 March 1995, San Diego, CA.

SESSION 4

Compliant Smart Materials and Complex Fluids I

Embedded PVF2 sensors for smart composites

Hugh B. Denham[a], Todd A. Anderson[b], Erdogan Madenci[b] and Paul Calvert[a]

[a]Arizona Materials Laboratories, 4715 E. Fort Lowell Road, Tucson, AZ 85712
[b]Department of Mechanical Engineering, University of Arizona, Tucson, AZ 85721

ABSTRACT

Piezoelectric polyvinylidenefluoride films have been embedded between layers of composite laminates and cured at temperatures up to 200°C. The films retain much of their piezoelectric response upon cooling even though the cure temperature exceeds the melting point of the film. The response of these embedded sensors to impact loading is discussed. We have also used embedded sensors to monitor curing of reinforced low temperature curing epoxy films sandwiched between polycarbonate sheets and subjected to an intermittent external load perpendicular to the surface. The sensor response drops as cure continues since the stiffer resin transfers less load to the film.

Keywords: PVF2, piezoelectric, embedded sensors, smart materials, cure monitoring

1. INTRODUCTION

Fiber based composite materials can exhibit strength to weight ratios several times those of steels and aluminum alloys. These would seem ideal materials for structural applications where weight is an issue, but their use is far from being totally exploited. One reason behind this is that the failure modes in composites are not as easily predicted and well known as metals. Composite material mechanical properties are very much dependent on the stress history of the material. Barely visible damage can dramatically decrease the structural integrity of a composite. For this reason, there is an interest in determining methods for monitoring composite materials to better predict their behavior. X-ray or ultrasonic methods can be used to detect damage but a permanently attached sensor allows frequent or continuous monitoring.

One choice for monitoring composites is to mount sensors externally. This method does not change the manufacturing of the composite material and so is fairly straightforward to implement. The sensors may also be removable and so can be used intermittently to check on the condition of a part. External sensors have the limitation that they are exposed to the environment and must endure its conditions. Piezoelectric sensors are generally small and instrument rather easily.

Islam et al. have used externally mounted PZT piezoelectric sensors to detect damage in laminate beams.[1] The use of externally mounted PZT sensors is limited by geometry as the piezoelectric ceramic is rigid. For this reason many researchers have looked into piezoelectric polymer sensors for external monitoring. The polymer sensors are thin (<100μm) and flexible and easily cut to shape or patterned. Externally mounted polymeric piezoelectric sensors have been used to detect and monitor damage, exploiting the inherent ability of the sensor to detect strain.[2, 3, 4, 5] The piezoelectric polymer can also be used as a transducer and sense damage with pulse and echo techniques.[6, 7]

Embedding sensors within the composite has advantages and disadvantages. The sensor is internal to the structure and protected from the external environment. There are other considerations as well. The embedding must become part of the fabrication process, so the sensor must survive the processing environment. However, the sensor could then also be used for process monitoring. The sensor becomes a

permanent part of the structure and thus becomes useful for in-life monitoring. The sensor and accompanying wiring will have an impact on the structural properties of the composite.

Numerous types of sensors have been embedded in various composite materials. Salzano *et al.* utilized embedded constantan wire strain gauges to monitor stress and strain in a graphite epoxy composite.[8] Embedded fiber-optic based sensors have been discussed in several papers by Measures[9, 10, 11], and also reviewed by Davidson *et al.*[12] The sensing techniques are many, but all involve placing optical fibers, which are typically 150-400 microns diameter, within the composite. There has been concern that these large fibers, when compared to the carbon fiber diameter of 8 microns, will weaken the composite, however experiment and modeling suggest that the effect is not serious.[13]

The analysis of signals from fiber optic sensors often requires elaborate equipment. Where signal transmission characteristics are measured, there is a problem of fiber optics being "universal sensors" which allow no deconvolution of changes due to strain, temperature or curing. A simple geometry for monitoring cure and water uptake in resin by near-IR spectroscopy with an embedded fiber has been described.[14]

Embedded piezoelectric PZT sensors have been used by Perrissin-Fabert *et al.* to monitor cure of thermosetting polymers.[15] Ceramic piezoelectric sheets are available down to thicknesses of 250 microns but are very fragile, with fracture strains of only about 0.1%. They are also limited by a loss of poling above the Curie temperature, 300-400°C for PZT, and can depole at stresses of 10-100MPa.[16] Polymer piezoelectrics offer the advantages of being thinner and tough but there are concerns about the temperature range and the piezoelectric coefficients are much less than those of the ceramics.

There are a number of known piezoelectric polymers, including several Nylons[17, 18] and copolymers of vinylidene cyanide.[19] Polyvinylidene fluoride (PVF2) was found to exhibit piezoelectric properties, when properly prepared, by Kawai.[20] Preparation involves stretching a film of PVF2 to induce a transformation to the beta phase and subjecting it to an electric field to pole the material by aligning the CF_2 dipoles, often at elevated temperatures. It has been generally observed that the piezoelectric response is lost at temperatures above the poling temperature.

We have found that piezoelectric PVF2 sensors can be cured within a thermosetting composite system and retain their activity despite exposure to temperatures above 160°C. In this paper we describe the temperature dependence of the response and test embedded sensors as cure and damage monitors.

2. EXPERIMENTAL

Polyvinylidene fluoride films were obtained from the Kureha Chemical Industry Co., Ltd. of Japan, under the tradename KF Piezo Film. The films are poled and the surfaces are electroded on both surfaces with aluminum, and are available in thicknesses of 9 and 30μm. For these experiments we used a film thickness of 30μm. Individual sensors were cut from the polymer sheet using a straight edge and scalpel to avoid smearing the electrodes and shorting the sensor. Sensor shape was chosen to make the film's stretch direction obvious. The sensor area was 1cm^2 to allow for ease of handling. Once cut to shape, copper lead wires were attached to the metallized surfaces with a copper adhesive tape (3M 1181). This structure will henceforth be referred to as PVF2 sensor assembly.

The composite material used for these experiments was a prepreg system consisting of cyanate ester resin and glass cloth. This material was provided by Lockheed Advanced Development Co. This system was proposed for use as an adhesive layer between composite skins and core materials. A typical cure cycle for this prepreg system is a two hour cure at 177°C, under autoclave conditions. Our curing was performed in a Fisher Scientific Isotemp Oven 718F, with the prepreg placed between metal blocks (to prevent warping, provide some constraint, and ensure uniform temperature). Temperature was monitored with an Omega WB-T21 analog data acquisition card and PC based computer.

The PVF2 sensors were measured by attaching the lead wires to a Tektronics model 2201 digital storage oscilloscope. BNC cabling was used from the oscilloscope and attached to the sensor lead wires. Electrical noise was reduced by surrounding the test assemblies with aluminum foil which was grounded to the oscilloscope. The voltage across the piezoelectric film was measured this way.

A Du Pont 910 series differential scanning calorimeter was used to verify the melting temperature and recrystallization temperatures for the PVF2 we obtained. A ramp rate of 10°C/min was used for heating, with cooling also limited by this rate.

Composite sandwich structures were fabricated by placing a PVF2 sensor assembly between 2.5cm x 15cm strips of cyanate ester prepreg, placing this between metal blocks and oven curing. During the curing cycle the sensor was agitated by dropping a metal rod, from a fixed height, onto the top of the metal block assembly. The sensor was monitored with an oscilloscope. This procedure was repeated at roughly 5°C increments while heating and curing the sample.

Composite coupons 10cm x 15cm were fabricated in the usual fashion with two embedded PVF2 sensor assemblies located to the left and right of center. These coupons were then impacted directly over the PVF2 sensors with an impact test rig, modeled after a NASA design. The impact tester consists of an instrumented dart dropped from a tower with variable height. The impact head has a 2.54cm diameter hemispherical end with a force transducer inside to measure impact force. The composite coupons were placed on a wooden block and impacted from a height of 30cm.

The PVF2 sensors were also used to monitor cure of a room temperature curing system. The system used was EPON 828 epoxy with triethylene tetramine curing agent. A mixture of 5:1 was found to provide a two hour cure at room temperature. To provide an environment for embedding the PVF2 sensors and allowing the sensor to receive mechanical input, the following system was chosen. Thin sheet of Lexan polycarbonate was cut into strips 2.5cm x 15cm. The whole was assembled by placing nylon mesh material at both ends of a Lexan strip, leaving a space in the middle for the PVF2 sensor. The epoxy was then mixed and poured over the screen and Lexan strip. A PVF2 sensor assembly was then placed in the gap between the screens and more epoxy applied to cover that. A second strip of Lexan was then placed over this and the assembly was placed into a fixture that supported the whole of the base and clamped the top. In this fashion, the epoxy was assured of a constant thickness and was not in a position to be squeezed out from around the sensor. The epoxy was then allowed to cure and the sensor was impulsed by dropping a rod from a fixed height onto the Lexan, centered over the embedded PVF2 sensor. The oscilloscope was used to measure voltage response to this impact at five minute increments for four hours.

3. RESULTS

Figure 1 shows the response of sensors embedded between glass fiber/cyanate ester sheets and cured for two hours at 177°C and 187°C. It can be seen that the response is linear with load in the mode used where a load is quickly removed from the sample. This method was chosen to avoid impact effects. The estimated stress under the cylindrical weight of 100g is 4000 Pa, the observed response does then correspond to a piezoelectric coefficient of 77 pC/V. Also shown are measurements on an as-received film clamped between two precured composite sheets. The response is weaker than in the cured sample.

Figure 2 shows the form of the signal in response to removing a weight of 80g. In principle a voltage step should be observed but signal leakage leads to a rapid decay. Based on a dielectric constant of 13 our sensors have a capacitance of 3.8×10^{-10}F. A leakage time of 100 msec for an 0.2V signal corresponds to a leakage resistance of about 400 Mohm. The leakage resistance of our samples exceeds 200 Mohm.

Unconstrained PVF2 film samples were also subjected to cure temperatures. This was accomplished by placing film samples in the curing oven in either aluminum pans or between glass slides. Once heat

cycled, the films were connected to the oscilloscope and checked for piezoelectric response to tapping. When heated unconstrained, the PVF2 films shrink dramatically and the electrodes turn white. When tested for piezoelectric response, the films did not exhibit any voltage response to mechanical tapping.

The peak voltage response of the embedded PVF2 sensor to the metal rod impacts during the cyanate resin cure is shown in figure 3. The sensor response decreases with increasing temperature and goes to zero in the region of the melting point. Throughout the rest of the cure, the sensor did not respond to impacts. Once cooled the sensor does exhibit piezoelectric response, although at a reduced capacity. An unconstrained sample subjected to a similar cycle shows a more rapid loss of response and no return on cooling.

These results can be compared with a DSC heating and cooling trace for the same material at 10°C/min, shown in figure 4. Melting occurs at 174°C and crystallization occurs on cooling at 145°C. As in all polymers, there is a melting range, which is dependent on the processing conditions, rather than a sharp melting point. The recrystallization at 145°C would be to the alpha phase which occurs when PVF2 is cooled from the melt, but is not piezoelectric.

The impact tester recorded force-time curves for the impacts; a typical curve shown in figure 5. The impact tester takes data at a fixed rate starting at a set time. The impact event is seen to occur over a time of about 2 ms. With a peak force of 5300N, this would generate a stress of 10 Mpa, if the film were rigidly constrained. The PVF2 sensor was set to acquire data for a set time sweep once a signal of 2 volts was sensed. The corresponding PVF2 sensor response is shown in figure 6. The sensor response is seen as a positive voltage followed by a negative voltage, which represent compression and tension, respectively, in the film. The impact event as seen by the embedded sensor is also about 2 ms.

Cure monitoring of the epoxy system is represented by the peak voltage sensor response to impact over time, as shown in figure 7. The voltage response decreases as the epoxy cures. After 120 minutes the sensor response has settled to just below 2 volts, and continues to decrease to around 1 volt at 200 minutes.

4. DISCUSSION

The d_{33} coefficient for the embedded PVF2 samples based on weight removals comes out slightly larger than theory. This may be due to the embedding process combined with the heating. It is well known that the melting point of oriented polymer fibers is affected by constraint. If the polymer is free to contract a much lower melting point is observed, while a clamped sample may melt above the normal melting point. This reflects both the thermodynamic effect of chain elongation in reducing the melting entropy and the physical cross-linking by residual crystallites near the melting point. These effects can explain why orientation and the beta structure should be retained after cycling to above the normal melting point of PVF2. It is less clear why the poling should also be retained since chain rotation between crosslinks should be possible at the melting temperature.

The behavior of the as-received samples clamped between cured sheets of glass fiber/cyanate ester is likely due to the geometry. The embedded sensors are very much a part of the composite while the sensor clamped between sheets becomes an intermediate layer and responds differently. The load may not be distributed evenly over the sensor area, and this could explain the lower reading.

The signal generated by lifting off a weight (figure 2) is a function of the speed at which the sample is removed. This is due to signal leakage and encouraged the use of impact loadings for other experiments. Impact loadings are more complicated than step weights but were found to be more repeatable.

The result of the impact testing (figures 5 and 6) left an indentation in the wood and therefore the wood absorbed some of the impact. The PVF2 sensor compression peak height corresponds to a stress of 2.5

Mpa, a factor of 4 lower than what the impact head recorded. This indicates that the impact loading was either distributed over the composite or over time. The compressive load was followed by a tensile load suggesting that some reflection of the loading occurred.

The cure monitoring results were encouraging. This system can be viewed as a composite of epoxy and PVF2 loaded in parallel. The load is shared between the two elements on the basis of equal strain. As the elastic modulus of the epoxy rises, the stress carried by the sensor decreases. During curing the epoxy modulus is expected to increase from about 1MPa to about 3GPa. The modulus of the PVF2 is in the region of 0.3-1 GPa. If we assume constant and approximately equal loaded areas for the sensor and matrix, the 85% decrease in load observed by the sensor corresponds to an increase in epoxy modulus from much less than the sensor to about 6-fold that of the sensor.

Thus the sensor does monitor the curing of the resin in terms of elastic modulus. However in most resins, the modulus increases to a maximum during the precuring cycle and decreases again during heating to the postcuring temperature. The glass transition is a much better measure of extent of cure than is the modulus at any particular temperature.

5. CONCLUSIONS

We have found that piezoelectric PVF2 can be used as an embedded sensor in a thermosetting composite even though the curing temperature is very near the melting point of the film. This has been shown to occur when there is some constraint on the film to inhibit melting. The response of an embedded PVF2 sensor to step loadings with weights is linear. Embedded PVF2 sensors were also used to detect impact loadings. For a room temperature curing epoxy system, embedded PVF2 sensors were used to monitor cure.

6. REFERENCES

1. A. S. Islam, K. C. Craig, "Damage detection in composite structures using piezoelectric materials", *Smart Mater. Struct.* **3**, 318-328 (1994).
2. S. C. Galea, W. K. Chiu, J. J. Paul, "Use of piezoelectric films in detecting and monitoring damage in composites", *J. Intel. Mat. Sys.Struct.* **4**, 330-336 (1993).
3. H. Zhang, S. C. Galea, W. K. Chiu, Y. C. Lam, "An investigation of thin PVDF films as fluctuatuing-strain-measuring and damage-monitoring devices", *Smart Mater. Struct.* **2**, 208-216 (1993).
4. W. K. Chiu, S. C. Galea, H. Zhang, R. Jones, Y. C. Lam, "The use of piezoelectric thin film sensors for structural integrity monitoring", *J. Intel. Mat. Sys.Struct.* **5**, 683-693 (1994).
5. M. Egashira, N. Shinya, "Local strain sensing using piezoelectric polymer", *J. Intel. Mat. Sys.Struct.* **4**, 558-560 (1993).
6. B. Tang, J. Mommaerts, R. K. Duncan, J. C. Duke, D. A. Dillard, "Nondestructive evaluation of model adhesive joints by PVDF piezoelectric film sensors", *Exper. Mechanics* **33**, 102-109 (1993).
7. J. F. Campbell, E. G. Vanderheiden, L. A. Martinez, D. S. Cairns, M. G. Abdallah, "A multi-purpose sensor for composite laminates based on a piezoelectric film", *J. Comp. Mat.* **26**, 334-349 (1992).
8. T. B. Salzano, C. A. Calder, D. W. DeHart, "Embedded strain sensor development for composite smart structures", *Exper. Mechanics* , 225-229 (1992).
9. R. M. Measures, "Smart composite structures with embedded sensors", *Composites Engineering* **2**, 597-618 (1992).
10. R. M. Measures, "Fiber optic sensing for composite smart structures", *Composites Engineering* **3**, 715-750 (1993).
11. R. M. Measures, "Advances toward fiber optic based smart structures", *Optical Engineering* **31**, 34-47 (1992).
12. R. Davidson, D. H. Bowen, S. S. J. Roberts, "Composite materials monitoring through embedded fiber optics", *Intl. J. Optoelec.* **5**, 379-404 (1990).

13. Holl, M. and Boyd, S., "The effect of fiber optics on the mechanical properties of a composite host material", *SPIE* **1916**, 109-117, 1993.
14. Calvert, P., George, G., and Rintoul, L., "Monitoring of cure and water uptake in a freeformed epoxy resin by an embedded optical fiber", *Chem. Mater.*, **8**, 1298-1301, 1996.
15. I. Perrissin-Fabert, M. Feve, Y. Jayet, G. Merle, "Monitoring thermoset polymerization by using piezoelectric measurements",*J. App. Polym. Sci.* **46**, 1087-1093 (1992).
16. Moulson, A. J.and Herbert, J. M., *Electroceramics: materials, properties, and applications*, Chapman and Hall, London, 1990.
17. Litt, M., Hsu, C., and Basu, P., "Pyroelectricity and piezoelectricity in Nylon 11", *J. Appl. Phys.*, **48**, 2208, 1977.
18. Lee, J., Takase, Y., Newman, B. and Scheinbeim, J., "Effect of annealing on the ferroelectric behavior of Nylon-11 and Nylon-7", *J. Polym. Sci., Part B, Polym. Phys.*, **29**, 279, 1991.
19. Miyata, S., Yoshikawa, M., Tasaka, S., and Ko, M., "Piezoelectricity revealed in the copolymer of vinylidene cyanide and vinyl acetate", *Polym. J.*, **12**, 857-860, 1980.
20. H. Kawai, "The piezoelecticity of poly(vinylidene fluoride)",*Jap. J. App. Phys.* **8**, 975-976 (1969).
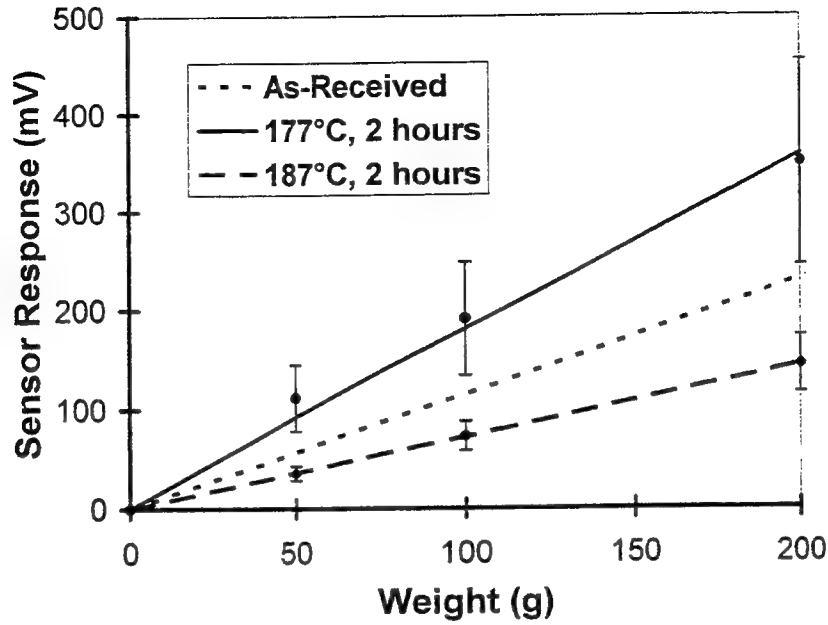
Figure 1. Response of PVF2 sensor embedded in cyanate ester resin laminate to weight being removed from directly over the sensor. Shown for two different cure conditions, and an as-received sensor clamped between two cured laminate layers.
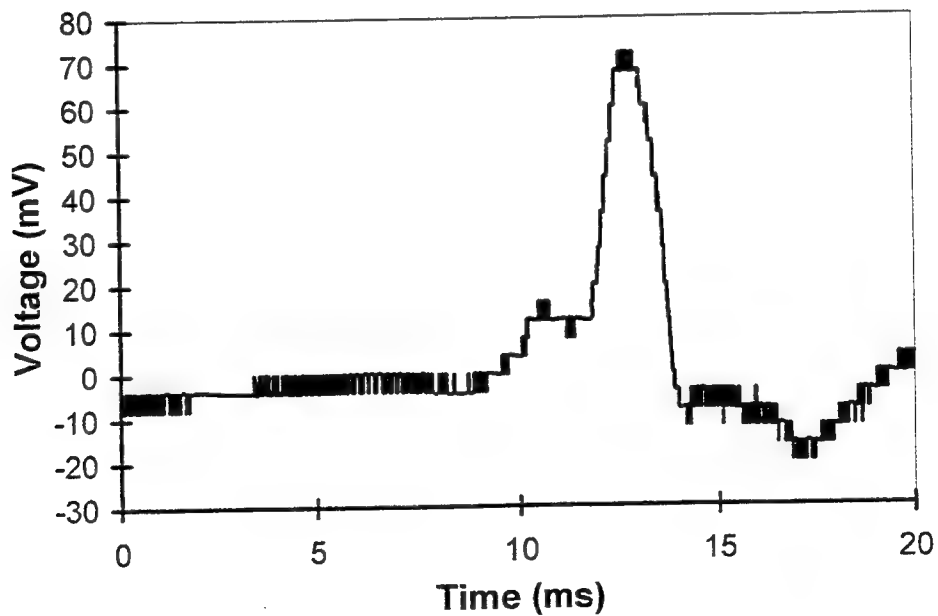
Figure 2. Oscilloscope trace of PVF2 sensor response to 80g weight being removed. Sensor is as-received and was clamped between cured sheets of cyanate ester resin. .
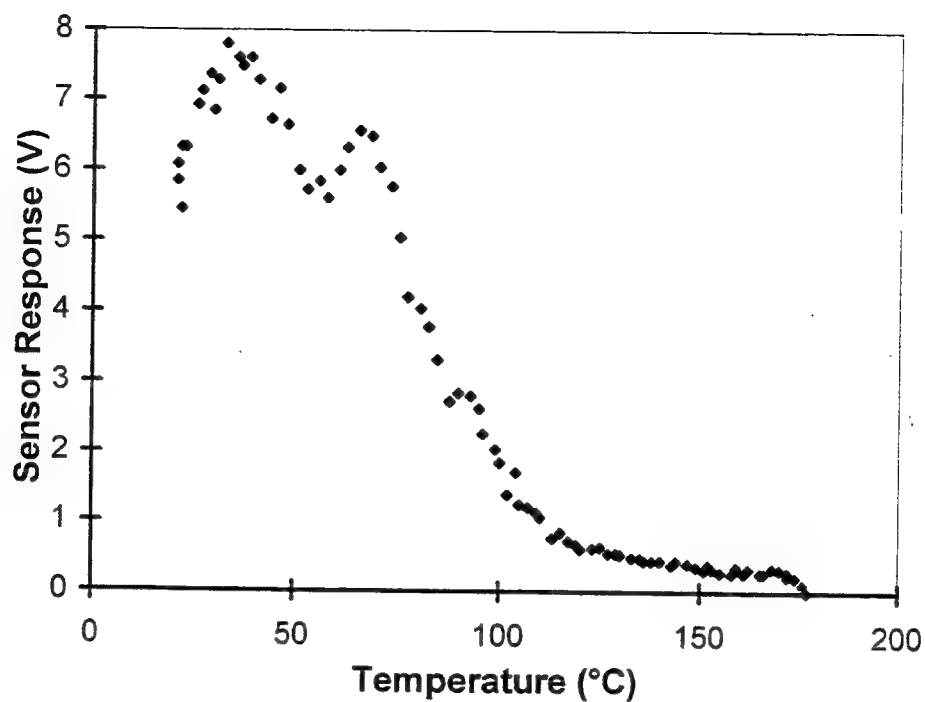
Figure 3. As-received PVF2 sensor placed between cyanate ester resin sheets and constrained with aluminum blocks. This assembly was then impacted with a 200g rod dropped from a height of 10cm. Measurements taken while heating to the cure temperature (177°C).
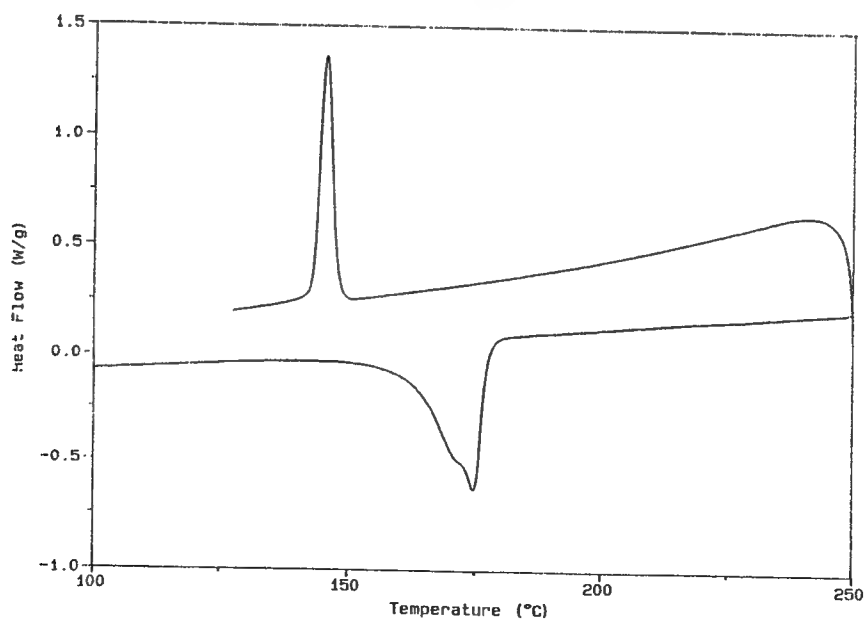
Figure 4. DSC curve for PVF2 film sensors heated and cooled at 10°C/min.
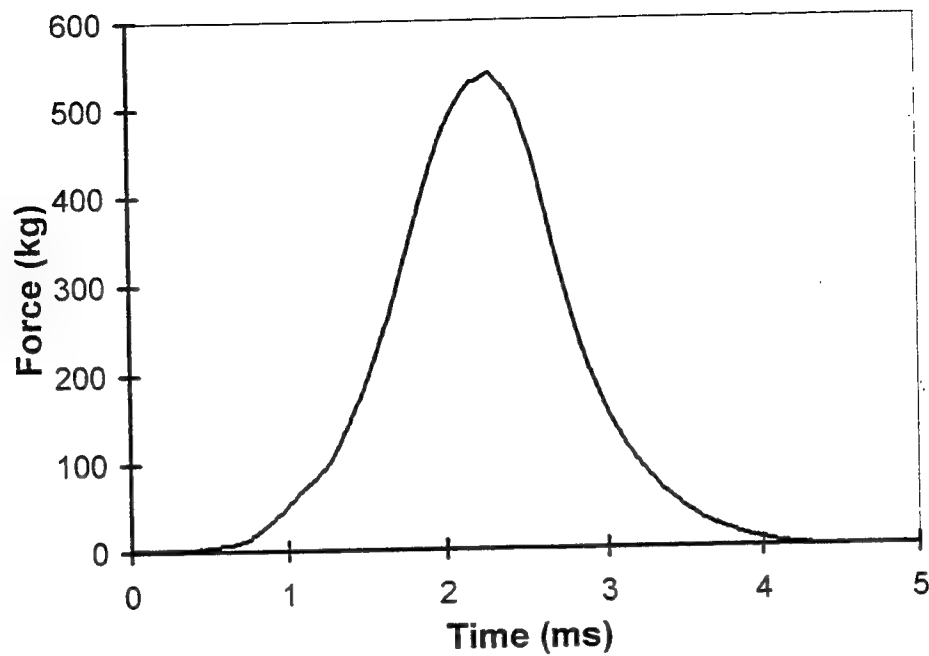
Figure 5. Force transducer output from impact testing head dropped from a height of 30cm onto a laminate of cyanate ester with embedded PVF2 sensors. The composite coupon was supported by a wooden block, and otherwise unconstrained.
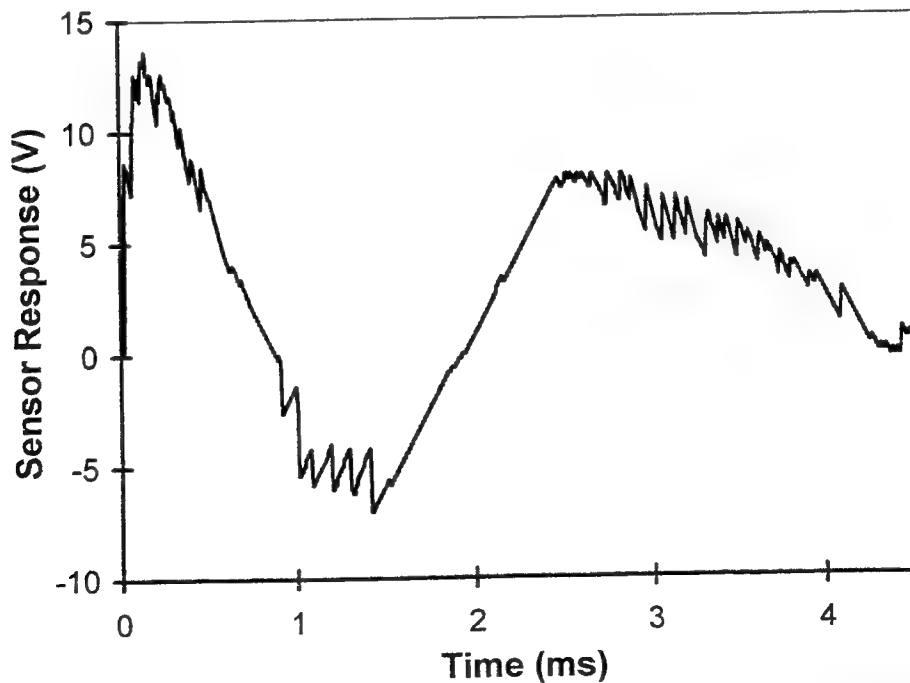
Figure 6. PVF2 sensor embedded within a cyanate ester laminate responding to the impact generated by a 2.54cm hemisphere. This curve corresponds to the force curve shown in figure 5.
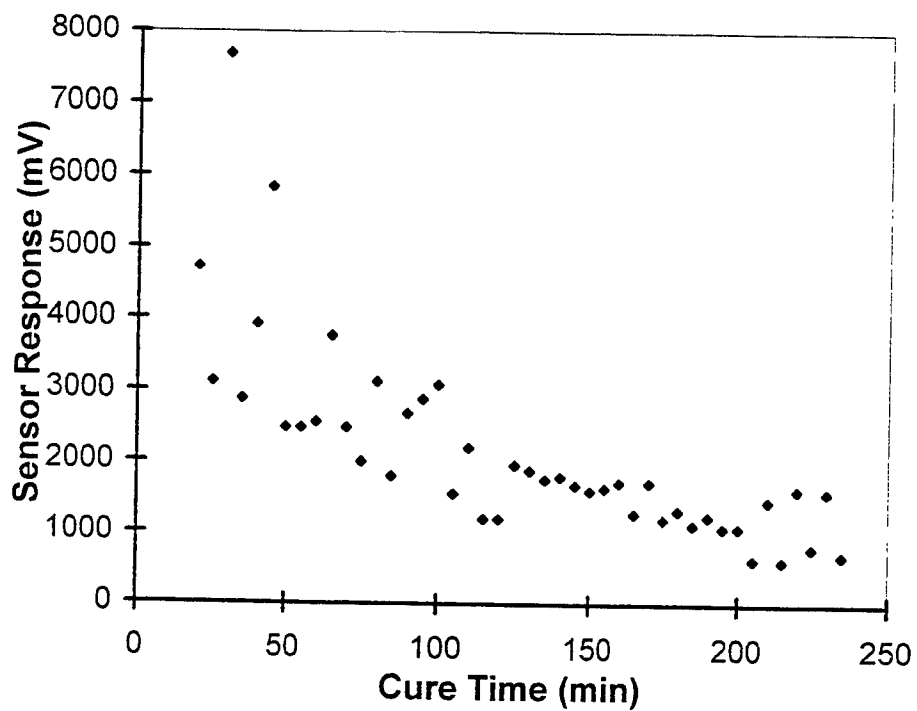
Figure 7. PVF2 sensor placed between sheets of polycarbonate, surrounded with EPON 828 epoxy and cured at room temperature. The whole assembly was impacted during the cure with a 20g rod dropped from a height of 8cm.

Mechanical properties of compliant piezoelectric composites

Steven Marra, K.T. Ramesh, and Andrew Douglas

Department of Mechanical Engineering
The Johns Hopkins University
Baltimore, Maryland 21218

ABSTRACT

The potential applications of pure piezoelectric ceramics as embedded sensors are limited by the stiffness and brittleness of these materials. To achieve a more compliant sensor, composites have been developed which incorporate calcium-modified lead titanate particles in a polymer matrix. Such compliant sensors, in thin film form, may be useful within thick composite structures such as tank hulls and helicopter blades. The mechanical response of 0-3 composite films of Ca-modified lead titanate in polyvinylidene fluoride-trifluoroethylene and Epon828 epoxy matrices is investigated in this work. The electrical response of these composites is currently being studied by Wenger et al. The viscoelastic properties of these thin film composites with various volume fractions have been measured over a wide range of frequencies and temperatures. The observed mechanical response of these heterogeneous materials is compared with the predictions of several simple models for such composites. Preliminary piezoelectric results are also presented.

Keywords: piezoelectric, viscoelastic, composite, sensor, lead titanate

1. INTRODUCTION

As thick-walled polymeric composite structures become increasingly utilized, new challenges arise in monitoring the mechanical state of these composites. Sensors such as strain gages and acoustic emission detectors can provide much information regarding the status of a structure through surface monitoring. However, many issues involving thick-walled composites, ranging from internal curing conditions and residual stresses to the progressive evolution of internal damage, would be better sensed from within the structure. Sensors which can be embedded in a composite are therefore advantageous.

Materials with the potential to be used for such sensors include piezoelectric ceramics. These materials possess a crystal structure which converts a mechanical deformation into an electrical potential, and vice versa. Barium titanate $(BaTiO_3)$[1,2], lead zirconate-titanate (PZT)[3,4], and lead titanate $(PbTiO_3)$[5-9] are well studied examples of such ceramics. $BaTiO_3$ and PZT possess large permittivities which make them more suited for applications as microactuators rather than as sensors. However, the permittivity of lead titanate is much lower than that of either $BaTiO_3$ or PZT, resulting in a larger electrical response. The magnitude of the d_{31} coefficient of $PbTiO_3$ is also lower, which results in a larger hydrostatic piezoelectric coefficient, d_h (the larger hydrostatic coefficient is useful in detecting some of the deformation modes in composite plates). Because of these properties, $PbTiO_3$ is preferred over $BaTiO_3$ and PZT for use within sensors intended for embedding in composites. However, pure lead titanate is a highly anisotropic ceramic with a tetragonal crystal structure;[7] sintering is difficult due to the anisotropy, and internal stresses and cracking are induced during poling.[3] Calcium doping of $PbTiO_3$ improves the sinterability and poling characteristics by reducing the anisotropy and lowering the Curie temperature.[10,11]

Ideally, embedded sensors should have mechanical properties identical to their surroundings so as to avoid the inclusion-matrix problem. While Ca-modified $PbTiO_3$ possesses good sensing capabilities, it is too stiff and brittle (being a ceramic) to be used alone as an embedded sensor within polymeric composites. Dispersing the ceramic in a polymer matrix results in composites which combine piezoelectric and

viscoelastic properties. The resulting composites retain the sensing capabilities of the $PbTiO_3$, while remaining compliant. Such composites, when formed into thin films, can be easily embedded in thicker laminate structures. Polymer/ceramic composites of this type usually consist of either ceramic fibers or rods (1-3 connectivity) or ceramic particles (0-3 connectivity) dispersed in a polymer matrix.

The piezoelectric properties of lead titanate 1-3 composites have been studied by Chan et al.[12] and Ting et al.,[13] and the piezoelectric properties of lead titanate 0-3 composites have been studied by Chilton et al.,[14] Dias et al.,[15-18] and Wenger et al.[19] While 1-3 connectivity composites possess better piezoelectric properties in general, the difficulty and cost of fabrication is a great disadvantage. Composites with 0-3 connectivity, in contrast, are inexpensive to fabricate and can be formed into thin films much more easily.

The present work considers thin film composites consisting of Ca-modified $PbTiO_3$ particles dispersed in a matrix of either epoxy (Epon828) or polyvinylidene fluoride-trifluoroethylene (P(VDF-TrFE)). These matrix materials were chosen because the former represents a popular matrix material in laminate composites, and the latter is a piezoelectric polymer. Epon 828 is a well characterized epoxy with material properties similar to many polymeric laminate structures. This epoxy has been extensively studied by Agarwal and Teufel,[20] Vleeshouwers et al.,[21] and Engelberg and Tesoro,[22] and extensive physical properties are available.

Pure PVDF is a thermoplastic piezoelectric polymer which can crystallize into at least four different forms. The most common form, which is normally obtained from the melt, is non-polar. The most electroactive crystal structure of PVDF is obtained by stretching the polymer. The copolymer P(VDF-TrFE), however, crystallizes into a piezoelectric form directly from the melt without the need for stretching.[23] The piezoelectricity of PVDF and P(VDF-TrFE) has been studied by Koizumi et al.,[24] Tashiro et al.,[25] Tasaka and Miyata,[26] and Higashihata et al.[27]

Wenger et al.[19] are currently investigating the electrical and piezoelectrical properties of Ca-modified $PbTiO_3$/Epon828 and P(VDF-TrFE) 0-3 composites. This paper examines primarily the mechanical characteristics of these composites. Viscoelastic properties have been measured for composites of various ceramic volume fractions and the experimental results are compared with analytical and finite element models. Some further consideration is also given to the piezoelectric properties.

2. MATERIALS AND COMPOSITE FABRICATION

All of the composite films studied in this paper were fabricated by Wenger et al. at the School of Electrical Engineering and Computer Systems at the University of Wales, Bangor, U.K. The Ca-modified $PbTiO_3$ was provided by GEC-Marconi (UK) and has the following composition:

$$Pb_{0.76}Ca_{0.24}[Ti_{0.96}Co_{0.02}W_{0.02}]O_3 + MnO_2$$
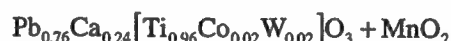
The Curie temperature of the ceramic is 260°C and the particle size is typically between 10μm and 60μm.

The epoxy resin is Epon828 (Shell Chemical Company) and the curing agent is K61B (Anchor Chemicals). The epoxy/ceramic composites were formed by adding a few drops of the curing agent and the desired amount of Ca-modified $PbTiO_3$ powder to 1cm^3 of epoxy. Stirring of the mixture resulted in an even distribution of ceramic throughout the matrix. The mixture was then placed in a vacuum to remove air and gases. After two hours the still-uncured composite was removed from the vacuum, placed on a smooth, clean sheet of aluminum foil, and returned to the vacuum for two hours at 60°C. The mixture was then removed from the vacuum and a second sheet of aluminum foil was placed on top. The composite was pressed between two steel plates at a maximum pressure of 25 MPa, after which it was cured for two to four hours at 60°C. The aluminum foil was then removed, leaving behind a smooth, thin (>100μm) unpoled film.

Epoxy/ceramic composite films with average ceramic volume fractions of 20, 30, 40, 50, 55, and 60% were supplied. Pure epoxy films were also provided. Upon inspection under a scanning electron

microscope (SEM), it was discovered that at low ceramic volume fractions (approximately 20-40%), the ceramic particles tended to settle to the bottom face of the film, creating an effectively layered structure. It is believed this settling occurred during the curing phase of the fabrication process. Films with ceramic volume fractions greater than 40% appeared to have a uniform distribution of particles throughout the thickness (see Figure 1). It was also discovered (by the University of Wales) that during the pressing phase of the fabrication process, the ceramic particles tended to migrate toward the edges of the film. As a result, different regions of the film had different local ceramic volume fractions.

10μm
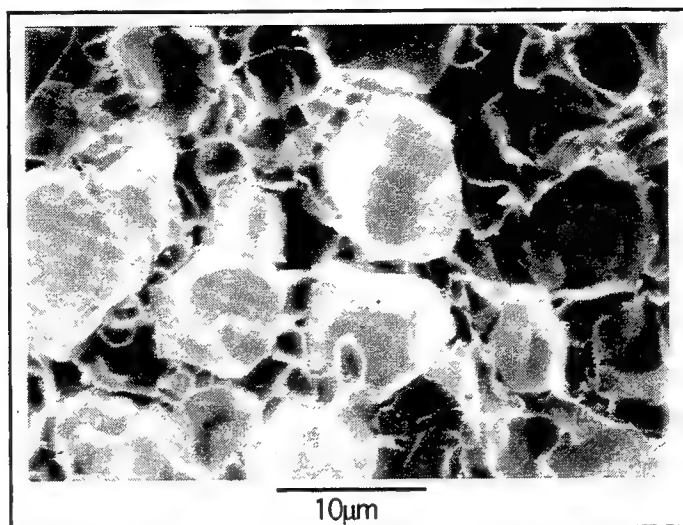
Figure 1 - SEM Micrograph of 45% Epon828/55% Ca-Modified PbTiO$_3$ Composite

The P(VDF-TrFE) was obtained from Piezotech and has a 75:25 mol% composition. Two different processes were used to form the P(VDF-TrFE)/ceramic composites. The first process consisted of melting the copolymer in a hot rolling mill at 170°C, adding the Ca-modified PbTiO$_3$ particles while mixing to ensure even ceramic distribution, then pressing the mixture at high temperature and pressure to form a thin (>100μm), composite film. The second process formed the P(VDF-TrFE)/ceramic composites by first dissolving the copolymer with methyl ethyl ketone, then adding the Ca-modified PbTiO$_3$ particles while mixing, during which some of the ketone evaporated. The mixture was then pressed at high temperature and pressure, which released the remainder of the ketone. No differences in the end properties of the composites have been observed between the two methods of fabrication.

P(VDF-TrFE)/ceramic composite films with average ceramic volume fractions of 40, 50, 55, and 60% were supplied. Pure P(VDF-TrFE) films were also provided. SEM inspection did not reveal settling of the ceramic particles as with the epoxy-ceramic films for these ceramic volume fractions. There were variations in the local ceramic volume fractions at different regions of the films, although not as pronounced as in the epoxy matrix composites. This may be due to the higher viscosity of the copolymer solution throughout the fabrication process.

3. MECHANICAL TESTING

Mechanical testing of the composite films was performed using a Rheometrics Solids Analyzer II (RSAII). The RSAII is a strain-driven testing machine capable of measuring the viscoelastic properties of films, fibers, foams, composites, and elastomers, depending on which tooling fixtures are used. The film fixtures used for this work consist of grips attached to an actuator and a force transducer mounted in the test station (see Figure 2). A test specimen is inserted into the grips. During a test, the actuator induces a prescribed strain in the specimen and the resulting force is measured with the transducer. A convection oven is used to perform tests at temperatures from ambient to 500°C.

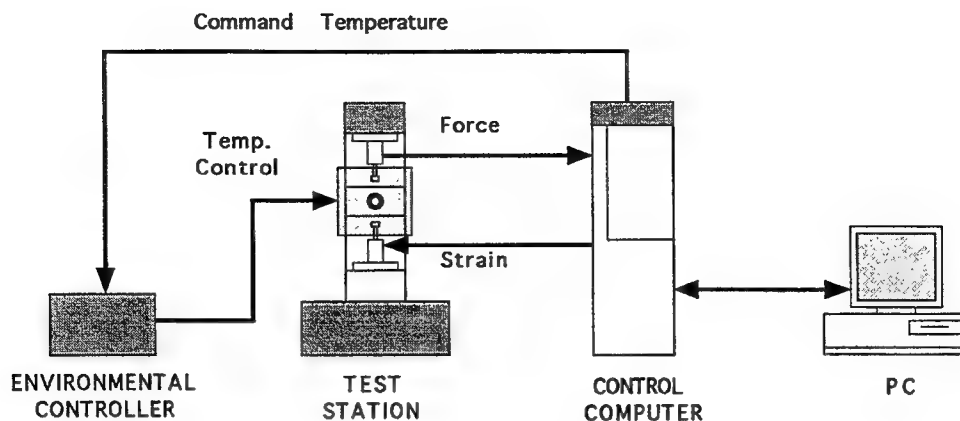Figure 2 - The Rheometrics Solids Analyzer II (RSAII)

Constant strain rate, frequency sweep, stress relaxation, creep, and temperature ramp tests can be performed using the RSAII. All test parameters are specified through a personal computer, which relays the information to a control computer, linked to the test station. Viscoelastic properties such as storage and loss moduli are determined for each test. The testing equipment has a displacement resolution of $\pm 1 \mu m$, a force measurement sensitivity of 9.81mN, and a maximum force of 9.81N. The actual testing frequency range is 0.001 to 100 rad/sec, although time-temperature superposition can be used to cover a much larger effective frequency range.

Before performing a test on the composites, the films must be cut into narrow specimen strips. A diamond wheel saw is used to section the film, resulting in strips with relatively smooth, parallel edges. The epoxy/ceramic composites specimens are cut into strips approximately 0.8mm wide, while the P(VDF-TrFE)/ceramic composite specimens are cut to widths of approximately 1.5mm. The composite specimens are then cleaned with methanol and placed in a dessicator to remove any remaining moisture. Because the ceramic volume fraction is not uniform throughout the film, the dimensions and weight of each composite specimen are measured. From these measurements, and using the known densities of the ceramic and matrix materials, the average ceramic volume fraction is calculated for each strip. The specimen is then inserted in the grips and tested. The actual test length of the specimens is approximately 23mm.

This work will focus primarily on the viscoelastic properties of compliant "smart" composites acquired through two mechanical tests:

- Frequency Sweep - A frequency sweep test consists of inducing a fixed-amplitude oscillatory strain in a specimen at constant temperature (all frequency sweep tests were performed at room temperature). The storage and loss moduli of each specimen are measured over a range of oscillatory frequencies (0.01 to 100 rad/sec for the epoxy/ceramic composites and 0.1 to 100 rad/sec for the copolymer/ceramic composites).

- Frequency-Temperature Sweep - A frequency-temperature sweep test is simply a series of frequency sweep tests performed for a given specimen over a range of temperatures. The resulting curves are then shifted using time-temperature superposition to create a master curve of the viscoelastic moduli, covering a wider range of frequencies at a fixed reference temperature. All master curves used in this work have been referenced to room temperature. Temperature ranges were from room temperature (approximately 27°C) to 100°C for the epoxy/ceramic composites and from room temperature to approximately 130°C for the copolymer/ceramic composites.

The strain amplitudes were kept relatively small (0.08% for the epoxy/ceramic composites and 0.02% for the copolymer/ceramic composites) in order to ensure that all specimens would remain in the linear viscoelastic range during the tests.

Viscoelastic Properties

A perfectly elastic material has a real Young's modulus E which is related to the bulk modulus K and the shear modulus μ. The Young's modulus of a viscoelastic material, however, is replaced by a complex Young's modulus E^* composed of a real storage modulus E' and an imaginary loss modulus E'': $E^* = E' + iE''$. The storage modulus is related to the recoverable energy due to elastic behavior, and the loss modulus is related to energy lost due to viscous effects. The ratio of loss modulus to storage modulus is referred to as the loss tangent: $\tan\delta_E = E''/E'$. Similarly, the bulk and shear moduli may be complex properties, and a loss tangent is related to each of these quantities.

4. EXPERIMENTAL RESULTS

Epon828 and Epon828/Ca-Modified PbTiO$_3$ Composites

The master curves for the pure epoxy and an epoxy/Ca-modified PbTiO$_3$ composite containing 44% ceramic are shown in Figure 3. It is apparent that the viscoelastic properties are frequency dependent for both materials. This dependence is not as pronounced at frequencies above approximately 10^{-2} rad/sec, where the epoxy behaves as a glassy polymer. However, as the frequency decreases from 10^{-2} rad/sec the properties change rapidly. These transitions correspond to the glass transition region of the polymer, since these measurements were taken at temperatures near and above the glass transition temperature of the epoxy (measured at approximately 65°C). As expected, the composite is much stiffer than the pure epoxy, except at very low frequencies, where the behavior of the matrix dominates. The increase in the loss tangents as the frequency decreases indicates the relative growth of viscous losses to stored energy. Note that it is unlikely that these composites will be used to sense such low frequency response.
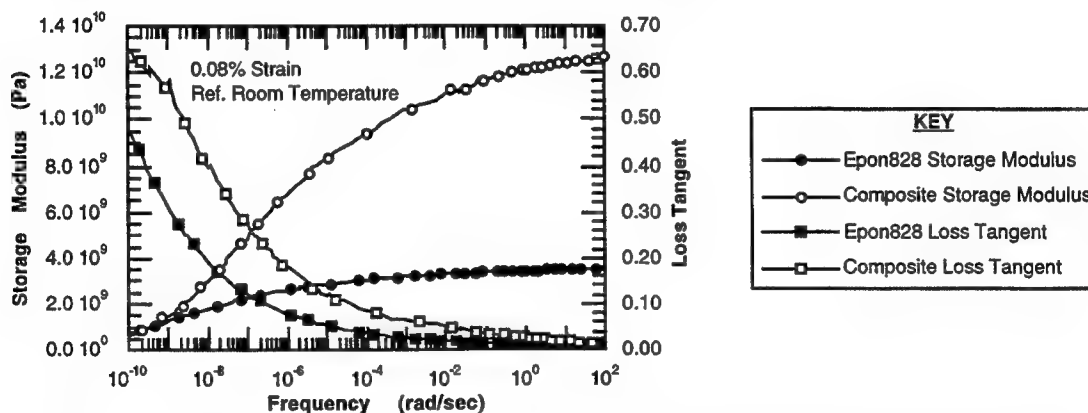
Figure 3 - Epon828 and 56% Epon828/44% Ca-Modified PbTiO$_3$ Composite Master Curves

A plot of the epoxy/ceramic composite storage modulus and loss tangent versus ceramic volume fraction at a fixed frequency of 10 rad/sec is shown in Figure 4 (similar behavior is observed at other frequencies). The ceramic is assumed to be totally elastic with a modulus of 127.6 GPa[11] and a loss tangent equal to zero. It is clear that as the amount of ceramic increases, the composite becomes stiffer. However, even at 60% particle content, the composite storage modulus is closer to that of the epoxy matrix than the ceramic. While the loss tangents of the composites tested appear to be scattered between 0.015 and 0.025, all are above the loss tangent of the pure epoxy. This is not intuitively expected; as the amount of ceramic increases, and hence the amount of polymer decreases, the viscous response should decline and the composite should behave more elastically. Therefore the loss tangent should ideally decrease with increasing ceramic volume fraction. However, this reasoning assumes perfect bonding between the matrix and particles. The increase in loss tangent of the composites may be a result of interface defects. Friction due to sliding contact between the ceramic and epoxy or debonding of the particles may be responsible for the increase in $\tan\delta_E$. It also appears for the composites tested that as the volume fraction of ceramic increases, the loss tangent

tends to decrease. A possible reason for this behavior is that as the ceramic volume fraction increases from zero, the losses due to interfaces dominate and the loss tangent increases. At some point, though, the effect of the interfaces reaches a maximum, and increasing the amount of ceramic does not increase the amount of interface losses (perhaps due to particle contiguity). Since the viscous effects decrease as the amount of ceramic increases, the loss tangent would then begin to decrease. Further study is necessary to determine if interfaces are indeed the cause of the higher lossy behavior.
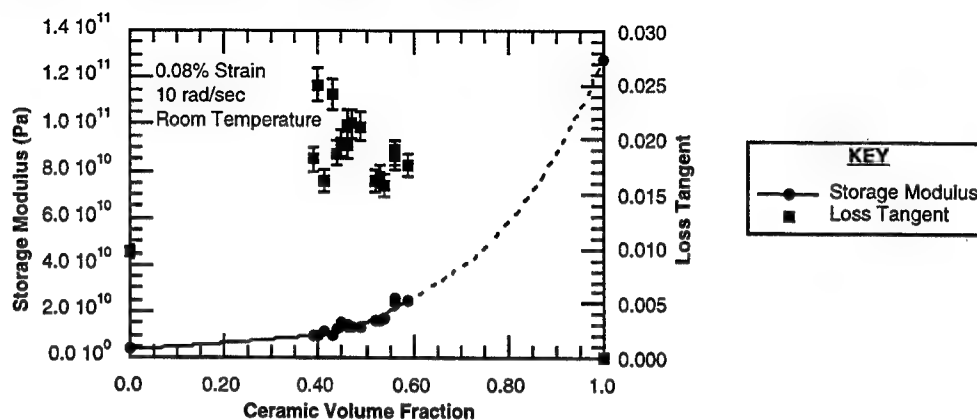
Figure 4 - Storage Moduli and Loss Tangents of Epon828/Ca-Modified PbTiO$_3$ Composites

P(VDF-TrFE) and P(VDF-TrFE)/Calcium-Modified PbTiO$_3$ Composites

The master curves for the pure P(VDF-TrFE) and a P(VDF-TrFE)/Ca-modified PbTiO$_3$ composite containing 56% ceramic are shown in Figure 5. Unlike the Epon828, the glass transition temperature of the copolymer is below room temperature (approximately -40°C[24]). As a result, the transitions which were apparent in the epoxy and epoxy/ceramic composites are not observed in these materials. Moreover, the storage moduli increase almost linearly with frequency over the range measured. As before, the composite is stiffer than the pure polymer, and the loss tangents increase as the frequency decreases.
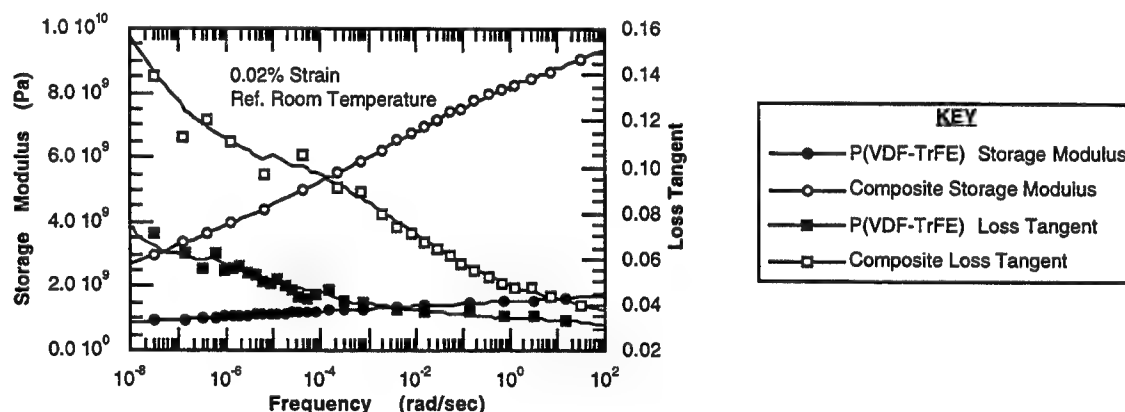
Figure 5 - P(VDF-TrFE) and 44% P(VDF-TrFE)/56% Ca-Modified PbTiO$_3$ Composite Master Curves

A plot of the copolymer/Ca-modified PbTiO$_3$ composite storage modulus and loss tangent versus ceramic volume fraction at a fixed frequency of 10 rad/sec is shown in Figure 6 (similar behavior is observed at other frequencies). As with the epoxy-matrix composites, the copolymer-matrix composites become stiffer with increasing amounts of ceramic. Again, the storage moduli of all the composites tested are closer to that of the polymer matrix than the ceramic. Also, as with the epoxy-matrix composites, the loss tangents of the copolymer composites are larger than that of the P(VDF-TrFE) alone. Again, this may be

due to interface defects. It also appears for the composites tested that as the volume fraction of ceramic increases, the loss tangent tends to increase. A possible reason for this behavior is that as the ceramic volume fraction increases, the number of interfaces increases. If the bonding between the matrix and particles is consistently weak for all volume fractions, then as the number of interfaces increases, the losses due to the interfaces increases.
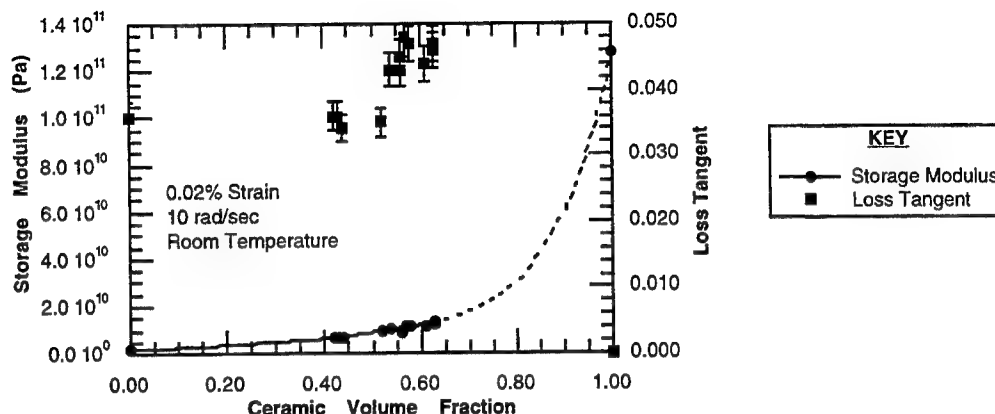
Figure 6 - Storage Moduli and Loss Tangents of P(VDF-TrFE)/Ca-Modified PbTiO$_3$ Composites

5. MECHANICAL MODELING

Analytical Model

The analytical model which is used to describe the viscoelastic properties of these 0-3 composites was developed by Hashin.[28] This model uses equations developed by Eshelby and Hashin for the bulk and shear moduli of elastic particulate composites, and applies them to a viscoelastic particulate composite with the following assumptions:

- The particles are purely elastic.
- The matrix is viscoelastic in shear and purely elastic in hydrostatic loading: $K'=K_m$, $K''=0$.
- The matrix shear loss tangent is small so that: $(\tan^2\delta_\mu)_m<<1$.

The 0-3 composite is modeled as a heterogeneous material made up of numerous cells, each containing one particle. The particles are assumed to be perfect spheres surrounded by a spherical shell of matrix material (see Figure 7). While all cells are not the same size, the ratio of the particle radius to the outer radius of the matrix shell is fixed for all cells. This ratio is equal to the particle volume fraction, c.
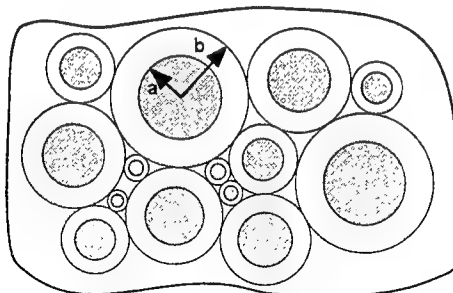
Figure 7 - Composite Spheres Model, c=a/b

154

Complex Bulk Moduli

For the perfectly elastic 0-3 composite, modeled according to Figure 7, the effective bulk modulus $\hat{K}$ was obtained as:[29]

$$\hat{K} = K_m + \frac{(K_p - K_m)(4\mu_m + 3K_m)c}{4\mu_m + 3K_p - 3(K_p - K_m)c} \qquad (1)$$

where the subscripts m and p refer to the matrix and particle material respectively, and μ_m is the matrix shear modulus. The real and complex viscoelastic bulk moduli are determined by replacing the matrix shear modulus with its complex components:

$$\hat{K}' = K_m + \frac{(K_p - K_m)(4\mu'_m + 3K_m)c}{4\mu'_m + 3K_p - 3(K_p - K_m)c} \qquad (2)$$

and
$$\hat{K}'' = \left[\frac{K_p - K_m}{4\mu'_m + 3K_p - 3(K_p - K_m)c} \right]^2 12\mu''_m c(1-c) \qquad (3)$$

Complex Shear Moduli

The effective shear modulus, $\hat{\mu}$, of an elastic particulate composite was obtained as:[29]

$$\hat{\mu} = \mu_m \left[1 + \frac{c}{\dfrac{1}{\gamma - 1} + A(1-c) - \dfrac{c(1-c^{\frac{2}{3}})^2}{Bc^{\frac{7}{3}} + C}} \right] \qquad (4)$$

where $\gamma = \mu_p/\mu_m$, and A, B, and C are functions of γ and the Poisson's ratios of the matrix and particle materials. The values of the Poisson's ratios used in modeling the composites are 0.205 for the Ca-modified PbTiO$_3$,[11] 0.36 for the Epon828[30], and 0.392 for the P(VDF-TrFE)[31]. The real part of the complex shear modulus of the composite, $\hat{\mu}'$, is found by replacing μ_m with μ'_m in (4). The imaginary part of the complex shear modulus is calculated from the composite effective shear loss tangent $\hat{\mu}'' = \hat{\mu}' \tan \hat{\delta}_\mu$ where the effective shear loss tangent is determined from:

$$\tan \hat{\delta}_\mu = \left(\frac{\mu'_m}{\hat{\mu}'} \right) \left(\frac{\partial \hat{\mu}'}{\partial \mu'_m} \right) (\tan \delta_\mu)_m \qquad (5)$$

The effective complex Young's modulus of the composites are computed from the effective complex bulk and shear moduli.

Finite Element Model

In addition to the analytical model, these viscoelastic particulate composites were also modeled using the finite element program ABAQUS. The composites are idealized as an array of space-filling hexagonal cells, and the behavior of a hexagonal cell is further approximated by an axisymmetric cell consisting of a spherical particle in a cylinder of matrix. Only one quarter of the cross-section of a cell is considered due to the symmetry of the model (see Figure 8). An oscillatory displacement is applied to the nodes at the top of the cell. The nodes along the x-axis are restricted to movement only in the x-direction, and the nodes along the y-axis are restricted to movement only in the y-direction. Further boundary conditions are imposed by constraining all nodes along the top of the cell to move with the same displacement in the y-direction, and all nodes along the outer (right) side of the cell to move with the same displacement in the x-direction. The

viscoelastic properties of the composite are calculated from the reaction force and phase angle which are extracted from the model. As with the analytical model, the particles are assumed to be elastic.
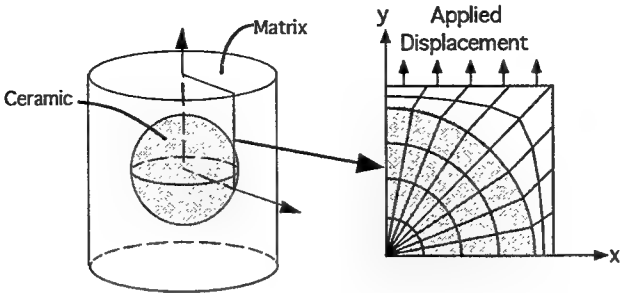
Figure 8 - Composite Unit Cell Finite Element Model

Figures 9 and 10 compare the experimental storage moduli and loss tangents with the predicted properties for the two composite materials. Both analytical and computational models predict the storage moduli fairly well for the ceramic volume fractions tested, although the finite element model is slightly more accurate. It should be noted that in practice, these composites will not contain more than 65% ceramic due to poor film quality at higher volume fractions.
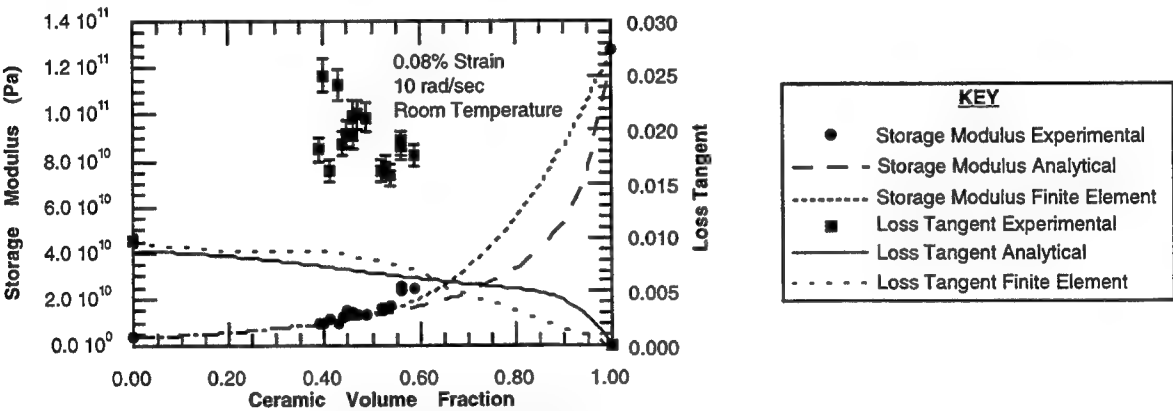
Figure 9 - Experimental and Predicted Storage Moduli and Loss Tangents of
Epon828/Ca-Modified PbTiO$_3$ Composites
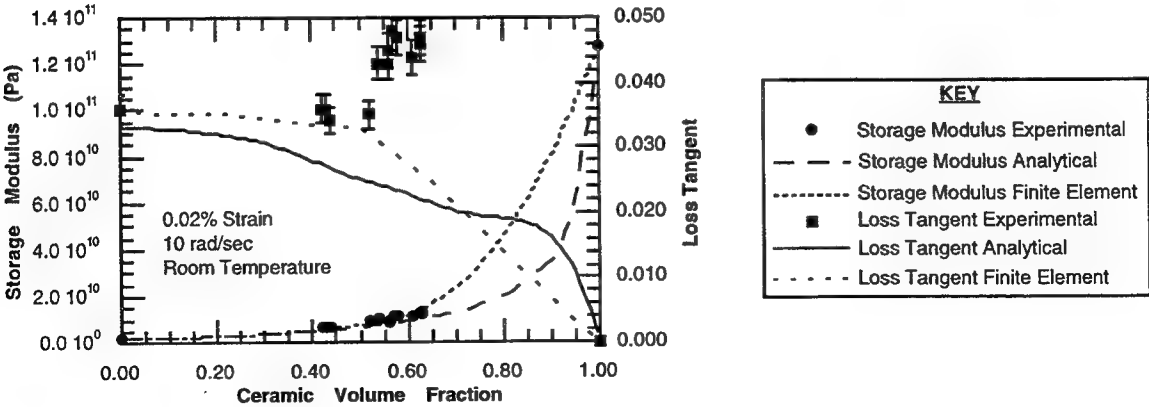
Figure 10 - Experimental and Predicted Storage Moduli and Loss Tangents of
P(VDF-TrFE)/Ca-Modified PbTiO$_3$ Composites

Both analytical and computational models assume perfect bonding between the particles and matrix, and hence, the predicted loss tangents decrease with increasing ceramic content. The next step in modeling these composites is to introduce a third (interphase) layer between the ceramic and polymer which will represent the interface. The bulk and shear moduli of this phase can then be manipulated to represent slip and debonding conditions.

6. PIEZOELECTRIC EFFECTS

Preliminary results on the piezoelectric response of these composites under mechanical loads are now presented. P(VDF-TrFE)/Ca-modified $PbTiO_3$ composites with ceramic volume fractions of approximately 55% and 60% have been poled successfully. This was achieved by first depositing gold-palladium electrodes (approximately 1000Å thick) on the composite films, which were then placed between two stainless steel plates and submerged in a bath of insulating silicon oil (see Figure 11). The oil was heated to approximately 100°C while an electric (DC) field was gradually applied across the plates. The field strength was increased to a maximum of 25MV/m and remained at that level for 30 minutes. The oil bath was then cooled to room temperature, after which the electric field was gradually decreased to zero. The poled films were sectioned into specimens as previously described.
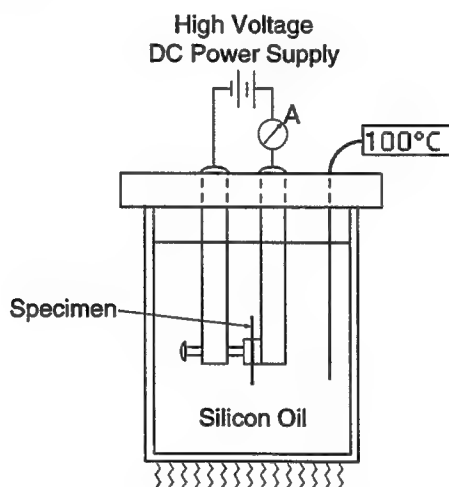
Figure 11 - Poling Apparatus

The piezoelectric response of these composites is measured by performing constant frequency tests using the RSAII. A poled specimen is placed in the grips and wire leads are attached to the electrodes. These leads connect to an oscilloscope which measures the voltage output across the thickness of the film. The strain signal from the RSAII is also sent to the oscilloscope.

Figure 12 shows the electrical response and strain for a P(VDF-TrFE)/Ca-modified $PbTiO_3$ composite with 60% ceramic at 100 rad/sec and room temperature. It is apparent that there is a phase difference between the electrical response and the applied strain, indicating that the piezoelectric coefficients are complex quantities. These coefficients have also been found to depend on the frequency of the applied strain.
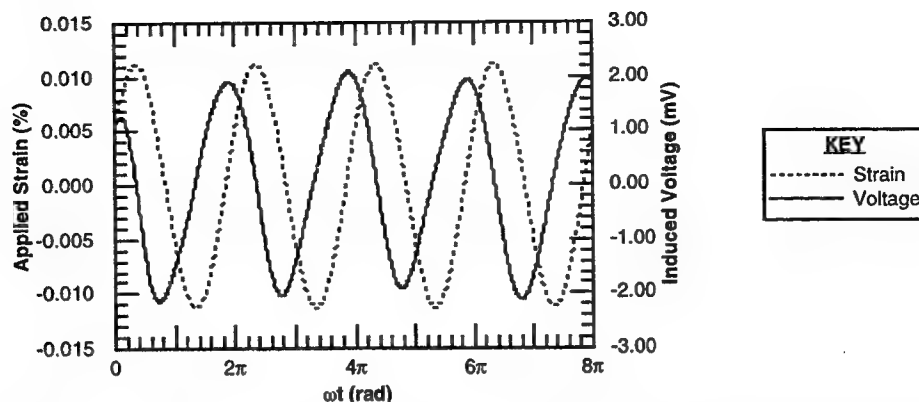
Figure 12 - Piezoelectric Response of 40%P(VDF-TrFE)/60%Ca-Modified PbTiO₃ Composite at 100 rad/sec

7. SUMMARY

The viscoelastic and piezoelectric properties of 0-3 composites consisting of Ca-modified PbTiO$_3$ particles in P(VDF-TrFE) and Epon828 matrices have been investigated. The frequency response of these composites with ceramic volume fractions between 40% and 63% were studied. As expected, the composites behave stiffer as the frequency increases. The composites also become stiffer with increasing amounts of ceramic; however, the stiffness is dominated by the matrix at ceramic volume fractions below approximately 60%. The loss tangents of the composites tested were generally larger than those of the matrix materials, indicating possible interface losses.

Analytical and computational models have been shown to predict the storage moduli of the composites fairly well. However, both models predict a decrease in the loss tangent with increasing amounts of ceramic, whereas the experimental results show an increase in the loss tangent. This is possibly due to the perfect bonding assumptions inherent in the models. Future work will consider the effect of the interfaces on the viscoelastic properties of the composites.

P(VDF-TrFE)/Ca-modified PbTiO$_3$ composite films have been poled successfully and preliminary results show that the piezoelectric coefficients of these composites are complex. The piezoelectric response is presently being investigated more thoroughly, particularly with respect to the effects of frequency and ceramic volume fraction. Thermal effects will also be considered.

ACKNOWLEDGMENTS

REFERENCES

1   Devonshire, A.F., "Theory of barium titanate - part I.," *Philos. Mag.*, 40, pp. 1040-1063, 1949.
2   Devonshire, A.F., "Theory of barium titanate - part II.," *Philos. Mag.*, 42, pp. 1065-1079, 1951.
3   Jaffe, B., R.S. Roth, and S. Marzullo, "Properties of piezoelectric ceramics in the solid-solution series lead titanate-lead zirconate-lead oxide: tin oxide and lead titanate-lead hafnate," *J. Res. National Bureau of Standards*, 55 (5), pp. 239-254, 1955.
4   Jaffe, H., "Piezoelectric applications of ferroelectrics," *IEEE Transactions on Electronic Devices*, 16, pp. 557-561, 1968.
5   Gavrilyachenko, V.G., R.I. Spinko, M.A. Martynenko, and E.G. Fesenko, "Spontaneous polarization and coercive field of lead titanate," *Soviet Physics - Solid State*, 12 (5), pp. 1203-1204, 1970.

6 Gavrilyachenko, V.G. and E.G. Fesenko, "Piezoelectric effect in lead titanate single crystals," *Soviet Physics - Crystallography*, 16 (3), pp. 549-550, 1971.

7 Haun, M.J., E. Furman, S.J. Jang, H.A. McKinstry, and L.E. Cross, "Thermodynamic theory of PbTiO$_3$," *J. Appl. Phys.*, 62 (8), pp. 3331-3338, 1987.

8 Rossetti, G.A., K.R. Udayakumar, M.J. Haun, and L.E. Cross, "Thermodynamic theory of single-crystal lead titanate with consideration of elastic boundary conditions," *J. Am. Ceram. Soc.*, 73 (11), pp. 3334-3338, 1990.

9 Nelmes, R.J. and W.F. Kuhs, "The crystal structure of tetragonal PbTiO$_3$ at room temperature and at 700 K," *Solid State Communications*, 54 (8), pp. 721-723, 1985.

10 Wersing, W., K. Lubitz, and J. Mohaupt, "Anisotropic piezoelectric effect in modified PbTiO$_3$ ceramics," *IEEE Trans. Ultrason., Ferroelec. Freq. Control*, 36 (4), pp. 424-433, 1989.

11 Yamashita, Y., K. Yokoyama, H. Honda, and T. Takahashi, "(Pb,Ca)((Co$_{1/2}$W$_{1/2}$),Ti)O$_3$ piezoelectric ceramics and their applications," *Jpn. J. Appl. Phys.*, 20 (Supplement 20-4), pp. 183-187, 1981.

12 Chan, H.L.W., J. Unsworth, and T. Bui, "Mode coupling in modified lead titanate/polymer 1-3 composites," *J. Appl. Phys.*, 65 (4), pp. 1754-1758, 1989.

13 Ting, R.Y., A.A. Shaulov, and W.A. Smith, "Piezoeletric properties of 1-3 composites of a calcium-modified lead titanate in epoxy resins," *Proceedings of the IEEE 1990 Ultrasonics Symposium*, 2, pp. 707-710, IEEE, Honolulu, Hawaii, USA, 1990.

14 Chilton, J.A., G.M. Garner, R.W. Whatmore, and F.W. Ainger, "0-3 Composite sensitivity," *Ferroelectrics*, 109, pp. 217-222, 1990.

15 Dias, C., D.K. Das-Gupta, Y. Hinton, and R.J. Shuford, "Polymer/ceramic composites for piezoelectric sensors," *Sensors and Actuators A*, 37-38, pp. 343-347, 1993.

16 Dias, C.J. and D.K. Das-Gupta, "Electroactive polymer/ceramic composites," *Proceedings of the 1994 IEEE 4th International Conference on Properties and Applications of Dielectric Materials*, 1, pp. 175-178, IEEE, Brisbane, Aust., 1994.

17 Dias, C.J., M.P. Wenger, Y. Kaminorz, U. Hopfner, and D.K. Das-Gupta, "Electro-active properties of intelligent ferroelectric ceramic/polymer composite sensors," *Proceedings of the 8th International Symposium on Electrets*, pp. 589-593, IEEE, Paris, France, 1994.

18 Dias, C.J. and D.K. Das-Gupta, "Piezo- and pyroelectricity in ferroelectric ceramic-polymer composites," *Key Engineering Materials*, 92-93 , pp. 217-248, 1994.

19 Wenger, M.P., P. Blanas, C.J. Dias, R.J. Shuford, and D.K. Das-Gupta, "Ferroelectric ceramic/polymer composites and their applications," *Ferroelectrics*, 187, pp. 75-86, 1996.

20 Agarwal, R.B. and L.W. Teufel, "Epon828 epoxy: a new photoelastic-model material," *Experimental Mechanics*, 23 (1), pp. 30-35, 1983.

21 Vleeshouwers, S., A.M. Jamieson, and R. Simha, "Effect of physical aging on tensile stress relaxation and tensile creep of cured Epon828/epoxy adhesives in the linear viscoelastic region," *Polymer Engineering and Science*, 29 (10), pp. 662-670, 1989.

22 Engelberg, P.I. and G.C. Tesoro, "Mechanical and thermal properties of epoxy resins with reversible crosslinks," *Polymer Engineering and Science*, 30 (5), pp. 303-307, 1990.

23 Yagi, T., M. Tatemoto, and J. Sako, "Transition behavior and dielectric properties in trifluorethylene and vinylidene fluoride copolymers," *Polymer Journal*, 12 (4), pp. 209-223, 1980.

24 Koizumi, N., N. Haikawa, and H. Habuka, "Dielectric behavior and ferroelectric transition of copolymers of vinylidene fluoride and trifluoroethylene," *Ferroelectrics*, 57, pp. 99-119, 1984.

25 Tashiro, K., H. Tadokoro, and M. Kobayashi, "Structure and piezoelectricity of poly(vinylidene fluoride)," *Ferroelectrics*, 32, pp. 167-175, 1981.

26 Tasaka, S. and S. Miyata, "The origin of piezoelectricity in poly(vinylidene fluoride)," *Ferroelectrics*, 32, pp. 17-23, 1981.

27 Higashihata, Y., J. Sako, and T. Yagi, "Piezoelectricity of vinylidene fluoride-trifluoroethylene copolymers," *Ferroelectrics*, 32 , pp. 85-92, 1981.

28 Hashin, Z., "Complex moduli of viscoelastic composites -I. General theory and application to particulate composites," *Int. J. Solids Structures*, 6, pp. 539-552, 1970.

29 Hashin, Z., "The elastic moduli of Heterogeneous Materials," *J. Appl. Mech.*, 29, pp. 143-150, 1962.

30 Personal communication, Shell Chemical Company.

31 Nalwa, H.S., *Ferroelectric Polymers*, p. 210, Macel Dekker, Inc., New York, 1995.

Electroassembly of Smart Polymer Structures
(Role of Polyelectrolytes)

Gordon G. Wallace

Intelligent Polymer Research Laboratories, Department of Chemistry,
University of Wollongong, Northfields Avenue, Wollongong, NSW 2522

Samuel B. Adeloju, Shannon J. Shaw
Centre for Electrochemical Research and Analytical Technology
Chemistry Department, University of Western Sydney, Nepean
PO Box 10, Kingswood, NSW 2747

Polymers are ubiquitous in nature, owing to their use as both structural and active components in dynamic, living systems. From a synthetic point of view man has utilised the excellent structural properties of polymers (light weight/high strength) for some decades now. However, the integration of active functional polymers into engineered systems and structures is a more recent endeavour with numerous challenges still to be overcome.

Conducting electroactive polymers such as polypyrroles, polythiophenes and polyanilines are a fascinating group of functional polymers. They are electronic conductors and in addition they respond to chemical or electrical stimuli in a number of ways (Schematic 1). They are truly *electrofunctional* polymers.

This unique combination of properties has led to the use of conducting polymers for electronic components (1, 2), chemical sensors and biosensors (3, 4), membranes for solution (5, 6) or gas (7, 8) separations, electromechanical actuators (9, 10), electro-optical devices (11, 12), biomaterials capable of controlled release of drugs or stimulation of biological processes (13, 14), and for corrosion protection (15).

Schematic 1: The unique attributes of Conducting Electroactive Polymers
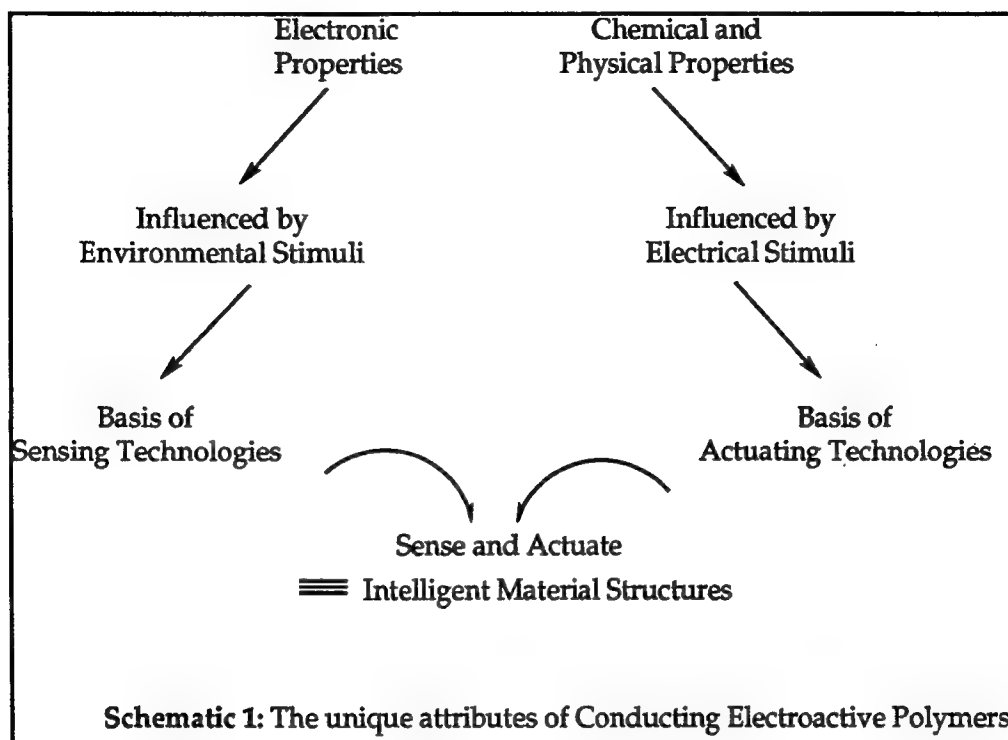
Each of these applications requires the ability to form, process and fabricate the conducting polymer in a way that enables a range of chemical compositions to be produced. For example, when formed polypyrroles have the following general formula:
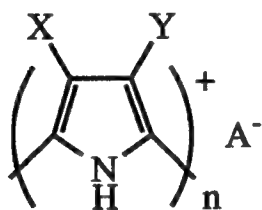
The composition and hence the chemical, physical, mechanical and electrofunctional properties of the polymer can be manipulated by control of X, Y or A⁻. Chemical derivatisation to attach X or Y is a time consuming and expensive option that often deteriorates the mechanical or electrical properties of the polymer. Variation of A⁻ during **electrosynthesis** according to:
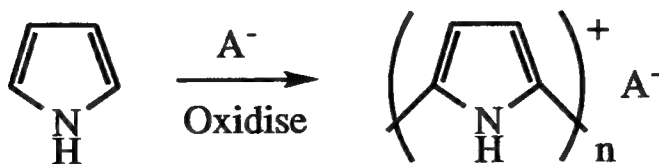
However is a more convenient and favoured option (16). Electrosynthesis enables a wide range of counterions to be incorporated from the supporting electrolyte employed. In addition, the energy injected into the system can be controlled in-situ, enabling accurate and dynamic control of the polymerisation process. These attributes of electrosynthesis are particularly important for processing of bioactive materials where "delicate" entities such as enzymes (17), other proteins (18) or even whole living cells (19) need to be incorporated.

Another requirement is to produce the conducting polymers in a number of shapes or forms that enables micro devices (eg. for sensors) or larger structures (eg. coatings for membranes or corrosion protection) to be produced.

Recent advances in the electroassembly of conducting polymers as well as structures or devices containing them, addresses each of these issues. This manuscript uses examples from our own laboratories to illustrate the usefulness of electroprocessing of conducting polymers.

EXPERIMENTAL

PPy-Urease Film Formation

A platinum working electrode was employed for deposition of the polypyrrole film. The polypyrrole-urease film was formed with 0.5 M pyrrole and 4000 mg/L urease. A three electrode voltammetric cell was used for all electropolymerisation procedures. Pt and Ag/AgCl were the auxiliary and reference electrodes respectively. A current density of 0.5 mA/cm^2 was applied between the working and auxiliary electrodes for a period of 3 minutes to promote polypyrrole formation. Samples for amino acid analysis were electropolymerised for 60 minutes onto a platinum sheet electrode (surface area 2 cm^2).

Instrumentation

A potentiostat/galvanostat designed and built at the University of Western Sydney (Nepean) was employed for the electropolymerisation. The cyclic voltammograms were performed on a BAS 100B analyser from Bioanalytical Systems Inc which was computer controlled and attached to a colour plotter. A Waters Picotag amino acid analyser was utilised for the determination of amino acids in the conductive polymer.

Chemicals and Standard Solutions

The pyrrole was distilled under water vacuum prior to use and was stored covered with aluminium foil in the refrigerator to prevent UV degradation. The KCl, NaH$_2$PO$_4$.2H$_2$O, Na$_2$HPO$_4$ and urea were of AR grade purity.

Procedure

After electropolymerisation the polymer was rinsed several times with milli-Q water to remove any weakly bound urease molecules. The experimental parameters used for the cyclic voltammetry were as follows: deoxygenation period, 300 s; number of cycles, 3; scan rate varied; initial potential, 600 mV and final potential, -900 mV.

The polymer film used for the amino acid analysis was grown on a platinum sheet. The film was removed from the substrate by heating to 110°C and it was peeled away from the platinum surface, and finally weighed on a microbalance. The polymer was then placed into hydrolysis tubes and frozen at -3°C until analysed. The amino acid detection was based upon the Waters Picotag standard procedure.

RESULTS AND DISCUSSION

Variable Polymer Composition

Conducting polymers can be coated on to other conductors by direct electroplating using a conventional electrochemical cell. The composition may be varied by changes in A^-. However in some cases this may compromise the electronic or mechanical properties of the polymer to an unacceptable extent. In recent work we have shown how even subtle changes in the molecular structure of some sulfonated aromatics (as A^-) can influence the mechanical and electrical properties of the resultant polymer (20). It is also important to ensure that the functional properties of A^- are not compromised by the incorporation process.

Consequently the molecular structure of A^- is important and ideally the anchoring site $\ominus$ should be separated from, yet in close proximity to the (bio) chemically active site (Schematic 2a). For example, in designing a polymer for metal complexation (21) or protein interactions (22) incorporation of a range of sulfonated dyes has proven particularly useful. Another successful approach involves the incorporation of multifunctional macromolecular polyelectrolytes (Schematic 2b). Again the functionality to be introduced can be separated from the anchoring sites to introduce the chemical properties while maintaining the physical and electrical properties required.

Schematic 2a

Schematic 2b

⊖ Anchoring sites
● Active sites
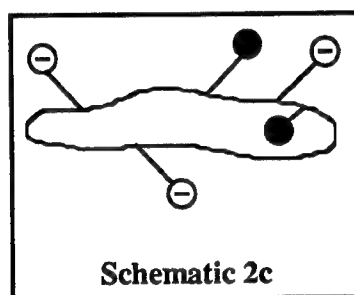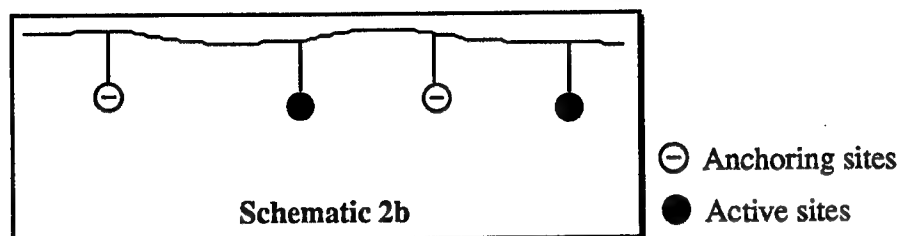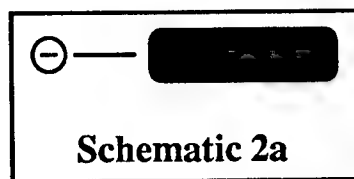
Schematic 2c

Direct incorporation of biomacromolecular species is also an exciting alternative. Enzymes, antibodies or living cells in themselves could be considered polyelectrolytes (Schematic 2c) capable of introducing biochemical properties to the resultant CP structure!! Hence the incorporation of such entities can be carried out without loss of bioactivity. Some work we have carried out in this area however serves to highlight the importance of optimising the parameters encountered during the electropolymerisation process and this is discussed below.

Phosphate Buffer as the Electrolyte for Electropolymerisation

Most incorporation experiments of enzyme into a polymer are performed in phosphate or tris buffers. These buffers maintain a constant pH which is critical for maximum enzymatic activity. The addition of phosphate buffer increased the initial polymerisation potential from 500 mV to 2000 mV over 50 seconds when galvanostatic growth was employed. The potential for the polypyrrole-phosphate system continued to increase slowly after this time. After 50 seconds, the potential for the polypyrrole-phosphate-urease reaction began to decrease. The reduction of potential occurred because there was an increase in conductivity due to the formation of polypyrrole. The chronopotentiogram obtained in a phosphate buffer showed that no polymerisation occurred during the reaction, as the potential continued to increase as a function of time, and it was also visually observed that no polymer was deposited.

The Effect of Chloride Ions in the Polymerisation Solution

The voltammograms for polypyrrole-urease films formed with urease and varying concentrations of potassium chloride were recorded. An increase in the Cl^- ion concentration with a constant urease concentration of 4000 mg/L caused a reduction in the polymerisation potential, and this corresponded to an increase in the amount of polymer deposited on the substrate.

The chloride concentration in the polymerisation electrolyte had a significant effect on the cyclic voltammetric behaviour of the electroactive polymers formed, as illustrated in Figure 1 (**Sammy good copy**). At the lower chloride concentrations (0.01-0.001 M) the cyclic voltammogram resembled that of a polypyrrole-urease film. At higher chloride concentration (0.1 M) the voltammogram was identical to that of a polypyrrole-chloride film. Evidently, the cyclic voltammogram was dominated by the more conductive and mobile counterion. The enzyme has only a small negative charge due to the carboxyl group on the amino acids, and is much more bulky than Cl^-. Therefore, the enzyme is less likely to be incorporated into the polypyrrole film than the chloride ion.

Table 1 shows the concentration of amino acids found in the polymer film as a function of the concentration of KCl. The results show generally a reduction in the concentration of urease in the films when KCl was added to the electropolymerisation solution.

Table 1

Amino acid composition of polypyrrole-urease films produced with varying concentrations of potassium chloride and 4000 mg/L of urease.

Polypyrrole Film	[Total Amino Acid] (mg/g Polymer)
0.1 M KCl & Urease	6.2 ± 1.5
0.01 M KCl & Urease	1.8 ± 0.4
0.001 M KCl & Urease	2.9 ± 0.5
Urease in water	20.1 ± 2.4

The bioactivity of the incorporated enzyme was deduced from results obtained using the conducting polymer as a potentiometric biosensor (17). The effect of chloride ion concentration on the magnitude of the response of the polypyrrole urease potentiometric biosensor was investigated. The greatest potential change was obtained when the polypyrrole-urease film was grown from urease dissolved in water and

pyrrole. The polypyrrole-urease film grown in phosphate buffer, 1 mM at pH 7, somewhat inhibited the urea response. This may be due to the phosphate ions competing for the counterion positions or by the inhibition of the enzymatic reaction.

The above results indicate that the incorporation of biomacromolecular "polyelectrolytes" is possible and that the species can be anchored while bioactivity is retained. The addition of other small molecules to the electropolymerisation solution enhances the electrochemical properties of the resultant polymer but compromises the bioactivity.

From Microstructures to Macrostructures

Recent advances in electropolymerisation protocols allows either micron sized devices or macrostructures to be coated. Micron sized devices can be coated directly if the substrate to be coated is conductive (23). For example, silicon coated chips produced by photolithographic techniques can be used to provide the conducting pattern. Interestingly deposition on small structures is not efficient due to the enhanced transport from the electrode surface (24). This is particularly so when larger molecules are to be incorporated (21). For example, attempts to directly deposit antibodies or enzymes have not been successful in work carried out in our laboratories. Recently, however, we have found that deposition of larger molecules can be enhanced by precoating the micro structure with an insoluble polyelectrolyte such as Nafion (21).

To coat larger structures (eg. high surface area membranes) directly by using electrochemical techniques may not be appropriate. The electrochemical production of conducting polymers in a form that is subsequently processable (eg. can be used to coat other larger scale conducting or non conducting materials) has many attractions. Recently hydrodynamic controlled electrochemical systems have been designed, developed and utilised for making colloidal "soluble materials" albeit colloidal dispersions (25).

The role of macromolecular polyelectrolytes is again very important in this area since they function as stabilisers and/or dopants. We have recently shown that proteins can be incorporated into "soluble" dispersions using this approach and in fact act as dopants (26).

CONCLUSIONS

Electroassembly can be used to produce conducting polymers with varying compositions. All elements of the electrochemical cell are important in determining the chemical, physical and electrical properties of the resultant materials. Of particular interest recently has been the incorporation of macromolecular polyelectrolytes including biospecies such as enzymes. Recent advances have enabled the electroprocessing of both micro and macro structures that utilise conducting electroactive polymers.

REFERENCES

1. C.H. McCoy and M.S. Wrighton, "Potential - Dependent Conductivity of Conducting Polymers Yields Opportunities for Molecule Based Devices: A Microelectrochemical push-pull Amplifier Based on Two Different Conducting Polymer Transistors". Chem. Mater. 1993, 5, 914-916.

2. M. Satoh, H. Ishikawa, K. Amano, E. Hasegawa and K. Yoshino. "Characterisation of a Tantulum Capacitor fabricated with a conducting polypyrrole as a counter electrode". Synth. Met. 1995, 71, 2259-2260.

3. P.R. Teasdale and G.G. Wallace. "Molecular Recognition on Conducting Polymers: Basis of an Electrochemical Sensing Technology". Analyst. 1993, 118, 329-334.

4. S.B. Adeloju and G.G. Wallace. "Conducting Polymers and the Bioanalytical Sciences". Analyst. 1996, 121, 699-703.

5. H. Zhao, W.E. Price, C.O. Too, G.G. Wallace and D. Zhou. "Parameters Influencing transport across conducting electroactive polymer membranes". J. Memb. Sci. 1996, 119, 199-212.

6. H. Zhao, D. Zhou, W.E. Price and G.G. Wallace. "Electrochemically controlled transport using a dual conducting polymer membrane system". J. Memb. Sci. 1995, 24, 157-164.

7. S. Kuwabata and C.R. Martin. "Investigation of the Gas Transport properties of polyaniline". J. Memb. Sci. 1994, 91, 1-12.

8. K. Kamada, J. Kamo, A. Motonaga, T. Iwasaki and H. Hosokawa. "Gas Permeation properties of conducting polymer/porous media composite membranes I". Polymer Journal. 1994, 26, 141-149.

9. P. Chiarelli, A. Della Santa, D. DeRossi and A. Mazzadi. "Actuation Properties of Electrochemically Driven Polypyrrole Free Standing Films". J. Int. Mat. Syst. Struct. 1995, 6, 32-37.

10. M.R. Gandhi, P. Murray, G.M. Spinks and G.G. Wallace. "Mechanism of electromechanical actuation in polypyrrole". Synthetic Metals. 1995, 73, 247-256.

11. K. Hyodo. "Electrochromism of Conducting Polymers". Electrochim Acta. 1994, 39, 265-272.

12. G.A. Sotzing and J.R. Reynolds. "Electrochromic Conducting Polymers via Electrochemical Polymerisation of Bis (2-(3, 4 - ethylenedioxy)thieny) Monomers". Chem. Mater. 1996, 8, 882.

13. R.L. Williams and P.J. Doherty. "A preliminary assessment of poly(pyrrole) in nerve guide studies". J. Mat. Science: Materials in Medichem. 1994, 5, 429-433.

14. A.J. Hodgson et al. "Reactive Supramolecular Assemblies of Muco polysaccharide polypyrrole and protein as controllable biocomposites for a new generation of Intelligent Biomaterials". Supramol. Sci. 1994, 1, 77-83.

15. N. Ahamad and A.G. MacDiarmid. "Inhibition of corrosion of steels with the exploitation of conducting polymers". Synth. Met. 1996, 78, 103-110.

16. G.G. Wallace. "Dynamic Conduct". Chem In Britain. 1993, Nov., 967-970.

17.   S.B. Adeloju, S.J. Shaw and G.G. Wallace. "Polypyrrole based Potentiometric Biosensor for Urea. Part I: Incorporation of Urease". Anal. Chim. Acta. 1993, 281, 611-620.

18.   A.J. Hodgson, M.J. Spencer and G.G. Wallace. "Incorporation of proteins into Conducting Electroactive Polymers". Reactive Polym. 1992, 18, 77-85.

19.   A.J. Hodgson et al. "Integration of biocomponents with synthetic structures - use of conducting polymer polyelectrolyte composites". Smart Structures and Materials. SPIE. 1996, 2716, 164-176.

20.   H. Zhao, W.E. Price and G.G. Wallace. "Effect of the counterion employed during synthesis on the properties of polypyrrole membranes". J. Memb. Sci. 1994, 87, 47-56.

21.   J.N. Barisci, P. Murray, C. Small and G.G. Wallace. "Conducting polymer microsensors for determination of aluminium". Electroanal. (In Press).

22.   W. Lu and G.G. Wallace. "Conducting polymer sensors for the amperometric detection of proteins in a flow system - use of sulfonated dye counterions to induce selectivity". Electroanal. (In Press).

23.   R. John and G.G. Wallace. "Microelectrode and Microarray Conducting Polymer Based Sensing Systems". Electroanal. (In Press).

24.   R. John and G.G. Wallace. "The use of microelectrodes to probe the electropolymerisation mechanism of heterocyclic conducting polymers". J. Electroanal. Chem. 1991, 306, 157.

25.   H. Eisazadeh, K.J. Gilmore, A.J. Hodgson, G. Spinks and G.G. Wallace. "Electrochemical production of conducting polymer colloids". Colloids and Surfaces. 1995, 103, 281-288.

26.   J.N. Barisci, A.J. Hodgson, L. Liu, G.G. Wallace and G. Harper. "Electrochemical Processing of Conducting polymer colloids". Colloids and Surfaces. (To be Submitted).

Some Experimental Results
On The Dynamic Performance of PAN Muscles

Karim Salehpoor, Mohsen Shahinpoor and Mehran Mojarrad
Artificial Muscles Research Institute
School of Engineering, University of New Mexico
Albuquerque, NM 87131

ABSTRACT

The objective of these characterization tests was to find the optimum conditions that maximize the length variation of the chemically activated polyacrylonitrile (PAN) muscles. There are two steps of annealing and chemical treatment in the developement of the PAN muscles. The effects of the annealing temperature, the duration of annealing, and the duration of the boiling in the NaOH solution on the variation of the length of PAN muscle were studied. The effect of the pH of the saturating solution on the expansion-contraction behavior of the PAN muscle was further studied. The expansion-contraction behavior of the PAN muscle when saturated with HNO_3, H_2SO_4, and HCl was also studied.

Keywords : Polyacrylonitrile (PAN) fiber, pH activated muscle, artificial muscle

2-INTRODUCTION

Ionic polymeric gels are three-dimensional networks of cross-linked macromolecular polyelectrolytes that swell or shrink in aqueous solutions on addition of alkali or acids, respectively. Katchalsky [1], and Kuhn [2] originally reported on the possibility that certain copolymers can be chemically contracted or swollen like a synthetic muscle (pH muscle) by changing the pH of the solution containing them. As originally reported by Kuhn, Horgitay, Katchalsky, and Eisenberg [3], a three-dimensional network, consisting of polyacrylic acid, can be obtained by heating a foil of polyacrylic acid containing a polyvalent alcohol such as glycerol or polyvinyl alcohol. The resulting three-dimensional networks are insoluble in water but swell enormously in water on addition of alkali and contract enormously on addition of acids. Chemically stimulated pseudo-muscular actuation has also been discussed recently by Li and Tanaka [4], De Rossi, Chiarelli, Buzzigoli, Domenici, and Lazzeri [5], Caldwell and Taylor [6], De Rossi, Kajiwara, Osada, and Yamauchi [7], Segalman, Witkowski, Adolf, and Shahinpoor [8], [9], and Harland and Prud'homme [10]. Shahinpoor and Mojarrad [11] used PAN muscles in a circulatory system of acid and base to activate a musculoskeletal structure. The possibility of electrically-induced contraction and expansion of polyacrylonitrile (PAN) muscles has been explained by Salehpoor, Shahinpoor and Mojarrad [12].

3-EXPERIMENTAL

PAN fibers were cut at a length of 6 inches. They were heated for some time and at some temperature. We refer to these as the annealing time and annealing temperature, respectively. The fiber length changed after heating. This new fiber length, which is referred to as the annealed length, was measured. A bundle was made of 10 of the annealed fibers. The ends of the fibers were tied together such that the bundle length, the end-to-end distance was 3 inches. The bundle was then left in a boiling sodium hydroxide solution (one normal) for some time. The time is referred to as the boiling time hereafter.

At the end of the boiling time the muscle length, the end-to-end distance was measured. At this step the muscle could contract and expand if saturated with acid and base, respectively. Two normal solutions of NaOH and HCl were used to test the muscle for expansion and contraction. The muscle saturation changed from acid to base or distilled water repeatedly and irregularly. At each saturation the end-to-end distance was measured. The change in muscle length was then calculated considering the muscle lengths at the current and the previous saturation. The results were consistent. That is, for example, the reduction in muscle length remained the same whenever the muscle saturation changed from base to acid. Throughout the discussion of the results, by variation in muscle length it is meant the increase in the muscle length when muscle saturation changed from acid to base. The results generally indicated muscle contraction when saturated with acid and muscle expansion when saturated with base. However, there were some cases in which muscle expanded when saturated

with acid and contracted when saturated with base. When a muscle that had already been saturated with base, was saturated with distilled water it exhibited more elongation. When the muscle was then saturated with base again, it contracted. This happened repeatedly and the lengths of the muscle at saturation with base and distilled water were recovered each time. In another case, when saturation changed between distilled water and acid, the muscle expanded when saturated with acid and contracted when saturated with distilled water. this observation was repeatable and the magnitude of the expansion when the muscle was saturated with acid was 0.25 inches. In this case, the muscle lengths when saturated with acid and distilled water were 2 and 1.75 inches, respectively.

The effects of the annealing time, annealing temperature, boiling time, and the pH of the saturating solution on the variation in muscle length were studied. The effects of different acids at the same pH on the contraction-expansion behavior of the muscle were also tested.

4-RESULTS

Annealing temperatures of 210, 220, 230, 240, and 250 °C were tested. At each temperature, annealing time of 1, 1.5, 2, 2.5, and 5.5 hours were tested. The variation of the annealed length is shown in Figure 1.
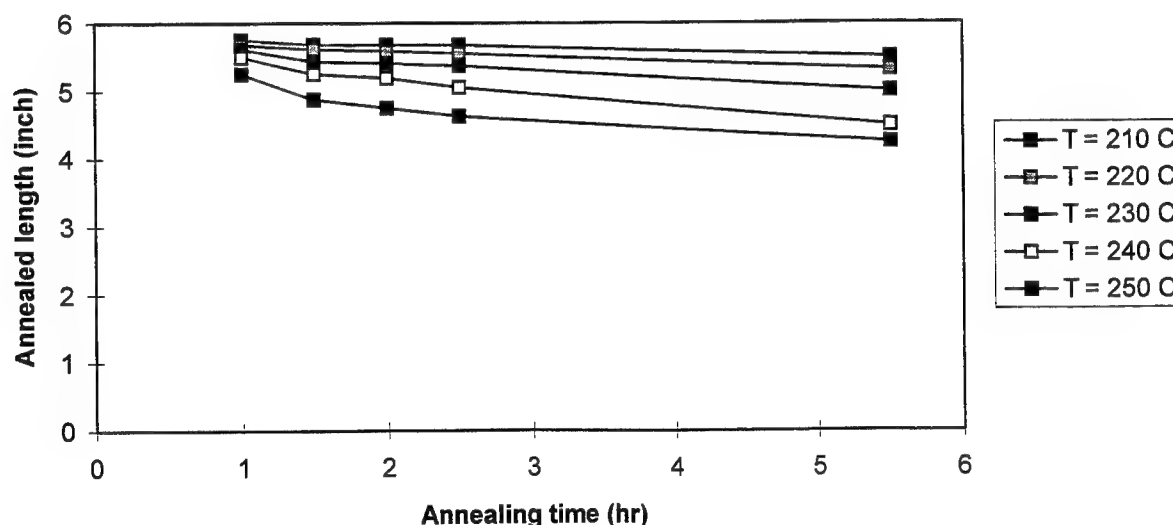
Figure 1- Effect of annealing time on annealed length.

In general, the fibers shrank as a result of heating. At all temperatures the annealed length decreased by increasing the annealing time. The decrease in the annealed length was more severe at upper limits of the annealing temperature and annealing time. Note that the initial fiber length was 6 inches.

The variation in the muscle length at different annealing temperature and annealing time is shown in the Figure 2. As it can be seen, the variation in the muscle length at all temperatures depends on the annealing time. At a temperature of 210 °C, no variation in length was observed when the annealing time was two hours or shorter. The same observation happened for the annealing temperature of 220 °C when the annealing time was one and half hours or shorter. At annealing temperatures of 230 °C and higher the variation in the muscle length first increased by increasing the annealing time. For annealing time of more than two hours, the variation in length started to decrease. As it can be seen, the optimum annealing temperature and annealing time are 240 °C and 2 hours, respectively. The optimum variation in the muscle length was about 1.55 inches which was equivalent to about %100 change in the muscle length. All the muscles which have been prepared at these conditions thereafter, whatever the number of fibers in the muscle and the muscle length might be, have exhibited the same variation in the length, i.e., a muscle that is 12 inches long in the expanded state becomes 6 inches long in the contracted state and vice versa.

After the fibers that had already been heated, were boiled in the NaOH solution, their lengths changed. This change in the length was governed by the annealing time. As shown in Figure 3, the muscles that were annealed at 210 and 220 °C, shrank as a result of boiling in the NaOH solution whatever the annealing time might be.
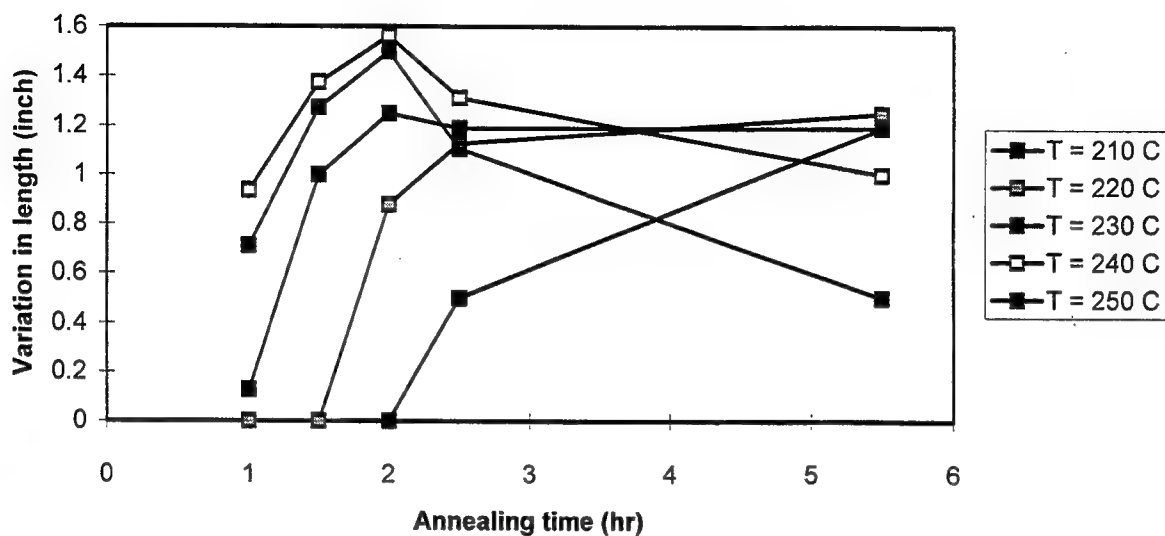
Figure 2- Effect of annealing time on variation in length.

At annealing temperatures of 230, 240, and 250 °C the muscle might either contract or expand as a result of boiling in the NaOH solution depending on the annealing time. Note that the initial muscle length before boiling, i.e., the end-to-end distance, was 3 inches.
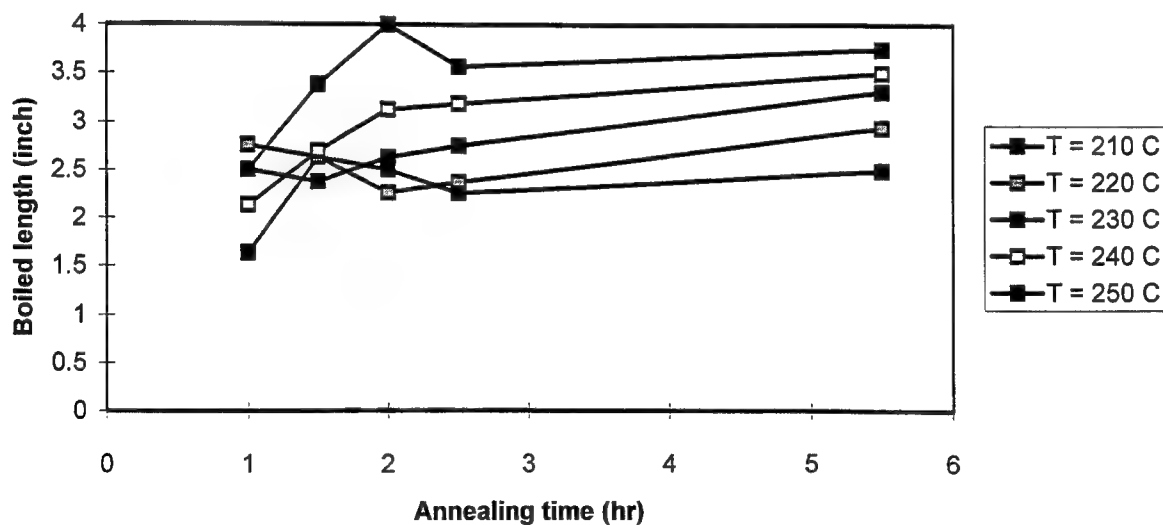
Figure 3- Effect of annealing time on boiled length.

The effect of the boiling time on the muscle length variation is shown in Figure 4. As it can be seen, the variation in length, almost, continuously increases as the boiling time is increased. However, since no change in the trend was observed for the whole interval, more tests are necessary to see the effect of boiling time of longer than 90 minutes.
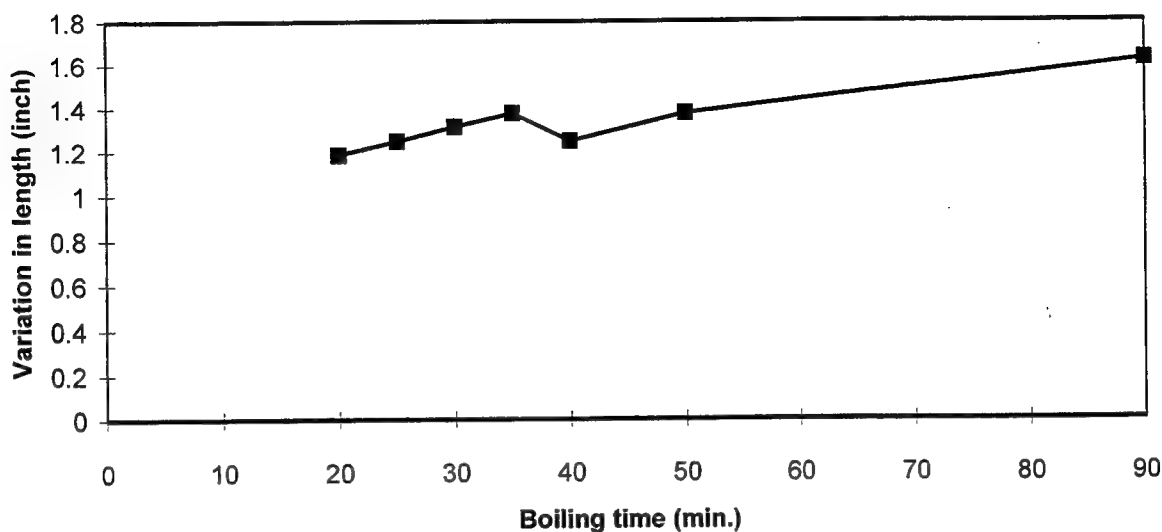
Figure 4- Effect of boiling time on variation in length.

In testing the effect of the pH of the saturating solution, the pH of the saturating solution first was increased from 0 to 14 and then reduced from 14 to 0. At each pH, the muscle was immersed in the solution for 1 minute. The corresponding change in the muscle length is shown in Figure 5.
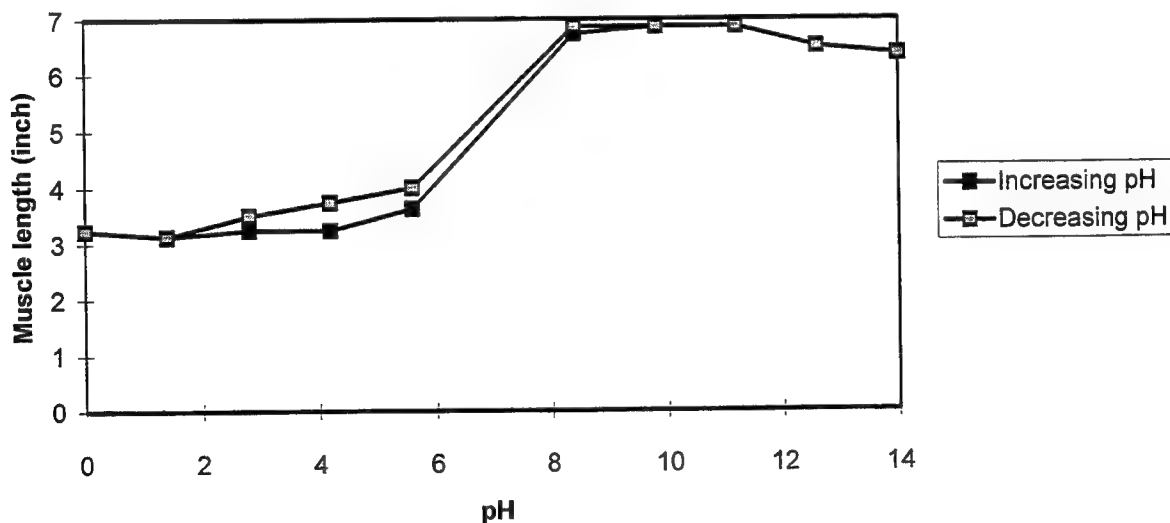
Figure 5- Effect of the pH of the saturating solution on the length of the PAN muscle.

As it can be seen, in both cases of increasing or decreasing the pH, when the muscle was in the same environment (i.e., in an acid or a base), there was not a significant change in the muscle length. However, in changing from acidic environment to

basic and vise versa a significant change in the muscle length appeared. The envelope that is made at the pH interval of 2-10 is believed to be eliminated if the muscle is left in the solution for longer than 1 minute time. In that case, the variation in the muscle length with increasing or decreasing the pH will almost overlap. In other words, no hysteresis in the PAN fiber behavior was observed.

Figure 5 displays one important information, that is, when the nature or material properties of the saturating solution changes, i.e., the saturating solution changes from an acid to a base, a significant change occurs in the PAN fiber length. On the other hand, when the material properties are kept constant while the pH is changed, i.e., in the ranges of pH = 0~6 and 8~14, the change in the fiber length is insignificant. As mentioned in an earlier paper [12] several factors may contribute to the expansion-contraction behavior of the PAN fibers. To verify the effect of the material properties, three different acids with the same pH were used, one at a time, to saturate the muscle. HNO_3, HCl, and H_2SO_4 all at a pH of 0 (1 normal solution) were used. No change in the muscle length was observed when saturation changed from one acid to another. By the combination of these results with the information obtained from Figure 5, it turns out that the relevant material property of the saturating solution that dominates the contraction-expansion behavior of the PAN fiber is the same in acids but different in bases and acids. This material property is most likely due to the presence of H^+ ions in acids and the presence of OH^- ions in bases. As a result of this, the electrostatic (Coulomb) forces seem to dominate the contraction-expansion behavior of the PAN fibers.

5-CONCLUSIONS

The result of this work led to the manufacturing of the artificial PAN muscles capable of showing a deformation of %100. While the PAN fiber muscles are well known as pH activated muscles, it turns out that the deriving force dominating the contraction-expansion behavior of the PAN fibers is the intermolecular Coulomb forces. Hysteresis in the PAN fiber contraction-expansion behavior was not observed.

6-REFERENCES

1-Katchalsky, Experientia, vol. 5, pp. 319-320, (1949).
2-Kuhn W., Experientia, vol. 5, pp. 318-319, (1949).
3-Kuhn W., Horgitay B., Katchalsky A., and Eisenberg H., Nature, vol. 165, pp. 514-516, (1950).
4-Li Y., and Tanaka T., J. Chem. Phys., vol. 92, pp. 1365-1371, (1990).
5-De Rossi D.E., Chiarelli P., Buzzigoli G., Domenici, and Lazzeri L., Trans. Am. Soc. Artif. Intern. Organs, XXXII, pp. 157-162, (1986).
6-Caldwell D. G. and Taylor P.M., Int. J. Engr. Sci., vol. 6, pp. 797-808, (1990).
7-De Rossi D. E., Kajiwara K., Osada Y., and Yamauchi A., Proc. Int. Symp. Polymer Gels, Tsukuba, Japan, 18-21 September, Plenum Press, New York, (1991).
8-Segalman D., Witkowski W., Adolf D., and Shahinpoor M., Proc. ADPA/AIAA/ASME/SPIE Conf. on Active Materials and Adaptive Structures, edited by Knowles G. J., Nov. 1991, Alexandria, Va., IAP Press, pp. 335-345, (1992).
9-Segalman D., Witkowski W., Adolf D., and Shahinpoor M., Smart Materials and Structures Int. J., vol. 1, Nov. 1, pp. 95-100, (1992).
10-Harland R. S. and Prud'homme R. K., Proc. Am. Chem. Soc. Symp. Series, Nov. 11-16, 1992, Chicago, Ill., Am. Chem. Soc. Publication, (1992).
11-Shahinpoor M. and Mojarrad M., Active Musculoskeletal Structures Equipped with a Circulatory System and a Network of Ionic Polymeric Gel Muscles, Proc. of the 1994 Int. Conf. on Intelligent Materials, pp. 1079-1085, (1994).
12-Karim Salehpoor, Mohsen Shahinpoor and Mehran Mojarrad, Electrically controllable artificial PAN muscles. SPIE, vol. 2716, pp. 116-124 (1996).

Manufacturing and characterization of magnetorheological fluids

Osama Ashour, Dawn Kinder, and Victor Giurgiutiu

Center for Intelligent Material Systems and Structures
Virginia Polytechnic Institute and State University
Blacksburg, Virginia 24061-0261

Craig Rogers

College of Engineering, Dean
University of South Carolina
Columbia , South Carolina 29208

ABSTRACT

Magnetorheological (MR) fluids are stable suspensions of magnetic particles in a carrying fluid exhibiting controllable rheological behavior in the presence of a magnetic field. Magnetorheological effect represents a reversible increase, due to an external magnetic field, of effective viscosity. MR fluids and devices have the potential to revolutionize the design of hydraulic systems, actuators, valves, active shock and vibration dampers, and other components used in mechanical systems. MR fluids that are currently available suffer from high initial viscosity values and low stability. Hence, there is a compelling need to optimize the MR fluid manufacturing process to produce optimum MR fluid characteristics. The present study proposes to manufacture an optimum composition of a MR fluid in terms of its quality and properties. A high-speed bead mill blending machine is used to manufacture the fluid. Characterization studies are conducted to evaluate the produced fluid.

Keywords: magnetorheological fluids, optimum composition, bead mill machine, characterization

2. INTRODUCTION

Magnetorheological (MR) fluids are stable suspensions of very fine ferromagnetic particles in a non-magnetic carrying medium exhibiting controllable rheological behavior in the presence of an applied magnetic field. In moderate fields, the apparent viscosity of MR fluids increases by more than two orders of magnitude. Electrorheological (ER) fluids, which are composed of suspended dielectric particles in a non-polar medium, exhibit a similar behavior to MR fluids in the presence of an external electric field. Both MR and ER fluids are part of a new class of controllable fluids that has the potential to revolutionize the design of hydraulic and electromechanical systems.

The first observations of a controllable fluid behavior in the presence of an electric field were reported by Konig[1] and Duff[2]. However, ER fluids were first invented by Winslow[3] when he filed a patent on a ER clutch-type relay. This clutch closed the relay contacts in response to a vacuum tube photocell connected in series with a supply of 120 volts. This ER controllable fluid behavior was, ever since, referred to as the Winslow effect. On the other hand, MR fluids were invented by Rabinow[4] when he devised a magnetic fluid clutch. Since then, there have been hundreds of patents and conducted research on these controllable fluids. However, until the last decade, the development of these fluids was largely ignored. As Winslow himself puts it[5], this might have been "since no great necessity for this invention could be imagined" at that time.

Nowadays, proposed applications of controllable fluids are both numerous and of enormous potential value. Changes in a variety of material properties, such as magnetic, electrical, thermal, acoustic, and other mechanical and physical properties can be observed in MR or ER fluids upon the application of a magnetic or electric field, respectively. However, most of the applications that have been studied in some detail are based on the controllable rheological properties of these fluids (elasticity, plasticity, and viscosity). They include electrically-controlled torque and pressure levels in clutches, brakes, valves, seals, and hydraulic systems. They also include damping devices, as well as systems to control the elastic response of

structural members. Employing controllable fluids in the transport industry; automotive, air and marine, where utilizing controllable fluids could result in large savings in fuel and energy, can be easily understood. At present, vibration control and vibration isolation applications may have the greatest commercial interest.

Both MR and ER fluids exhibit unique controllable rheological characteristics which can be successfully used in all shock and vibration control approaches: passive, semi-active, and active. The most important feature of these fluids is their ability to change from a free-flowing liquid into a solid in milliseconds when exposed to the corresponding field, and to return just as quickly to the liquid state when the field is removed. Unlike their conventional hydraulic or electromechanical counterparts, devices based on these fluids can be controlled directly through electrical input. This offers fast switching speed, miniaturization potential, and continuously varying control. The resultant systems are simpler and have fewer or no moving parts. Hence, they experience less wear, are quieter, and have longer life expectancy. Active shock and vibration control designs based on these controllable fluids have the ability to adjust the system's characteristics in response to rapidly changing external environments. This greatly enhances their vibration control levels and ranges over passive system.

Until recently, most of the research on controllable fluids has been concentrated on ER fluids, since such fluid-based devices were thought to be easier to construct. However, ER fluids require thousands of volts to operate and expensive high-voltage power supplies. Hence, safety and packaging are clear design problems for ER fluids. In contrast, MR fluid devices require current-driven low-voltage power supplies, such as a 12 volt car battery. They can become widely available at relatively low cost. In addition, Pinkos, Shtarkman and Fitzgerald[6] pointed out that electrorheological fluids result in low shear stresses (less than 2 psi when the applied field is 4000 V/mm), while MR fluids generate very high shear stresses (about 45 psi when the applied voltage is 12 V). Also, Carlson and Weiss[7] have proved that yield stress values in excess of 80 kPa are easily obtained in MR fluids, while the best ER fluids have a yield stress around 3 kPa. Magnetorheological fluids, also, have a greater stability and less temperature dependence than electrorheological fluids. Another major drawback of ER fluids is that they cannot tolerate common impurities encountered during manufacturing or use. Hence, expensive quality control is required during manufacturing.

Magnetorheological fluids are distinguishable from colloidal magnetic fluids or ferrofluids. In colloidal ferrofluids, the particles are typically 5 to 10 nanometers in diameter. Upon the application of a magnetic field, a colloidal ferrofluid does not exhibit particles' chain structuring or the development of a resistance to flow. This is due to the effect of the thermal Brownian motion on the ferromagnetic particles which hinders the particles' approach to each other. Hence, no yield stress is developed and a minimal or no increase in rheological properties is observed. Instead, in the presence of a magnetic field, colloidal ferrofluids experience a body force on the entire material that is proportional to the magnetic field strength. This force causes the entire fluid to be attracted to regions of high magnetic field gradient.

In the past few years, there has been an increasing interest in the study of magnetorheological fluids and their various applications. The most notable contributions to this field include the studies of Shulman et al.[8], Kordonsky et al.[9], and Kordonsky[10]. Also, several patents on MR materials and devices have been obtained (Shtarkman[11]; Carlson and Chrzan[12]; Carlson and Weiss[13]; Kordonsky et al.[14,15]). A great deal of understanding of the magnetic, structural, and rheological characteristics of MR fluids, including both microscopic and macroscopic properties, has been recently achieved.

Experimental studies on MR fluids include the work of Lemaire, Bossis, and Grasselli[16] who measured the yield stresses of a MR fluid composition as a function of the external magnetic field. Their results showed a good agreement with the theoretical model of Klingenberg and Zukoski.[17] However, most of such experimental studies have concentrated on understanding the mechanism of structure formation in MR fluids upon the application of an external magnetic field. Liu et al.[18] have studied the static and dynamic properties of chain formation in MR fluids. Their work focused on the initial stage of the structure transition. Time dependence of the structure formation as a function of the field strength was studied by light scattering techniques. More recently, Promislow and Gast[19] studied the MR fluid aggregate shape as a function of field strength, particle size, and magnetic susceptibility. They found that the most favorable aggregate shape at high fields was that of an ellipsoid with spiked ends. However, at low fields, elongated shapes were favored. The influence of particle size on the yield stress of MR fluids has been studied by Lemaire et al.[20] They defined a coupling parameter as the ratio of magnetostatic energy to thermal energy. By relating this parameter to the size of the particles, they found that for small

particles, the yield stress strongly increased with the particle size. For very high values of the coupling parameter (around 10^9) they reported no dependence of the yield stress on the particle size. In their work, they utilized a structural model based on the deformation of simple chains of particles.

Investigators at Lord Corporation[13] have managed to manufacture MR fluids using iron alloy particles. Their research included iron-cobalt alloys and iron-nickel alloys. They found that MR fluids prepared with iron alloy particles exhibited higher yield stresses than those prepared using traditional iron particles, such as carbonyl particles. The drawback, however, is the high cost of such alloys in comparison to carbonyl iron particles.

New MR fluid-based devices were developed by Gorodkin, Kordonskii, and Protasevich[21] who studied the characteristics and dynamics of a MR fluid-based seal. They concluded that employing MR fluids significantly increases the seal efficiency. The critical pressure, at which the sealing ring would be broken, was raised in both static and dynamic cases. A variety of prototype MR fluid dampers have been constructed at Lord Corporation to evaluate the potential of this technology[7]. Linear shock absorbers were constructed to replace the current passive automotive shock absorbers. The damper was operated at various stroke rates, with an overall stroke distance of 20 mm. A current of 2 A was needed to generate the magnetic field, and the force output reached a maximum of 3500 N. Equally interesting, Pinkos, Shtarkman, and Fitzgerald[6] have managed to develop an actively damped passenger car suspension system using MR fluids. They utilized a rotary shock absorber configuration coupled with MR fluid as an adaptive suspension system. The design provides greater flexibility in the styling of exterior and interior envelopes, improves passenger safety and comfort, and provides easily adjusted vehicle suspension control. The damping force of the rotary shock absorber varies as a function of the applied magnetic field. The product has been tested on actual vehicles and proved to be more advantageous than the conventional baseline vehicle.

At present, there is a compelling need to manufacture a competitive composition of MR fluid. The existing MR fluid compositions suffer from one of the following drawbacks, which hinder their full industrial utilization and their wide commercial availability: particle settling during extended periods of time, relatively high initial viscosity, and high manufacturing cost. For example, the two MR fluid compositions manufactured by Lord Corporation; versaflo MR-100 and versaflo MRX-135CD have a 15-20% particle-liquid separation as indicated on the specification sheet. High manufacturing cost of these fluids add another drawback (sale price is $500/liter).

The work presented here deals with the manufacture of a competitive MR fluid composition which does not suffer from the above-mentioned drawbacks and, at the same time, provides very high yield stresses at high magnetic fields. The manufacturing cost of the proposed technology is relatively low.

3. COMPOSITION OF MAGNETORHEOLOGICAL FLUIDS

Magnetorheological fluids consist of three major components: dispersed ferromagnetic particles, a carrier liquid, and a stabilizer.

3.1 Dispersed ferromagnetic particles

Iron and iron-base alloys are the principal magnetosoft (soft ferromagnetic) materials in use today. Control of magnetic properties can be achieved primarily by controlling chemical impurities and crystal orientation. The term "pure iron" generally refers to irons of 99.9% purity. Impurities that have the greatest effects on magnetic properties are the nonmetallic elements carbon, oxygen, and nitrogen which enter the lattice interstitially. In magnetosoft particles, there appear domains of spontaneous magnetization. The domains are aligned primarily along the axis of magnetization. However, when an external magnetic field is absent, the material is not magnetized as a whole, as the direction of the magnetic moments of separate domains is random. The external magnetic field aligns the elementary magnetic moments. Hence, magnetosoft materials are multi-domain particles. These particles exhibit superparamagnetic behavior in that they have a large saturation magnetization but no remanence or coercivity. On the other hand, magnetosolid (solid ferromagnetic) materials have high remanence and coercivity. This is mainly useful in recording materials where the objective is to store information. In practice, magnetosolid materials are made of fine single-domain particles and, thus, have their own ordered direction of magnetic moments.

In this work, we use a mixture of coarse magnetosoft particles and fine magnetosolid particles. The magnetosoft particles are spherical in shape with a diameter size ranging from 1-10 μm. The density of such particles is also high (7-8 g/cm³). A preferred magnetizable particle is carbonyl iron magnetosoft powder grade S-3700, which is known for its high magnetic permeability and produced by International Specialty Products (ISP). Other carbonyl iron powders and magnetite can also be used. Carbonyl iron is manufactured by the decomposition of iron pentacarbonyl $Fe(CO)_5$. This process produces unreduced spherical and very fine particles. The particles are physically soft and compressible. Table 1 below gives physical and chemical properties for grade S-3700 magnetosoft powder carbonyl iron:

TABLE 1: Properties of magnetosoft powder carbonyl iron grade S-3700 produced by ISP

Appearance	Average Diameter (μm)	Apparent Density (g/cm³)	True Density (g/cm³)	% Iron (Min.)	% Carbon (Max.)	% Oxygen (Max.)	% Nitrogen (Max.)
Uniform	1-3	1.5-3.0	7.5-7.8	98	1	0.7	1

Volumetric concentration of the dispersed particles can be as high as 50% of the total fluid volume. In the presence of a magnetic field, the particles become polarized and thereby organized and structured into chains of particles within the fluid. This chain of particles acts to increase the apparent viscosity or flow resistance of the overall material. In the absence of a magnetic field, the particles return to an unorganized state and the apparent viscosity is reduced to original state.

The magnetosolid particles used in this work are made of chromium dioxide. Chromium dioxide (CrO_2) is prepared by thermal decomposition of anhydrous chromium trioxide CrO_3 under pressure. Chromium dioxide was first introduced by Du Pont in the late sixties as a material for magnetic recording surfaces. The particles are easily dispersed and oriented and exhibit the needed high coercivity and remanence. These particles are acicular in shape and have a needle-like structure. This abrasive nature of CrO_2 increases the viscosity of the resulting MR fluid composition under a magnetic field. The particle size ranges from 0.1 to about 1.0 μm, which is about 10 times smaller than the magnetosoft particles. This smaller particle size is needed, so as to allow the chromium dioxide particles be adsorbed on the surfaces of the carbonyl iron particles. By this, a brush-like effect is imparted to the magnetosoft particles. This has shown to give the resulting fluid composition a higher stability and improved rheological behavior under the magnetic field. Chromium dioxide has a single-domain particles. They have their own magnetic moment which keeps them attached to the carbonyl iron particles.

3.2 Carrier Liquid

The second component of a magnetorheological fluid is a carrier liquid which serves as a continuous isolating medium. This can be any medium conventionally employed in a fluid responsive to a magnetic field. Preferably, the carrier liquid should have a viscosity value in the range: 0.01-1.0 Ns/m² at 40 °C. Some of the preferred carrier liquids are: Silicon oil, kerosene, and synthetic oil. The choice of a suitable carrier liquid in preparing a MR fluid is very important, since the stability of the system (as will be explained later) and the overall rheological behavior under the magnetic field depends on this choice. In this work, we use a synthetic ozone-friendly EAL (Environmental Awareness Lubricant) Arctic 15 produced by Mobil. This is chosen for its environmentally-safe properties, non-flammable characteristic, low volatility, good anti-corrosion properties, wide-range temperature stability, and low initial viscosity. It also meets all other standard hydraulic demands. Mobil EAL Arctic Series lubricants are used in refrigeration compressors. Optionally, some additives may be added to the carrying fluid to enhance its overall rheological and mechanical properties. Table 2 below lists physical characteristics of Mobil EAL Arctic 15.

TABLE 2: Physical characteristics of Mobil EAL Arctic 15 carrier liquid

Specific Gravity	Flash Point (°C)	Viscosity at 40 °C (Ns/m²)	Viscosity Index, ASTM D 2270	Color, ASTM D 1500	Water Content (ppm)	Copper Corrosion, ASTM D 130
0.995	235	0.016	117	0.5	<100	1A

3.3 Stabilizer

The third component of a magnetorheological fluid is a stabilizer, which serves to keep the particles suspended in the fluid. Stability of MR fluids is one of the most important properties of the fluid. It determines to a large extent the life time and durability of the fluid. There are three distinct kinds of stability associated with magnetorheological fluids: Agglomerative stability, sedimental stability, and thermal stability. Agglomerative stability refers to the resistance of the particles to the formation of aggregates. Sedimental or settling stability ensures that the particles do not settle down with time. Thermal stability has two aspects: first, the ability of the fluid to function at reduced and elevated temperatures. Secondly, The fluid's resistance to degradation when held at elevated temperatures over long periods of time. Most of the work on stability of MR fluids and magnetic fluids, in general, has been on the first two kinds of stability. Hence, we present here a brief background on the first two kinds of stability.

3.3.1 Agglomerative stability

Agglomeration (clustering of solid particles) occurs under the action of the attractive van der Waals force between particles closely approaching each other. Disperse systems, in which solid particles are suspended in a liquid, are characteristic of a developed specific surface and, accordingly, of large surface energy. Therefore, processes accompanied by decreasing surface energy, such as aggregation of particles, easily occur in such systems. It is even easier to occur in colloidal systems, such as magnetic fluids. This is so, because colloidal particles are in constant Brownian movement, which results from the thermal energy of the particles. During this perpetual movement, the particles experience interactions of various kinds, the magnitudes of which strongly depend on the particles' transient mutual distances. If no stabilizing method is present, the particles will stick together, in which case destabilization (coagulation or flocculation) occurs.

To retain their individuality, and hence stabilize the system, particles must be stabilized through forces of repulsion. The two known forces of repulsion are electrostatic and steric forces. In electrostatically stabilized systems, the particles are electrically charged. Electrostatic repulsion must exceed the van der Waals attraction. At short and large separations, the van der Waals force always dominates the electrostatic repulsion, but at intermediate distances the electrostatic force can dominate, provided that the particles are sufficiently charged and that little screening of these charges occurs by dissolved electrolytes. In addition to the charged particles, electrostatically stabilized systems must have a polar medium in the carrier liquid. As such, this is not the preferred way of stabilizing MR fluids. Also, the electrostatic repulsive forces decrease rather rapidly with increasing distance. A more desirable way of stabilizing MR fluids and magnetic fluids, in general, involves the use of polymers (surfactants) in non-polar media. This is referred to as steric stabilization.

In sterically stabilized systems, each particle is coated with adsorbed surface layers that hinder the particles' approach to each other to distances where van der Waals forces dominate. The thickness of the adsorbed layer is determined by the length of chain in the polymer (surfactant). When two particles containing an adsorbed layer approach each other to a separation distance that is less than twice the adsorbed layer thickness, interference of the chains occurs. This interaction leads to repulsion as a result of three main effects. The first effect arises from mixing of the adsorbed layers, which is unfavorable due to the lower chemical potential of the carrier fluid (solvent) medium in the overlap region. As a result, diffusion of solvent from bulk solution to this overlap region takes place, which leads to particle repulsion. The second repulsive effect results from the loss of configurational entropy of the chains on the approach of a second surface. As a result of such an approach, the volume available for the adsorbed chain becomes restricted, leading to loss of configurational entropy. This effect is usually referred to as the volume-restriction effect. The third repulsive effect arises from the increase in local osmotic pressure in the overlap region which reacts against particle approach. Three conditions must be met if stable dispersions are to be prepared: First, the carrier liquid must be a good solvent for the adsorbed surfactant. Secondly, the surface coverage must be complete and the adsorbed surfactant must be firmly attached to resist displacement under shearing conditions. Thirdly, the depth of the steric barrier must be sufficient to prevent flocculation. A surfactant is, therefore, specially chosen for each carrier liquid.

Surfactants are polymers that comprise a polar head and a non-polar tail. The polar head is preferably anchored to the solid particle surface through a weak chemical bond, although physically adsorbed surfactants are also known. On the other

hand, the tail of the polymer should have no affinity to the solid particle material. Otherwise, it is localized on the particle surface. Surfactants can be anionic, cationic, or non-ionic. Oleic acid $CH (CH_2)_7COOH$ is the most widely used stabilizer of magnetite particles in hydrocarbon bases. It is an unsaturated fatty acid which is maintained in the form of triglyceride in all vegetable and animal fats. The presence of the negative (OH) group in the head of the chain makes oleic acid an anionic surfactant. This allows the formation of a weak ionic bond with the surface of the solid ferromagnetic particles. Another widely used stabilizers include unhydrated inorganic silicone compounds, such as silica gel (SiO_2). which is an amorphous silica powder comprising ultrafine particles. Here, the stabilizer particles are much smaller in size than that of the dispersed particles. This leads to a large surface area (100-300 m^2/g). Each particle is highly non-porous. The ferromagnetic dispersed particles become mechanically held by the surface structure of the silica gel and thus uniformly dispersed in the carrying fluid. However, the main disadvantage of this stabilizer is the formation of a gel-like structure which is unsuitable for hydraulic applications.

For MR fluids, the choice of surfactant depends on the type and concentration of the dispersed particles. .The type of surfactant should also be carefully chosen, such that it complies with the carrying fluid and works together with other used surfactants. Agglomerative stability is maintained by one of two methods: Course-dispersed small-concentration systems (up to 10%) can be stabilized by the use of gel-forming stabilizers, such as silica gel. These stabilizers form a protective colloidal structure in the bulk of the carrier. The strength of this structure should allow reversible thixotropic transformations and not to inhibit the system structurization in the magnetic field. On the other hand, fine-dispersed concentrated (up to 50%) suspensions are stabilized by the introduction of surfactants (ionic or non-ionic), which form a spatial structure from the ferromagnetic particles without forming a gel.

In this work, the high concentration of carbonyl iron (50% by volume) makes the stability of this fluid a major concern. We use two types of surfactants: an anionic surfactant, oleic acid, to maintain agglomerative stability of the fluid and a non-ionic surfactant (polyoxythylene 10 lauryl ether) is also used to create a soft net in the bulk of the carrier liquid.

3.3.2 Sedimental stability

The tendency of the solid particles to settle under gravity causes severe problems. However, sedimentation may be tolerated, to a certain percentage, if the sediments are easily redispersed. Irreversible coagulation of particles can be avoided by steric stabilization, as was discussed in the previous section. Settling of particles is usually measured in the most elementary way; by allowing the fluid to sediment under gravity and following the height of the clear fluid as it develops over time. Sedimentation is a direct consequence of the greater density of the particles relative to that of the carrier liquid. However, when the particle size is sufficiently small, i.e. in the colloid range (<1 μm), the gravitational force is opposed by a diffusional force associated with the thermal Brownian motion. This makes magnetic liquids highly stable. To study the parameters affecting the speed of settling (V), we use the famous Stokes' formulation for a sphere moving slowly under gravitational forces. The result is:

$$V = \frac{2a^2(\rho - \rho_0)g}{9\eta}, \qquad (1)$$

where a is the sphere diameter, ρ is the density of particles, ρ_0 that of the carrier liquid, η is the viscosity of the carrier liquid, and g is the gravitational acceleration. Of course, this formulation is very simplistic in that it ignores the interaction of the particles and, hence, is invalid for highly concentrated systems. A number of correctional formulas exist in the literature for both low and high concentration of solid particles[22]. However, the above formula gives us a qualitative understanding of the parameters affecting the rate of settling (in addition to the concentration of particles). To lower this rate, the particle diameter should be small, the difference in density between the particles and the carrier liquid should be minimized, and the viscosity of the liquid should be increased. In reality, however, many restrictions prevent one or more of these conditions. To obtain a non-colloidal MR fluid, the particle size should be fairly large (>1 μm). Also, the density difference between the particles and the carrier liquid is also high for MR fluids and even if the density difference is minimized at a certain temperature, the densities of liquids can vary significantly at another temperature.

For MR fluids, highly-concentrated surfactants are used. They form organized structures that are referred to as liquid-crystalline phases. Three types of organized systems are frequently found. These are: (a) the hexagonal phase, which is composed of cylindrical units; (b) the viscous isotropic phase, which is composed of spherical units in a cubic arrangement; and (c) the lamellar phase, which is composed of sheets of molecules. Both hexagonal and cubic phases give a highly viscous gel-like structure, which can be used for prevention of claying and settling. Silica gel, which was mentioned as an agglomerative stabilizer, is an example of such stabilizers. In this work, however, we avoid using any gel-forming stabilizers. A non-ionic surfactant (polyoxythylene 10 lauryl ether) is used to create a lamellar phase and, hence, reduce the settling rate.

4. METHOD OF MANUFACTURING

Preparing the MR fluid consists of three steps:
(1) Preparing the dispersed phase.
(2) Fabricating the dispersion medium.
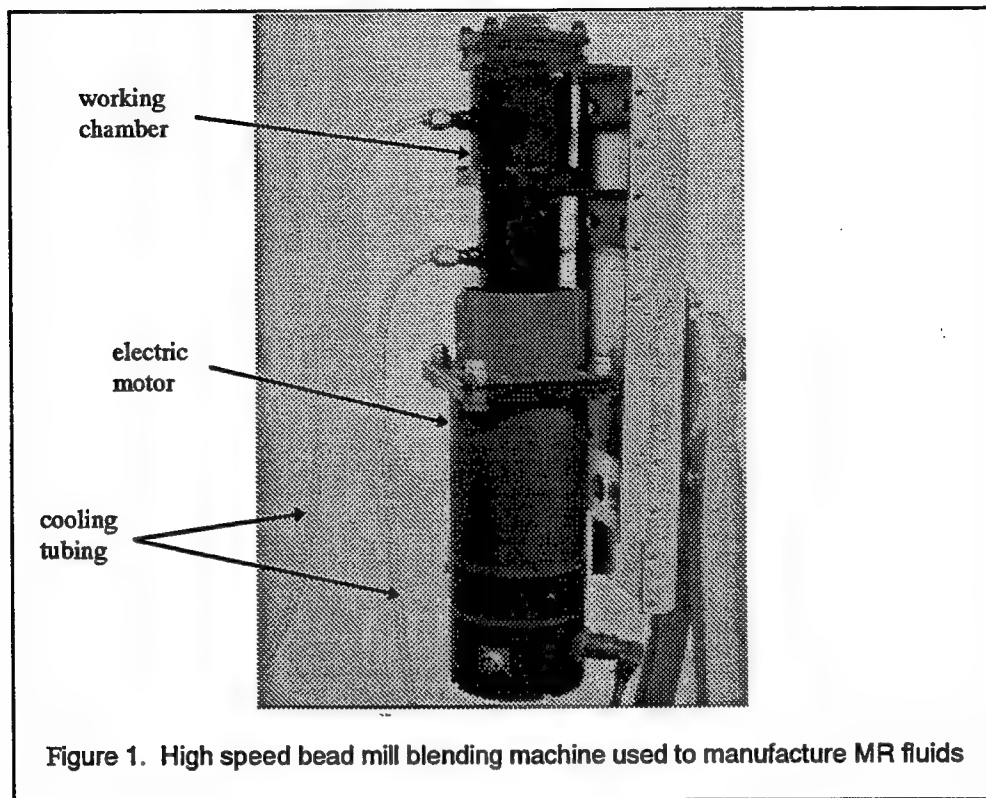(3) Mixing the components in the bead mill machine.

Preparing the dispersed phase involves two operations, purifying the carbonyl iron particles and, then, coating the particles surfaces with oleic acid. For the current study, the used carbonyl iron particles are produced by ISP and have a maximum of 0.2% impurities. Hence, the particles are virtually pure, and the purification operation is not needed. Otherwise, the particles would have to be washed and boiled with water. Impurities would, then, have been removed by skimming off the forming foams and bubbles on the surface of water. Coating the carbonyl iron particles with oleic acid is done by dissolving oleic acid in a good solvent, such as ethyl alcohol or toluene. The prepared solution is then poured on the carbonyl iron particles and mixed together. After some time, the solvent evaporates and leaves the ferromagnetic particles coated with oleic acid. The percentage of oleic acid concentration is a very important parameter which influences the fluid's behavior.

Fabricating the dispersion medium requires dissolving the non-ionic surfactant (polyoxythylene 10 lauryl ether) in the carrier liquid (Mobil oil EAL Arctic 15). Again, the percentage of the non-ionic surfactant is another vital parameter to ensure a highly-stable MR fluid.

There are several known methods to mix the components. Among which are grinding methods, condensation methods, and precipitation methods. The first magnetic fluid was prepared by S. S. Papell in the mid sixties by grinding magnetite in a ball mill in the presence of oleic acid in kerosene. At that time, it took three months of continuous mill operation to produce a stable colloidal system. This method has many advantages: It is very simple; it is sufficient to fill a mill with magnetic fluid components and switch on. It is possible to attain a desired degree of particle dispersion (specified by the milling time), there is no solvent loss, and various ferromagnetic materials can be used with various carrier liquids. The main disadvantages of this method, however, is the long grinding time and the resulting small yield of final product. The long grinding time can be dramatically reduced using a high speed bead mill. In this work, we use a grinding method which utilizes a high-speed bead mill machine. Hence, the grinding time is shortened to about a half of an hour. The final product volume is still low (about 150 ml). This problem can be easily solved, however, by modifying the manufacturing process to be continuous.

Figure 1 shows a picture of the bead mill blending machine. Another advantage of choosing this kind of machine is that it depends on a mixing process as its principle of operation. Such a mixing process meets the requirements of obtaining a rheologically complex thixotropic mediums, such as a MR fluid. A bead mill machine is distinguishable from all other types of mills (ball, attrition, jet, pestle) in that it intensively mixes the entire charged volume and, at the same time, it carefully grinds the ingredients between solid surfaces. In its basic form, the bead mill consists of a motor which rotates a shaft, on which three impellers are mounted, a working vessel, a cooling system, and metal beads (2 mm in diameter). The principle of operation can be simplified as follows: Upon the charging of MR fluid ingredients, the impellers on the high-speed rotating shaft capture the beads and throw them at random along the periphery of the working vessel. In doing so, the beads intensely collide among themselves and with the walls of the working vessel, and at the same time squeeze the fluid

ingredients in between. Hence, grinding and mixing of the ingredients take place. The bead mill can rotate with speeds up to 2000 rpm.

Figure 1. High speed bead mill blending machine used to manufacture MR fluids

To mix the MR fluid components in the bead mill, five equally weighed portions of the processed carbonyl iron as well as the chromium dioxide particles are prepared. The dispersion medium is fed in the machine first. Then, one portion at a time of the ferromagnetic particles (carbonyl iron and chromium dioxide) is fed in the machine according to a pre-determined grinding time. The machine has to be in the horizontal position for optimum grinding conditions.

5. OPTIMIZATION OF MR FLUID CHARACTERISTICS

MR fluids are characterized by the following main characteristics:
- Initial viscosity μ_0 (or initial shear stress τ_0).
- Shear stress (or yield stress) as a function of the applied magnetic field H.
- Shear stress increment or working range of shear stress.
- Working temperature range.
- Qualitative long term stability behavior.

In order for the fabricated MR fluid composition to be "good", the following characteristics are needed:
- Initial viscosity of the fluid (when H=0) must be low (about 0.5 Pa s at a shear rate of $100 \, s^{-1}$).
- The Shear stress in the field H=100 KA/m must be of the order τ=10 kPa.
- The maximum allowable shear stress at H=500 KA/m must be of the order τ=100 kPa.
- The working temperature range is T=-50 to +150 ^{0}C.
- The fluid is highly stable both sedimentally and agglomeratively.

181

Due to the limited available testing facilities, we have confined our optimization study to include initial viscosity and stability of the fluid. Several experiments were conducted and the resulting fluid's viscosity and stability were measured. Viscosity was measured in a Brookfield DV-III rheometer at 25 ^{0}C. Stability was measured by the percentage of sediment volume to the total volume. The fluid samples were left in graduated cylinders for a month before the readings were taken. The three controlled parameters in these experiments were: the concentration of oleic acid, the concentration of the non-ionic surfactant, and the concentration of chromium dioxide particles. To identify each parameter's effect on the behavior of the fluid, the other two parameters are kept constant when changing the third parameter.

5.1 Results for optimizing stability

Table 3 below lists the results for optimizing the fluid's stability.

TABLE 3: Results for stability measurements

Sample	Non-ionic surfactant	Oleic acid	Chromium dioxide	% Separation
1	2.70g	0.42g	2.50g	9.50
2	1.55g	0.42g	2.50g	1.10
3	3.50g	0.42g	2.50g	3.10
4	2.70g	0.20g	2.50g	1.50
5	2.70g	0.80g	2.50g	4.00
6	2.70g	0.42g	2.00g	10.00
7	2.70g	0.42g	3.00g	5.10

The effect of each parameter is now clear. The optimum amounts of the three parameters, to have the most stable composition, are as follows: non-ionic surfactant (1.55g), oleic acid (0.20g), and chromium dioxide (3.00g). So, the new "optimum" composition was found and produced in the bead mill. However, the produced fluid, although resulted in 0 % separation and thus was highly stable, was very viscous (about 45 Pa s at a shear rate of 1.02 s^{-1} and a temperature of 25 ^{0}C). This result should be expected, since highly viscous dispersion systems are more stable, as was indicated by the Stokes' formulation. Hence, there exists a trade-off between the viscosity of the fluid and its stability.

5.2 Results for optimum viscosity

After conducting the stability experiments, a study for the effect of the three parameters on viscosity was conducted. Table 4 shows the viscosity results for some samples.

TABLE 4: Results for viscosity measurements

Sample	Non-ionic surfactant	Oleic acid	Chromium dioxide	Viscosity, Pa s 1.02 s^{-1}, 25 ^{0}C
8	1.55g	0.42g	2.50g	36.23
9	3.50g	0.42g	2.50g	36.45
10	1.55g	0.20g	2.50g	24.30
11	1.55g	0.20g	3.00g	44.51

It is clear from the results of samples 8 and 9 that the effect of the non-ionic surfactant on the viscosity of the produced fluid is minimal. On the other hand, increasing the amount of either chromium dioxide or oleic acid significantly increases the viscosity of the produced fluid.

Hence, comparing these results to those found for the stability study, one arrives at the conclusion that the following composition results in the optimum stability and viscosity requirements: oleic acid (0.2g), non-ionic surfactant (1.55g), and chromium dioxide (2.5g). This composition is sample #10. The measured stability was 1.4%. As long as this small amount

of sediment is easily redispersed, this provides an adequately stable fluid. Figure 2 below shows the viscosity behavior as a function of shear rate for this composition.

Figure 2: Viscosity variation for the optimum composition
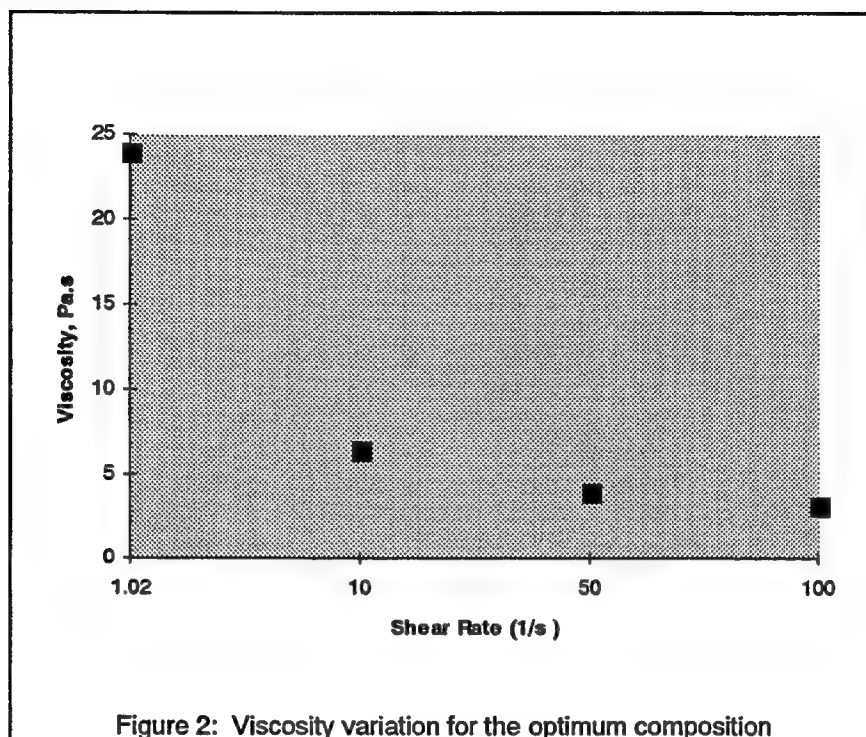
6. CONCLUSIONS

A laboratory scale magnetorheological fabrication facility was constructed at the Center for Intelligent Materials Systems and Structures CIMSS at VA Tech. A high speed bead mill blending machine was used to manufacture the fluid. Several experiments were conducted to optimize the composition of MR fluid, which results in the needed highest qualities. An optimum composition was found to minimize the initial viscosity of the fluid and maximize its stability.

7. REFERENCES

1. Konig, W., 1885. *Ann. Phys.*, Vol. 25, p. 618.
2. Duff, A. W., 1896. *Phys. Rev.*, Vol. 4, p. 23.
3. Winslow, W. M., 1949. "Induced Vibration of Suspensions," *Journal of Applied Physics*, Vol. 20, No. 12, pp. 1137-1140.
4. Rainbow, J., 1948. "Magnetic Fluid Clutch," *Technical News Bulletin*, Vol. 32, No. 5, pp. 54-60.
5. Winslow, W. M., 1989. "The Winslow Effect," Proceedings, *Second International Conference on ER Fluids*, Raleigh, NC, 7-9 August, 1989; in press.
6. Pinkos, A., E. Shtarkman, and Th. Fitzgerald, 1994. "An Actively Damped Passenger Car Suspension System With Low Voltage Electro-Rheological Magnetic Fluid," Proceedings, *SPIE's 1994 North American Conference on Smart Structures and Materials*, Vol. 2190, pp. 28-35, Orlando, Fl.
7. Carlson, J. D. and Weiss, K. D., 1994. "A Growing Attraction to Magnetic Fluids," Machine Design, Vol. 66, No. 15, pp. 61-64, August 8, 1994.

8. Shulman, Z. P., W. I. Kordonsky, E. A. Zaltsgendler, I. V. Prokhorov, B. M. Khusid, and S. A. Demchuk, 1986. "Structure, Physical Properties and Dynamics of Magnetorheological Suspensions," *Int. J. Multiphase Flow*, Vol. 12, No. 6, pp. 935-955.

9. Kordonsky, W. I., Z. P. Shulman, S. R. Gorodkin, S. A. Demchuk, I. V. Prokhorov, E. A. Zaltsgendler, and B. M. Khusid, 1990. "Physical Properties of Magnetizable Structure-Reversible Media," *Journal of Magnetism and Magnetic Materials*, Vol. 85, pp. 114-120.

10. Kordonsky, W. I., 1992. "Elements and Devices Based on Magnetorheological Effect," Proceedings, *Recent Advances in Adaptive and Sensory Materials and Their Applications*, Technomic Publishing Co., Inc., lancaster, PA. pp. 755-764.

11. Shtarkman, E., 1991. "Fluid Responsive to a Magnetic Field," U.S. Patent 4,992,190.

12. Carlson, J. D. and M. J. Chrzan., 1994. "Magnetorheological Fluid Dampers," U.S. Patent 5,277,281.

13. Carlson, J. D. and K. D. Weiss., 1995. "Magnetorheological Materials Based on Alloy Particles," U.S. Patent 5,382,373.

14. Kordonsky, W. I., S. R. Gorodkin, A. V. Kolomentsev, V. A. Kuzmin, A. V. Lukianovitch, N. A. Protasevich, I. V. Prokhorov, and Z. P. Shulman, 1994. "Magnetorheological Valve And Devices Incorporating Magnetorheological Elements," US Patent 5,353,839.

15. Kordonsky, W. I., Gorodkin, S. R., Kolomentsev, A. V., Kuzmin, V. A., Lukianovitch, A. V., Protasevich, N. A., Prokhorov, I. V., and Shulman, Z. P. 1995. "Magnetorheological Valve And Devices Incorporating Magnetorheological Elements," US Patent.5,452,745.

16. Lemaire, E., Bossis, G., and Grasselli, Y., 1993. "Yield Stress and Structuration of magnetorheological suspensions," *Journal of Magnetism and Magnetic Materials*, Vol. 122, No. 1-3, April 1993, pp. 51-52.

17. Klingenberg, D. and Zukoski, C., 1990. *Langmiur*, Vol. 6, p. 15.

18. Liu, J., Hagenbuchle, M., Sheaffer, P., and Zhu, Y., 1996. "Static and Dynamic Properties of Chain Formation in a Dilute Magnetorheological Fluid," *Advances in the Astronautical Sciences*, Vol. 95, No. 664, pp. 431-439.

19. Promislow, J., and Gast, A., "Magnetorheological Fluid Structure in a Pulsed Magnetic Field," 1996. Langmiur, Vol. 12, pp. 4095-4102.

20. Lemaire, E., Meunier, A., Bossis, G., and Liu, J., 1995. "Influence of the Particle Size on the Rheology of Magnetorheological Fluids," 1995. *Journal of Rheology*, Vol. 39, No. 5, pp. 1011-1020.

21. Gorodkin, S., Kordonskii, V., and Protasevich, N., "Estimates as to the Possibility of Utilizing Magnetorheological Suspensions in Compression Equipment," 1989. *Magnetohydrodynamics*, Vol. 24, No. 4, pp. 511-514.

22. Solid/ Liquid Dispersions, Edited by Tadros, Th. F., 1987. Academic Press, Orlando, Fl., pp. 226-230.

Magnetic and magnetorheological properties of flowable compositions based on barium and strontium ferrites and iron oxides

Tatiana G. Lazareva and Ilya G. Shitik

Institute of General and Inorganic Chemistry of the Academy of Sciences of Belarus, Minsk, Belarus

ABSTRACT

Magnetic and magnetorheological properties of a number of compositions are examined. The compositions are based on barium and strontium ferrites, magnetite, and γ-Fe_2O_3, both commercial and synthesized using specially developed methods, suspended in transformer oil and synthetic binders based on phenol-formaldehyde, epoxyacrylic and pentaphthalic resins. The influence of numerous factors, such as the type and magnetic properties of the filler, type of the binder, magnetic properties of the composition on the orienational effect of the filler in a magnetic field was evaluated. The latter was judged by a magnitude of magnetorheological effect.

Keywords: magnetic, magnetorheological properties, barium and strontium ferrites, iron oides.

INTRODUCTION

A wide range of smart and intelligent materials can be obtained on the basis of fluid compositions with dispersed fillers possessing magnetic properties. Of special interest are fluid media with inert binders, e.g. oil, and those with polymeric binders. The latter are capable of forming anisotropic structures in external fields, which may be used as different sensors, actuators, measuring elements, etc[1]. In this aspect, we have performed a comparative examination of magnetic and magnetorheological properties of compositions based on barium and strontium ferrites, magnetite, and γ-Fe_2O_3 suspended in oil and polymeric binders based on pentaphthalic (commercial varnish PF-060) epoxyacrylic (varnish EAS-510) and phenol-formaldehyde resins.

EXPERIMENTAL

For experiments, commercial barium and strontium ferrites and magnetite with particle sizes of 5-6 μm (type FB, FS and MG) and 1-2 μm (type FB*, FS* and MG*), as well as powders synthesized by us at different heat treatment temperatures, viz. magnetite (type MGS1, MGS2, MGS3) and γ-Fe_2O_3 with a particle size of about 1 μm and barium ferrite sized 0.1 μm. Magnetite and γ-Fe_2O_3 were obtained by precipitating iron hydroxide, $Fe(OH)_3$, by ammonia from $FeSO_4$ aqueous solutions with subsequent heating of the mixture to 70-80 °C. The precipitate was filtered out, dried and heat treated in an inert atmosphere in the temperature range of 100-400 °C. For obtaining γ-Fe_2O_3, heat treatment in air was carried out in the temperature range of 150-300 °C.

The magnetic properties of fillers and composites were evaluated using automated vibration magnetometer with maximal field intensity of 1260 kA/m and sensitivity of 10^{-6} Gs for magnetization. Magnetorheological properties were judged by the relative viscosity $\Delta\eta/\eta$, $\Delta\eta=\eta_1-\eta$, where η_1 and η are the viscosities with and without external field. The viscosity was assessed using rotary viscometer "Rheotest-2" with a specially designed headpiece which permits generating the magnetic induction of 0-100 μGs in the gap. The suspensions of powders in a binder were prepared using ultrasonic dipergating unit UZDM-2 with the frequency of 44 kHz.

RESULTS AND DISCUSSION

The magnetic properties of the examined fillers for magnetorheological compositions are presented in Table 1, where ρ is density, g/cm^3, σ_s is the saturation magnetization, $Gs\cdot cm^3/g$, σ_r is the residual magnetization, $Gs\cdot cm^3/g$, B_s is the saturation magnetic induction,

Gs, B_r is the residual magnetic induction, Gs, H_c is the coercive force, Oe, μ_0 is the initial magnetic permeability, μ_{max} is the maximal magnetic permeability.

The data shown in Table 1 allow definite conclusions on the effect of the synthesis conditions of iron oxides on their magnetic properties. The coercive force of MGS does not depend on the heat treatment temperature in an inert atmosphere (He) within the examined temperature range. The oxidation of MGS in air at 400 °C until the formation of γ-Fe$_2$O$_3$ causes the coercive force of the powder to decrease by 30%. The residual magnetization in the sequence MgS1, MGS2, MGS3 and MG increases from 5 to 9.8 Gs·cm^3/g, which is apparently connected with coarsening of γ-Fe$_2$O$_3$ particles at elevated temperatures.

Table 1. Magnetic properties of fillers

Filler	ρ	σ_s	σ_r	B_s	B_r	H_c	μ_0	μ_{max}
FB	1.8	22	16	506	360	1346	10	350
FS	1.9	11	8	275	200	1311	13	200
FBS	1.0	15	8.8	197	112	3000	56	1275
MG	2.1	40	12	1050	312	319	32	260
MGS1	1.5	70	5	1312	-	92	44	75
MGS2	1.5	52	7	975	-	108	90	112
MGS3	1.4	76	9.8	1337	-	92	142	166
γ-Fe$_2$O$_3$	1.5	50	5	875	-	67	70	78

Figures 1 and 2 present the obtained results on magnetization and relative viscosity for compositions based on FB, FS (particle size 5-6 μm), FB*, FS* (particle size 1-2 μm) and MG (particle size 5-6 μm) in transformer oil, the concentration of the filler being 30 wt%. Magnetization was estimated using the Hall sensor by measuring magnetic induction when the composition was placed between the poles of an electromagnet. The magnetic field intensity was changed reversibly from 0 to 200 kA/m (the hysteresis loop). As follows from Fig.1, the compositions possess significant residual magnetization, which is maximal for compositions with FB and FS and somewhat lower for MG-containing suspensions. These results correspond to the magnetic properties of the fillers. Decreasing the particle size from 5-6 to 1-2 μm brings about a certain increase in residual magnetization of compositions.
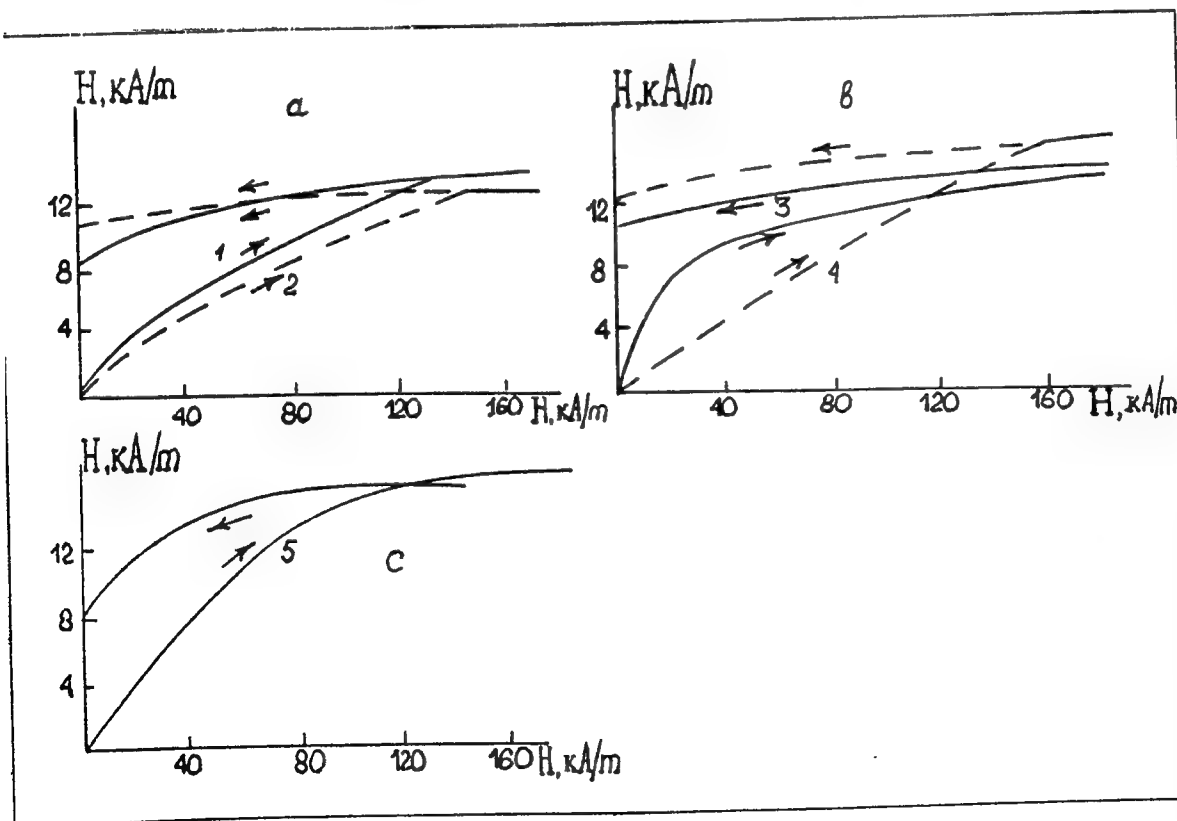

Fig. 1. Magnetization curves (the hysteresis loop) for compositions containing FB (curve 1), FB* (curve 2), FS (curve 3), FS* (curve 4) and MG (curve 5) in transformer oil.

As seen from Fig.2, relative viscosity, i.e. the response of the system on an external field, decreases with lowering shear rate, the effect being more pronounced at higher magnetic

field intensity. For the examined compositions, magnetorheological effect decreases in the series $\gamma\text{-Fe}_2\text{O}_3 > \text{SrFe}_{12}\text{O}_{19} > \text{BaFe}_{12}\text{O}_{19}$, and is stronger for fillers with a particle size of 5-6 μm. Decreasing the particle size to 1-2 μm weakens the effect. The use of a freshly prepared magnetite obtained at a higher heat treatment temperature, MGS3, results in a stronger effect as compared with commercial powder MG (Fig.3). Compositions with $\gamma\text{-Fe}_2\text{O}_3$ possess lower properties in comparison with MGS-based compositions.
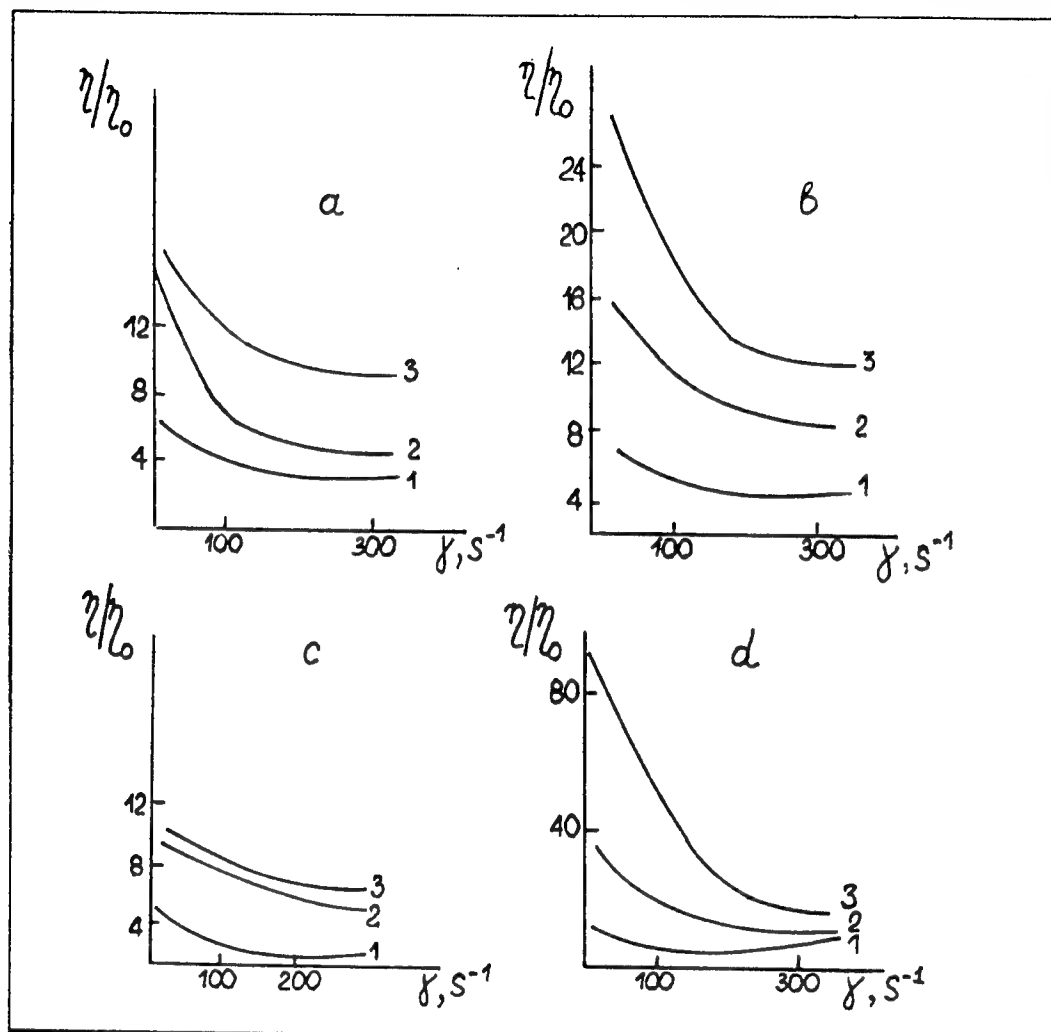
Fig. 2. Relative viscosity versus shear rate for suspensions of FB (a), FS (b), FS* (c) and MG (d) in transformer oil.

Thus, the obtained results has clearly demonstrated that magnetorheological effect decreases in the following series of fillers: MGS3>MGS1>γ-Fe$_2$O$_3$>MG>FS>FB> FS*>FB*.

Basing on the results listed in Table 1, we conclude that a stronger magnetorheological effect is characteristic of compositions which possess higher values of saturation magnetization (σ_s) and magnetic permeability (μ_0). For example, for the above presented series of iron oxide-based fillers, s changes as follows: 76, 70, 50, 40. The values of residual magnetization (σ_r) and coercive force (H_c) do not influence the magnetorheological effect.

The results listed in Table 2 indicate that magnetic properties of compositions depend on type and properties of both a filler and a binder. In particular, the properties of MG-containing compositions are optimal for binders based on pentaphthalic (varnish PF-060) and phenol-formaldehyde resins (PFR), and are lower for varnish EAS-510 based on epoxyacrylic resin. For compositions with FB, optimal magnetic properties are attained in varnish PF-060; phenol-formaldehyde resins give worse results. Decreasing the particle size from 5-6 to 0.1 μm for fillers FB and FBS brings about a decrease in the σ_s, σ_r, B_s, B_r, μ_0 and μ_{max} values and an increase in the coercive force (H_c).
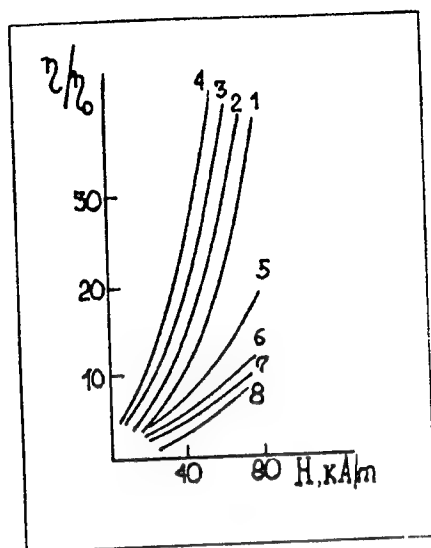
Fig.3. Relative viscosity versus the magnetic field intensity for compositions containing MG, MGS1, MGS2, MGS3, FS, FB, FS* and FB* (curves 1 to 8, correspondingly) at a shear rate of 100 s^{-1}.

Table 2 lists the measured magnetic properties of flowable compositions which contain 30 wt% solid ferromagnetic phase in different binders.

Table 2. Magnetic properties of flowable compositions

Binder	Filler	ρ	σ_s	σ_r	B_s	B_r	H_c	μ_0	μ_{max}	K
PF-060	MG	0.9	31.0	15.5	350	175	168	4.7	120	0.5
	MGS	1.22	26.0	8.5	425	162	118	12.8	130	0.3
	FB	1.18	10.0	7.7	147.5	112.5	185	4.4	96	0.7
	FBS	1.16	4.7	3.0	68.7	43	203	0.1	45	0.6
EAS-510	MG	1.39	8.4	4.2	145	72.5	208	3.3	71	0.5
FFS	MG	0.95	32.0	16.0	375	188	247	9	162	0.5
	FB	0.93	5.8	4.5	64	52	355	1	47	0.7

As follows from Fig.4, the values of relative viscosity are optimal for binders based on pentaphthalic resins (varnish PF-060) and are lower for the binder based on epoxyacrylic resin (varnish EAS-510). For the same binder, e.g. varnish EAS-510 or PF-060, with different fillers, magnetorheological effect decreases in the following series MGS>MG>FBS.
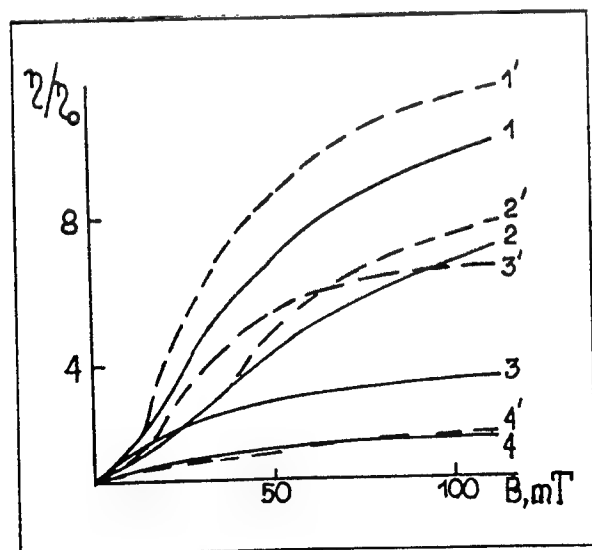

Fig. 4. Relative viscosity versus the induction of an applied magnetic field for 10% dispersions of magnetic fillers MGS (curves 1 and 1'), MG (curves 2 and 2'), FB (curves 3 and 3') and FBS (curves 4 and 4') in varnishes EAS-510 (curves 1 through 4) and PF-060 (curves 1' through 4').

It should be noted that the σ_s and B_s values of the fillers decrease in the same sequence. Lowering the particle size from 5 to 0.1 μm (fillers FB and FBS) weakens magnetorheological effect.

CONCLUSION

The results obtained in this research are indicative of a substantial influence of a polymeric binder on magnetorheological effect. This is connected with different values of saturation magnetization of the compositions. Besides, it is established that orientational effects in a magnetic field are more pronounced for iron oxides and less substantial for compositions based on barium and strontium ferrites; these effects depend also on the particle size, saturation magnetization, saturation induction and initial magnetic permeability of a filler.

REFERENCES

1. T.G. Lazareva, E.V. Korobko. "Electroreological Film-Forming Media Based on Polysaccharides & Metal Oxides. Second International Conference of Intelligent Materials". 5-8 June, 1994, Williamsburg, VA.

SESSION 5

Compliant Smart Materials and Complex Fluids II

Linear and Platform Type Robotic Actuators
Made From Ion-Exchange Membrane-Metal Composites

Karim Salehpoor, Mohsen Shahinpoor and Mehran Mojarrad

Artificial Muscles Research Institute
School of Engineering, University of New Mexico
Albuquerque, NM 87131

ABSTRACT

In this research, feasibility of using ion-exchange-membrane-metal composite artificial muscles as linear platform type actuators was studied. In order to achieve linear motion from these typically bending type actuators, a series of muscles made from ion-exchange-membrane-metal composites were cut in strips and attached either end-to-end or to one fixed platform and another movable platform in a cylindrical configuration. By especially prepared electrodes embedded within the platforms one can convert the bending response of each strip into linear movement of the mobile platform. By applying a low voltage the movement of free end of the actuator could be calibrated and its response could be measured, accordingly. A theoretical model was developed and was compared to experimental results. Ion-exchange-membrane-metal composites are highly active actuators that show very large deformation in the presence of low applied voltage and exhibit low impedance.

Keywords: Linear Actuator, Ion-Exchange-Membrane-Metal Composite Actuator, Platform Actuator, Parallel Actuator, Linear Artificial Muscles, Biomechanical Muscles, Ionic Polymeric Actuators, Composite Film Actuators

2. INTRODUCTION

Ion-exchange-membrane (IEM) metal composites are highly active actuators that show very large deformation in the presence of low applied voltage and exhibit low impedance. They operate best in a humid environment and can be made as a self-contained encapsulated actuators to operate in dry environments as well. They have been modeled as both capacitive and resistive element actuators that behave like biological muscles and provide an attractive means of actuation as artificial muscles for biomechanics and biomimetics applications. Grodzinsky[1], Grodzinsky and Melcher[2,3], were the first to present a plausible continuum model for electrochemistry of deformation of charged polyelectrolyte membranes such as collagen or fibrous protein. Kuhn[4] and Katchalsky[5] however should be credited to have been the first investigators to report the ionic chemomechanical deformation of polyelectrolytes such as polyacrylic acid (PAA), polyvinyl chloride (PVA) systems. Kent, Hamlen and Shafer[6] were also the first to report the electrochemical transduction of PVA-PAA polyelectrolyte system. Recently revived interest in these area with concentration on artificial muscles can be traced to Shahinpoor[7,8], Shahinpoor and Mojarrad[9,10], Osada[11], Oguro, Asaka and Takenaka[12], Asaka, Oguro, Nishimura, Mizuhata and Takenaka[13], Guo, Fukuda, Kosuge, Arai, Oguro and Negoro[14].

Essentially polyelectrolytes possess many ionizable groups on their molecular chain. These ionizable groups have the property of dissociating and attaining a net charge in a variety of solvent medium. According to Alexanderowicz and Katchalsky[15] these net charge groups which are attached to network of macromolecules are called polyions and give rise to intense electric fields of the order of 10^{10} V/m. Thus, the essence of electromechanical deformation of such polyelectrolyte systems is their susceptibility to interactions with externally applied fields as well as their own internal field structure. In particular if the interstitial space of polyelectrolyte network is filled with liquid containing ions, then the electrophoretic migration of such ions inside the structure due to an imposed electric field can also cause the macromolecular network to deform accordingly. Shahinpoor[16,17,18,20,23,24,26,27,29,30,31,32,33,34] and Shahinpoor and co-workers[19,21,22,25,28] have recently presented a number of plausible models for micro-electro-mechanics of ionic polymeric gels as electrically controllable artificial muscles in different dynamic environments. The reader is referred to these papers for the theoretical and experimental results on dynamics of ion-exchange membranes -platinum composite artificial muscles. Most Ion exchange polymeric membranes swell in solvents and by and large are hydrophilic. This gives rise to ability of the membrane to swell in water which can be controlled in an electric field due to ionic nature of the membrane. Furthermore by placing two electrodes in close proximity of the membrane

walls and applying a voltage, the forced transport of ions within a solution through membrane becomes possible at microscopic level. For a solvent such as water then local swelling and deswelling of membrane can be controlled depending on polarity of the electrode nearby more like the behavior of the bimorphic materials. This can be achieved by chemical or other possible means of plating of conductive materials on membrane surfaces. Platinum is one such conductor that can be deposited on the IEM.

Also being ionic in microscopic structure, IEM has the ability to shift its mobile ions of the same charge polarity within itself when it is placed in an electric field which results in ionic attraction or repulsion between the fixed charges of opposite polarity contained in the side groups within the polymer molecular chain. This leads to local collapse or expansion of the polymer membrane macroscopically. Physically this causes a stress gradient on opposite sides of the membrane causing it to bend. Therefore by applying an alternating signal at low voltage one can achieve membrane oscillation proportional to frequency and amplitude of the input signal. This bending oscillation can be utilized in various applications as in a linear or platform type actuators.

In this paper strips of polyelectrolyte Ion-Exchange membrane (IEM) were used as legs for linear and platform type robotic actuators. The ion-exchange membrane strips were chemically plated with platinum. A small function generator circuit was designed and built to produce approximately ±4.0V amplitude square wave at varying frequency up to 60 Hz. By setting the signal frequency to the desired value and thereby setting the frequency of bending oscillation of the membrane, a proportional dynamic linear actuation of each leg of a platform type robotic actuator could be obtained. The results were compared to experimental data which showed close agreement In order to study the feasibility of using ion-exchange-membrane-metal composite artificial muscles as linear platform type actuators, a series of muscles made from ion-exchange-membrane-metal composites were cut in strips and attached either end-to-end or to one fixed platform and another movable platform in a cylindrical configuration. By especially prepared electrodes embedded within the platforms the bending response of each strip could be converted to linear movement of the mobile platform. By applying a low voltage the movement of free end of the actuator could be calibrated and its response could be measured, accordingly. A theoretical model was developed and was compared to experimental results.

3. DESIGN OF LINEAR & PLATFORM TYPE ACTUATORS

For detailed dynamics description and analysis of the dynamic theory of ionic polymeric gels the reader is referred to Shahinpoor[16,17,18,20,23,24,26,27,29,30,31,32,33,34] and Shahinpoor and co-workers[19,21,22,25,28]. Since ionic polyelectrolytes are for the most part three dimensional network of macromolecules cross-linked nonuniformly, the concentration of ionic charge groups are also nonuniform within the polymer matrix. Therefore the mechanism of bending is related to migration of mobile ions within the network due to imposition of an electric field as shown in Figure 1 below.
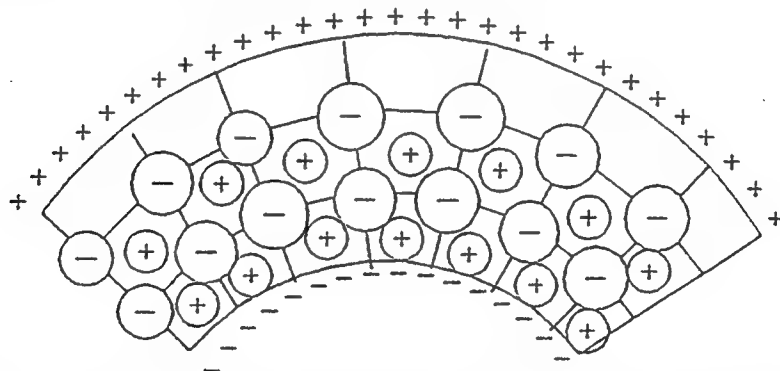

Figure 1- Bending of IEM-Pt composite muscles due to ionic rearrangement within the network

Ion exchange membrane (IEM) chemically treated with platinum salt solution gives rise to IEM-platinum composites that undergo large deformations in an electric field of a few volts (1.5-3.0 V/mm^2 depending on the size and thickness of the membrane). They also show remarkable vibrational characteristics (30 Hz or higher depending on mass and geometry of membrane) bandwidth. For experimental evidence on the dependence of deformation amplitude on the imposed voltages and frequencies the reader is referred to other papers by this author and his co-researchers in this conference

A simple one-dimensional model of electrically-induced deformation of ionic polymeric gels is such that :

$$\sigma = (1/3)E(C_0, C_i) \, (\lambda - \lambda^{-2}) , \qquad (1)$$

$$\sigma = \kappa \, (C_0, C_i) \, E^{*2} \qquad (2)$$

where σ is the stress, λ is the stretch, $E(C_0, C_i)$ is the corresponding Young's modulus of hyper-elasticity, C_0 is the polymer solid concentration, C_i, $(i=1,2,....,N)$'s are the molal concentration of various ionic species in the aqueous medium, $\kappa \, (C_0, C_i)$ is an electromechanical coefficient and E^* is the local electric field. Thus bending can occur due to differential contraction and expansion of outer most remote fibers of a strip if an electric field is imposed across its thickness as shown below in Figure 2.
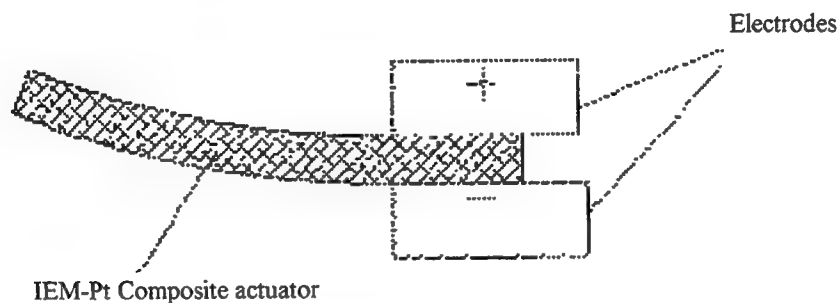
Figure 2- Bending of IEM-Pt composite muscles under an electric field

Figure 3 depicts the bending deformation of a typical strip with varying electric field, while Figure 4 displays the variation of deformation with varying frequency of alternating electric field.
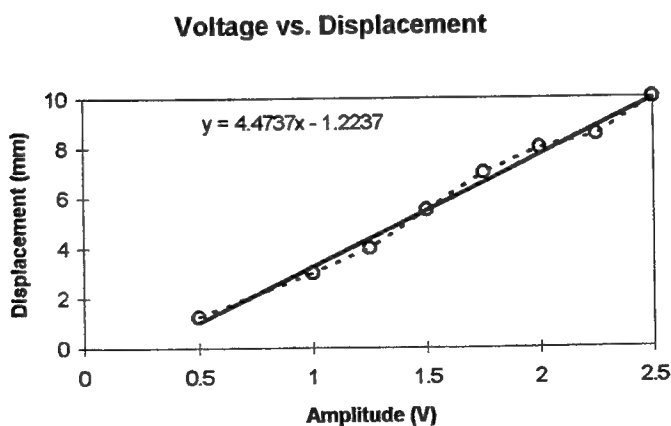
Figure 3-Bending Displacement versus Voltage for a typical strip of 0.17mmx5mmx20mm.
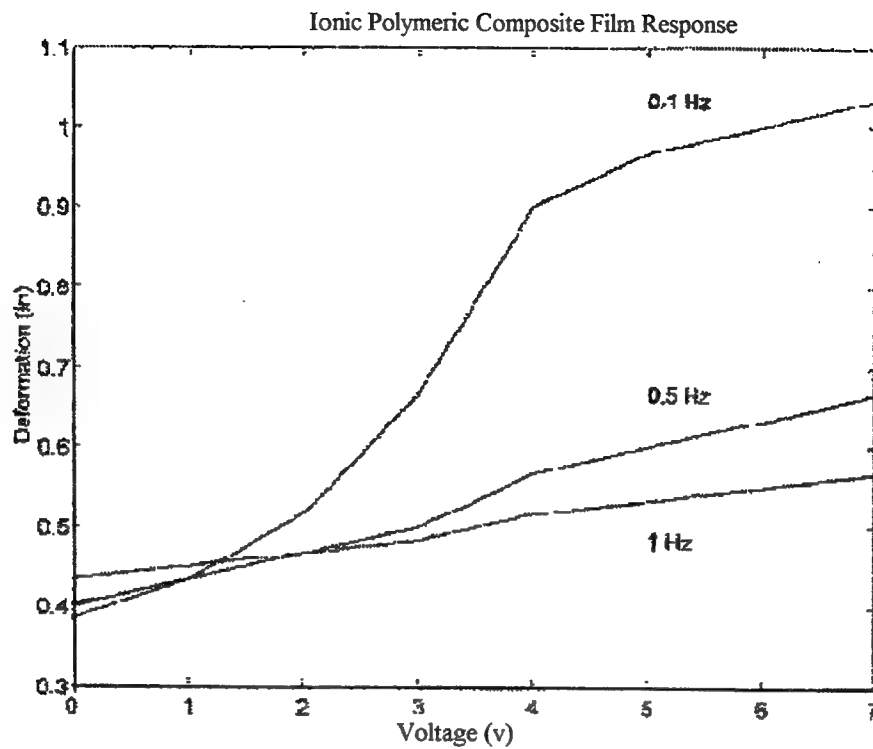
Figure 4-Frequency dependence of bending deformation of IEM-Pt composite muscles

Based on such dynamic deformation characteristics, linear and platform type actuators can be designed and made dynamically operational. These types of actuators are typically shown in Figures 5 and 6.
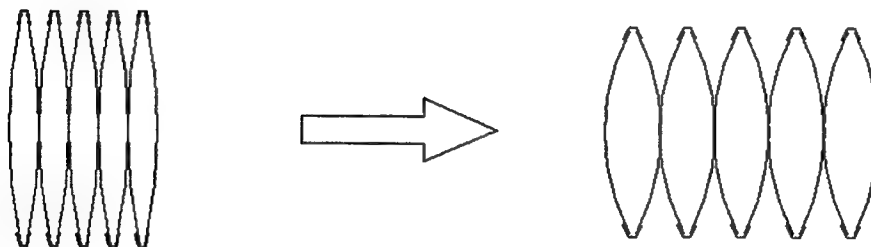

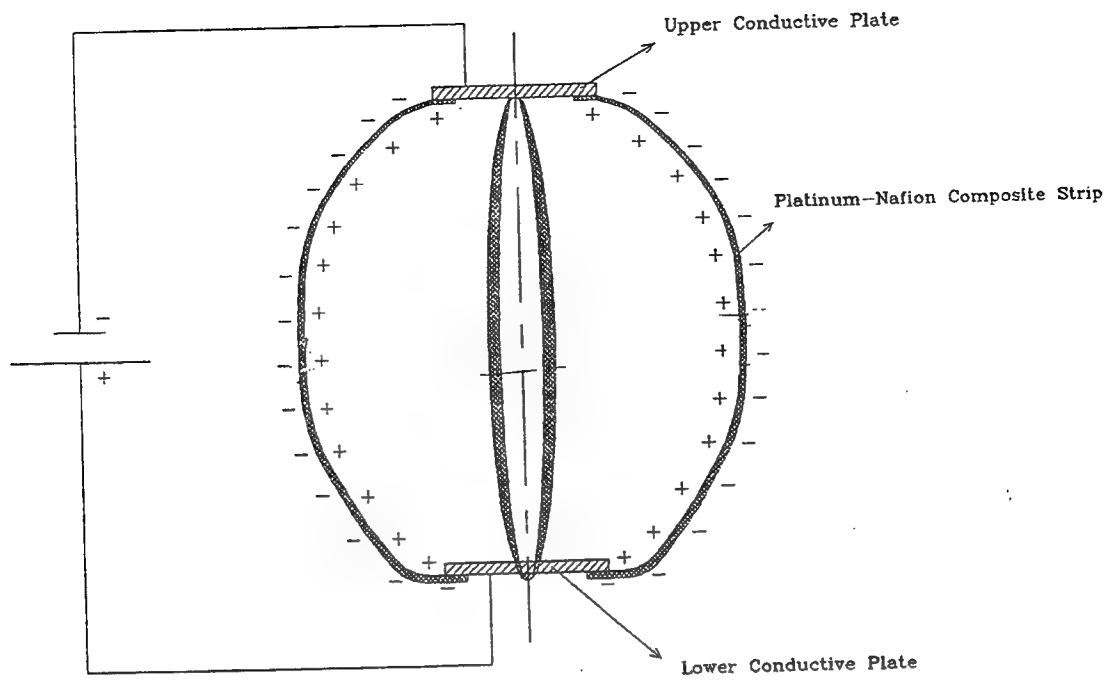Figure 5- A typical linear-type robotic actuators made with IEM-Pt composite legs

Figure 6- A typical platform-type actuator made with an assembly of IEM-Pt composite bending strip muscles

Figure 7 shows an assortment of such actuators made in our laboratory. The experimental results on the deformation of these actuators as depicted in Figure3 and 4 have been found to agree with the theoretical predictions as presented in references [16] through [34].
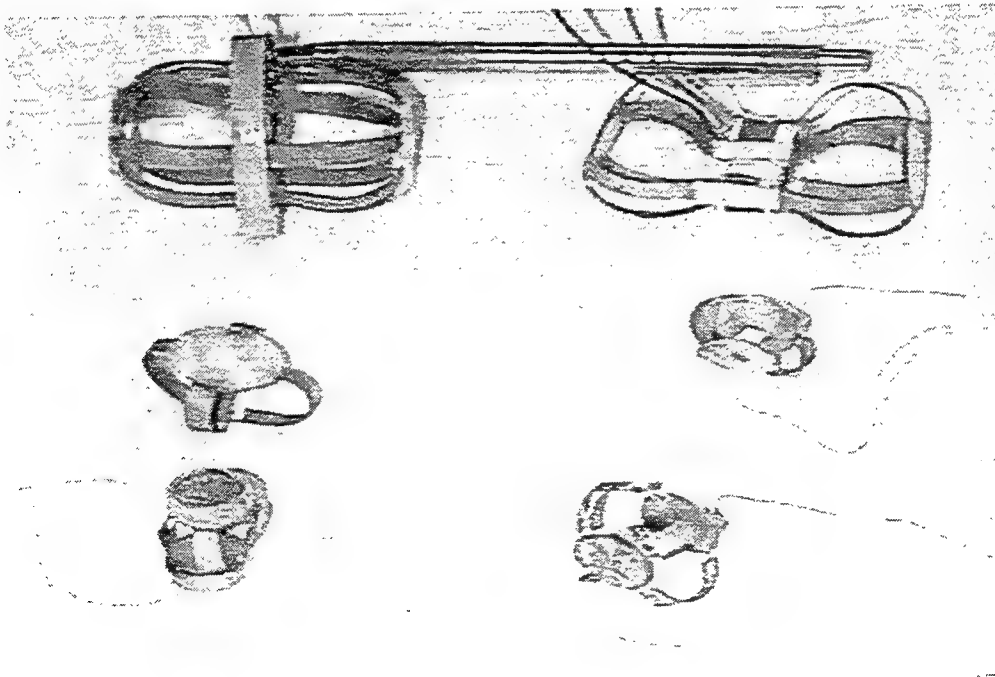
Figure 7- An assortment of linear and platform type actuators made in our laboratory.

4. CONCLUSION

In this paper the feasibility of designing linear and platform type robotic actuators made with a polyelectrolyte ion exchange membrane-metal composite artificial muscle were presented. In order to achieve linear motion from these typically bending type actuators, a series of muscles made from ion-exchange-membrane-metal composites were cut in strips and attached either end-to-end or to one fixed platform and another movable platform in a cylindrical configuration. By especially prepared electrodes embedded within the platforms one can convert the bending response of each strip into linear movement of the mobile platform. By applying a low voltage the movement of free end of the actuator could be calibrated and its response could be measured, accordingly. A theoretical model was developed and was compared to experimental results.

ACKNOWLEDGMENT

REFERENCES

1. A.J. Grodzinsky, "Electromechanics of Deformable Polyelectrolyte Membranes", Sc.D. dissertation, Dept. of Elec. Eng., MIT, Cambridge, June 1974.
2. A. J. Grodzinsky, Melcher, J. R., "Electromechanics of Deformable, Charged Polyelectrolyte Membranes", Proc. 27th Annu. Conf. Engineering in Medicine and Biology, Vol. 16, 1974, paper 53.2.
3. A. J. Grodzinsky, Melcher, J. R., "Electromechanical Transduction with Charged Polyelectrolyte Membranes", IEEE Transactions on Biomedical Engineering, Vol. BME-23, No. 6, pp421-433, November 1976.
4. W. Kuhn, Reversible Dehnung und Kontraktion bei Anderung der Ionisation eines Netzwerks Polyvalenter Fadenmolekulionen", Experientia, Vol. V, pp318-319, 1949.
5. A. Katchalsky, "Rapid Swelling and Deswelling of Reversible Gels of Polymeric Acids by Ionization", Experientia, Vol. V, pp319-320, 1949.
6. R. P. Hamlen, Kent, C. E., Shafer, S. N., "Electrolytically Activated Contractile Polymer", Nature, Vol. 206, pp1149-1150, 1965.
7. M. Shahinpoor, "Continuum Electromechanics of Ionic Polymeric Gels as Artificial Muscles for Robotic Applications", Smart Material and Structures Int. J., Vol. 3, pp. 367-372, 1994.
8. M. Shahinpoor, "Microelectro-Mechanics of Ionic Polymeric Gels as Artificial Muscles for Robotic Applications", Proceeding of the IEEE Robotics & Automation Conf., vol. , pp. , 1993.
9. M.Shahinpoor, Mojarrad, M., "Active Musculoskeletal Structures Equipped with a Circulatory System and a Network of Ionic Polymeric Gel Muscles", Proceedings of the 1994 International Conference on Intelligent Materials, pp. 1079-1085, 1994.
10. M.Shahinpoor, Wang, G., Mojarrad, M., "Elctro-Thermo-Mechanics of Spring-Loaded Contractile Fiber Bundles with Applications to Ionic Polymeric Gel and SMA Actuators", Proceedings of the International Conference on Intelligent Materials" ICIM'94, Williamsburg, VA., pp. 1105-1116, 1994.
11. Y. Osada, "Electro-Stimulated Chemomechanical System Using Polymer Gels (An Approach to Intelligent Artificial Muscle System)", Proceeding of the International Conference on Intelligent Materials, pp155-161, 1992.
12. K.Oguro, Asaka, K., Takenaka, H., "Polymer Film Actuator Driven by Low Voltage", Proceedings of 4th International Symposium on Micro Machine and Human Science at Nagoya, pp39-40, 1993.
13. K.Asaka, Oguro, K., Nishimura, Y., Mizuhata, M., Takenaka, H., "Bending of Polyelectrolyte Membrane-Platinum Composites by Electric Stimuli, I. Response Characteristics to Various Waveforms", Polymer Journal, Vol. 27, No. 4, pp436-440, 1995.
14. S.Guo, Fukuda, T., Kosuge, K., Arai, F., Oguro, K., Negoro, M., "Micro Catheter System with Active Guide Wire Structure, Experimental Results and Characteristic Evaluation of Active Guide wire Using ICPF Actuator", Osaka National Research Institute, Japan, pp191-197, 1994.
15. A. Alexanderowicz, Katchalsky, A., "Colligative Properties of Polyelectrolyte Solutions in Excess of Salt", Journal of Polymer Science, Vol. 1A, pp3231-3260, 1963.
16. M. Shahinpoor, "Nonhomogeneous Large Deformation Theory of Ionic Polymeric Gels in Electric and pH Fields", Proceedings of the 1993 SPIE Conference on Smart Structures and Materials, Feb. 1-4, Albuquerque, Vol. 1916, pp. 40-50, 1993.

17. M. Shahinpoor, "Micro-Electro-Mechanics of Ionic Polymeric Gels as Electrically Controlled Artificial Muscles," Proc. 1994 Int. Conf on Intelligent Materials, ICIM'94, June 1994, Williamsburg, VA, pp. 1095-1104, 1994

18. M.Shahinpoor, "Conceptual Design, Kinematics and Dynamics of Swimming Robotic Structures Using Ionic Polymeric Gel Muscles", Smart Materials and Structures Int. J., Vol. 1, pp. 91-94, 1992.

19. D.Segalman, Witkowsky, W., Adolf, D., Shahinpoor, M., "Electrically Controlled Polymeric Muscles as Active Materials used in Adaptive Structures", Proceedings of ADPA/AIAA/ASME/SPIE Conference on Active Materials and Adaptive Structures, Alexandria, VA, November 1991.

20. M. Shahinpoor, "Micro-Electro-Mechanics of Ionic Polymeric Gels As Electrically-Controllable Artificial Muscles,", Int. J. Intelligent Material Systems, vol. 6, no. 3, pp. 307-314, 1995

21. M. Mojarrad and M. Shahinpoor "Noiseless Propulsion for Swimming Robotic Structures Using Polyelectrolyte Ion-Exchange Membranes,", Proc. SPIE 1996 North American Conference on Smart Structures and Materials, February 27-29, 1996, San Diego, California, vol. 2716, paper no. 27, 1996

22. M. Shahinpoor and M. Mojarrad, "Ion-Exchange Membrane-Platinum Composites As electrically Controllable Artificial Muscles,", Proc. 1996 Third International Conference on Intelligent Materials, ICIM'96, and Third European Conference on Smart Structures and Materials, Lyon, France, SPIE Publication No. ICIM'96 , pp. 1171-1184, June 1996

23. M. Shahinpoor, "Electro-Mechanics of Bending of Ionic Polymeric Gels as Synthetic Muscles for Adaptive Structures,", ASME Publication AD-Vol. 35, Adaptive Structures and Material Systems, edited by G.P. Carman and E. Garcia, Vol. AD-35, pp.11-22, 1993

24. M.Shahinpoor, "Electro-Mechanics of Resilient Contractile Fiber Bundles with Applications To Ionic Polymeric Gel and SMA Robotic Actuators" Proc. 1994 IEEE International Conference on Robotics & Automation , vol. 2, pp. 1502-1508, San Diego, California, May 1994

25. M. Shahinpoor and M. Mojarrad, "Ion-Exchange Membrane-Platinum Composites As Electrically Controllable Artificial Muscles,", Proc. 1996 Third International Conference on Intelligent Materials, ICIM'96, and Third European Conference on Smart Structures and Materials, June 1996, Lyon, France

26. M. Shahinpoor, "The Ionic Flexogelectric Effect" Proc. 1996 Third International Conference on Intelligent Materials, ICIM'96, and Third European Conference on Smart Structures and Materials, June 1996, Lyon, France

27. M. Shahinpoor, "Design and Development of Micro-Actuators Using Ionic Polymeric Micro-Muscles,", Proc. ASME Design Engn. Technical Conference, Boston, MA, September (1995)

28. M. Shahinpoor and M.S. Thompson, "The Venus Flytrap As A Model For Biomimetic Material With Built-In Sensors and Actuators," J. Materials Science & Engineering, vol.C2, pp. 229-233, (1995)

29. M. Shahinpoor, "Design and Modeling of A Novel Spring-Loaded Ionic Polymeric Gel Actuator," Proc. SPIE 1994 North American Conference on Smart Structures and Materials ., February 94, Orlando, Florida, vol. 2189, paper no. 26, pp.255-264, (1994)

30. M. Shahinpoor, "Microelectro-Mechanics of Ionic Polymeric Gels As Synthetic Robotic Muscles," Proc. SPIE 1994 North American Conference on Smart Structures and Materials, February 94, Orlando, Florida, vol. 2189, paper no. 27, pp.265-274, (1994)

31. M. Shahinpoor, "Micro-Electro-Mechanics of Ionic Polymeric Gels as Electrically Controlled Synthetic Muscles,", Biomedical Engineering Recent Advances, Editor : J.Vossoughi, University of District of Columbia Press, Washington, D.C., April 1994, vol.1, pp.756-759, (1994)

32. M.Shahinpoor, "Electro-Mechanics of Resilient Contractile Fiber Bundles with Applications To Ionic Polymeric Gel and SMA Robotic Actuators" Proc. 1994 IEEE International Conference on Robotics & Automation , vol. 2, pp. 1502-1508, San Diego, California, May (1994)

33. M. Shahinpoor, "Electro-Thermo-Mechanics of Spring-Loaded Contractile Fiber Bundles with Applications To Ionic Polymeric Gel and SMA Actuators," Proc. 1994 Int. Conf. on Intelligent Materials, ICIM'94, June 1994, Williamsburg, VA, pp. 1105-1116, (1994)

34. M. Shahinpoor, "A New Effect in Ionic Polymeric Gels : The Ionic "Flexogelectric Effect," Proc. SPIE 1995 North American Conference on Smart Structures and Materials, February 28-March 2, 1995, San Diego, California, vol. 2441, paper no. 05, (1995)

SESSION 6

Biomimetics and Biotechnology

Biochemically Designed Polymers as Self Organized Materials

K. Shridhara Alva,[†] Rupmoni Sarma, Kenneth A. Marx, Jayant Kumar,[†] and Sukant K. Tripathy
Departments of Chemistry and [†]Physics, Centers for Advanced Materials and Intelligent Biomaterials, University of Massachusetts Lowell, Lowell MA 01854.

Joseph A. Akkara and David L. Kaplan
Biotechnology Division, US Army Natick RD&E Center, Natick, MA 01760

ABSTRACT

Self assembled molecular systems are a focus of attention for material scientists as they provide an inherent molecular level organization responsible for enhanced material properties. We have developed polymeric molecular systems with interesting optical properties by biochemical engineering, which can be self assembled to thin films. Horseradish peroxidase catalyzed polymerizations of phenolic monomers: 8-hydroxyquinoline-5-sulfonic acid, acid red and decyl ester (d&l isomers) of tyrosine, have been achieved in the presence of hydrogen peroxide. The polymer of 8-hydroxyquinoline-5-sulfonic acid acts as a polymeric ligand that can be used for metal ion sensing. The polymer of acid red, with azo functional groups in the polymer backbone, shows interesting optical properties. Amphiphilic derivatives of tyrosine self assemble into tubules from micelles in aqueous solutions. These tubules have been enzymatically polymerized to polymeric tubules. The tubules are of 5μm average diameter and >200 μm length. The formation and properties of these tubules are discussed.

1. INTRODUCTION

Ultrathin organic films are currently gaining interest in many areas such as integrated optics, sensors, coatings and surface orientation layers. A recent approach to build multilayer assemblies is by consecutive alternate adsorption of anionic and cationic polyelectrolytes.[1,2] This layer-by-layer deposition technique through electrostatic interaction of polyelectrolytes has become an attractive technology for the fabrication of thin film devices with molecular level control on the organization. This deposition results in 100% coverage of the substrate independent of the substrate size and topology.[1] Polymers with a wide range of properties such as electrical conductivity, electroluminescence, nonlinear optical and redox properties can be assembled into thin films with controlled supramolecular architecture.[2]

Chemical synthesis of polymers with electroactive properties, though very extensively studied, is environmentally harmful. Enzyme catalysis, on the other hand, is becoming increasingly popular in organic synthesis.[3-5] Enzymes provide a means of synthesis of specialty chemicals in the purest forms possible under environmentally mild chemical conditions. Horseradish peroxidase catalyzed oxidative free radical coupling of phenols have been explored in various experimental conditions: in aqueous, solvent

mixtures, micelles, reverse micelles and at the air-water interface to control the molecular weight, organization and ordering of the resulting polymer.[5-9] Scheme 1 provides the mechanism of HRP catalyzed polymerization of phenols.[10] The oxidized form of the enzyme (compound I) reacts with two molecules of electron donors, which in turn get oxidized to their respective free radicals. These free radicals, with possible resonance stabilization, undergo oxidative free radical coupling reactions, which will result in the growth of the polymer chain.

Step 1:   HRP + H_2O_2 $\longrightarrow$ Compound - I + H_2O

Step 2:   Compound - I +   [phenol OH] $\longrightarrow$ Compound - II +   [phenoxy radical structure]

Step 3:   Compound - II +   [phenol OH] $\longrightarrow$ HRP +   [phenoxy radical structure]

Step 4:   [resonance structures of phenoxy radical] $\longrightarrow$ [biphenol structure with two OH groups]
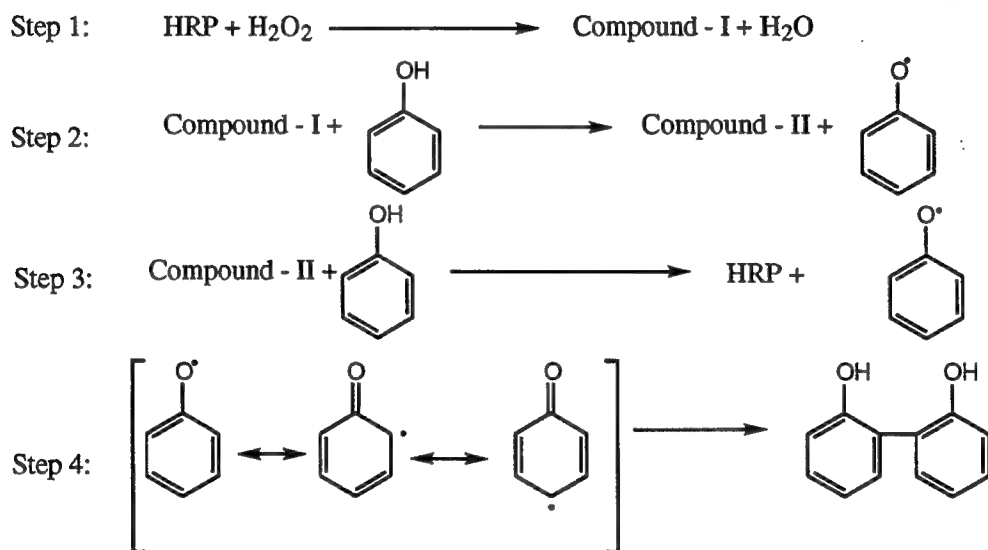
Figure 1: Mechanism of HRP catalyzed polymerization of phenols

In this paper, we discuss the synthesis of some of the polyphenols. We describe the potential applications of these polymeric systems. Also, the post-organization of these polymers to ultrathin films through the layer-by-layer deposition technique is discussed. We also report the self assembly of amphiphilic phenolic monomers into tubules and some of the properties of these structures.

2. MATERIALS AND METHODS

2.1 Materials

Horseradish peroxidase was purchased from Sigma Chemicals Co. Acid red, 8-hydroxyquinoline-5-sulfonate and hydrogen peroxide were obtained from Aldrich Chemicals Co. The decyl esters of tyrosine were synthesized by the esterification of tyrosine with decanol. All other chemicals were of analytical grade.

The spectroscopic characterization of the polymer and the polymerization reaction were followed using a Perkin Elmer Lambda 9 UV-Vis-near IR spectrophotometer. The scattering experiments to determine the cmc were carried out using a SLM 8100 spectrofluorometer. The NMR experiments were carried out using a Bruker DPX 200

spectrometer. Scanning electron microscopy (Amray 1400 Scanning Electron Microscope) was used to study the surface morphology of the tubules.

2.2 Experimental Procedures

Horseradish peroxidase catalyzed polymerization of phenolic derivatives has been carried out at pH 6.0. The monomers (~ 100mg) were dissolved in 10 ml of the phosphate buffer and 10 units enzyme was introduced to the monomer solution. The polymerization reaction was initiated by the addition of 5 μl of 30% hydrogen peroxide solution into the reaction medium. To ensure the completion of the polymerization, additional aliquots of hydrogen peroxide were added to the reaction medium with one hour time intervals such that the substrate induced inhibition of the enzyme is minimized.

Self assembly of the poly(acid red) on a glass slide was carried out by the layer-by-layer deposition technique.[2] A glass slide treated with alkali (Chemsolv®) was exposed to polycation and polyanion solutions repeatedly with in between washes to transfer monolayers of these polyelectrolytes per every exposure. 1mg/10ml solution of poly(diallyldimethylammonium chloride) (PDAC) at pH 2.5 was used as the polycation while 1mg/10ml solution of polyphenol also at pH 2.5 was used as the polyanion. The glass slide was exposed to the polyelectrolyte solution for 10 minutes and washed with water at pH 2.5 to remove any unbound polymer from the surface. This process was repeated to obtain the desired number of bilayers.

Amphiphilic tyrosine derivatives (C10 esters) were dissolved in aqueous solution at pH 3.0 and then the solution pH was increased to 6.0. At concentrations above cmc, when the solution was allowed to stand for over an hour, the micelles organize themselves into tubules. These tubules are then polymerized.

3. RESULTS AND DISCUSSION

3.1 Enzymatically designed polymeric ligand

Figure 2: Structure of 8-hydroxyquinoline-5-sulfonate

Quantitative estimation of heavy metal ions in environmental samples is important in order to monitor and remediate the environmental pollutants. A large number of approaches have been attempted for efficient fabrication of metal ion sensors. We propose a complexometric approach based on a polymeric ligand utilizing the characteristic spectral properties of the metal-complex. 8-hydroxyquinoline is a bidentate ligand, which forms complexes with metal ions such as Fe(III). 8-Hydroxyquinoline-5-sulfonate (HQS) (Fig. 2) has been enzymatically polymerized to produce a water soluble polymer (PHQS). PHQS is a polymeric ligand. It has been established by *in-situ* proton NMR studies that the oxidative free radical coupling takes place at positions 2, 4 and 7, with the order of preference being 7≥2>4.[11] Polymerization reaction is rapid and the polymer is soluble in water and methanol. The polymerization was confirmed by both proton and ^{13}C NMR spectral studies. Fig. 3 gives the ^{13}C spectra of the monomer and the
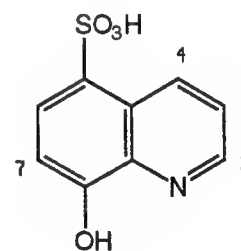
polymer. The complex spectral characteristics of the polymer as compared with the monomer supports the structural changes observed during *in-situ* studies.
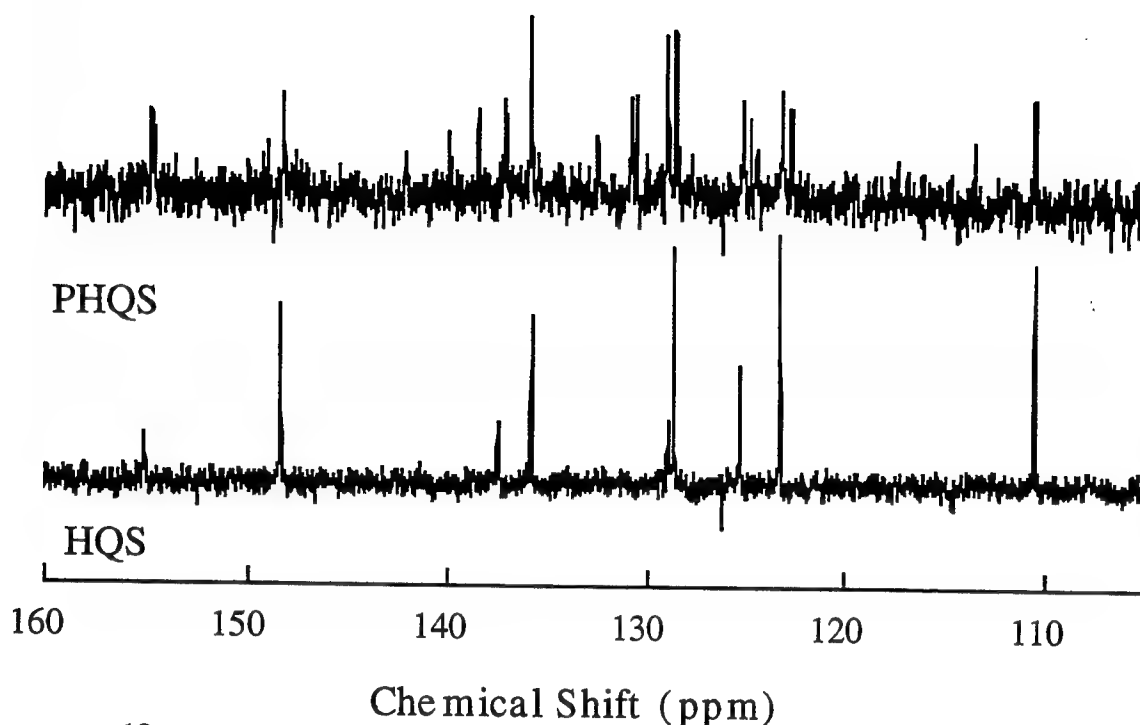

Figure 3: ^{13}C spectra of the monomer and the polymer of HQS

The complexing capability of the polymeric ligand PHQS has been studied with Fe(III). The absorption spectra of the polymer and the polymer-Fe(III) complex in water is given in Figure 4. The complex shows a spectrum with absorption maxima at 450 and 580 nm respectively. The characteristic spectral features of the complex can be used as a probe for the colorimetric detection of metal ions. In this illustration, we have used the absorption band at 450 nm as a measure of the concentration of the complex, which in turn is the concentration of the metal ion present in solution. Figs. 5 and 6 represent plots of absorbance at 450 nm as a function of concentration of the metal ion and the ligand for a fixed concentration of the ligand and the metal ion respectively. The absorbance increases linearly till the metal - ligand concentrations attain the stoichiometric ratio and then saturates. These observations suggest that desired dynamic ranges for the detection of metal ion can be achieved by the proper control of the ligand concentration. The ligand has different co-ordination strengths with different transition metal ions. The spectral features of the complex will depend on the metal ion in the complex, which suggests that one can use this ligand for the complexation and quantitative estimation of metal ions. One can use this polymeric ligand in the immobilized form for the fabrication of a sensitive metal ion sensor. With the development of the layer-by-layer multilayer deposition technique based on the charge compensation of polyelectrolyte pairs, one can assemble these polymeric ligands into organized multilayers, that can be used as solid state sensors for the metal ions. Moreover, these films can used for the separation of metal ions

in trace amounts based on the binding capacities of the metal ions with the polymeric ligand.
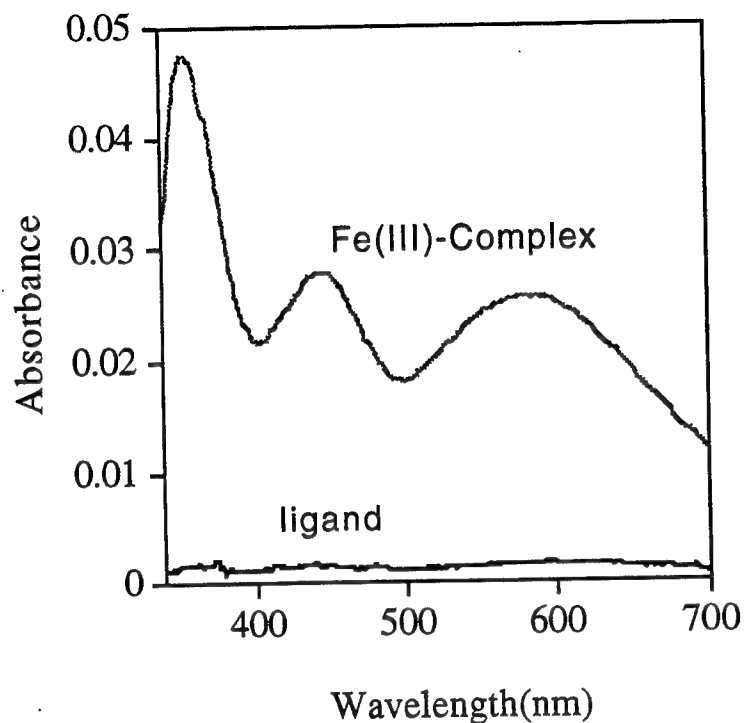
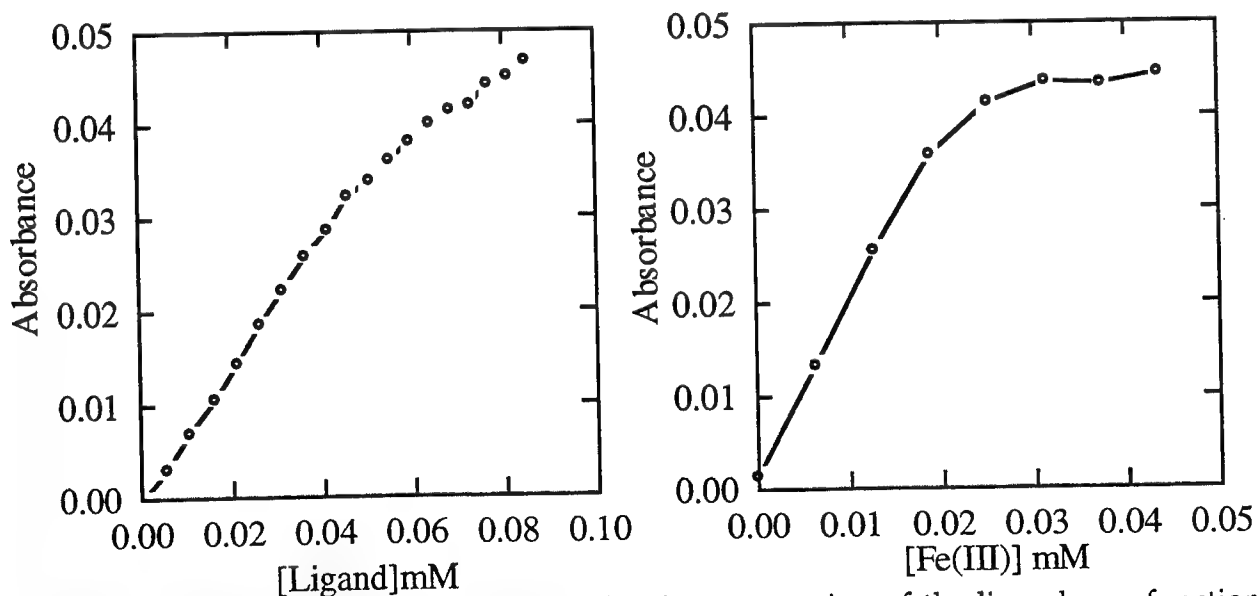Figure 4: Absorption spectra of the polymer and polymer-Fe(III) complex

Figure 5: The change in absorbance for a fixed concentration of the ligand as a function of Fe(III) concentration. [Fe(III)] = 0.03mM

Figure 6: The change in absorbance for a fixed concentration of Fe(III) as a function of ligand concentration. [Ligand] = 0.06mM

3.2 Layer-by-layer deposition of poly(acid red)
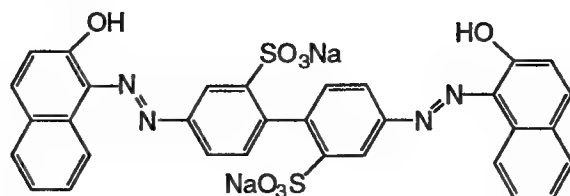
Figure 7. Structure of acid red

Azopolymers are gaining considerable interest in the recent years due to their capability to undergo cis-trans isomerization which can be used to various device applications. Acid red (Figure 7) is a phenolic azodye, which can be enzymatically polymerized to a polyphenol with azo functionality built in the molecule. This polymer is soluble in all solution pH conditions, because of the sulfonic acid groups. This makes it a perfect 'command layer' for the fabrication of thin films by the layer-by-layer deposition technique. This polymer can be used as polyanion with a variety of other polycations of interest. In the preliminary studies on fabrication of multilayers by this techniques, we have demonstrated that one can build multilayers of this polyphenol with polydiallydimethylammonium chloride under acidic pH conditions. Figure 8 gives the absorption spectra of some of the bilayers of these deposited on a glass slide at pH 2.5. Since PDAC is not absorbing in the spectral region scanned in this study, the absorbance is solely due to the polyphenol.
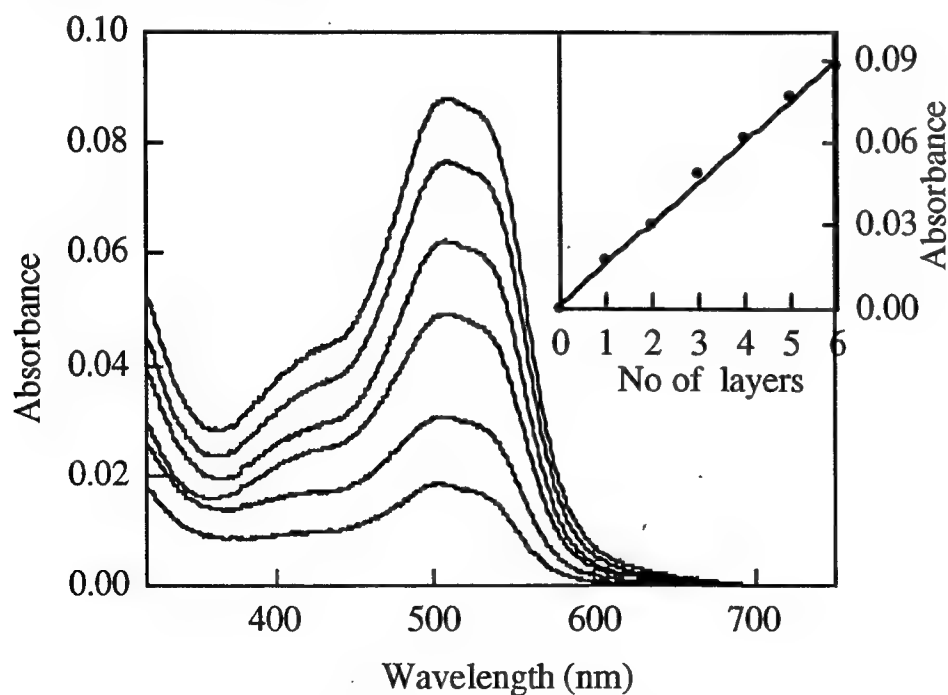
Figure 8: Self assembled multilayers of acid red on a glass slide.

The absorption spectrum of the multilayer assembly gives the absorption maxima at 510 nm, which increases linearly with the number of bilayers as shown in the inset. The constant change in absorbance per bilayer indicates that one can build thin films with precise control over thickness and organization. The average thickness per bilayer is about $35Å^2$, which indicates the coiled nature of the polymers in the molecular assembly. The orientation of the chromophore in the self assembled films was studied by polarized UV-Vis spectroscopy. Figure 9 summarizes such a study, which indicates that the chromophores are randomly oriented in the plane of the slide. This approach of making thin films can be extended, for example, to the fabrication of thin films of biomolecules sandwiched between conjugated polymer layers for biosensing applications.
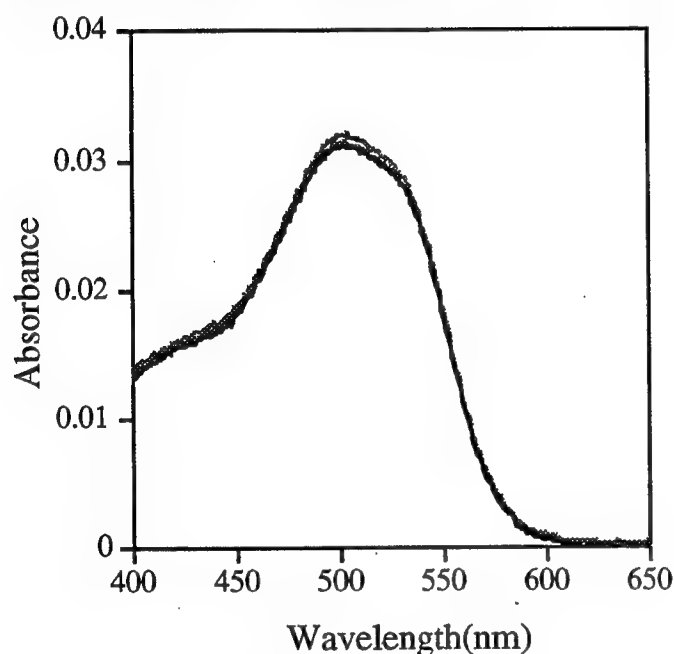
Figure 9: Polarized UV-Vis spectra of the poly(acid-red) deposited on glass slide via layer-by-layer deposition technique. The spectra represented here are recorded under conditions of unpolarized, parallel and perpendicular polarizations with respect to the dipping direction.

3.3 Self organized decyl esters of tyrosine

Amphiphilic molecules, self assemble in aqueous medium forming various types of molecular aggregates such as micelles, vesicles, etc. Micelle size and shape depends on the concentration of the amphiphiles[12] and the presence of counterions.[13] Elongated micelles also referred to as *tubules*, usually results from spherical micelles, when certain changes, as mentioned above, are made to the system. These microstructures were reported to consist of bilayers wrapped around a hollow core.[14-16]

Decyl esters of d (DEDT)and l (DELT) isomers of tyrosine, whose structures are shown in Figure 10, were found to assemble into macroscopic structures, which are a result of tubule-tubule aggregation.[17] This happens only when the concentration of the amphiphiles exceeds 0.31mM, and at a pH above 6.0. This concentration is above the

critical micelle concentration (cmc) of the amphiphiles. The cmc. of both DEDT and DELT were found to be about 0.15mM, based on Raman scattering experiments (Figure 11).
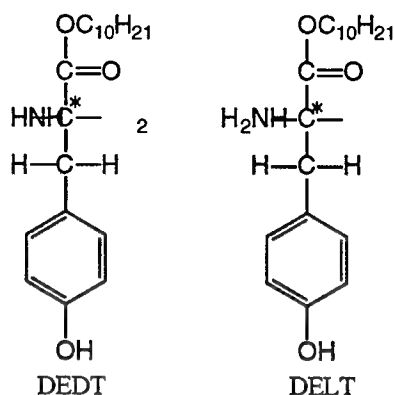
Figure 10: Structure of decyl ester of tyrosine

Under the 0.31mM monomer concentration conditions, the solution was at first observed to become turbid. Formation of the macrostructures were visualized only after allowing the solution to stand for a few hours. The rate could be accelerated by stirring the solution occasionally and by increasing the concentration of the amphiphiles and the pH. The structures appear to be the result of very weak interactions, since the structures disperse upon gentle stirring. However, we have been able to polymerize these structures enzymatically using HRP. By so doing we hope to render these self assembled macrostructures rugged and stable for practical applications. The reaction with HRP was found to be very fast and the color of the tubules becomes yellow within a few minutes of the reaction initiation.
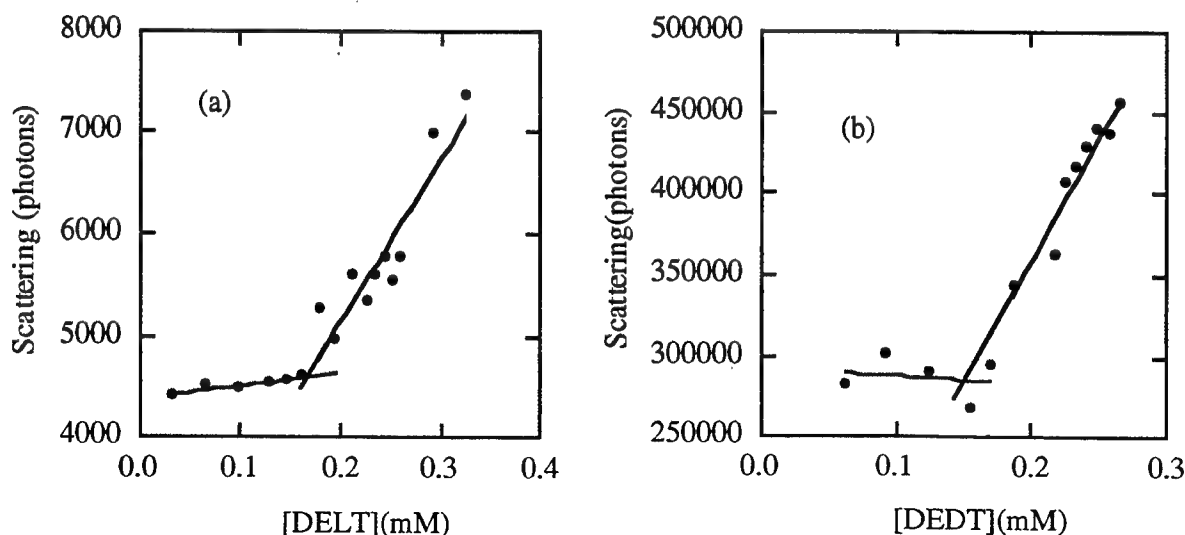
Figure 11: CMC of (a) DELT and (b) DEDT by Raman scattering experiment

Scanning electron miscrographs of the tubules of the DEDT monomer (Figure 12) and polymerized DEDT tubules (Figure 13) had been used to visualize the monomeric and polymeric tubular structures. The images revealed that the tubules were 5μm average diameter. However, the polymeric tubules appear to be more highly organized and have greater length (>200um) than the monomeric counterparts. The polymerized tubules, in addition, were found to be more stable as compared to the unpolymerized monomeric tubules. We could obtain higher magnification images of the polymeric tubules, while under identical conditions, the monomeric tubules disintegrated in the SEM. The tubule formation and the surface morphology are not influenced by the chirality of the monomer. A detailed investigation of the system is in progress.

10μm   10KeV   X1000
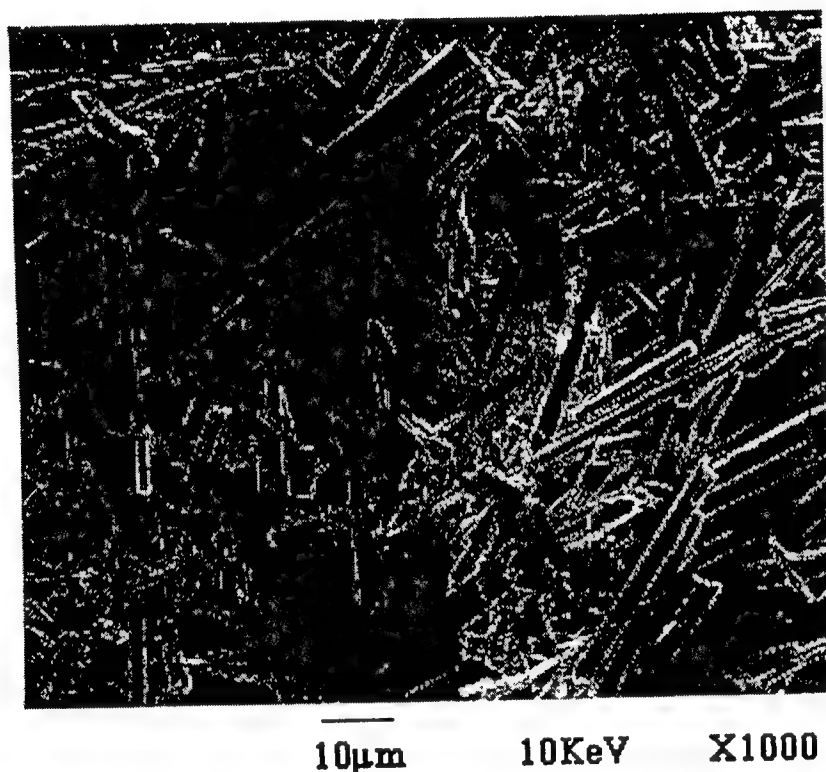
Figure 12: SEM image of monomeric d-DEDT tubules.

REFERENCES
1. G. Decher, J.D. Hong and J. Schmitt, "Buildup of ultrathin multilayer films by a self-assembly process: III. Consecutively alternating adsorption of anionic and cationic polyelectrolytes on charged surfaces", *Thin Solid Films*, , Vol. 210-211, pp. 831-835. 1992.
2. J.H. Cheung, A.F. Fou and M.F. Rubner, "Molecular self-assembly of conducting polymers", *Thin Solid Films*,, Vol. 244, pp. 985-989, 1994.
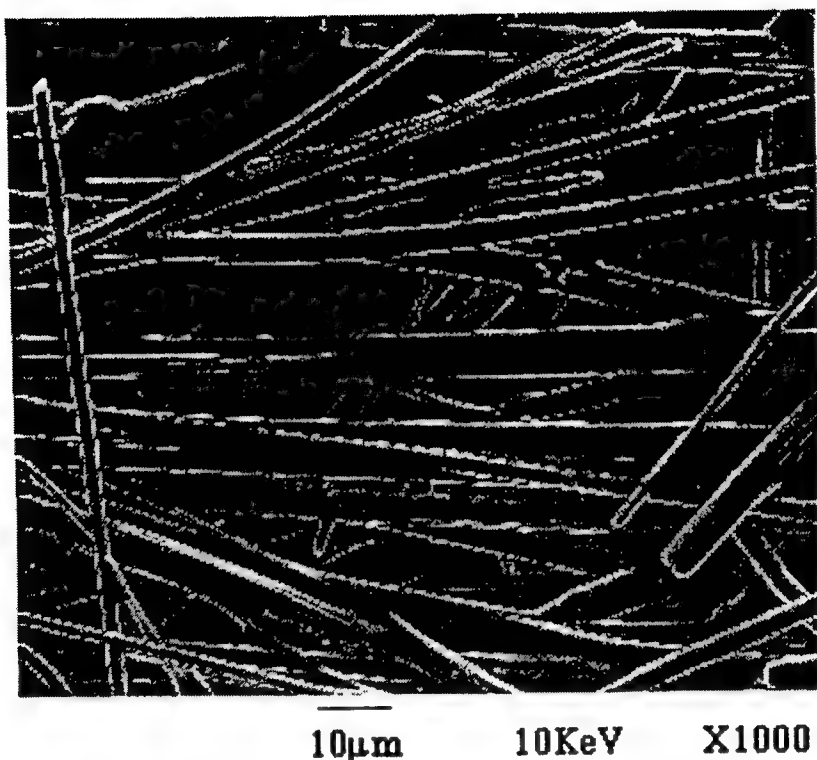
10μm   10KeV   X1000

Figure 13: SEM image of polymerized tubules of d-DEDT.

3. H. Kurioka, I. Komatsu, H. Uyama and S. Kobayashi, "Enzymatic oxidative polymerization of alkylphenols", *Macromol. Rapid Commun.* vol 15, 507-512, 1994.

4. R. Ikeda, H. Uyama and S. Kobayashi, "Novel synthetic pathway to a poly(phenylne oxide). laccase-catalyzed oxidative polymerization of syringic acid", *Macromolecules*, vol. 29, 3053-3054 1996.

5. J. A. Akkara, K. J. Senecal and D.L. Kaplan, "Synthesis and characterization of polymers produced by horseradish peroxidase", *J. Poly. Sci.: A: Polym. Chem.*, vol. 29, 1561-1574, 1991.

6. 14. M. S. Ayyagari, K. A. Marx, S. K. Tripathy, J. A. Akkara and D. L. Kaplan, "Controlled free-radical polymerization of phenol derivatives by enzyme-catalyzed reactions in organic solvents", *Macromolecules*, vol. 28, 5192- 5197, 1995.

7. F. F. Nando, J. A. Akkara, L. A. Samuelson, D. L. Kaplan, B. K. Mandal, K. A. Marx, J. Kumar and S. K. Tripathy, "Enzymatic mediated synthesis of conjugated polymers at the Langmuir trough air-water interface", *Langmuir*, vol 11, 889-892, 1995.

8. K. S. Alva, K. A. Marx, J. Kumar, and S. K. Tripathy, "Biochemical synthesis of water soluble polyanilines: poly(p-amino benzoic acid)," *Macromol. Rapid Comm.* vol. 17, 000-000, 1996.

9. R. Sarma, K. S. Alva, K. A. Marx, S. K. Tripathy, J. A. Akkara and D. L. Kaplan, "Enzymatic polymerization of amphiphilic alkyl tyrosine derivatives from emulsions", Materials Science and Engineering, vol. C00, 000-000, 1996.

10. C. Walsh in *"Enzymatic Reaction Mechanisms"*, W. H. Freemand & Co., New York, pp, 488-493, 1979.

11. K. S. Alva, K. A. Marx, J. Kumar and S. K. Tripathy, "Mechanistic study of enzyme catalyzed polymerization of 8-hydroxyquinoline-5-sulfonate using nuclear magnetic resonance spectroscopy", *Macromol.Rapid Comm.* vol 18, 0000, 1997.

12. C.M. Paleos, *Polymerization in organized media*, Gordon and Breach Science Publishers, Chapter 3, pp. 184, Philadelphia, PA, 1992.

13. K.L.Mittal and B. Lindman, *Surfactants in Solution*, Plemun Press, New York and London. Vol 2, Part III, 825, 1982.

14. P.Yager and P.E. Schoen, "Formation of tubules by a polymerizable surfactants", *Mol. Cryst. liq. Cryst.*, vol 106, 371, 1984.

15. P. Yager, P. E. Schoen, C. Davies, R. Price and A. Singh, "Structure of lipid tubules formed from a polymerizable lecithin", *Biophys. J* , vol. 48, 899, 1985.

16. J. H. Georger, A. Singh, R. R. Price, J. M. Schnur, P. Yager, P. E. Schoen, " Helical and tubular microstructures formed by polymerizable phosphatidylcholines", *J. Am. Chem. Soc.*vol, vol. 109, 6169, 1987.

17. M. Lu, J. B. Lando, J. A. Mann Jr.,R. G. Petschek and C. Rosenblatt, "Aggregation of aqueous suspensions of Phospholipid tubules", *Langmuir* , vol. 7, 1988-1990, 1991.

Molecular Recognition and Optical Detection of Biological Pathogens at Biomimetic Membrane Interfaces

John J. Pan and Deborah Charych[*]

Center for Advanced Materials, Materials Sciences Division, Lawrence Berkeley Laboratory, Berkeley, CA 94720

Abstract

Molecular recognition sites on cell membranes serve as the main communication channels between the inside of a cell and its surroundings. Upon receptor binding, celular messages such as ion channel opening or activation of enzymes are triggered. In this report, we demonstrate that artificial cell membranes made from conjugated lipid polymers (polydiacetylene) can, on a simple level, mimic membrane processes of molecular recognition and signal transduction. The ganglioside, GM1 was incorporated into polydiacetylene liposomes. Molecular recognition of cholera toxin at the interface of the liposome resulted in a change of the membrane color due to conformational changes in the conjugated (ene-yne) polymer backbone. The 'colored liposomes' might be used as simple colorimetric sensors for drug screening or as new tools to study membrane-membrane or membrane-receptor interactions.

Keywords

biosensor, pathogen, molecular recognition, biomimetic, liposome, cholera, toxin, detection, polydiacetylene, optical

Introduction

The surface of a cell membrane is a mosaic of highly specific molecular recognition receptor sites. When specific ligand binding occurs at these sites, the binding event is often transduced into a cellular message. Cell membrane recognition sites may trigger, for example, the opening of ion channels or the activation of intracellular enzymes. From the materials science point of view, the cell membrane may be considered a completely self-contained biosensing system wherein molecular recognition is directly linked to signal transduction. We have been interested in the design of synthetic membranes that attempt to mimic, on a very simple level, the complex molecular choreography of cell membranes.[1] These simplified constructs allow the study of fundamental receptor-ligand interactions and, in a more practical sense, the application of receptor-ligand binding to biosensor design. The synthetic membranes are organized supramolecular structures that resemble natural cell surfaces at the interfacial region, but possess a chromophoric conjugated polymer at its interior. The latter part serves as an optical 'transducer' of molecular recognition events occuring at the interface.[2,3,4,5] Signalling occurs by a simple color change of the chromophoric unit from blue to red.

Previously, we demonstrated that polydiacetylene (PDA) thin films and liposomes functionalized with sialic acid molecular recognition groups can bind and colorimetrically detect influenza virus.[3,4] The multi-valent nature of viral binding at the interface triggered large conformational changes in the polymer side chains followed by disruption of conjugation in the chromophoric polymer backbone. The result was a visible color change from blue to red, similar to color changes previously observed in PDA

induced by heat (thermochromism) [6,7] and mechanical stress (mechanochromism).[8] For the viral binding study, the ligand molecule for the bio-target was a synthetic diacetylenic lipid compound derivatized with the binding ligand. The ligand-lipid could be cross-linked with the remaining diacetylene groups forming the conjugated polymer backbone. More recently, we showed that naturally derived lipophilic molecules can be incorporated into polydiacetylene Langmuir-Blodgett films.[9] In this report, we show that these molecules can also be formed into liposomes when mixed with a polymerizable monomer lipid.

Gangliosides are a complex subclass of sphingolipids that are derivatives of ceramide. The large polar head is made up of several carbohydrate units. The membranes of the human nervous system contain at least 15 different gangliosides of which little is known about their function. However, in addition to its natural role in animal cells, the ganglioside, G_{M1}, (1), is the point of attachment of cholera toxin as it attacks the cell. This interaction provides a useful model to demonstrate molecular recognition between the protein toxin and the lipid-polymer matrix.
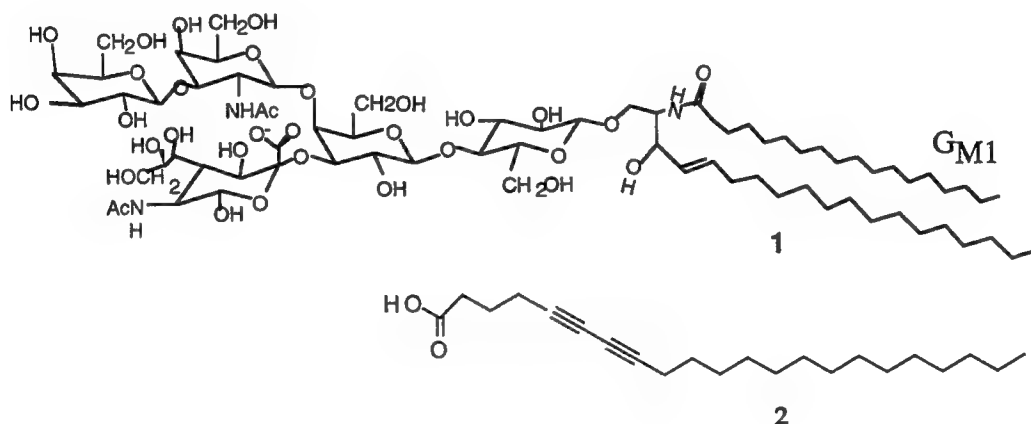
Experimental Section

Materials. Ganglioside, G_{M1}, cholera toxin from *Vibrio cholerae* , human serum albumin and wheat germ agglutinin were purchased from Sigma. 5,7 docosadiynoic acid (**2**) was a kind gift from Professor Alice Deckert. De-ionized water was obtained by passing distilled water through a Millipore uF ultrapurification train. Solvents used were reagent grade.

Liposome formation. Compounds **1** and **2** were dissolved in methanol and chloroform, respectively. The solutions were mixed in appropriate volumes to achieve a lipid mixture of 5 % by mole of GM1 and total lipid content of 2 umoles. The solvent was evaporated by rotary evaporation and 2 ml of de-ionized water added to the dried lipid. The suspension was probe sonicated[10], cooled and polymerized for 60 minutes using a hand-held UV lamp (254 nm). The resulting blue/purple liposome suspension was stored in the dark at 4°C.

Colorimetric Assay Cholera toxin was diluted to 1mg/ml in 50 mM Tris buffer, pH 7.0. In a 500 uL glass cuvette, blue phase liposomes were diluted 1:5 in 50 mM Tris buffer, pH 7.0. The liposomes were pre-incubated in the buffer for 15-30 minutes to ensure stability of the blue phase prior to the addition of cholera toxin. No color changes were observed during this period. Cholera toxin was added to the cuvette by the method of successive additions. After each addition, the contents were mixed and the visible absorption spectrum was recorded as a function of time. Typically, 95% of the absorption changes were observed to occur within the first two minutes after addition of toxin. After each experiment, the contents of the cuvette were transferred to a single well of a white microtiter plate. The pink-orange color of the cholera-treated liposomes was verified visually with a blue negative control.

Results and Discussion

Cholera toxin is an enterotoxin of the gram-negative bacterium *Vibrio cholerae* that causes potentially lethal diarrheal disease in man.[11] The cholera-G_{M1} interaction is well-characterized[12] and the G_{M1} lipid can be easily incorporated into liposomes. Cholera toxin is composed of two subunits: A (MW 27 kDA) and B (MW 11.6 kDa) with the stoichiometry AB_5. The B components bind specifically to G_{M1} gangliosides on cell surfaces, ultimately leading to translocation of the A1 fragment through the membrane [13]. Previous studies have shown that cholera toxin could be recognized by G_{M1}-containing supported lipid membranes [14] and polymerized Langmuir-Blodgett films containing G_{M1} and a carbohydrate 'promotor' lipid [9,15].

The ganglioside G_{M1} was mixed at 5 mole percent with the diacetylene 'matrix lipid' monomers, **2**. Liposomes were prepared using the probe sonication method and polymerized by UV irradiation (254 nm). The solid-state polymerization proceeds as a 1,4 addition controlled by the packing of the monomers (scheme 1).
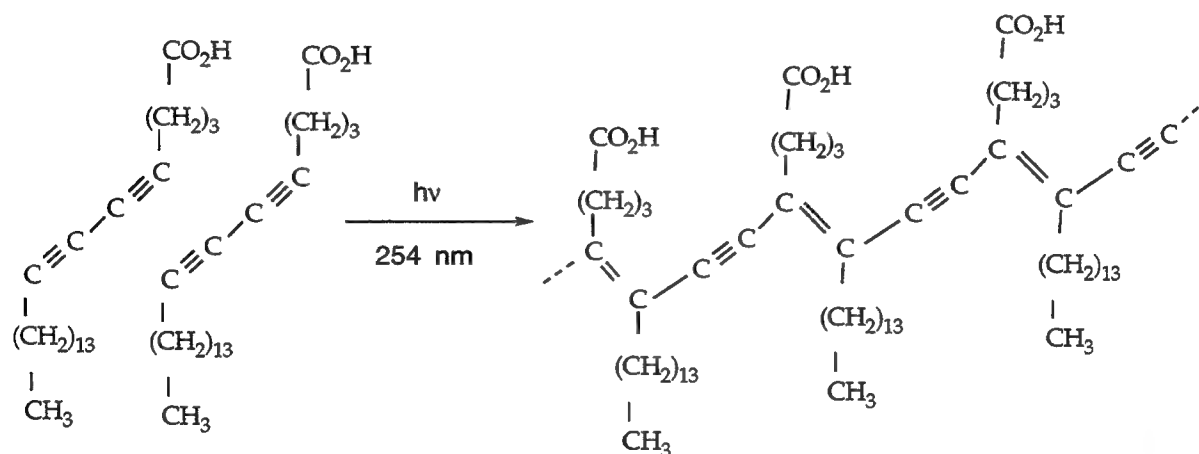

Scheme 1. Polymerization of lipophilic diacetylene monomers by UV irradiation. The reaction proceeds as a 1,4 addition.

The time course of the polymerization is shown in Figure 1. The visible absorption arises from the conjugated ene-yne system that comprises the polymer backbone. (The monomer absorption occurs at wavelengths less than 300 nm). The absorption intensity increases with the UV irradiation time and nearly saturates after a total energy dose of 7.2 J/cm^2. The absorption peak at 620 nm is designated as the PDA

blue form [16]. The appearance of the colored polymer provides a sensitive and simple test of molecular order in the self-assembled nanostructure. 'Looser' structures such as micelles would not form the conjugated polymer due to the topochemical nature of the polymerization reaction. The formation of liposomes in sonicated samples of amphiphilic diacetylenes has been previously demonstrated by electron microscopy [17,18]. Transmission electron microscopy of the liposomes composed of 5% G_{M1} and 95% 2 indicate an oblong shape with a mean length of 600nm.

The conjugated ene-yne backbone of polydiacetylene liposomes results in the appearance of a deep blue/purple solution [19,20]. The visible absorption spectrum of the freshly prepared purple liposomes is shown in Figure 2A. The spectrum can be analyzed by determining the initial percentage of blue phase (%B) in the preparation by comparing the intensity of the peak at 620 nm to the red absorption maxima at 490nm. Typically, %B $\approx$ 50 for the initial liposome preparation. When cholera toxin is added to the liposomes composed of 5% G_{M1} and 95% 2, the solution immediately changes to an orange color, and the 'red phase' absorption of polydiacetylene dominates, Figure 2B with %B $\approx$18. The colorimetric response (%CR) is measured as the percent change in the absorption at 620 nm (blue phase polydiacetylene) relative to the total absorption maxima at 620nm and 490nm [21]. A positive response is obtained if the %CR is greater than 7%. These color changes are easily seen with the naked eye, particularly if the liposome solution is placed in a white 96-well microtiter plate. If the ganglioside GM1 was mixed with a matrix lipid composed of 10,12 pentacosadiynoic acid instead of 5,7 docosadiynoic acid, (2), the colorimetric response was significantly reduced. The enhanced sensitivity of the system composed of matrix lipid 2 most likely arises from the positioning of the optical reporter group nearer to the interface (three methylene units compared to eight). We have previously shown by FTIR spectroscopy that small rotations about the C-C bond β to the polymer backbone are sufficient to change the effective conjugated length [4]. These conformational changes are more easily transduced through shorter alkyl chain length.
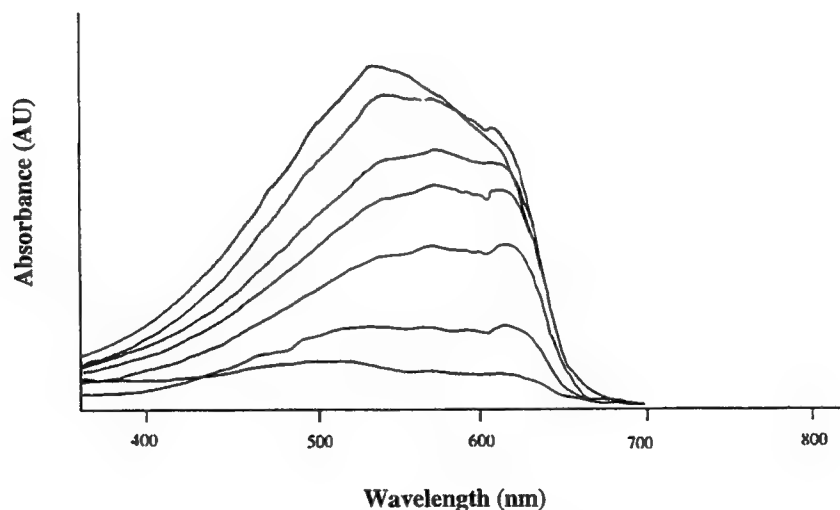
Figure 1. Visible absorption spectra of polydiacetylene liposomes composed of 5% GM1 ligand, 1, and 95 % matrix lipid, 2 as a function of UV irradiation time. The liposomes were exposed to a total energy dose of 7.2 J/cm². Each spectrum (in order of increasing absorption) corresponds to a dose of 0.8, 1.6, 2.4, 3.2, 4.0, 5.6 and 7.2 J/cm².

A negative response was observed if the ganglioside, G_{M1} ligand was removed from the liposomes (for example, for 233 ug/ml cholera toxin the %CR was ≈ 6 compared to ≈ 43 with the ganglioside present). Similarly, negative responses were obtained when comparable quantities of other proteins besides cholera toxin were added to the G_{M1}-containing liposomes. These include, human serum albumin, avidin and wheat germ agglutinin.

Kinetic experiments indicate that greater than 95 % of the color change occurs within the first two minutes of adding the toxin. The color transition is not an all or nothing effect but depends on the quantity of toxin titrated into the solution, Figure 3. The sigmoid behavior suggests cooperativity of the colorimetric transition. This may indicate that the binding itself is cooperative in the sense that binding of toxin to the G_{M1} ligand makes the binding of subsequent toxins more favorable. Alternatively this result might more appropriately be understood in terms of the lipid-polymer side chain conformation and its result on the effective conjugated length of the polydiacetylene backbone. Once the effective conjugated length is reduced as a result of toxin binding, subsequent perturbation of the remainder of the lipid-polymer backbone becomes more favorable. This might be explained as a reduced activation barrier of the blue to red conversion. Temperature-dependent studies of the blue to red transition induced by molecular recognition as well as by heat (thermochromism) may shed light on the relative energetics of the blue-red transition. In addition, the effects of liposome size and G_{M1} mole density on the absolute sensitivity of this approach will be examined.
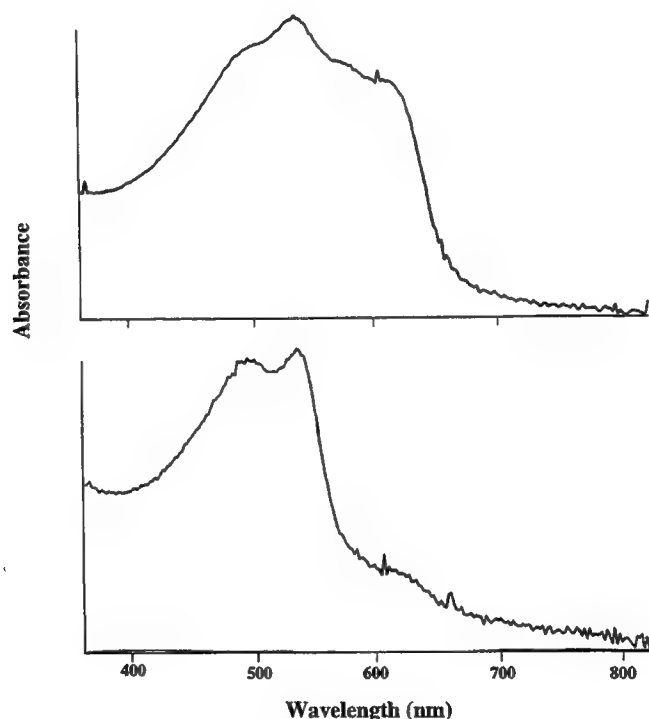
Figure 2. Colorimetric detection of cholera toxin by polymerized diacetylene liposomes (5% GM1 and 95% 2). (**A**) Visible absorption spectrum of blue/purple liposome solution prior to addition of cholera toxin. Liposomes were diluted in Tris buffer, pH 7.0 to a final concentration of 100 mM total lipid. (**B**) Visible absorption spectrum of liposomes after the addition of cholera toxin to a final concentration of 310 ug/ml. The incubation time with the liposomes was 2 minutes.

In summary, we have demonstrated that protein-ligand molecular recognition occurs at the interfacial region of polymerized liposomes and that molecular recognition can be directly linked to signal transduction. Such artificial membranes resemble the organization and functionalization of cell membranes but have the added benefit of a built-in synthetic 'trigger' that signals molecular recognition events by an easy to measure color change. Non-specific adsorption if it occurs, does not appear to effect the color of the liposome solutions. These preliminary results suggest that polymerized supramolecular assemblies may offer an alternative approach to investigating molecular recognition at tailored interfaces.
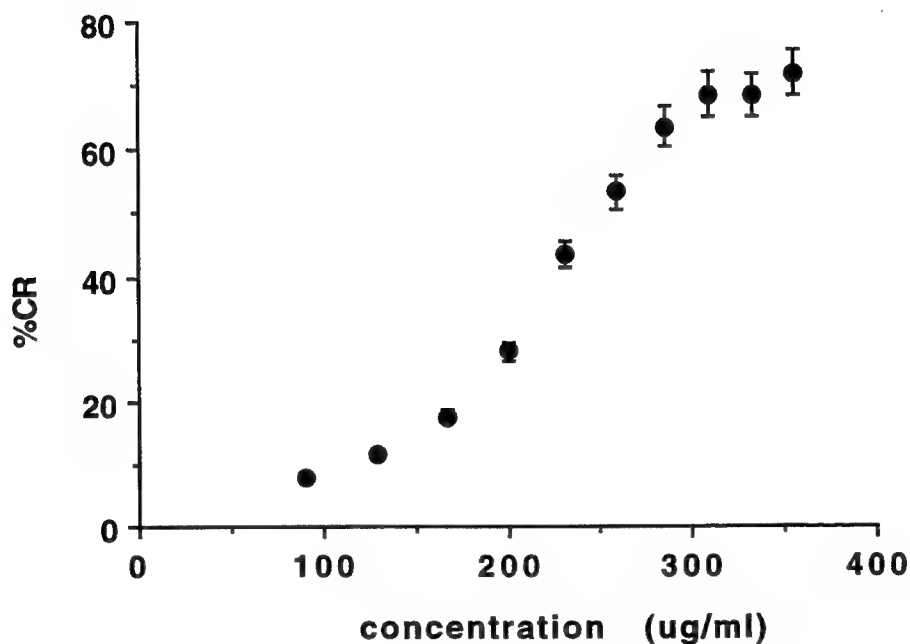
Figure 3. Colorimetric response (%CR) of polymerized liposomes (5% GM1 and 95% **2**) after successive additions of cholera toxin. The liposomes were incubated with toxin for 2 minutes after each addition and the spectrum recorded as in Figure 2. The %CR was calculated from the spectrum according to Footnote 21.

[1]Spevak, W.; Nagy, J.O.; Charych, D.H., *Adv. Mater.* **1995**, *7*, 85.

[2]Charych, D.H.; Nagy, J.O.; Spevak, W.; Bednarski, M.D. *Science* **1993**, *261*, 585.

[3]Reichert, A; Nagy, J.O.; Spevak, W.; Charych, D.; *J. Am. Chem. Soc.*, **1995**, *117*, 829.

[4]Berman, A; Ahn, D.J.; Reichert, A.; Lio, A.; Salmeron, M.; Charych, D., *Science*, **1995**, *259*, 515.

[5]Muller, W.; Ringsdorf, H.; Rump, E.; Wilburg, g.; Zhang, x.; Angermaier, L.; Knoll, W.; Liley, M.; Spinke, J., *Science,* **1993**, *262*, 1706.

[6]Chance, R.R.; Patel, G.N.; Witt, J.D., *J. Chem. Phys.*, **1979**, *71*, 206.

[7]Mino; N; Tamura, H.; Ogawa, K. *Langmuir* **1992**, *8*, 594.

[8]Nallicheri, R.A.; Rubner, M.F. *Macromolecules* **1991**, *24*, 517.

[9]Charych, DH, Cheng, J., Reichert, A., Kuziemko, G., Stroh, M., Nagy, J.O., Spevak, W., Stevens, R.C., *Chemistry and Biology*, **1996**, *3*, 113.

[10]New, R.R.C. In *Liposomes: A Practical Approach*; New, R.R.C., Ed.; Oxford University Press: Oxford, 1990; pp 33-104.

[11]Barua, B. *Cholera*, D. Barua and Greenough, W.B. III, Eds: Plenum, New York, 1992; pp. 1-36.

[12]Cuatrecasas, P., *Biochemistry*, **1973**, *12*, 3547.

[13]Fishman, P.H. *ADP-Robosylating Toxins and G-Proteins: Insight into Signal Transduction*; Moss, J., Vaughan, M., Eds.; American Society of Microbiology: Washington, DC, 1990.

[14]Terrettaz, S.; Stora, T.; Duschl, C.; Vogel, H., *Langmuir*, **1993**, *9*, 1361.

[15]Cheng, J.; Stevens, R.C., *Langmuir*, **1996**, in press.

[16]Chance, R.R. Baughman, R.H., Muller, H., Eckhardt, J.G., J. Chem. Phys., 1977, *67*, 3616.

[17]Hub, H.H., Hupfer, B., Koch, H., Rongsdorf, H., *Angew. Chem., Int. Ed. Engl.* **1980**, *19* 938.

[18]O'Brien, D.F., Whitesides, T.H., Klingbiel, R.T., *J. Polym. Sci., Polym. Lett. Ed.*, **1981**, *19*, 95.

[19]Day, D.; Ringsdorf, H., *J. Polym. Sci., Polym. Lett. Ed.*, **1978**, *16*, 205.

[20]Bader, H.; Ringsdorf, H., *J. Polym. Sci: Polym. Chem. Ed.*, **1982**, *20*, 1623.

[21]In order to quantify the response of a liposome solution to a given amount of toxin, the visible absorption spectrum of the liposome solution without the toxin was analyzed as:

$$B_o = I_{620}/(I_{620}+I_{490})$$

The same value was calculated for liposome solutions exposed to cholera toxin (B_{ct}). The colorimetric response (%CR) is defined as the percentage change in B upon exposure to toxin:

$$CR = [(B_o - B_{ct})/B_o] \times 100 \%$$

Synthesis of self-assembled photo-sensitive molecules in mesoporous silicates

*Itaru HONMA and #H-S.ZHOU

*Electrotechnical Laboratory, Energy Division, AIST, Umezono 1-1-4, Tsukuba, Ibaraki,305 Japan, e9513@etl.go.jp, tel: +81-298-58-5797, fax: +81-298-58-5805:   #Frontier Research Program, The Institute of Physical and Chemical Research (RIKEN), Hirosawa 2-1, Wako, Saitama, 351-01, Japan. tel: 048-462-1111 (ext6223),   fax: 048-466-2736

ABSTRACT

Self-assembled functional molecules in mesoporous materials are synthesized directly either by co-assembly of dye-bound surfactant of ferrocenyl TMA with silicate or Pc (phthalocyanine) molecules doped in the C_{16}TMA micelles with oxides framework such as V_2O_5, MoO_3, WO_3 and SiO_2. The process provides well-organized molecular dopoed mesoporous structure by direct and simple procedure.

INTRODUCTION

Mesoporous materials invented by scientists of the Mobil Corporation[1-3] have attracted considerable interest since the first announcement in 1992[4,5]. The formation mechanism of mesoporous materials designated as MCM products have been studied by many groups[6,7] and phase change behavior among lamellae, hexagonal and cubic are understood in terms of charge matching at the interface as well as a free energy argument in the organized organic/inorganic system[8]. The MCM products are widely synthesized in silica (SiO_2) framework and there are interests for extending other

oxides such as TiO_2[9], V_2O_5[10,13], WO_3[11,12,13], MoO_3[13], because their potential applicability to adsorbents and catalytic processes. Hexagonal tungsten, vanadium and titanium oxides have been successfully produced respectively, and other oxides mesophase were examined in Pb, Fe, Mn, Zn, Al, Co, Ni to form lamellae structure. Besides extending framework oxides to other class of transition oxides, it's quite attractive to investigate a novel process of mesoporous film formation. Attempts have been made for silica mesoporous film either on the substrate[14,15] or air-water[16] interface. Those films might be used for device's application as optical, electric and chemical sensors as well as membranes.

In this work, we have investigated to synthesize photo-sensitive mesoporous materials for optical device applications where the photo-absorbing dyes are doped in the mesochannels by direct self-organizing process of the surfactants, not by external doping after the calcination of the channel. If the synthetic path is found to dope functional molecules to mesochannels by self-organized co-assembly process, it will open a wide controllable design to produce functional mesoporous materials for optical application such as sensors or luminescent materials.

EXPERIMENT & RESULTS

In order to make self-assembled functional molecules in mesoporous materials, we have investigated two different methods for dye-doped MCM products. The first one is by using dye-bound surfactant ; Fe-TMA(11-ferrocenylundecylammonium bromide where the trimethylammonium surfactant has a ferrocenyl dye at the end of the tail. The other is by using C_{16}TMA (hexadecyltrimethylammonium chloride) and the Pc (phthalocyanine ($C_{32}H_{18}N_8$), phthalocyanine blue ($C_{32}H_{16}N_8Cu$)) molecules are doped in a co-assembly within a C_{16}TMA micelles. In the latter case, Pc molecules are, supposedly, self-assembled between the C_{16}TMA's hydrophobic tails and organized with a periodic array of the lipid micelle structures. The schematic diagram of the two new synthetic process are described in Figure 1. The Fe-TMA surfactant has a ferrocenyl ligand at the lipid tail and a distance of eleven carbons to trimethylammonium cation. The isolated molecules have an absorption band at 440 nm which is coloured to yellow. The latter case, C_{16}TMA as well as Fe-TMA was used to make Pc-doped MCM with various metal oxides framework where the doping ratio and the mesophase structure was changed by a combination of Pc-dyes and framework oxides.   In the first case, we have synthesized Fe-TMA-MCM in a similar way as an acidic synthesis of Silica MCM while C_{16}TMA was replaced by Fe-TMA. The molar ratio of the synthetic precursors were as follows; 1.0 TEOS : 9.0 HCl : 0.12 Fe-TMA : 130 H_2O, which is an exactly same molar ratio as a first acidic hexagonal silica MCM synthesis[17] as is shown in table 1.   In spite of the lower concentration of the surfactants, hexagonal phase were successfully produced and the products were colored (yellow green) by the surfactant's ferrocenyl ligands. Fig. 2 (a) shows a low angle XRD scan for Fe-TMA-MCM and the fundamental reflection pattern of the hexagonal mesophase was clearly observed. The d-spacing of the products was 37 A which is as twice long as the Fe-TMA surfactant and those are basically same products as silica MCM where lipid micelle forms the mesochannel structure. Slight shift of the molar ratio of surfactant to silicate was proved to result in the same hexagonal MCM products. Figure 2 (b) shows a transmission electron microscopy (TEM) photograph of the Fe-TMA-MCM and the hexagonal array of the mesoporous channels are clearly observed. As far as an eye-observation on the whole area of the low magnification view, only hexagonal phase was produced and other phase such as cubic or lamellae was not observed.

The result shows that the Fe-TMA surfactants can synthesize hexagonal mesophase in a similar way as silica MCM and this is a first complete synthesis of the mesoporous products through ferrocenyl surfactants. As a Fe-TMA surfactant carries ferrocenyl dye at the end of the lipid tail, the initial products possess an optical absorption band in a visible light wavelength region and those are colored in light green or yellow green. Figure 3 shows an absorption spectrum of Fe-TMA-MCM powders and two absorption band at 440 nm and 640 nm were clearly seen. The absorption at 440nm was ascribed to a reduced state of the ferrocenyl ligand of Fe-TMA and the one at 640 nm was an oxidized state. Because of the ferrocenyl dyes are incorporated in the channel by self-assembly process, the absorption of the products are coming from concentrated dyes at the channel's center. The absorption band of 440 nm is a reduced state and identical to the absorption of isolated Fe-TMA molecules in the solution, while the one at 640 nm is an oxidized state and the peak appeared by the reaction with air (oxygen) after the synthesis. As the products are exposed to air at ambient temperature, the absorption intensity of 640 nm
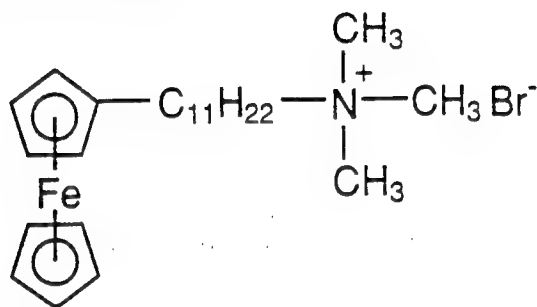
Self-assembled synthesis of dye -doped MCM

1. Fe-TMA (Ferrocenyl TMA)
    11-Ferrocenyltrimethylundecylammonium bromide
    Dye-bound surfactant
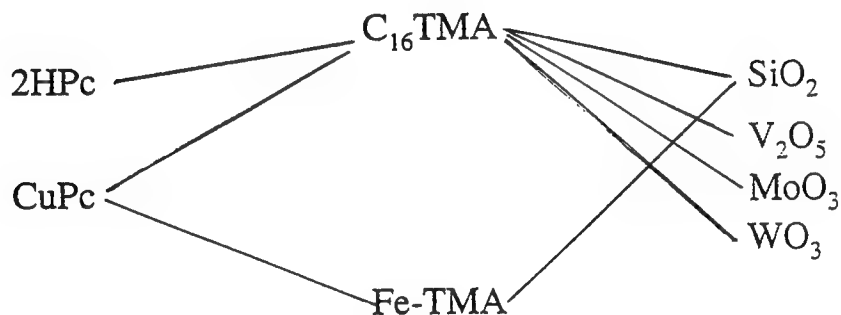

2. C_{16}TMA
    Pc-doped in the micelle

Figure 1. Two different ways of self-assembled synthesis of Pc-doped MCM. The former is by using Fe-TMA surfactants and the latter is by using C_{16}TMA surfactants.

Fe-TMA-MCM

	weight	molar ratio	SiO₂ MCM*
Fe-TMA	: 0.12 g	(0.12)	C_{16}TMA
TEOS	: 0.45 g	(1.0)	TEOS
H₂O	: 5.00 g	(130)	H_2O
HCl (35%)	: 2.00 g	(9)	HCl

Table 1   The synthetic condition for Fe-TMA-MCM. The molar ratio is as same as an acidic synthesis of Silica MCM.
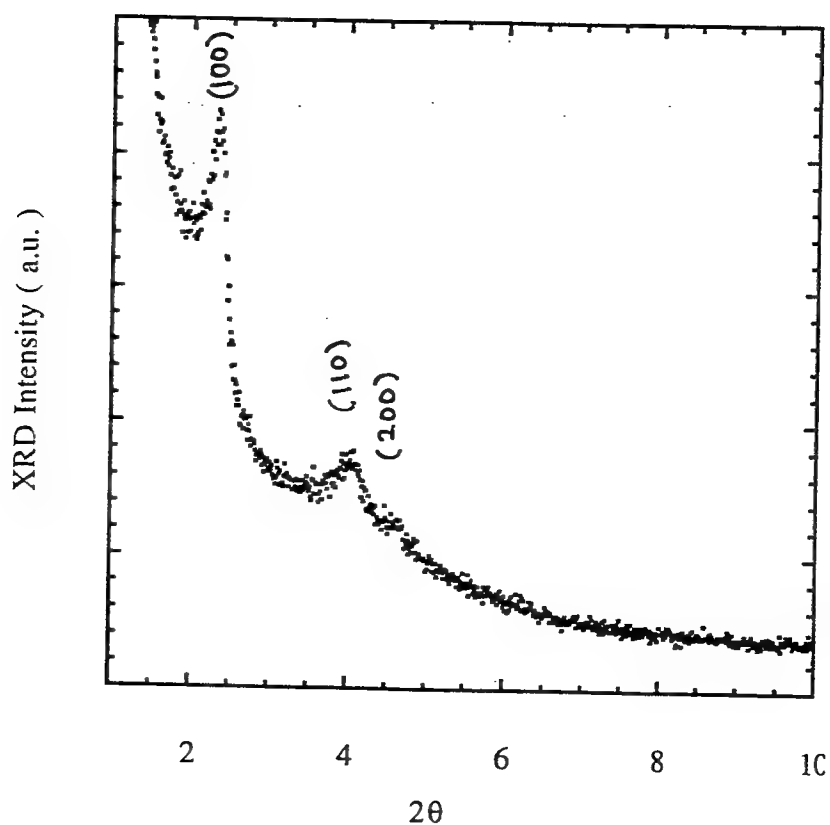
Fig.2(a) Low angle XRD spectrum for Fe-TMA-MCM
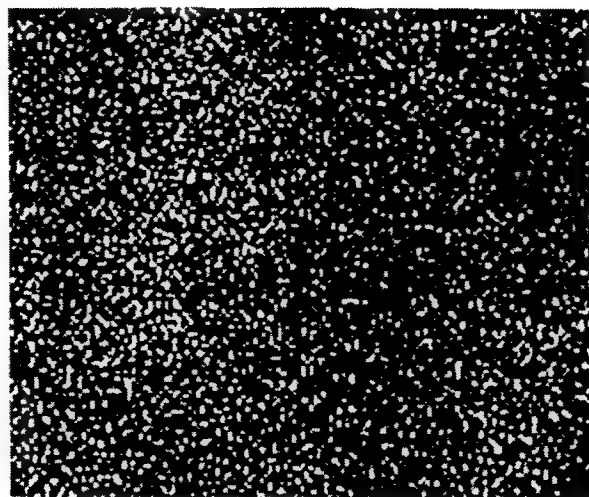
Fig.2(b)   Transmission electron micrograph
for Fe-TMA-MCM
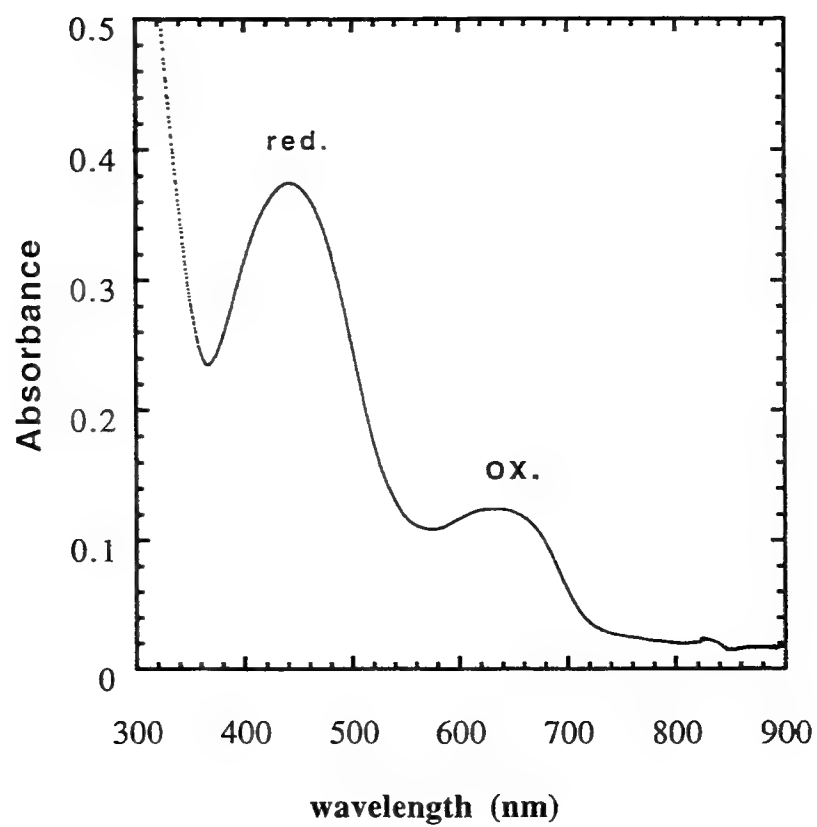
Fig. 3 Optical absorption spectrum for
Fe-TMA-MCM

increases with time. In this new process, it is not necessary to dope molecules into mesoporous channels after the pore become open by calcination. The process provides economic and more efficient way to dope heavily in the mesochannels. The molar ratio of ferrocenyl dye to silica is as high as 12% which is higher doping ratio than other conventional method to silicate materials.

The second method to make self-assembled molecules in a mesoporous materials is by mixing dye molecules among the surfactant's hydrophobic tails where the dye molecules are inserted in a periodic manner within a mesoporous channels, which are basically similar system to chloroplast in the natural plants. In the present work, We have chosen Pc (phthalocyanine ($C_{32}H_{18}N_8$), phthalocyanine blue ($C_{32}H_{16}N_8Cu$)) molecules as dopants and metal oxides of V_2O_5, WO_3, MoO_3, PbO, and SiO_2 as mesoporous framework. The synthetic procedures of Pc-doped MCM by C16TMA and Pc are schematically drawn in figure 4. For example, in Pc-doped V_2O_5 MCM case, the process is as follows; the ammoniumvanadate (NH_4VO_3) ; 1.0 g, was first dissolved in a aqueous water (18g) with an addition of amount of NaOH (1.2g) to be solvated completely. And the C_{16}TMA (0.54g) are dissolved in the above solution with no precipitation at this high pH condition. And, the various amount of Pc (0.043g - 0.34g) were added to the above solution and stirred for 1 hour. Surprisingly, the Pc molecules were solvated quite well in the surfactant solution, which becomes completely blue because of the Pc molecules are isolated within the surfactant micelles. In the present experiment, the molar ratio of Pc to C_{16}TMA was changed from 0.0 to 1/2.5, so that, in heavy doping case, Pc are inserted in every several surfactant molecules. After stirring Pc/C_{16}TMA solution, HCl (5N) are added drop wise to gradually decrease a solution pH to around 1.0. As HCl adding, vanadium oxides start precipitating at the surface of the micelle and mesoporous vanadium oxides with Pc molecules doped in the mesochannel were made. Similarly, Pc-doped WO_3-MCM as well as Pc-doped MoO_3-MCM were produced; the ammonium tungstate para pentahydrate ($(NH_4)_{16}W_{12}O_{41}5H_2O$) were dissolved in water with C_{16}TMA at high pH and Pc were well solvated in the above surfactant solution with stirring. The WO_3-MCM was formed by a drop wise addition of HCl and green-blue colored Pc-doped MCM powder was precipitated. In the case of Pc-MoO_3-MCM, ammonium phosphomolybdate trihydrate ($(NH_4)_3PO_4$ $12MoO_3$ $3H_2O$) was used as a precursor chemical for the MCM products. In silica (SiO_2) case, Pc was first dissolved in the C_{16}TMA surfactant solution at low pH (acidic) condition and TEOS (tetraethoxysilane) was added to precipitate Pc-doped MCM powders. The molar ratio of Pc to C_{16}TMA was changed from 0 to 1/2.5 and the products were characterized by TEM, low angle XRD and optical absorption measurements. The change of d-spacing as well as mesophase structure induced by the Pc-doping was examined.

Figure 5 (a) shows a low angle XRD (LAXRD) scan for Pc-doped V_2O_5 MCM with a variation of Pc-doping ratios. LAXRD of the pure V_2O_5 MCM was also shown in the figure. The as-prepared V_2O_5 MCM products are amorphous mesostructure which is confirmed by a broad fundamental reflection at about 2.5 - 3.0 degree[10,13]. The amorphous structure in this case means that the material has a mesoporous structure but the pores are not regularly arranged, not forming crystalline symmetry of the mesoporous chammels. Supposedly, the V_2O_5 primarily building unit of Keggin salts is a crystal

Pc-doped V_2O_5 MCM   synthesis

Pc/C_{16}TMA (molar ratio)	0	1/20	1/10	1/5	1/2.5
Pc	0.0 g	0.043 g	0.085 g	0.17 g	0.34 g
C_{16}TMA	0.54 g	0.54 g	0.54 g	0.54 g	0.54 g
NH_4VO_3	1.0 g	1.0 g	1.0 g	1.0 g	1.0 g
H_2O	18 g	18 g	18 g	18 g	18 g

Synthetic process

NH_4VO_3
$((NH_4)_3PO_412WO_33H_2O,$
$(NH_4)_3PO_412MoO_33H_2O)$

C_{16}TMA
NaOH
H_2O

C_{16}TMA
Pc
H_2O
HCl

stirring

Pc (in micelle)

TEOS

HCl addition

Pc-doped MCM

Pc-doped MCM

Characterization

Characterization
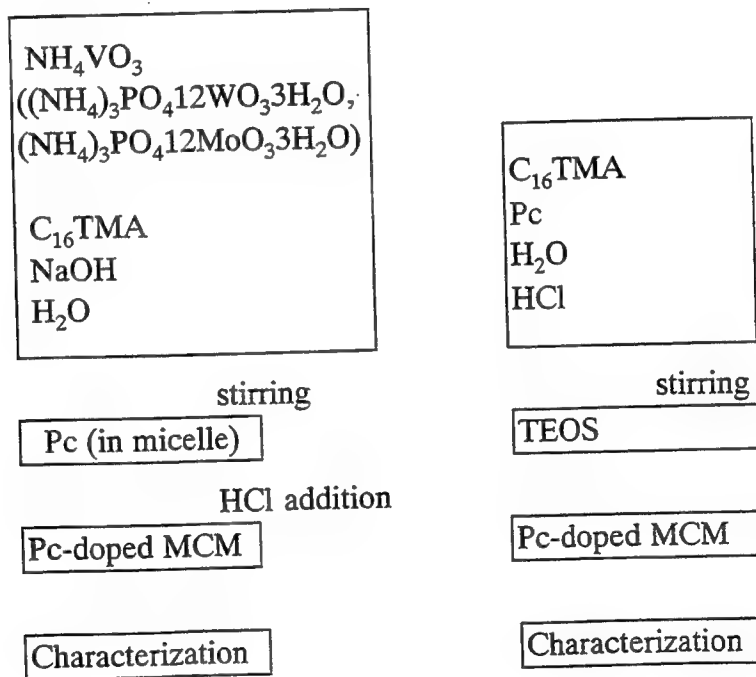
Fig. 4   Various synthetic procedure pathways for Pc-doped MCM

224
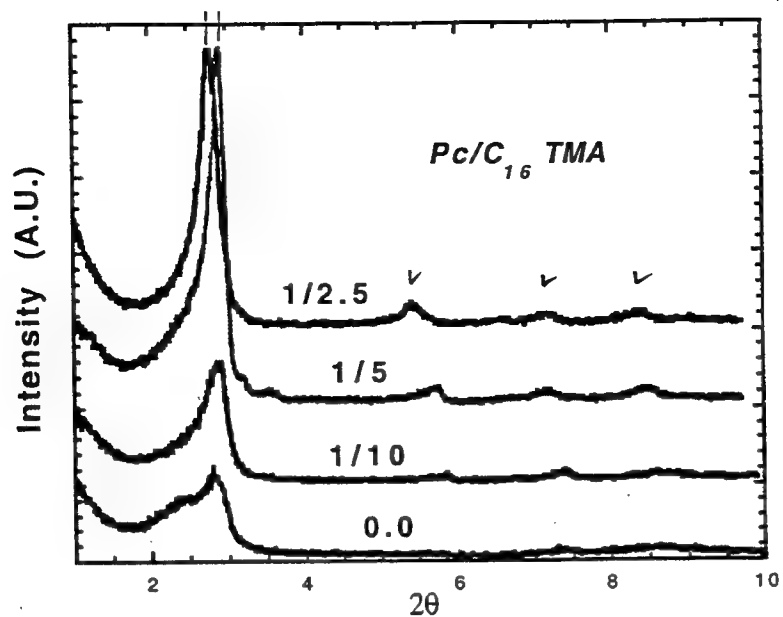
Fig. 5 (a)   Low angle XRD spectra for
Pc-doped V_2O_5 MCM
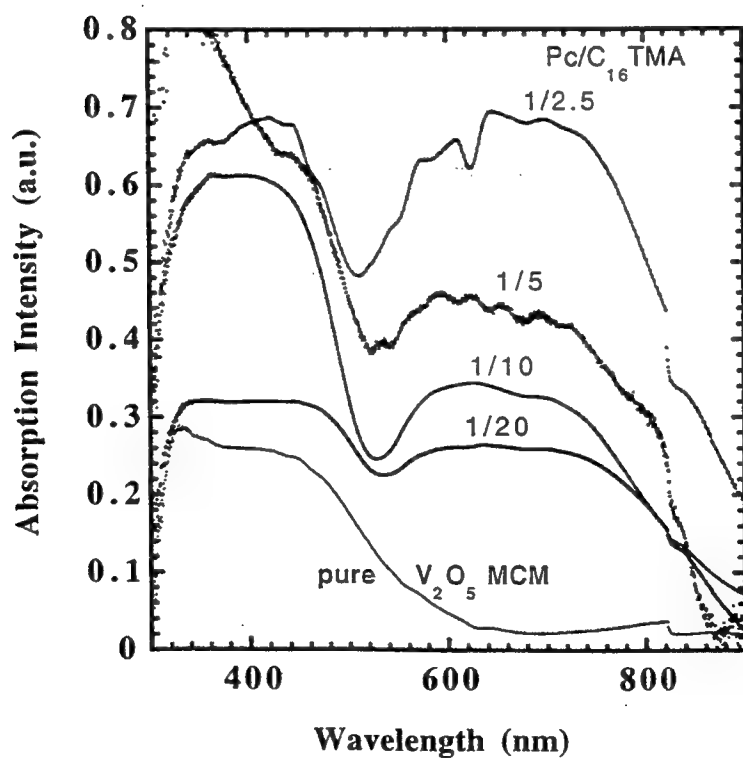
Fig.5 (b) Optical absorption spectra for
Pc-doped V_2O_5 MCM

structure so that it is not possible to form directly hexagonal or cubic phase which have curved interior surfaces of the mesochannel walls, although, in the SiO_2 case, easy by the flexibility of the random amorphous network of the silica. Supposedly, because of the insersion of Pc modify the channel structure and the metal oxides unit can be arranged to have proper position to form a crystalline mesophase, Phase stability changed by the Pc-insersion. In V_2O_5 case, as a Pc-doping ratio increases, the phase becomes unstable, especially, at the $Pc/C_{16}TMA$ ratio of around 1/20 where the initial amorphous structure changes and the pattern shifts by minor experimental conditions. And further increase of the Pc-doping makes a MCM structure stable and a crystalline mesophase appeared that is different from the initial amorphous phase. In other words, the insertion of Pc molecules in the mesochannel stabilizes a crystalline phase possibly because of the modification of the channel wall shape. It is also observed that the peak position of the fundamental reflection of the mesophase shifts toward low angle with the Pc doping, i.e., the d-spacing of the V_2O_5 MCM becomes larger slightly by the expansion of the mesochannel. The d-spacing is 30.55A at Pc/C16TMA ratio of 1/5, shifts to 31.87A at the ratio of 1/2.5. Although there is a small expansion from the pure V_2O_5 MCM to Pc-doped MCM, the main peak position does not change significantly, which indicates that the Pc molecules are doped, perhaps, in between the surfactants hydrophobic tails of the lipid micelle, not in the center position of the micelle as in the expander molecules of trimethylbenzene (TMB)[7]. Pc molecules inserted between the surfactant expand slightly the channel size, at the same time, stabilize the vanadium oxides framework. Figure 5 (b) shows an optical absorption data for Pc-doped V_2O_5 MCM and the absorption from the doped Pc was clearly seen. The powder is green and as the doping ratio increases, the absorption intensity increases with the doping. The absorption at short wavelength region is coming from the V_2O_5 framework. We have investigated structures of Pc-doped MoO_3-MCM. The doped MoO_3 mesoporous structure was made in a similar way as a V_2O_5-MCM. Figure 6 (a) shows a low angle XRD scan of Pc-doped MoO_3 -MCM with a variation of the Pc-doping molar ratio ($Pc/C_{16}TMA$) from 0.0 (pure MoO_3 MCM) to 1/2.5. In this materials, the mesostructure was amorphous, lacking in crystalline symmetry of the channels' array, throughout the whole Pc-doping ratio with a broad scattering between 2 and 9 degree, which is quite different from the V_2O_5-MCM. In this case, the incorporated Pc molecules does not act as stabilizer molecules for the crystalline hexagonal phase. In the amorphous phase, the average pore spacing derived by LAXRD was not changed so much by Pc-doping and ,at the same time, the randomness structure was not changed. The difference is presumably comes from a shape difference of the primarily oxides building units. Figure 6 (b) shows absorption spectra of the doped MoO_3-MCM and the absorption of Pc was observed through a transparent MoO_3 framework from 500nm to 900nm wavelength region. As the doping ratio increases, the absorption intensity increases without a shift of the spectra's shape. Additionally, Pc-doped SiO_2-MCM was successfully synthesized and the hexagonal mesophase was retained for high Pc doping condition and optical absorption spectra of the doped phase was similar to those of other oxides. The results of LAXRD and optical absorption of Pc(blue, Cu)-doped SiO2 MCM were shown in figure 7 (a) and (b). The differences from V_2O_5 and MoO_3 MCM were clear and we are continuously investigating the mechanism of formation in the doped mesostructure materials.
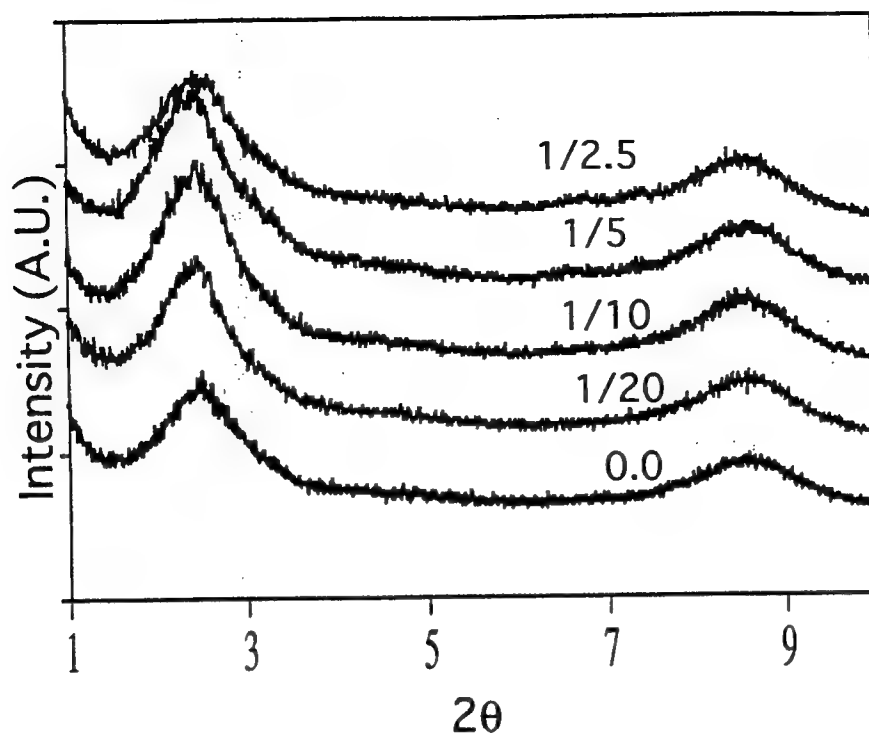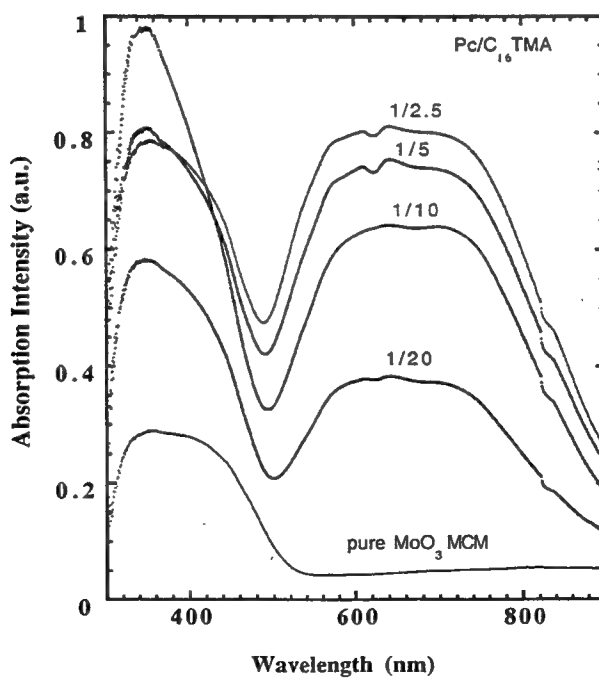
Fig. 6 (a) Low angle XRD spectra for
Pc-doped MoO_3 MCM

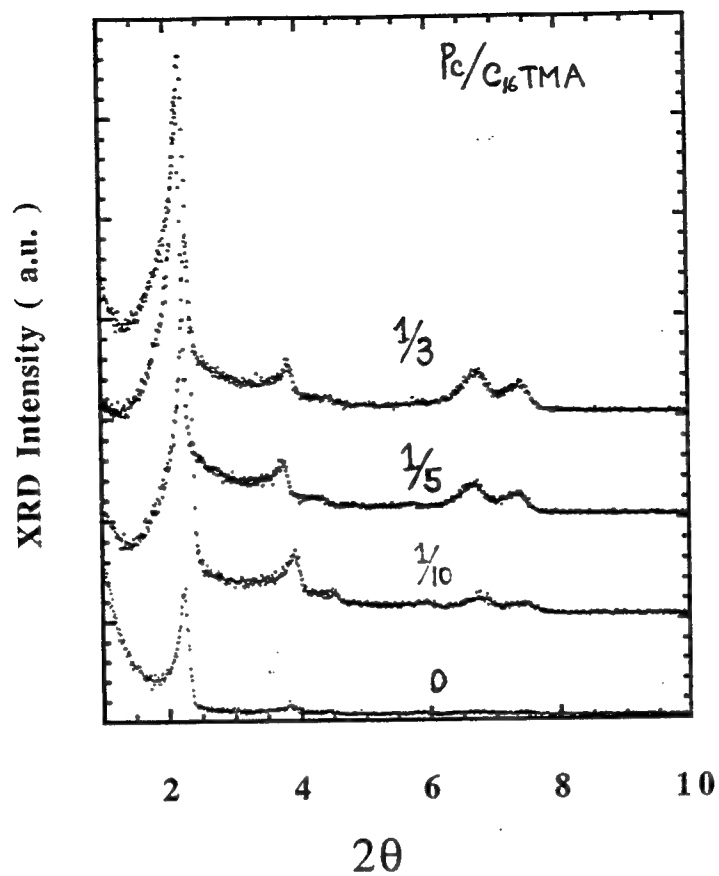

Fig. 6 (b) Optical absorption spectra for
Pc-doped MoO_3 MCM

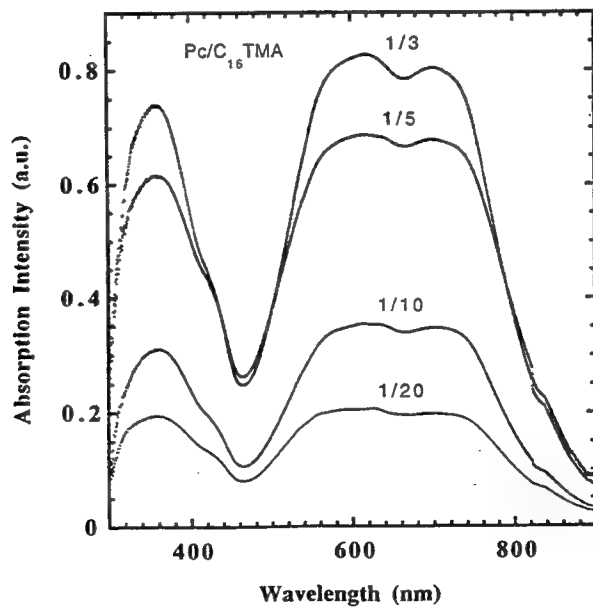Fig. 7 (a) Low angle XRD spectra for Pc(Cu)-doped SiO_2 MCM

Fig. 7 (b) Optical absorption spectra for Pc(Cu)-doped MoO_3 MCM

CONCLUSIONS

We have successfully synthesized Pc-doped metal oxides mesoporous materials in a V_2O_5, MoO_3, WO_3 and SiO_2 framework materials as well as a direct synthesis of dye-doped MCM through a co-assembly of ferrocenyl TMA surfactants . There is a different role of the doping Pc to the host mesophase; in V_2O_5 case, Pc plays a stabilizing agent for crystalline mesoporous phase, i.e., amorphous phase of the pure V_2O_5 MCM transforms to crystalline phase with the doping, although, in the MoO_3-MCM case, the amorphous phase remains by the doping. However, Pc-doped SiO_2-MCM was successfully made to be a hexagonal phase.

REFERENCES

1. J.S.Beck, US Pat., **5** 507 296, (1991)
2. C.T.Kresge,M.E.Leonowicz,W.J.Roth and J.C.Vartuli, US Pat.,**5** 098 684,(1992)
3. J.S. Beck et al., US Pat., **5** 108 725, (1992)
4. C.T.Kresge, M.E.Leonowicz, J.C.Vartuli and J.S. Beck, Nature, **359**, 710 (1992)
5. J. S. Beck et al., J. Am. Chem. Soc., **114**, 10834 (1992)
6. A. Monnier et al., Science, **261**, 1299 (1993)
7. A. Firouzi et al., Science, **267**, 1138 (1995)
8. Q. Huo et al., Chem. Mater., **6**, 1176 (1994)
9. D.M.Antonelli and J.Y.Ying, Angew. Chem. Int. Ed. Engl., **34**, 2014 (1995)
10. V. Luca et al., Chem. mater. , **7**, 2220 (1995)
11. A.Stein et al., Chem. Mater., **7**, 304 (1995)
12. U. Ciesla et al., J. Chem. Soc. Commun., 1387 (1994)
13. G.G.Janauer et al., Chem. Mater., **8**, 2096 (1996)
14. I.A.Aksay et al., Science, **273**, 892 (1996)
15. H. Yang et al., Nature, **381**, 589 (1996)
16. H. Yang et al., Nature, **381**, 589 (1996)
17. Q. Huo et al., Nature, 368, 317 (1994)

Structural design for dynamic loading using a biomimetic approach

R.Wardle*and G.R.Tomlinson[†]
Dynamics Research Group,
Department of Mechanical Engineering,
University of Sheffield,
Mappin Street,
Sheffield S1 3JD
United Kingdom

ABSTRACT

A common method of reducing vibration levels in structures is to coat the surfaces of the structure with a layer of viscoelastic material which dissipates the elastic strain energy induced by the dynamic loading. The passive damping material is placed in areas of high strain energy to extract as much energy as possible from the structure, but the exact location of the material can tend to be arbitrary. A more systematic approach is demonstrated which uses an evolutionary method which allows viscoelastic surface coatings to be gradually built up until the required damping is achieved. In this way the material can be placed in a more efficient manner, and it is proposed that this leads to a better damping performance.

Keywords: shape optimisation, topology optimisation, viscoelastic, passive damping, biomimetics, cellular automata.

1   INTRODUCTION

The optimisation of structural geometries and materials is an active area of engineering research. While optimisation for statically loaded structures has enjoyed much attention, the optimisation of dynamically loaded structures is a less well-developed field, in part due to the many possible approaches. Some attempts at geometry optimisation for dynamically loaded structures are reported by Xie and Steven[8,9]. Lumsdaine and Scott[3] studied the optimisation of viscoelastic damping layers and give a brief review of damping layer optimisation in general. Gordon and Hollkamp[2] investigated the optimisation of damping characteristics through the use of viscoelastic damping in cavities in a blade structure.

A novel approach to the problem of optimisation is to consider the structure to be a 'biological system' which responds to the undesirable symptoms of loading, such as large strain energies, by 'growing' some additional structure or changing the mechanical properties of the existing structure in order to reduce the effects of the loading. The benefits of adding extra material are often balanced against the resulting additional mass.

This paper reports an investigation into the application of the 'biological' or evolutionary approach to dynamics

*e-mail: r.wardle@sheffield.ac.uk
†e-mail: g.tomlinson@sheffield.ac.uk

problems. The specific optimisation technique is the addition of free-layer viscoelastic damping and extends work carried out in a previous paper by the same authors.[7] The vibration of a cantilever beam, modelled using a finite element package, was reduced by the addition of a viscoelastic covering of the free-layer type. The layer was evolved on the surface of the beam through a cellular automata 'growing' algorithm which used the state of the surface strain energy field and the presence of existing viscoelastic to produce new viscoelastic material.

2 VISCOELASTIC DAMPING

2.1 Review of viscoelastic material behaviour

We will briefly review the assumptions made in the use of modelling of viscoelastic materials. A comprehensive introduction to the theory of viscoelastic materials can be found in Tschoegl's book.[6] Viscoelastic materials exhibit behaviour which is partly elastic and partly fluid or viscous, making them suitable materials for the dissipation of mechanical energy. We assume an element of viscoelastic material to be linearly elastic and subject to a harmonic excitation. Then the stress and strain in the material for unidirectional loading is given by

$$\sigma_{ij} = \hat{\sigma}_{ij} \sin(\psi) \; ; \; i,j = 1,2,3 \tag{1}$$

$$\varepsilon_{ij} = \hat{\varepsilon}_{ij} \sin(\psi - \phi) \; ; \; i,j = 1,2,3 \tag{2}$$

where the strain lags the stress by some angle ϕ, $\hat{\varepsilon}$ is the maximum strain and $\hat{\sigma}$ is the maximum stress. The quantities σ_{ij} and ε_{ij} are the stress and strain tensors indexed in the usual way by the suffices i and j. The *complex elastic modulus*, E^*, is defined as

$$E^* = \frac{\sigma_{ii}}{\varepsilon_{ii}} = \frac{\hat{\sigma}_{ii}}{\hat{\varepsilon}_{ii}} \cos\phi + i \frac{\hat{\sigma}_{ii}}{\hat{\varepsilon}_{ii}} \sin\phi \; ; \; i = 1,2,3 \tag{3}$$

$$\Rightarrow E^* = E' + i E'' \tag{4}$$

E' is the *storage* or *elastic* modulus, E'' is the *imaginary* or *loss* modulus, and the ratio $\eta = \frac{E''}{E'} = \tan\phi$ is called the *loss factor* (the difference between the use of i as an index and the use of i to represent $\sqrt{-1}$ is evident). In a similar way, the *complex shear modulus* is defined as $G^* = G' + i G''$. Both moduli are assumed to be homogeneous and isotropic.

The energy dissipated per volume of viscoelastic over a cycle due to the internal damping force, $F_d(x)$, is given by

$$W_d = \oint F_d(x) \, dx \tag{5}$$

which reduces to

$$\widehat{W}_d^{ii} = \oint \sigma_{ii} \, d\varepsilon_{ii} = \pi E' \eta \hat{\varepsilon}_{ii}^2 \; ; \; i = 1,2,3 \tag{6}$$

Similarly, the energy dissipated per unit volume per cycle for a cyclic shear loading can be shown to be

$$\widehat{W}_d^{ij} = \pi G' \eta \hat{\varepsilon}_{ij}^2 \; ; \; i = 1,2,3 \; ; \; j = 1,2,3 \; ; \; i \neq j \; ; \; \widehat{W}_d^{ij} = \widehat{W}_d^{ji} \tag{7}$$

The magnitude of the dissipated energy can be seen to be proportional to the maximum strain energy density in the material, giving the following relationships;

$$\widehat{W}_d^{ii} = 2\pi\eta U^{ii} \; ; \; i = 1,2,3 \tag{8}$$

$$U^{ii} = \frac{1}{2} E' \hat{\varepsilon}_{ii}^2 \tag{9}$$

$$\widehat{W}_d^{ij} = 2\pi\eta U^{ij} \; ; \; i = 1,2,3 \; ; \; j = 1,2,3 \; ; \; i \neq j \; ; \; \widehat{W}_d^{ij} = \widehat{W}_d^{ji} \tag{10}$$

$$U^{ij} = \frac{1}{2} G' \hat{\varepsilon}_{ij}^2 \tag{11}$$

2.2 Optimal placement of viscoelastic material for damping

In the previous section we saw how the energy dissipated in a viscoelastic is proportional to the square of the peak strain experienced by the viscoelastic under cyclic loading. In considering the optimum layout problem for free-layer damping we require a measure or indicator of the best sites for damping location. To construct this measure we must make some assumptions about the behaviour of the viscoelastic material in the free-layer treatment. If we examine an elemental piece of the free-layer, it can be seen to be forced on one face, is free on the opposite face and is partially constrained on the other four faces. If we assume that the sides of the element perpendicular to the forced surface remain perpendicular, then the element is subjected to two-dimensional extensional and shear strain only. This strain is produced by the deformation of the base structure under load, and shear introduced by bending is not considered. The viscoelastic is thus subject solely to direct strains ε_{11} and ε_{22}, and the shear strain ε_{12}. We also assume that the viscoelastic has negligible effect on the base structure, i.e. the strain on the base structure drives the strain in the viscoelastic. Hence, the peak strain energy density in the viscoelastic element under cyclic loading will be

$$\widehat{U} = \frac{1}{2} \left(E' \, \hat{\varepsilon}_{11}^2 + E' \, \hat{\varepsilon}_{22}^2 + G' \, \hat{\varepsilon}_{12}^2 \right) \tag{12}$$

A well-known relationship between the elastic modulus, E, the bulk modulus, B, and the shear modulus, G, is

$$E = \frac{9BG}{3B + G} \tag{13}$$

Elastomers are considered to be practically incompressible, a condition of the material which dictates $B \gg G$ (and also that Poisson's ratio, $\nu = 0.5$), which reduces the relationship between the elastic modulus and the shear modulus to

$$E = 3G \tag{14}$$

and hence we can write the total strain energy density as

$$\widehat{U} = \frac{1}{2} E' \left(\hat{\varepsilon}_{11}^2 + \hat{\varepsilon}_{22}^2 + \frac{1}{3} \hat{\varepsilon}_{12}^2 \right) \tag{15}$$

or

$$\widehat{U} = \frac{1}{2} E' \, \mathcal{E} \; ; \; \mathcal{E} = \left(\hat{\varepsilon}_{11}^2 + \hat{\varepsilon}_{22}^2 + \frac{1}{3} \hat{\varepsilon}_{12}^2 \right) \tag{16}$$

The energy dissipated in the viscoelastic is related to $\widehat{U}$ by the expression $\widehat{W}_d = 2 \pi \eta \widehat{U}$. $\widehat{W}_d$ is thus proportional to $\mathcal{E}$, and we can use the quantity $\mathcal{E}$, which is a straightforward function of strain, as an indicator of the most suitable location for the viscoelastic damping material.

3 CANTILEVER BEAM MODEL

3.1 The model beam

A model cantilever beam (Figure 1) was available for the application of viscoelastic free-layer treatment. The cantilever was 635mm long, 127mm wide and 6.3mm thick, and was made of mild steel, exact composition unknown. For simulation purposes the mechanical material properties were taken to be: elastic modulus $E = 209 \times 10^9$ N/m^2, Poisson's ration $\nu = 0.3$, mass density $\rho = 7850$ kg/m^3. The evolution of the viscoelastic layer was based around a real model beam to allow for future experimental verification of results.

3.2 Finite element model

The addition of viscoelastic damping material to the beam using the evolutionary approach naturally had to be performed by simulation. The cantilever was modelled with finite elements. The finite element solver ABAQUS was used to perform the analyses. Two constraints on the mesh were necessary; the mesh on the top surface of the
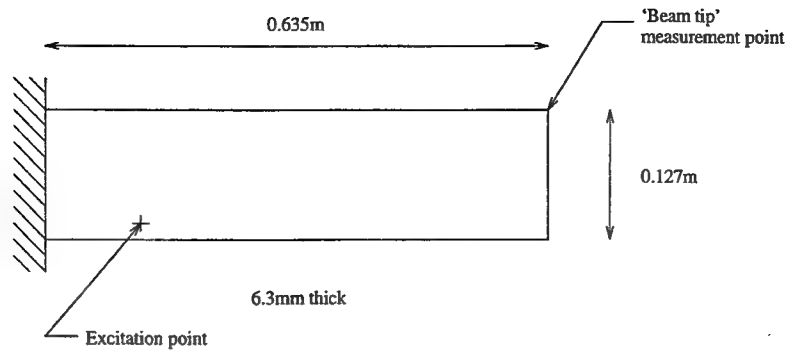
Figure 1: Cantilever beam model

Mode no.	Mode type	Frequencies (Hz)			Error
		Analytical	FE model	Actual	
1	Bending (z)	13.0	13.2	12.5	5.6%
2	Bending (z)	81.6	82.6	81.6	1.2%
3	Torsion	124.7	130	135.6	4.1%
4	Bending (z)	228.5	232	230.6	0.6%
5	Bending (y)	262.5	255	—	—
6	Torsion	374.1	397	408.1	2.7%
7	Bending (z)	447.8	455	446.9	1.8%
8	Torsion	623.4	686	703.8	2.5%
9	Bending (z)	740.3	754	735.6	2.5%

Table 1: Comparison of actual and calculated natural frequencies (all values in Hz)

cantilever had to be sufficiently dense to allow sensible 'growth' of the viscoelastic layer, and a relatively accurate measure of strain was required on this top surface. A mesh of 40 × 8 elements was adjudged to be sufficiently dense for the top surface, and produced square elements. The thickness of the beam was made up of two layers; a thick 'base' structure 5.7mm thick, and a thin top surface having a thickness of 0.6mm. This allowed the surface strains to be approximated by the thin surface element centroidal strains. This was additionally useful in that the element centroids were also the desired locations for the viscoelastic growth stimulus. Extrapolated nodal strains were found to be a) not appropriate locations for the growth stimulus, and b) not sufficiently accurate (particularly in direction) in regions of high strain and at the edges of the mesh.

A verification test was performed to identify the natural frequencies of the beam and compare them with the FE model and analytical formulations (see for example Blevins[1]) for the natural frequencies — the results of this test are shown in Table 1. Considering that the material properties were estimated for the model, this can be considered to be an adequate representation of the real cantilever.

4   EVOLUTION OF STRUCTURAL DAMPING

4.1   General Method

A viscoelastic damping covering of the free-layer type was to be evolved on the top surface of the cantilever plate. The surface was divided into a 40 × 8 cell lattice, which corresponded to the finite element mesh division on the top surface. The evolution of the viscoelastic was performed using a cellular automaton rule on the surface lattice — in fact two coincident lattices, one containing the surface strain energy values, the other a lattice of binary values with a
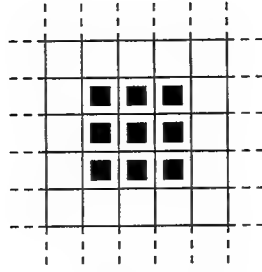
Figure 2: The Moore neighbourhood

'1' indicating the presence of viscoelastic. The automaton used a Moore neighbourhood (an area three cells by three cells on the lattice; see Figure 2). The neighbourhood of a given cell x^t is the set of all cells in the neighbourhood with respect to that cell x^t at iteration number t, denoted by $X^t(x)$. Thus in Figure 2, the centre shaded cell is the cell x^t and the set of all the shaded cells is the set $X^t(x)$. The measure $|X|$ is the number of cells in X; in the case of the Moore neighbourhood this is 9. The cellular automaton rule for the evolution of the viscoelastic is given in Equation 20; this, and the accompanying definitions are presented in compact form mostly for completeness, and the rule is explained more clearly in the following text.

$$I = \{1, \ldots, |X|\} \tag{17}$$

$$X^t(x) = \{x_1^t, x_2^t, \ldots, x_{|X|}^t\} \tag{18}$$

$$X^t(\mathcal{E}) = \{\mathcal{E}_1^t, \mathcal{E}_2^t, \ldots, \mathcal{E}_{|X|}^t\} \tag{19}$$

$$x^{t+1} = (x^t = \max(\{\neg X^t(x)_i \land X^t(\mathcal{E})_i \mid i \in I\})) \tag{20}$$

The rule described in Equation 20 is interpreted as follows. A viscoelastic element is 'grown' at a particular location or cell, x, on the surface if the strain energy measure, $\mathcal{E}$, for that cell is larger at this location than at any of the neighbouring locations specified by the neighbourhood of cells, X (Figure 2, with the cell in question the centre cell of the 9). It is assumed that the boundaries of the plate meet the condition $\mathcal{E} = 0$, so cells on the edges of the top surface always have a higher strain energy measure than the boundary. Neighbouring locations which have already 'grown' viscoelastic are assumed to have a $\mathcal{E}$ of zero (it can be imagined that they cease to register a strain signal once viscoelastic has been deposited). Hence, initial 'nucleation' sites with the largest local $\mathcal{E}$ start off the growth of viscoelastic, which then 'grows out' from these points to cover more of the plate. As a result, the viscoelastic is placed in areas of high strain energy first where it should dissipate more energy, only later in the evolution 'growing' where it is less likely to have significant effect.

4.2 Free-Layer Treatment

Free-layer damping was added to the cantilever using the cellular automaton described in the previous section. The viscoelastic was taken to be 5mm thick Viton E40/1839 fluorocarbon elastomer at 20°C (see the master curve, Figure 3), and was added as single 5mm thick elements onto the surface mesh (8x40 elements as stated above). The damping of the cantilever beam was modelled by assuming it to be made of a viscoelastic with $E' = 209 \times 10^9$ N/m^2 and $\eta = 0.01$.

A dynamic analysis of the cantilever beam was simulated using the finite element program ABAQUS. The beam was excited at a point 92.25mm along and 15.875mm from the edge of the beam (the cross point indicated in Figure 1, corresponding to a mesh node between the 6th and 7th elements along and the 1st and 2nd elements across the beam) by a 10N sinusoidal force perpendicular to the top surface of the beam; the force was deliberately offset from the longitudinal centre-line of the cantilever so that the torsional modes would be excited. In many practical applications, the forcing function does not act on individual modes but has some power spectrum over a moderately well-defined frequency range. A previous study[7] has looked at the effect of evolving viscoelastic on a structure excited
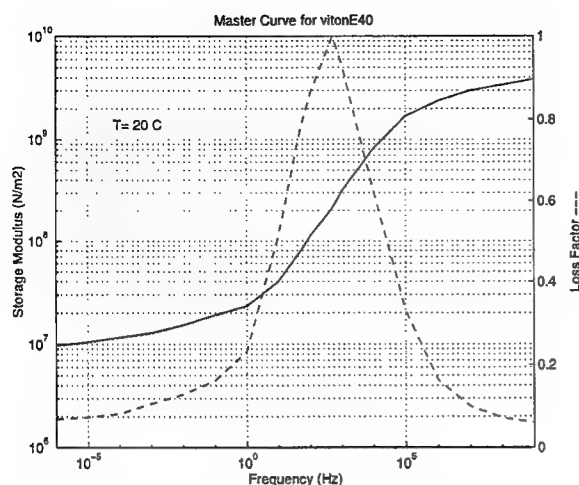
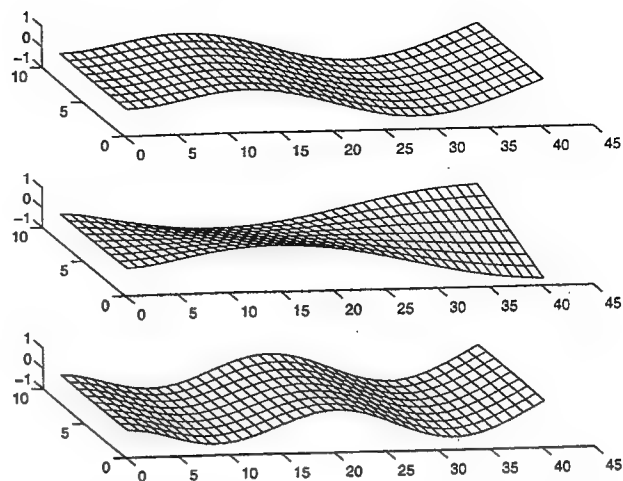Figure 3: Master curve for Viton E40/1839

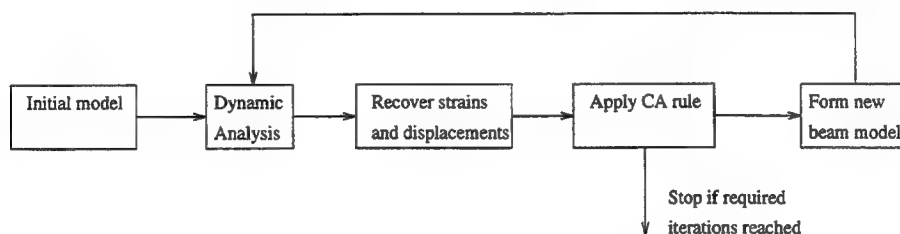
Figure 4: 4th, 6th and 7th modes of the cantilever

Figure 5: The evolutionary process

at a single resonant frequency; for the present study it was decided to excite a range of modes and to attempt to reduce the overall vibration in the given bandwidth. The exciting force was chosen as constant over a bandwidth of 200–500Hz, exciting the 4th, 6th and 7th modes of the cantilever (the 5th mode is a lateral vibration about an axis perpendicular to the large top surface of the beam, and is not excited by this force). See Figure 4. The beam was excited at 120 equally-spaced frequencies in this bandwidth using a direct integration forced-response method, and the strains and nodal displacements in the model recorded. The measure $\mathcal{E}$ used in the cellular automata was calculated as the sum of $\mathcal{E}$ over the excited frequencies.

The completion of the analysis for all 120 frequencies marked the end of an iteration and the calculation of the position of new viscoelastic material. The procedure was repeated for a total of 30 iterations, after which time the beam was almost totally covered with free-layer damping — see Figure 5 for a representation of the process as a flow chart.

The coverage of the viscoelastic damping layer was recorded at each step, along with the nodal displacements. The modal damping was calculated from the frequency response functions (FRFs) at both the forcing node and the tip of the beam furthest away from the forcing point on the top surface of the beam at each iteration point. In the absence of phase information the modal damping was estimated by fitting a rational polynomial to each mode, calculating the peak response, and calculating the half-power bandwidth from the half-power points of the fitted response curve. The presence of phase information would have allowed a linear model fit and direct extraction of the half-power bandwidths. The evolution of the modal damping in the model due to the progressive addition of free-layer damping is shown in Figure 6, where the cross symbols represent the loss factor estimated from the response at the excitation point, while the asterisks represent the loss factor estimated from the tip of the beam furthest from

	Mode 4		Mode 6		Mode 7	
	tip	load	tip	load	tip	load
η — No coverage	0.0110	0.0105	0.0106	0.0102	0.0105	0.0105
η — Total coverage	0.0161	0.0160	0.0163	0.0165	0.0185	0.0179

Table 2: Loss factors per mode for no and total viscoelastic coverage

the excitation point.

Due to the time limitations in conducting the simulation, the evolution was not carried out until the entire top surface of the beam was covered with viscoelastic, but was terminated after 30 iterations. The final modal damping values were, however, calculated extra to the evolution. These values are shown in Table 2. Figure 7 shows qualitatively the reduction in the response due to total coverage of the beam. Figures 8 to 14 show, at selected iteration points, how the viscoelastic 'grows' across the surface of the cantilever as the evolution progresses.

Some comment on these results is required. It may be noticed that some data appears to be missing from the plots in Figure 6; this is the result of occasional errors in the curve-fitting exercise which produced erroneous loss factor estimates, leading to the discarding of the data at those points. This in no way detracts from the overall demonstration of the results.

It can be seen that the evolutionary method reduces the vibration of the beam at all three modes simultaneously in the excitation region; the total vibration of the beam is reduced uniformly by the evolution. It is not clear whether the fluctuations in loss factor at mode 4 are real or an artifact of the loss factor estimation, and further investigation needs to be done. What is not clear from Figure 6 is whether the curves do in fact represent a upper limit of loss factor for a given mass of viscoelastic. It may be imagined that they do, given that the evolutionary method attempts to place the material in the most useful position on the beam, but some tests with arbitrarily placed material need to be conducted to verify this.

For reasons of space, only a selected few steps in the iteration are shown in Figures 8 to 14, but the spread of the viscoelastic can be readily seen. It is interesting to note the patches left uncovered as the evolution proceeds, which seem to correspond to areas of high curvature (and hence high surface strain energy) in mode 7 (Figure 4) — however, the magnitude of the mode 7 resonance is less than that of the other modes, and hence does not contribute as much to the overall strain energy in the excited frequency range.

5 CONCLUSIONS

In this speculative study it has been shown that a method of locating viscoelastic damping layers based on the idea of a biological 'stimulus-growth' model can produce free-layer layouts which qualitatively appear to represent 'good' use of the material, i.e. high energy dissipation for a given mass of viscoelastic. However, a number of questions remain.

In determining the growth measure $\mathcal{E}$, strain energy introduced by the bending of the elements was not considered. Further study should be undertaken to see whether this is significant or not.

The increase in loss factor over the iteration is relatively slight, although still significant. It is believed that the low increase in loss factor is due to the inherently low effectiveness of free-layer techniques when compared to constrained-layer or active methods. Free-layer techniques were used in this study to simplify some of the analysis, but further work may require consideration of constrained-layer methods. No attempt was made to optimise the thickness of the layer, a parameter which is known to have significant effects on the damping performance[3,4,5]. Also, no attempt was made to optimise the material, although the viscoelastic selected was found to be operating in the optimum range for energy dissipation. Finally, the inherent damping in the cantilever may have been over-estimated,
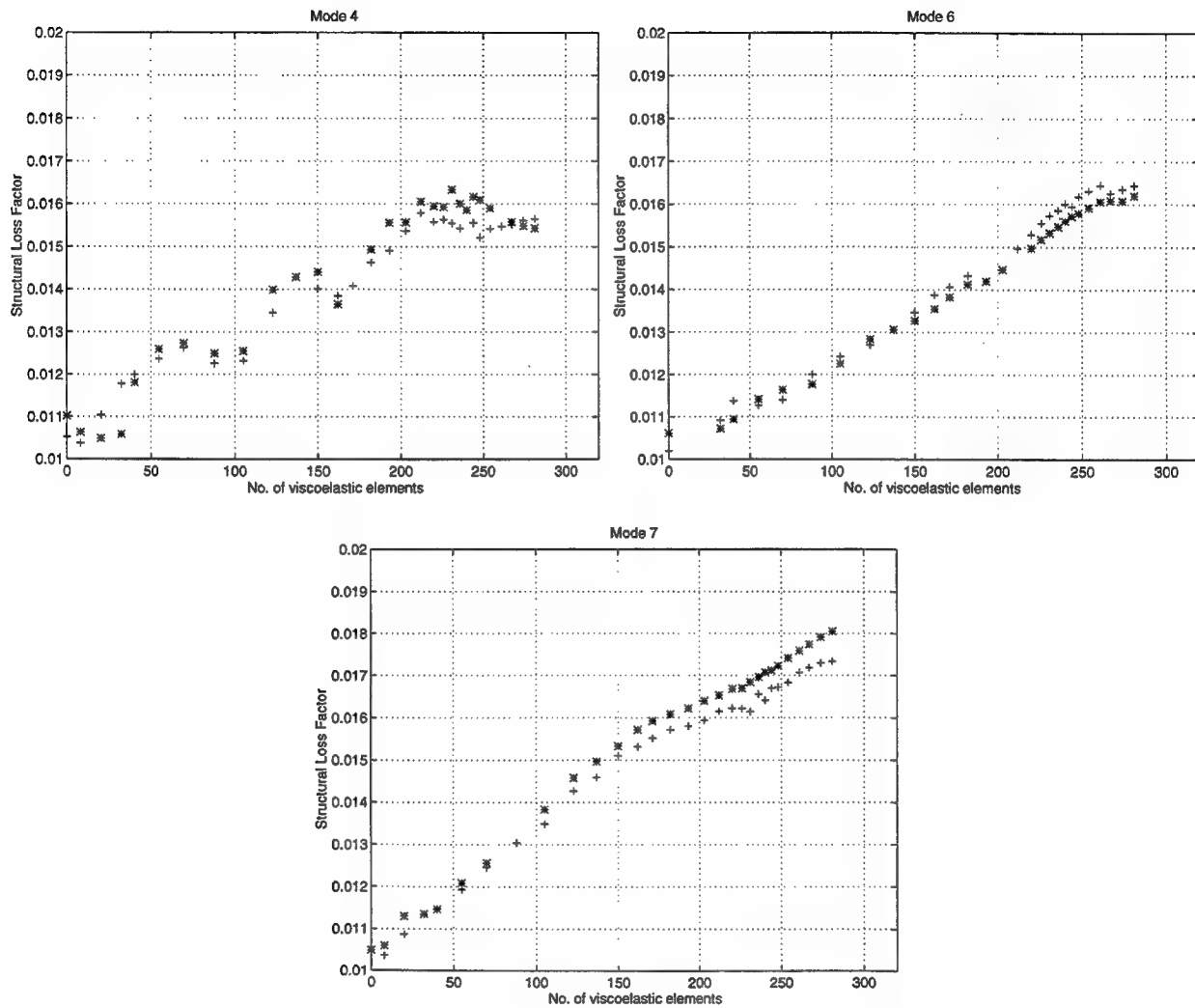
Figure 6: Evolution of the modal damping — the crosses refer to the damping calculated at the excitation point, the asterisks to the damping calculated at the beam tip
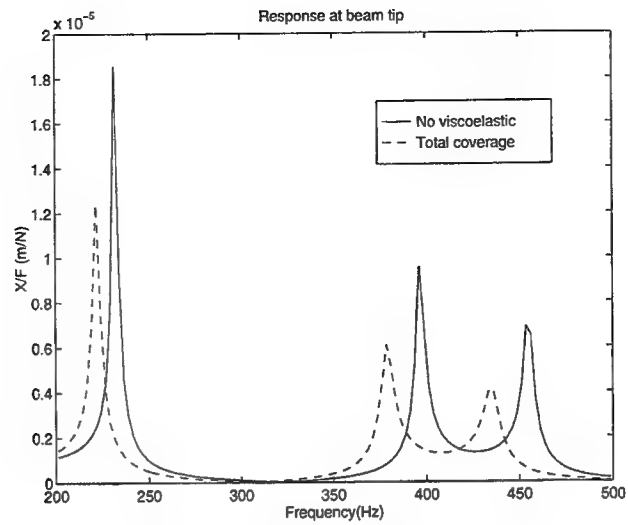
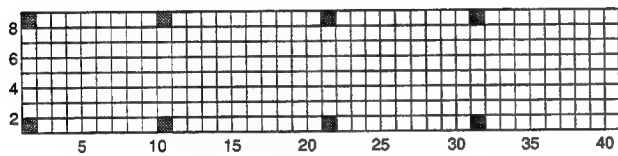Figure 7: FRF at the beam tip

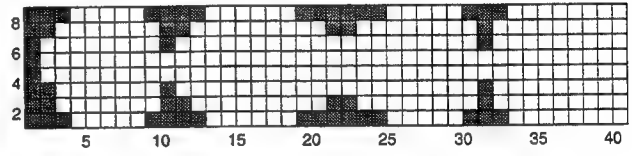Figure 8: 1 iteration, 8 elements, 2.5% coverage

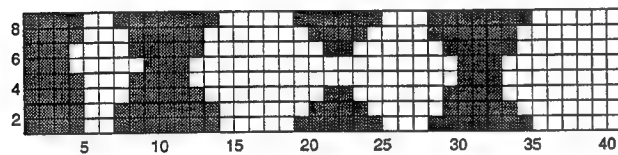Figure 9: 5 iterations, 20 elements, 6.25% coverage

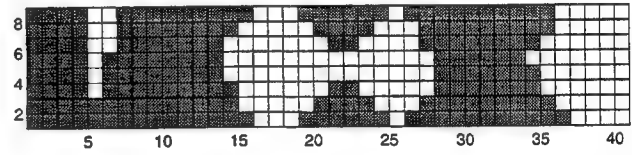Figure 10: 10 iterations, 137 elements, 42.81% coverage

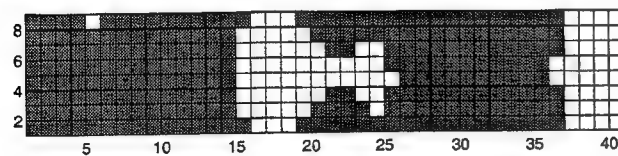Figure 11: 15 iterations, 193 elements, 60.31% coverage
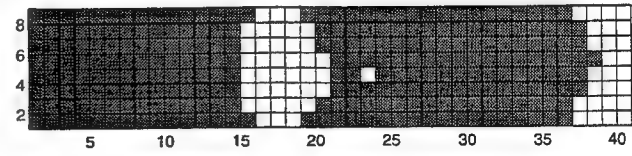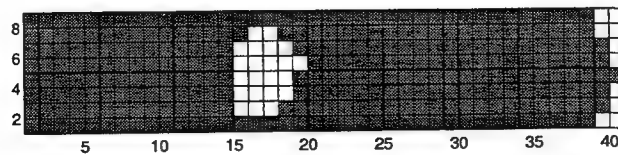

Figure 12: 20 iterations, 231 elements, 72.19% coverage

Figure 13: 25 iterations, 254 elements, 79.38% coverage

Figure 14: 30 iterations, 288 elements, 90.0% coverage

238

leading to a lower increase in loss factor than might have been anticipated. This could be corrected by performing some experiments with the real model.

Following the biological analogy, a further development would be to set an acceptable vibration level (e.g. modal loss factor) and allow removal of material as well as growth. In this way a 'set point' or normal level could be decided and the viscoelastic adapted to satisfy this point and no more. It would be possible to 'help' the process by starting with an initial estimate of the optimum layout and then allowing the cellular algorithm to 'grow' the material to the best configuration. This was not a worthwhile exercise within the current study, given the low increase in loss factor, but would be useful for a system where large decreases in vibration amplitudes are possible but at a cost of monetary expense and mass of material.

As mentioned in the previous section, it will be necessary to compare the damping layouts produced by the evolutionary method with layouts produced by other means, such as randomly, per mode or perhaps by expert estimation based on the knowledge of the mode shapes. It may then be possible to test the various layouts experimentally to determine which provides the best loss factor for a given viscoelastic mass.

6   ACKNOWLEDGEMENTS

7   REFERENCES

[1] Robert D. Blevins. *Formulas for Natural Frequencies and Mode Shape.* Krieger Publishing Company, 1979.

[2] Robert W. Gordon and Joseph J. Hollkamp. A comparison of damping treatments for gas turbine blades. In Conor D. Johnson, editor, *Passive Damping and Isolation*, volume 2720 of *Smart Structures and Materials 1996*, pages 3–12. SPIE — The International Society for Optical Engineering, SPIE, February 1996.

[3] Arnold Lumsdaine and Richard A. Scott. Shape optimization of unconstrained layer beam and plate damping layers. In *Design Engineering Technical Conferences*, volume 84–3C, pages 15–22. ASME, 1995.

[4] A. D. Nashif, D. I. G. Jones, and J. P. Henderson. *Vibration Damping.* John Wiley & Sons, 1985.

[5] G. R. Tomlinson. Using viscoelastic materials for practical damping applications. Notes for one-day course, Department of Mechanical and Process Engineering, University of Sheffield, UK, December 1995.

[6] Nicholas W. Tschoegl. *The Phenomenological Theory of Linear Viscoelastic Behaviour.* Springer-Verlag, 1989.

[7] R. Wardle and G. R. Tomlinson. A novel approach to structural design using biological models. In *Smart Structures and Materials: Implications for Military Aircraft of New Generation*, number AGARD-LS-205 in AGARD Lecture Series 205, pages 7–1 to 7–7. AGARD, October 1996.

[8] Y. M. Xie and G. P. Steven. A simple approach to structural frequency optimization. *Computers and Structures*, 53(6):1487–1491, 1994.

[9] Y. M. Xie and G. P. Steven. Evolutionary structural optimization for dynamic problems. *Computers and Structures*, 58(6):1067–1073, 1996.

Telemetry System for Monitoring Anterior Cruciate Ligament Graft Forces In vivo

by

Eric Lynn McKee
Research Assistant in
Biomedical Engineering

M. L. Hull
Professor of Mechanical
Engineering and
Chair of Biomedical Engineering

Stephen M. Howell
Associate Professor of
Mechanical Engineering

University of California
Davis, CA 95616

Abstract

Quantifying changes in the tension of an anterior cruciate ligament (ACL) graft in vivo during rehabilitative exercises is vital for developing the optimal rehabilitation for patients who have had reconstructive surgery. The purpose of this project was to design, build, and test a telemetry system that can measure the in vivo ACL graft tension postoperatively.

A commercially available fixation device was modified to sense the graft tension, house electronic components, transmit an output signal, and pass the power generating signal. A transcutaneous inductive link was used to power the implanted telemetry electronics. The current difference technique (Bergmann et al, 1988) was used to measure changes in two strain gages that monitored shear strain developed on the femoral fixation device by the ACL graft. This current regulated a frequency modulated output signal and transmitted it, by using the ionic properties of body tissue as the medium, to external EMG surface electrodes. A signal conditioning board detected and converted the output to an analog voltage for collection by a computer data acquisition system. A performance evaluation demonstrated that the telemetry system either met or exceeded all of the criteria necessary for the application.

Keywords: Implantable, telemetry, anterior cruciate ligament, graft, tension, transducer

Introduction

Rehabilitation is important to the success of an anterior cruciate ligament (ACL) reconstruction. The goal of rehabilitation is to restore full functionality to the reconstructed knee as quickly as possible without either stretching the graft or losing fixation both of which can cause recurrent instability. In recent years, an aggressive rehabilitation approach emphasizing early motion and weight bearing has been pursued to avoid the complications stemming from a more conservative approach which immobilizes the knee and avoids weight bearing (Shelbourne and Nitz, 1990; Pomphrey, 1992). However, a potential complication of aggressive rehabilitation is that the graft may be exposed to excessive tension. Excessive tension could cause failure of either the graft or the initial fixation and compromise the remodeling and maturation process (Markolf et al., 1994). Consequently, to avoid this complication, the graft tension must be determined for various rehabilitation activities.

Although there are several approaches for determining graft tension such as mathematical models (e.g., Harrington, 1976) and in vitro measurements (e.g., Markolf et al., 1993), in vivo measurement offers the advantage of monitoring and modifying the rehabilitation program if necessary. In vivo tension measurements have been obtained using the goat model (Holdens et al., 1994; Lewis et al., 1994). However, the results of the goat study are useful only in the design and interpretation of other animal studies and can not be extrapolated to humans (Holden et al., 1994). In human studies, sutures attached to an ACL graft were secured to load cells mounted externally on the tibia (Shino et al., 1994; Wallace et al., 1996). Data could be collected only in the operating room and during simple knee extension exercises against gravity (Shino et al., 1994). Such exercises do not encompass the full spectrum of activities in an aggressive rehabilitation program.

Because of the limitations inherent in the previous studies which have measured ACL graft tension in vivo, there is a need for instrumentation that can be implanted into ACL reconstructive patients so that the graft tensions can be measured during the rehabilitation process. The purpose of this project was to design, build, and test a prototype telemetry system that can directly measure the in vivo ACL graft tension for several weeks postoperatively. The remainder of this paper describes the design of the telemetry system, presents an evaluation of performance, and discusses how well the design meets the established criteria.

Design Description

Several criteria were established for developing the instrumentation to measure the ACL graft forces in vivo.

1. The device must be entirely integrated within a present fixation device and fit into its geometric constraints so that modification of the surgical procedure is not needed.

2. Since the device requires a power source and will be implantable, the device must be inherently safe to protect the patient from any possible harmful side effects.

3. The device must minimize power drain.

4. The device must be capable of operating up to 12 weeks, the maximum expected time for the graft to become fixed biologically so that the device no longer senses load.

5. The device must have a resolution of at least 1 % of full scale output and a non-linearity of less than 1 %. The output signal rise time must be less than 10 ms, so that relatively fast changes in the ACL graft tension can be monitored.

6. The device must incorporate diagnostic capabilities so that the functionality of the device while implanted can be determined.

To meet the criteria outlined above, the system diagrammed in Figure 1 was designed and constructed. The ACL telemetry system incorporates a power transmission system, a telemetry device, and a data acquisition system. Power is inductively coupled into the telemetry implant by external and internal coils. The ACL graft tension is monitored by the telemetry fixation device and a data signal is transmitted via the body's ionic fluids and detected by surface electrodes. This signal is amplified, converted to an analog voltage signal, and captured by the computer data acquisition system for analysis and storage. The following paragraphs describe in detail the modifications to the present fixation device, the implantable telemetry electronics, the power transmission system, and the data acquisition system.

Fixation Screw Design

The commercially available bone mulch screw fixation device (Arthrotek, Ontario, CA) was modified for sensing graft tension, housing electronic components, transmitting an output signal, and receiving the inductive power generating signal (Figure 2). To appreciate the modifications, an understanding of how the device is used for ACL graft fixation is useful. A tibial tunnel, through which the graft bundles pass, is drilled from the anterior-medial side of the tibia up through the tibial plateau (Figure 3). Another tunnel is drilled into the femur by inserting a drill through the tibial tunnel. The fixation device is screwed into a second closed-end femoral tunnel so that the graft bundles can be looped over the beam. The bundles are then securely fastened to the tibia with a screw and studded washer.

To create a dynamometer for measurement of graft tension, two foil strain gages are mounted on the facing sides of the inside of the hollow rectangular section, which is integral with the beam. Oriented at opposite 45 degree angles with respect to the vertically applied load, the gages detect shear strain which is independent of the center of pressure.

To achieve a hermetically sealed enclosure while at the same time providing a high coupling coefficient for the inductive power link, the screw is manufactured from different materials joined by various methods. The threaded portion of

the screw is manufactured out of alumina ceramic facilitating passage of the inductive power magnetic field. A titanium collar is brazed to the alumina so that the titanium beam can be laser welded to the threaded portion of the screw. Two platinum wires, cut flush to the exterior surface on the hex head end of the fixation device, provide the signal output connections. A glass seal around the wires completes the hermetic seal.

Telemetry Device Design

For ease of description and understanding, the design can be conceptually separated into three sections: power supply, signal transduction, and signal transmission (Figure 4). In the power supply section, a custom-designed inductive pick-up coil L1 receives the transmitted magnetic field. The coil consists of 40 turns of 34 AWG wire wrapped around a ferrite core (length = 6.4 mm, diameter = 4.6 mm). Capacitor C1 develops a resonant circuit at the power transmission frequency significantly increasing the coupling efficiency of the power coupling link. Diode D1 and capacitor C2 provide rectification and filtering of the incoming AC voltage supplying a stable DC voltage to voltage regulator U1. Resistors R1 and R2, along with U1, establish the circuit power supply voltage at 3.25 V. Capacitor C3 and C6 provide additional filtering reducing any spurious noise that may have been transmitted from the power generating portion of the circuit.

Signal transduction is achieved by using two current sources, U2 and U3, connected in series using the current difference technique (Bergmann et al, 1988). The output of the current sources is regulated by the resistance value of each of the strain gages, SG1 and SG2. The interconnection between the two current sources provides the current difference that is used in the signal transmission section. Resistor R4 maintains a permanent offset so that current always flows out of the interconnection point providing charging current to capacitor C4. If resistor R4 is not used, then U3 might require more current than could be provided by U2 making the circuit inoperable. The output frequency can be adjusted by slightly altering the value of R4, which changes the charging current available.

An innovative approach, exploiting the ionic and volume conduction properties of body fluids, is used for data transmission. The frequency-modulated output signal is transmitted through the tissue medium and received by external surface electrodes. The transmitted signal is at a higher frequency, nominally 5 kHz, than normal muscle activation frequencies so that the signal both can be distinguished from them and does not cause spurious muscle contractions. Also, this reduces the amount of noise introduced into the data signal at the transmission frequency.

The general-purpose timer U4 is connected as an astable multivibrator for generation of the frequency-modulated output. The current from the signal transduction section charges capacitor C4 until it triggers U4 causing the output to go low and the capacitor to be discharged through resistor R3. At the end of the discharge cycle the output will return to a high state and charging of the capacitor will proceed as previously. The time for charging capacitor C4 is regulated by the current difference between the two current sources and, thereby, modulates the output frequency of the timer which is nominally set at about 5 kHz. Resistor R5 is used to limit the amount of current sourced by the circuit for driving the signal through the tissue's ionic medium. A tradeoff exists between higher resistance, thus lower output current and lower power requirements, and the ability to detect the signal with the EMG leads. By increasing the value of resistor R5 the output current can be reduced but it also decreases the amplitude of the output voltage pulse making signal detection more difficult.

Power Transmission System

The power transmission system includes a benchtop DC power supply, inductive power supply, 6 meter cable and coil (Figure 1). The benchtop power supply provides +/- 20 V to the inductive power supply where it is regulated to +/- 15 V to supply the internal components and the signal conditioning board with power. The external coil is tethered by a long cable to the power supply to allow for movement of the patient during data collection.

Following the procedure described by Troyk and Schwan (1992), the inductive power supply consists of a class E power supply to generate the magnetic field (Figure 5). The general-purpose timer, U1, generates the frequency signal that maintains the oscillations across the output coil. Resistors R1 and R2 can be used to adjust both the frequency and duty cycle of oscillation. A comparator with an open collector output buffers the timer output signal.

The actual power generating section of the inductive power supply involves transistor U3, inductors L1 and L2, and capacitors C1 and C2. When the switching transistor U3 is open, current is supplied to inductor L2 through capacitor C2 and current is also supplied to capacitor C1 creating a positive voltage across the switch. While the switch is closed, L2 and C2 supply current back to the switch creating a positive voltage. By switching the transistor on and off oscillations are established at the switching frequency. A design frequency of 200 kHz was chosen because tissue is translucent at this frequency (Johnson and Guy, 1972).

The external coil consists of 48 turns of 24 AWG wire wrapped around a plastic bobbin form (length = 12.2 mm, inside diameter = 25.4 mm). The chosen diameter allows for the expected movement of the external coil, relative to the internal coil, without appreciably decreasing the coupling coefficient and, thereby losing power transfer. However, the external coil diameter has been minimized so that coupling with the internal coil can be maximized (Soma et al., 1987).

Data Acquisition System

The data acquisition system consists of EMG leads with amplifier, 6 meter cable, signal conditioning board, and computer with an installed data acquisition board (Figure 1). Placed near the knee on the lateral side, silver/silver-chloride surface electrodes monitor the output of the internal telemetry device. An instrumentation amplifier (1NA 101) amplifies the telemetry output signal and transmits the signal to the signal conditioning board. The amplifier is configured to provide a high-pass filter with a cutoff frequency of 33 Hz eliminating low-frequency noise. As in the case of power transmission, a cable tethers the patient to the ACL telemetry system.

The signal conditioning board receives the amplified EMG signal and converts the frequency to an analog voltage for input into a computer data acquisition board (Figure 6). A comparator U1, whose output goes high when the input exceeds the threshold set by resistor R4, detects the incoming frequency and converts it to a TTL compatible signal. Flip-flop U2 generates a 50 % duty cycle digital signal at one-half the input frequency, which is then used to drive the frequency-to-voltage converter (FVC). The operational amplifier U4, along with R12 and R11, provides a dc offset and variable gain factor to the FVC output to make maximum use of the input dynamic range of the data acquisition system. Resistor R15 and capacitor C9 yielded a low-pass filter with a 370 Hz frequency cutoff to reduce output noise. The output, which is set as a 0 to 5 V signal, is connected to a data acquisition board.

Performance Evaluation

Performance evaluation of the ACL telemetry system can be separated into the three system components as described above: the power transmission system, the telemetry device, and the data acquisition system. The purpose of the power transmission system is to provide sufficient power to the implanted electronics for it to operate properly at the required external and internal coil separation. Although the design frequency was 200 kHz, due to inaccuracies of the design procedure, the available component values, and the inductance of the output coil the actual operating frequency is approximately 167 kHz. This operating frequency was chosen by adjusting the frequency of oscillation until the voltage across the transistor is minimized during the onset of transistor conduction, thereby, minimizing the power loss and the heat dissipation in the transistor.

When the frequency is set so that the transistor turns on immediately at the end of the first half cycle the voltage across the output coil is 300 V peak-peak. The present design generates sufficient magnetic field to provide the telemetry device with the required 9 mW of power at a coil separation of 20 mm. The estimated separation for the two coils during experimental trials is 10 mm to 15 mm so some room for variability does exist. Lateral movement of the internal coil relative to the external coil has no effect on power transfer until the outer edges of the two coils begin to line up, where the expected rapid drop-off occurs.

It was observed during testing of the inductive power supply that sufficient power is radiated from the external coil to cause significant heating. In fact, the coil, which reached a temperature of 111 degrees C, would cause severe burns if held in contact with tissue.

The functionality and performance of the electronic circuitry of the telemetry device was tested on the bench at ambient temperature. The telemetry electronics were powered from a DC power supply; thus the inductive power link was not used. The beam was placed in a custom designed holder and securely held in a benchtop vise so that weights could be hung from the beam. The output of the circuit was connected to the signal conditioning board through the 6 meter cable and recorded using a data acquisition computer. The output voltage was recorded under various loading conditions to quantify different performance characteristics.

To measure the hysteresis and non-linearity of the device, weights were applied incrementally during loading and unloading. The response was linear with a full scale voltage range of 4.25 V for a maximum load of 290 N. The maximum non-linearity for the loading condition was 0.63 % of full scale load. The hysteresis showed a maximum deviation of only 0.65 %.

A drift test was conducted at four different loads: 0 N, 110 N, 200 N, and 290 N. Data were collected for a 30 minute time period for each of the loads. No low frequency drift was present for any of the four tests. Noise in the telemetry system limited the resolution to a typical value of 1.15 % of full scale output. The worst case resolution was 1.29 %, which occurred for the 110 N load. Therefore, a typical signal-to-noise ratio of 39 dB was obtained.

The dynamic response of the system was measured by momentarily switching in a parallel resistance with one of the strain gages. This simulated a step input in the loading. The time to reach 90 percent of the final output (rise time) was 9 ms with a 5 ms time constant. Different rise times can be obtained by changing the integrating capacitor, C7, for the FVC. However, resolution of the system will also change because a smaller capacitor will lead to shorter rise times but the integrator output ripple will increase (Figure 7).

The most important aspect of the data acquisition system is the ability of the comparator to detect signal pulses. The signal conditioning board was tested on the benchtop measuring the hysteresis and threshold levels. The present circuit requires a minimum of 100 mV peak input signal for the output to change states and has a hysteresis band of 25 mV to eliminate false triggering during a state transition.

Discussion

The objective of this project was to design, build, and test a telemetry system that can monitor ACL graft forces in vivo during rehabilitation. Many physiological quantities have been measured using implantable telemetry devices, especially with the advent of microcircuitry and hybrid circuit design (Jeutter, 1983). Telemetry devices have been used extensively in hip implants to monitor human hip cartilage surface pressures (Carlson et al, 1974), hip joint forces (Graichen and Bergmann, 1991; Kilvington and Goodman, 1981), and strain measurements (Barlow et al, 1984; Taylor et al, 1992). However, due to the unique nature of the application here, no previous system built around these devices satisfied the design criteria. Accordingly, the design of a new system was undertaken.

To meet the first design criterion of using a current fixation device so that the surgical procedure did not need to be modified, the bone mulch screw was selected. The internal components were designed to fit into the geometric constraints of the screw, which severely limited the number of components allowed and the construction technique to be used. Some modifications to the screw were required but the basic form and function were not altered. Accordingly, the modified screw can be used without affecting the surgical procedure.

The second criterion of insuring the patients' safety was also met. The packaging for an implantable telemetry device must provide protection of the electronic and mechanical components from the hazardous body environment, protection of the patient from any possible harmful effects, and compatibility with the body (Ko and Spear, 1983). A hermetically sealed enclosure is ideal because polymers do not provide the same protection due to a finite permeability to moisture (Ko and Spear, 1983). An hermetically sealed enclosure was realized by using both glassy and metallic seals (Donaldson, 1988).

The third design criterion was to minimize the power drain of the implanted electronics. Most designs utilizing strain gages employ Wheatstone bridges and operational amplifiers for amplification of the small resistance change, but this requires a large number of components and has a high power demand. To reduce both the component count and the power

demand, the current difference method was used (Bergmann et al., 1988) This method was ideally suited to the application because both current source outputs were regulated by the two strain gage resistances. The current difference was used to modulate the frequency of a carrier signal.

Space limitations for the internal circuitry severely restricted the available options for data transmission. Radio frequency transmission could not be employed because a coil, needed for transmitting the signal, required too much space. A transcutaneous optical data link could not be used because it required an optical path, which was unavailable (Mitamura et al, 1990). Likewise, the transcutaneous power link could not be used because the coupling coefficient between the external and internal coils was so small that any change in the internal coil inductance had a negligible effect on the external coil inductance (Donaldson, 1986). Therefore, an innovative approach was taken harnessing the ionic and volume conduction properties of the body fluids for data transmission.

The new data transmission technique was developed and tested. Testing demonstrated that an electrical signal, which constituted the data signal, could be transmitted into the body fluids containing ions that were used as charge carriers and then easily detected using surface electrodes. The signal's frequency needed to be high enough so that interference with signals naturally existing in the body did not occur. Current limiting, thereby limiting power consumption, was easily obtained by placing a resistor in series with the output before the signal entered the body fluids.

To insure that the circuitry diagrammed in Figure 4 could be housed within the hollow of the screw (Figure 2), a design for a hybrid circuit board was completed. Although the circuitry in Figure 4 could be accommodated, the space limitation precluded any additional circuitry for diagnostic purposes. Therefore the sixth design criterion could not be met. However, analysis of the data transmission signal does provide information regarding the functionality of the electronics.

The fourth design criterion required that the device operate for a minimum of 12 weeks after implantation. Batteries were eliminated from consideration because present technology does not provide a battery with sufficient power, even when using switches to extend the battery life, that can be housed in the required enclosure. Thus, transcutaneous power coupling was the only possible solution and allowed for longer experimental times, more experimental trials, and repeated experiments. However, a poor coupling coefficient resulted both because of the 10 mm to 15 mm separation between the internal and external coils and because of the size difference between the two coils. Therefore, a class E power supply design was chosen because it provides greater efficiency of power generation than other power supply designs (Troyk and Schwan, 1992). Nevertheless, due to the large power requirements, a pack to carry enough batteries was too heavy and cumbersome so that instead the patient was tethered to a 6 meter cable.

Because significant heat was generated in the external coil, a sheet of thermally nonconductive material must be placed between the patient and the coil to prevent discomfort to the patient. However, the separation between the internal and external coils needs to be kept at a minimum so that sufficient power can be transferred to operate the telemetry device.

The fifth criterion concerning resolution, non-linearity, and dynamic response was satisfied. The non-linearity of the device was less than ±1 % with a typical resolution of 1.1 %. The dynamic response produced a 9 ms rise time and a 5 ms time constant. In vivo dynamic ACL force measurements in humans have not been obtained. However, in vivo ACL force measurements in quadrupeds showed a worst case loading rate of 1572 N/ms during normal walking (Holden et al, 1994). This leads to an error of 7.8 N (error = slope * time constant), which corresponds to 2.7 % of full scale load, in the present system. Typically, leg movement immediately postoperative is limited due to swelling and pain. Therefore, a relatively slow loading rate is expected.

Conclusion

Because a safe and effective rehabilitation program for ACL reconstructive patients depends upon knowing the graft tension during rehabilitative exercises, the goal of this project was to design and build a telemetry system that can monitor the ACL graft tensions in vivo. The performance evaluation demonstrated that the design satisfied all of the criteria important to the application. Accordingly, much progress toward developing an ACL telemetry device that can monitor ACL graft tension in vivo has been made. The next step for developing an implantable telemetry device is to implant a prototype and test its functionality in an animal model.

References

1. Barlow, J.W., Goldie, I.F., Horwood, J.M.K., Lee, A.J.C. and Ransom, R.P. (1984). In-vivo telemetry of strain in a total hip joint, *IMechE*, C216/84:55-61.

2. Bergmann, G., Graichen, F., Siraky, J., Jendrzynski, H. and Rohlmann, A. (1988). Multichannel strain gauge telemetry for orthopaedic implants, *J Biomechanics*, 21:169-176.

3. Carlson, C.E., Mann, R.W. and Harris, W.H. (1974). A radio telemetry device for monitoring cartilage surface pressures in the human hip, *IEEE Trans Biomed Eng*, 21:257-264.

4. Donaldson, N. (1988). Low-technology sealing method for implantable hermetic packages, *Med Biol Eng Comput*, 26:111-116.

5. Donaldson, N. (1986). Passive signaling via inductive coupling, *Med Biol Eng Comput*, 24:223-224.

6. Graichen, F and Bergmann, G. (1991). Four-channel telemetry system for in vivo measurement of hip joint forces, *J Biomed Eng*, 13:370-374.

7. Harrington, I.J. (1976). A bioengineering analysis of force actions at the knee in normal and pathological gait, *J Biomed Eng*, 11:167-172.

8. Holden, J.P., Grood, E.S., Korvick, D.L., Cummings, J.F., Butler, D.L. and Bylski-Austrow, D.I. (1994). In vivo forces in the anterior cruciate ligament: direct measurements during walking and trotting in a quadruped, *J Biomechanics*, 27:517-526.

9. Jeutter, D.C. (1983). Overview of biomedical telemetry techniques, *Eng Med Biol*, 2:17-24.

10. Johnson, C.C. and Guy, A.W. (1972). Nonionizing electromagnetic wave effects in biological material and systems, *Proc. IEEE*, 60:692-718.

11. Kilvington, M. and Goodman, R.M.F. (1981). In vivo hip joint forces recorded on a strain gauged 'english prosthesis using an implanted transmitter, *Eng Med*, 10:175-187.

12. Ko, W.H. and Spear, T.M. (1983). Packaging materials and techniques for implantable instruments, *Eng Med Biol*, 2:24-38.

13. Lewis, J.L., Lew, W.D., Smith, J., Engebretsen, L. and Poff, B. (1994). Force magnitudes and effect of force on acl graft properties: an in vivo study in the goat, Second World Congress of Biomechanics, Amsterdam, The Netherlands, pp 85.

14. Markolf, K.L., Burchfield, D.M., Shapiro, M.S. and Finerman, G.A.M. (1994). Comparison of forces in the acl and patellar tendon autograft, Second World Congress of Biomechanics, Amsterdam, The Netherlands, pp 86.

15. Mitamura, Y., Okamoto, E. and Mikami, T. (1990). A transcutaneous optical information transmission system for implantable motor-driven artificial hearts, *ASAIO Trans*, 36:M278-M280.

16. Pomphrey, M.M. (1992). Aggressive rehabilitation following anterior cruciate reconstruction: an update and protocol, *Missouri Med*, 89:358-361.

17. Shelbourne, K.D. and Nitz, P. (1990). Accelerated rehabilitation after anterior cruciate ligament reconstruction, *Am J Sports Med*, 18:292-299.

18. Shino, K., Hamada, M., Tanaka, M. and Matsui, Y. (1994). ACL graft load measurement, Second World Congress of Biomechanics, Amsterdam, The Netherlands, pp 87.

19. Soma, M., Galbraith, D.C. and White, R.L. (1987). Radio-frequency coils in implantable devices: misalignment analysis and design procedure, *IEEE Trans Biomed Eng*, 34:276-282.

20. Taylor, S.J., Donaldson, N., Meswania, J. and Perry, J. (1992). A telemetry system for in vivo strain measurement in orthopaedic endoprostheses, *Proc Intl Conf Experimental Mechanics*, pp 4-5.

21. Troyk, P.R. and Schwan, M.A. (1992). Class E driver for transcutaneous power and data link for implanted electronic devices, *Med Biol Eng Comput*, 30:69-75.

22. Wallace, M.P., Howell, S.M., and Hull, M.L. (1996). In vivo tension measurements in a double-looped hamstrings graft for anterior cruciate ligament replacement, *ORS Trans*, pp 74.
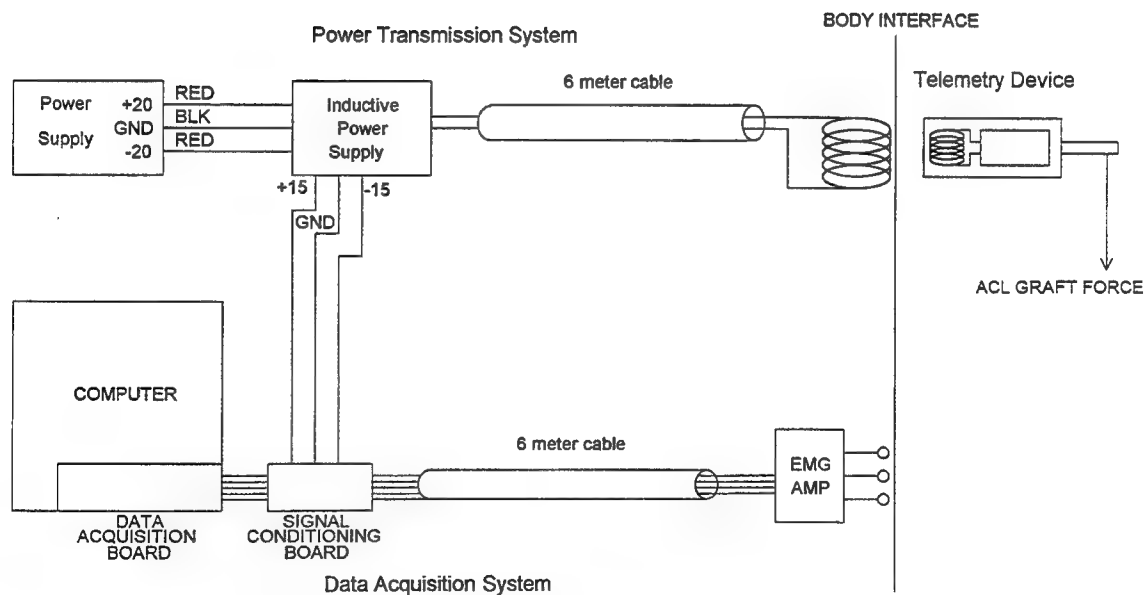
Figure 1: System design.
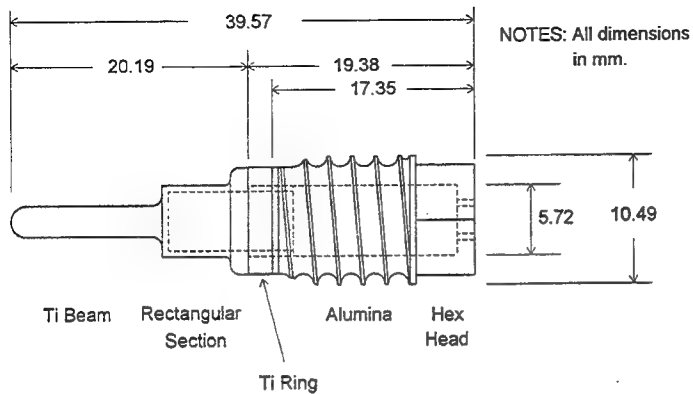
Figure 2: Fixation device.
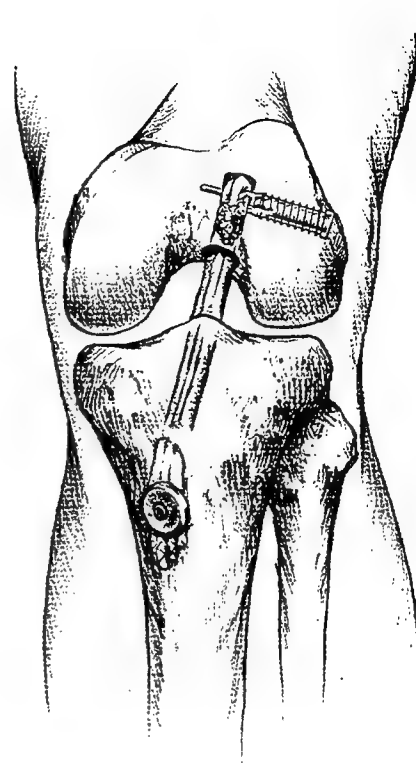
Figure 3: Completed ACL reconstruction.
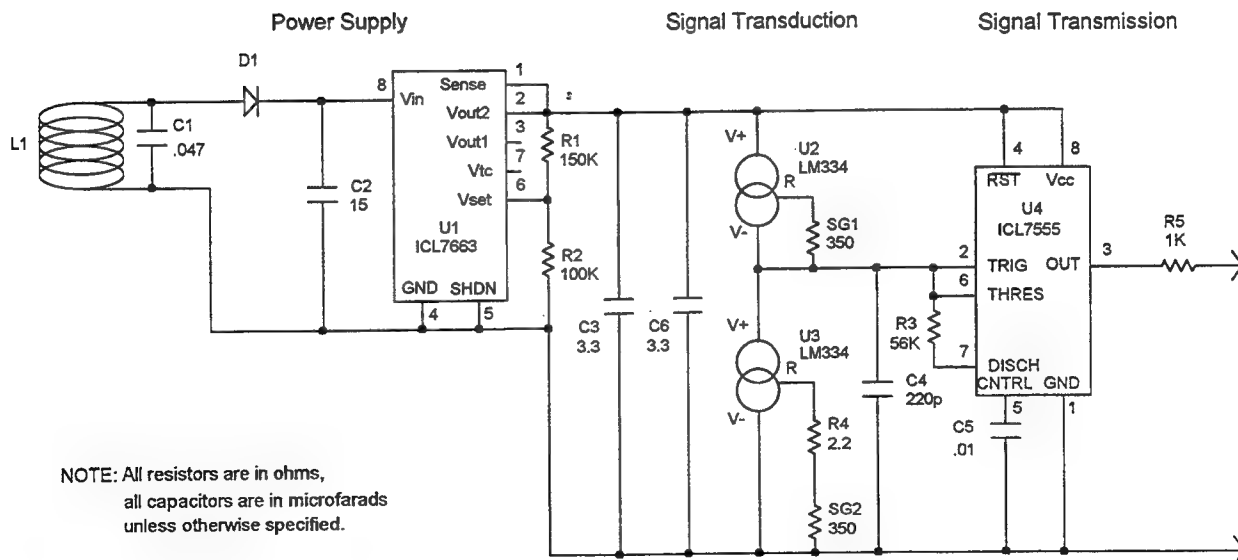
Figure 4: Implant electronics, schematic diagram.
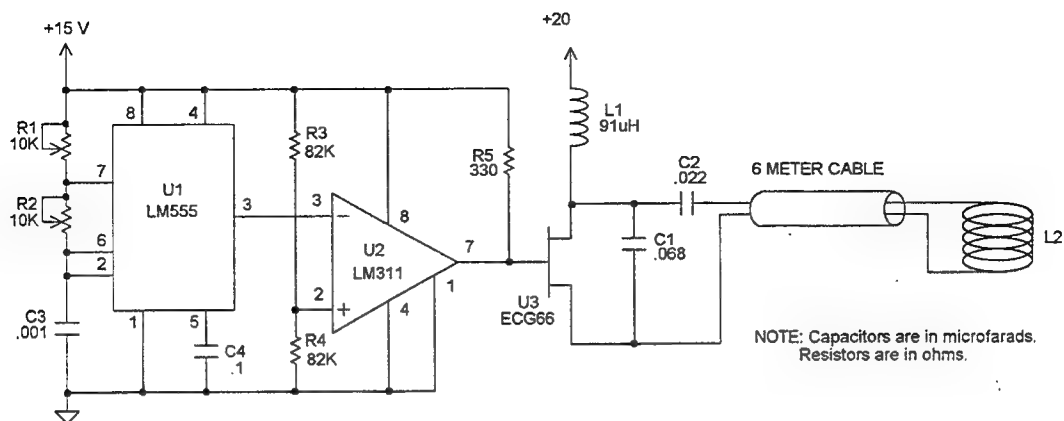
Figure 5:   Inductive power supply, schematic diagram.
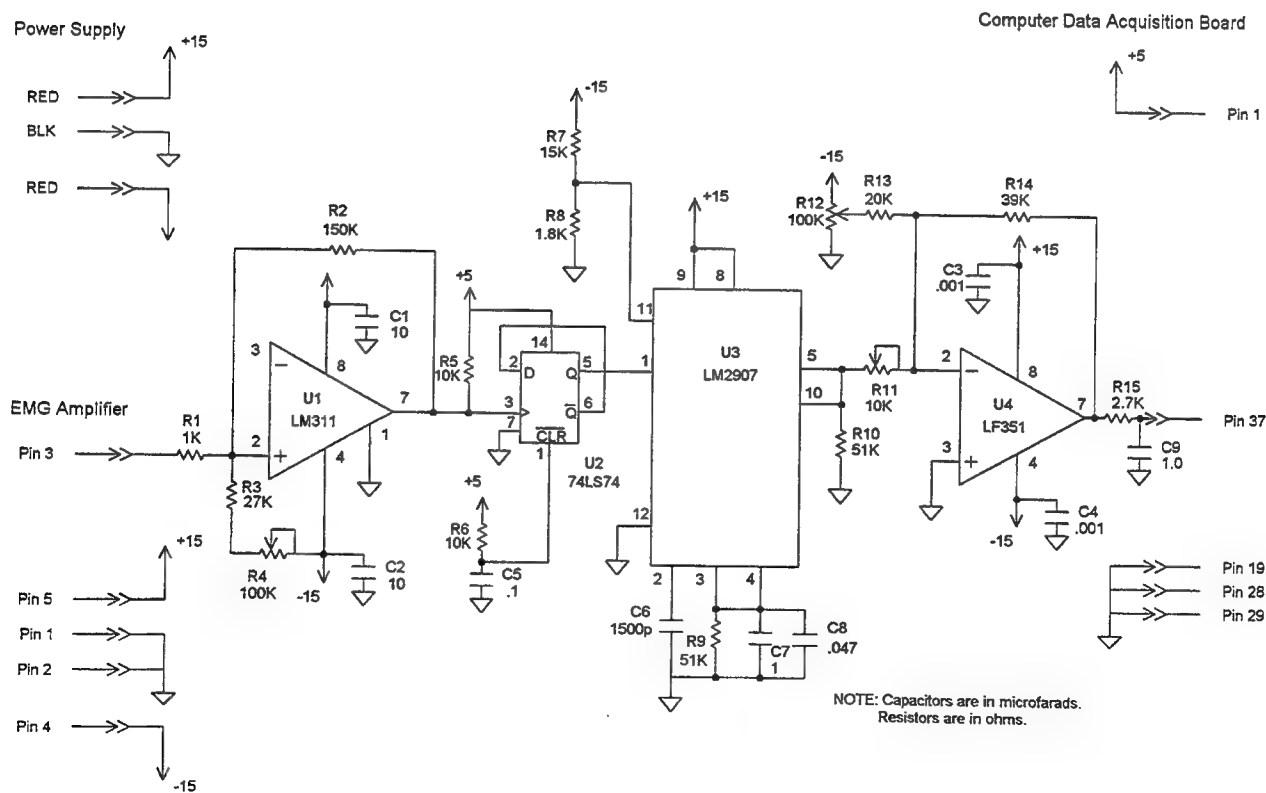
Figure 6:   Signal conditioning board, schematic diagram.
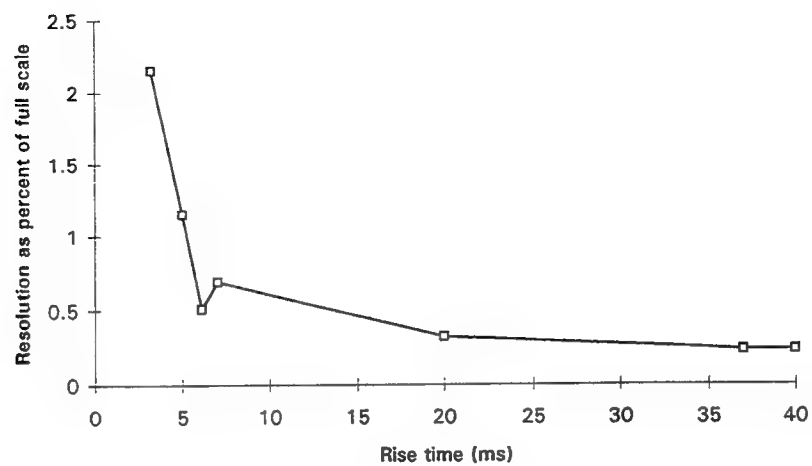
Figure 7:   Resolution of percent of full scale versus time constant.

Biomimetic   Bone-like Polymer Cementitious Composite

Carolyn Dry, Professor
Carrie Warner, Graduate Research Assistant

School of Architecture-Building Research Council
University of Illinois @ Urbana-Champaign
Champaign, Illinois

ABSTRACT

This paper outlines the progress in the development of a biomimetic, prefabricated synthetic building material that is to have the superior properties of bone. The goal was to make polymer/ceramic composite which mimics bone in both process of fabrication and resultant properties and bond between phases, because bones and shells have been found to have greater toughness and strength than conventional ceramics alone due to the presence of organic bonding materials. The intimate connection between material phases is due to careful growth sequences, i.e. the fibers are made first and the matrix grown around them as opposed to conventional ceramics in which any fibers are added to the matrix. We followed the rules under which bone material naturally forms albeit at a macroscale, as spelled out by researchers in biological materials.

Keywords: Biomimetic, bone, composites, building materials, polymer, ceramic, bone formation

1. Introduction

1.1 Rules of Bone Formation

The goal is to mimic bone material formation to obtain superior performance properties. The rules of natural bone formation are as follows:

"Bone is made up of an oriented matrix which is secreted by bone-forming cells: the osteoblasts. This organic matrix is first made of structural molecules which serve as a scaffolding and which are laid down in a very precise, oriented pattern of fibrils into and onto which the inorganic crystalline phase forms. The formation of the first crystals of inorganic salt of calcium phosphate is referred to as the initiation or nucleation site which appear at regular intervals along this complex organic scaffolding of collagen laid down by osteoblast. Once nucleation has occurred, the next major process involves the continuation of crystalline growth from the nucleation sites outward along the fabric of the organic matrix and eventually between the molecules which serve as scaffolding. As crystal growth continues and forms a dense, inorganic matrix, there is a loss of organic components which are designed to reserve space in this matrix for the ever-expanding inorganic phase."[1]

"The important landmarks of the organizational rules that can be deduced are as follows:
1. Oriented multi-component organic matrix of fibrils as secreted by osteoblasts.
2. The formation of these oriented structural molecules serve as scaffolding (fibrils) and nucleation sites.
3. Initiation or nucleation of this inorganic, calcium phosphate crystalline phase on the sites.
4. The continuation of crystal growth with simultaneous rearrangement or elimination of components from the organic matrix."[1]

1.2 The Biomimetic Processes In the Simplest Case

Following the above rules in the self-growing structure (see figure 1): porous walled hollow polymer fibers would release organic polymer chemicals into an inorganic matrix. The fibers would act as the organic template of fibrils onto which forms the calcium phosphate from the matrix, creating a strong structural bone-like composite. The chemicals released from the fibers are designed to form a linked organic/inorganic matrix. The chemicals are monomers which release water when polymerizing. Reactions in which the water released (as they crosslink) hydrates the calcium phosphate cement.

The structural design of the matrix organization to resist particular stresses can be built into the formation process by the application of prestressing. More particularly, these generated lines of force can cause the charged cementitious ions to migrate along them. The prestressing forces on the composite would thus generate the appropriate microstructure, metal fibers could be used as the fibers which carry an electrical change.

Ongoing self-healing over the life of the structure would be accomplished by reuse of the original void fibers. These porous walled hollow fibers would deliver repair chemicals if and when damage to the matrix occurs, such as cracking. In other research we have shown this type of repair improves strength, toughness and ductility.

Referring back to the organization of rules, the 1) organic scaffolding of fibrils is mimicked by the hollow porous polymer fibers. 2) Structural molecules that are scaffolding and nucleation sites are the polymers which are created near the fiber release points by crosslinking from the monomer in the matrix and the catalyst released from the fiber. 3) Initiation of the inorganic crystallizing phase in the polymer is caused by the released water which hydrates in the cement, and 4) continuation of crystal growth and simultaneous rearrangement of the organic matrix is mimicked by ions which migrate along stress lines generated by electricity from metal fibers.

The significance of this work is 1) that brittle cement materials will have ductile fibers bonded in the matrix and a polymer/cement inherently bonded and therefore the composite will have superior strength properties, 2) the morphology and controlled reaction between phases in the matrix will impart superior properties, 3) the material will be formed under the actual stress environment and therefore perform in a superior way in the field and, 4) the material will be self-repairing.

## 2. DEVELOPMENT OF A PROCESS FOR BIOMIMETIC MATERIAL PRODUCTION

We have investigated a polymer condensation reaction and the method for inducing this polymerization and ensuring the hydration of the cements. The chemistry had the following constraints: the reaction must take place near room temperature; the reactants and products must be relatively harmless; the resulting polymer must be cross-linked once it has been released in the matrix; the resulting polymer must not be water soluble; the polymer structure must provide a suitable interface for the link up with hydrated cement crystals; the chemical constituents must be widely available and relatively inexpensive; and the polymer must give off enough water to hydrate the cement and not need mixing.

These reactions were symbiotic. The polymerization produced the water necessary to hydrate the portland cement, and the hydration of the portland cement absorbed the water byproduct of the condensation reaction, thereby driving the polymerization reaction to produce more polymer. (the polymerization process usually required a vacuum in order to remove the water from the condensation reaction.)

Time sequencing and developing a suitable system for introducing the liquid monomer
is essential in our experimentation. The delivery system was required to evenly distribute the liquid monomer to all portions of the powder matrix. As this liquid reached the powder, the liquid monomer and the monomer in the matrix polymerized and gave off water which hydrated the portland cement powder.

### 2.1 Investigation of the properties of biomimetic composite material

This early research was done to find a process which successfully produced the material by following the time sequencing of bone formation. Once the process was successful, we began to study the properties of the product. Samples were made to study the basic properties of the composite in comparison with cement. Butter stick samples (1"x1"x8") and compression cubes (2"x2"x2") were made of both materials (cement and composite) to compare the bending and compressive strengths and behaviors of the materials.
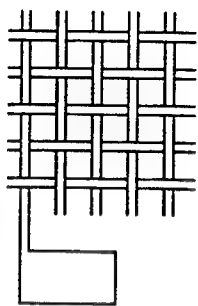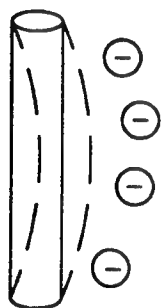
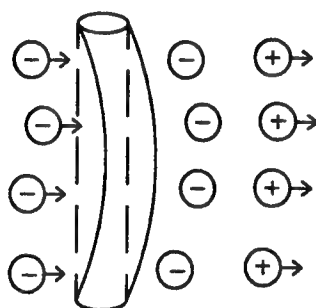Initiator is pumped or released through the fibers. It crosslinks with the monomer in the matrix.
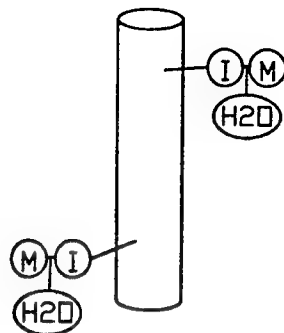
Polymer is formed by reaction between monomer and initiator, giving off water.
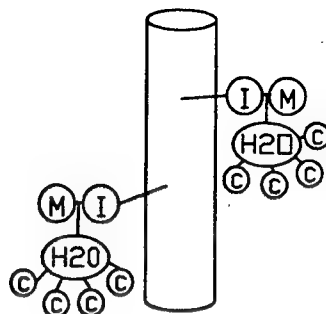
Water from polymer condensation reaction hydrates cement powder.

Some fibers are piezo-electric and give off a charge when stressed (in a prestressing mode).

Charged ions in the cement polymer matrix are migrated away from the fiber bend and charged ions are attracted, e.g. the negative ions fill (beef up) a stressed member.
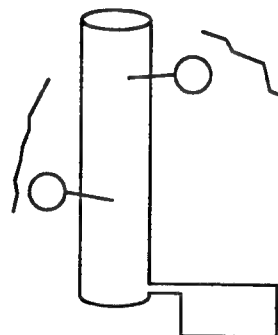
Some of the hollow fibers are used to deliver repair chemicals to change the matrix' interior microstructure.

Figure 1. The sequence of forming the biomimetic bone-like polymer cementitious composite.

2.2 Test Results

Three-point bending tests revealed that the composite material did not suffer the same brittle failure of typical cements. A comparison was made of the behavior of the composite material to a polymer sample and a cement sample (all made with the same delivery system), see figure 2. The cement sample initially carried very low loads, but upon sudden brittle failure, the load capacity increased significantly as the load was transferred to the steel reinforcing. However, the composite material never experienced such a brittle failure, rather a gradual increase in load capacity can be seen in the more flexible composite, as microcracking absorbs the load energy, preventing build up to sudden failure.
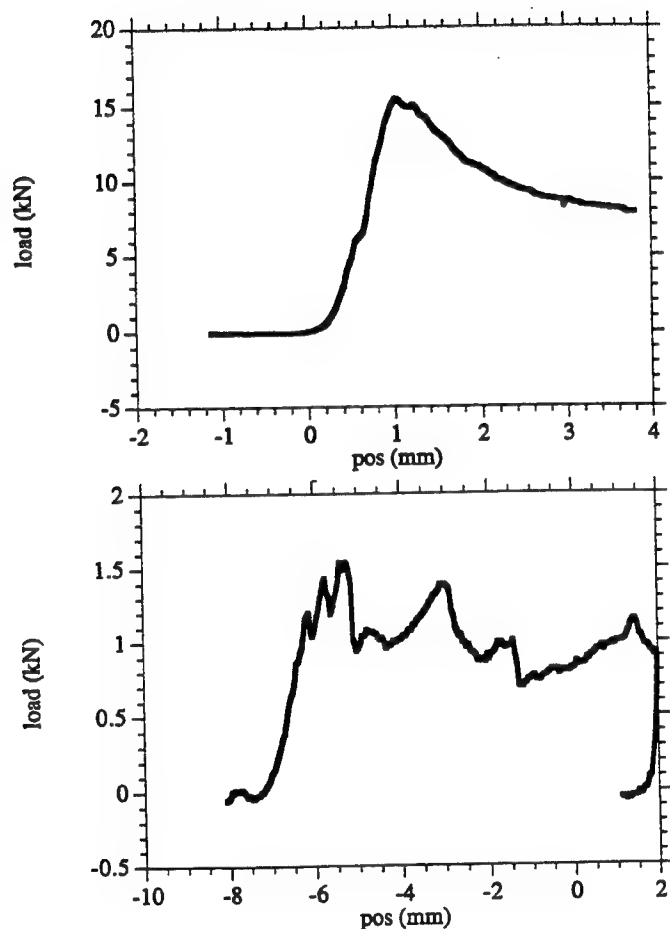
Figure 2. Load diagrams of cement control and polymer/cement composite.

Compression tests showed the compressive strength of the new composite to be less than that of cement.

A closer look at the materials confirms that the composite material is meeting some, but not all, of the rules outlined for mimicking bone formation. Scanning electron microscope photographs show composite with some cross linking (Figure 3 and 4). At 250X enlargement, it can be seen that the composite material is indeed a combination of the polymer and cement materials, therefore the process of polymerization and cement hydration is successful. At 2500X enlargement, the is further confirmed, while it becomes apparent that the two materials seem to be linked only mechanically due to proximity in space.
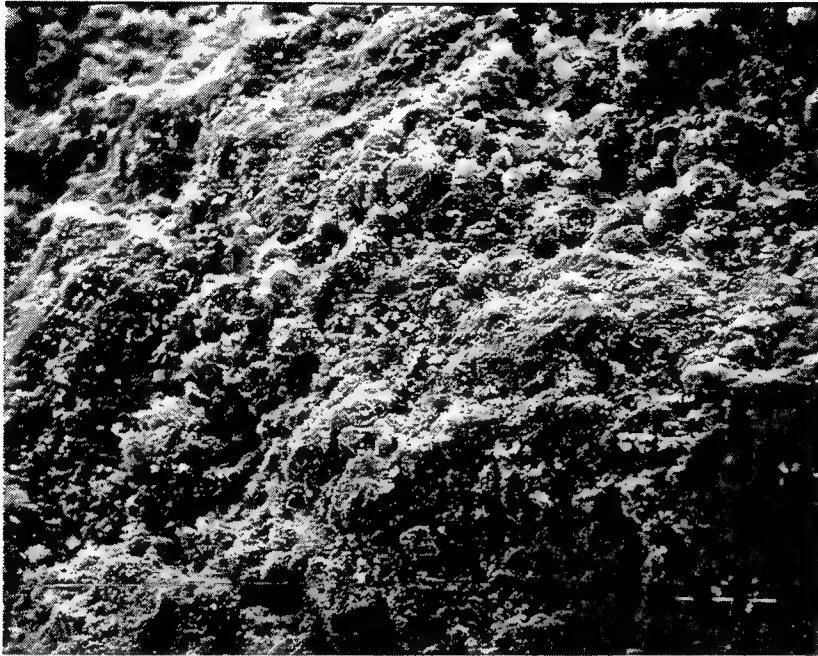
254

Figure 3.   Scanning electron microscope photo of composite sample at 250X enlargement

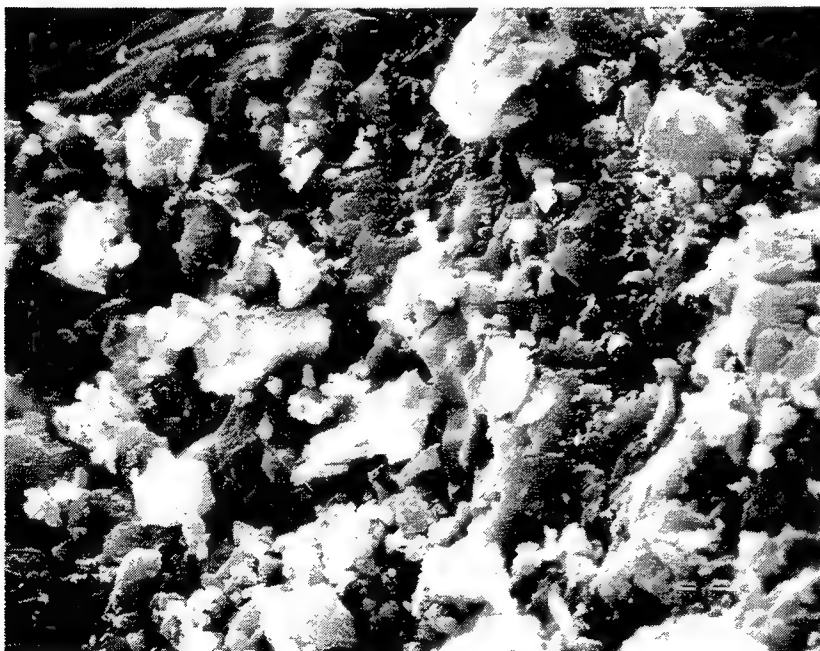

Figure 4. Scanning electron microscope photo of composite sample at 2500X enlargement.

3. CONCLUSIONS

This research has led to a process of mimicking bone production. The polymerization and resulting cement hydration is a symbiotic reaction that leads to a mechanically bonded polymer-cement composite material. Through testing, it was found that the bending behavior of the polymer-cement composite was less like typical cement (with its brittle failure) and failed in a more ductile manner, with more deflection and flexure. The process of delivering the liquid monomer into the powder matrix must be improved to reach greater material strengths, and different polymers are also being investigated. However, the properties of bone are becoming more attainable as this research proves the possibility of matching the bone production process.

REFERENCES

1. Caplan, Arnold, "Bone Foundation, The Rules for Fabricating a Composite." *Ceramic. Mat. Res. Soc. Symp. Proc.* Vol. 174, pp. 9-10 (1990).

2. Billmeyer, Fred W. *Textbook of Polymer Science, 2nd ed.* John Wiley and Sons, Inc. New York. p. 435.

Chemical Microsensors Based on "Smart" Surface-Bound Receptors

DeQuan Li,[*] Jing-Xuan Shi, Kendall Springer, and, Basil I. Swanson

Los Alamos National Laboratory
P.O. Box 1663
Los Alamos, NM 87545

ABSTRACT

Cyclodextrin thin films were fabricated using either self-assembled monolayers (SAM) or sol-gel techniques. The resulting host receptor thin films on the substrates of surface acoustic wave (SAW) resonators were studied as a method of tracking organic toxins in vapor phase. The mass loading of surface-attached host monolayers on SAW resonators gave frequency shifts corresponding to typical monolayer surface coverage for SAM methods and "multilayer" coverage for sol-gel techniques. Subsequent exposure of the coated SAW resonators to organic vapors at various concentrations, typically 5000 parts per millions (ppm) down to 100 parts per billions (ppb) by mole, gave responses indicating middle-ppb-sensitivity (~50 ppb) for those sensor-host-receptors and organic-toxin pairs with optimum mutual matching of polarity, size, and structural properties.

Keywords: sensor, cyclodextrin, receptor, surface acoustic wave, self-assembly, self-assembled monolayer, sol-gel, host polymer, thin-film.

2. INTRODUCTION

Chemical microsensors are desired for cost-effective environmental monitoring, site remediation, and industrial process characterization,[1] and are expected to play a growing role in these applications. The analyses of volatile organic compounds (VOCs) are currently performed with standard analytical instruments such as gas chromatography and mass spectrometry. By integrating a surface acoustic wave (SAW) measurement platform with a selective sensing layer, a desired chemical microsensor is constructed, which provides some of the functionality of analytical instrumentation, but with drastically reduced cost, size, and power consumption.

Moreover, chemical microsensors have also found demanding applications in other areas. These include worker safety assurance and detection of the presence of special substance or odor. The benefit of using chemical sensors is great because early detection and warning of the presence of specific chemicals will lead to proper procedures that can remediate the situation. In general, sensors are smart devices which provide important information for making critical decisions that could benefit us from environmental safety to increased productivity in industrial process.

There has been numerous work on SAW device fabrications not only for chemical sensors but also for communication devices such as frequency filters and cellular phones. Little, however, has been done on engineering the selective sensing layers. In this paper, we focus on a novel approach to construct new host receptors as a sensing layer on SAW devices using innovative molecular self-assemblies and sol-gel techniques. The sensing layer can be regarded as a smart skin of the detection device; they preferentially interact with and absorb specific organic molecules in the vapor phase. By modifying the sensing layer characteristics, the sensor properties can be designed and tuned so that desired selectivity and sensitivity can be achieved. Here, we report the studies of nature-occurring cyclodextrin molecules, which are known to form inclusion complexes with organic compounds, as a superior sensing layer on SAW devices.
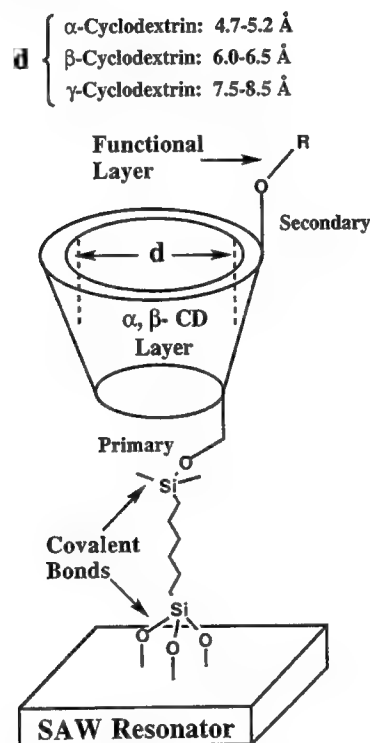
3. RESULTS AND DISCUSSIONS

Cyclodextrins are chiral, toroidal-shaped enzymatic products formed by the action enzyme cyclodextrin transglycosylase on hydrolyzed starch. They contain $m = 6$ to 12 glucose units bonded together through α-(1,4)-linkage, whose characteristic sleeve-like-cavity size and shape are defined by m. The three smallest homologs, α- ($m = 6$), β- ($m = 7$), and γ- ($m = 8$) cyclodextrins, are commercially available. These host cavities exhibit hydrophobic behavior; depending on the variety, they

---

[*] To whom correspondence should be addressed

have the size and chemical environment to readily incorporate specific chemical agents or target organics through "host" and "guest" interactions. Furthermore, the polarity and the size of the cyclodextrin's cavity can be chemically modified and structurally tuned to further enhance molecular recognition ability.

The self-assembled monolayers of cyclodextrin receptors on SAW surfaces were prepared by reacting cyclodextrin derivatives with a bifunctional bis(1,6-trichlorosilylhexane) (BTCSH) derivatized oxide surface to create covalently bound sensing layer with tailored selectivity as shown in Scheme I.[2] The surface attached nanometer-sized host molecules are predominantly aligned upward[3] and endowed with a locally modified chemical environment to complex volatile organic compounds.

Scheme I

d { α-Cyclodextrin: 4.7-5.2 Å
β-Cyclodextrin: 6.0-6.5 Å
γ-Cyclodextrin: 7.5-8.5 Å

Functional Layer → R

Secondary

d

α, β- CD Layer

Primary

Si

Covalent Bonds

Si

SAW Resonator

Using efficient molecular engineered cyclodextrin host monolayers, we have achieved sensitivity comparable to that of thicker polymer spin-casted or spray-coated films.[4] The optimized interactions between hosts and guests are attributable to the proper alignment, lipophilic cavity, and functionalization of the upper rim.

The general synthetic strategy is first blocking the primary side (bottom of the molecular bucket) of the cyclodextrin and then functionalizing the secondary side by reacting various organic substitutes with the secondary hydroxyl groups. When the proper functional groups were introduced at the desired level on the secondary side, the blockers in the primary side is then hydrolyzed off to recover the primary hydroxyl group for surface attachment. We have selected 1,6-bis(trichlorosilyl)hexane as our first linker because it reacts readily with hydroxyl groups. In our vapor-phase-monolayer deposition, we found little amount of the 1,6-bis(trichlorosilyl)hexane forming loop-like structures on the silica surfaces. This might be due to the fact that the extended chains are the energetically favorable structures.

The asymmetric host molecules used in this study include α-cyclodextrin dodeca(2O,3O)-benzoate (**1**), β-cyclodextrin tetradeca(2O,3O)-benzoate (**2**), β-cyclodextrin tetradeca(2O,3O)-acetate (**3**). Host compounds **1** and **3** were prepared according to the reported literature procedures;[5] whereas, host compound **2** was synthesized by treating β-cyclodextrin with *t*-butyldimethylsilyl chloride followed by benzoation reaction using benzoyl chloride in pyridine. The host monolayer thin films were prepared by exposing the cleaned SAW substrates to the vapor of 1,6-bis(trichlorosilyl)hexane by bubbling argon through a trap-bubbler-trap system at 150 mL/min at 70 °C. The silane derivatized substrates were then immersed in the ~1.0-5.0 mM corresponding cyclodextrin solutions for about 2 hrs at room temperature to allow the formation of self-

assembled host monolayers. The sol-gel precursors were synthesized by reacting cyclodextrin with isocyanatopropyl-triethoxy-silane in pyridine at 75 °C for 48 hours, followed by removing of the solvent and redissolving the sol-gel precursors in DMF. The sol-gel films were prepared by simply immersing the corresponding SAW devices in the above 10 mM sol-gel precursor solution in DMF at room temperature for a period of time up to two days.
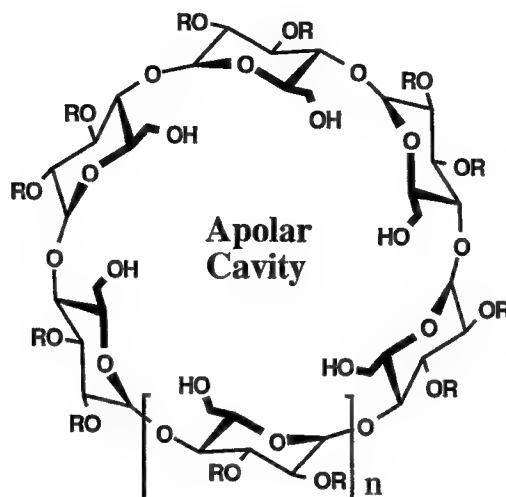
1: R = -COC$_6$H$_5$, n = 1
2: R = -COC$_6$H$_5$, n = 2
3: R = -COCH$_3$, n = 2

SAW resonators (200 MHz) were used to measure sensor response to organic analytes.[6] The phase velocity of this acoustic wave—and therefore the resonant frequency of the device—is a sensitive function of the physical properties of any contacting materials. In the present case of thin, nonconductive thin films, electrical and viscoelastic effects are minimal and the resonant frequency shift (Δf)[6d] depends mainly on the mass loading per unit area ($\Delta m/A$) of the sensing monolayer[7] and any adsorbed vapors according to eq. (1), where $K = 1.3 \times 10^{-6}$ s·cm^2/g.

$$\Delta f = - K f^2 \frac{\Delta m}{A} \qquad (1)$$

For cyclodextrin-based monolayers, we have observed a chemical sensor with a sensitivity of about 50-5 ppm towards typical organic molecules such as chloroform, perchloroethylene, and xylenes. SAW measurements indicate that the interaction of the sensing layer with organic vapors produces a maximum mass-loading of a typical monolayer. This result further suggests that each surface-bound receptor interacts with one or less organic analytes on average. The sensor sensitivity depends on two factors: the ultimate sensitivity of the SAW devices and the affinity of the sensing layer to the target molecules. The sensitivity of SAW devices has little improvement now, but the sensing layer can be adjusted to obtain a large range of sensitivity for target organic compounds by tuning the equilibrium constant.

For a given system, the sensor sensitivity increases with the increase of the sensing layer thickness. Therefore, a monolayer system is useful in understanding specific molecular interactions between analytes and sensing layers, but a multilayer system is practical for sensor applications. Aforementioned self-assembled systems offer an approach of controlled synthesis to multiple layer thick films. Sol-gel techniques offer an alternative approach to thick films with less control of the molecular structure but with great simplified synthetic route.

Figure 1 shows real-time reversible, rapid (~sec) sensor response for a cyclodextrin sol-gel film to acetone at a concentration range from 25 ppm to 2 ppm. Over five orders of vapor concentrations (~5,000 ppm-50 ppb), a nonlinear behavior was observed at extreme organic vapor partial pressures; whereas sensor exhibits a linear response within a narrow concentration range, especially at low concentrations. For xylene and perchloroethylene, the vapor concentrations as low as ~50 ppb were traced by the present cyclodextrin sol-gel microsensors.
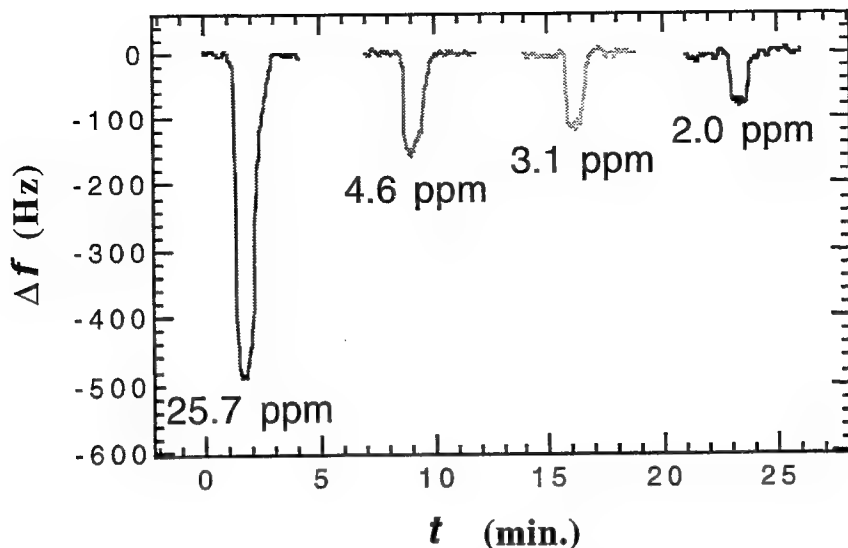
Figure 1. The cyclodextrin-coated, surface-acoustic-wave-based sensor responds to 1-minute-wide acetone pulses at the particular concentrations shown. The film was prepared from β-cyclodextrin with 14 equivalent amount of isocyanatopropyltriethoxysilane on both primary and secondary sides.
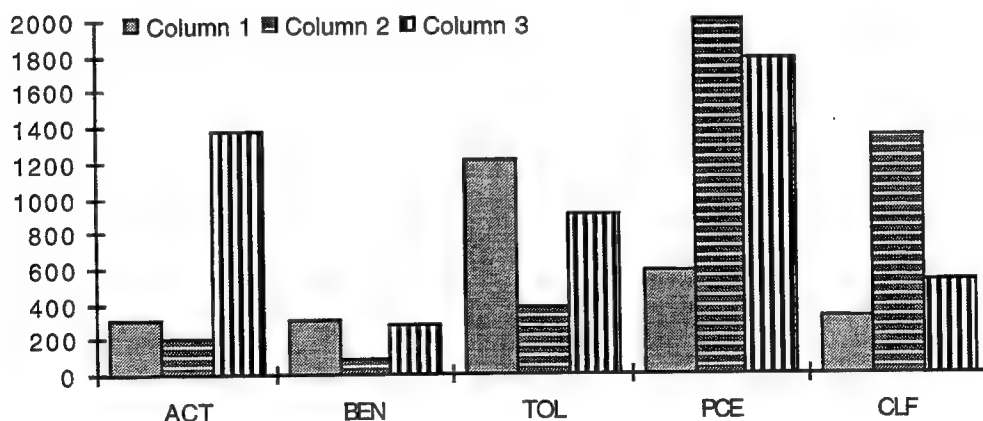
Figure 2. The bars represent the distinct responses (frequency shifts in Hz) of 5 volatile [Acetone(ACT), Benzene (BEN), Toluene (TOL), Perchloroethylene (PCE), and Chloroform (CLF)] organic compounds to 3 different host monolayers (from left to right, sensing layer consists of host compound **1**, **2**, or **3**).

Sensor selectivity depends on optimum chemical or physical interactions between the analyte and the sensing layer such as mutual matching of polarity, size, and structural properties. The cyclodextrin monolayers show appreciable selectivities within a group of organic template analytes chosen for their variety of structures and polarities to probe the cavities of the host compounds (Figure 2). The observed selectivities are expected, as the inclusion complexes of phenyl units into α-cyclodextrin and the optimum fit of perchloroethylene into β-cyclodextrins are well-documented by UV-vis,[8] NMR,[9] and X-ray crystallography[10] in the literature. The sensor each shows a distinct set of relative responses among a group of analytes, attributable to inherently different local host chemical environments. Conversely, a judicious assortment of sensing layers in an array of microsensors can be used to provide a unique characteristic pattern of responses for each compound. For instance, the response of chloroform as illustrated in Figure 2 to an array of microsensors coated with monolayers of host **1**, **2**, and **3** is a sharp peak. The same sensor array responds to toluene with a "doublet," and each compound has its own characteristic

response to this sensor array. VOCs which closely resemble each other, for instance, benzene and toluene, yield similar patterns.

4. CONCLUSION

To summarize, we have successfully synthesized cyclodextrin-based monolayers and sol-gel films which were shown to have ppm-ppb sensitivity to targeted organic analytes. Pattern recognition with an array of microsensors appears to be a feasible approach for identifying a particular VOC.

ACKNOWLEDGMENTS

REFERENCES AND NOTES

1. (a) F. W. Cornell: Proc. *Natl. Symp. on Measuring and Interpreting VOCs is Soil: State of the Art and Research Needs*, Las Vegas, NV, Environmental Liability Management, Inc., Princeton, NJ (1993).
    (b) A. D. Henricks, D. E. Grant,*The Cost Effectiveness of Field Screening for VOCs, Emerging Technology Symposium*, Los Alamos National Laboratory, Los Alamos, NM (1993).
2. (a) L. W. Moore, K. N. Springer, J.-X. Shi, X. Yang, B. I. Swanson, D. Li, *Adv. Mater.* 7, 729-731 (1995).
    (b) D. Li, B. I. Swanson, *Langmiur*, 9(12), 3341-3344 (1993).
    (c) D. Li, M. A. Ratner, T. J. Marks, C. Zhang, J. Yang, G. K. Wang, *J. Am. Chem. Soc.*, 112, 7389-90 (1990).
3. All host compounds (1-3) have hydroxyl functional groups *only* at the bottom rim and therefore these hosts can only align upward.
4   F. L. Dickert, P. A. Bauer, Adv. Mater., 3, 436 (1991).
5. (a) J. Boger, R. J. Corcoran, J. M. Lehn, *Helvetica Chimica Acta* , 61, 2190 (1978).
    (b) K. Takeo, K. Uemura, H. Mitoh, *J. Carbohydrate Chem.*, 7(2), 293. (1988).
    (c) C. D. Gutsche, L. G. Lin, *Tetrahedron*, 42, 1633 (1986).
6. (a) C. Campbell: *Surface Acoustic Wave Devices and Their Signal Processing Applications*; Academic Press, Boston, 1989.
    (b) M. Feldmann, J. Henaff:*Surface Acoustic Wave for Signal Processing*; Artech House, Boston (1989)
    (c) J. W. Grate, A. Snow, D. S. Ballantine Jr., H. Wohltjen, M. H. Abraham, R. A. McGill, P. Sasson, *Anal. Chem.*, 60(17), 869-75 (1988).
    (d) Grate, J. W.; Klusty, M. *Anal. Chem.*, 63(17), 1719-27 (1991).
7. (a) J. W. Grate, M. Klusty, R. A. McGill, M. H. Abraham, G. Whiting, J. Andonian-Haftvan, *Anal. Chem.* 64, 610 (1992).
    (b) R. Anderson, G. L. Larson, C. Smith (Ed.): *Huls Silicon Compounds: Register and Review*; Huls America Inc: Piscataway, NJ, 1991, pp. 93.
8. F. Cramer, H.-Ch. Spatz, *J. Am. Chem. Soc.*, 89, 14 (1967).
9. M. Teiichi, H. Kazuaki, M. Satoshi, *Chem. Express*, 4, 645-8 (1989).
10. K. Harata, *Bull. Chem. Soc. Jpn.*, 48, 2049 (1975).

SESSION 7

Poster Session

Electrical resistivity of smart composites with electromechanical coupling

Xiangdong CHEN,Daben YANG,Yadong JIANG,Zhiming WU,
Shaohong WANG,Dan LI

Department of Materials Science and Engineering,
University of Electronic Science and Technology
Chengdu 610054, China

ABSTRACT

This paper describes the effect of electromechanical phase on electrical resistivity of a composite consisting of magnetostrictive phase, conductive phase and insulating phase. It is found that the resistance of three-phase composite increases with increase of applied magnetic field beyond a certain value of magnetic field. This resistivity vs. magnetic field characteric seems to be a novel magnetoresistance effect, which is different from the conventional magnetoresistors. The mechanism of resistance variation of three-phase composite with applied magnetic field is analysed, and the influence of material parameter of the polymer matrix like elastic modulus on the resistance vs. magnetic field characterics is discussed.

Keywords: composites, electrical resistivity, smart materials

1. INSTRUCTION

Recently, the field of "smart" materials has progressed remarkably in the last ten years.[1-2] Various smart materials may sense a change in the environment and make a useful response.[3] Electronic materials like varistors and thermistors are important part of smart materials, which are also called as smart electronic materials.[4] Polychromatic percolation and product properties of composite materials are an effective approach to develop smart electronic materials.

2.PRODUCT PROPERTIES AND POLYCHROMATIC PERCOLATION OF COMPOSITE MATERIALS

The sum and product properties of composites were introduced by J. Van Suchtelen.[5] For a sum property, the composite property coefficient depends on the corresponding coefficients of its constituent phases.

Product properties are more complex and more interesting involving different properties in its constituent phases with the interactions between the phases often causing unexpected results. A product property utilizes different properties in the two phases of a composite to produce yet a third property through the interaction of the phases. By combining different properties of two or more constituents, surprisingly large product properties are sometimes obtained with a composite. Indeed, in a few cases, product properties are found in composites which are entirely absent in the phases making up the composite.

Transport by percolation through two or more materials can be visualized in terms of colors.[6] Black and white patterns illustrate percolation in a diphasic solid. Three kinds of percolation are possible : (I) percolation through an all-white path. (ii) percolation through an all-black path, and (iii) percolation

through a combined black-white path. From a composite point of view, the third possibility is the most interesting because it offers the possibility of discovering new phenomena that are not present in either phase individually. Foremost among these effects are the interfacial phenomena that arise by inserting a thin insulating layer between particles with high electrical conductivity. PTC thermistors and boundary layer capacitors are examples.
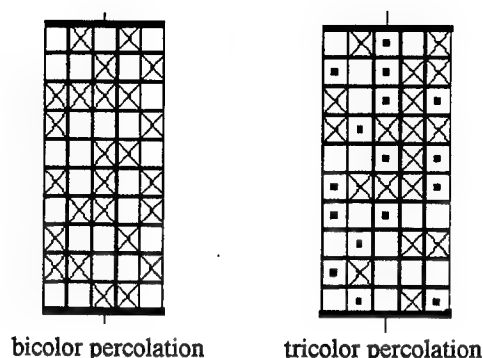

bicolor percolation   tricolor percolation

Figure 1.

Three-color percolation is illustrated in Figure 1. Seven kinds of conduction paths are possible: three monocolor, three bicolor, and a tricolor. When all three are present in equal amounts, it is possible that there will be no monocolor transport. In this case bicolor and tricolor paths become important. Monocolor conduction paths become increasingly important as volume fractions become unbalanced.

3. FUNDAMENTALS OF RESISTIVITIES OF CONDUCTIVE COMPOSITES

The properties of composite systems are understood in terms of percolation phenomena;[7-9] when a sufficient amount of conductive filler is loaded into an insulating polymer matrix, the composite transforms from an insulator to a conductor, the result of continuous linkages of filler particles. This is shown graphically in Fig. 2;[10] as the volume fraction of filler is increased, the probability of continuity increases until the critical volume fraction, beyond which the electrical conductivity is high, comparable to the filler material.
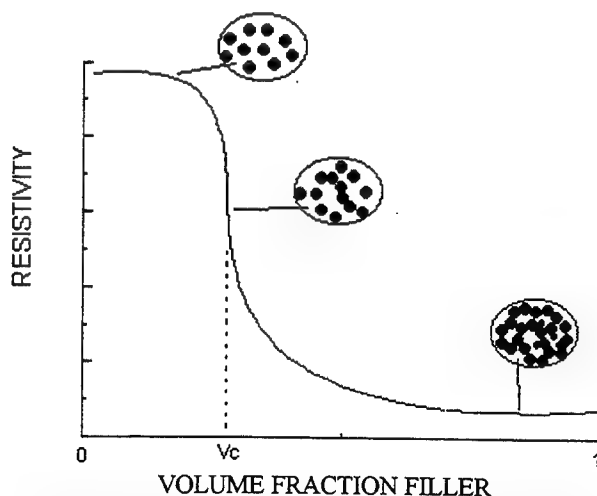
. **Figure 2.** Percolation theory, as applied to conductive composites. The formation of the first complete particle linkage results in a sharp drop in resistivity at Vc.

Effective-media theories attempt to quantify the resistance of these systems. When speaking of effective-media approximations in electrically conductive composites, a continuous linkage of conductive particles is often thought of as a single conductive filament; however, this is not accurate. Rather, each percolated linkage should be thought of as a series of resistors, with each particle and each particle-particle contact contributing to the total resistance in the filament. There are two important contributions to the particle-particle contact resistance: constriction resistance and tunneling resistance.

The other important limitation to the conductivity of two spheres is the resistance associated with any insulating film which be completely coating each filler particle. This film may be present in varying thickness, providing an insulating layer between two spheres. According to classical mechanics (and the Bruggeman asymmetric effective media or Hashing coated-spheres models), this would result in a high series resistance, but this is not the case. For thin films on the order of $100 \overset{\circ}{A}$ or less, quantum-mechanical tunneling can occur, resulting in lower resistivities.

The physics of quantum-mechanical tunneling shows that the relative probability that an electron will "tunnel through", rather than surmount, a potential barrier is proportional to the work function of the conductor, the thickness of the film, and the relative dielectric permittivity of the film. The surprising result is that the resistivity of the film is not a factor in tunneling, so that organic, polymers, and oxides, most with similar work functions and permittivities, will have similar tunneling resistivities for similar film thicknesses.

The dependence of tunneling resistivity on the insulating film thickness has been derived mathematically, Dietrich[10] pioneered the work on this problem, and presented a general tunneling curve (based on TiO_2 film on Ti), empirically derived but thought to be approximately applicable to all materials(see Figure 3).

Conventional magnetoresistors are usually prepared from semiconductors such as indium antimonide. Further, those magnetoresistors need special fabrication techniques like unidirectional solidfication of eutectics or realisation of semiconductor films or crystals with specific geometry. There is a need to develop magnetoresistors which can be realised with simpler technology. Polychromatic percolaton and product properties of composites suggest that magnetoresistance effect can be realised with by proper coupling of interactions in a multiphase composite material. This paper reports the attempts made to develop a novel magnetoresistor using electromechanical coupling effect.
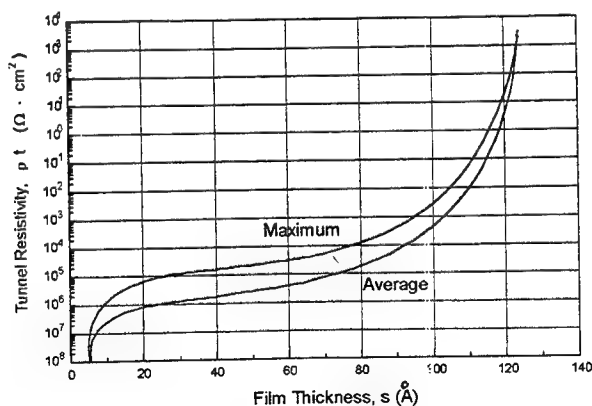
Figure 3. Tunnel resistivity for thin films of TiO_2 on Ti as a function of film thickness.

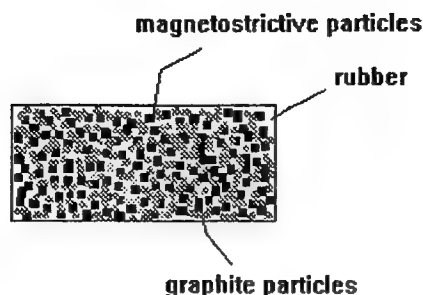**Figure 4.** Cross section of the sample

4. SAMPLE PREPARATION

The cross section of 0-3 composite structure is shown in Figure 4. $Co_xFe_yO_4$ ferrite and graphite particles are dispersed in a rubber solution. The mixture is then air dried and vulcanized at about 120 for three hours. Samples are cut to suitable dimensions from larger sheets. Electrodes are realised by covering the lateral faces of the sheets with silver paint. Their thickness is about 2 mm. The samples with different compositions have been prepared. In the similar way, epoxy resin based composite samples loaded with $Co_xFe_yO_4$ and graphite particles have been formed.

5. RESULTS AND DISCUSSION
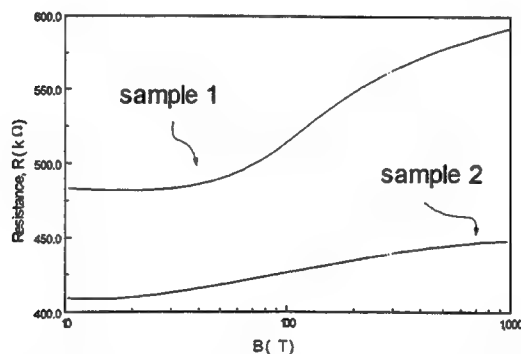
Figure 5. Measured variation of resistance of rubber based composites with magnetic field.
sample 1: v_g =0.14, v_f =0.26, v_r =0.60
sample 2: v_g =0.18, v_f =0.22, v_r =0.60
where v_g is the volume fraction of graphite, v_f is the volume fraction of magnetostrictive ferrite ,
v_r is the volume fraction of rubber.

The R-B characteristics of rubber based composites have been measured. Figure 5. shows the resistivity vs. magnetic field characterics of 0-3 rubber based composite. From this figure, the change in resistance of the sample is small at low field. At higher field, the change in resistance increases with magnetic field and tends finally to saterate. It is seen from this figure that the magnetic field coefficient of resistance depends on the composition of the sample. This R-B characteristics of three-phase composite

is caused by product property of three-phase composite.

The steady-state for the resistivity minima of composites is based on the notion that the composite is the result of a series of a large number of resistors combined in series and parallel. There are three separate contributions to the resistance: constriction resistance at the contacts, tunneling resistance at the contacts, and the intrinsic filler resistance through each particle. Tunneling resistance generally dominates the magnitude of the overall resistance.

Electrical conduction of composite is controlled by an electron emission process between adjacent conducting particles across the thin film of rubber separating them. This electron emission process is determined by the electrical field across the rubber film. The electrical field is related to two factors, the applied voltages and the gaps between the conducting particles.

At low field, the strain of magnetostrictive phase may be negligible, the change in gap between graphite particles is small, thereby the resistance of 0-3 composite hardly change initially with increase of magnetic field. However, at higher field, electromechanical properties of magnetostrictive ferrite particles begin to affect electrical resistance of 0-3 composite. In fact, 0-3 composite with electromechanical coupling is a passively smart structure at high field; the magnetostrictive particles sense a field to create a strain and passes this strain to the film between conducting particles, leading to an increase in thickness of the gap between the conducting particles, tending to give rise to a decrease in conduction. When the influence of magnetostrictive phase on electron emission process dominates beyond a certain value of field, the resistance of composite begins to increase with magnetic field and exhibits a positive magnetic field coefficient.
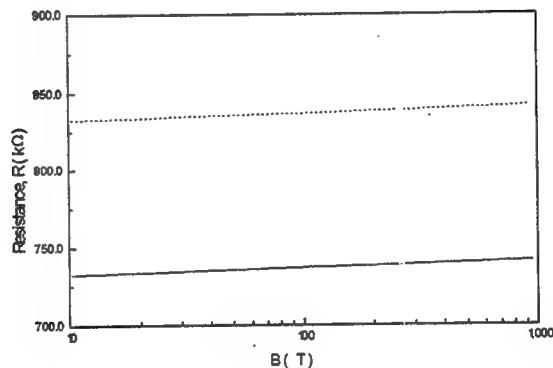

Figure 6. Measured variation of resistance of epoxy resin based samples with magnetic field.
short dot line: v_g =0.16, v_f =0.26. v_e =0.58
solid line: v_g =0.19, v_f =0.22, v_e =0.59
where v_g is the volume fraction of graphite, v_f is the volume fraction of magnetostrictive ferrite ,
v_e is the volume fraction of epoxy resin.

Figure 6. shows the resistivity vs. magnetic field characterics of epoxy resin based composites. In this figure, the resistance of epoxy resin based composite hardly change with magnetic field. An expected positive magnetic field coefficient of resistance has not been found in epoxy resin based samples. This shows that the resistance vs. magnetic field characterics of three-phase composites are related to a parameter of polymer material used as the matrix.

If the cross section area of the tunnel is known, a tunneling resistance R_t may be expressed as

$$R_t = \rho_t t \qquad (1)$$

where ρ_t is the tunneling resistivity, t is the thickness of the insulating film between adjacent conducting particles, which can be expressed as

$$t = t_0 + \triangle t \qquad (2)$$

where t_0 is the thickness of polymer film between two adjacent conducting particles in the absence of applied magnetic field and $\triangle t$ is the increase in thickness of the polymer film caused by the magnetostrictive effect of ferrite particles. This increase in thickness must be a function of the applied pressure on the polymer gap between adjacent conducting particles due to magnetostrictive strain and the deformation that occurs as a result of this applied pressure, hence, it is proportional to this stress, so

$$\triangle t = \sigma_i / E \qquad (3)$$

where σ_i is the applied pressure on the polymer gap between adjacent conducting particles due to magnetostrictive strain, E is the elastic modulus of the polymer matrix.

Substituting Eq. (2) and Eq. (3) into Eq. (1) gives

$$\triangle R_t = \rho_t \, \sigma_i / E \qquad (4)$$

where $\triangle R_t$ is the increase of resistance caused by the increase in thickness of the polymer gap between conducting particles.

From Eq. (4), it is seen that the increase of resistance is inversely proportional to the elastic modulus of the polymer matrix when the stress σ_i is the same. This is why the change in resistance of epoxy resin based sample is always small with applied field. The elastic modulus of epoxy resin is much larger than rubber, hence, the thickness change of gap between two adjacent conducting particles in epoxy resin based sample due to magnetostrictive coupling is too small to result in a noticeable change of resistance of composite.

6. CONCLUSION

In this paper, we introduce electromechanical phase into the study of smart electronic materials. The results show that it is possible to realize a novel magnetoresistance effect using electromechanical coupling, which is different from conventional semiconductor magnetoresistors. The resistance vs. magnetic field characterics of three-phase composite are related to the material parameter of polymer matrix like elastic modulus.

REFERENCES

1. R. E. Newnham, "The golden age of electroceramics", *Adv. Ceram. Mater.* **3**, pp. 12-16, 1988.
2. H. Yanagida, "Intelligent materials-a new frontier", *Angew. Chem.* **100**, pp. 1443-46, 1988.
3. R. E. Newnham, Q. C. Xu, S. Kumar, and L. E. Cross, "Smart ceramics", *Ferroelectrics* **102**, pp. 1-8, 1990.
4. Robert E. Newnham and Gregory R. Ruschau, "Smart electroceramics", *J. Am. Ceram. Soc.* **74**, pp. 463-80, 1991.
5. J. Van Suchtelen, "Product properties: a new application of composit materials", *Philips Res. Repts* **27**, pp. 28-37, 1972
6. R. E. Newnham, "Composite electroceramics", *Ferroelectrics* **68**, pp. 1-32, 1986.
7. David S. Mclachlan, Michael Blaszkiewicz, and Robert E. Newnham, "Electrical resistivity of

composite", *J. Am. Ceram. Soc.* **73**, pp. 2187-2203, 1990.

8. N. Deprezand, D. S. Mclachlan, "The analysis of the electrical conductivity of graphite powders during   compaction", *J. Phys. D: Appl. Phys.* **D21**, pp. 101-107, 1988

9. S. M. Aharoni, "Electrical resistivity of a composite of conducting particles in an insulating matrix", *J. Appl. Phys.* **43,** pp. 2463-65, 1972.

10. G. R. Ruschau, S. Yoshikawa, and R. E.Newnham, "Resistivites of conductive composites", *J. Appl. Phys.* **72**, pp. 953-959, 1992.

Novel vapor sensor based on chemical coupling effect of composite

Xiangdong Chen, Daben Yang, Yadong Jiang, Zhiming Wu, Shaohong Wang, Dan Li
Department of Materials Science and Engineering,
University of Electronic Science and Technology,
Chengdu 610054, China

ABSTRACT

A novel sensing material has been developed for constructing a sensor of solvent vapours using chemical coupling effect of composite, which is different from conventional electron-moving chemiresistors for use as gas sensors. The composites consisting of polymer loaded with conductive filler near the percolation threshold exhibit sensitive characters comparable to that of conventional semiconductor gas sensor but can be realized with much simpler technology and operated at room temperature. This sensor can also obtain better selectivity by choosing different polymer matrix. Theoretic analysis and experimental results show sensitive properties of composite sensor greatly depend on composition of composite and grain size of conducting particles. In general resistance variation R/R_0 in the presence of vapor is more for higher volume fraction of filler and larger grain size of conducting particles.

Keywords: gas sensors, composites, electrical resistivity

1. INTRODUCTION

Increasing concern with environmental and personal protection together with wide spread requirements for more accurate process control has been created a need for new or improved sensors for measuring both physical and chemical parameters. This need for better sensors is strongly influenced by the increasing use of intelligent microelectronics for monitoring and control.

The sensing effect of conventional chemiresistors used as gas sensor is due to electron density moving between the sensitive film and the vapor and the relative magnitude of the electronegativity of the vapor and the work function of the sensitive film determines properties of sensors. Sensitive materials for these sensors are usually a metal oxide such as SnO_2 or ZnO. However, current designs that are based mainly on SnO_2, suffer from certain shortcomings that militate against their wider application. Prominent among these are their relative lack of selectivity to toxic gases and vapors. Another serious disadvantage is the requirement in most applications for operation at 300   or above. The development of gas-sensitive materials which could be sensitive to a wider range of gases and particularly to toxic gases and vapors, which could show significant selectivity and could be also could operate closer to ambient temperature would permit consideration of this type of device for a much wider range of applications

than is Satisfied at present.[1-2]

J. Van Suchtelen proposed that a new physical property could be realized by product properties of composite, in which the phases or submaterials of the composite are selected in such a way that an effect in one of the phases or submaterials leads to a second effect in the other phase.[3] The transfer can be brought about by coupling mechanisms of several kinds. Electrical, optical, magnetic, thermal and chemical coupling all is possible. A typical example is to realize a polymer based PTC thermister with a positive voltage coefficient of resistance using thermal coupling.[4]

In this paper we describe results on a composite gas sensor with chemical coupling which show some promise for the detection of toxic gases at room temperature.

2. STRUCTURE AND FABRICATION OF SENSORS

The sensor studied is a composite film deposited on a substrate with electrodes. The resistor is prepared by screen-printing a thick film paste consisting of PMMA solution and graphite powder. The resistor is a composite film of thickness o.o25cm. The resistor is rectangular in shape with length 1.0cm and width 0.5cm. Various resistors have been printed using pastes containing graphite powder of different grain sizes and compositions. Electrodes of evaporated copper are deposited on one side of the composite film only, with a narrow gap separating them. The structure of the device is shown in Fig. 1.
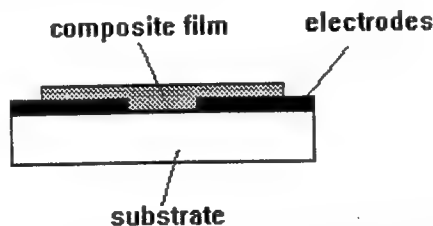
Figure 1. Cross section of the structure of the sensor.

3. MEASUREMENTS

As a vapor penetrates the composite film, the conduction path changes and bulk resistance is measured. Resistance measurements (d.c.) are taken as a function of exposure time for the sensor samples. For measurements in solvent vapor, the samples are electrically connected to a digital multimeter and suspended in a sealed 10ml glass bottle with 2ml of $CHCl_3$ or CH_2Cl_3 solvent to provide sufficient vapor pressure. Resistance readings are taken manually and normalized against the initial resistances. Thus all data are in the form of resistance ratios R/R_0, where R_0 is the initial resistance of the sensor.

4. RESULTS AND DISCUSSIONS

The order of magnitude of resistance of the composite film depends upon the volume fraction of graphite. It is typically about 200k for a volume fraction of 0.25 and about 6k at a volume fraction of 0.30. It has been found that the variation of resistance with time t in the presence of vapor. Typical variations of resistance with time t are shown in Fig. 2. From this figure, it is found that the electrical resistance of the composite film always increases in the presence of vapor. Percolation theory is proposed to explain this positive coefficient of resistance in the presence of vapor with time t.

The resistivity characteristics of such a system can be described by percolation theory (see Fig. 3), in which conductive filler particles are surrounded by a polymer matrix.[5-6] At low volume fraction of conductor, the electrical resistance of the composite is high (region A), i.e., dominated by the polymer, and approaches the bulk resistivity of the polymer. As more filler is loaded into the composite, the resistivity decreases steadily until a critical volume fraction is reached (region B). This volume fraction is known as the percolation threshold, and marks the formation of the first
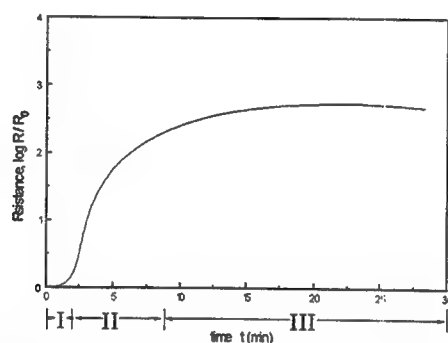
Figure 2. Typical variations of resistance with time t.

continuous conducting filament of particle-particle contacts. The resistance then drops sharp with a small increase in filler volume fraction. Once loaded to the conduction limit (region C), additional filler will have a much less dramatic effect on the resistivity. At high volume fractions of conductor, the electrical resistance of the composite is relatively low, dominated by the filler, and approaches the bulk resistivity of the pure filler.

From percolation theory of conductive composite, the resistance of composite will increase if percolation paths of conductive particles are broken by certain physical or chemical coupling. Swelling may be such a coupling. In part I (see Fig. 2), the evaporation of liquid solvent, the changes in resistance are slow; in part II, the vapor is absorbed into the composite film, the vapor causes swelling of polymer matrix, so the volumetric concentration of the conductor phase decreases, a few or many of the conducting paths formed between the conductor particles are broken (see Fig. 4),
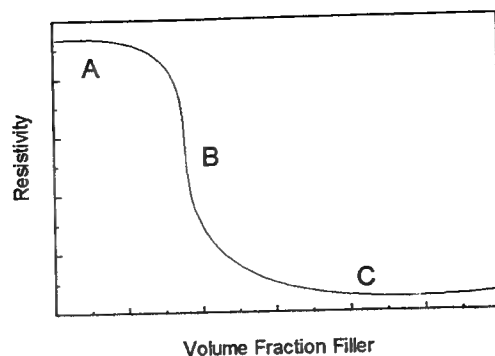
Figure 3. Dependence of resistivity of composites on the volume fraction of conductor filler.

it causes a decrease in conductivity of the sample, the resistance reaches the largest value in a short time; in part III, the stabilization of sample resistivity occurs.
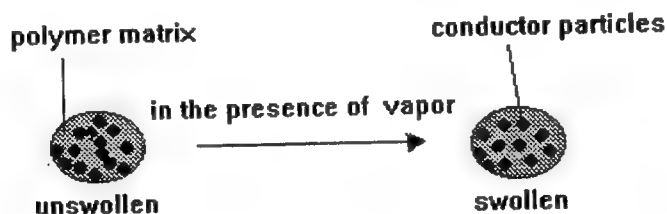
Figure 4. Schematic of composite sensor response

The result in Fig. 2 is obtained at room temperature. This shows that this composite sensor can be operated at room temperature but has sensitive characterics comparable to that of conventional semiconductor gas sensor, and this sensor can be realized with much simple technology and obtain better selectivity by choosing different polymer matrix.

Figure 5 shows resistance variation dependence for different values of volume fraction of filler, it is found resistance ratios varied greatly for different systems. In general the increase in resistance is more for higher values of higher volume fraction of graphite. However, presence of vapor can hardly cause an obvious change in the resistance of composite film when volume fraction of filler is beyond certain value. This dependence of resistance variation of sensor on volume fraction of filler may be determined by properties of tunneling resistivity between conductor particles.
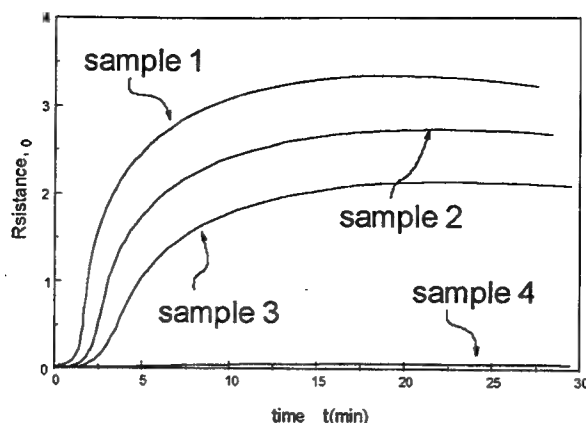
Figure 5. Time-dependent sensor response for different values of volume fraction of graphite:
Sample 1: 0.20, Sample 2: 0.25, Sample 3: 0.30, Sample 4: 0.50

The steady-state model for the resistivity minima of composite is based on the notion that the composites the result of a series of a large number of resistors combined in series and parallel. There are three contributions to the resistance: constriction resistance at the contacts, tunneling resistance at the contacts, and the intrinsic filler resistance through each particle. Tunneling resistance generally dominates the magnitude of the overall resistance.[7] Therefore, the resistance of the insulating gaps between the conducting particles decides the total resistance of film.

It is assumed that the change L (increase) in length of the thick film resistor along electric field caused by swelling effect is given by

$$L = S(t)L \qquad (1)$$

where $S(t)$ is the swelling coefficient of polymer matrix in vapor, which is a function of time t, and L is the length of the resistor along electrical field.

This increase in length of the film due to swelling effect leads to an increase in the thickness of the insulating film separating adjacent graphite particles. If there are N_0 contacts between graphite particles along the length, then

$$N_0 = \frac{L}{(D + d_0)} \qquad (2)$$

where D is the diameter of the graphite particle and d_0 is the thickness of the insulating film between

adjacent particles in the absence of vapors.

The thickness of the insulating gap in the presence of the vapor can be expressed as

$$d = d_0 + \frac{L}{N_0} \tag{3}$$

When swelling effect results in an increase in thickness of the insulating gap, the electric field across the thin polymer film between adjacent conducting particles becomes

$$E' = \frac{(V / N_0)}{d} = \frac{V}{N_0 d_0 + S(t)L} \tag{4}$$

Assuming that the current flow between the conductor particles through the polymer gap is by field emission, the resistance R_g of one gap between conductor particles can be obtained through the Fowler-Nordheim equation as

$$R_g = \frac{(V / L)(D + d_0)}{aAE'^2 \exp(-b / E')} \tag{5}$$

where a is the cross sectional area for current flow, A and b are constants in the Flower-Nordheim equation. The total resistance of the thick film R, considering the number of the contacts along the thickness and width, is given by

$$R = R_g(\frac{L}{W})\frac{D + d_0}{h} \tag{6}$$

where W is the width of the film and h is the thickness. From (5) and (6), R can be expressed as

$$R = \frac{(D + d_0)^2}{aAhWV}[N_0 d_0 + S(t)L]^2 \exp\{\frac{b[N_0 d_0 + S(t)L]}{V}\}$$

$$= R_0[1 + \frac{S(t)L}{L - N_0 D}]^2 \exp\frac{bS(t)L}{V} \tag{7}$$

From this equation, we can see that resistance variation R/R_0 in presence of vapor increases with increasing of N_0, and N_0 is proportional to volume fration of filler, therefore, resistance variation R/R_0 is more for higher values of volume fraction of filler. However, this equation is only suitable to B region. When volume fraction of filler is in C region, (see Figure 3), the electrical resistance is very low, approaches the bulk resistivity of the pure filler, volume change due to swelling is too to cause an obvious resistance variation.

Figure 6 shows resistance variation dependence for different values of grain size of conductive particles, the increase in resistance is also more for higher values of larger grain size of graphite particles. This result can also be obtained from Eq. 7.
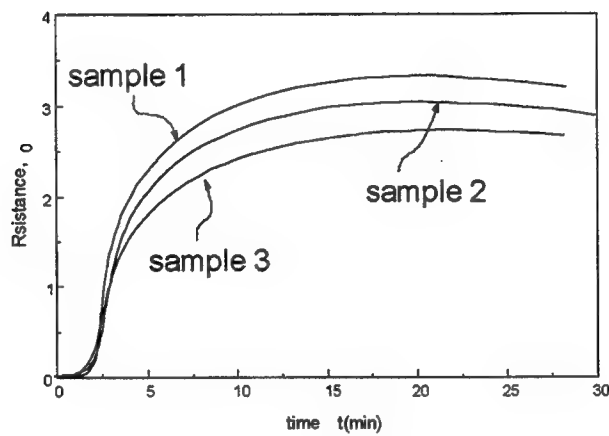
Figure 6. Time-dependent sensor response for different values of grain size of graphite particles: Sample 1: 40 μm, Sample 2: 60 μm, Sample 3: 90 μm

Substituting Eq. (2) into Eq. (5) and Eq. (7) gives

$$E' = \frac{(V/L)(D+d_0)}{d_0 + S(t)(D+d_0)} \tag{8}$$

$$R = \frac{L^2}{\alpha A h W V}[d_0 + S(t)(D+d_0)]^2 \exp\{\frac{b[d_0 + S(t)(D+d_0)]}{(V/L)(D+d_0)}\}$$

$$= R_0 [1 + S(t)(\frac{D}{d_0} + 1)]^2 \exp\frac{bS(t)L}{V} \qquad (9)$$

The insulating gap d_0 of adjacent conducting particles decreases with increasing of grain size D of conducting particles when volume fraction of filler is the same, therefore, D/d_0 increases with increasing of grain size D, and R/R_0 is more for larger diameter of conductive particles.

5. CONCLUSIONS

The PMMA-graphite composite film with chemical coupling is a good sensing material for constructing a detector of $CHCl_3$ and CH_2Cl_3 vapours. It exhibits sensitive characterics comparable to that of conventional semiconductor gas sensor based on electron-moving chemiresistor but can be realized with much simpler technology and operated at room temperature. This sensor can obtain better selectivity by choosing different polymer matrix. Theoretic analysis and experimental results have shown that sensitive properties of composite sensor greatly depend on composition of composite and grain size of conducting particles. Resistance variation R/R_0 in the presence of vapor is more for higher volume fraction of filler and larger grain size of conducting particles.

REFERENCES

1. H. Shurmer, A. Fard, J. Barker, P. Bartlett, G. Dod and U. Hayat, "Development of an electronic nose," *Phys. Technol.* **18**, pp. 170-176, 1987.

2. Jan J. Miasik, Alan Hooper, Bruce C. Tofield, "Conducting polymer gas sensors," *J. Chem. Soc., Faraday Trans. I* **82**, pp. 1117-1126, 1986

3. J. Van Suchtelen, "Product properties: a new application of composite materials," *Philips Res. Repts* **27**, pp. 28-37, 1972.

4. K. A. Hu, D. Moffatt, J. Runt, A. Safari and R. E. Newnham, "V_2O_5-polymer composite thermisters," *J. Am. Ceram. Soc.* **70**, pp. 583-39, 1987.

5. I. Balberg, C. H. Anderson, S. Alexander, and N. Wagner, "Excluded volume and its relation to the onset of percolation," *Phys. Rev. B: Condens. Mater.* **B30**, pp. 3933-43, 1984.

6. S. M. Ahharoni, "Electrical resistivity of a composite of conducing particles in an insulating matrix," *J. Appl. Phys.* **33**, pp. 3125-31, 1962.

7. G. R. Ruschau, S. Yoshikawa, and R. E. Newnham, "Resistivities of conductive composites," *J. Appl. Phys.* **72**, pp. 953-959, 1992.

Smart Materials Based on the Vinyledene Fluoride Copolymers

Tatiana G. Lazareva, Tatiana N. Vorob'eva, Elena V. Vashuk

Institute of General and Inorganic Chemistry of the Academy of Sciences of Belarus, Minsk, Belarus

ABSTRACT

Structure-sensitive materials, or the so-called "smart materials", which change their properties under the action of external fields (e.g. electric, light or temperature field) can find a wide use in various industrial applications as sensors, measuring elements of various types, radiation detectors, membranes, etc. In this connection, we have examined the conditions of formation of electrosensitive films based on copolymers of vinyledene fluoride (VDF) with tri- and tetrafluoroethylene. The films have been prepared from solutions in organic solvents (acetone, dimethyl sulfoxide (DMCO), dimethyl formamide (DMFA) and ethyl acetate). Based on the results of investigations of the temperature dependencies of the dielectric permittivity, surface charge density and tangent of dielectric losses, we have evaluated the effect of film formation conditions and a copolymer type on the molecular mobility, formation of electrets and charge relaxation in the temperature range 20-200 °C.

It has been concluded that in the non-orientated films there exists a relationship between the charge relaxation and the molecular mobility of the C-F dipoles in amorphous and crystalline regions of the polymer matrix. At the same time, the charge relaxation in orientated materials occurs in the crystalline regions of the polymer matrix. The optimal conditions have been specified for the production of such materials from solutions in organic solvents.

Keywords: electrosensitive films,

INTRODUCTION

In literature some polymer materials are known that respond to an electric field. Those are cellulose derivatives, in particular, monocarboxycellulose[1], polymethylgluconate, polycaprolactam, polyvinyl fluoride, polycarbonate[2], polyacrylonitrile[3], polymthyl methacrylate[4]. In the presence of an electric field of sufficient intensity these polymers undergo polarization transformations that occur both in kinetic links and in macromolecule as a whole. This makes it possible in the presence of an electric field to form ordered or modified, due to the electric field, structures of a number of polymers. Some polarization changes remain until a polymer is exposed to an electric field. It is a known fact, however, that in some solid-state polymers at temperatures substantially lower than their vitrification temperature some portion of acquired polarization still remains long after deenergizing the field[5-7]. It is stated that an electric field causes formation of electroinduced polar structures, changes a degree of crystallinity which is accompanied by ordering of polymer macromolecules or vise versa - disorientation processes.

In literature much attention is given to the electric effect exercised by polyvinyledene fluoride. Prehistory of investigations of an influence of the electric field on a polymer structure, of passing from measurement of piezo-, pyroelectric, mechanical properties to investigation of a polymer structure and its change in the presence of an electric field by an X-ray method and IR-spectroscopy is well traced. The interest to polyvinylidene fluoride owes to the discovery in 1969 of the substantial pyro- and piezo-electric response of the films exposed to an electric field[8,9]. It is reported about an influence of the electric field of different intensity on the structure and properties of polymer fluoride. Electrosensitivity of the latter is related with a change of its lattice in the presence of an electric field[10], formation of an active phase with a define layout of links in the lattice. Electrosensitive films find applications in electronics, instrument manufacture, robotics, acoustics, medicine. At present one of the best polymeric films is polyvinyledene fluoride (PVDF). However, along with its good quality, the PVDF film possesses such disadvantageous features as the complicated polymer synthesis and a low degree of crystallinity. Moreover, the orientation process yields many defects which deteriorates piezocharacteristics. Therefore we face the necessity of developing new electrosensitive films, in particular, those based on the copolymers of vinyledene fluoride whose synthesis is an easier technological process and their electrophysical properties rank on a par with the polyfluoride films.

EXPERIMENTAL RESULTS AND DISCUSSION

In investigations we used the films of vinyledene fluoride with tri- (I) and tetrafluoroethylene (II) copolymers, which were prepared from the following solvents: ethylacetate, dimethylformamide, dimethylsulfoxide, and acetone. The films were obtained by pouring a certain volume of the solution of the prescribed concentration onto a glass surface. The films were dried in air with use of ethyl acetate and acetone and then subjected to final drying in a desiccator at 50 °C. When dimethylsulfoxide and dimethylformamide were used, the films were dried in a desiccator at 150 °C till complete disappearance of the solvent.

A film structure was evaluated by a relaxation technigue involoving measurement of temperature dependences of the tangent of dielectric losses (tgδ) as well as by the method of X-ray analysis and IR-spectroscopy. Moreover, we also determined such electrophysical properties as dielectric permittivity (ε) and a surface charge density (Q/S) after polarizing the films by a d.c. electric field.

In measurements, the film sample was pressed between two metallic electrodes under certain loading and then placed into a cell where it was subjected to heating. To measure electrophysical characteristics of the polarized samples, prior to measurements the films were polarized for 1 h by a d.c. field with the prescribed electric intensity at the fixed temperature and then cooled in the presence of the applied field. To determine structural changes in the presence of the applied field and change relaxation, we measured the temperature dependencies of tg δ, ε, and Q/S.

As is known, the PVDF electrosensitivity is related with a crystal-line phase of the polymer. PVDF crystallized to form three crystalline phases, namely, α, β и γ[10]. A polymer cooled at the atmospheric pressure after extrusion from a melt crystallizes to form a crystalline α-form (spherulites with a size to 400 nm) of γ-form (finer spherulites sized to 100 nm). Spherolites have a typical star-like structure having both crystalline and amorphous region. In the crystalline α-form links of the molecules are arranged in the sequence: trans-gosh-trans-gosh (TGTG). The crystalline structure is such that the molecules form a weakly twisted coil, the CF_2 dipoles are aligned so that their vectors run in the opposite directions and total polarization in the crystalline cell is close to zero. The dipole moment of the link in $-CF_2-CF_2-$ in the zigzag conformations is 7×10^{-30} C/m, an elementary cell consists of four such links and has the dimension 0,966×0,496×0,464 nm. A great dipole moment leads to the substantial energetic interaction with an applied field. In the course of mechanical oriented stretching the initial spherulite structure fails and yields ordered crystals in which macromolecules are aligned in the direction of the applied mechanical load. If such deformation occurs at elevated temperatures (140-150 °C), the initial TGTG conformation remains unchanged since the chains freely slip relatively each other and the crystalline α-formis preserved. If deformations occur at low temperatures (< 90 °), then in the course of stretching the macromolecules become elongated, their conformation becomes more prolonged and corresponds to the crystalline β-form. A size of the monomer link increases along the chain from 0,231 до 0,256 nm. The elementary cell of the β-form is orthorhombic, the dipole moments of two chains in the elementary cell are aligned parallel to the major chain.

Such an extended conformation is polar since the dipoles are aligned perpendicularly to the macromolecule axes. The PVDF film prepared from a solution as well as upon slow cooling from a polymer solution has the crystalline γ-form[9]. Polarization of the polymer in the crystalline α-form in the presence of d.c. electric field causes partial rearrangement of the structure and, as a result, dipoles turn by 180 °. This is the crystalline polar-α_p-form. It is formed during polarization in the field with E equal up to 150 mV/m in the temperature range 243 °C. Polarization in the fields of higher intensity (240-400 mV/m) makes the structure to be rearranged from the α_p to β-form.

IR-spectra of the films of VDF copolymers formed from different solvents show distinctly the absorption bands corresponding to rocking and deformations vibrations of the CF_2 links (at 510, 480, 490 cm^{-1}). According to literature data[11] the bands at 490, 530, 610, 765, 975 cm^{-1} are assigned to the α-phase, while those at 422, 510, 340 cm^{-1}- to the β-phase. Experimental IR-spectroscopy data indicate that percentage of the α- and β-phases essentially depends on the way of film formation. For instance, the samples of VDF copolymers, in particular, with trifluoroethylene, obtained from dimethylsulfoxide display the bands corresponding to the α-phase, more distinctly, the bands of the dimethylformamide-based films are weaked and for the acetone-based films this series (530, 610, 765, 975 cm^{-1}) is not manifested itself. At the same time for the VDF copolymers obtained from dimethylformamide the absorption bands at 510 and 840-850 cm^{-1} typical of the β-phase are more pronounced.

Fig. 1a shows the temperature dependencies of tg δ for the films based on the vinyledene fluoride - trifluoroethylene copolymer which were prepared from 3% copolymer solutions in dimethylformamide, dimethylsulfoxide, acetone, and ethyl acetate.
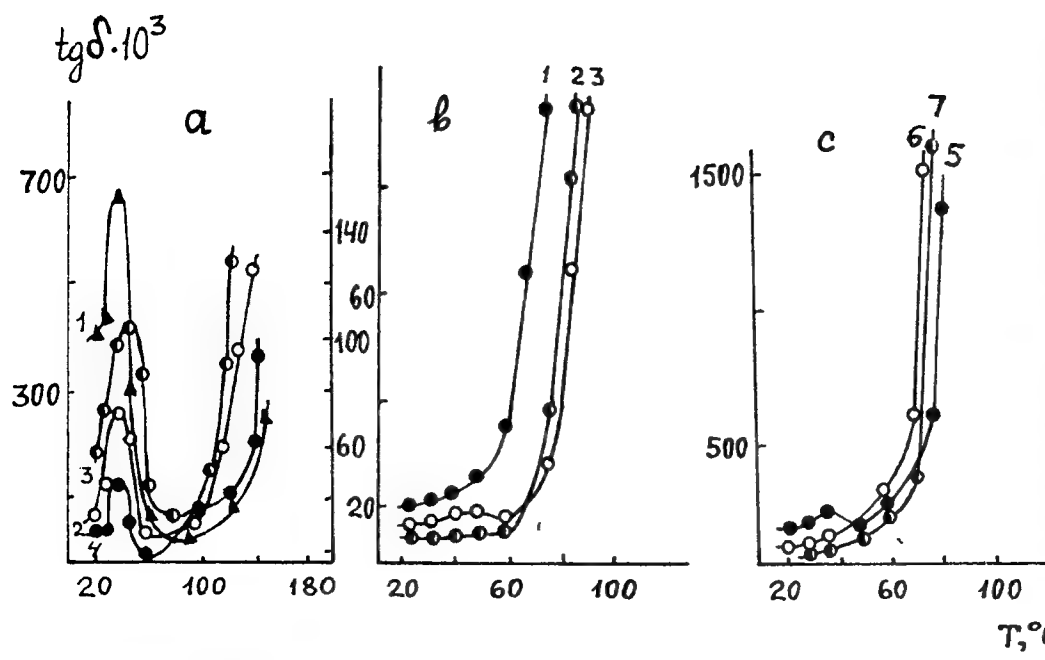
Fig.1. Temperature dependences of tgδ for the unpolarized (a), polarized at the temperature of 80 °C and E = 8 V/μm (b) samples prepared from the 3% copolymer solutions in dimethylformamide, dimethylsulfoxide, acetone, and ethyl acetate (1-4) as well as for the unpolarized samples formed from the 3% VDF-trifluoroethylene copolymer solutions in dimethylformamide and subjected to mechanical orientation (c), (5 initial unoriented sample; 6, relative elongation is 20%; 7, relative elongation is 30%).

All the samples show relaxation transitions in the temperature ranges 40-50 °C and 100-140 °C. This may be associated with the relaxation transitions in the amorphous and crystalline regions of the polymers being the fragments of the polymer chain, in particular, C-F[12,13]. As it follows from Fig. 1a, the molecular mobility depends on the solvent type and as far as molecular mobility enhances the solvents are arranged in the following sequence: acetone, dimethylformamide, dimethylsulfoxide, ethyl acetate.

Film polarization by a d.c. field or mechanical orientation leads to degeneracy of the relaxation transition in the range 40-50 °C and a shift of the latter towards lower temperatures in the range 100-140 °C (see Fig. 1b).
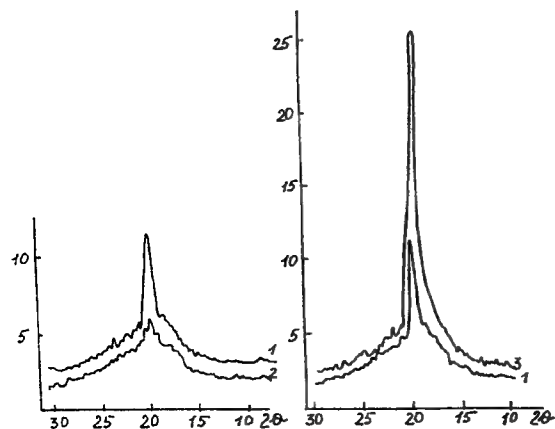
Fig.2. X-ray patterns of the unpolarized samples prepared from the 3% copolymer solutions in dimethyl-formamide (1) and ethyl acetate (2) and the sample, polarized at 80 °C and E = 8 V/μm, prepared from dimethylforma-mide (3).

This is indicative of formation of an ordered structure which is confirmed by the results of X-ray analysis shown in Fig. 2 where X-ray patterns of the unpolarized films and those polarized by a d.c. field formed from dimethylformamide and ethyl acetate are represented. Fig. 3 shows temperature-dependent dielectric permittivity for the polarized and unpolarized copolymer samples. Here, the dielectric permittivity is at its maximum in the temperature range 80-100 °C, a value of the maximum depends on the type of the solvent. Film polarization causes an increase in ε. The presence of the maximum in this temperature interval is apparently associated with polarization of the C-F-dipoles in the crystalline region of the polymer matrix.
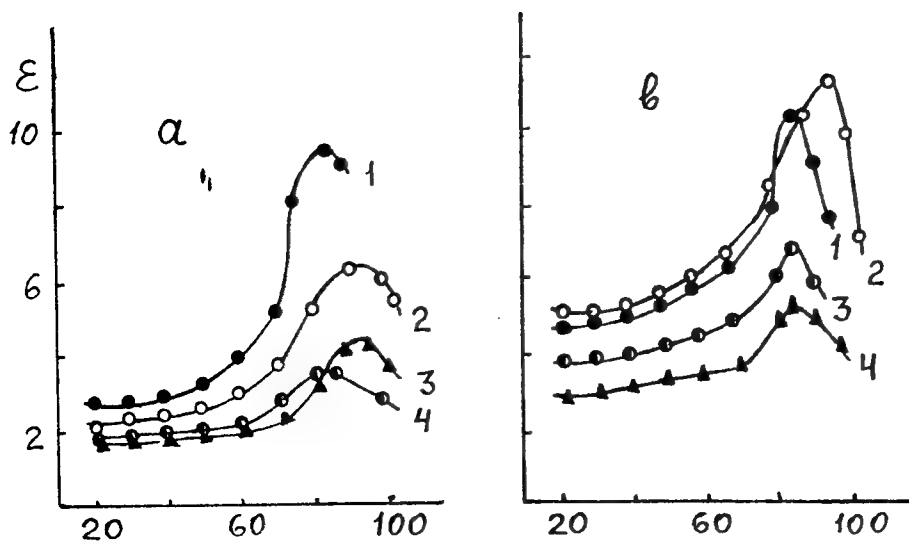
Fig.3. Temperature dependences of ε for the unpolarized (a) and polarized at 80 °C and E = 8 V/μm (b) copolymer samples prepared from the 3% copolymer solutions in acetone, dimethylformamide, dimethylsulfoxide and ethyl acetate (1-4).

As follows from Fig. 4, the relaxation maximum for the VDF-tetrafluoroethylene copolymer is manifested at temperatures higher than 100 °C and is, apparently, associated only with the transition in the crystalline phase of the copolymer. The dielectric permittivity (ε) is at its maximum in the temperature range of 140-170 °C, it essentially depends on a solvent type and decreases in the sequence DMFA > acetone > DMSO.
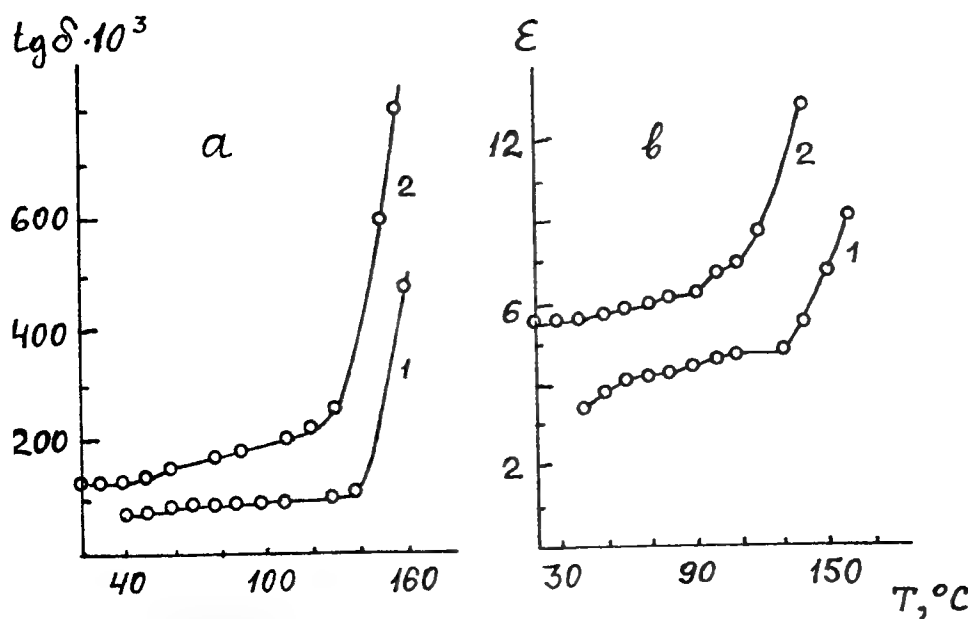
Fig. 4. Temperature dependences of tgδ (a) and ε (b) for the polarized samples of copolymer I formed from DMSO (1) at T = 100 °C, E = 3,0 V/μm and DMFA (2) at T = 80 °C, E = 3,0 V/μm.

In order to evaluate an influence of an electric field, we measured a surface charge density. With polarization, an electret , i.e. a material with a sufficiently high charge density, is formed in the electric field. For the investigated material based on the VDF-trifluoroethylene copolymer, electret formation may be related with structural changes in the amorphous and crystalline phases upon dipole orientation. Fig. 5 a, b shows the temperature dependencies (Q/S) for the unpolarized and polarized samples formed from various solvents. It is seen (Fig. 5) that the unpolarized films have a certain charge density, its value depends on the solvent type. It is interesting that the investigated films manifest two types of the electret property carriers. This is evidenced by the presence of /Q/S/ maxima in two temperature intervals, namely, 40-60 °C and 75-100 °C. As seen from Fig. 5, on polarization the position of the relaxation maxima remains unchanged but the charge density increases, approximately, by two orders of magnitude. The results obtained may be associated with the orientation processes in the field of C-F dipoles in the ordered and unordered regions of the polymer matrix the polarization of which and, correspondingly, the charge relaxation occur in different temperature intervals. It is established that an increase in the electric intensity from 4 to 17 V/mt causes an increase in the charge density both in low and high-temperature regions. An increase in the charge density

is also achieved by rising a polarization temperature of the sample from 20 to 80 °C. In this case, the choice of a maximum temperature depends on the presence of a maximum of the dielectric permittivity. An optimal temperature is 80 °C. At low polarization temperatures a relaxation maximum is not observed in the high-temperature region.
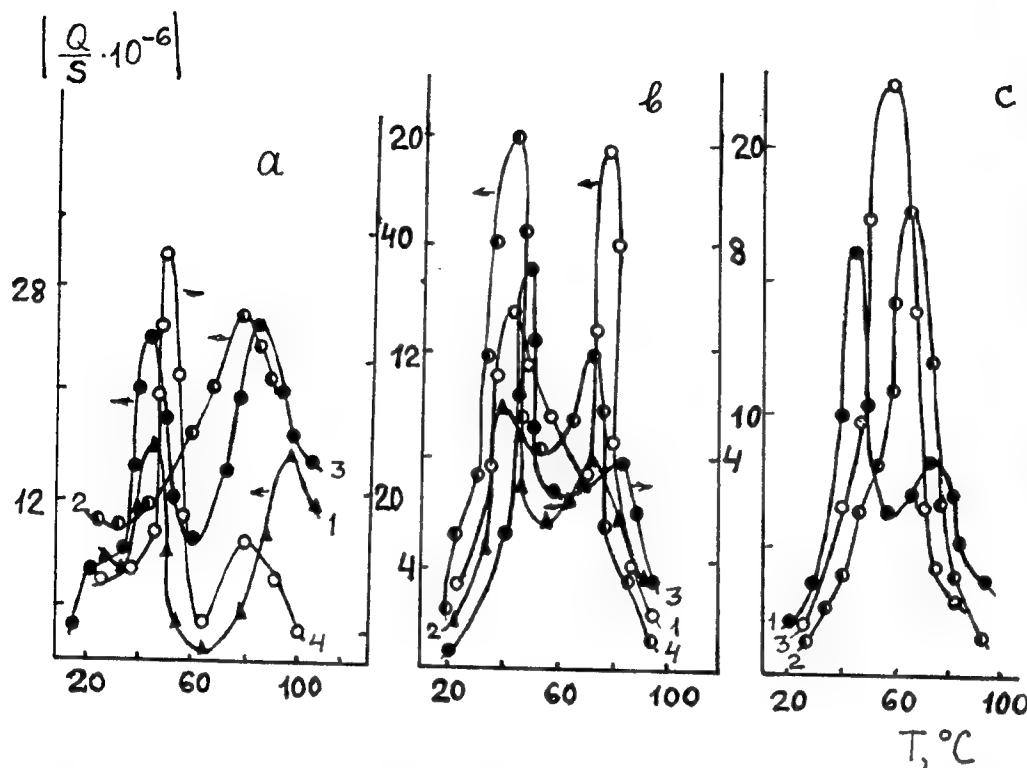

Fig.5. Temperature dependences of the specific charge density /Q/S/ for the unpolarized (a) and polarized at 80^{0}C and E= 8 V/μm (b) samples prepared from the 3% copolymer solutions in dimethylsulfoxide, dimethylformamide, ethyl acetate and acetone (1-4) as well as for those prepared from the 3% copolymer solutions in dimethylformamide polarized at 80 °C and E = 8 V/μm · and preliminarily subjected to mechanical orientation (5, initial unoriented sample; 2, relative elongation of the sample is 20; 3, relative elongation is 30%).

To clarify an effect of mechanical actions on electret properties of the films, the latter were subjected to orientational pulling. Relative elongation was 20-30%. In the course of mechanical orientational pulling the initial spherulitic structure undergoes destruction followed by formation of ordered crystallites in which the macromolecules are aligned in the direction of the applied mechanical load. Fig. 5c shows the temperature dependences of charge relaxation of the polarized films preliminarily subjected to mechanical orientation. As it follows from Fig. 1c, stretching of the films results in disappearance of the relaxation maximum in the tgδ vs. temperature curve in the range 40-50 °C. In this case, the temperature dependence of Q/S for the polarized samples preliminarily subjected to mechanical orientation has a maximum in the region 60-70 °C. Relaxation of the surface charge density for polarized samples of the vinyledene fluoride-trifluoroethylene copolymer are manifested in the temperature range of 80-100 °C.

CONCLUSIONS

1. The results obtained allow us to conclude that the electrets based on the copolymer I may be formed due to orientational processes in the amorphous and crystalline regions and those based on the copolymer II - in the crystalline region of the polymer.

2. Formation of copolymers from solutions of various solvents (DMSO, DMFA, acetone, etc.) leads to the formation of different crystalline forms that possess different electrosensitivity.

3. Mechanical orientation prior to polarization causes ordering of the amorphous part of the matrix thus enhancing the electrosensitivity due to an increase of the concentration of C-F dipoles in the crystalline region which affects the temperature interval of charge relaxation.

4. The processes of mechanical orientation and polarization in the electric field cause similar changes in the structure and electrophysical properties of the investigated copolymers, with the electret stability being increased at temperatures up to

80-100 °C. For the discussed copolymers the optimal electret properties can be achieved by way of polarization in an electric field without additional mechanical orientation.

REFERENCES

1. I.N. Ermolenko, G.N. Savastenko, V.V. Komar, et al., *Light Sensitive Materials Based on Polymer with Acidic Groups* [in Russian], Nauka i Tekhnika, Minsk, 1988.
2. T.D. Shermerger, and N.N. Strel'tsov, *Film Piezoelectrics* [in Russian], Radio I Svyaz', Moscow, 1986.
3. G.A. Lushcheikin, V.E. Gul', and V.K. Shatalov, "Mechanical Properties of Polarized Polymers", *Dokl. Akad. Nauk SSSR*, **25**, pp. 801-803, 1975.
4. S.I. Stupp, and S.H. Carr, "Electricfield Induced Structure in Poly(acrylonitrile)", *Colloid and Polym. Sci.*, **257**, pp. 913-919, 1979.
5. B. Jangnikel, "Kerr Effect Relaxation Measurements on Glassy Amorphous Poly(methylmetacrylate)", *Polymer*, **22**, pp. 720-725, 1981.
6. M.L. Miller, "Persistent Polarization in Polymers. I. Relationship between the Structure of Polymers and Their Ability to Become Electrically Polarized", *J. Polym. Sci. Polym. Phys.*, **4A-2**, pp. 685-695, 1966.
7. R.A. Creswell, and M.M. Perlman, "Thermal Currents from Corona Charges Mylar", *J. Appl. Phys.*, **41**, pp. 2365-2375, 1970.
8. A.C. Lilly, L.L. Stewart, and M.H. Rosemary, "Thermally Stimulated Currents in Mylar", *J. Appl. Phys.*, **41**, pp. 2007-2014, 1970.
9. G.T. Davis, J.E. McKinney, M.G. Brodhurst, and S.C. Roth, "Electric-Field-Induced Phase Changes in Poly(vinylidene Fluoride)", *J. Appl. Phys.*, **49**, pp. 4498-5002, 1978.
10. J.I. Scheinbein, K.T. Chung, K.D. Pac, and B.A. Newman, "The Dependence of the Piezoelectric Response of Poly(vinylidene Fluoride) on Phase-I Volume Fraction", *J. Appl. Phys.*, **50**, pp. 6101-6105, 1979.
11. R.M. Aliguliev, R.M. Khiteeva, and A.G. Kazbekov, "Influence of the Phase Composition and Morphology on the Polyvinyledenfluoride and Tetrafluoroethylene copolymers on the Vertification Temperature", *Azerb. Khim. Zh.*, pp. 58-63, 1986.
12. B.I. Sazhin (ed.), *Electric Properties of Polymers* [in Russian], Khimiya, Leningrad, 1986.
13. G. Sessler (ed.), *Problems in the Applied Physics* [Russian translation], Mir, Moscow, 1983.

Thermo-mechanical Characteristics of Composites Reinforced with Shape Memory Alloy Wires

Zheng Wang [a], Jiansheng Wu [a], Jianwei Dong [a], and Guojun Sun [b]

[a] The NCE Open Lab for High-Temperature Materials and Testing, Shanghai Jiao Tong University, Shanghai, 200030
[b] Dept. of Engineering Mechanics, Shanghai Jiao Tong University, Shanghai, 200030

Abstract

In composites reinforced with Shape Memory Alloy (SMA) wires, SMA wires play a role of distributed actuators to achieve adaptive functions while in service. This paper presents the theoretical study on the thermo-mechanical characteristics of composites reinforced with SMA wires, based on the one-dimensional constitutive relation of SMA. Experimental results derived from tension, free recovery and restrained recovery of composites reinforced with SMA wires are presented and compared with the simulated results.

Keywords : smart composites, reinforced composites, Shape Memory Alloy, constitutive relation, experimental analysis

1. Introduction

Smart composites are a class of advanced materials which combine the structure characteristics of advanced composites with the sense and actuation capabilities of embedded sensors and actuators. These smart composites can respond to varying external environments or internal conditions by changing their properties adaptively, therefore, they are able to keep in the best or better state.

Shape Memory Alloy (SMA) is first used as actuator to create such adaptivity in a series of smart composites. The advantages of SMA actuators are several transformation types, large transformations, good compatibility with matrix materials, obvious elastic moduli change caused by the phase transformations and great recovery forces in the restrained recovery. Thus composites reinforced with SMA wires can meet the need of adaptability. To predict the adaptability of composites reinforced with SMA wires, it is necessary to research on the thermo-mechanical characteristics of the composites as the fundamental data .

2. One-dimensional constitutive relation for composites embedded with SMA wires

SMA is a kind of functional alloy which exchanges the thermal energy with the mechanical energy by its internal phase transformations (martensitic phase transformation and its reverse transformation). According to the thermodynamics principles, the one-dimensional constitutive relation of SMA in a range of small strain during the course of stress-induced martensitic transformation or the reverse transformation can be described in the differential form as

$$\dot{\sigma} = E \dot{\varepsilon} + \theta \dot{T} + \Omega \dot{\xi} \tag{1}$$

where $\dot{\sigma}$ and $\dot{\varepsilon}$ are the differentials of stress and strain of SMA with respect to time respectively, $\dot{T}$ is the differential of temperature with respect to time and $\dot{\xi}$ is the differential volume fraction of martensite ($0 < \xi < 1$) with respect to time. E, θ and Ω are elastic modulus, thermo-coefficient and phase-transformation coefficient of SMA, respectively.

Cosine function can be used to describe the dependence of ξ on T and σ[1].
During the phase transformation from martensite to austensite, ξ is given by

---

$$\xi = \frac{1}{2}\,\xi_M \left\{ \cos\left[a_A\,(T-A_s) - \frac{a_A}{C_A}\,\sigma_a \right] + 1 \right\} \qquad (2)$$

and during the martensitic transformation, i.e., from austenite to martensite

$$\xi = \frac{1-\xi_A}{2}\cos\left[a_M(T-M_f)\frac{a_M}{C_M}\,\sigma_a \right] + \frac{1+\xi_A}{2} \qquad (3)$$

where ξ_A and ξ_M are initial martensite volume fractions when the A→M or M→A transformation starts, C_A and C_M are equivalent coefficients of σ and T during the M→A or A→M transformation, and a_A and a_M are the material constants of SMA

$$a_A = \frac{\pi}{A_f - A_s} \qquad\qquad a_M = \frac{\pi}{M_s - M_f} \qquad (4)$$

where A_s and A_f are the austenite start and finish temperatures under stress-free conditions respectively, M_s and M_f are the martensite start and finish temperatures under stress-free conditions respectively.

Considering the effect of changeable elastic modulus, E, of embedded SMA on the stiffness of the SMA-reinforced composite structure, it is assumed that E is a function of ξ. Equation (1) can be written in the following differential form

$$d\sigma_a = E(\xi)d\,\varepsilon_a + \Omega d\,\xi + \theta dT \qquad (5)$$

where the subscript 'a' indicates SMA actuator, and the elastic modulus $E(\xi)$ is assumed to be in the form

$$E(\xi) = \frac{E_A - E_M}{2}\,(\cos\xi\,\pi + 1) + E_M \qquad (6)$$

where E_A and E_M are elastic moduli of SMA in the case of austenite and martensite, respectively.

Along the SMA wire's direction, the stress and strain of the composite matrix are denoted σ_m and ε_m, the elastic modulus and the thermal expansion coefficient of the matrix are denoted E_m and α_m, the volume fraction of the SMA wires and the matrix are denoted V_a and V_m, and the stress and strain of the composite reinforced with SMA wires are denoted σ and ε, respectively.

As shown in Fig.1, when the composite reinforced with SMA wires is uniaxially stressed, the strain of the SMA wires and the matrix are assumed to be the same and to equal the composite's strain

$$d\varepsilon_m = d\varepsilon_a = d\,\varepsilon \qquad (7)$$

Fig.1 A composite lamina reinforced with SMA wires

From the mechanical equilibrium considerations, it can be derived as

$$d\,\sigma = V_a d\,\sigma_a + V_m d\,\sigma_m \qquad (8)$$

The one-dimensional thermo-elastic constitutive relation of the matrix is

$$d\,\varepsilon_m = \frac{d\sigma_m}{E_m} + \alpha_m dT \qquad (9)$$

Eliminating $d\sigma_m$ from Equation (8) and (9) leads to

$$d\,\varepsilon_m = (d\,\sigma - V_a d\,\sigma_a)/E_m V_m + \alpha_m dT \qquad (10)$$

Using the relation $\quad d\,\xi = \dfrac{\partial \xi}{\partial \sigma_a}d\,\sigma_a + \dfrac{\partial \xi}{\partial T}dT$

Equation (5) can be described as

$$d\,\varepsilon_a = \frac{1}{E(\xi)}\left\{ (1 - \Omega\frac{\partial \xi}{\partial \sigma_a})d\,\sigma_a - (\theta + \Omega\frac{\partial \xi}{\partial T})d\,T \right\} \qquad (11)$$

From Equations (7),(10) and (11), the one-dimensional differential constitutive equation of the composite reinforced with SMA wires can be obtained as

$$[E(\xi)+\frac{V_m E_m}{V_a}(1-\Omega\frac{\partial\xi}{\partial\sigma_a})]\,d\varepsilon=\frac{1-\Omega\dfrac{\partial\xi}{\partial\sigma_a}}{V_a}\,d\sigma+$$

$$[\frac{1-\Omega\dfrac{\partial\xi}{\partial\sigma_a}}{V_a}E_m\alpha_m V_m-\theta-\Omega\frac{\partial\xi}{\partial T}]\,dT \tag{12}$$

where $\dfrac{\partial\xi}{\partial\sigma_a}$ and $\dfrac{\partial\xi}{\partial T}$ can be given from Equation (2) and (3).

From martensite to austenite

$$\frac{\partial\xi}{\partial\sigma_a}=\frac{\xi_M}{2}\frac{a_A}{C_A}\sin[a_A(T-A_s)-\frac{a_A}{C_A}\sigma_a]$$

$$\frac{\partial\xi}{\partial T}=-\frac{\xi_M}{2}a_A\sin[a_A(T-A_s)-\frac{a_A}{C_A}\sigma_a] \tag{13}$$

and from austenite to martensite

$$\frac{\partial\xi}{\partial\sigma_a}=\frac{1-\xi_A}{2}\frac{a_M}{C_M}\sin[a_M(T-M_f)-\frac{a_M}{C_M}\sigma_a]$$

$$\frac{\partial\xi}{\partial T}=-\frac{1-\xi_A}{2}a_M\sin[a_M(T-M_f)-\frac{a_M}{C_M}\sigma_a] \tag{14}$$

where σ_a is related to σ and ε in the form

$$\sigma_a=\frac{1}{V_a}\{\sigma-V_m E_m[\varepsilon-\alpha_m(T-T_0)]\} \tag{15}$$

where T_0 is the initial temperature.

Equation (12) gives the differential relation of the total stress and strain of the composite reinforced with SMA wires to temperature. If one variable, among the variables σ, ε and T, is settled down, the relation of the two others can be obtained by numerical integration.

3. Experiments and numerical simulations of the thermo-mechanical characteristics for composites reinforced with SMA wires

In the experimental process, the composite sample reinforced with SMA wires is schematically shown in Fig.2. The matrix is glass-fiber/epoxy, E_m=6.82 GPa and α_m=6.6×10^{-6} /^{0}C. SMA wires are 1.45mm diameter 50.8 at%Ni-Ti wires which contain 3% plastic strain, and V_a=10% .The material properties of the 50.8 at %Ni-Ti wires in use are assumed and listed in Table 1.

Fig.2 A composite sample reinforced with SMA wires

Table 1. Material properties of the 50.8 at %Ni-Ti wires

E_A	E_M	Ω	θ	M_f	M_s	A_s	A_f	C_A	C_M
(MPa)			(MPa/^{0}C)	(^{0}C)				(MPa/^{0}C)	
2.04×10^4	1.56×10^4	-489.8	-0.4	-3	2	45	63	14.8	14.8

Tensile properties

. The experimental tensile curves of the composite sample reinforced with SMA wires at 14^0C , 50^0C and 65^0C are shown in Fig.3(a) while the corresponding simulated curves are shown in Fig.3(b). In both Fig.3(a) and Fig.3(b), the elastic moduli of the sample decrease as the temperature increases, and the relation between the stress and strain of the sample can be regarded as linearity. Furthermore, in the simulated calculations there is little difference whether the modulus of SMA wires is constant or variable of ξ because the volume fraction of SMA wires is low, and the tensile property of the sample mainly depends on the property of the glass-fiber /epoxy matrix. The simulated curves at 14^0C and 50^0C fit the experimental curves better,but there is obvious difference between the two curves at 65^0C. This is because the matrix softens at 65^0C, leading to a large transformation of the sample. The theoretical model, however, has the assumption of small strains.

Fig.3 The tensile curves
(a) experimental curves
(b) simulated curves

Restrained recovery

Restrained recovery is to keep the strain increment of the sample being zero, i.e. $d\varepsilon$ =0, throughout the experiment at continuously changing experimental temperatures. The sample stress, σ, can be obtained from the equation $\sigma = V_a\sigma_a + V_m\sigma_m$. Fig.4 gives the relation of the total stress and the temperature of the sample under restrained recovery (ε=0) . The solid curve shows the experimental results while the dotted curve shows the numerical simulation. In Fig.4, the changing tendency of the two curves is almost uniform, and at the two turn points in the curve the phase transformation from martensite to austensite starts and finishes. The phase transformation temperatures have increased due to the effect of stress. Before the phase transformation of SMA wires, the thermal expansion of the sample is dominant, and the total stress of the sample is constrictive. As the temperature increases, the phase transformation starts. Then the constrained SMA wires exert large recovery stress and the total stress becomes tensile. At the same temperature, there is a stress difference between the experiment and the simulation. One reason is also the matrix softening. The SMA wires may constrict slightly as the matrix softens, thus the state varies compared with the restrained recovery state. So the experimental value is lower than the simulated value. Besides, the materials constants in the simulation, heating speed, the thermal conduction state, and etc., also have some influence on the difference.

Fig.4 Restrained recovery

Free recovery

Free recovery is to keep the sample free, i.e., the total stress of its cross section is zero, throughout the experiment. The relation of the sample surface strain and the temperature is shown in Fig. 5. The solid curve is experimental results while the dotted curve is numerical simulations. From 35 ^{0}C to 57 ^{0}C, the simulated curve fits the experimental curve well. Before the phase transformation of SMA wires, the thermal expansion of the sample is dominant, and the total strain is tensile. During the phase transformation, the total strain becomes constrictive. This is caused by the recovery of SMA wires, which are constrained by the matrix. SMA wires apply to the matrix axial constriction, which is much larger than the thermal expansion action of the matrix. In the free recovery, the interaction between SMA wires and the matrix completely depends on their interfaces. When the temperature is beyond 60 ^{0}C, the matrix softens, and the capability of load carrying on the interfaces becomes weaker and weaker. In the simulation, the above mentioned points are not considered leading to the obvious difference between the two curves above 60 ^{0}C.

Fig.5 Free recovery

4. Conclusion

Recently there is much interest in composites reinforced with SMA wires due to its adaptive functions. But it is difficult to completely describe the constitutive relation of composites reinforced with SMA wires using one model or formula because of the complicated thermo-mechanical properties of SMA. In this paper, an one-dimensional constitutive relation of composites reinforced with SMA wires is derived, utilising the Tanaks's model of SMA and assuming that the modulus of SMA is the

cosine function of the martensite fraction. Both the experimental and simulated results show that the thermo-mechanical model can describe the mechanical properties of the reinforced composites at some extent. The further research should be done. Besides, attentions should be paid to the influence of the temperature on the matrix properties and the compatibility of SMA wires with the matrix.

Reference

1. C.Liang and C.A.Rogers, "One-dimensional thermomechanical constitutive relations for Shape Memory Materials", AIAA-90-1027-CP
2. M.W.Lin and C.A.Rogers, "Analysis of stress distribution in a Shape Memory Alloy composite beam", AIAA-91-1164-CP
3. G. Sun and C. T. Sun, "One-dimensional constitutive relation for shape-memory-alloy reinforced composite lamina", J. of Mater. Sci. 28(1993), pp. 6323-6328
4. Zheng Wang, "Study on Shape Memory Alloy applied in adaptive composite structures", Ph.D dissertation , Nanjing University of Aeronautics & Astronautics, June 1995
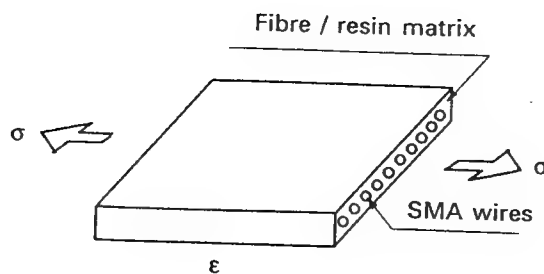
Fig.1
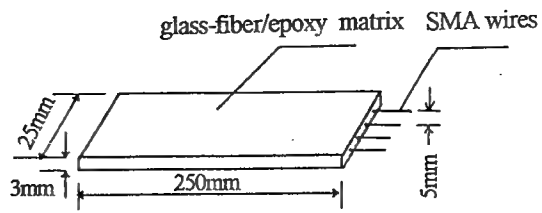
Fig.2
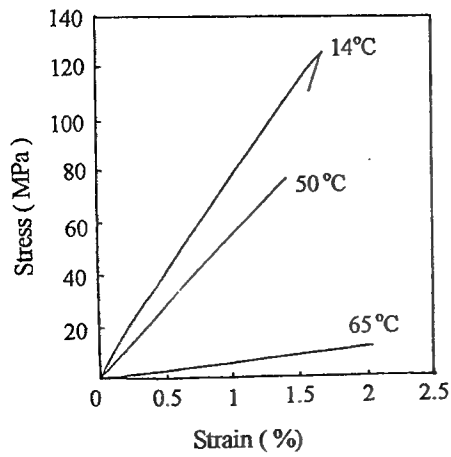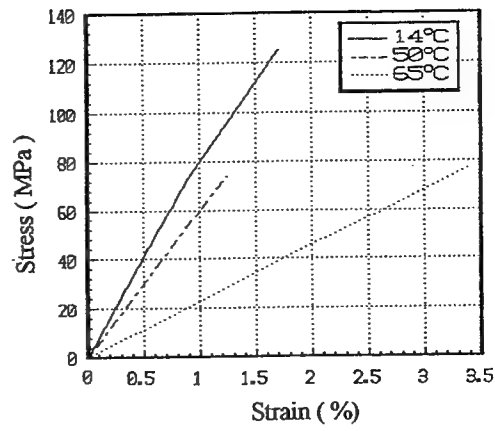
(a)　　Fig.3　　(b)
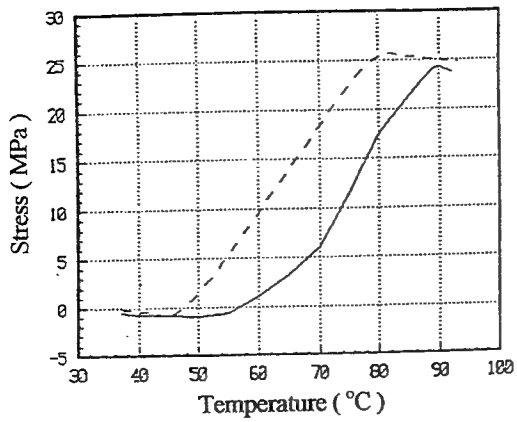
Fig.4
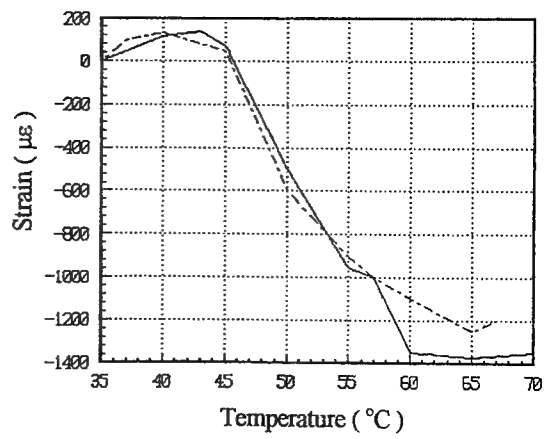
Fig.5

Study of Ti(C,N) film formed by ion beam assisted deposition

Liu Hanwei[@], Chen Yunru[@] and Cai Haitao[#]

[@]Department of material engineering, Southwest Jiaotong University, Chengdu, PRC
[#]Department of physics, Hong Kong University, Hong Kong

ABSTRACT

The Ti(C,N) film has been synthesised by ion beam assisted deposition in our study, in which a TiC target was bombarded by argon ion beam. Sputtreing deposition of Ti, C and bombardment with argon ion beam were done simultaneously under the environment of nitrogen gas. The component depth profiles and structure of the film were analysed by means of AES and X-ray diffraction. Our results shows that the Ti(C,N) film was composed of TiC crystallites with random orientation and composed of TiN crystallites with preferential orientation and with small grain size. It was confirmed that there is a wide intermixed region of Ti, C, N and Fe at interface between the film and the substrate. The Ti(C,N) film formed by ion beam assisted deposition exhibits superior hardness and improvement over the wear resistance and friction properties.

Keywords: ion beam assisted deposition, Ti(C,N) film.

1. INTRODUCTION

Ion beam assisted deposition is very useful for improving adhesion between film and substrate, and for controlling chemical component and thickness of film and possibility of synthesising film, and for growing film at low temperature. The TiN film formed by this method exhibits good wear resistance, but the hardness of the film is lower than that prepared by PVD or CVD[1-4]. In this paper, we studied how to synthesised the Ti(C,N) films by ion beam assisted deposition and the result of investigation on composition, structure and mechanical properties of the film are also presented.

2. EXPERIMENTAL

The synthesis of Ti(C,N) film was carried out using an ion beam assisted deposition system, in which a polished Cr12MoV steel substrate was bombarded by nitrogen ion beam before TiC target was bombarded by argon ion beam. Sputtering deposition of Ti, C and bombardment with argon ion beam onto Cr12MoV steel substrate were done simultaneously. The Deposition rate of Ti, C was 2.8 nm/s. Finally, thickness of films was about 2μm.

The composition and structure of the film was analysed by means of AES and X-ray diffraction. The microhardness of the film was measured by use of a microhardness tester with a load weight of 0.25 N. The coefficient of friction of the film was measured on a fine coefficient of friction tester with a load weight of 2.9N and sliding speed of 1mm/s. The wear tests were conducted on the "come-and-back" wear testing machine. The 20N, 30N, 40N and 50N load were applied respectively. The cross of wear trace was measured by the outline measurement and the micrographs of that was observed by means of SEM.

3. RESULT AND DISCUSSION

The AES spectrum of the Ti(C,N) film deposition on a Cr12MoV steel substrate is shown in Fig.1. It can be seen that each component is well distributed with depth profiles of the film. There is a wide intermixed region of Ti, C, N and Fe at the interface between the film and the substrate. It can be presaged that the film is very high bonded with the substrate. Fig.2 is the X-ray diffraction pattern of the Ti(C,N) film, which was composed of TiC and TiN crystallites. The order of peak strength and the half width of peaks imply that the TiC with random orientation, TiN with preferential orientation and with small grain size. Fig.3 shows that the cross of wear trace of the Cr12MoV
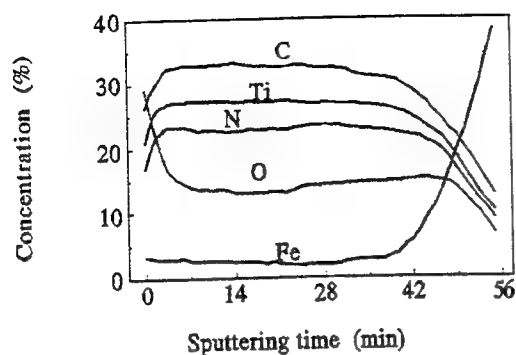
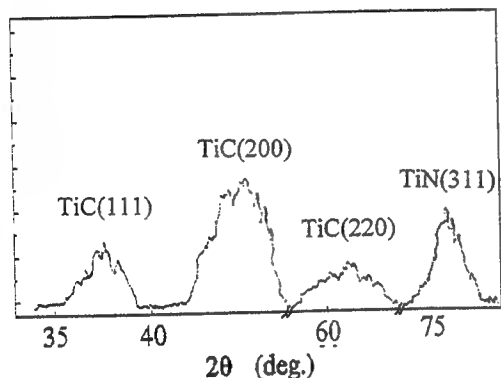Fig.1 Depth profiles of Ti(C,N) film components.
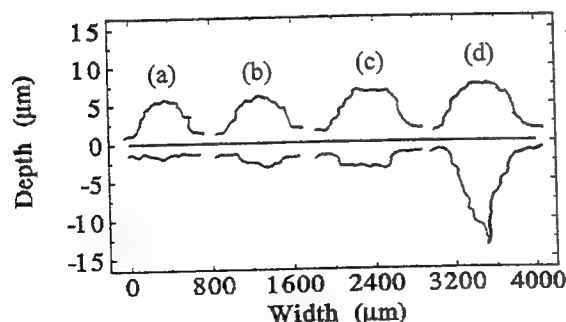

Fig.2 X-ray diffraction pattern of Ti(C,N).

Fig.3 The cross pf wear trace pf Cr12MoV steel without and withTi(C,N) film under (a)20N, (b)30N, (c)40N, (d)50N load respectively.

steel without and with Ti(C,N) film under 20N, 30N, 40N and 50N load. The micrographs of wear trace of the Cr12MoV steel without and with the Ti(C,N) film are very crude and smooth respectively. The highest depth of wear trace of the Cr12MoV steel without the Ti(C,N) film is 0.5μm. but there is a very shallow wear trace on the Cr12MoV steel with the Ti(C,N) films. When the depth of wear trace of the Cr12MoV steel with the Ti(C,N) film get to about 2μm, the width of wear trace increase continuously and depth of that don't increase. Under loading 50N, the depth of wear trace of the Cr12MoV steel with the Ti(C,N) film suddenly increase greatly and that of the Cr12MoV steel without Ti(C,N)film increase slowly, which are concerned in intermixed region of Ti,C,N and Fe at the interface between the film and the substrate. More detailed investigation about these problems will be studied in our future work.

The microhardness of the Cr12MoV steel with the Ti(C,N) film (HV>1600) is about 3 times that of the Cr12MoV steel (HV650). The coefficient of friction of the Ti(C,N) film ($\mu=0.09$) is 7 times less than that of the Cr12MoV steel ($\mu=0.62$). The Ti(C,N) film formed by ion beam assisted deposition exhibit superior hardness and improvement over the wear resistance and friction properties.

4. CONCLUSION

The Ti(C,N) film formed by ion beam assisted deposition is composed of the TiC crystallites with random orientation, and composed of the TiN crystallites with preferential orientation and with small grain size. There is a wide intermixed region of Ti, C, N and Fe at the interface between the film and the substrate.

The Ti(C,N) film formed by ion beam assisted deposition exhibits superior hardness and improvement over the wear resistance and friction properties.

REFERENCES

1. S.M. Rossnagel and Cuomo, "Ion-beam assisted deposition and synthesis," MRS Bulletion, Vol.16, pp40-49, 1987.

2. T.Satou, K. Ohata, N.Asahi, Y.Dno, Y.Oka, I.Hashimoto and K.Arimatsu, "Surface treatment of aluminum alloy at room temperature with titanium nitride films by dynamic mixing," Nucl. Instru. Meth. Phys. Res., Vol. B19/20, pp644-647, 1987.

3. H.Ito, Y.Yoshida, S.Yamaji, Y. Maeyama, T. Ina and Y.Minowa, "Titanium nitride deposited by dual ion beams," Nucl. Instru. Meth. Phys. Res.,Vol. B39, pp174-177,1989.

4. F.A.Smidt, "Use of ion beam assited deposition to modify the microstructure and properties of thin films," iNT. mATER. rEV., vOL.35,PP60-62, 1990.

Ion-exchange-metal composite artificial muscle actuator load characterization and modeling

Mehran Mojarrad and Mohsen Shahinpoor

Artificial Muscles Research Institute
School of Engineering, University of New Mexico
Albuquerque, NM 87131

ABSTRACT

Reported in this work are load characterization of electroactive films made out of polymeric ion-exchange membrane materials treated with a noble metal such as platinum. Load characterization under oscillating voltage input on the resulting composite samples was then performed using a PC-platform data acquisition system, variable signal generator, amplifier and load cells. For fixed signal frequency, various shape signals at low voltage amplitudes were then applied and the corresponding induced forces measured by the load cells and recorded via the data acquisition setup. The applied input signals consisted of sinusoid, square, saw tooth, and triangular form in order to observe the difference in behavior and the resulting output forces of the actuators. A brief description of a proposed theory for this type of actuator was then discussed. The results showed that these actuators exhibit good force to weight characteristics in the presence of low applied voltages.

Keywords: Ion-Exchange-Membrane-Metal Composite, Soft Actuator, Artificial Muscle Membrane, Biomimetic Actuators, Polymeric Actuators, Composite Film Actuators, Actuator Fins

2. INTRODUCTION

Ion-exchange-membrane-metal composites are highly active actuators that show very large deformation in the presence of low applied voltage and exhibit low impedance. They operate best in a humid environment and can be made as a self-contained encapsulated actuators to operate in dry environments as well. They have been modeled as both capacitive and resistive element actuators that behave like biological muscles and provide an attractive means of actuation as artificial muscles for biomechanics and biomimetics applications. Grodzinsky[1], Grodzinsky and Melcher[2,3] were the first to present a plausible continuum model for electrochemistry of deformation of charged polyelectrolyte membranes such as collagen or fibrous protein. Kuhn[4] and Katchalsky[5] however should be credited to have been the first investigators to report the ionic chemomechanical deformation of polyelectrolytes such as polyacrylic acid (PAA), polyvinyl chloride (PVA) systems. Kent, Hamlen and Shafer[6] were also the first to report the electrochemical transduction of PVA-PAA polyelectrolyte system. Recently revived interest in these area with concentration on artificial muscles can be traced to Shahinpoor[7,8], Shahinpoor and Mojarrad[9,10], Osada[11], Oguro, Asaka and Takenaka[12], Asaka, Oguro, Nishimura, Mizuhata and Takenaka[13], Guo, Fukuda, Kosuge, Arai, Oguro and Negoro[14].

Essentially polyelectrolytes posses many ionizable groups on their molecular chain. These ionizable groups have the property of dissociating and attaining a net charge in a variety of solvent medium. According to Alexanderowicz and Katchalsky[15] these net charge groups which are attached to network of macromolecules are called polyions and give rise to intense electric fields of the order of 10^{10} V/m. Thus, the essence of electromechanical deformation of such polyelectrolyte systems is their susceptibility to interactions with externally applied fields as well as their own internal field structure. In particular if the interstitial space of polyelectrolyte network is filled with liquid containing ions, then the electrophoretic migration of such ions inside the structure due to an imposed electric field can also cause the macromolecular network to deform accordingly. Shahinpoor[16,17,18,20,23,24,26,27,29,30,31,32,33,34] and Shahinpoor and co-workers[19,21,22,25,28] have recently presented a number of plausible models for micro-electro-mechanics of ionic polymeric gels as electrically controllable artificial muscles in different dynamic environments. The reader is referred to these papers for the theoretical and experimental results on dynamics of ion-exchange membranes -platinum composite artificial muscles. Most Ion exchange polymeric membranes swell in solvents and by and large are hydrophilic. This gives rise to ability of the membrane to swell in water which can be controlled in an electric field due to ionic nature of the membrane. Furthermore by placing two electrodes in close proximity of the membrane walls

and applying a voltage, the forced transport of ions within a solution through membrane becomes possible at microscopic level. For a solvent such as water then local swelling and deswelling of membrane can be controlled depending on polarity of the electrode nearby more like the behavior of the bimorphic materials. This can be achieved by chemical or other possible means of plating of conductive materials on membrane surfaces. Platinum is one such conductor that can be deposited on the Ion-Exchange Membrane (IEM). Also being ionic in microscopic structure, IEM has the ability to shift its mobile ions of the same charge polarity within itself when it is placed in an electric field which results in ionic attraction or repulsion between the fixed charges of opposite polarity contained in the side groups within the polymer molecular chain (Fig. 1). This leads to local collapse or expansion of the polymer membrane macroscopically. Physically this causes a stress gradient on opposite sides of the membrane causing it to bend. Therefore by applying an alternating signal at low voltage one can achieve membrane oscillation proportional to frequency and amplitude of the input signal. This bending oscillation can be utilized in various applications as propulsion and robotic actuators.
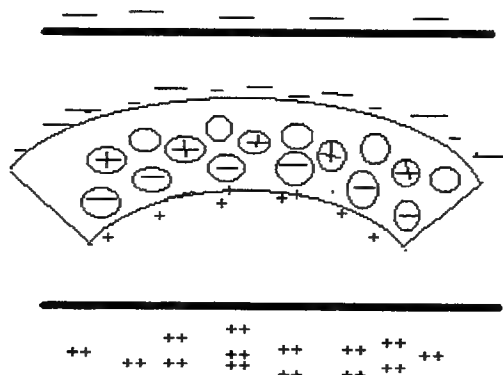
Figure 1. Bending due to ion redistribution in ionic polymer under imposed electric field.

3. Electrodynamic Modeling

For detailed dynamics description and analysis of the dynamic theory of ionic polymeric gels the reader is referred to Shahinpoor[16,17,18,20,23,24,26,27,29,30,31,32,33,34] and Shahinpoor and co-workers[19,21,22,25,28]. Since ionic polyelectrolytes are for the most part three dimensional network of macromolecules cross-linked nonuniformly, the concentration of ionic charge groups are also nonuniform within the polymer matrix. Therefore the mechanism of bending is related to migration of mobile ions within the network due to imposition of an electric field (Fig. 2).
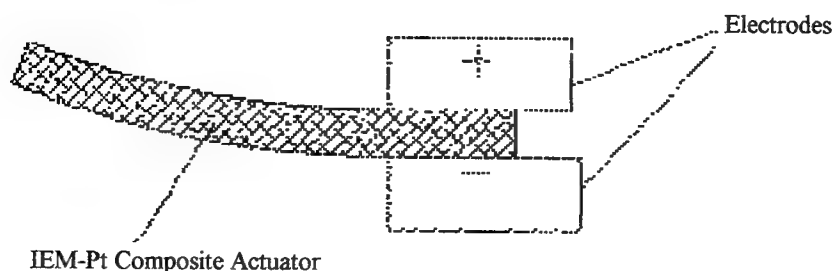
Figure 2. Bending of IEM-Pt composite muscles due to ionic rearrangement within the network

Ion exchange membrane (IEM) chemically treated with platinum salt solution gives rise to IEM-platinum composites that undergo large deformations in an electric field of a few volts. They also show remarkable vibrational characteristics of about 30 Hz bandwidth. For experimental evidence on the dependence of deformation amplitude on the imposed voltages and frequencies the reader is referred to other papers by this author and his co-researchers in this conference.

A simple one-dimensional model of electrically-induced deformation of ionic polymeric gels is such that :

$$\sigma = (1/3)E(C_0, C_i)\,(\lambda - \lambda^{-2})\,, \tag{1}$$

$$\sigma = \kappa\,(C_0, C_i)\,E^{*2} \tag{2}$$

where σ is the stress, λ is the stretch, $E(C_0, C_i)$ is the corresponding Young's modulus of hyper-elasticity, C_0 is the polymer solid concentration, C_i, $(i=1,2,....,N)$ is the molal concentration of various ionic species in the aqueous medium, $\kappa\,(C_0, C_i)$ is an electromechanical coefficient and E^* is the local electric field. Thus bending can occur due to differential contraction and expansion of outer most remote fibers of a strip if an electric field is imposed across its thickness as shown below in Figure 2. Comparing above equations, for constant stress developed in the membrane actuator and small λ, a simple linear correlation between electric field E^*, and stretch λ is observed. This relation was in fact verified by the author and co-workers in laboratory measurement[22].

4. EXPERIMENTAL WORK

Nafion-117[TM] polymeric ion-exchange membrane was acquired from commercially available source. This membrane is about 0.17mm thick and can be purchased as wide as one meter and any desired length. The membrane was then chemically cleaned and treated with platinum to form a composite that is active under electric field of low voltage. The thickness after chemical plating was about 0.2mm. The membrane was then fully hydrated in pure water bath. It was then cut in standard size of 15mm×5mm which was measured to be 0.04grams in weight. A load cell (Transducer Techniques, model GS-30, 30 grams capacity) and corresponding signal conditioning module (Transducer Techniques, model TMO-1) together with a power supply was setup and connected to a PC-platform data acquisition and signal generation system composed of a 12-bit analog output board (National Instrument AT-AO-10) and a 16-bit multi-input-output board (National Instrument AT-MIO-16XE-50). A Nicolett scope was used to monitor the input and output waveform. Labview[TM] software was used to write a program to generate various waveform such as sinusoid, square, saw tooth, and triangular signals at desired frequency and amplitude (Fig. 3). Also a program was written to convert the output data from the load cell to force values and display on the monitor. The membrane actuator was then attached at one end to the load cell (load application point) and freed at the other end to be placed between two platinum electrode plates of 0.1mm thick (Aldrich Chemicals) which formed the jaws of a plastic forceps (Fig. 4). Therefore the effective length of the membrane was 10mm when 5mm of the total length was placed between the electrodes.
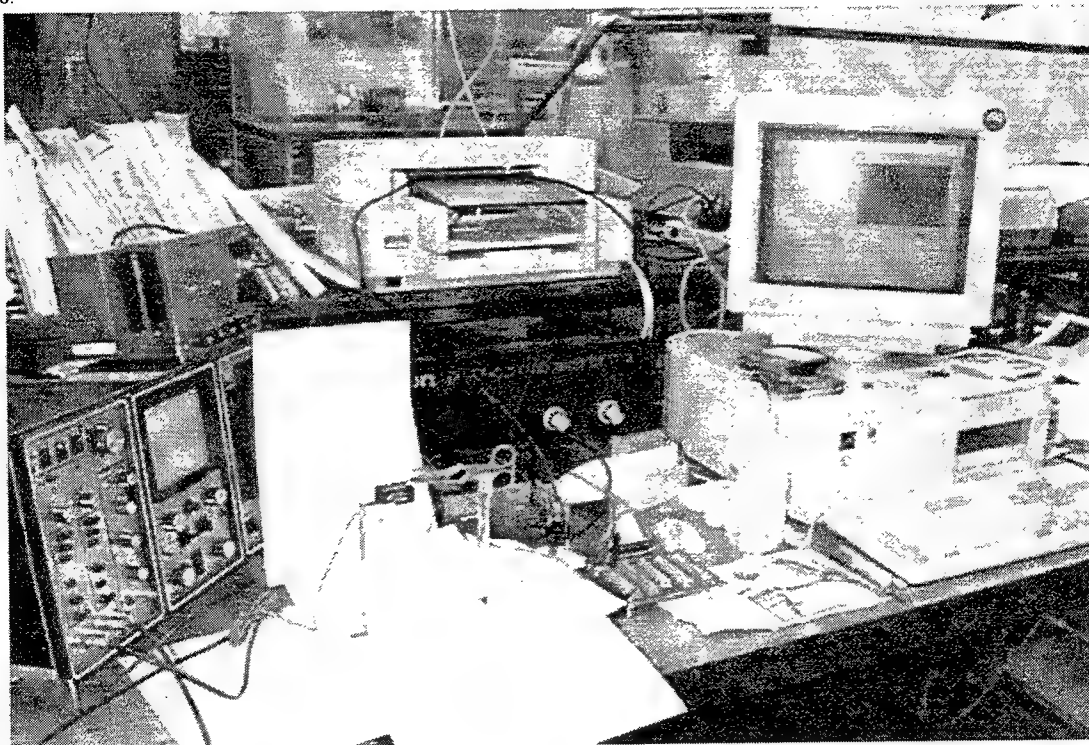

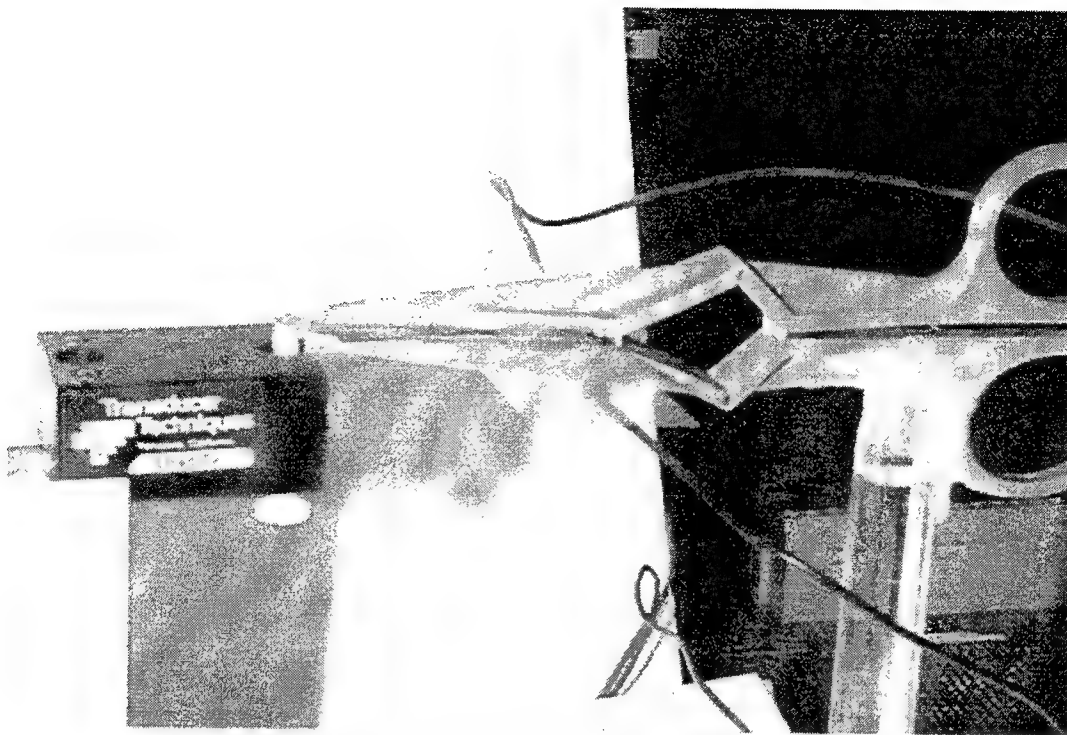Figure 3. Overall load cell-data acquisition setup with corresponding instrumentation.

Figure4. Load cell and composite membrane actuator interface.

A baseline was first established for each waveform with membrane actuator attached to load cell and electrodes to measure the initial pre-load and noise before actuation. Then a series of force data was generated by using a load cell correction factor of 0.255 and a constant frequency (0.5 Hz) signal input of 1.5, 2.0, 2.5, and 3.0 V rms amplitude voltages respectively. The resulting graphs were then adjusted for initial noise and pre-load and plotted over 5 seconds period (2.5 cycles).

5. RESULTS AND DISCUSSION

The results showed that sinusoid and triangular waveform input to the IEM-pt actuator generate more symmetric output forces, meaning they are relatively equal in either direction of travel (Fig. 5). The maximum forces were generated at higher input voltage amplitudes (3.0 V rms maximum) for most wave forms. The square and saw tooth input wave forms produced more nonuniform results in a sense that all or most of the generated forces were in one direction (Fig. 6). This can be attributed to the fact that there is insufficient time for ion travel to take place when the signal switches its polarity. However for the saw tooth signal, the voltage starts at zero and reaches a maximum in positive direction which results in force in one direction alone where in this case resulted in tension or downward movement of the IEM-pt actuator. The next paragraph explains in details the effect of individual input waveform on the membrane actuator.

Sinusoid Input: This wave produced a uniform force in either direction of travel (tension and compression of the load cell). The output followed input best at 2.5 V amplitude. However the maximum forces were generated at 3.0 V input and reached 0.5 grams (10 times actuators mass) in either directions. This input shape appears to be more suitable for robotic controls where application of forces are involved for proper calibration and desired force response and command inputs.

Square Input: This wave generated the maximum output forces of all input wave forms reaching 1.25 grams (over 31 times actuators mass) in upward movement (load cell in compression) at 2.5 V amplitude. The reason for lower output at 3.0 V is not clear but square voltage causes sudden change of polarity which can attribute to rapid dehydration and heating of the membrane actuator all of which lead into increase in output in one direction only and may lead into actuator failure. At higher voltages, the generated forces appeared to shift toward negative (load cell in compression or upward movement).

Saw Tooth Input: This signal generated uniform forces in downward motion (load cell in tension) only reached a maximum of 0.65 grams (16 times actuators mass) at 3.0 V input.

Triangular Input: This wave form also produced a uniform force in both direction of travel and reached a maximum of 0.7 grams (17.5 times actuators mass) at 3.0 V in upward direction. However the best symmetry was observed to be at 1.5 V.
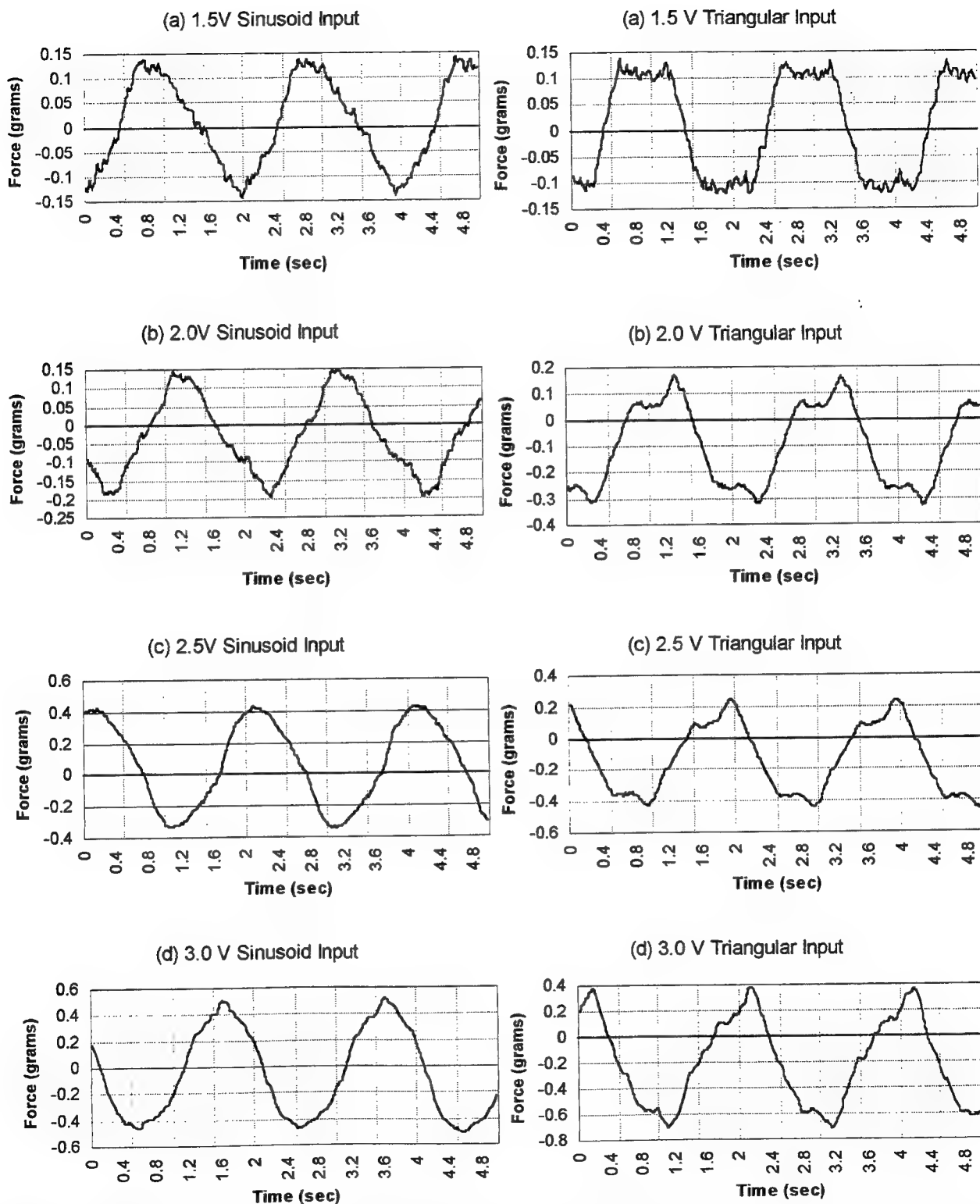
Figure 5. IEM-Pt actuator response for sinusoid and triangular wave input at (a) 1.5, (b) 2.0, (c) 2.5, and (d) 3.0 Volts rms.
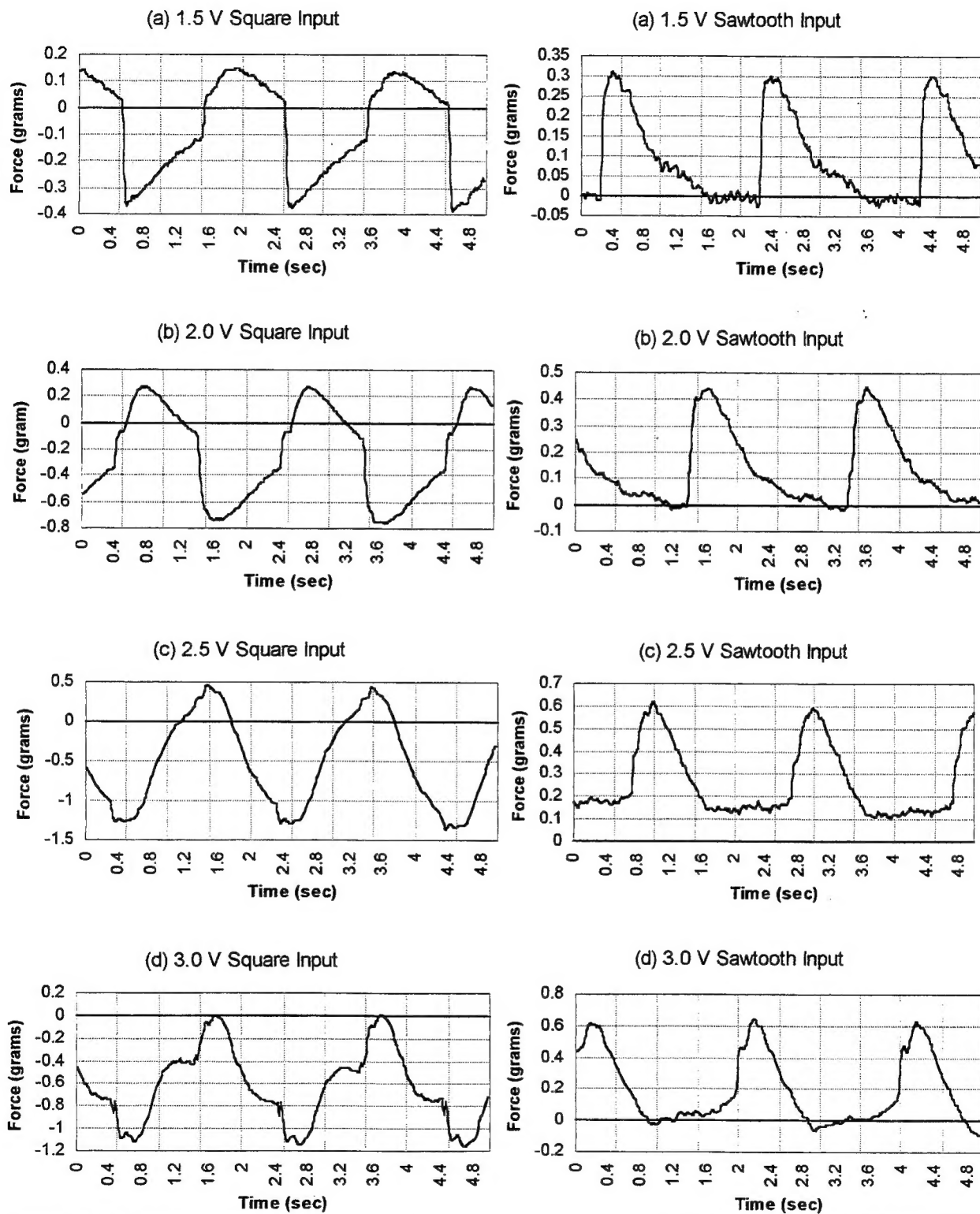
Figure 6. IEM-Pt actuator response for square and saw tooth wave input at (a) 1.5, (b) 2.0, (c) 2.5, and (d) 3.0 Volts rms.

6. CONCLUSION

Polymer composite actuators such as IEM-Pt proved to be practical for applications requiring small load and possibly in micro-actuation. These materials exhibit remarkable force to mass ratio (as high as 30 for these samples) and are inexpensive to manufacture. Depending on quality of manufacturing process control, actuators producing force in the order of over 50 times their mass have been observed previously in laboratory. The experimental results showed that they are also sensitive to the shape as well as the amplitude of the applied input signal and result in different force responses accordingly.

For robotic controls, sinusoidal input at low amplitudes produce more uniform response but at low magnitudes. This will enable a simple controls circuitry requirement to integrate the IEM-Pt actuator in a robotic system such as gripper.

ACKNOWLEDGMENT

REFERENCES

1. Grodzinsky, A. J., "Electromechanics of Deformable Polyelectrolyte Membranes", Sc.D. dissertation, Dept. of Elec. Eng., MIT, Cambridge, June 1974.
2. Grodzinsky, A. J., Melcher, J. R., "Electromechanics of Deformable, Charged Polyelectrolyte Membranes", Proc. 27th Annu. Conf. Engineering in Medicine and Biology, Vol. 16, 1974, paper 53.2.
3. Grodzinsky, A. J., Melcher, J. R., "Electromechanical Transduction with Charged Polyelectrolyte Membranes", IEEE Transactions on Biomedical Engineering, Vol. BME-23, No. 6, pp421-433, November 1976.
4. Kuhn, W., "Reversible Dehnung und Kontraktion bei Anderung der Ionisation eines Netzwerks Polyvalenter Fadenmolekulionen", Experientia, Vol. V, pp318-319, 1949.
5. Katchalsky, A., "Rapid Swelling and Deswelling of Reversible Gels of Polymeric Acids by Ionization", Experientia, Vol. V, pp319-320, 1949.
6. Hamlen, R. P., Kent, C. E., Shafer, S. N., "Electrolytically Activated Contractile Polymer", Nature, Vol. 206, pp1149-1150, 1965.
7. Shahinpoor, M., "Continuum Electromechanics of Ionic Polymeric Gels as Artificial Muscles for Robotic Applications", Smart Material and Structures Int. J., Vol. 3, pp. 367-372, 1994.
8. Shahinpoor, M., "Microelectro-Mechanics of Ionic Polymeric Gels as Artificial Muscles for Robotic Applications", Proceeding of the IEEE Robotics & Automation Conf., vol. , pp. , 1993.
9. Shahinpoor, M., Mojarrad, M., "Active Musculoskeletal Structures Equipped with a Circulatory System and a Network of Ionic Polymeric Gel Muscles", Proceedings of the 1994 International Conference on Intelligent Materials, pp. 1079-1085, 1994.
10. Shahinpoor, M., Wang, G., Mojarrad, M., "Elctro-Thermo-Mechanics of Spring-Loaded Contractile Fiber Bundles with Applications to Ionic Polymeric Gel and SMA Actuators", Proceedings of the International Conference on Intelligent Materials" ICIM'94, Williamsburg, VA., pp. 1105-1116, 1994.
11. Osada, Y., "Electro-Stimulated Chemomechanical System Using Polymer Gels (An Approach to Intelligent Artificial Muscle System)", Proceeding of the International Conference on Intelligent Materials, pp155-161, 1992.
12. Oguro, K., Asaka, K., Takenaka, H., "Polymer Film Actuator Driven by Low Voltage", Proceedings of 4th International Symposium on Micro Machine and Human Science at Nagoya, pp39-40, 1993.
13. Asaka, K., Oguro, K., Nishimura, Y., Mizuhata, M., Takenaka, H., "Bending of Polyelectrolyte Membrane-Platinum Composites by Electric Stimuli, I. Response Characteristics to Various Waveforms", Polymer Journal, Vol. 27, No. 4, pp436-440, 1995.
14. Guo, S., Fukuda, T., Kosuge, K., Arai, F., Oguro, K., Negoro, M., "Micro Catheter System with Active Guide Wire Structure, Experimental Results and Characteristic Evaluation of Active Guide wire Using ICPF Actuator", Osaka National Research Institute, Japan, pp191-197, 1994.
15. Alexanderowicz, A., Katchalsky, A., "Colligative Properties of Polyelectrolyte Solutions in Excess of Salt", Journal of Polymer Science, Vol. 1A, pp3231-3260, 1963.

16. Shahinpoor, M., "Nonhomogeneous Large Deformation Theory of Ionic Polymeric Gels in Electric and pH Fields", Proceedings of the 1993 SPIE Conference on Smart Structures and Materials, Feb. 1-4, Albuquerque, Vol. 1916, pp. 40-50, 1993.

17. Shahinpoor, M., "Micro-Electro-Mechanics of Ionic Polymeric Gels as Electrically Controlled Artificial Muscles," Proc. 1994 Int. Conf on Intelligent Materials, ICIM'94, June 1994, Williamsburg, VA, pp. 1095-1104, 1994

18. Shahinpoor, M., "Conceptual Design, Kinematics and Dynamics of Swimming Robotic Structures Using Ionic Polymeric Gel Muscles", Smart Materials and Structures Int. J., Vol. 1, pp. 91-94, 1992.

19. Segalman, D., Witkowsky, W., Adolf, D., Shahinpoor, M., "Electrically Controlled Polymeric Muscles as Active Materials used in Adaptive Structures", Proceedings of ADPA/AIAA/ASME/SPIE Conference on Active Materials and Adaptive Structures, Alexandria, VA, November 1991.

20. Shahinpoor, M., "Micro-Electro-Mechanics of Ionic Polymeric Gels As Electrically-Controllable Artificial Muscles,", Int. J. Intelligent Material Systems, vol. 6, no. 3, pp. 307-314, 1995

21. Mojarrad, M., Shahinpoor, M., "Noiseless Propulsion for Swimming Robotic Structures Using Polyelectrolyte Ion-Exchange Membranes,", Proc. SPIE 1996 North American Conference on Smart Structures and Materials, February 27-29, 1996, San Diego, California, vol. 2716, pp183-192, 1996.

22. Shahinpoor, M., Mojarrad, M., "Ion-Exchange Membrane-Platinum Composites As electrically Controllable Artificial Muscles,", Proc. 1996 Third International Conference on Intelligent Materials, ICIM'96, and Third European Conference on Smart Structures and Materials, Lyon, France, SPIE Publication No. ICIM'96 , pp. 1171-1184, June 1996

23. Shahinpoor, M., "Electro-Mechanics of Bending of Ionic Polymeric Gels as Synthetic Muscles for Adaptive Structures,", ASME Publication AD-Vol. 35, Adaptive Structures and Material Systems, edited by G.P. Carman and E. Garcia, Vol. AD-35, pp.11-22, 1993

24. Shahinpoor, M., "Electro-Mechanics of Resilient Contractile Fiber Bundles with Applications To Ionic Polymeric Gel and SMA Robotic Actuators" Proc. 1994 IEEE International Conference on Robotics & Automation , vol. 2, pp. 1502-1508, San Diego, California, May 1994

25. Shahinpoor, M., Mojarrad, M., "Ion-Exchange Membrane-Platinum Composites As Electrically Controllable Artificial Muscles,", Proc. 1996 Third International Conference on Intelligent Materials, ICIM'96, and Third European Conference on Smart Structures and Materials, June 1996, Lyon, France

26. Shahinpoor, M., "The Ionic Flexogelectric Effect" Proc. 1996 Third International Conference on Intelligent Materials, ICIM'96, and Third European Conference on Smart Structures and Materials, June 1996, Lyon, France

27. Shahinpoor, M., "Design and Development of Micro-Actuators Using Ionic Polymeric Micro-Muscles,", Proc. ASME Design Engnn technical Conference, Boston, MA, September (1995)

28. Shahinpoor, M., Thompson, M. S., "The Venus Flytrap As A Model For Biomimetic Material With Built-In Sensors and Actuators," J. Materials Science & Engineering, vol.C2, pp. 229-233, (1995)

29. Shahinpoor, M., "Design and Modeling of A Novel Spring-Loaded Ionic Polymeric Gel Actuator," Proc. SPIE 1994 North American Conference on Smart Structures and Materials ., February 94, Orlando, Florida, vol. 2189, paper no. 26, pp.255-264, (1994)

30. Shahinpoor, M., "Microelectro-Mechanics of Ionic Polymeric Gels As Synthetic Robotic Muscles," Proc. SPIE 1994 North American Conference on Smart Structures and Materials, February 94, Orlando, Florida, vol. 2189, paper no. 27, pp.265-274, (1994)

31. Shahinpoor, M., "Micro-Electro-Mechanics of Ionic Polymeric Gels as Electrically Controlled Synthetic Muscles,", Biomedical Engineering Recent Advances, Editor : J.Vossoughi, University of District of Columbia Press, Washington, D.C., April 1994, vol.1, pp.756-759, (1994)

32. Shahinpoor, M., "Electro-Mechanics of Resilient Contractile Fiber Bundles with Applications To Ionic Polymeric Gel and SMA Robotic Actuators" Proc. 1994 IEEE International Conference on Robotics & Automation , vol. 2, pp. 1502-1508, San Diego, California, May (1994)

33. Shahinpoor, M., "Electro-Thermo-Mechanics of Spring-Loaded Contractile Fiber Bundles with Applications To Ionic Polymeric Gel and SMA Actuators," Proc. 1994 Int. Conf. on Intelligent Materials, ICIM'94, June 1994, Williamsburg, VA, pp. 1105-1116, (1994)

34. Shahinpoor, M., "A New Effect in Ionic Polymeric Gels : The Ionic "Flexogelectric Effect," Proc. SPIE 1995 North American Conference on Smart Structures and Materials, February 28-March 2, 1995, San Diego, California, vol. 2441, paper no. 05, (1995)

Author Index